THE NATURE OF THE LOW MASS SUPERGIANTS: RV TAURI AND R CORONAE BOREALIS VARIABLES

A THESIS
SUBMITTED IN PARTIAL FULFILMENT
OF THE REQUIREMENTS FOR THE DEGREE
OF
DOCTOR OF PHILOSOPHY IN ASTRONOMY
IN THE
UNIVERSITY OF CANTERBURY
BY

KAREN R. POLLARD

University of Canterbury
1994

Contents

List of Tables

List of Figures

Abstract

A programme of photometric and spectroscopic observations has been undertaken in order to investigate the physical and chemical characteristics of the RV Tauri and R Coronae Borealis variables. These characteristics have, in turn, been used to examine a variety of theoretical models that attempt to describe the pulsation mechanisms, the underlying physical nature and the evolutionary status of these low mass supergiant variables.

Long time baseline *BVRI* photometry was obtained at the Mt John University Observatory (MJUO) over intervals of between 750 and 1300 days for eleven of the RV Tauri variables. RV Tauri stars from both the RVa (constant mean magnitude) and RVb (varying mean magnitude) photometric subclasses and from all three spectroscopic Preston subtypes (A, B and C types) were included in the programme.

Fourier and least-squares analyses of the light and colour variations have revealed the dominant periodicities and the stability of the pulsation in these stars. A harmonic $(f + 2f)$ fit was found to be a good representation of the "deep–shallow" nature of both the light and colour curves in most stars.

Contemporaneous high-resolution spectroscopy of these objects was acquired at MJUO and at the Mt Stromlo Observatory. This enabled us to link the photometric variations and the radial motions in these stars' atmospheres and to relate any photometric and spectral peculiarities. The appearance and phase-dependent behaviour of the Hα line profiles and the radial velocities were examined. Shock-related features, such as line doubling and recombination emission lines, were observed in all the programme stars. The observed Hα profiles were consistent with two enhancements of Hα emission following the passage of the primary and secondary shock waves through the photosphere around phases 0.2 and 0.6. In addition, the metallic lines showed profiles characteristic of an atmospheric shock wave at these phases.

The derived spectroscopic and the photometric characteristics have been used to examine a variety of theoretical models that attempt to describe the pulsation mechanisms and the underlying physical nature of the RV Tauri stars.

The nature of the RVb subclass and the interpretation that the RVa and RVb stars actually represent a continuum of properties is discussed in detail. A model of a binary system which undergoes periodic eclipses by dust or which interacts at certain orbital phases is presented. Two scenarios were proposed to explain the observed properties: an 'obscuration' model where the star is eclipsed by dust in the binary system; or an 'interaction' scenario where the two stars interact in some manner at a particular orbital phase. The interaction model generally has better agreement with the observed properties although it is quite likely, in a system where circumstellar and/or circumbinary material is known to exist, that a combination of obscuration and interaction is possible.

A detailed analysis of the chemical composition of a number of RCB stars in the Galaxy and the Large Magellanic Cloud is presented. This study made use of high-resolution échelle spectra obtained at the Anglo-Australian Telescope. The results for the galactic star, SU Tau, revealed very similar properties to a number of other warm galactic RCB stars, most notably R CrB. This was the first abundance analysis completed for any extragalactic RCB stars and showed a similar abundance distribution to the galactic RCB stars. All these objects (galactic and extragalactic) have a reasonably consistent set of properties, providing evidence that it is possible for this phenomenon to exist in different nucleosynthetic environments.

Chapter 1

Introduction

Astronomical objects with peculiar photometric and spectroscopic properties are the ones that attract the attention of astronomers, so encouraging them to find out the nature (and cause) of their peculiarities. These types of objects enable astronomers to make connections with the more 'normal' objects and hence investigate links between the different phases of evolution.

Such a link would be extremely desirable with respect to the RV Tauri and R Coronae Borealis (RCB) stars — variables whose evolutionary status is rather uncertain. The RV Tauri stars are usually associated with low mass post-AGB stellar variability, while the RCB objects have been linked with various evolutionary scenarios (e.g. recycled white dwarfs).

The RV Tauri and RCB stars are therefore an important probe of at least one phase of post-AGB (and possibly pre-planetary nebula) evolution. The post-AGB phase of evolution is rather short by normal stellar standards (only a few thousand years), which is consistent with the rarity of the RV Tauri and RCB stars. It is possible that evolutionary effects such as period changes (in particular period decreases) may be detectable, or that the lack of any change may at least constrain the evolutionary models proposed for these variables.

Both classes of variable occupy a region of the HR diagram that is populated by a large variety of different luminous variable stars (see Fig. 1.1). Evolved luminous stars of low mass (e.g. RV Tauri, RCB, UU Her, SRd and post-AGB transition objects) occupy a similar region in the HR diagram as those more massive Population I stars (e.g. Cepheids).

Such a situation provides us with an opportunity to investigate not only the evolutionary connections mentioned above, but also allows a comparison of

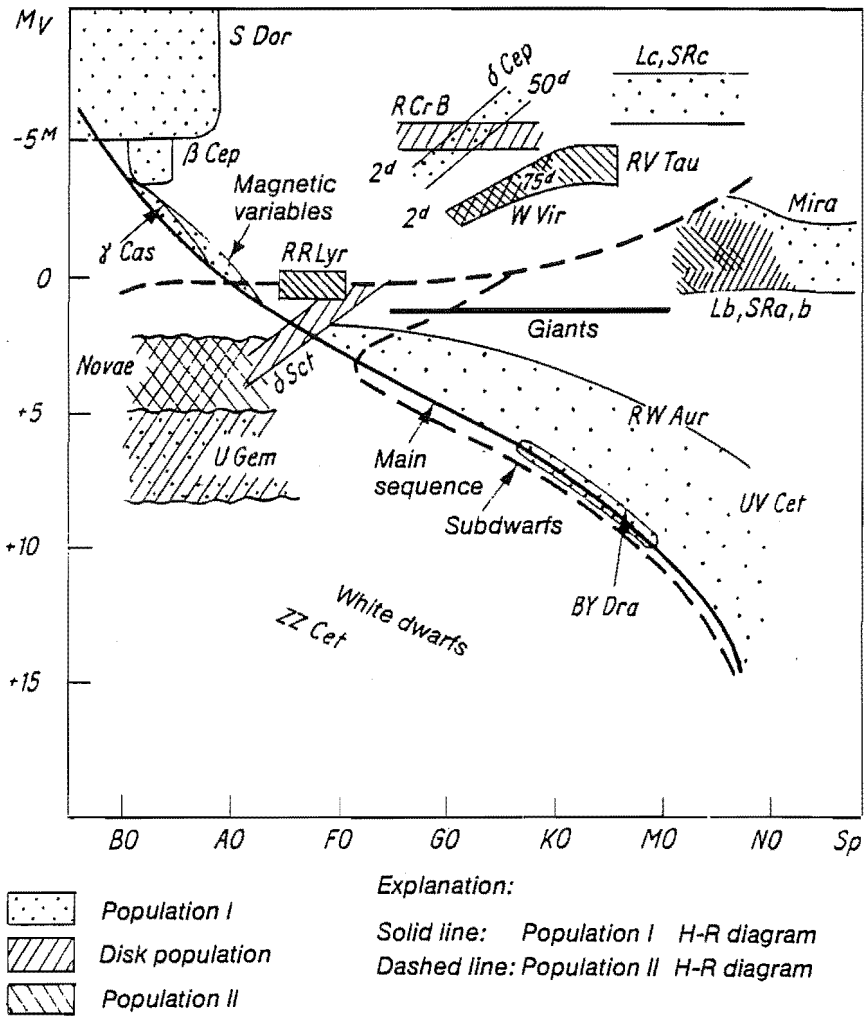

Figure 1.1: The positions of various classes of variable stars on the Hertzsprung-Russell diagram. Population types are also indicated. (Reproduced from Hoffmeister et al. 1985.)

the pulsation mechanisms in low mass and high mass stars. The higher mass variables, of which the classical Cepheids are the best known example, are well understood in terms of the pulsation mechanism. The low mass supergiants may have similar temperatures and luminosities as some Cepheids, but their different masses imply a different internal structure and hence different pulsational characteristics.

The study of the chemically peculiar RCB variables in the Galaxy and the Large Magellanic Cloud provides important clues to their evolutionary history. These objects, with their peculiar photometric and spectroscopic 'decline' behaviour, unusual abundance distributions and infrared excesses indicative of circumstellar dust shells, are linked with various evolutionary scenarios. Abundance analyses allow us to test these evolutionary scenarios and nucleosynthetic models in both a galactic and extragalactic environment. In addition, the interrelationship between the members of this class, and the links to other variables which display similar characteristics, can then be investigated.

1.1 The RV Tauri variables

1.1.1 Basic properties

The RV Tauri stars[1] are a small class of radially-pulsating variables which are located in the brightest part of the Cepheid II instability strip. They are believed to consist of old disk and population II stars. The RV Tauri variables are generally characterized by:

- a light curve which displays alternating deep and shallow minima;
- 'formal' periods[2] between about 30 and 150 days;
- spectral type F–K and luminosity class Ia–II.

The last of these criteria was introduced in order to exclude the various red variables that satisfy the first two conditions.

A recent review of the properties of the RV Tauri variables (Wahlgren 1992) notes that the study of these stars is confused by a number of incorrectly classified

[1]The origin of the term 'RV Tauri-type' to describe these variables stars is discussed by Zsoldos (1993b), who states that this term was used as early as 1912.

[2]For RV Tauri stars the 'formal' or 'double' period is defined as the time interval between successive *deep* minima while the 'fundamental' or 'single' period is the time between successive minima.

variables that have been placed in this class. Approximately 120 RV Tauri stars are listed in the General Catalogue of Variable Stars (Kholopov et al. 1985).

The second edition of the General Catalogue of Variable Stars (Kukarkin et al. 1958) subdivides the RV Tauri stars into two *photometric* subclasses based on the appearance of their light curves. The RVa subclass exhibit a constant mean magnitude, whereas the subclass RVb was created to describe those objects that possessed an additional periodicity, such as RV Tau itself. This additional periodicity appears as a long-term ($\sim$600–3000 day) variation of the mean V magnitude superimposed on the short-term ($\sim$30–150 day) variations due to pulsation.

Most field members of the RV Tauri class exhibit peculiar infrared excesses (Gerhz & Woolf 1970, Gerhz 1972, Gerhz & Ney 1972, Lloyd Evans 1985, Goldsmith et al. 1987) indicative of extensive circumstellar dust shells. An infrared excess has also been detected for a globular cluster RV Tauri variable (Nook & Cardelli 1989). In addition, a number of RV Tauri stars display intrinsic and phase-dependent polarization (Raveendran & Kameswara Rao 1988, Raveendran et al. 1989, Nook et al. 1990, Nook & Nordsieck 1991, Polyakova 1992).

As a consequence of these properties, it has been suggested (Jura 1986) that the RV Tauri stars are low mass objects in transition from the AGB to the white dwarf phase and hence are the likely progenitors of planetary nebulae. However, if the evolution of these objects to the blue in the HR diagram is very slow, then photoionization of their surrounding gas may not take place.

1.1.2 The alternating behaviour in RV Tauri stars

It can be shown that the form of the characteristic RV Tauri light curve can be reproduced by the addition of two sinusoidally-varying functions (Gerasimovič 1929). This would correspond to the simultaneous excitation of two pulsational modes in the star. If one mode has a period almost twice that of the other, then a simple resonance between the two modes will result in alternating deep and shallow minima[3] as displayed in Fig. 1.2. This figure shows the two constituent sinusoids that result in a light curve of the RV Tauri type. If the phase difference

[3]It should be noted that for the RV Tauri stars, a convention is used where phase 0.0 defines the deep (or *primary*) minimum and phase 0.5 defines the shallow (or *secondary*) minimum. The maxima following the primary and secondary minima are known as the primary and secondary maxima respectively.

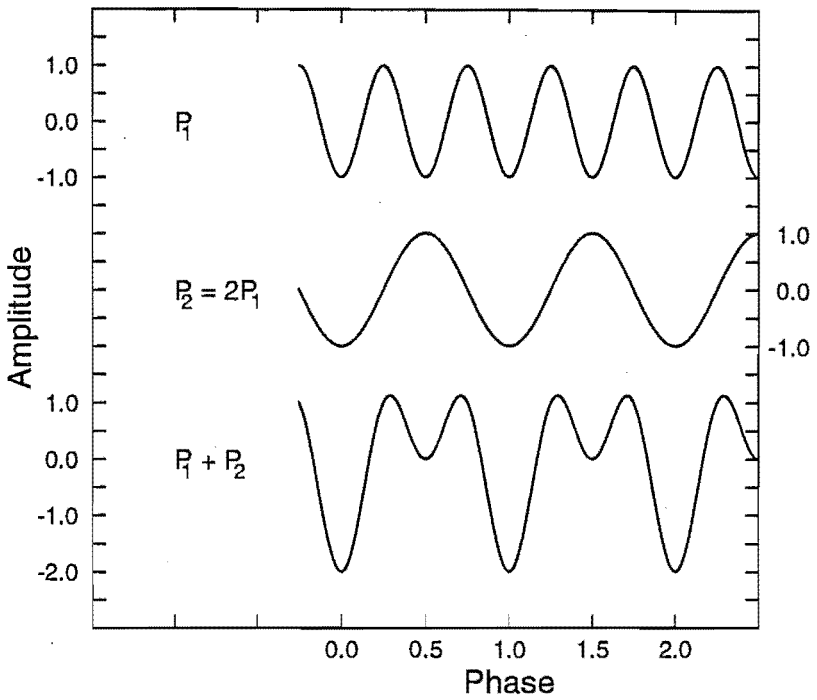

Figure 1.2: The form of the characteristic RV Tauri light curve can be reproduced if $P_2 = 2P_1$ and the two modes of pulsation have a specific phase relationship (as pictured).

between the two constituents is such that the period P_1 is at its minimum whenever the period P_2 ($= 2P_1$) is at its maximum, then the characteristic RV Tauri light variation will result.

There have been a number of suggestions in the literature to explain the *physical* origin of the alternating behaviour in RV Tauri stars (Deupree & Hodson 1976, Takeuti & Petersen 1983, Fadeyev 1984, Aikawa & Bruegman 1987, Buchler & Kovacs 1987). However, many theoretical studies of RV Tauri stars are based mainly on the numerical results obtained for W Vir, RR Lyrae or even Population I models.

Sasselov (1992) states that due to the mass distribution in a low mass post-AGB star and the virtually zero density gradient in the envelope, any pulsations excited in a low mass supergiant will be strongly non-adiabatic and nonlinear, unlike those of a Cepheid with the same effective temperature and luminosity.

The resonance hypothesis, proposed by Takeuti & Petersen (1983), suggests that a 2:1 resonance exists between the fundamental mode and the first overtone. A recent theoretical study (Fokin 1993) of the nonlinear pulsations of luminous

($3123 < L/L_{\odot} < 7000$), low mass ($0.6M_{\odot}$) RV Tauri models supports this long standing resonance hypothesis by revealing a 2:1 period ratio for the fundamental mode and first overtone. The alternating behaviour appears due to the enhancement of the first overtone. The fundamental mode in the models appears to correspond to the 'formal' period in the RV Tauri stars.

Further evidence to support the resonance hypothesis is provided by the linear non-adiabatic pulsation analysis of low mass ($0.5 < M/M_{\odot} < 0.8$), high luminosity ($10^3 < L/L_{\odot} < 10^4$) models by Tuchman et al. (1993). These models are found to reproduce the observed periods and temperatures of RV Tauri stars and, in most of the models, the period of the fundamental mode is nearly twice that of the first overtone.

Alternative explanations for the pulsations in RV Tauri stars are provided by: coupling between the radial oscillation and large amplitude convective motions (Deupree and Hodson 1976), a non-linear mode-coupling between two or more periodic effects (Aikawa & Bruegman 1987) or a deterministic chaotic process associated with a low-dimensional attractor (Buchler & Kovács 1987, Kovács & Buchler 1988, Saitou et al. 1989, Kolláth 1990).

The W Vir models of Buchler & Kovács (1987) showed that a typical series of period doubling bifurcations and a transition to chaotic pulsations occurred as the effective temperature was decreased. Behaviour similar to that displayed by W Vir, RV Tauri and semi-regular stars was reported. Aikawa (1993), extending an earlier study (Aikawa 1991) of low mass post-AGB stars to higher luminosities in order to obtain a better representation of RV Tauri atmospheres, found the transition from regular to chaotic behaviour occurred as the luminosity was increased. There are a few RV Tauri stars which may show signs of chaotic behaviour (for R Sct, see Veldhuizen & Percy 1989, Kollàth 1990), but many studies are limited by the paucity of photometry and frequent gaps in the data sets.

Another possibility to explain the characteristic RV Tauri light curve, suggested by Shenton et al. (1992) to describe the carbon-rich RV Tauri star AC Her, is a model where a radial and a non-radial mode are simultaneously excited. The non-radial pulsation has a period exactly twice that of the radial mode, so that at successive light minima the star oscillates between an oblate and prolate spheroid.

1.1.3 Spectroscopic properties

In addition to their photometric subclasses, the RV Tauri stars can be divided into three *spectroscopic* subtypes (Preston et al. 1963):

A *G–K type variables:* All spectral features indicate type G or K, although irregularities may occur in the strength of the CN bands, the λ4175 blend or the G band. TiO bands, indicating a spectral type as late as M5, may appear at minimum light.

B *Fp(R) variables:* These stars are generally characterized by weak metal-line absorption. Spectral classification based on the hydrogen line intensities gives spectral type of about F5–G0, while the Ca II line give earlier spectral types. Variations in the strength of the CH and CN bands with phase are observed. The members of this group show evidence of enhanced carbon.

C *Fp variables:* The bands of CN and CH are weak or absent at all phases. Otherwise the spectra are similar to those of the Preston B subtype.

There are a number of general spectroscopic studies of the RV Tauri stars which are mostly concerned with the brighter members of this class (R Sct, U Mon and AC Her). One of the most striking spectral peculiarities of the RV Tauri stars is the presence of strong Balmer and metallic emission lines and the doubling of some absorption lines. As discussed by Wallerstein & Cox (1984), these features provide strong evidence that shock waves are present in the atmospheres of these stars. High dispersion studies of the RV Tauri stars to investigate the radial velocity variations, the stratification and structure of the atmosphere and the effects of shock waves have included those by: Sanford (1931, 1933, 1955), Abt (1955), Preston (1962, 1964, 1972), Baird (1982, 1984), Gillet et al. (1989, 1990), Lèbre & Gillet (1991a, 1991b) and Gillet (1992).

An intriguing observation was made by Mozurkowich et al. (1987) who found that high-resolution, infrared (2μm) spectra revealed a different pulsational periodicity than the optical studies. In addition, no evidence of shock waves was seen at this wavelength.

Studies to determine the photospheric composition have been presented for the following RV Tauri stars: U Mon (Aliev 1967), AC Her (Yoshioka 1979), R Sct (Luck 1981, Luck & Bond 1984), IW Car (Giridhar et al. 1994) and RU Cen, AI CMi and U Mon (Luck & Bond 1989). Most studies suggest that the stars

are metal deficient and, in the case of AC Her, RU Cen and IW Car, carbon enhancements are seen. Luck (1981) and Giridhar et al. (1994) have speculated that the envelopes of the RV Tauri stars may be enriched in helium and deficient in hydrogen.

1.2 The R Coronae Borealis variables

The atmosphere of an RCB star is extremely hydrogen deficient. Coupled with the presence of numerous C I lines (and C_2 Swan bands in the cooler stars), this suggests that the atmospheres of these stars are now dominated by nuclear processed material. A comprehensive review of the spectroscopic properties of the RCB stars has been presented by Lambert (1986). An updated review including results for a further 18 galactic RCB stars has been published recently (Lambert & Kameswara Rao 1994).

The photometric variability displayed by this class is unique – at irregular intervals, the stars fade rapidly or 'decline' by up to 7 magnitudes. A 'decline' is attributed to the obscuration of the star by a cloud of carbon dust grains which have condensed from carbon-rich gas previously ejected from the star. The general characteristics for the RCB class are as follows:

- $M_{bol} \sim -5$;
- $M \sim 0.8 M_{\odot}$;
- T_{eff} of typically 5000 to 7000 K, but there are a few members that have $T_{eff} > 10000$ K;
- extreme hydrogen deficiency of generally 10^{-5} times the solar abundance, carbon overabundance of about 10 times solar;
- some have lithium or s-process element enhancement;
- infrared excesses due to the presence of a 700–900 K circumstellar dust shell;
- low amplitude variations in luminosity ($\Delta V = 0.1$–0.7 magnitudes) that are usually associated with radial pulsations;
- large amplitude declines of up to 7 magnitudes.

The RCB stars appear to be closely related to the hydrogen-deficient carbon (HdC) stars, which are generally considered to be cooler objects. The HdC stars do not display the characteristic RCB-type declines and show a much lower amplitude in their photometric (ΔV = 0.0–0.1) and radial velocity variations. The photometric characteristics of the RCB and HdC stars have been surveyed by Lawson et al. (1990). Both classes of star are extremely rare. In the case of the RCB stars, only about 25 Galactic and 4 LMC members are known. Only six HdC stars are known in the Galaxy. However, this small galactic HdC population may be due in part to the difficulty in detecting these stars, since they do not have 'declines' or particularly large amplitude pulsations.

Both the HdC and RCB stars are generally presumed to be the low temperature extension of the extreme helium (eHe) stars (Drilling 1986). Photometric and radial velocity variability in the eHe stars has been observed (Lawson et al. 1993). The periods and temperatures obtained for these stars are consistent with the evolution of the RCB and HdC stars to the eHe star region.

1.3 Connections

The brightest stars of the RV Tauri and the R Coronae Borealis class, R Sct and R CrB respectively, were both discovered in 1795 by Pigott (1797). Many authors refer to the similarities which exist between these two classes of variables. Both classes of object:

- are semi-regular, pulsating variable stars;
- have inferred low masses (in the range $0.6 < M/M_{\odot} < 1.0$);
- have high luminosities;
- exhibit strong infrared excesses, indicative of cool circumstellar dust shells;
- are evolved, possibly post-AGB stars and are believed to be precursors to planetary nebulae.

In addition, carbon enhancement is seen in some RV Tauri stars (see Section 1.1.3) and all RCB stars. The possibly of helium enhancement and hydrogen deficiency in the RV Tauri stars has been discussed by Luck (1981), Lambert (1986) and Giridhar et al. (1994). Carbon enhancement and hydrogen deficiency are two of the key findings for all RCB stars.

Further similarities are suggested by Howell et al. (1983) who even asked the question "Do RV Tauri stars evolve to RCB stars?". A spectrum of the RV Tauri star, R Sct, taken during an extremely deep pulsation showed chromospheric lines very reminiscent of that seen in RCB stars during their characteristic 'declines' (Howell et al. 1983).

Shock waves are present in the atmospheres of most RV Tauri stars and have been linked to the mass loss processes in these stars (Baird 1981). Recent work on the times of onset of RCB declines has revealed that the mass loss episodes in these stars may also be related to the pulsational period (Lawson et al. 1992). There is strong evidence for shock waves in the atmosphere of the RCB star, RY Sgr (Cottrell & Lambert 1982). This star displays line doubling (or 'splitting') and a shock amplitude of $\sim 35\,\mathrm{km\,s^{-1}}$(Lawson 1990, Lawson et al. 1990) which is comparable with that exhibited by the RV Tauri stars. The phase relationship between the light, colour and radial velocity curves in RY Sgr is also similar to that seen in the RV Tauri stars.

The alternating deep and shallow light curve behaviour of RV Tauri stars are characteristics displayed by some RCB stars, U Aql and RT Nor, which both pulsate in this manner at irregular intervals (Lawson 1990, Lawson et al. 1990).

Consequently, the scene is set to investigate these connections with the acquisition of long time baseline colour photometry and contemporaneous spectroscopic observations. This should enable links to be made between the photometric variations and the radial motions in the atmospheres of these stars and to relate any photometric and spectral peculiarities. In addition, such observations will allow us to examine any long term variations in the spectroscopic nature and the radial velocities of these objects.

1.4 Introduction to the thesis

In this thesis the photometric and spectroscopic observations of the RV Tauri stars are presented and discussed with a view to obtaining a better understanding of the nature of these pulsating variables. A detailed analysis of the chemical composition of a number of galactic and LMC R Coronae Borealis stars allows links to be investigated between these two classes of low mass, high luminosity variables.

In Chapter 2 the RV Tauri photometric programme is discussed, including the instrumentation, the acquisition of these data and their preliminary reduction.

The photometric programme was carried out at the Mt John University Observatory (MJUO), where up to four years of multicolour *BVRI* photometry has been obtained for eleven stars which have been classified[4] as RV Tauri variables. This long term monitoring is only able to be maintained with the dedication of the resident observers at MJUO, allowing unique programmes of long timescale multicolour photometry to be undertaken.

The analysis techniques which were employed to identify the dominant periodicities in the MJUO photometric data are described in detail in this chapter. Particular emphasis is placed on the correct identification of the dominant periodicities and the complications that arise from the effects of window functions, aliasing and the presence of multiple periodicities in the photometry.

The presentation and analysis of the photometric data for the RV Tauri stars of the subclasses RVa and RVb is presented in Chapters 3 and 4 respectively. (These photometric data are also tabulated in Appendix A.) Each of the stars in the RV Tauri programme is discussed in a separate section which presents the Fourier power spectra, a tabulated summary of the Fourier and least-squares analyses, and phased light and colour curves. RU Cen and U Mon were selected as typical examples of the RVa and RVb subclasses respectively. The detailed discussion of each of these two stars is presented first in its appropriate chapter.

Chapter 5 summarizes the results from the RV Tauri photometric programme and discusses the general characteristics of the programme stars that are evident from the photometric analyses. Additional infrared photometry and IRAS fluxes are used to derive some stellar and dust shell properties for the RVb star U Mon. These properties and their time variability will be used later in the investigation into the nature of the RVb type stars (see Section 9.1.2).

The CCD detector system, the échelle spectrograph and the 1.0-m reflecting telescope at MJUO are discussed in Chapter 6. (More extensive details of the CCD system's characteristics and performance are included in Appendix 2.) In addition, this chapter describes the steps used in the reduction of the CCD échelle spectra of the programme RV Tauri stars. The MIDAS software package was employed for the reduction of raw CCD frames to one-dimensional, wavelength-calibrated spectra. (The specific sequence of MIDAS commands for reduction of CCD échelle spectra are listed in Appendix C.) Further analysis techniques, such

[4]The General Catalogue of Variable stars (Kukarkin et al. 1985) and the Sky Catalogue 2000.0 (Hirshfeld & Sinnott 1985) were used to select the RV Tauri stars for the photometric and spectroscopic programme.

as line profile fitting, the measurement of radial velocities and the derivation of orbital elements are also outlined in this chapter.

Chapters 7 and 8 present the spectroscopy of the RV Tauri stars. Following the format that was used for the chapters dealing with their photometric observations, the results for each star are discussed individually, with the RVa stars and RVb stars being presented in separate chapters. More spectra were obtained of R Sct (RVa subclass) and U Mon (RVb subclass) as a consequence of their being the two brightest RV Tauri variables. These two stars are discussed first, and in greater detail, in their respective chapters. Due to the faintness of some of the programme RV Tauri stars, only a few spectra were obtained.

A discussion of the photometric and spectroscopic characteristics of the two subclasses of RV Tauri star in the framework of our current understanding of these pulsating stars is presented in Chapter 9. The various models that have been proposed to explain the alternating deep–shallow light variations in the RV Tauri stars are considered. In addition, the nature of the long-term secondary light variation in the RVb stars is investigated and a model for the RV Tauri stars is discussed.

In Chapter 10 a detailed analysis of the chemical composition of a number of galactic and Large Magellanic Cloud RCB stars is presented. Various evolutionary scenarios and nucleosynthetic models are discussed.

A summary of the main findings of this thesis and general suggestions for future work are presented in Chapter 11.

Preliminary photometric and spectroscopic results for the RV Tauri stars from Chapters 3, 4, 7 and 8 were presented as a poster paper at IAU Colloquium 139 *New Perspectives on Stellar Pulsation and Pulsating Variable Stars* and subsequently appeared in the proceeding for this conference (abstract only) and in *Southern Stars* (Pollard, Kilmartin, Gilmore & Cottrell 1993).

Chapter 10 is based on a paper that was published recently in *Monthly Notices of the Royal Astronomical Society* (Pollard, Cottrell & Lawson 1994).

Appendix 2 first appeared as *The Mt John Photometrics CCD System Use and Performance Notes* Numbers 2 and 3 (Pollard 1989a, 1989b). The first of these was concerned with the linearity of the MJUO CCD system, while the second was an evaluation of the variation of the CCD system at a number of different wavelengths and for various chip operating temperatures.

Chapter 2

Photometric observations and analysis techniques

2.1 Telescope and instrumental details

Photometric *BVRI* observations of eleven RV Tauri stars were obtained with the Boller & Chivens (B&C) and Optical Craftsmen (OC) 0.61-m telescopes at MJUO. Both telescopes were equipped with automated single channel photometers. Photometric observations obtained between 1990 August and 1993 July were made with EMI 9558B photomultiplier tubes. In 1993 July, the tubes in the photometers on both the B&C and the OC telescopes were replaced with EMI 9202B photomultiplier tubes. However, due to an unacceptably high dark current in one of the new tubes, an EMI 9558B tube was re-installed in the B&C photometer in 1993 October. The filters used to obtain the photometric observations were similar to those described by Bessell (1976).

2.2 Acquisition and preliminary reduction of data

The computer program, PTM UBVRI, written by A.C. Gilmore, is used at the telescope for data acquisition and preliminary reduction. The program utilizes the current transformation and mean extinction coefficients for the particular combination of telescope, filter wheel and photometer that is being used. These coefficients are determined from observations of E-region standard stars (Cousins 1983). A reference file containing the V magnitudes, colour indices and positions (precessed to the observation date) is kept for each programme star and its

comparison and check stars.

Observations are usually taken in the sequence S–C–V–K–V–C–S, where the letters S, C, V and K represent the sky, comparison, variable and check star readings respectively. Integration times for different filters vary, with longer integrations in the U and I filters where the counts are generally lower.

Once the observations have been obtained, sky counts are interpolated and subtracted from all star data before any other reductions. The heliocentric Julian Date (HJD) is calculated for the midtime of the V integrations and air masses are calculated for the time of observation in the bluest filter.

The comparison star's counts and air mass are interpolated for the time of observation of the variable star. The differential V magnitude and colours of the variable are calculated from the interpolated comparison counts. The differential magnitude of the variable is then transformed to the standard system using the photometric constants and the difference in air mass. The differential magnitudes can then be added to the comparison V magnitude and colours in the reference file to give standard V magnitudes and colours. The check star is reduced in exactly the same manner as the variable, and thus is an indicator of the internal accuracy of the differential photometry.

A direct reduction of the comparison star magnitudes and colours using the current photometric coefficients is useful as a check on the applicability of the constants to the actual night of observation.

2.3 The RV Tauri photometric programme

Photometric monitoring of eight RV Tauri stars was initiated in 1990 August. An additional three stars (AI Sco, RY Ara and AR Sgr) were added to the observing programme in 1991 August. For each RV Tauri star in the photometric programme, photometric observations were obtained differentially with respect to several nearby comparison and check stars. In many cases, comparison and check stars from previous differential photometry were available and the magnitudes and colours were adopted from the literature. Otherwise, comparison and check stars were chosen on the basis of having similar spectral types and magnitudes to the variable star. In this case, the comparison and check stars were observed on several nights and magnitudes and colours were obtained differentially with respect to E-region standard stars. The comparison and check stars for the RV Tauri photometric programme, together with their adopted mean magnitudes

and colours, are given in Table 2.1.

The zero point errors for the comparison V magnitude (and hence the differentially determined check and variable star magnitudes) are generally better than 0.03 magnitudes. For the colour indices, the error is better than $\sim$0.02 magnitudes. The scatter between the observations of the variable and check star on a particular night and the direct reduction of the comparison star were used to determine the quality of the night for photometric observations. Care was taken to ensure that only photometric data from nights of reasonable quality were used. Criteria used for the rejection of photometric observations were:

- inconsistent check star magnitudes;
- a large scatter in repeated observations of the same object;
- measurements of the variable or comparison star that are clearly in error, for example, observing the wrong star.

Nightly mean magnitudes for the variable star were then calculated. The internal accuracy of the differential photometry over the time of the observations was determined from the constancy of the check star magnitudes. For the V magnitudes and all colours, the internal accuracy was generally better than 0.01 magnitudes.

2.4 Analysis of the RV Tauri photometry

The RV Tauri photometric data from MJUO (tabulated in Appendix A) were then analysed to determine the dominant periodicities present. Of particular importance is the identification of these periodicities with physical processes, such as pulsational modes (either radial or nonradial) of the star, or binary motion. The relationship between the light, colour and radial velocity curves over a large time baseline is required for this investigation.

2.4.1 The Fourier power spectrum method

When searching for the presence of periodic signals in a data set, one standard technique that is often employed is that of Fourier analysis in the form of a Fast Fourier Transform (FFT). One inherent limitation of this method is the requirement that the data be evenly sampled – a restriction that becomes problematic

Table 2.1: The adopted magnitudes and colour indices for the comparison and check stars in the RV Tauri photometric programme.

Star[a]	α_{1950} h m s	δ_{1950} ° ′	V	(B-V)	(V-R)	(V-I)	SAO	Chart[b]
U Mon	07 28 24	-09 40						
C	07 28 36	−10 00	6.55	1.62	0.85	1.82	152986	–
K	07 28 12	−08 57	7.60	1.40	0.64	1.19	134769	–
AR Pup	08 01 10	-36 27						
C	08 00 56	−36 06	8.37	0.92	0.47	0.93	198737	83 (149)
K	08 02 17	−36 16	8.72	0.54	0.29	0.60	198762	87 (149)
IW Car	09 25 43	-63 25						
C	09 23 13	−63 30	8.62	0.62	0.34	0.73	250565	89 (861)
K	09 27 35	−63 00	8.82	0.37	0.20	0.47	250592	– (861)
RU Cen	12 06 48	-45 09						
C	12 09 33	−44 53	9.30	0.33	0.19	0.45	223247	93 (123)
K	12 10 57	−46 19	7.54	0.54	0.30	0.70	223263	76 (123)
V820 Cen	14 10 54	-37 52						
C	14 08 08	−37 40	8.35	1.23	0.64	1.24	205274	–
K	14 12 47	−37 22	8.49	1.26	0.62	1.20	205365	–
RY Ara	17 17 09	-51 04						
C	17 17 25	−51 04	7.74	0.61	0.33	0.58	244656	–
K	17 17 52	−51 18	8.58	1.62	0.87	1.67	244664	–
V453 Oph	17 24 13	-02 22						
C	17 24 44	−01 40	10.17	0.77	0.46	0.85	141674	–
K	17 23 04	−03 20	9.17	0.55	0.32	–	141657	–
AI Sco	17 53 00	-33 48						
C	17 51 06	−33 36	8.44	0.66	0.35	0.58	209445	– (664)
K	17 52 11	−34 09	8.57	1.82	0.99	2.30	209464	– (664)
R Sct	18 44 49	-05 46						
C	18 47 00	−05 58	5.99	1.60	0.83	1.55	142661	–
K	18 43 21	−06 18	7.92	1.26	0.65	1.30	142598	–
AD Aql	18 56 25	-08 14						
C	18 56 04	−08 19	8.86	0.50	0.30	0.65	142864	–
K	18 58 13	−08 08	9.78	0.48	0.30	0.63	142916	–
AR Sgr	18 56 40	-23 47						
C	18 58 22	−23 18	7.78	1.08	0.57	1.03	187581	a (677)
K	18 58 31	−24 13	9.15	0.70	0.39	0.67	187582	c (677)

[a]The letters C and K denote the comparison and check star respectively.

[b]Variable stars charts were obtained from the Variable Star Section (VSS) of the Royal Astronomical Society of New Zealand. The first designation identifies the comparison star and the number in brackets is the corresponding VSS chart number.

when dealing with astronomical data. Converting the unevenly spaced data to equal sampling steps by interpolation or some other method may alter the perceived frequency and strength of a periodic signal.

Lomb (1976) and Scargle (1982) have developed a technique that detects weak periodic signals and evaluates their significance in the case where the observation times are unevenly spaced. The method involves calculating the normalized periodogram (Fourier spectrum) of the non-uniform data set, requiring a slight modification (by introducing a time offset factor, τ) to the definition of the classical periodogram for evenly spaced data. This modification has two main effects. It causes the normalized periodogram to be completely independent of a translation in time and it makes the periodogram analysis approximately equivalent to the least-squares fitting of sine waves to the data.

For a set of observations $y_i, i = 1, \ldots, N$ taken at times t_i, Lomb fits the model

$$y_i = a_1 \cos\omega(t_i - \tau) + a_2 \sin\omega(t_i - \tau)$$

to these data in a least-squares sense, where a_1 and a_2 are unknowns for a given value of the frequency, ω. The time-offset term, τ, is defined by the equation

$$\tan(2\omega\tau) = \frac{\sum_i \sin 2\omega t_i}{\sum_i \cos 2\omega t_i}.$$

The constant τ makes the calculated periodogram completely independent of shifting all the t_i values by any constant. This method evaluates data, sines and cosines, only at the times of observation, thus considering these data on a per point basis rather than a per time interval basis.

The Lomb-Scargle method has the additional advantage of providing a measure of the significance of the height of a peak in the periodogram, through the calculation of a 'false-alarm' probability. This can only be done when the periodogram power is normalized by the total variance of the noise in the data, σ^2. The Lomb-Scargle normalized periodogram (spectral power as a function of ω) is defined as

$$P_N(\omega) = \frac{1}{2\sigma^2}\left\{\frac{[\sum_i (y_i - \bar{y})\cos\omega(t_i - \tau)]^2}{\sum_i \cos^2\omega(t_i - \tau)} + \frac{[\sum_i (y_i - \bar{y})\sin\omega(t_i - \tau)]^2}{\sum_i \sin^2\omega(t_i - \tau)}\right\}.$$

Scargle (1982) defines the expected power signal-to-noise ratio, Z, as

$$Z = N\left(\frac{A}{2\sigma}\right)^2$$

where N is the number of observations in the data set, A is the amplitude of the signal and σ is the noise level in the data set. In most practical cases, the peak signal-to-noise ratio is estimated from an inspection of the power spectrum in the region of the peak of interest. The power of the peak is divided by the power due to the noise and observational uncertainties to obtain an estimate of the peak signal-to-noise ratio. There are a number of factors which can complicate this procedure. Enhancements in the power of the noise due to spurious peaks introduced by the window function may result in an overestimation of the noise level. Alternatively, we may look at the noise level after the peak of interest has been removed from the periodogram by subtracting the contribution of the signal from the data set (sometimes known as 'prewhitening'). However, this may underestimate the noise level if the peak of interest was merely a result of noise fluctuations in the first instance. Because of these complicating factors, it can be seen that the value of the peak signal-to-noise ratio, Z, may be rather uncertain due to the difficulty in making a correct estimate of the noise level, σ, from the power spectrum.

The false-alarm probability tells us the probability that a peak of height z or greater will occur in a spectrum of pure noise. If M independent frequencies are sampled, the false-alarm probability is

$$P(>z) = 1 - (1 - e^{-z})^M.$$

A low value of the false-alarm probability ($P(>z) \sim 0.01$) indicates there is only a small chance that the peak could have arisen from chance noise fluctuations alone. The significance level of the peak, and therefore the possibility of a periodic signal being present at that frequency, is correspondingly high. To evaluate $P(>z)$, the number of independent frequencies, M, needs to be calculated. Since we are interested in the regime where $P(>z)$ is small, the equation above can be series expanded to give

$$P(>z) \approx M\, e^{-z}.$$

As practical significance levels are spaced apart by factors of 5 or 10, fairly large errors in M can be tolerated. The uncertainty in calculating $P(>z)$ is therefore much more dependent on the value of z. For a periodogram normalized in the correct manner, the value of the peak height z is effectively the peak signal-to-noise ratio Z. If the sampling is up to the mean Nyquist frequency of the data set, f_N, then the number of independent frequencies, M, is approximately equal to

the number of data points, N. When more frequencies are sampled, M increases proportionally. In addition, if these data are clumped in time by a certain factor, then the value of M is reduced by the same factor. If required, Monte Carlo simulations can be used to determine M for a particular data set.

From the above discussion, it can be seen that the false-alarm probability is much more dependent on a correct evaluation of the peak signal-to-noise level in the periodogram than on the number of independent frequencies. Just how well the value of the peak signal-to-noise level can be estimated places a limitation on the use of the false-alarm probability, even if the frequency has been determined very accurately.

2.4.2 The window function and aliasing

It is possible to have several significant peaks in the Fourier power spectrum which arise not from the presence of multiple periodicities in the data set, but from the effects of the natural window function. The spurious peaks introduced into the power spectrum by the window function are characteristic of a particular set of photometric data and arise from two main effects. First, non-uniform data spacing can introduce several 'aliases' for each of the 'true' signals present in the data set. The term aliasing generally refers to spectral power from higher frequencies leaking to lower frequencies. Second, the sharp truncation at the ends of the data set can cause sidelobes of significant height to appear around the 'true' peak (or peaks) in the power spectrum.

To examine the effect of the window function upon the periodicities identified in a data set, a synthetic time series can be constructed for a perfect (i.e. noise free) sine wave (or sine waves) at the same spacing as the original data. When the Fourier power spectrum of this synthetic time series is compared with that determined for the original photometry, the effect of the data spacing on the appearance of the spectral pattern as a whole (both side lobes and aliases) will be apparent. Peaks that arise from the effect of the window function are able to be identified as spurious. This will be important when we come to identify further periodicities that are present in the data set.

2.4.3 Fitting multiple periods using the Fourier technique

The first method used to fit multiple periods to the photometric data is an extension of the Fourier power spectrum technique. The presence of multiple periods in

the data set complicates the analysis. Multiple periodic signals present in a data set will introduce the corresponding peaks in the Fourier spectrum, as well as the associated sidelobes and aliases caused by the window function. Interference terms may arise from the interaction of the spectral patterns of the different signal components, causing further complications in interpreting the original power spectrum.

To overcome the complications that arise from aliasing, one periodic term at a time is identified from the Fourier power spectrum and this 'known' constituent is removed from the data set by 'prewhitening'. This technique involves removing the contribution of the most significant periodicity from the data set by subtracting a sine wave of the correct amplitude, phase and frequency. Thus the direct influence of the periodic signal, as well as the sidelobes and interference terms should be eliminated. This procedure can be repeated until the variance of the residuals is comparable to the variance of the noise in the data set, assuming that each period is independent and is modelled correctly.

Since we are looking for physical connections between these periods and the pulsation modes of the star, the assumption that each period is independent should be regarded with a degree of caution. This 'prewhitening' of the data assumes that the derived values for the amplitude, phase and frequency are exact and that the contribution of this periodicity has been modelled perfectly. In reality, there are uncertainties associated with the determination of the amplitude, phase and frequency and these uncertainties will be introduced into the data set (in some manner) as the sine wave is removed. Further, the modelling of the signal will be inadequate when dealing with non-sinusoidal variations. In such cases, the fit may be improved by including higher Fourier harmonics in the known constituents. Breger (1982) has shown that for a Cepheid-like light curve, it is better to adopt an $(f + 2f)$ fit, where f is the frequency. Additionally, it is possible that part of the power of the second periodicity is attributed to the first when this power is evaluated in order to prewhiten these data. Several authors (Mantegazza 1985, Antonello et al. 1986) have noted that the orthogonality of the Fourier components of the signal is destroyed by the unequal data spacing if the technique of prewhitening is used. This can lead to an incorrect identification of the spectral components in the power spectrum.

2.4.4 Fitting multiple periods using the least-squares technique

Due to the uncertain effects introduced by the prewhitening of the data set as described above, an alternative technique of fitting multiple periods was applied to the MJUO photometric data. This method is based on the generalized least-squares procedure, proposed by Vaníček (1971), that has been used in a number of analyses investigating the spectral content of multi-periodic pulsating variables (Antonello et al. 1986, Andreasen 1987, Poretti 1989, Poretti et al. 1992). In this scheme, a least-squares solution is made simultaneously for the amplitudes of all known constituents of the data, together with the amplitude and phase of the sine wave with the trial frequency. Because the amplitude and phase of each known periodicity is calculated while scanning the data set for the next most significant frequency, no prewhitening of the data is required.

In applying this alternate 'simultaneous least-squares technique' to the photometric data, the frequencies determined from the Fourier power spectrum technique are used as the starting values for the analysis. The first frequency found from the Fourier method is included as the first known constituent. A series of least-squares fits are made to the data set for a range of trial periods, where the amplitude, phase and frequency for the first known component, as well as those associated with the trial frequency, are allowed to vary. In this way, a simultaneous fit of two or more constituent sinusoids is made to the data set without the need to fix the values of the amplitude, phase or frequency of the previously determined component. The rms residuals of the final fits are compared with those obtained from the Lomb-Scargle Fourier technique.

If the presence of further independent periodicities are suspected in the data set, the first two periodicities are included as the known constituents and further trial frequencies can then be investigated. Specifically, for a set of observations $y_i, i = 1, \ldots, N$ taken at times t_i, the photometric data are fitted in a least-squares sense on the model:

$$y_i = A_0 + \sum_{j=1}^{n-1} \{A_1 \cos[\omega_j(t_i - t_0) + \phi_j]\} + A_n \cos[\omega_n(t_i - t_0) + \phi_n]$$

where the $\omega_1, \ldots, \omega_{n-1}$ are the previously identified periodicities present in the data set (that is, the 'known constituents'), and ω_n is the new trial frequency to be determined. For each new trial frequency, ω_n, the coefficients $A_0, \ldots, A_n$, $\phi_0, \ldots, \phi_n$ and frequencies $\omega_1, \ldots, \omega_{n-1}$ are calculated to best fit the photometric data in a least-squares sense.

In Chapters 3 and 4, a further least-squares fit is typically employed in the period analysis, where the frequency, f_1, and its first harmonic, $2f_1$, are included as the known constituents. This specific fit can characterize either a non-sinusoidal (Cepheid-type) light curve or an alternating deep–shallow (RV Tauri-type) light curve. During the analysis, it was found that the algorithm used to minimize the squares of the residuals (the Nelder-Meade simplex search algorithm for multivariable minimization) was quite dependent on the initial starting values for the frequency and phase. Each set of data was analysed with a number of initial input values to verify that the same local minimum could be found. In addition, the various intermediate iterations were displayed together with the original photometry to visually check that a reasonable fit had been obtained.

The two techniques described above (the Fourier spectrum and least-squares method) are employed to analyse the MJUO photometric data for unknown periodicities. The analysis of each star makes use of both techniques. The rms residuals of the best fit to the observed data are compared for each method of analysis. In Chapter 3 the analysis of the RV Tauri stars of the RVa photometric type (constant mean magnitude) is described and Chapter 4 presents the analysis for the RVb subclass (varying mean magnitude).

Chapter 3

Photometry of the RVa stars

In this chapter, the stars belonging to the RVa subclass in the RV Tauri photometric programme are discussed individually. The photometric *BVRI* magnitudes and colour indices for the programme stars are presented in graphical form. The photometric data obtained for all the stars in the RV Tauri programme at MJUO are tabulated in Appendix A. The photometric data are analysed to search for any periodicities. Two different techniques are used to ensure that the dominant periodicities present in the data set are determined correctly.

The photometric data are initially analysed using the Lomb-Scargle Fourier method described in Chapter 2. Power spectra and synthetic curves are calculated using the computer program of W.A. Lawson (see Lawson et al. 1990). In the second method of analysis the dominant periodicities found in the data set, together with their associated amplitudes and phases, are used as initial conditions for a simultaneous least-squares fit of a number of sinusoids. The rms residuals of the various fits to the photometric data are compared for both techniques.

RU Cen is a typical example of the RVa subclass and a more detailed analysis and discussion of this star is presented in Section 3.1. The next three stars discussed in this chapter (AR Sgr, AD Aql and V453 Oph) show similar light variations to RU Cen and display reasonably regular light variations. The more irregular members of the RVa class (R Sct, RY Ara and V820 Cen) are presented at the end of the chapter.

3.1 RU Cen

3.1.1 Background

RU Cen was discovered to be a variable star by Kapteyn (1896), but the first period determination was completed by Hertzsprung (1928). Based on estimates from 669 Harvard plates, he concluded that RU Cen was an eclipsing binary of the β Lyrae type, with a period of 64.74 d and two minima of unequal depth.

Voûte (1932b) published estimates of the variable from photographic plates taken at Lembang from 1926 to 1932 and a mean light curve with a period of 64.789 d was presented. The main features of the mean light curve were its asymmetrical appearance, with the rise to both maxima being steeper than the descent to the minima and a larger than usual scatter in the observations, especially at secondary minimum.

Using estimates of the variable from photographic plates taken at Johannesburg, Rybka (1934, 1935) published a mean light curve of RU Cen which also showed irregularities. It was suggested at this stage that the variable was of the RV Tauri class.

Since these initial studies, subsequent observers and catalogues have alternatively classed RU Cen as an RV Tauri-type star or as an eclipsing binary. In 1961 O'Connell published a study of the light curve from 1926 to 1951, based on the estimates published by Voûte (1932b) and Rybka (1934, 1935) and his own estimates from 841 Riverview Observatory plates, which showed that RU Cen was a member of the RV Tauri class of variable. The period determined in this work, 64.727 ± 0.006 d, is the value quoted in most catalogues.

The General Catalogue of Variable Stars (Kholopov et al. 1985) gives a photographic magnitude range of 8.7–10.7. Few photoelectric data on RU Cen have been published. Light and colour curves in four-colour *uvby*, Hβ and *VRI* photometric systems were presented for RU Cen in Eggen's (1986) study of 20 supergiants of the RV Tauri and related classes.

A number of authors have obtained a few nights of optical and infrared photometry of selected RV Tauri stars in order to model the stellar and dust shell environment (Gehrz 1972, Gehrz & Ney 1972, Lloyd Evans 1985, Goldsmith et al. 1987).

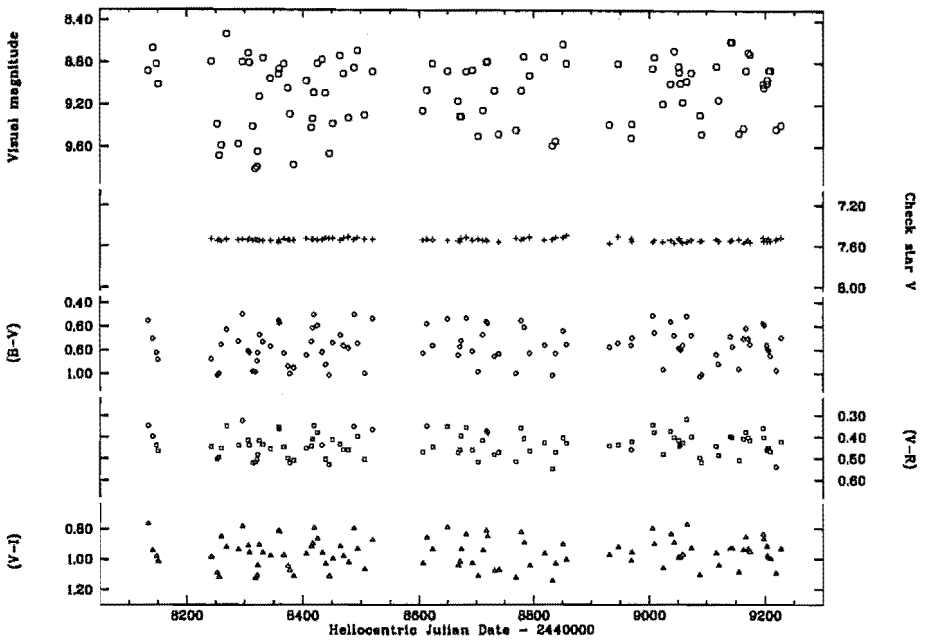

Figure 3.1: The V light and $(B–V)$, $(V–R)$ and $(V–I)$ colour curves for RU Cen.

3.1.2 Photometry from MJUO

Photometric *BVRI* observations of RU Cen were obtained with the B&C and OC 0.61-m telescopes at MJUO between 1990 August and 1993 August, during which a total of 103 night-averaged observations of RU Cen were obtained. SAO 223247 was the comparison star and an E-region standard, SAO 223263, was the check star (see Table 2.1). The internal accuracy of the V photometry is 0.014 magnitudes. The initial check star (SAO 223282) was replaced in 1990 September, when a close bright companion was unable to be excluded from the aperture when the check was being observed.

The V magnitudes and colour indices of RU Cen are displayed in Fig. 3.1. Also included on this graph are the V magnitudes for the check star. These are plotted on the same scale as the RU Cen V magnitudes to give a visual indication of the accuracy of the differential photometry. Individual B, R and I magnitudes were calculated from the photometric data and are presented together with the V magnitudes in Fig. 3.2.

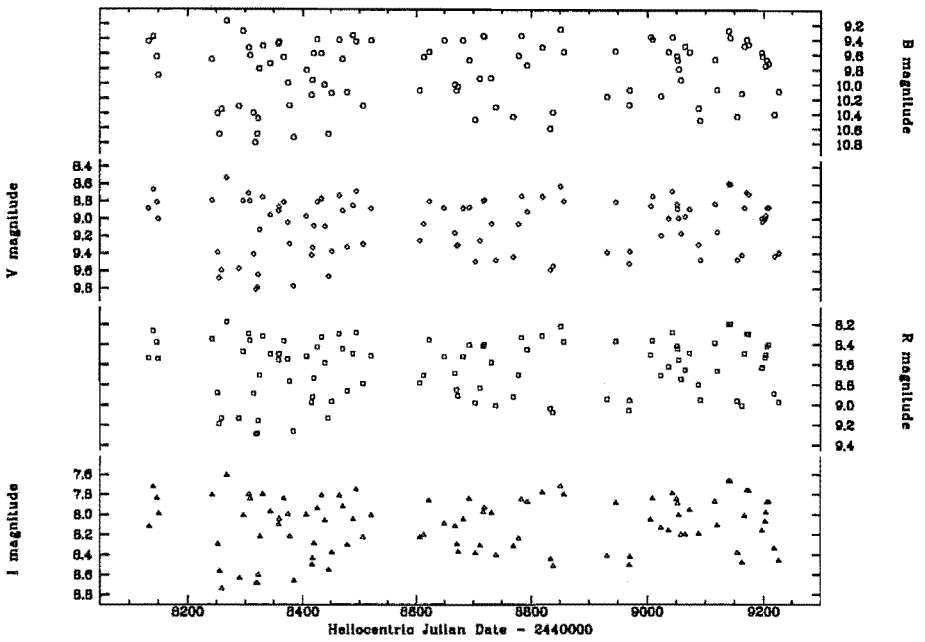

Figure 3.2: Individual B, V, R and I magnitudes for RU Cen.

3.1.3 Fourier analysis of the photometric data

The MJUO V photometric data for RU Cen were initially analysed using the Lomb-Scargle Fourier technique. The power spectrum for the RU Cen V photometry (see Fig. 3.3, solid line) shows an obvious peak at $f_1 = 0.03096\,\mathrm{d}^{-1}$ corresponding to a period of $P_1 = 32.30\,\mathrm{d}$.[1] The Lomb-Scargle false-alarm probability for the dominant peak is calculated in this case by estimating the noise from the power (or amplitude) spectrum itself. The estimated value of the amplitude signal-to-noise of 6.89 gives a value for the power signal-to-noise, Z, of 47.4. The derived value for the false-alarm probability using the equation $F = 1-(1-e^{-z})^M$ is 2.5×10^{-19} indicating that this peak is not due to chance fluctuations in the data set. The very high significance of this periodicity is not unexpected as it is well known that the light variations of RU Cen are extremely regular.

The natural window function for the particular photometric data spacing that was obtained for the RU Cen V photometry is shown in Fig. 3.3 (dotted line). Several small peaks in the power spectrum, particularly around the main peak,

[1] The reader is reminded that the 32.30 d period is the 'single' or 'fundamental' period which is defined as being the time interval between two successive minima. The 'double' or 'formal' period is the time interval between successive *deep* minima.

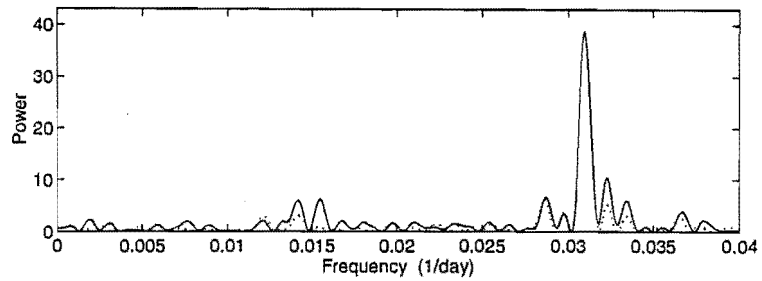

Figure 3.3: The power spectrum from the Fourier analysis of the V photometry for RU Cen (solid line). The dominant peak is at $f_1 = 0.03096\,\mathrm{d}^{-1}$ ($P_1 = 32.30\,\mathrm{d}$). The dotted line shows the natural window function.

are introduced by the window function. A peak at $f \sim 0.015\,\mathrm{d}^{-1}$ is seen to have higher power than can be attributed to the window function.

The 32.30 d period was subtracted from the photometric data and these 'prewhitened' data were reanalysed to search for further periodicities. The Fourier power spectrum for the prewhitened data (see Fig. 3.4) shows the next-most significant peak is found at a frequency of $0.01566\,\mathrm{d}^{-1}$ ($P_2 = 63.86\,\mathrm{d}$). This peak has an amplitude signal-to-noise of 4.45, and the corresponding Lomb-Scargle false-alarm probability is calculated to be 2.6×10^{-7}. This is also a very significant periodicity.

A synthetic light curve was then constructed as the sum of the identified periodicities using the derived values for the frequency, amplitude and onset phase for each constituent. Fig. 3.5 shows the comparison of the V photometric data for RU Cen and the synthetic light curve constructed as the sum of the two periodicities identified from the Fourier power spectra. It can be seen that this synthetic light curve represents the V photometric data very well, with the main differences being in the depths of the minima in the first season of observation.

The fact that the second period is almost double the first period results in an alternation of deep and shallow minima in the two-sinusoid fit to the photometric data. This deep–shallow alternation of minima in light curve is one of the characteristics that define the RV Tauri class of variables. If the first period is not *exactly* twice the second, the characteristic deep–shallow light curve will gradually become less well-defined. This can be seen occurring outside the range of the data for some of the synthetic light curve fits or in less well sampled regions of the long data set (see Fig. 3.5 HJD 2448900–2449300). Table 3.1 shows the

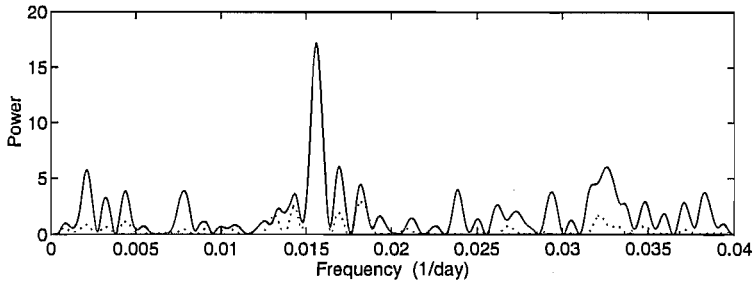

Figure 3.4: The Fourier power spectrum (solid line) for the RU Cen V photometry prewhitened for a period of 32.30 d. The largest peak is found at a frequency of 0.01566 d^{-1} ($P_2 = 63.86$ d). The dotted line is the natural window function.

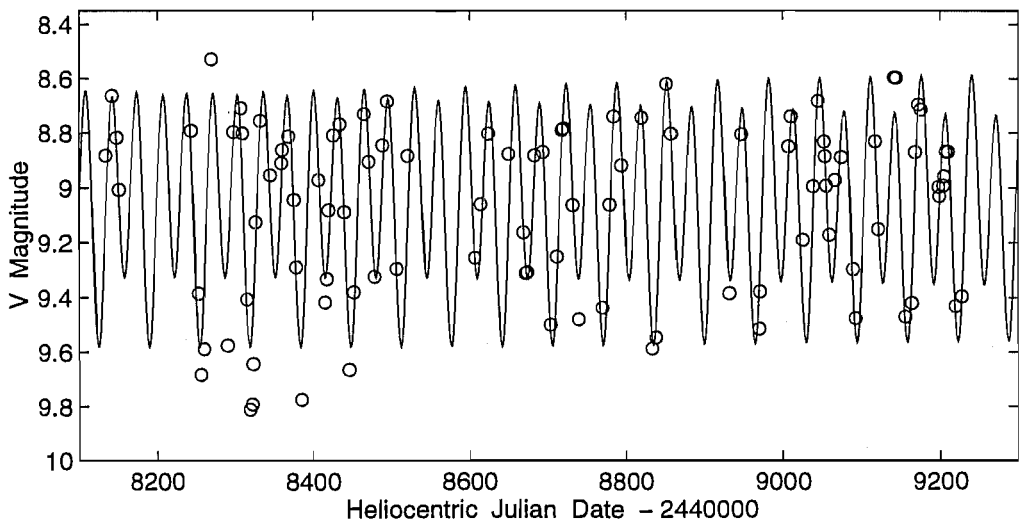

Figure 3.5: The two-period synthetic light curve fit to the RU Cen V photometry.

Table 3.1: The Fourier analysis of the B, V, R, I, $(B–V)$, $(V–R)$ and $(V–I)$ photometric data for RU Cen. Each data set consists of 100 photometric points, except for the $(V–I)$ and I data sets where there are 98 points.

Data	Fit[a]	f_1 (d^{-1})	P_1 (d)	A_1 (mag)	ϕ_1 (°)	f_2 (d^{-1})	P_2 (d)	A_2 (mag)	ϕ_2 (°)	rms
B	A	0.03098	32.28	0.48	109	–	–	–	–	0.227
	B	0.03098	32.28	0.48	109	0.01549	64.56	0.22	66	0.169
	C	0.03098	32.28	0.48	109	0.01558	64.18	0.23	47	0.166
V	A	0.03096	32.30	0.40	95	–	–	–	–	0.148
	B	0.03096	32.30	0.40	95	0.01548	64.60	0.12	64	0.121
	C	0.03096	32.30	0.40	95	0.01558	64.18	0.13	43	0.119
R	A	0.03096	32.30	0.37	88	–	–	–	–	0.119
	B	0.03096	32.30	0.37	88	0.01548	64.60	0.09	62	0.100
	C	0.03096	32.30	0.37	88	0.01558	64.18	0.09	42	0.099
I	A	0.03094	32.32	0.35	85	–	–	–	–	0.110
	B	0.03094	32.32	0.35	85	0.01547	64.64	0.07	65	0.097
	C	0.03094	32.32	0.35	85	0.01554	64.35	0.07	50	0.096
$B-V$	A	0.03104	32.22	0.17	148	–	–	–	–	0.089
	B	0.03104	32.22	0.17	148	0.01552	64.43	0.10	63	0.057
	C	0.03104	32.22	0.17	148	0.01556	64.18	0.10	54	0.057
$V-R$	A	0.03106	32.20	0.05	138	–	–	–	–	0.036
	B	0.03106	32.20	0.05	138	0.01553	64.39	0.03	54	0.027
	C	0.03106	32.20	0.05	138	0.01558	64.18	0.03	43	0.027
$V-I$	A	0.03106	32.20	0.10	138	–	–	–	–	0.062
	B	0.03106	32.20	0.10	138	0.01553	64.39	0.05	49	0.050
	C	0.03106	32.20	0.10	138	0.01560	64.10	0.05	34	0.049

[a]Fit A is fitting a single sinusoid of frequency f_1; Fit B is fitting one sinusoid plus its harmonic; Fit C is fitting two independent sinusoids.

Fourier components from the analysis of the RU Cen V photometry.

Another fit to the photometric data was obtained by setting the second period to be exactly twice the first period (that is, an $(f+2f)$ or 'harmonic' fit, where f is the frequency). The effect of fixing the second period in this manner is that the characteristic light curve is preserved with no variation in amplitude or shape, even outside the range of the data. This may have some greater relationship to the real physical situation where the form of the light variations is known to be extremely stable over several decades (O'Connell 1961).

Although it is clear that RU Cen exhibits extremely regular light variations, there are still disturbances or fluctuations in its light curve that remind us that the RV Tauri stars are actually semi-regular variables. RU Cen is known to possess variations in the depth of the 'shallower' or secondary minimum. In addition, 'flipping' or interchanges of deep and shallow minima have been observed to

occur in this particular star (O'Connell 1961) and for other stars of this class (for example, R Sct, see Lèbre 1991a and Section 3.5).

The periodicities, amplitudes and phases of the individual B, V, R and I magnitudes, together with the relative behaviour of $(B–V)$, $(V–R)$ and $(V–I)$ colour indices may hold important clues as to the nature (and cause) of the RV Tauri variability. To investigate the luminosity and colour variations in greater detail, the photometric B, R and I magnitudes were calculated and analysed via the Lomb-Scargle Fourier technique. The frequencies, periods, amplitudes and onset phases identified from the Fourier analyses are included in Table 3.1 and the power spectra are shown in Fig. 3.6. A trend of increasing amplitude for bluer filters is seen for both the 32 d and 64 d periodicities present in the photometric data. In addition, the onset phases show that the B variations lead the V, R and I variations by an average of 14°, 21° and 24° respectively.

It is assumed that the periods for the B, V, R and I data sets should be identical and calculate a mean period from the four individual analyses. This also gives us an estimate of the uncertainties in the identification of the dominant periodicities in the RU Cen photometry. However, the period determinations in the different filters are *not* independent due to the fact that the sampling is essentially the same. The standard deviation quoted will therefore be an underestimate of the uncertainty. The average frequency determined for the four data sets is $\overline{f_1} = (0.0310 \pm 0.0001)\,\mathrm{d}^{-1}$, which corresponds to a mean period of $\overline{P_1} = (32.30 \pm 0.01)\,\mathrm{d}$. For the second periodicity, a mean frequency of $\overline{f_2} = (0.0156 \pm 0.0002)\,\mathrm{d}^{-1}$ is determined, implying a mean period of $(\overline{P_2} = 64.23 \pm 0.07)\,\mathrm{d}$.

The power spectra for the photometric $(B–V)$, $(V–R)$ and $(V–I)$ data were also calculated. Table 3.1 shows that periods at ~ 32 d and ~ 64 d were found in the data sets. The amplitude of variation for both periodicities is largest in the $(B–V)$ data and smallest in the $(V–R)$ data. The $(V–R)$ and $(V–I)$ colours are virtually in phase and the $(B–V)$ colour curve has a slight phase lead. The colours are at their bluest as the V variations are rising to maximum light.

In order to examine the repeatability of the light and colour curves and to investigate the nature of the deviations from the mean light curve in greater detail, the photometric data were phased to a period of 64.60 d (twice the mean period of 32.30 d). The 64.60 d $(= 2\overline{P_1})$ period is used instead of the 64.2 d $(= \overline{P_2})$, since the former period is much more well-defined from the period analysis, and

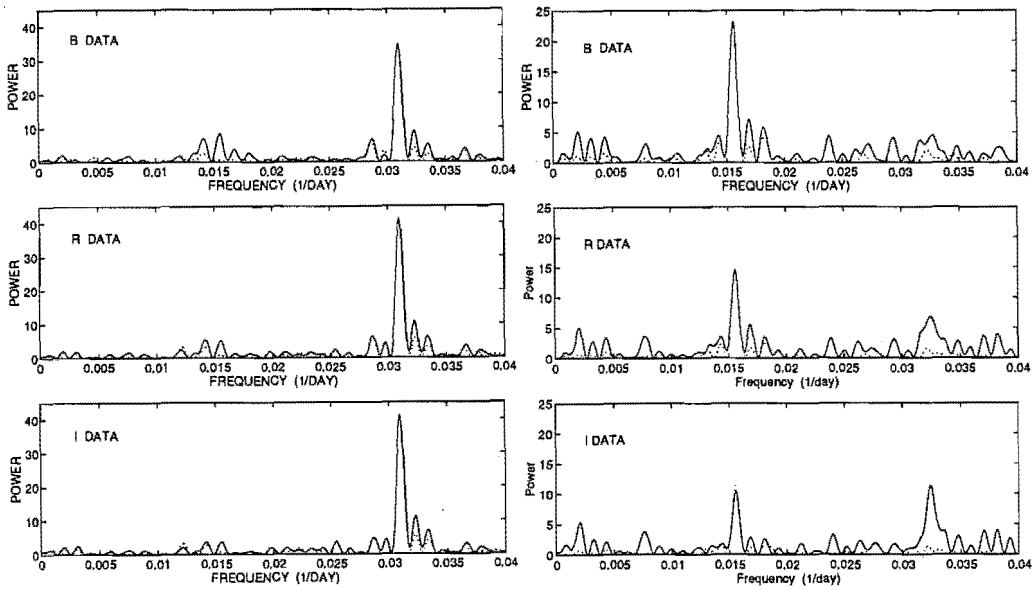

Figure 3.6: The Fourier power spectra for the B, R and I photometry for RU Cen. The dominant peaks occur at $\sim 0.0310\,\mathrm{d}^{-1}$ (left panels). The first periodicity was subtracted from the photometry and the recalculated power spectra (right panels) show peaks occurring at $\sim 0.0156\,\mathrm{d}^{-1}$.

is not derived from prewhitened data which may increase the uncertainties in the analysis. As discussed earlier, the use of the double period may be a more realistic model of the light variations. In addition, phasing to this period separates the primary and secondary minima, allowing the fluctuations in depth and shape of each type of minimum to be investigated.

The phased B, V, R and I photometric data are displayed in Fig. 3.7. The data from phases 1.0–2.0 are a repetition of those data from phase 0.0–1.0, so that the form of the B, V, R and I light curves can be appreciated more readily. The light curves in the different filters are all asymmetric, with the rise to both maxima being steeper than the descent to the minima. The mean light curves in the bluer filters have greater amplitudes and more asymmetrical appearances than the redder light curves. This is most obvious during the rise to maximum light (phase 0.0–0.3). The B light curve takes about 0.2 of a cycle to rise to maximum from primary minimum, whereas the I light curve takes about 0.3 of a cycle.

The phased light curves show there is a greater difference in the mean depths of the primary and secondary minima in the bluer filters. In the B filter, the difference in depth of the two types of minima is typically about 0.5 magnitude while for the I filter, the difference is less than 0.25 magnitudes. This effect can also be inferred from the amplitude of the f_2 periodicity, which decreases from 0.22 magnitudes in B to 0.07 magnitudes in I. When the second periodicity is much smaller than the first periodicity, as is the case here, the second periodicity can be thought of as a *modulation* of the depths of both the minima – increasing the depth of the primary minimum slightly while making the secondary minimum slightly shallower. This is true so long as the f_1 and f_2 components are approximately in phase at the primary minimum (phase=0.0).

The depth variations of the secondary minima (phase ~ 0.5) and the following maxima (phase ~ 0.7) are indicated by the larger scatter at these phases. This scatter is more apparent in the B and V filters than in the redder filters, indicating that variations may be present in the portion of the spectrum sampled by the B and, to a lesser extent, the V filter. The bluer filters tend to sample more of the line features in the spectrum, while the redder filters sample more of the stellar continuum. The increased scatter in the B filter is consistent with the fact that the strengths of the emission lines is observed to be the greatest during the rising branch of the V light curve (Preston et al. 1963). Observations show that

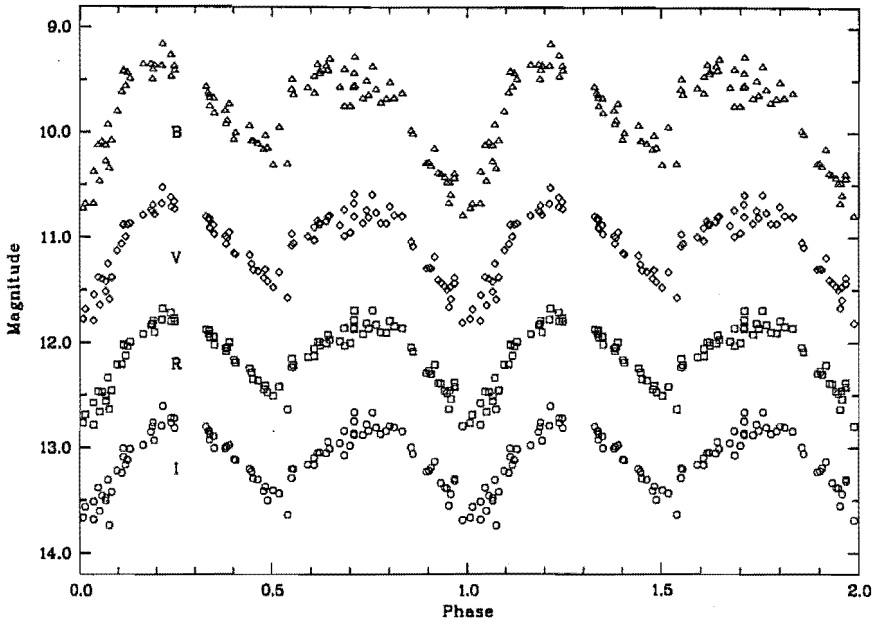

Figure 3.7: The phased (period = 64.60 d) B, V, R and I photometry for RU Cen. Offsets of 2.0, 3.5, 5.0 magnitudes have been applied for the V, R and I data respectively.

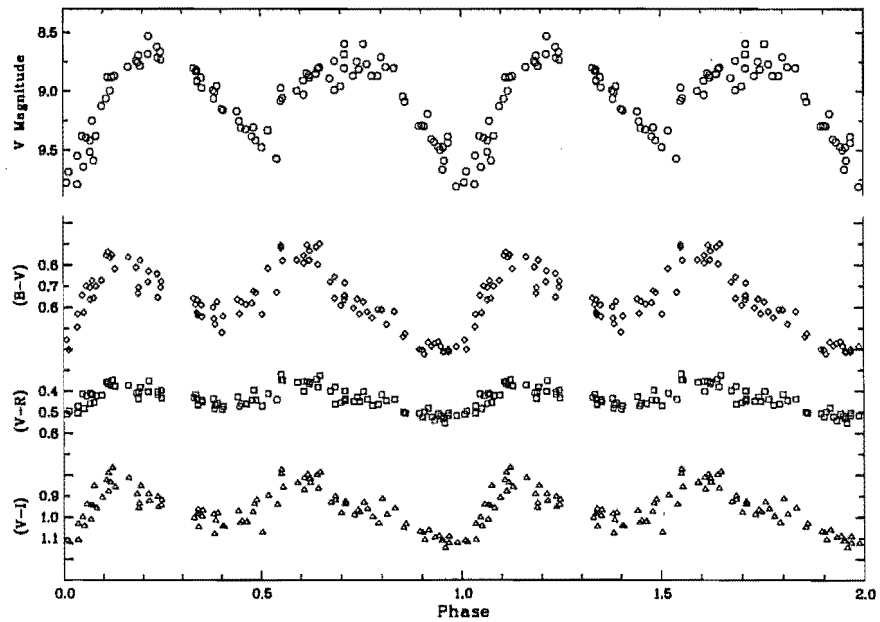

Figure 3.8: The phased V, $(B–V)$, $(V–R)$ and $(V–I)$ photometry for RU Cen.

the photometric colours are also very blue during these phases. Variations in the strength of the shock-produced emission lines (which appear in greater numbers in the bluer filters) may cause such photometric variations from cycle-to-cycle. However, we must be cautious of the possible effect of the Hα line, which shows highly variable emission and appears in the photometric R band. The variability of emission line strengths will be discussed further in Chapters 7 and 8, where an investigation of the spectroscopic variations in the RV Tauri stars is presented.

The phased $(B–V)$, $(V–R)$ and $(V–I)$ data are displayed in Fig. 3.8 with the V data included for reference. The colour curves are less symmetrical in appearance than the V light curve. The relative 'skewness' of the light and colour curves results in varying phase differences throughout a cycle. For instance, the minima of the colour curves occur about 0.05 in phase before the V light curve primary minimum (at phase ~ 0.0), but later in the cycle (at phase ~ 0.7) the maxima of the colour curves lead the mean light curve by about 0.15 in phase.

The primary minima of the colour curves are quite well defined and have less scatter than in the V light curve. The relative amplitudes of variation for the colour curves are obvious from this figure, with the smallest maximum-to-mean amplitude of 0.05 mag displayed by the $(V–R)$ curve. The relative flatness of the $(V–R)$ curve may reflect the fact that these stars' flux distributions peak at around 525–725 nm so that the $(V–R)$[2] colour index tends to sample across the peak of the flux distribution. It is also possible that there are anomalous features present which can cause peculiar effects in the $(V–R)$ colour index. Features such as the Hα line and the molecular bands of TiO, of which there are several strong examples in the photometric R band, could cause colour anomalies.

The next step in the analysis of the light variations of RU Cen is to investigate any amplitude changes that may be present. By re-inspecting Fig. 3.5, it can be seen that the amplitude of the V variations appears to be different in each of the observing seasons, with 1991 (HJD 2448200–2448500) data displaying a larger amplitude of variation than the 1992 or 1993 data. To investigate this further, the V photometry was divided into the individual years of observation. The data from each year were then analysed separately to determine if any amplitude variations were apparent. The power spectra obtained from an analysis of the V photometry for the three individual years is displayed in Fig. 3.9. The panels on the left indicate that the dominant period for each year is around 32 d. This

[2]The effective wavelengths of the V and R filters for a K5 star are 549 nm and 676 nm respectively (Bessell 1979).

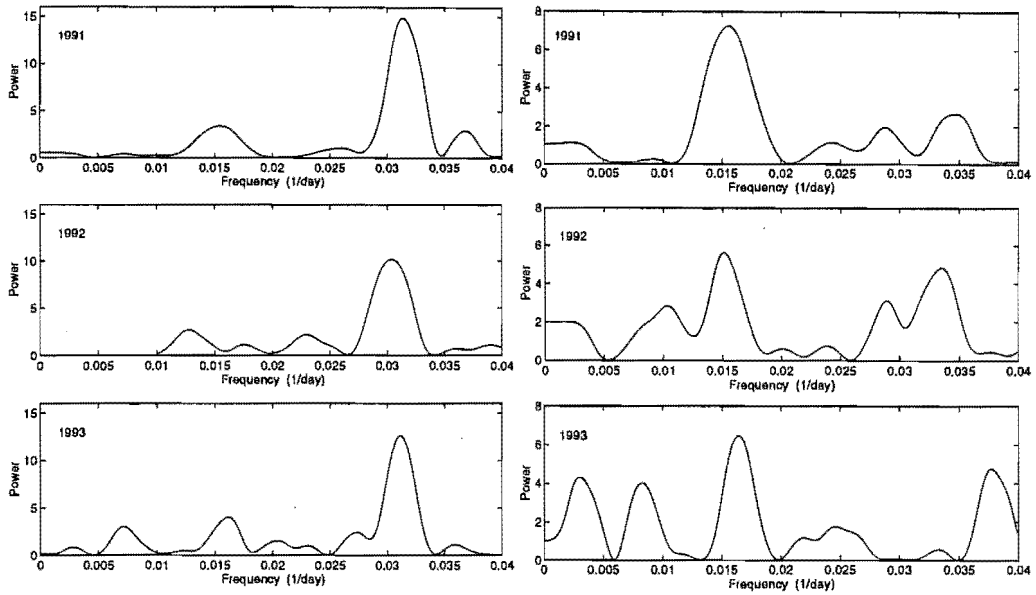

Figure 3.9: The Fourier power spectra for the 1991, 1992 and 1993 V photometry for RU Cen.

Table 3.2: The analysis of the individual years of RU Cen V photometry.

Data	N^a	f_1 (d^{-1})	P_1 (d)	A_1 (mag)	ϕ_1 (°)	f_2 (d^{-1})	P_2 (d)	A_2 (mag)	ϕ_2 (°)
all	100	0.03096	32.30	0.40	95	0.01558	64.19	0.15	43
1991	38	0.03136	32.89	0.45	216	0.01546	64.27	0.15	293
1992	24	0.03038	32.92	0.41	5	0.01510	66.23	0.12	206
1993	34	0.03118	32.07	0.35	335	0.01644	60.83	0.13	124

[a] N is the number of data points

constituent was then subtracted from the corresponding data set and each year was reanalysed for further periodicities (right panels). In each case, the second most significant peak occurs at ~ 64 d or about double the first period.

The amplitudes, phases and periods derived from the Fourier analysis of the entire V data set, together with the results for the individual years, are shown in Table 3.2. The amplitude for the dominant frequency f_1 seems to decrease year by year, whereas the amplitude of the second frequency f_2 is smallest in 1992 and largest in 1991.

A comparison between the yearly fits and the fit derived for the entire data set is plotted together with the V photometric data in Fig. 3.10. Also displayed

in this figure is the synthetic light curve obtained by setting the second period to be exactly twice the 32.30 d period (as was used previously for the phasing of the data). There is little difference between the synthetic light curves from the original ($P_1 = 32.30$ d, $P_2 = 64.3$ d) fit and the fit with the second period fixed ($P_1 = 32.30$ d, $P_2 = 64.60$ d). The largest difference is in less well-sampled regions of the long data set and in the brightness of the maxima in the 1993 season.

There are several interesting features displayed in Fig. 3.10. In the 1991 data, the primary minima are reasonably deep (~ 9.7 mag). The secondary minimum at HJD ~ 2448285 is almost as deep as the primary minima, whereas two out of the three secondary minima that have been sampled appear to be shallower (~ 9.3 mag). A similar effect is seen in 1992. One secondary minimum is seen to be almost as deep as the primary minima and most of the other secondary minima appear to be shallower.The 1993 data show evidence of some very shallow secondary minima, which also appear to have quite asymmetric shapes and be offset in phase. The minimum at HJD $\sim$2449200 is a good example of this. Such minima have also been seen in previous studies of RU Cen (Voûte 1932b, O'Connell 1961), where large variations in the depth and shape of the secondary minima are noted.

It is possible that the apparent amplitude change from 1991 to 1993 is due to poor sampling in the data sets since, for instance, the 1992 data set contains only 24 point for the entire season. To determine whether the yearly data is sampled at a reasonable range of phases, a plot of phase versus V magnitude was constructed for the individual years (see Fig. 3.11). The V photometric data are phased using the 64.60 d period.

There are few data points defining the primary minimum (phase ~ 0.0) in the 1993 data, so that the actual mean depth of the minima during this year will be fainter than ~ 9.6. In 1992, the data are poorly sampled over the descent to primary minima (phase range 0.8–0.95) and at the minimum itself (also see Fig. 3.10). Thus, it is possible that there are amplitude variations over the years 1991–1993, but poor phase sampling prior to and including the primary minima in 1992 and 1993 decreases the accuracy of the calculated amplitudes. Although amplitude variations in RU Cen have been noted in previous studies, these seem to occur in a random manner and mean light curves derived from decades of photographic data indicate that the long-term mean amplitude is relatively constant.

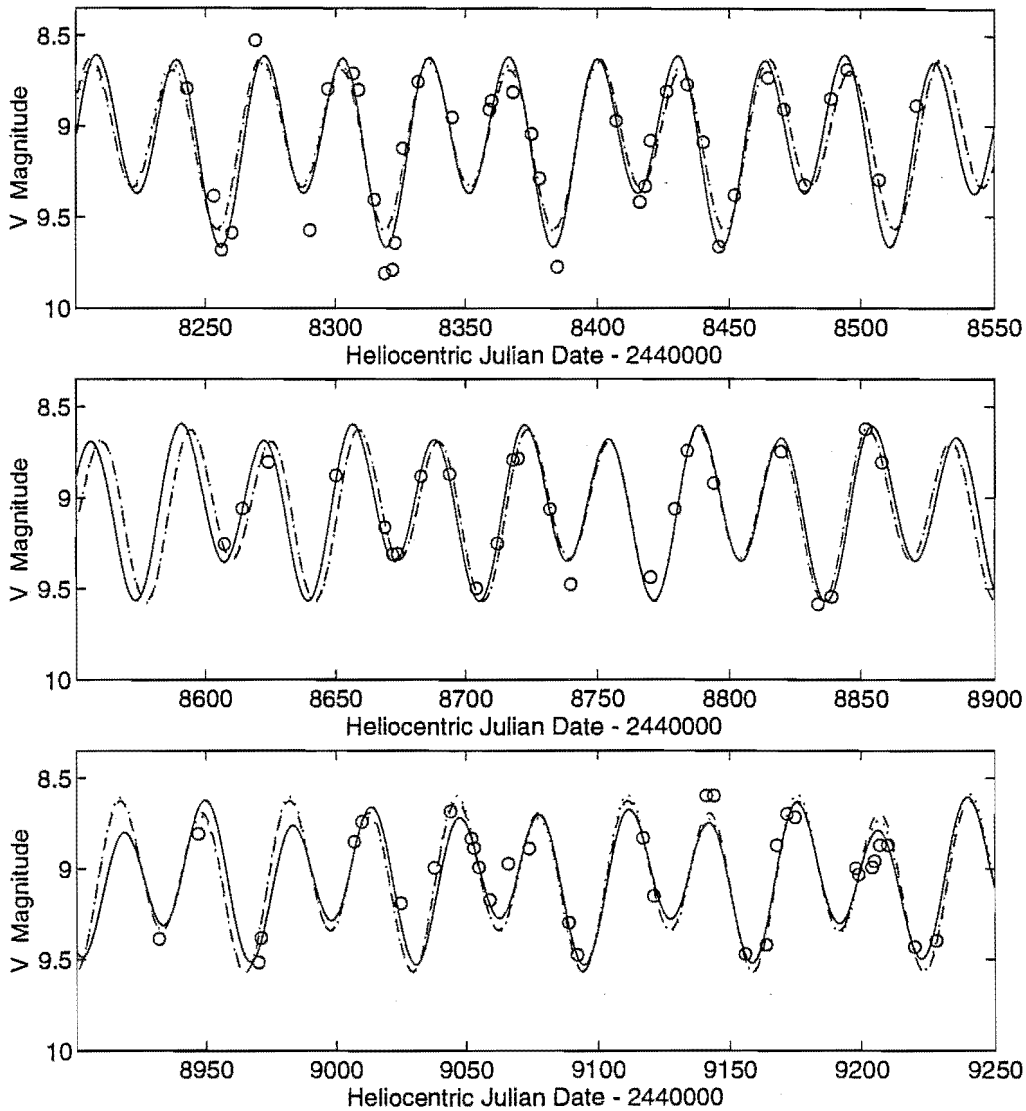

Figure 3.10: The synthetic light curves for the RU Cen V photometry. The fit to all the V photometry (dotted line) and the fit obtained from analysing each year of data individually (solid line) are compared with the harmonic fit (dashed line) obtained by fixing the second period at exactly twice the dominant 32.30 d period. Top to bottom: 1991, 1992, 1993.

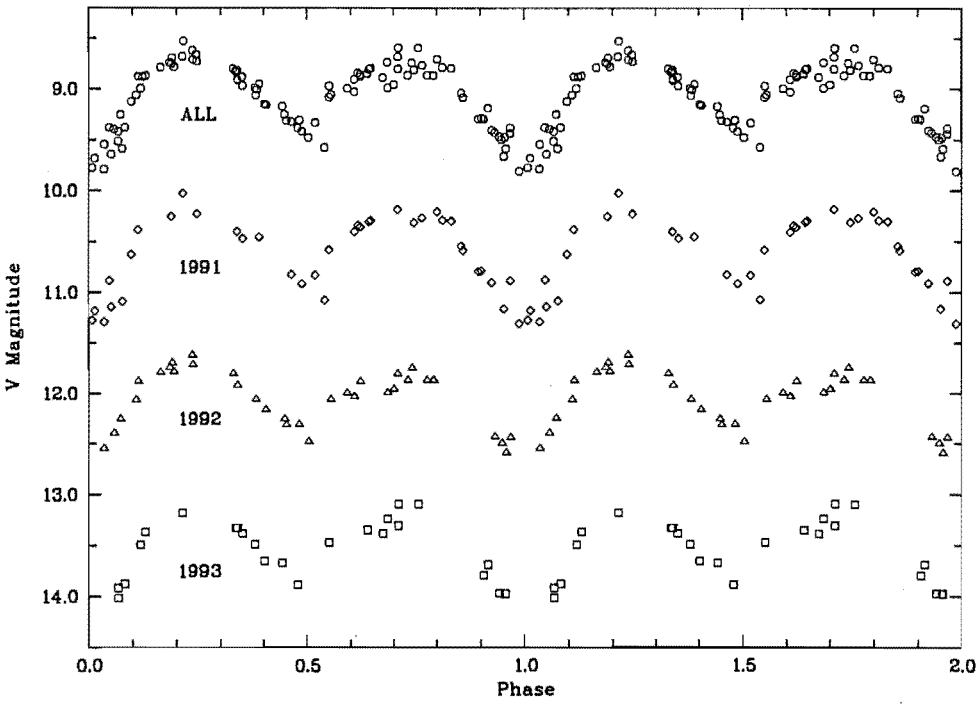

Figure 3.11: The 1991, 1992 and 1993 RU Cen V photometry plotted versus phase. This figure shows the phase coverage obtained in each year of observation.

In their photographic studies of the light curve of RU Cen, both Hertzsprung (1928) and O'Connell (1961) noted that the maximum following the secondary minimum tended to be fainter than that following the primary minimum, especially if the secondary minimum was relatively shallow. This characteristic is also evident in the MJUO RU Cen data in Fig. 3.10. The shallow secondary minimum at HJD $\sim$ 2449200 is one example of this effect. In addition, Fig. 3.11 shows that the secondary maximum (phase 0.6–0.8) has more scatter when there are larger variations in the depth of the secondary minimum, as occurred in 1993.

3.1.4 Least-squares analysis of photometric data

In this second method of analysing the photometric data for RU Cen, the dominant periodicities previously found using the Lomb-Scargle Fourier technique were used as initial conditions for a simultaneous least-squares fit of a number of sinusoids. This avoided the need to prewhiten the data or fix the values of any of the parameters describing each constituent signal.

The individual B, V, R and I magnitudes were analysed by the least-squares method. First, a one-sinusoid fit was made to each of the data sets using the f_1 periodicity found using the Fourier technique as the starting point. This fit was done in order to make a comparison with the Lomb-Scargle technique and to verify that f_1 has been correctly identified. Second, a two-sinusoid 'harmonic' ($f_1 + 2f_1$) fit was used to model the photometric data. Third, a two-sinusoid fit was calculated using the previously identified f_1 and f_2 periodicities (from the Fourier analyses) as initial conditions. The (B–V), (V–R) and (V–I) photometric data were analysed in exactly the same way. Table 3.3 presents the results of the least-squares analyses for the individual magnitudes and for the colour data.

It can be seen that the dominant periodicities are those that define the deep–shallow nature of the variations, and not the skewness of the light curve. The results using the two analysis techniques are quite similar, with the rms residuals for the least-squares technique being slightly less than those obtained from the Lomb-Scargle Fourier method. This is a confirmation of what Lomb (1976) found when comparing the Fourier spectrum (or periodogram) method to Vaníček's (1971) simultaneous least-squares analysis, namely that "This scheme [Vaníček's] ...provides only a marginal improvement to the accuracy of the simple LS [periodogram] spectrum".

Table 3.4 presents a comparison of the two analysis techniques for the B

Table 3.3: The least-squares analyses of the RU Cen photometric data. Each data set consists of 100 photometric points, except for the $(V–I)$ and I data sets where there are 98 points.

Data	Fit[a]	f_1 (d^{-1})	P_1 (d)	A_1 (mag)	ϕ_1 (°)	f_2 (d^{-1})	P_2 (d)	A_2 (mag)	ϕ_2 (°)	rms
B	A	0.03098	32.28	0.48	109	–	–	–	–	0.227
	B	0.03101	32.25	0.47	107	0.01550	64.50	0.22	62	0.166
	C	0.03100	32.26	0.48	109	0.01558	64.18	0.22	46	0.164
V	A	0.03095	32.31	0.41	96	–	–	–	–	0.147
	B	0.03097	32.29	0.39	94	0.01549	64.58	0.12	63	0.121
	C	0.03097	32.29	0.40	96	0.01559	64.14	0.12	41	0.119
R	A	0.03095	32.31	0.38	89	–	–	–	–	0.117
	B	0.03096	32.30	0.37	88	0.01548	64.60	0.09	62	0.099
	C	0.03096	32.30	0.37	89	0.01558	64.17	0.09	41	0.098
I	A	0.03095	32.31	0.37	84	–	–	–	–	0.108
	B	0.03095	32.31	0.36	83	0.01548	64.62	0.07	66	0.096
	C	0.03095	32.31	0.36	84	0.01557	64.24	0.07	47	0.095
$B-V$	A	0.03104	32.22	0.16	149	–	–	–	–	0.089
	B	0.03105	32.21	0.17	150	0.01552	64.42	0.10	61	0.057
	C	0.03104	32.22	0.17	151	0.01555	64.29	0.10	55	0.056
$V-R$	A	0.03105	32.20	0.06	139	–	–	–	–	0.036
	B	0.03107	32.18	0.06	139	0.01554	64.37	0.03	52	0.027
	C	0.03106	32.20	0.06	141	0.01558	64.19	0.03	42	0.027
$V-I$	A	0.03105	32.21	0.10	141	–	–	–	–	0.061
	B	0.03106	32.19	0.11	141	0.01553	64.38	0.05	48	0.049
	C	0.03105	32.21	0.11	143	0.01560	64.12	0.05	35	0.048

[a]Fit A is fitting a single sinusoid of frequency f_1; Fit B is fitting one sinusoid plus its harmonic; Fit C is fitting two independent sinusoids.

Table 3.4: A comparison of the Fourier and least-squares analysis for the RU Cen B photometry. The Δ symbol represents the absolute difference between the parameters derived using the two different techniques.

Fit[a]	Technique	f_1 (d^{-1})	A_1 (mag)	ϕ_1 (°)	f_2 (d^{-1})	A_2 (mag)	ϕ_2 (°)	rms
B	Fourier	0.03098	0.48	109	0.01549	0.22	66	0.169
	Least-squares	0.03101	0.47	107	0.01550	0.22	62	0.166
	Δ	0.00003	0.01	2	0.00001	0.00	4	0.003
C	Fourier	0.03098	0.48	109	0.01558	0.23	47	0.166
	Least-squares	0.03100	0.48	109	0.01558	0.22	46	0.164
	Δ	0.00002	0.00	0	0.00000	0.01	1	0.002

[a]Fit B is fitting one sinusoid plus its harmonic; Fit C is fitting two independent sinusoids.

photometry of RU Cen. The largest differences between the parameters derived using the two methods are obtained for the B filter and thus this table shows the largest uncertainties introduced by the choice of analysis technique. For each light and colour curve, the $(f_1 + f_2)$ fit returns the smallest residuals, although this is often only marginally better that the $(f + 2f)$ fit. Using the $(f + 2f)$ fit has the advantage that the RV Tauri-like light curve is defined outside the range of the photometric data and thus may be a better model of the long-term pulsations in the star. This fit also has the advantage of being able to predict the times of maxima and minima. In the subsequent analyses of the additional programme stars of the RVa subtype, the harmonic $(f + 2f)$ fit was adopted as the more realistic model of the photometric variations in the RV Tauri stars. Only the harmonic fit results are tabulated. The fits using the Fourier and the least-squares techniques are presented and the residuals are compared for both techniques.

3.2 AR Sgr

3.2.1 Background

AR Sgr was discovered early this century and was originally thought to be a classical Cepheid with a period of 44 d. From Harvard plates taken between 1915 and 1920, Gerasimovič (1929) showed that AR Sgr was a RV Tauri variable with a 'fundamental' period (the time between successive minima) of 44.45 d

corresponding to a double period of 88.90 d. The observed range in photographic brightness was 9.5–11.5. Payne-Gaposchkin et al. (1943) estimated the brightness of AR Sgr on 874 photographic plates. The derived period and epoch are 87.87 d and JD 24421113.1 respectively, with a photographic brightness ranging from 9.6 to 11.5. Sky Catalogue 2000.0 (Hirshfeld & Sinnott 1985) classifies AR Sgr as an RV Tauri star with no subclass designation. The range of the photographic variations is stated as 9.1–13.5.

3.2.2 Photometry from MJUO

AR Sgr was added to the RV Tauri programme in 1991 August. Between this date and 1993 November, a total of 55 night-averaged *BVRI* photometric observations were obtained using the B&C and the OC 0.61-m telescopes. Table 2.1 shows the position and adopted photometric magnitudes for the comparison star (SAO 187581) and the check star (SAO 187582) that were used in obtaining the differential photometry. The internal accuracy of the V photometry is 0.009 magnitudes.

The V magnitudes and colour indices for AR Sgr are displayed in Fig. 3.12. The V magnitudes for the check star SAO 187582 are included in this figure and are plotted on the same scale as for AR Sgr to give a visual indication of the internal accuracy of the differential photometry. Individual B, R and I magnitudes were calculated from the photometric data and are presented in Fig. 3.13.

3.2.3 Analysis of the photometric data

The photometric data for AR Sgr were analysed to search for the dominant periodicities. The Fourier power spectra obtained from the analysis of the AR Sgr V photometry are shown in Fig. 3.14. The top panel shows the dominant periodicity occurs at $f_1 = 0.02240\,\mathrm{d}^{-1}$ ($P_1 = 44.64\,\mathrm{d}$) and the lower panel shows the power spectrum obtained after the V photometry has been prewhitened for the 44 d period. The second periodicity occurs at $f_2 = 0.01120\,\mathrm{d}^{-1}$ ($P_2 = 89.29\,\mathrm{d}$). The natural window function is represented by the dotted line in each panel. The power spectra from the analysis of the (B–V) photometry are shown in Fig. 3.15. The dominant periodicity obtained in this case is the 88 d period (upper panel) with the 44 d period obtained once the 88 d constituent had been subtracted from the data (lower panel).

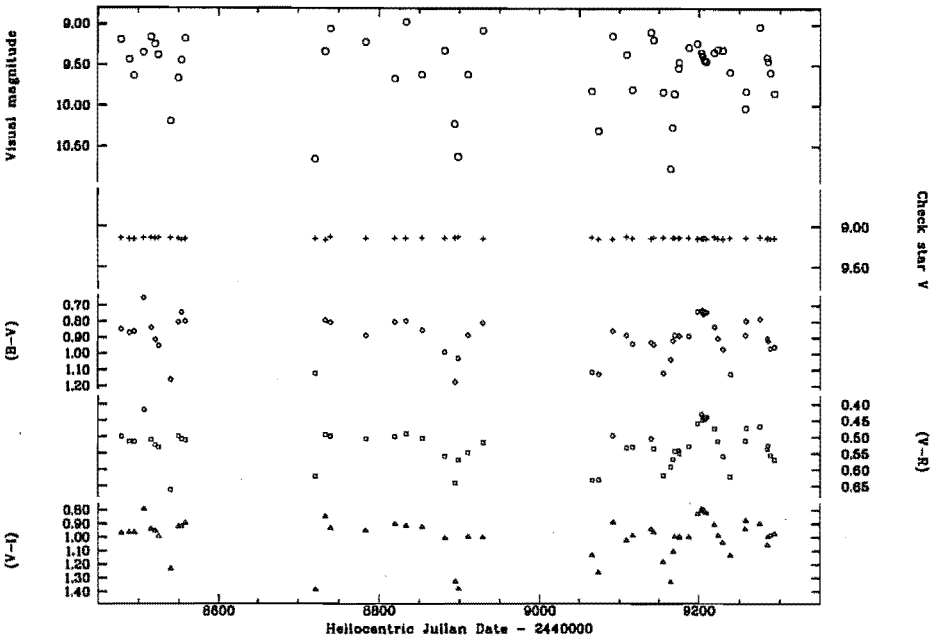

Figure 3.12: The V light and $(B–V)$, $(V–R)$ and $(V–I)$ colour curves for AR Sgr.

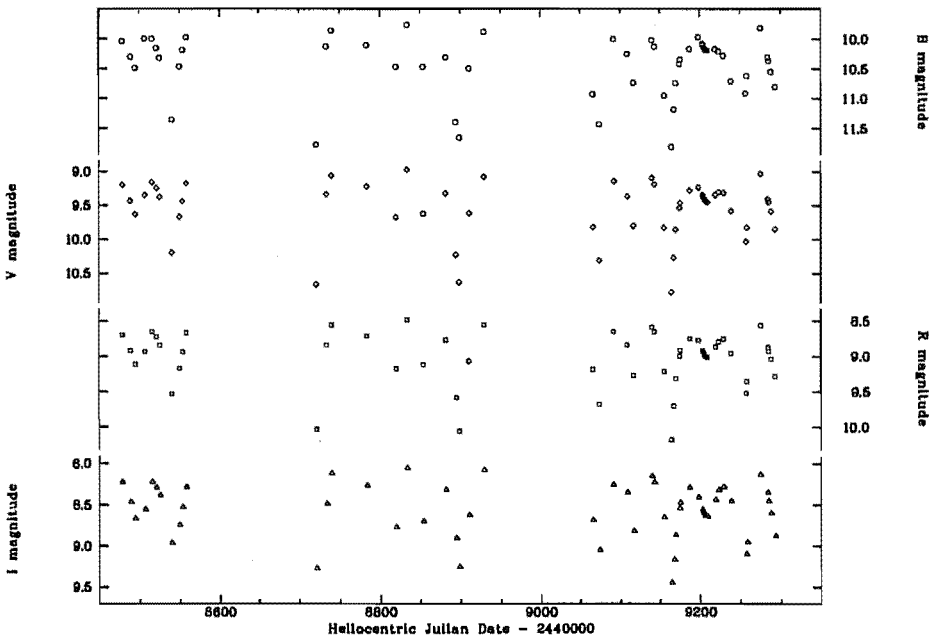

Figure 3.13: Individual B, V, R and I magnitudes for AR Sgr.

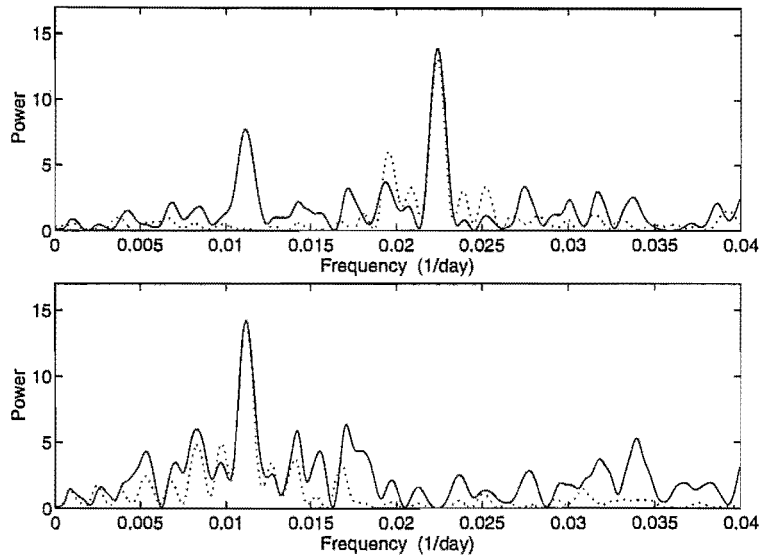

Figure 3.14: The Fourier power spectra from the analysis of the AR Sgr V photometry. The dominant peaks occur at 0.02240 d^{-1} (upper panel) and 0.01120 d^{-1} (lower panel) corresponding to periods of 44.64 d and 89.29 d respectively. The dotted line shows the natural window function.

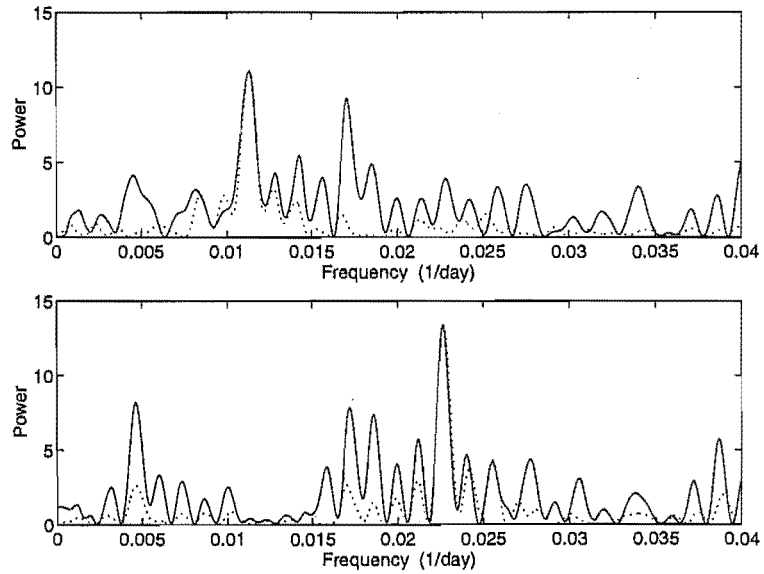

Figure 3.15: The Fourier power spectra from the analysis of the AR Sgr (B–V) photometry. The dominant peaks occur at 0.01132 d^{-1} (upper panel) and 0.02264 d^{-1} (lower panel) corresponding to periods of 88.34 d and 44.17 d respectively. The dotted line shows the natural window function.

Table 3.5: The analysis of the photometric data for AR Sgr. Each data set consists of 55 photometric points.

Data	Fit[a]	f_1 (d^{-1})	P_1 (d)	A_1 (mag)	ϕ_1 (°)	f_2 (d^{-1})	P_2 (d)	A_2 (mag)	ϕ_2 (°)	rms
B	F	0.02236	44.72	0.47	228	0.01118	88.45	0.39	134	0.268
	L	0.02252	44.41	0.47	227	0.01126	88.82	0.48	119	0.222
V	F	0.02240	44.64	0.41	216	0.01120	89.29	0.31	125	0.200
	L	0.02250	44.43	0.42	217	0.01125	88.87	0.34	116	0.173
R	F	0.02242	44.60	0.45	210	0.01121	89.21	0.23	125	0.180
	L	0.02250	44.45	0.41	213	0.01125	88.90	0.28	115	0.158
I	F	0.02246	44.52	0.37	201	0.01123	89.05	0.16	120	0.123
	L	0.02251	44.42	0.37	203	0.01126	88.84	0.19	114	0.112
$B-V$	F	0.01132	88.34	0.13	131	0.02264	44.17	0.10	264	0.067
	L	0.01131	88.39	0.14	121	0.02263	44.20	0.11	267	0.065
$V-R$	F	0.01130	88.50	0.05	117	0.02260	44.25	0.04	270	0.033
	L	0.01132	88.34	0.06	107	0.02264	44.17	0.05	264	0.031
$V-I$	F	0.01126	88.81	0.14	120	0.02252	44.40	0.10	269	0.092
	L	0.01132	88.32	0.15	105	0.02264	44.16	0.11	251	0.088

[a]F is the Fourier harmonic fit; L is the least-squares harmonic fit.

As was found for RU Cen, the harmonic ($f+2f$) fit and the two-independent-frequencies (f_1+f_2) fit give very similar synthetic curves and rms errors. Table 3.5 displays the results of the harmonic fit for both the Fourier method and the least-squares technique. The latter technique gives smaller rms residuals, particularly for the analysis of the light curves. The periods derived from the analysis of the B, V, R and I data for AR Sgr using the least-squares technique and the harmonic fit were used to determine the average period and uncertainties associated with this determination. A mean period of (44.43 ± 0.01) d was determined which corresponds to a double period of (88.86 ± 0.03) d. As was seen in RU Cen, the amplitudes of the light variations tend to be larger in the bluer filters and the B light curve has an increasing lead over the V, R and I light curves.

The photometric data for AR Sgr were phased using the 88.86 d (double) period in order to separate the primary and secondary minima. Fig. 3.16 displays the phased B, V, R and I photometric data. There are many similarities that can be drawn with RU Cen. There is a trend of increasing asymmetry for bluer colours in the shape of the individual B, V, R and I light curves. As was seen in RU Cen, there is much more scatter in the bluer light curves than the redder light curves, which is possibly linked to the presence of (variable strength) emission lines at particular phases. The amplitude of variation in the B, V, R and I filters

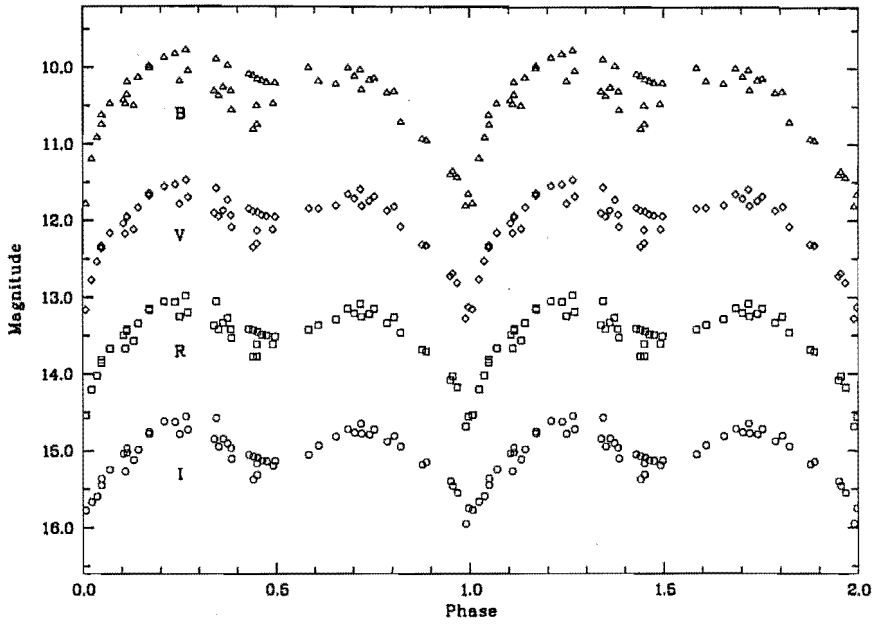

Figure 3.16: The phased (period = 88.86 d) B, V, R and I photometry for AR Sgr. Offsets of 2.5, 4.5, 6.5 magnitudes have been applied to the V, R and I data respectively.

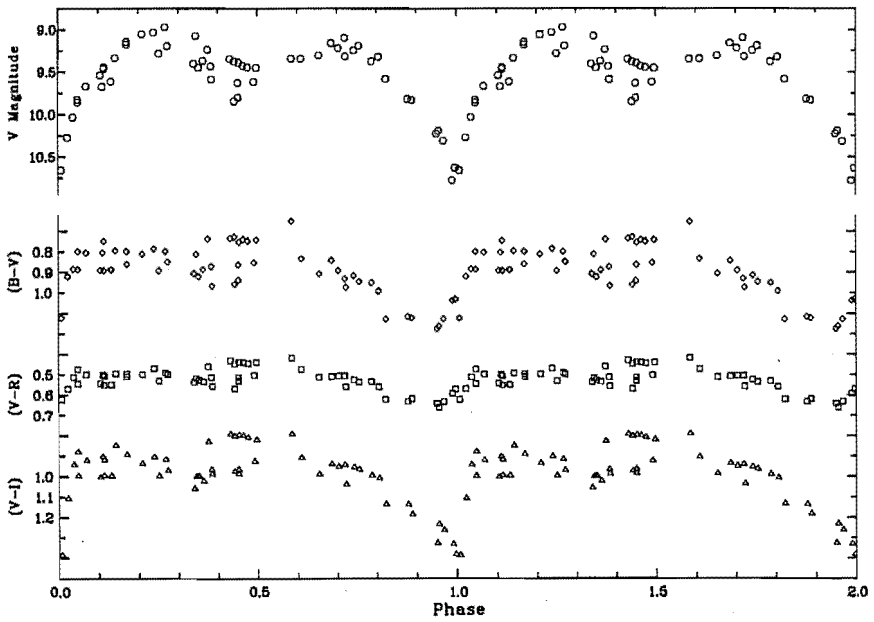

Figure 3.17: The phased V, $(B\text{–}V)$, $(V\text{–}R)$ and $(V\text{–}I)$ photometry for AR Sgr.

for AR Sgr are very similar to RU Cen for the f_1 component (the 44 d period in AR Sgr), but the amplitudes of f_2 component (the 88 d period in AR Sgr) are more than twice as large as those in RU Cen. This leads to a larger depth of the primary minimum in AR Sgr and a greater difference in the depths of the primary and secondary minima.

Of particular interest is the behaviour of the star's photometric light and colour curves during the variable secondary minimum and following maximum. An increased scatter at these phases (0.3–0.7) is obvious in the figure and cycle-to-cycle variations are readily apparent. There is a possible phase shift in the secondary minima with 'deeper' secondary minima reaching their faintest before the 'shallower' secondary minima. However, this effect may only be due to the relatively small number of secondary minima sampled and further photometric data, covering the secondary minima in particular, would be useful. In the Fourier analysis of the colour curves for AR Sgr, the double (88 d) period was found to be the dominant period in the data sets. The phased colour curves (Fig. 3.17) indicate why this is so. The reddening of the colours prior to the primary minimum in the V light curve is readily apparent in all the colour curves. However, prior to the secondary minimum in the V light, the colours curves show an increased amount of scatter but do not tend to become much redder. For the *mean* colour curves, the secondary minimum colour changes are thus very small and the 44 d period becomes less distinct for the colour curves.

One secondary minimum (at HJD $\sim$ 2449210) has been sampled reasonably well with six photometric points following the star's descent to a very shallow minimum. The colour variations during this minimum are quite intriguing. For the six points defining the shallowest secondary minimum, the $(B–V)$, $(V–R)$ and $(V–I)$ colours are, in actual fact, very blue. By identifying specific photometric points, it can be determined that the deeper secondary minima and redder colours are closely correlated between phases 0.4–0.5. The scatter in the depths of the secondary minima result in an increased scatter in the colours at phases 0.3–0.5.

It can be seen that the colour curves are quite asymmetric with the $(V–I)$ curve, in particular, having an extremely steep rise at primary minimum. The $(V–I)$ colour curve has the largest amplitude of the colours. As was seen in RU Cen, the $(V–R)$ curve for AR Sgr is very flat. The amplitudes of the f_1 component (the 44 d period) and the f_2 component (the 88 d period) are very similar for each colour curve, resulting in a much greater difference in the colour

changes between the primary and secondary minima.

3.3 AD Aql

3.3.1 Background

Very few observations have been obtained of this star – its relative faintness making it a difficult target for visual observers and less popular for long-term photoelectric observations with smaller telescopes.

A total of 270 visual observations were obtained of AD Aql between 1925 April and 1929 September (as reported by Brancewicz et al. 1976), but these data were unable to be obtained by the author. DuPuy (1973) observed a number of RV Tauri stars photoelectrically including five *UBVR* observations of AD Aql. Although the range in V is quoted as being 8.83–13.42, the 8.83 measurement is probably in error with the other points giving a range of 11.27–13.52. The General Catalogue of Variable Stars (Kholopov et al. 1985) gives the range in photographic magnitude for AD Aql as 11.5–13.5, with a period of 65.4 d and classifies it as a member of the RVa subclass.

3.3.2 Photometry from MJUO

Between 1990 August and 1992 November a total of 46 *BVRI* night-averaged photometric observations were obtained for AD Aql on the 0.61-m B&C and OC telescopes at MJUO. The comparison and check stars used were SAO 142864 and SAO 142916 respectively. The adopted magnitude and colour values for the comparison and check stars are given in Table 2.1. Figs 3.18 and 3.19 present the photometric data obtained at MJUO in graphical form. The internal accuracy of the AD Aql V photometry of 0.009 magnitudes is determined from the scatter in the check's V magnitudes. Due to the relative faintness of AD Aql (which is ~ 3 mag fainter than RU Cen and ~ 2 magnitudes fainter than AR Sgr), the precision of the photometry may be slightly less than indicated by the check due to the increased importance of the background sky counts. For the I filter in particular, where the counts are relatively low, there may be an increased amount of scatter in the data.

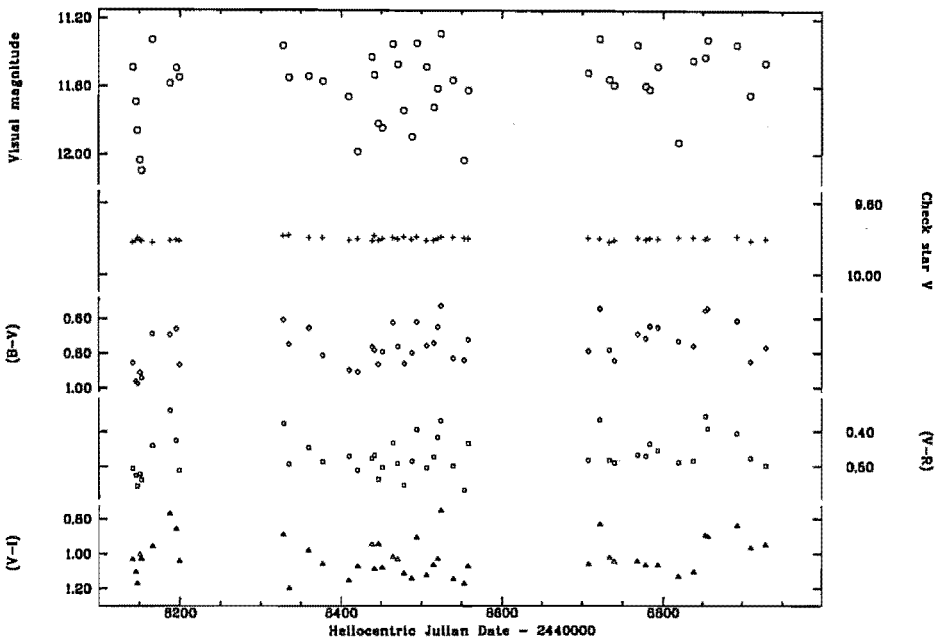

Figure 3.18: The V light curve and the $(B–V)$, $(V–R)$ $(V–I)$ colour curves for AD Aql.

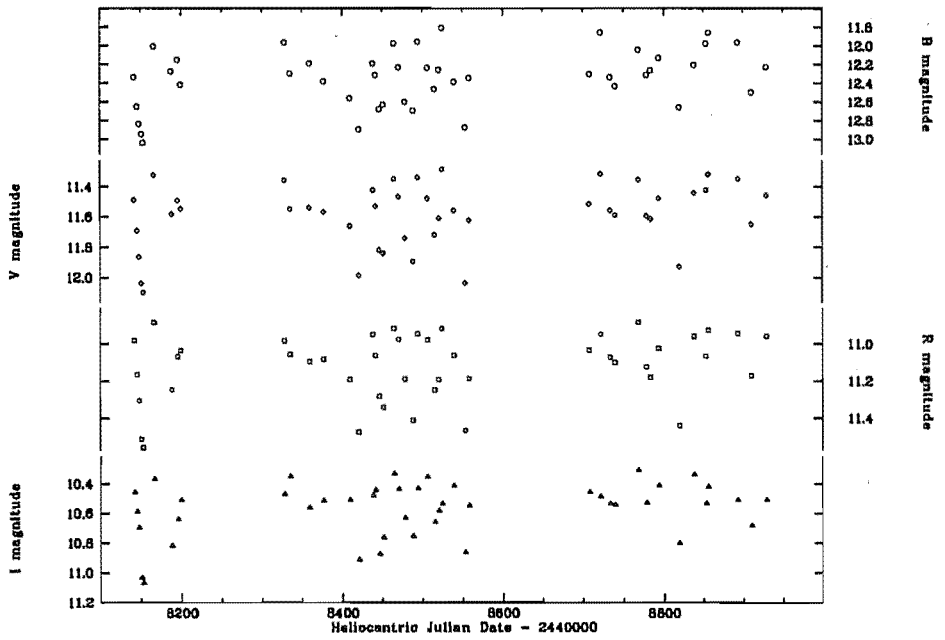

Figure 3.19: Individual B, V, R and I magnitudes for AD Aql.

3.3.3 Analysis of the photometric data

The dominant periodicities present in the photometric data for AD Aql were determined using both the Fourier analysis and the least-squares technique. The initial Fourier analysis revealed that three dominant periodicities are present in the photometry and these occur at frequencies of around $0.015\,\mathrm{d}^{-1}$, $0.030\,\mathrm{d}^{-1}$, and $0.045\,\mathrm{d}^{-1}$. In every data set (B, V, R, I, (B–V), (V–R) and (V–I)) the dominant periodicity corresponds to $f_1 \approx 0.030\mathrm{d}^{-1}$ or a period of about 33 d. Fig. 3.20 displays the power spectra obtained by analysing the V photometry for AD Aql. The three panels show that the dominant periodicities present in the V photometry are $f_1 = 0.03020\,\mathrm{d}^{-1}$ ($P_1 = 33.11\,\mathrm{d}$), $f_2 = 0.01510\,\mathrm{d}^{-1}$ ($P_1 = 66.23\,\mathrm{d}$) and $f_3 = 0.03020\,\mathrm{d}^{-1}$ ($P_3 = 22.11\,\mathrm{d}$). If we identify f_2 as the fundamental frequency of pulsation, then the harmonics $2f_2$ and $3f_2$ are also seen to be present in the data set.

As for AR Sgr, the harmonic ($f + 2f$) fit was employed as the more realistic model of the light variations. Table 3.6 presents the results of both the Fourier and the least-squares analyses. The periods derived from the analysis of the B, V, R and I photometry were used to obtain a mean period and the scatter of the period derived from the different filters gave an indication of the accuracy of the period determination. The average period is calculated to be $(33.05 \pm 0.02)\,\mathrm{d}$ which corresponds to a double period of $(66.09 \pm 0.05)\,\mathrm{d}$. As for RU Cen and AR Sgr, the bluer filters tend to have larger amplitudes of variation and lead the redder light curves.

The 66.09 d period was used to phase the photometric observations. The phased B, V, R and I photometric data are displayed in Fig. 3.21 and the phased V, (B–V), (V–R) and (V–I) data are shown in Fig. 3.22. It is obvious from the appearance of the B, V, R and I light curves that the B light curve has a greater amplitude than the redder light curves. The bluer light curves also show a much slower descent to primary minimum and a much steeper rise to primary maximum and they reach secondary maximum before the redder light curves (the difference between the B and I curves being about 0.1 in phase). Due to insufficient sampling, it is difficult to discern what the phase difference is around the primary maximum.

The form of the light curves during secondary maximum to primary minimum (phases 0.6–1.0) is quite 'bumpy' and asymmetric for the B and V filters, whereas the R and I curves have a much smoother shape. Related to this is that the

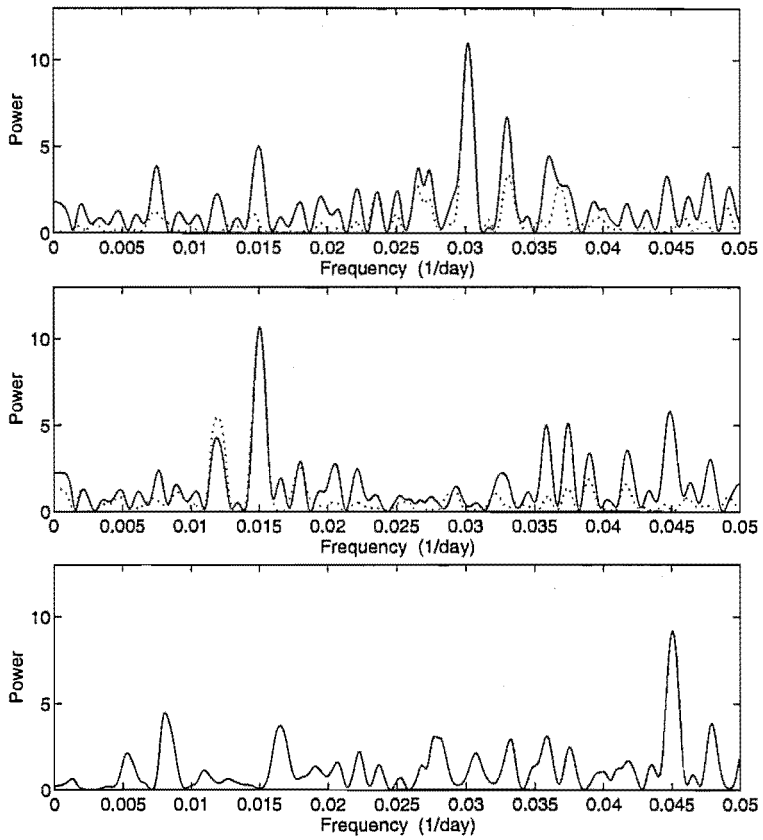

Figure 3.20: The Fourier power spectra from the analysis of the AD Aql V photometry. The dominant peaks occur at $0.03020\,\mathrm{d}^{-1}$ (upper panel), $0.01510\,\mathrm{d}^{-1}$ (middle panel) and $0.04508\,\mathrm{d}^{-1}$ (lower panel) corresponding to periods of 33.11 d, 66.40 d and 22.18 d respectively. The dotted line shows the natural window function.

Table 3.6: The analysis of the B, V, R, I, $(B–V)$, $(V–R)$ and $(V–I)$ photometric data for AD Aql. Each data set consists of 46 data point except for the I and $(V–I)$ data where 45 points were obtained.

Data	Fit[a]	f_1 (d^{-1})	P_1 (d)	A_1 (mag)	ϕ_1 (°)	f_2 (d^{-1})	P_2 (d)	A_2 (mag)	ϕ_2 (°)	rms
B	F	0.03026	33.05	0.27	262	0.01513	66.09	0.22	303	0.157
	L	0.03029	33.01	0.33	253	0.01514	66.03	0.23	303	0.152
V	F	0.03020	33.11	0.20	251	0.01510	66.23	0.14	305	0.110
	L	0.03027	33.04	0.24	240	0.01514	66.07	0.15	303	0.105
R	F	0.03018	33.13	0.19	243	0.01509	66.27	0.11	306	0.085
	L	0.03025	33.06	0.22	233	0.01512	66.12	0.12	305	0.081
I	F	0.03016	33.16	0.19	238	0.01508	66.31	0.08	311	0.100
	L	0.03023	33.08	0.23	229	0.01512	66.15	0.09	311	0.096
$B-V$	F	0.03032	32.98	0.12	290	0.01516	65.96	0.08	305	0.059
	L	0.03024	33.07	0.11	296	0.01512	66.14	0.08	309	0.058
$V-R$	F	0.03026	33.05	0.05	308	0.01513	66.09	0.03	301	0.036
	L	0.03017	33.14	0.04	305	0.01509	66.29	0.04	316	0.035
$V-I$	F	0.03000	33.33	0.08	342	0.01500	66.66	0.07	315	0.081
	L	0.02993	33.41	0.07	353	0.01497	66.82	0.07	317	0.080

[a]F is the Fourier harmonic fit; L is the least-squares $(f+2f)$ harmonic fit.

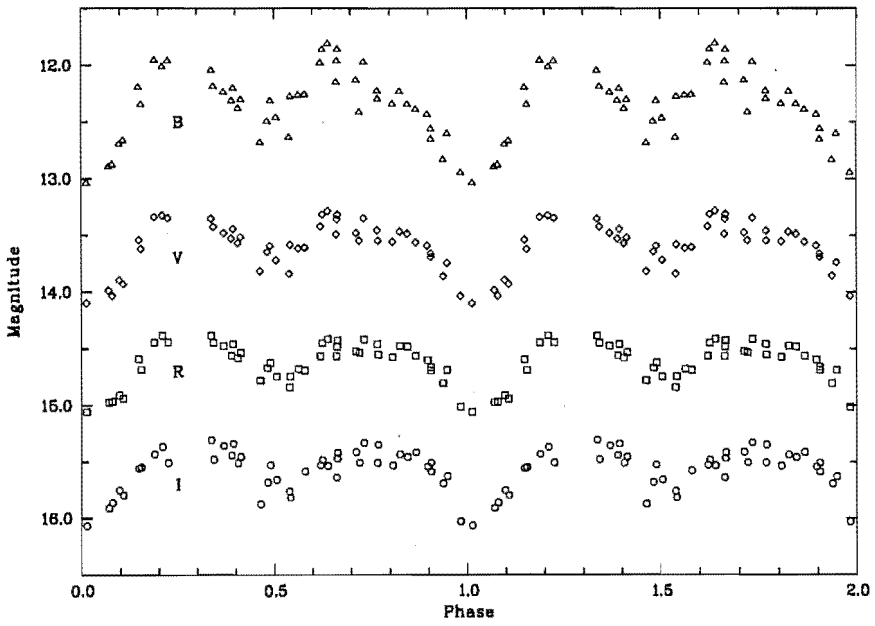

Figure 3.21: The phased (period = 66.09 d) B, V, R and I photometry for AD Aql. Offsets of 2.0, 3.5, 5.0 magnitudes have been applied to the V, R and I data respectively.

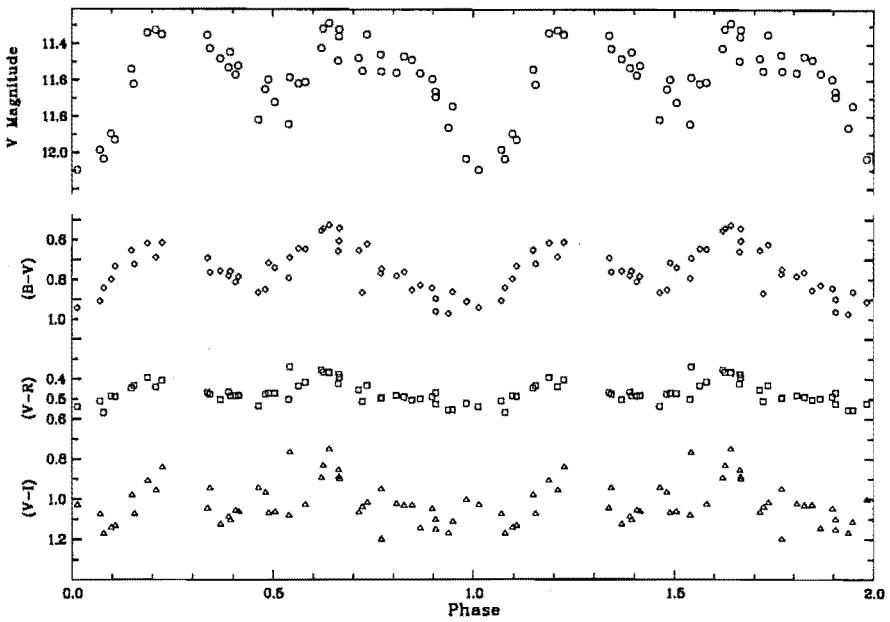

Figure 3.22: The phased V, $(B–V)$, $(V–R)$ and $(V–I)$ photometry for AD Aql.

secondary maximum in the B curve (and to a lesser extent, the V curve) appears to be brighter than the primary maximum, almost appearing like a 'peak' of increased light at this phase.

These two effects – the phase shift of the secondary maximum between filters, and the relative steepness and 'bumpiness' of the descent to primary minimum in the bluer filters – are more pronounced in AD Aql than either RU Cen or AR Sgr.

Fig. 3.22 shows that the colour curves for AD Aql are bluer during the rising branch to the V maximum and are bluest during the rise to the *secondary* maximum (phase ~ 0.6). The colour curves for RU Cen were much more equal for the two minima, although the $(B–V)$ colour curve also appeared to be slightly bluer following the secondary V minimum than the primary V minimum. In AR Sgr, one night's observations showed very blue colours at this phase also, although this part of the cycle was not sampled well.

The colour curves in AD Aql are quite asymmetric. They have a 'sawtooth' shape with a rapid rise to maximum and a slower decent to minimum. As was seen in RU Cen and AR Sgr, the $(V–R)$ curve has quite a low amplitude compared to the other colours. The $(V–I)$ curve shows a lot of scatter that is possibly due to having fewer counts above the sky background in the I filter.

3.4 V453 Oph

3.4.1 Background

Originally classed as a 0.97 d Cepheid, V453 Oph was confirmed as a member of the RV Tauri class in the study by Preston et al. (1963). A period of approximately 80 d was determined from 22 *UBV* photometric observations.

Estimates of the brightness of V453 Oph from 1127 photographic observations were published by Erleksova (1979). The ephemeris for the time of primary (deep) minima was determined to be:

$$\text{Primary Minimum} = \text{JD } 2437505 + 81.300\,E.$$

An analysis of the light variations of V453 Oph based on the measurements published by Erleksova have been presented by Mantegazza (1985). The doubling of peaks in the least-squares power spectrum led Mantegazza to exclude a model where the light variations are due to a single fundamental frequency with its higher harmonics. The alternative explanation given was that there are some nonradial modes excited and the double peaks are the result of stellar rotation lifting the degeneracy of the eigenfrequencies of these oscillations.

3.4.2 Photometry from MJUO

V453 Oph was an addition to the RV Tauri programme in 1991 May, and between this date and 1992 October, a total of 26 *BVR* observations were obtained. Photometric I data were not obtained for this star until 1992 April, so only 10 I and $(V–I)$ observations are available. The positions, adopted magnitudes and colour indices for the comparison star (SAO 141674) and the check star (SAO 141657) are presented in Table 2.1. The internal accuracy of the V453 Oph V photometry is 0.01 magnitudes. V453 Oph is the faintest of the programme stars and, as such, is likely to have the greatest uncertainty associated with having low counts relative to the sky background. The lowest counts are for observations in the I filter, of which there are also fewer observations in total.

Fig. 3.23 displays the V magnitudes for both V453 Oph and its check star as well as the colour indices for V453 Oph. The individual B, V, R and I magnitudes are plotted in Fig. 3.24.

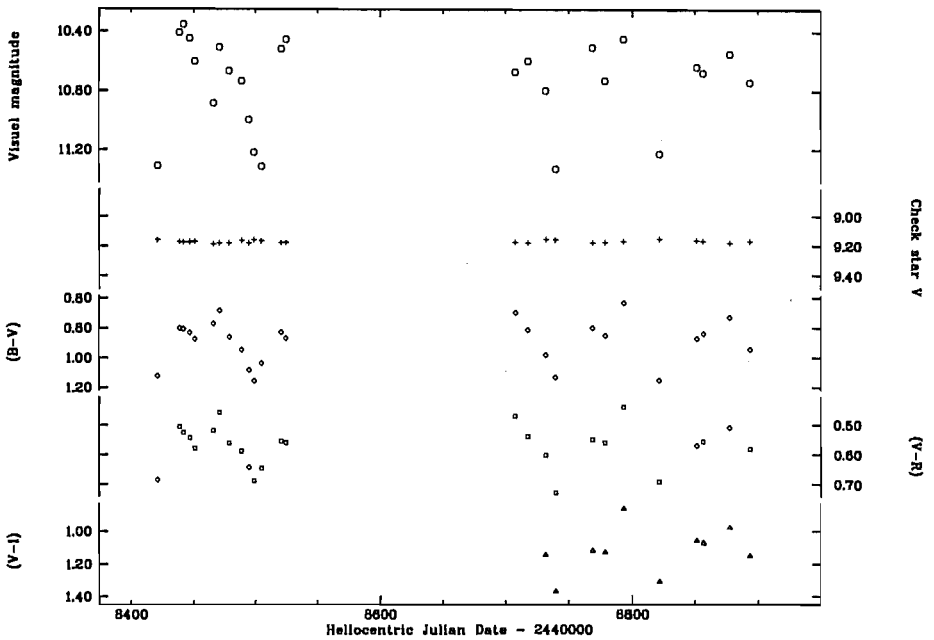

Figure 3.23: The V light and $(B–V)$, $(V–R)$ and $(V–I)$ colour curves for V453 Oph.

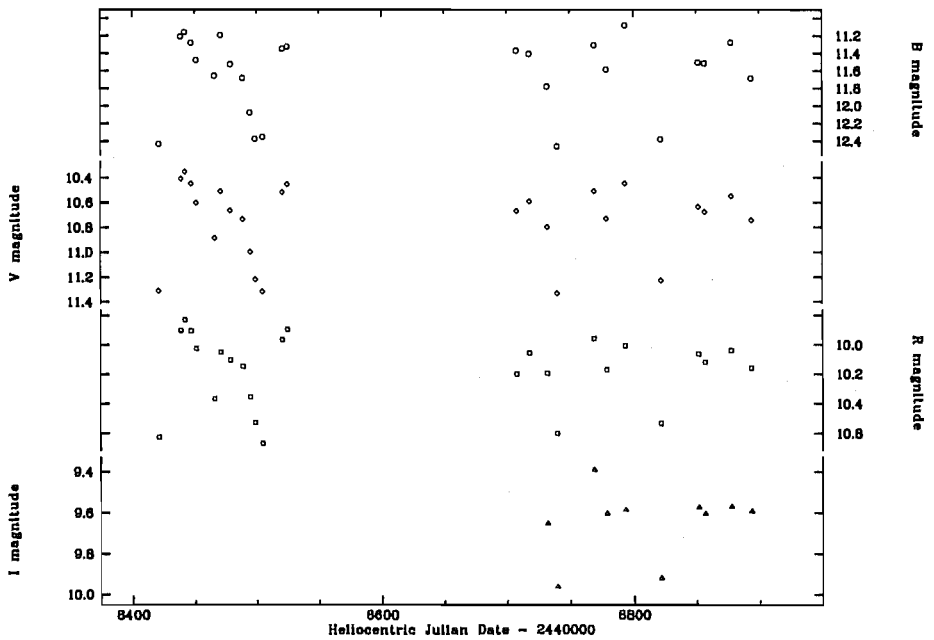

Figure 3.24: Individual B, V, R and I magnitudes for V453 Oph.

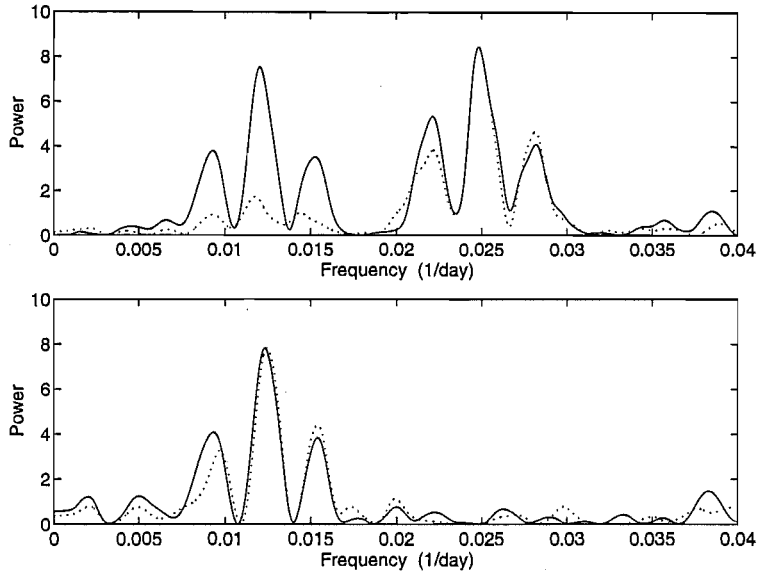

Figure 3.25: The Fourier power spectra from the analysis of the V photometry for V453 Oph. The dominant peaks occur at $0.02482\,\mathrm{d}^{-1}$ (upper panel) and $0.01232\,\mathrm{d}^{-1}$ (lower panel) corresponding to periods of 40.29 d and 81.17 d respectively. The dotted line shows the natural window function.

3.4.3 Analysis of the photometric data

The photometric data for V453 Oph were analysed to search for the dominant periodicities. Because of the smaller number of photometric points, the accuracy of the analysis is somewhat less than for the previously discussed stars. The Fourier analysis reveals that the dominant periodicities in the V, R and I data sets are ~ 40 d, while for the $(B\text{–}V)$, $(V\text{–}R)$, $(V\text{–}I)$ and B data sets the dominant periodicities are ~ 80 d. Fig. 3.14 shows the power spectra obtained from the Fourier analysis of the V photometry for V453 Oph. The top panel shows the dominant periodicity occurs at $f_1 = 0.02482\,\mathrm{d}^{-1}$ ($P_1 = 40.29$ d) and the lower panel shows the power spectrum obtained after the V photometry has been prewhitened for the 40 d period. The second periodicity occurs at $f_2 = 0.01232\,\mathrm{d}^{-1}$ ($P_2 = 81.17$ d). The dotted line in each panel is the natural window function for the data spacing and periodicity.

Table 3.7 presents the results of the Fourier power spectrum method and the least-squares technique for the harmonic $(f + 2f)$ fit. Using the periods determined from the harmonic fits to the B, V and R data sets (the I data were

Table 3.7: The analysis of the photometric data for V453 Oph.

Data	Fit[a]	f_1	P_1	A_1	ϕ_1	f_2	P_2	A_2	ϕ_2	rms
	(d^{-1})	(d)	(mag)	(°)	(d^{-1})	(d)	(mag)	(°)		
B	F	0.02420	41.32	0.22	43	0.01210	82.64	0.56	25	0.180
	L	0.02475	40.41	0.35	11	0.01237	80.81	0.38	1	0.125
V	F	0.02482	40.29	0.35	7	0.01241	80.58	0.19	4	0.105
	L	0.02480	40.33	0.29	358	0.01240	80.66	0.23	1	0.090
R	F	0.02484	40.26	0.28	357	0.01242	80.52	0.14	9	0.073
	L	0.02483	40.28	0.26	349	0.01241	80.56	0.16	5	0.066
I	F	0.02454	40.75	0.17	261	0.01227	81.50	0.11	314	0.053
	L	0.02451	40.81	0.19	246	0.01225	81.62	0.15	297	0.045
$B-V$	F	0.01220	81.97	0.16	11	0.02440	40.98	0.08	69	0.044
	L	0.01230	81.29	0.16	3	0.02460	40.64	0.08	55	0.041
$V-R$	F	0.01216	82.24	0.09	10	0.02432	41.12	0.03	71	0.031
	L	0.01230	81.29	0.07	0	0.02460	40.64	0.04	53	0.028
$V-I$	F	0.01236	80.91	0.17	284	0.02472	40.45	0.08	270	0.044
	L	0.01230	81.33	0.17	282	0.02459	40.66	0.09	277	0.040

[a]F is the Fourier harmonic fit; L is the least-squares harmonic fit.

not used due to the paucity of observations) a mean period of (40.34 ± 0.05) d corresponding to a double period of (80.68 ± 0.10) d is derived. Although this star has the least amount of data of the programme RV Tauri stars, the characteristic trends of the previous RVa stars are seen. The amplitude of variation increases with bluer filters and the onset phases also show that the bluer light curves lead the redder light curves.

The photometric data were phased to the double period of 80.68 d in order to separate the primary and secondary minima. Fig. 3.26 displays the phased B, V, R and I photometric data and Fig. 3.27 shows the colour curves with the V light curve included for comparison.

The bluer light curves appear less symmetric around primary minimum and show greater amplitudes than the redder curves. An increased 'bumpiness' and a shift in the phase of secondary minima are features that were seen in AD Aql. The (V–R) curve has the smallest amplitude of the colours, as was seen in all the previously discussed RV Tauri stars. The (B–V) curve is very blue during the rise to maximum V light which is, again, similar to the behaviour of AD Aql.

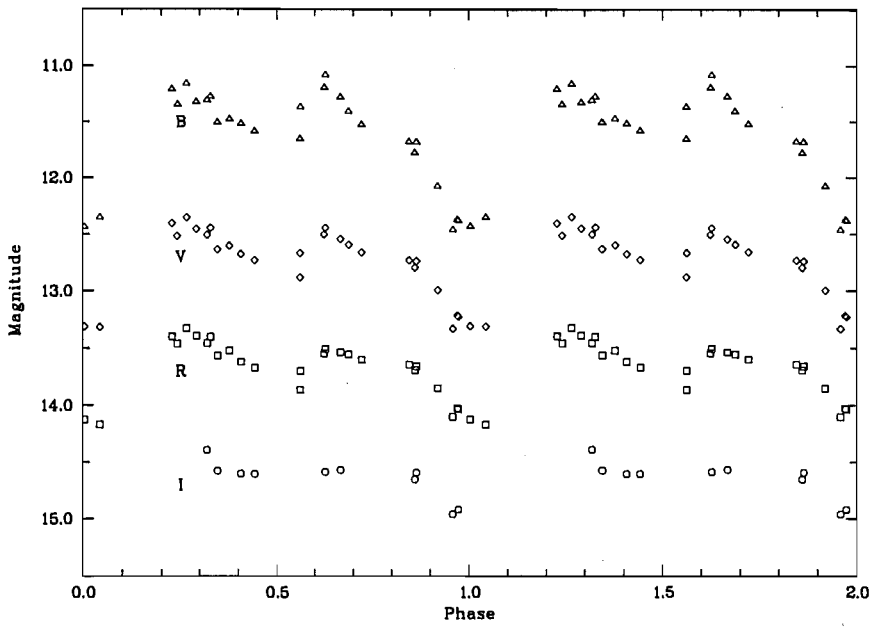

Figure 3.26: The phased (period = 80.68 d) B, V, R and I photometry for V453 Oph. Offsets of 2.0, 3.5,and 5.0 magnitudes have been applied to the V, R and I data respectively.

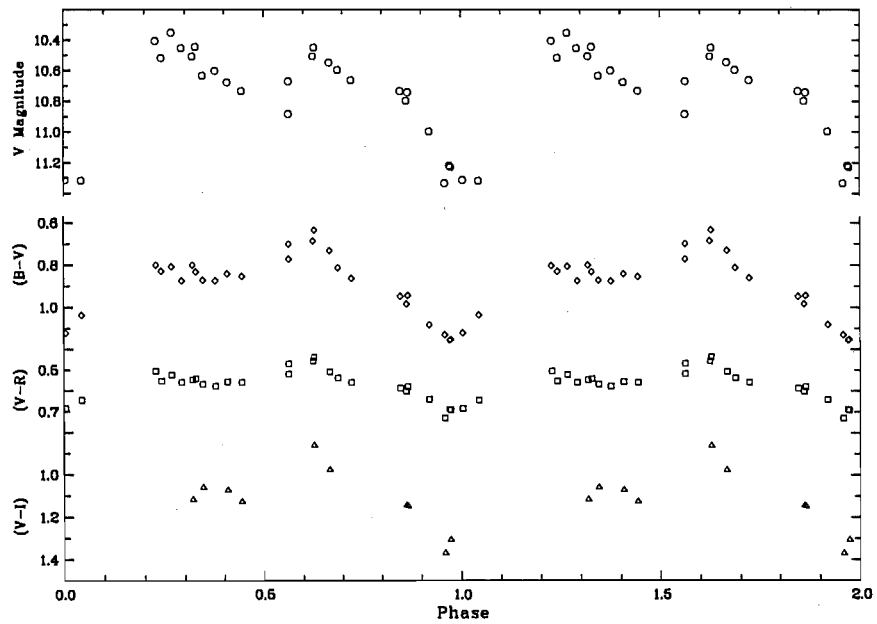

Figure 3.27: The phased V, $(B–V)$, $(V–R)$ and $(V–I)$ photometry for V453 Oph.

3.5 R Sct

3.5.1 Background

R Sct is the brightest and one of the most irregular members of the RV Tauri class. It was discovered by Pigott in 1795 who also found that it was a variable star. Argelander (1869) made the first analysis of the peculiarities of the light variations of R Sct.

The General Catalogue of Variable Stars (Kholopov et al. 1985) gives the range in V for R Sct as 4.45–8.2, with a double (or formal) period of 140.05 d, making it one of the longest period RV Tauri stars known. It is a member of the RVa subclass.

The original definition of the RVb subclass in the General Catalogue of Variable Stars (Kurkarkin et al. 1958) states that RVb stars are '... variables of the RV Tauri type that periodically vary in mean magnitude...'. Cardelli (1985) and Cardelli & Howell (1989) misinterpret this definition by stating that R Sct appears to be an extreme example of the RVb subclass. Although it is correct that the mean light level of R Sct is variable depending on whether R Sct is pulsating in a regular manner or not, it does not show the additional periodicity that Kukarkin et al. were using as the defining characteristic for the RVb subclass.

Variations in the period of R Sct are known to exist. There has been much discussion about whether these period changes are abrupt or cyclical in nature. An investigation into the period changes in R Sct was undertaken by Gerasimovič (1928) who determined that discontinuous jumps in the period had occurred and the accumulation of these jumps resulted in an apparent linear increase in phase over the 123 years (1798 to 1921) of visual and photographic data examined. More recently, Percy et al. (1991) investigated the period changes in the two brightest RV Tauri stars, R Sct and U Mon using 150 years of photographic and visual observations. They found that the fundamental period of R Sct decreased abruptly from 70.95 d to 70.0 d in 1941, giving an average rate of period decrease of 0.0687 days/year over 150 years.

3.5.2 Photometry from MJUO

Between 1990 August and 1993 October, a total of 78 night-averaged *BVRI* photometric observations were obtained of R Sct using the 0.61-m B&C and OC telescopes. The comparison star (SAO 142661) and the check star (SAO 142598)

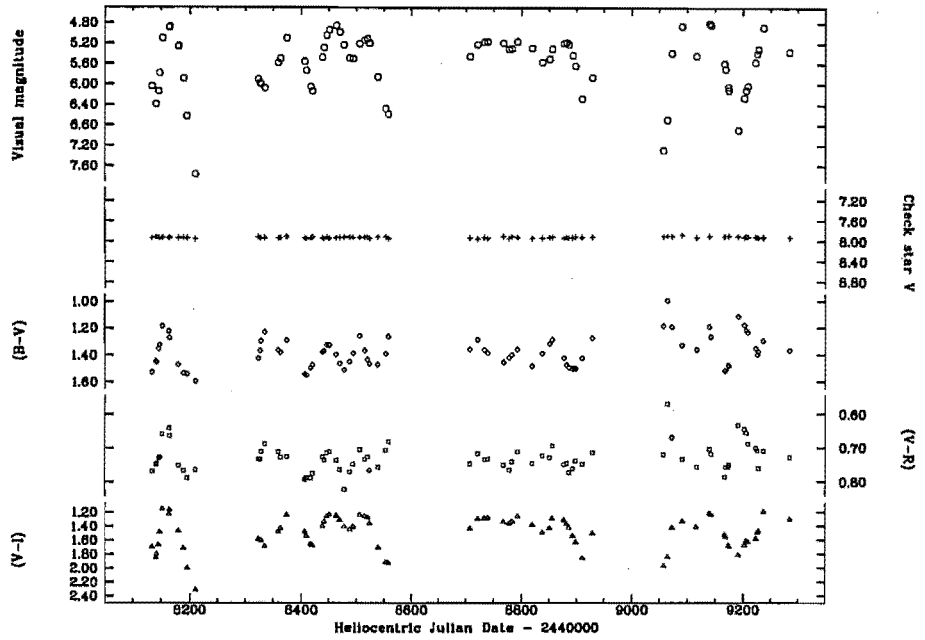

Figure 3.28: The V light and $(B–V)$, $(V–R)$ and $(V–I)$ colour curves for R Sct.

used in the differential photometry have their adopted magnitudes and colours tabulated in Table 2.1. The colour indices and V magnitudes for R Sct are displayed in Fig. 3.28 and the individual B, V, R and I magnitudes are shown in Fig. 3.29. The precision of the R Sct V photometry is derived from the standard deviation of the check star's V magnitudes and this is calculated to be 0.015 magnitudes. This value is rather large and indicates that either the comparison or the check star could be a low amplitude variable. The V magnitudes for the check star are plotted on the same scale as for R Sct in Fig. 3.28.

Compared to the four stars (RU Cen, AR Sgr, AD Aql and V453 Oph) that have already been presented, R Sct and the following two stars (RY Ara and V820 Cen) have much more irregular photometric variations. The MJUO photometric data for R Sct display such large variations in the depth of the minima that it is very difficult to determine which minima are primary and which are secondary. The 1990 data (HJD 2448130–2448210) display quite regular light variations which are in phase with, and are similar in appearance to, the variations in the 1993 data (HJD 2449050–2449290). The light variations in 1991 and 1992 have a reasonably small amplitude, are relatively irregular in appearance and show several 'flips' or interchanges of deep and shallow minima.

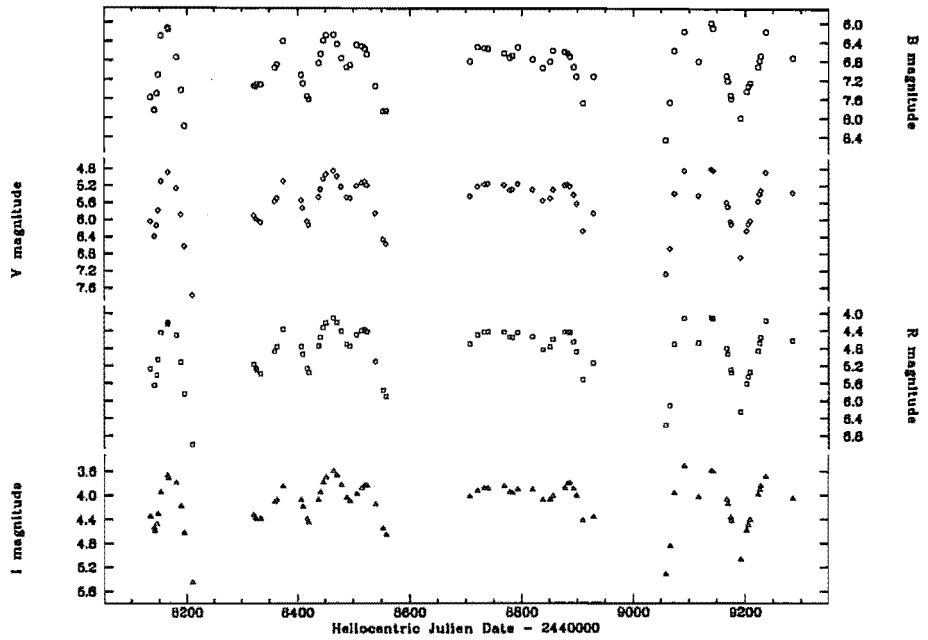

Figure 3.29: Individual B, V, R and I magnitudes for R Sct.

3.5.3 Analysis of the photometric data

The photometry for R Sct was analysed to investigate the dominant periodicities that are present in the data. In the case of R Sct, where the light curve is relatively irregular and shows the characteristic deep–shallow variations for only some of the time, the data were initially fitted by a single sinusoid. The Fourier power spectrum for the analysis of the V photometry is seen in Fig. 3.30. Although the power spectrum is noisier than those seen for the previous stars due to the more irregular nature of the pulsations in R Sct, a dominant peak is seen at a period of $P_1 = 70.62\,\mathrm{d}$ ($f_1 = 0.01416\,\mathrm{d}^{-1}$). The estimated value of the amplitude signal-to-noise of 3.54 (power signal-to-noise of 12.5), corresponds to a false alarm probability for this peak in the power spectrum of 2.86×10^{-4}. This periodicity is therefore quite strongly present in the photometric data set and is not likely to arise from random chance.

The general RV Tauri trends of increasing amplitude of variation and increasing phase lead with bluer filter are seen in the analysis of the R Sct photometry. The results for the B, V, R and I were averaged to obtain a mean period. From both the least-squares analysis and the Fourier analysis a mean period of

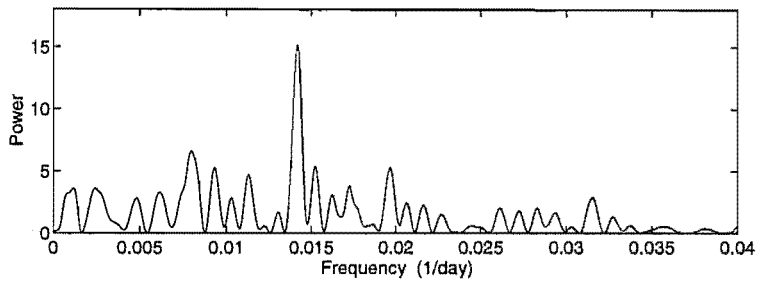

Figure 3.30: The power spectrum from the Fourier analysis of the R Sct V photometry (solid line). The dominant peak is at $f_1 = 0.01416\,\mathrm{d}^{-1}$ ($P_1 = 70.62\,\mathrm{d}$).

$(70.62 \pm 0.08)\,\mathrm{d}$ was obtained.

The photometric data were divided into two different subgroups of data to analyse in greater detail. The 1990 (HJD 2448130–2448210) data and the 1993 (HJD 2449050–2449290) data were grouped together since both years of data display regular, deep–shallow light variations of similar amplitude. The second subgroup of data consists of the 1991 (HJD 2448320–2448560) and the 1992 (HJD 2448700–2448930) data. Both these sets of data show smaller, more irregular light variations which contain a number of 'flips' or interchanges of deep and shallow minima. When analysed separately, the 'regular' data show a mean period (calculated from the B, V, R and I data) of $(70.58 \pm 0.06)\,\mathrm{d}$ and the 'irregular' data show a mean period of $(71.3 \pm 0.5)\,\mathrm{d}$. These same periods were derived using both the Fourier and the least-squares techniques. A summary of the single-sinusoid and harmonic fits to the various data sets are presented in Table 3.8.

The 'regular' data have a larger time baseline and a complex aliasing structure due to the time separation between the 1990 and the 1993 data. The power spectra for the V photometry are shown in Fig. 3.31. Most of the observed structure is produced by two dominant periodicities. The upper panel in this figure shows the comparison between the power spectra obtained for the 'regular' V data only (solid line) and for the entire V data for R Sct (dotted line). The dominant peak for both sets of data occurs at $f_1 = 0.01416\,\mathrm{d}^{-1}$ corresponding to a period of $P_1 = 70.62\,\mathrm{d}$. Once the first constituent is subtracted from the 'regular' data, a second periodicity at $f_2 = 0.01120\,\mathrm{d}^{-1}$ ($P_2 = 139.3\,\mathrm{d}$) is apparent (lower panel of Fig. 3.31). Some smaller peaks are also seen in this power spectrum. The 70 d and the 140 d periodicities were included in a harmonic $(f + 2f)$ fit to

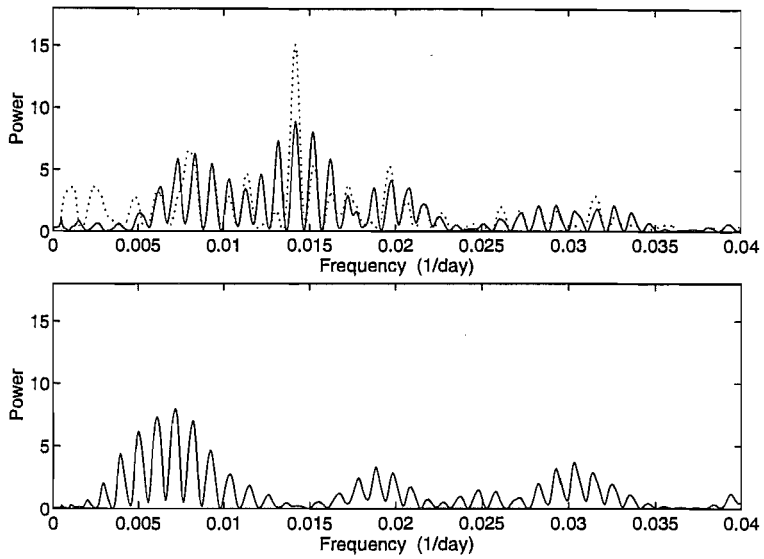

Figure 3.31: The Fourier power spectra for analysis of the 'regular' R Sct V photometry. Two dominant periodicities are present at $f_1 = 0.01416\,\mathrm{d}^{-1}$ ($P_1 = 70.62\,\mathrm{d}$) and $f_2 = 0.01120\,\mathrm{d}^{-1}$ ($P_2 = 139.3\,\mathrm{d}$). The dotted line in the upper panel is the power spectrum from analysing the entire V photometry.

the 'regular' data. The synthetic curve from this harmonic fit is shown together with the 'regular' data (circles) for R Sct in Fig. 3.32. The 'irregular' data are included in this figure (plus symbols) for comparison, but these data were not included in the analysis. This harmonic fit represents the 'regular' data well and reduces the rms residuals of the fit to the V photometry from 0.479 to 0.296 magnitudes. Using the B, V, R and I data, a mean period of $(70.15 \pm 0.04)\,\mathrm{d}$, corresponding to a double period of $(140.30 \pm 0.07)\,\mathrm{d}$, was derived.

The 'irregular' data show a more poorly defined period, but it should be remembered that these data have only half the time-baseline of the 'regular' data. The power spectrum for the 'irregular' V data is shown in Fig. 3.33. A peak is seen at a frequency of $f_1 = 0.01414\,\mathrm{d}^{-1}$ corresponding to a period of 71.23 d. The amplitude of variation in each of the filters is much smaller than that of the 'regular' data and no 140 d periodicity is apparent. The colour variations have power spectra that show multiple peaks, some of which are higher than the 70 d peak.

The photometric data were phased to a period of 140.30 d, the period derived from the harmonic fit to the 'regular' data set. The phased B, V, R and I

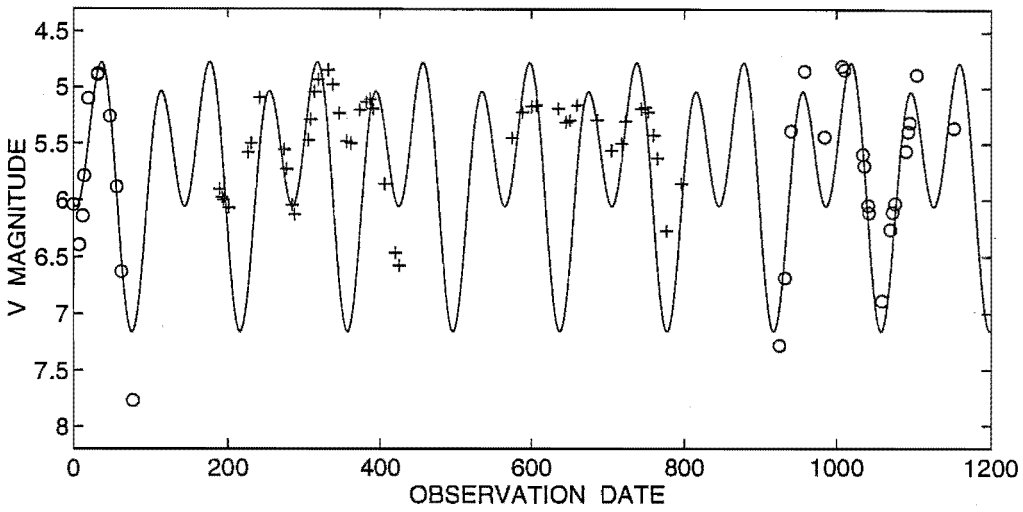

Figure 3.32: The synthetic light curve from the harmonic fit to the 'regular' V photometry (o) for R Sct. The 'irregular' V data (+) are included for comparison.

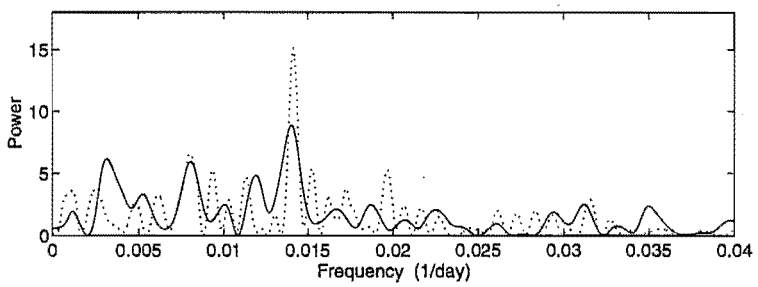

Figure 3.33: The Fourier power spectra from the analysis of the 'irregular' R Sct V photometry. The dominant periodicity is $f_1 = 0.01404\,\mathrm{d}^{-1}$ ($P_1 = 71.22\,\mathrm{d}$). The dotted line is the power spectrum from analysing the combined V photometry.

Table 3.8: The least-squares analysis of the R Sct photometry.

Data	N^a	Fit^b	$\overline{f}$ (d^{-1})	$\overline{P}$ (d)	$2\overline{P}$ (d)	$\overline{\mathrm{rms}}$
all	78	S	0.01416 ± 0.00002	70.62 ± 0.08	141.24 ± 0.16	0.419
all	78	H	0.01417 ± 0.00002	70.55 ± 0.09	141.10 ± 0.18	0.408
regular	32	S	0.01417 ± 0.00001	70.58 ± 0.06	141.16 ± 0.12	0.444
regular	32	H	0.01426 ± 0.00001	70.15 ± 0.04	140.30 ± 0.08	0.279
irregular	46	S	0.01402 ± 0.00002	71.32 ± 0.46	142.64 ± 0.92	0.206

[a] N is the number of data points
[b] S is a single sinusoid fit; H is a harmonic ($f + 2f$) fit

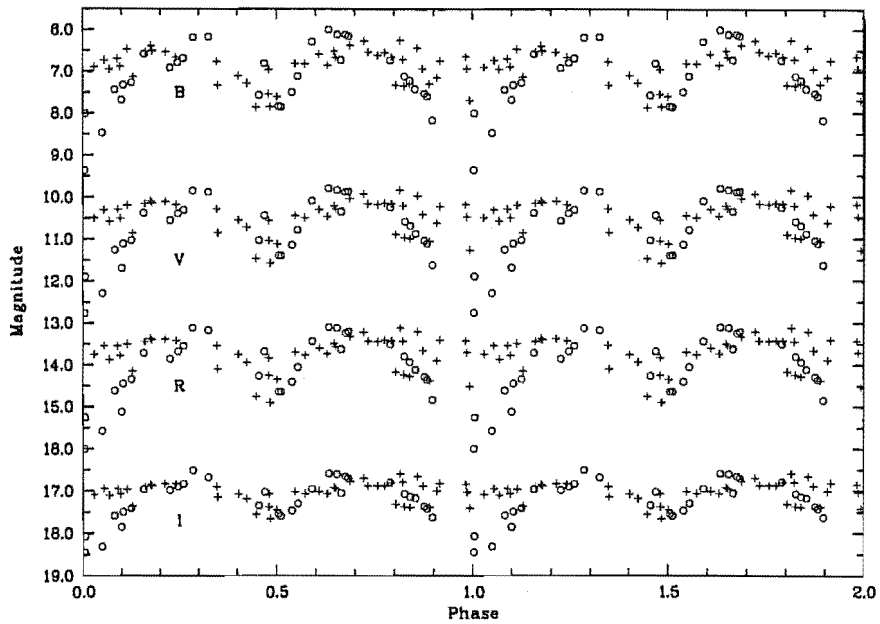

Figure 3.34: The phased (period = 140.30 d) B, V, R and I photometry for R Sct. Offsets of 5.0, 9.0, 13.0 magnitudes have been applied to the V, R and I data respectively. Both the 'regular' data (o) and the 'irregular' data (+) are plotted.

photometric data are displayed in Fig. 3.34 and the phased V, $(B–V)$, $(V–R)$ and $(V–I)$ data are displayed in Fig. 3.35. The 'regular' data (o) and the 'irregular' data (+) are plotted using different symbols so that any systematic or correlated changes in the behaviour of the light and colour variations of R Sct can be seen. The plot of the phased photometric data shows that the primary minima in the 'regular' data are much deeper than in the 'irregular' data in all the filters. The light variations in I have the lowest amplitude in both the sets of photometry. The primary and secondary maxima in the 'regular' data appear to be slightly brighter than the 'irregular' data. The phased colour curves show an interesting difference in the two sets of photometry. The $(B–V)$ and $(V–R)$ colour curves are systematically bluer in colour for the 'regular' data during rising V light, particularly during the rise from primary minimum to primary maximum. The $(V–I)$ colour curve seems to follow the behaviour of the V curve extremely closely. This is because the variations in the V band are much larger than those in the I band and therefore dominate the colour index term.

The first minimum in the R Sct V photometry appears to be the deepest but

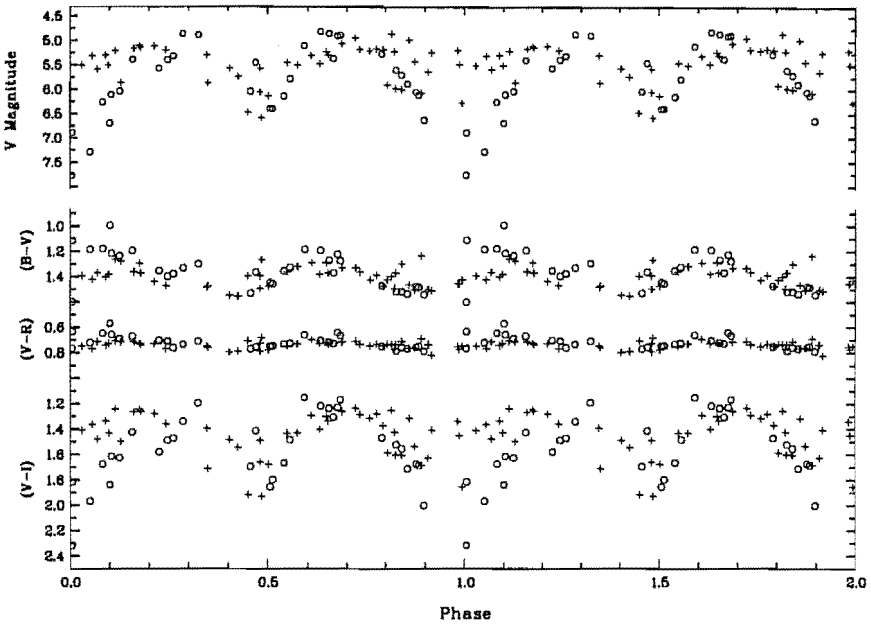

Figure 3.35: The phased V, $(B–V)$, $(V–R)$ and $(V–I)$ photometry for R Sct. Both the 'regular' data (o) and the 'irregular' data (+) are plotted.

is sampled only up until primary minimum itself. A reddening of the colours is seen for this minimum. The second minimum appears to be the second deepest and is only sampled after the primary minimum. The $(B–V)$ and $(V–R)$ colours show a sharp 'peak' as the colour get very blue during this rise to maximum light. The descent to minimum and the rise to maximum is sampled well for the third minimum, which is the shallowest of the three primary minimum in the 'regular' subgroup of data. The colours are seen to get blue very quickly, although they do not get as blue as for the second minimum.

3.6 RY Ara

3.6.1 Background

RY Ara was included in Rosino's (1951) list of members of the RV Tauri class. A photographic range of 9.2–12.1, a large mean amplitude of 2.9 magnitudes and a period of 143.5 d were noted.

The General Catalogue of Variable Stars (Kholopov et al. 1985) classifies RY Ara as an RV Tauri star, but Lloyd Evans (1985) notes that the limited

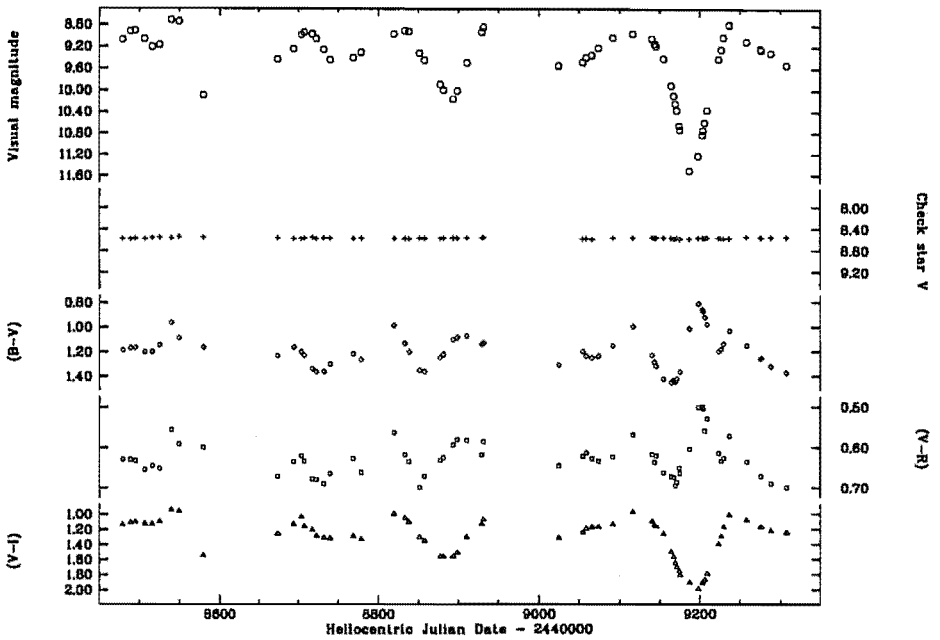

Figure 3.36: The V light and $(B–V)$, $(V–R)$ and $(V–I)$ colour curves for RY Ara.

optical data do not definitely establish RY Ara as a member of this class. Infrared observation by Gehrz & Ney (1972) reveal that RY Ara appears to radiate like a blackbody at wavelengths as long as 3.4 μm with no infrared excess. Optical and near-infrared photometry for RY Ara presented by Goldsmith et al. (1987) has also shown no evidence of a circumstellar dust shell. Using fluxes derived from these observations, a stellar effective temperature of 5800 K was estimated.

3.6.2 Photometry from MJUO

RY Ara was added to the RV Tauri programme in 1991 August and between this date and 1993 November, 63 night-averaged *BVRI* photometric observations were obtained using the 0.61-m B&C and OC telescopes at MJUO. The comparison star used for the differential photometry was SAO 244656 and the check star was SAO 244664. Table 2.1 shows the adopted magnitudes and colours for the comparison and check stars. The internal accuracy of the V photometry is 0.01 magnitudes. The photometric data for RY Ara are displayed graphically in Figs 3.36 and 3.37.

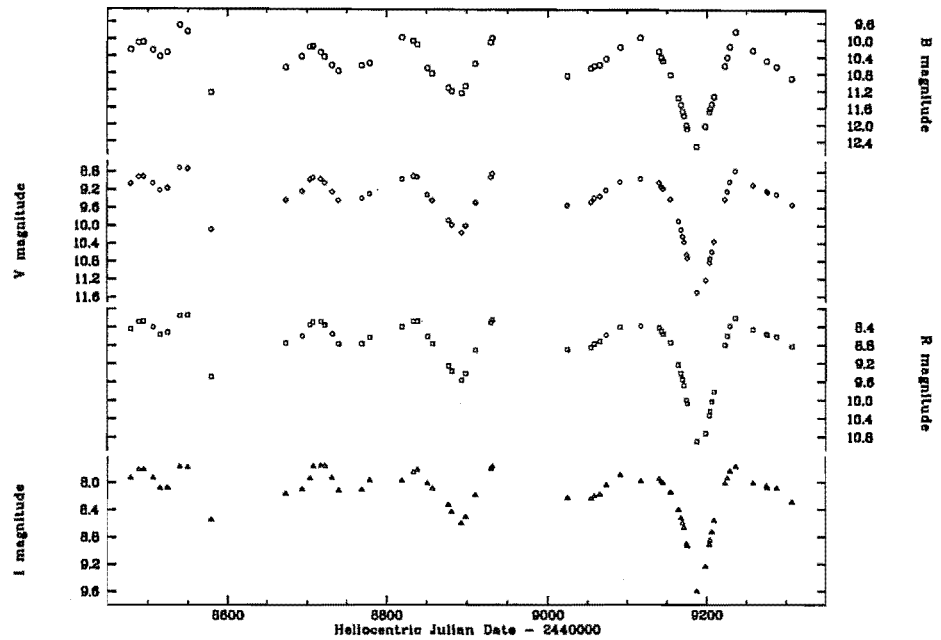

Figure 3.37: Individual B, V, R and I magnitudes for RY Ara.

3.6.3 Analysis of the photometric data

Due to the fact that the period of this star appears to be quite long, the photometry has only covered a few cycles, decreasing the accuracy of any period determination. Large variations in the depths of the minima in all filters are seen. The very deep minimum at HJD$\sim$ 2449200 is quite unusual, both in its relative faintness and in the behaviour of the $(B–V)$ and $(V–R)$ colours during the minimum. The $(B–V)$ and $(V–R)$ colour variations show two maxima as the V light increases to a maximum. Colour variations can usually be attributed to temperature changes in normal pulsating stars, but in RV Tauri stars there is the added complication of the presence of atmospheric shock waves. The shock waves produce emission lines during rising light which can cause the colours to become very blue. It is therefore possible that the two peaks in the colour curves are due to two different effects and the colour variations do not reflect the underlying period of pulsation at this particular time.

The photometric data for RY Ara were analysed to search for the dominant periodicities. For each of the B, V, R, I and $(V–I)$ data sets, a dominant periodicity of $\sim$ 145 d was present. The $(B–V)$ and $(V–R)$ data sets both showed a

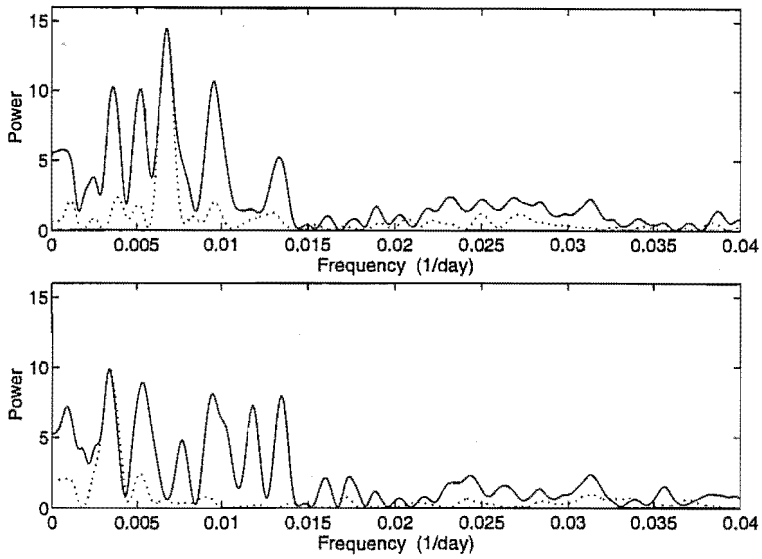

Figure 3.38: The Fourier power spectra from the analysis of the RY Ara V photometry. The dotted line shows the natural window function.

dominant periodicity at about 137 d. The dominant periodicity was subtracted from the data, which were then reanalysed to search for the next most dominant periodicity. For the V, R and $(V–I)$ data, the second periodicity, ~290 d, was approximately double the first. For the I data, the second period, ~73 d, was about half the first. The $(B–V)$ and $(V–R)$ data both showed periodicities at about 80 d. The power spectra for the analysis of the RY Ara V photometry is presented in Fig. 3.38. The dominant peaks occur at $0.00678\,\mathrm{d}^{-1}$ (upper panel) and $0.00338\,\mathrm{d}^{-1}$ (lower panel) corresponding to periods of 147 d and 296 d respectively.

Although the 145 d period is the most dominant periodicity in the data sets, it is unclear whether this is the fundamental period (with the 73 d period as the first overtone) or is the first overtone (with the 290 d period as the fundamental period). More recent MJUO photometry that has not been included in the above analysis suggests that the star appears to be pulsating with two dominant periodicities of approximately 150 d and 300 d, resulting in 'deep' minima about every 300 d. The harmonic fit using these two periodicities was adopted as the most likely current mode of pulsation and the results of this analysis are presented in Table 3.9. The harmonic $(f + 2f)$ fit to the photometry was only carried out for the light curves and the $(V–I)$ colour curve. The $(B–V)$ and the $(V–R)$ colour

Table 3.9: The analysis of the photometric data for RY Ara. Each data set consists of 63 photometric points.

Data	Fit[a]	f_1 (d^{-1})	P_1 (d)	A_1 (mag)	ϕ_1 (°)	f_2 (d^{-1})	P_2 (d)	A_2 (mag)	ϕ_2 (°)	rms
B	F	0.00682	146.6	0.65	71	0.00341	293.3	0.31	202	0.365
	L	0.00692	144.5	0.64	50	0.00346	288.9	0.35	190	0.356
V	F	0.00678	147.5	0.58	71	0.00339	295.0	0.36	205	0.389
	L	0.00689	145.2	0.58	46	0.00344	290.3	0.40	193	0.380
R	F	0.00678	147.5	0.59	68	0.00339	295.0	0.39	206	0.396
	L	0.00687	145.5	0.58	47	0.00344	291.0	0.42	196	0.388
I	F	0.00682	146.6	0.34	64	0.00341	293.3	0.21	206	0.261
	L	0.00694	144.1	0.32	36	0.00347	288.2	0.23	192	0.256
$B-V$	F[b]	0.00722	138.5	0.14	51	0.01256	79.62	0.10	153	0.086
	L[b]	0.00715	139.9	0.11	65	0.01366	73.21	0.10	251	0.092
$V-R$	F[b]	0.00734	136.2	0.04	35	0.01246	80.26	0.03	164	0.033
	L[b]	0.00663	150.8	0.03	217	0.01359	73.58	0.03	252	0.035
$V-I$	F	0.00676	147.9	0.28	73	0.00338	295.9	0.15	202	0.146
	L	0.00684	146.1	0.26	55	0.00342	292.2	0.17	192	0.142

[a]F is the Fourier fit; L is the least-squares fit.
[b]Two-independent-sinusoid fit

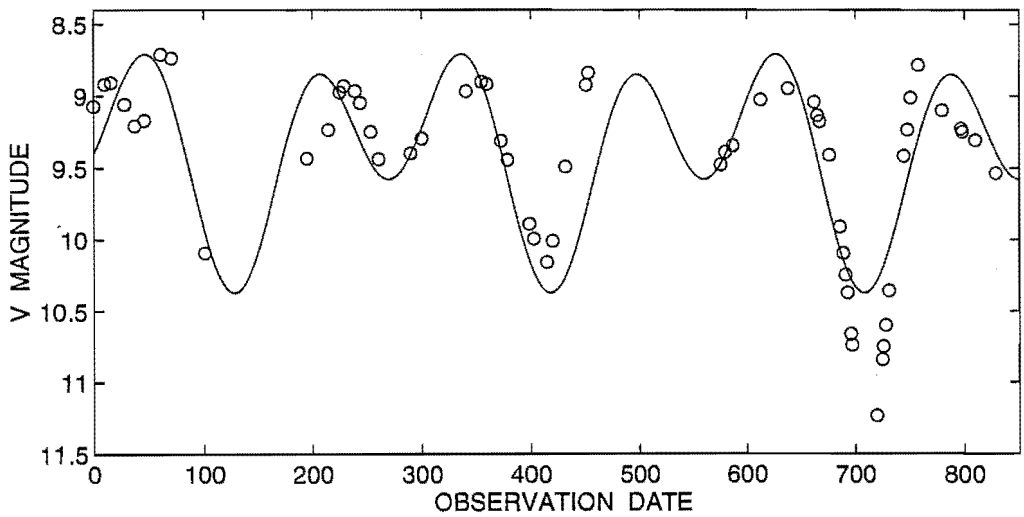

Figure 3.39: The synthetic light curve from the harmonic fit to the RY Ara V photometry.

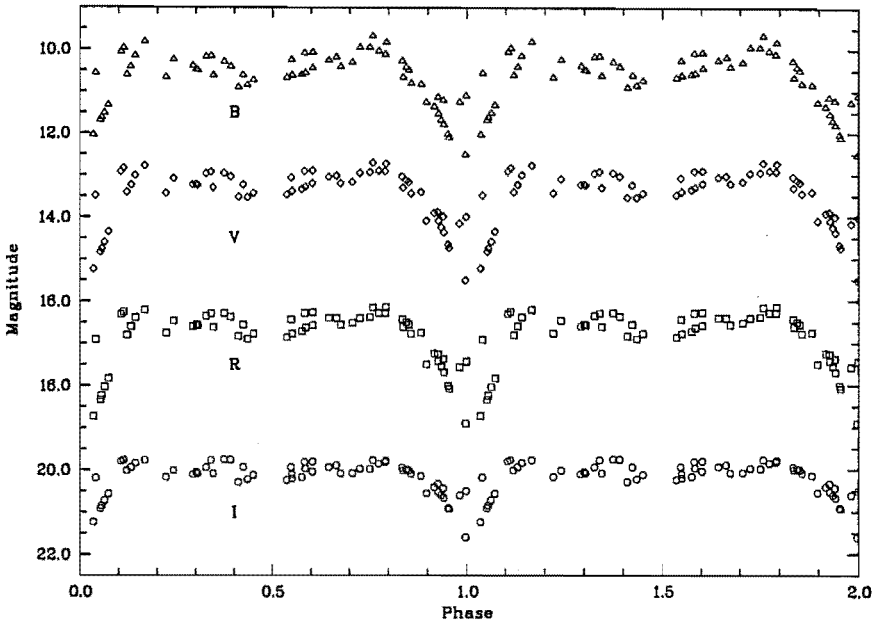

Figure 3.40: The phased (period = 289.6 d) B, V, R and I photometry for RY Ara. Offsets of 4.0, 8.0, 12.0 magnitudes have been applied to the V, R and I data respectively.

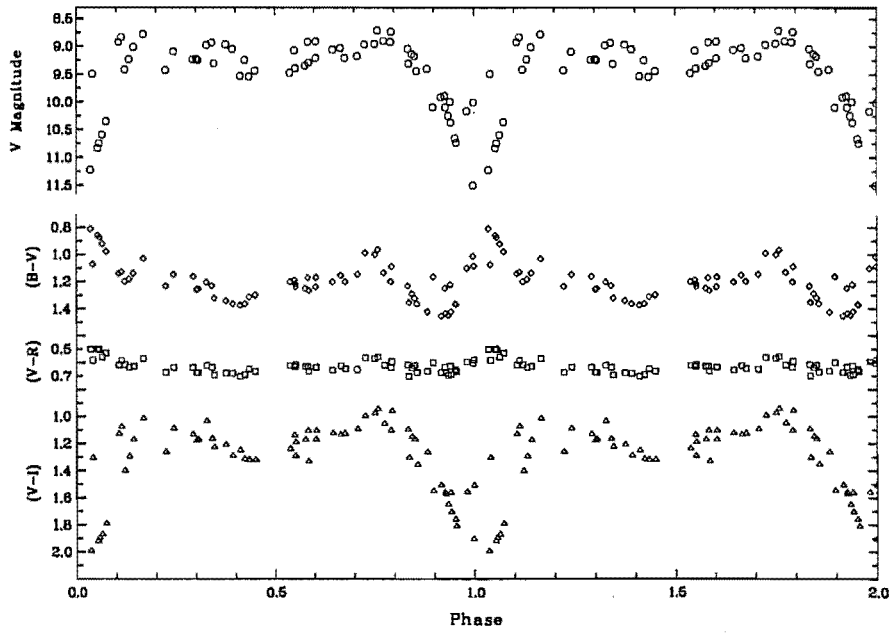

Figure 3.41: The phased V, $(B–V)$, $(V–R)$ and $(V–I)$ photometry for RY Ara.

curves displayed some unusual features that were associated with the very deep light minimum at HJD $\sim$ 2449200. For these colour curves, a two-sinusoid (f_1+f_2) fit was employed which showed that higher frequency features were present in the data. Whether this power at higher frequencies is merely due to transient features is unlikely to be determined from just the available photometry of this star. Spectra of RY Ara during the very deep minimum at HJD $\sim$ 2449200 would have been useful in determining the nature of the colour changes (and whether these were due to shock-related phenomena, chromospheric-type lines, TiO bands or other spectral peculiarities).

The V photometry for RY Ara, together with the synthetic curve from the analysis of these data, are shown in Fig. 3.39. The earliest photometry appears to show some higher frequency periodicities, but the general characteristics of the V light curve are modeled reasonably well by the harmonic ($f + 2f$) fit where $f = 0.00344\,\mathrm{d}^{-1}$ ($P = 290.3\,\mathrm{d}$). A mean period was derived from the fits to the B, V, R and I light curves. A mean fundamental period of $(144.8 \pm 0.6)\,\mathrm{d}$ was determined which corresponds to a formal period of $(289.6 \pm 1.1)\,\mathrm{d}$. The photometric data were phased using the formal period of 289.6 d and the resulting phased light and colour curves are shown in Figs 3.40 and 3.41.

The phased light curves show distinct primary minima but these appear to have a variable depth. The secondary minima are rather shallow. Other higher frequencies may be present in the photometry, as indicated by the number of other smaller minima in the light curves. The phased colour curves show that the colours all become quite blue preceding a deep minimum (phase $\sim$ 0.75–0.85). As RY Ara increased in brightness following the extremely deep light minimum at HJD$\sim$2449200, the (B–V) and (V–R) colours appear extremely blue while the (V–I) colour curve mimics the behaviour of the V curve. Some rather unusual colour behaviour is seen during this deep minimum, with two maxima apparent in the (B–V) and (V–R) colour curves as the V light increases to a maximum. A spectrum of R Sct, taken during an extremely deep light minimum, showed chromospheric-type emission lines reminiscent of that seen in RCB stars during their characteristic 'declines'. This may also have been the case for RY Ara during its very deep minimum, which would be one explanation for the peculiar colour behaviour at this time.

Like R Sct, RY Ara displays great irregularity in its light variations. These two stars have the longest pulsational periods in the MJUO photometric programme.

(V820 Cen may be another (see Section 3.7), although there is some doubt as to whether V820 Cen is an RV Tauri star or merely an irregular variable.) These stars also have very late spectral types. The extreme irregularity of the depths of the minima in RY Ara suggests that the star may be undergoing some sort of chaotic processes. The models of chaotic variations, where the pulsating variable star undergoes period-doubling bifurcations as the controlling parameter (usually the $T_{\rm eff}$) is decreased are consistent with what is seen for the very cool RV Tauri stars such as R Sct and RY Ara.

3.7 V820 Cen

3.7.1 Background

Few estimates of the visual magnitude from photographic plates and little photoelectric photometry of V820 Cen have been published. Two nights of *UBVRI* photometry from the South African Astronomical Observatory (SAAO) were reported by Wegner (1976). Observations of V820 Cen on the *uvby*, Hβ and *VRI* photometric systems were obtained between 1976 and 1980 by Eggen (1986), who presented light and colour curves for the intermediate band observations. A very deep minimum ($\Delta V \sim 2.0$ mag) was observed in 1977, where the usual amplitude of V variations was $\Delta V \sim 0.8$ mag. A mean cycle length of 150 d was determined and a range in V from 8.4 to <10.1.

The General Catalogue of Variable Stars (Kholopov et al. 1985) classifies V820 Cen as an RV Tauri star, but does not specify a subclass designation. This classification is based on the photometric V data presented by Eggen (1978), which is a subset of the data discussed in Eggen (1986). Less than one cycle was covered by Eggen (1978), making the classification of V820 Cen as an RV Tauri star a very tentative one.

3.7.2 Photometry from MJUO

A total of 64 night-averaged *BVRI* photometric observations were obtained using the B&C and the OC 0.61-m telescopes at MJUO between 1990 August and 1992 October. Table 2.1 shows the position and adopted photometric magnitudes for the comparison star (SAO 205274) and the check star (SAO 205365) that were used to obtain the differential photometry. The internal accuracy of the V photometry is 0.01 magnitudes.

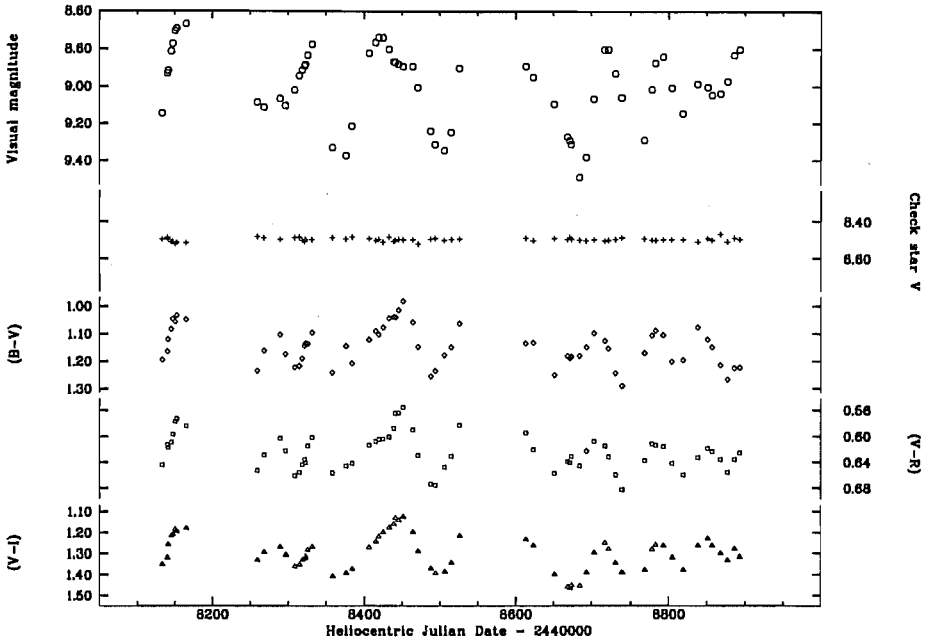

Figure 3.42: The V light and $(B–V)$, $(V–R)$ and $(V–I)$ colour curves for V820 Cen.

The V light curve and $(B–V)$, $(V–R)$ and $(V–I)$ colour curves for V820 Cen are plotted in Fig. 3.42. In order to give a visual indication of the precision of the differential photometry, the V magnitudes for the check star are also included in this plot and are displayed on the same scale as the V magnitudes for V820 Cen. Fig. 3.43 displays the individual B, R and I magnitudes that were calculated from the photometric data.

3.7.3 Analysis of the photometric data

The light and colour variations in V820 Cen appear to be quite irregular, with no consistent deep–shallow variations apparent. The 64 MJUO photometric points were analysed using the Fourier technique to search for the presence of any periodicities. Fig. 3.44 (top panel) displays the Fourier power spectrum obtained from this analysis. In addition, 117 V photometric points from Eggen (1986) were analysed and the power spectrum is shown in Fig. 3.44 (middle panel). Finally, an analysis of the combined V photometry from MJUO and Eggen gives the power spectrum in Fig. 3.44 (bottom panel).

The Fourier analysis of the MJUO data indicates that three main peaks are present in the power spectrum, at frequencies of $0.00675\,\mathrm{d}^{-1}$ ($\sim$ 148 d),

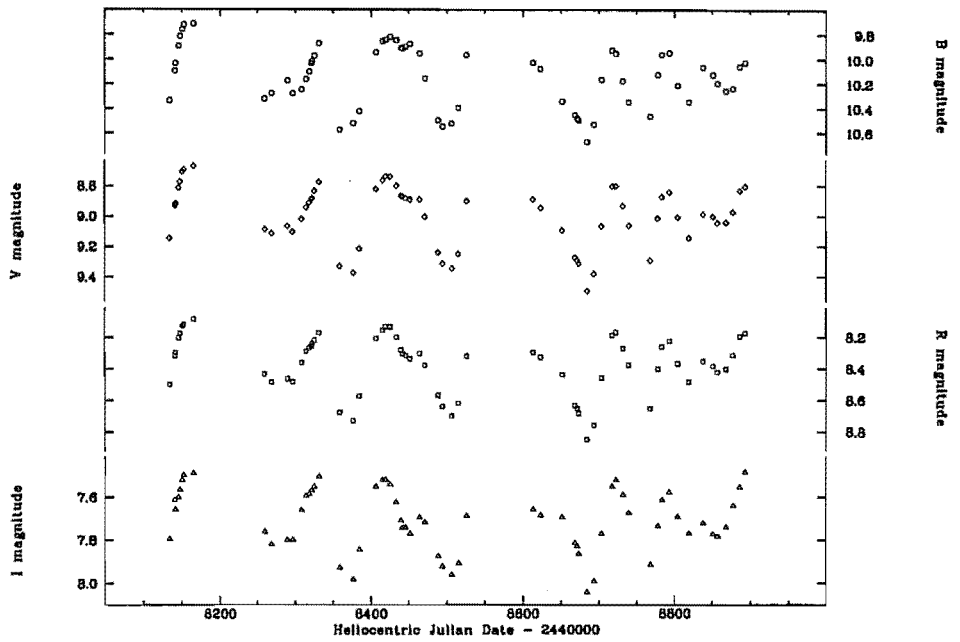

Figure 3.43: Individual B, V, R and I magnitudes for V820 Cen.

$0.01065\,\mathrm{d}^{-1}$ ($\sim$ 94 d) and $0.01250\,\mathrm{d}^{-1}$ ($\sim$ 80 d). Analysing Eggen's (1986) V photometry reveals a dominant peak at a frequency of $0.01255\,\mathrm{d}^{-1}$ ($\sim$ 80 d). However, the two highest peaks in the power spectrum of the MJUO data are each seen to be composed of two constituents in the power spectrum obtained from analysing the Eggen photometry. The power spectrum for the combined photometry is most similar to that of the Eggen data, but with a more complex structure arising from the window function. Table 3.10 presents the main periodicities found in each of the photometric data sets. When the MJUO photometric data from the different filters is analysed, the same three peaks appear in all the power spectra. The 80 d periodicity appears to be more variable in height and is strongest for the redder filters. Fig. 3.45 shows the power spectra for the B, V, R and I photometry from MJUO.

From the analysis of the combined photometry, it is not obvious that V820 Cen is an RV Tauri star. Although Eggen's data by itself suggests that the dominant periods are $\sim$ 80 d and $\sim$ 160 d, the presence of a number of other strong periodicities (at about 93 d, 100 d and 130 d) make the form of the light curve rather complex. It appears that two of the three main peaks in the analysis of the MJUO photometry are actually unresolved double peaks. The $\sim$ 80 d periodicity

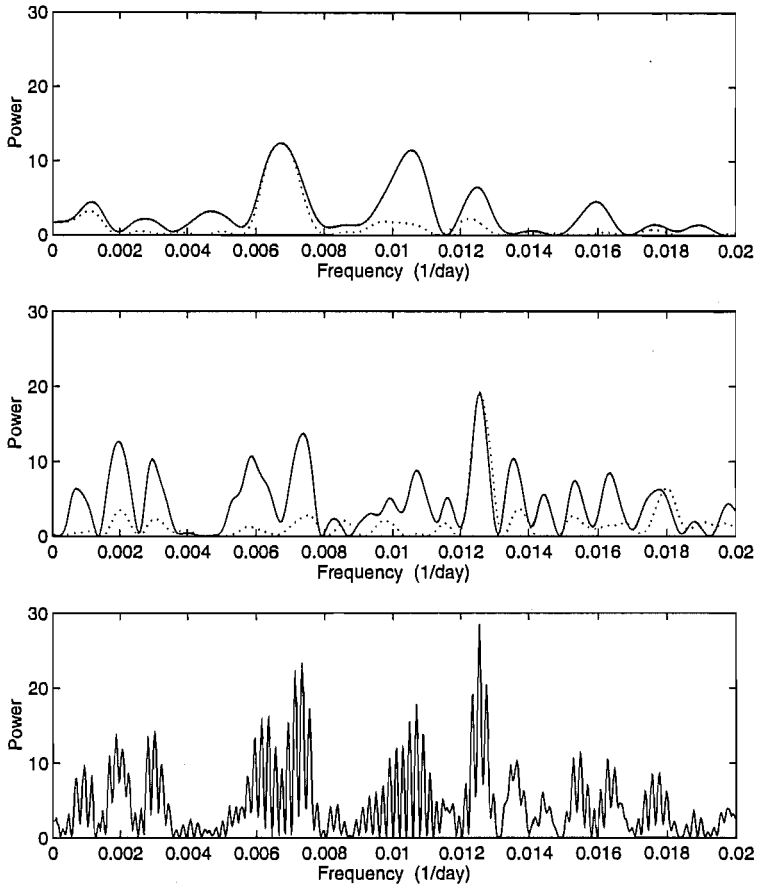

Figure 3.44: The power spectra from the Fourier analysis of the V820 Cen V photometry. The power spectra for the MJUO photometry (top panel), Eggen's (1986) photometry (middle panel) and the combined photometry (bottom panel) are shown. The dotted line shows the natural window.

Table 3.10: The Fourier analyses of the V820 Cen V photometry

Data		f (d^{-1})	P (d)	A (mag)	ϕ (°)	rms
V_{MJUO}	f_1	0.00675	148.1	0.18	137	0.155
	f_2	0.01065	93.9	0.11	106	0.129
	f_3	0.01600	62.5	0.11	34	0.105
V_{Eggen}	f_1	0.01255	79.7	0.19	84	0.216
	f_2	0.00630	158.7	0.17	252	0.194
	f_3	0.01075	93.0	0.12	344	0.174
$V_{(MJUO + Eggen)}$	f_1	0.01254	79.7	0.19	85	0.203
	f_2	0.01066	93.8	0.12	4	0.177
	f_3	0.01006	99.4	0.11	99	0.156

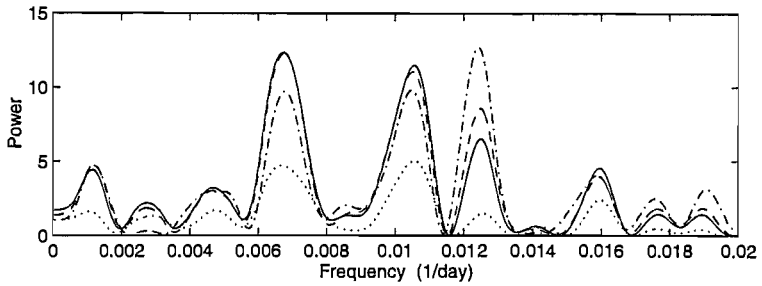

Figure 3.45: The power spectra from the Fourier analysis of the MJUO B (dotted), V (solid), R (dashed) and I (dot-dash) photometry for V820 Cen.

is present but is strongest in the I filter. No consistent deep–shallow alternations are obvious from the period analyses of the combined data set. The 80 d periodicity appears as the strongest peak.

The calculated synthetic light curves are compared with the MJUO and Eggen (1986) V photometric data in Fig. 3.46. Two synthetic light curves are shown. The first curve (solid line) represents the 79.8 d period. The second curve (dashed line) represents the addition of the first two periodicities (79.7 d + 93.8 d) from the Fourier analysis of the combined data set.

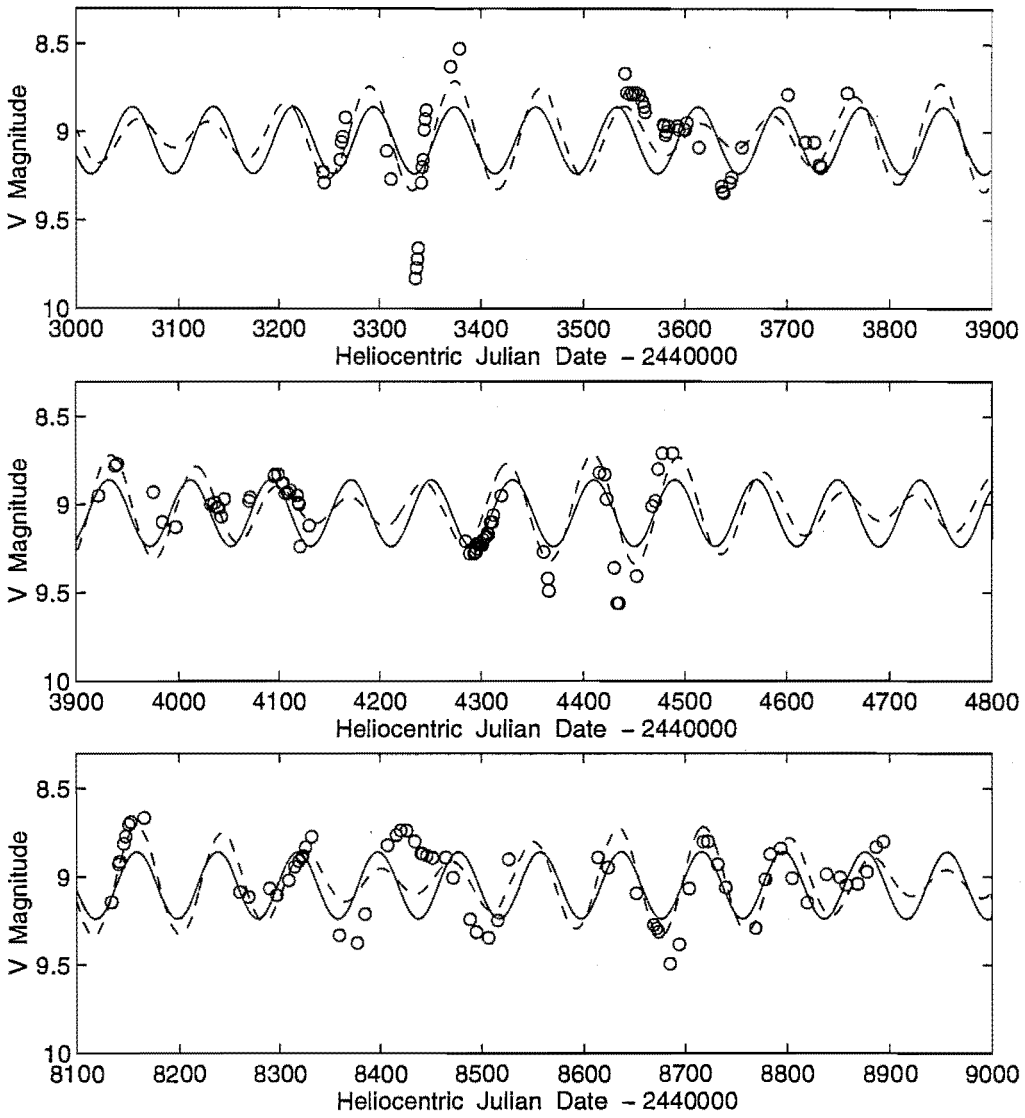

Figure 3.46: The synthetic light curves obtained from the analysis of the V820 Cen V photometry. The synthetic curves are shown for a one period fit (solid line) and a two-period fit (dashed line) to the combined MJUO and Eggen V photometry.

Chapter 4

Photometry of the RVb stars

This chapter presents the analysis of the MJUO photometric data for the four programme RV Tauri stars of the RVb subtype. The RVb subclass have a long-term (~600–2500 days) modulation of the mean V magnitude superimposed on the short-term period of ~30–150 days. Although it is well-established that the short-term light and colour variations are due to pulsations in these stars, the long-term variations are less well understood. Light curves from visual estimates and photographic observations appear to show that the long-term light variations are not strictly periodic, but are cyclic in nature. However, the long-term light behaviour is rather difficult to consider in isolation, due to the fact that the short-term pulsations are not completely regular and are thus not able to be modelled exactly. The short- and long-term light variations are typically of a comparable amplitude which complicates the procedure of disentangling the two, particularly if the light curve is sparsely sampled.

There is very little multicolour photometry published for these stars and none that is continuous over a long enough time baseline to study the long-term light and colour variations in these stars. Obtaining these data was one of the motivations for including a number of RVb stars on the RV Tauri photometric programme. The brightest star of the four programme RVb stars, U Mon, exhibits the typical characteristics of this subclass and is discussed in greatest detail (see Section 4.1). The other members of this subclass that have been included in the RV Tauri programme at MJUO are AI Sco, AR Pup and IW Car.

4.1 U Mon

4.1.1 Background

U Mon is the second brightest RV Tauri star and the brightest of the RVb photometric subtype. As a consequence of its relative brightness, U Mon has been observed quite extensively compared with other RV Tauri stars. The first recorded observations of this star date from 1873.

Gerasimovič (1929) includes U Mon in his study entitled "A General Study of RV Tauri Variables". A double period of 92.26 d is quoted and a visual magnitude range from 5.7 to 7.2 magnitudes.

From visual estimates of the variable's brightness, Loreta (1938) obtained a period of 2320 d for the long-term light variations. Other estimates of this long-term periodicity are taken from radial velocity studies of U Mon. Sanford (1933), Abt (1955), Preston (1964) determined periods of 2300 d, 2640 d or 1980 d and 1500 d or 3000 d respectively.

Recently, Percy et al. (1991) studied the visual and photographic data of U Mon from 1883 to 1988 in order to determine the long and short periods for the light variations. The short period variations were studied through the use of (O–C) variations of the phase in periods versus the Julian Date. This shows that the period decreased abruptly in 1957 (JD 2436000) from 46.117±0.003 d to 45.814±0.005 d. Plotting the visual magnitude versus Julian Date revealed a long period of about 2475 d.

4.1.2 Photometry from MJUO

Photometric *BVRI* observations of U Mon were obtained with the B&C and OC 0.61-m telescopes at MJUO between 1990 August and 1994 May. A total of 131 good-quality, night-averaged observations of U Mon were obtained. The comparison and check stars were SAO 152986 and SAO 134769 respectively. This comparison star has been used in the past for differential photometry (Preston et al. 1963, Wisse & Wisse 1973, Dawson 1979). The adopted V magnitudes and colours are presented in Table 2.1. The internal accuracy of the V photometry is 0.02 magnitudes. This value is quite large indicating that some low amplitude variability of the comparison or check star may be present.

Fig. 4.1 shows the V magnitudes and the colour indices obtained for U Mon. The individual B, V, R and I magnitudes are displayed in Fig. 4.2. The most

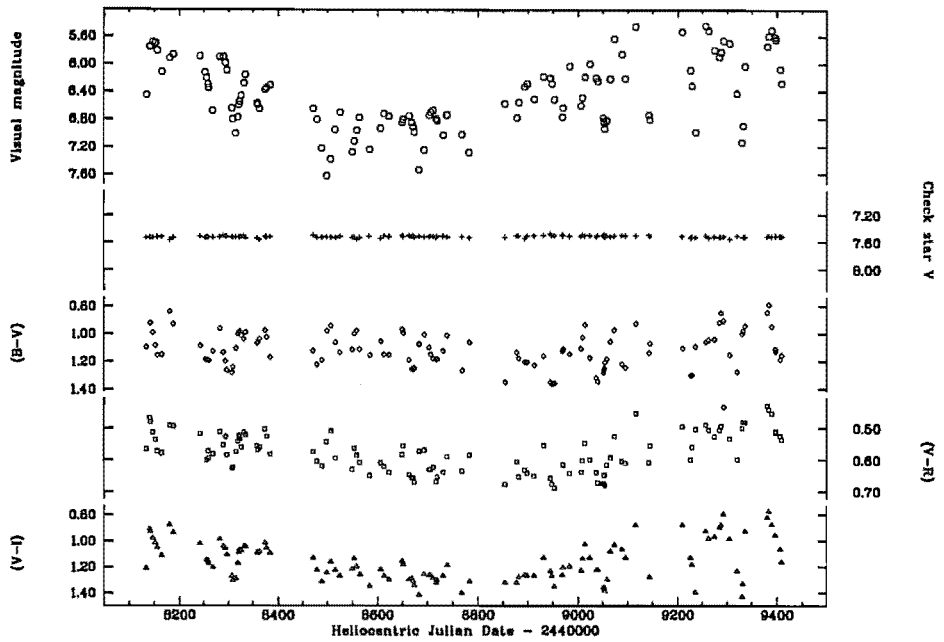

Figure 4.1: The V light curve and $(B–V)$, $(V–R)$ and $(V–I)$ colour curves for U Mon.

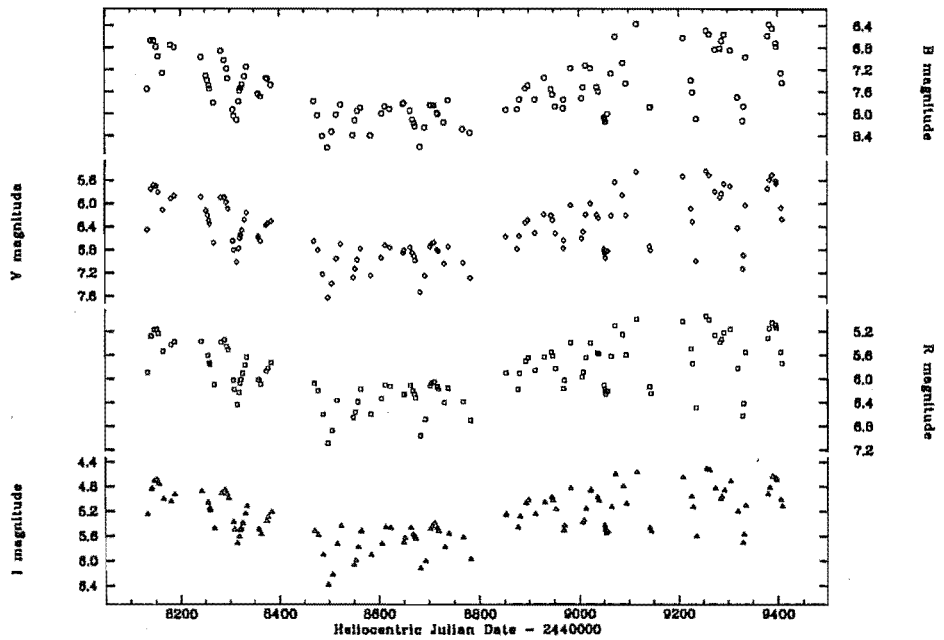

Figure 4.2: Individual B, V, R and I magnitudes for U Mon.

Table 4.1: The amplitude of the long-term variation in U Mon.

Filter	Amplitude (mag)	M_{max}[a] (mag)	M_{min}[b] (mag)
B	1.40	6.35	7.75
V	1.25	5.45	6.70
R	1.15	4.95	6.10
I	0.90	4.55	5.45
$(B-V)$	0.18	0.78	0.96
$(V-R)$	0.14	0.43	0.57
$(V-I)$	0.36	0.78	1.14

[a]Magnitude of the maxima during the long-term maximum

[b]Magnitude of the maxima during the long-term minimum

striking feature of this latter figure is the long-term modulation of the light curve which is apparent in all four filters. The amplitude of the long-term light variation is determined by measuring the change in the magnitude of the short-term (pulsational) light maxima from long-term minimum to long-term maximum. The amplitudes of variation in all four filters is estimated from the plotted photometric data and these are listed in Table 4.1. The light maxima are used since they are much less variable than the light minima.

The colour curves also show this long-term variation and it is particularly obvious in the $(V-R)$ and $(V-I)$ colours. The colours are redder during the minimum of the long-term oscillation. However, there appears to be a slight phase difference between the light and colour curves so that the reddest colours occur at a slighter later time than long-term minimum of the light curve. The amplitudes of the long-term colour variations are also shown in Table 4.1.

Another characteristic of the light and colour curves is the increase in the amplitude of the short-term variations at the maximum of the long-term cycle. There appears to be a greater increase in the amplitude in the B, V and R filters than in the I filter. For the colour curves, the increase in the amplitude is most apparent in the $(V-I)$ colour curve.

4.1.3 Analysis of the photometric data

The long-term modulation of the V light curve for U Mon appears to be reasonably sinusoidal until about HJD 2449100 when the light curve 'flattens out' and

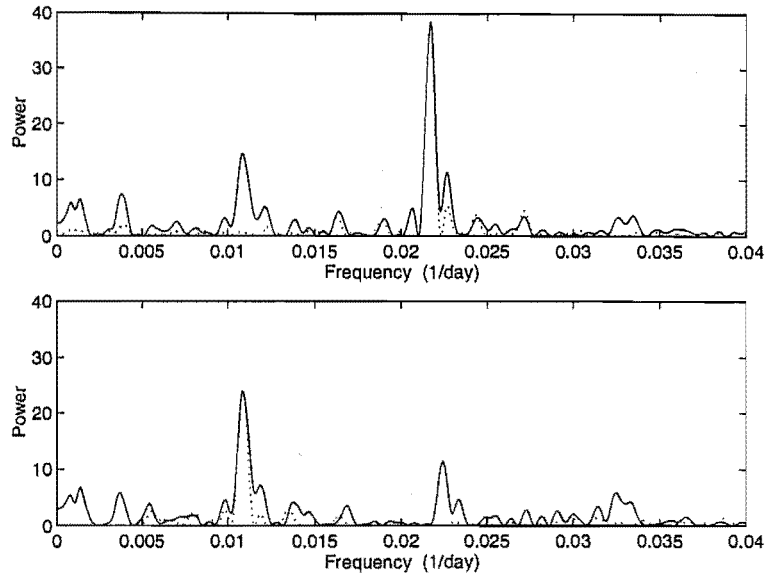

Figure 4.3: The power spectra from the Fourier analysis of the U Mon V photometry (solid line). The dotted line shows the natural window function for the photometry.

U Mon remains at maximum light. This appears to be a characteristic of some of the RVb stars and has been noted in studies based on photographic and visual estimates of both U Mon (Percy et al. 1991) and AI Sco (Voûte 1932a). These stars spend comparatively more time at maximum light with abrupt, periodic declines to the minimum of the long-term oscillation. Some researchers have claimed that these long term variations (particularly in the case of U Mon, see Preston (1964, 1972), Tsesevich (1975)) are not periodic at all, but are cyclic occurrences. However, Percy et al. (1991) have recently shown that a long-term period of 2475 d is a reasonable fit to the photographic observations and visual estimates of U Mon from JD 2425000–2447500 (1928 to 1988). It will be shown later (see Chapter 8) that the radial velocity variations for U Mon are in reasonable agreement with the light variations, giving a long period of about 2600 d.

The long-term light variations in U Mon were modelled by fitting smooth spline curves to the maxima of the photometric data (the maxima being much more well defined and not as variable as the minima). This was done for the light curves in each of the four filters and for the three colour curves. This long term trend was then subtracted from the photometric data, so that the short period could be determined.

Table 4.2: The analysis of the photometric data for U Mon. The B, V and $(B–V)$ data sets consist of 131 photometric points. There are 129 points in the R and $(V–R)$ data sets and 130 points in the I and $(V–I)$ data sets.

Data	Fit[a]	f_1 (d^{-1})	P_1 (d)	A_1 (mag)	ϕ_1 (°)	f_2 (d^{-1})	P_2 (d)	A_2 (mag)	ϕ_2 (°)	rms
B	F	0.02166	46.17	0.43	58	0.01083	92.34	0.25	23	0.242
	L	0.02165	46.19	0.42	61	0.01082	92.39	0.26	24	0.240
V	F	0.02168	46.13	0.40	37	0.01084	92.25	0.21	16	0.193
	L	0.02167	46.16	0.39	40	0.01083	92.31	0.26	20	0.192
R	F	0.02170	46.08	0.40	20	0.01085	92.17	0.19	13	0.183
	L	0.02167	46.14	0.38	31	0.01084	92.29	0.20	18	0.180
I	F	0.02170	46.08	0.33	16	0.01085	92.17	0.13	15	0.129
	L	0.02167	46.14	0.32	25	0.01084	92.29	0.13	20	0.127
$(B–V)$	F	0.02166	46.17	0.13	130	0.01083	92.34	0.05	45	0.074
	L	0.02167	46.14	0.12	130	0.01084	92.28	0.05	42	0.066
$(V–R)$	F	0.02166	46.17	0.04	114	0.01083	92.34	0.01	6	0.028
	L	0.02166	46.17	0.04	115	0.01083	92.34	0.01	6	0.028
$(V–I)$	F	0.02162	46.25	0.11	93	0.01081	92.51	0.08	20	0.077
	L	0.02163	46.24	0.10	93	0.01081	92.47	0.08	19	0.077

[a]F is the Fourier harmonic fit; L is the least-squares harmonic fit.

The dominant short-term or pulsational periodicities present in the U Mon photometry were then determined using both the Fourier analysis and the least-squares technique. The Fourier power spectra for the MJUO V photometry are displayed in Fig. 4.3. The long-term period has already been modelled and subtracted from the photometry so that no low frequencies should be present. A dominant periodicity is seen at 46.16 d ($f_1 = 0.02168\,d^{-1}$) in the upper panel of Fig. 4.3 and once this has been subtracted from the photometric data a period of 92.08 d ($f_1 = 0.010868\,d^{-1}$) is revealed. The power spectra for the B, V, R and I photometry all display these two dominant periodicities.

As for the RVa stars, the harmonic fit was adopted as the more realistic model of the light variations. Table 4.2 presents the results of the analysis for the harmonic fit. The short-term variations in U Mon appear to display the same general characteristics that were seen in the RVa stars. The bluer light curves have greater amplitudes and lead the redder light curves in phase. The $(V–R)$ curve has a much smaller amplitude than either of the $(B–V)$ or $(V–I)$ colour curves.

A mean period was derived from the average of the periods from the analysis of the B, V, R and I photometry. The accuracy of the period determination is

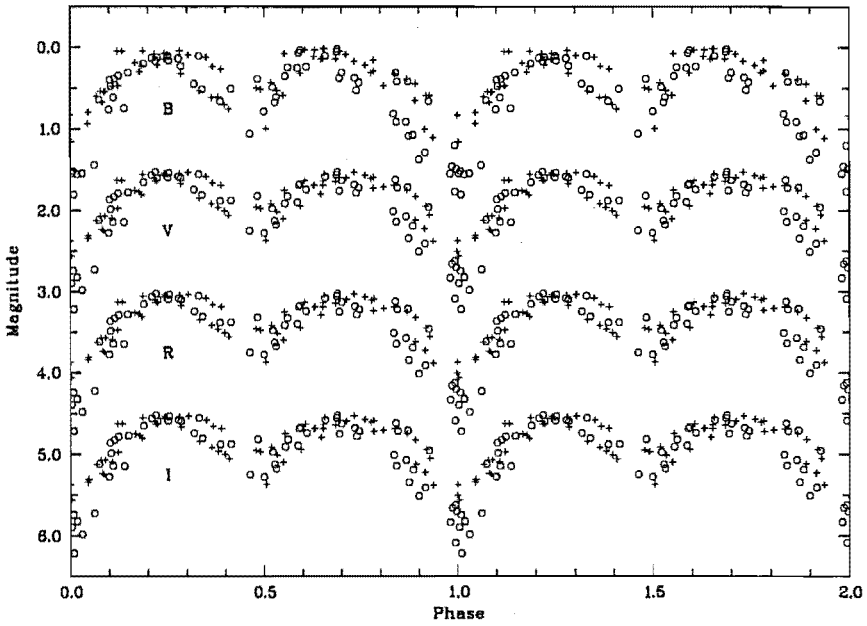

Figure 4.4: The phased (period = 92.32 d) residual B, V, R and I magnitudes for U Mon. Offsets of 1.5, 3.0, 4.5 magnitudes have been applied to the V, R and I data respectively. 1991 and 1992 (+), 1993 and 1994 (o).

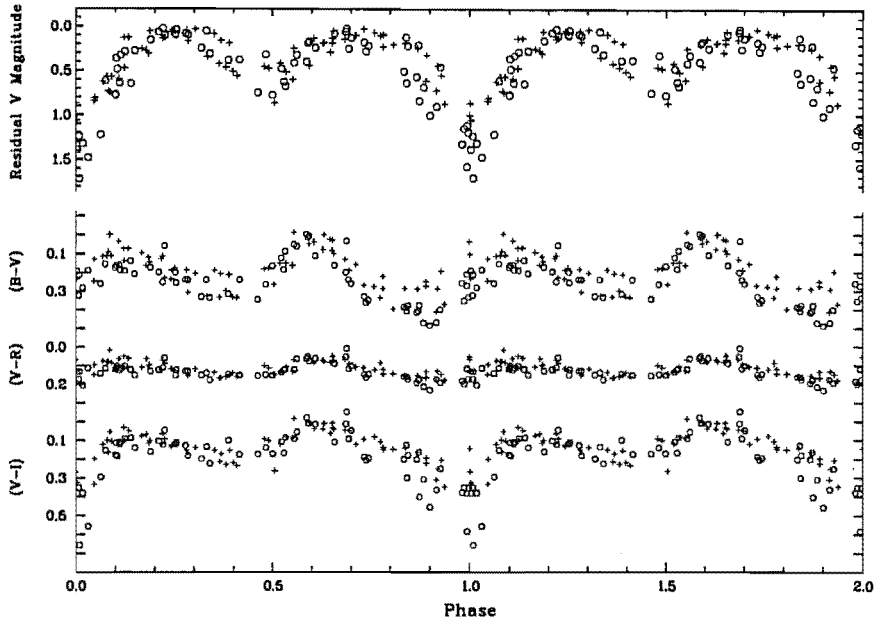

Figure 4.5: The phased residual V, $(B–V)$, $(V–R)$ and $(V–I)$ photometry for U Mon. 1991 and 1992 (+), 1993 and 1994 (o).

taken as the standard deviation of the value of the period in the different filters. The average period is calculated to be (46.16 ± 0.02) d, which corresponds to a double period of (92.32 ± 0.04) d. The photometry was phased using the double period and the phased light and colour curves are plotted in Figs 4.4 and 4.5. In these two figures, the photometry from the 1991 and 1992 observing seasons (+) and the photometry from the 1993 and 1994 observing seasons (o) are plotted with different symbols in order to reveal any trends from the different years of observations. (It should be remembered that the long-period trend has been removed from all the photometry), so that it is the *residual* magnitudes and colour index values that are being plotted in these figures. Since a smooth spline curve was fitted to the maxima of the data, this should define the zero-deviation level in the residuals.)

The light curves in Fig. 4.4 show a reasonable amount of scatter in both the primary and secondary minima. For the primary minima, most of this scatter is due to the increased amplitude of the light variations in the 1993 and 1994 observing seasons. Quite some variation is seen in the depth of the secondary minima also but this does not seem to be correlated with the changing amplitude

of the primary minima. As the star comes out of the long-term minimum (during the 1993 and 1994 season), it appears that the secondary minima do not get any deeper, even as the primary minima increase in amplitude.

The bluer light curves show slightly more asymmetry than the redder light curves. As a result, the phase differences between the four filters change with phase. The largest phase difference occurs around secondary maximum, which occurs at about phase 0.65 in the B light curve and at about phase 0.70–0.75 for the I curve.

The colour curves displayed in Fig. 4.5 have quite an asymmetric appearance, with the rise to maximum typically much steeper than the descent to minimum. The colours are bluer during increasing V light and redder during decreasing V light. During the rise from secondary minimum to secondary maximum (phase 0.5–0.7) the colours tend to reach their smallest (bluest) value. This is a tendency that was also seen in the 'regular' RVa stars.

In contrast to the colour curve behaviour displayed by R Sct where the deeper minima gave rise to bluer colours, the deeper minima in U Mon (which occurred in the 1993 and 1994 seasons) have little difference or are slightly redder in their $(B–V)$ and $(V–R)$ colours when compared with the shallower minima. *This contrasting behaviour suggests that the mechanism for producing the very deep minima in the RVa stars is different from that in the RVb stars.* The amplitude change in the short-term light variations in the RVb stars is periodic and is related to the long-term cycle[1], whereas for the RVa stars, the deeper light variations seem to occur in a reasonably random manner.

The change in amplitude of the light variations was then investigated by analysing each year of photometry separately. Table 4.6 shows the year-by-year analysis of the V and the I photometry for U Mon. Each season's observations consist of at least 30 photometric points. A least-squares harmonic fit was used for this analysis. It can be seen that the variations in the V filter tend to be larger than those in the I filter. The variations in 1991 and 1992 have a smaller amplitude than in the 1993 and 1994 seasons in both the V and the I filters. The amplitude of the f_2 periodicity is larger in 1993 and 1994. This larger amplitude means that there is a greater difference in the depths of the primary and secondary light minima during these seasons.

The synthetic curves from the analysis of the entire V data set is compared

[1]The light variation amplitude is smaller during the minimum of the long-term oscillation.

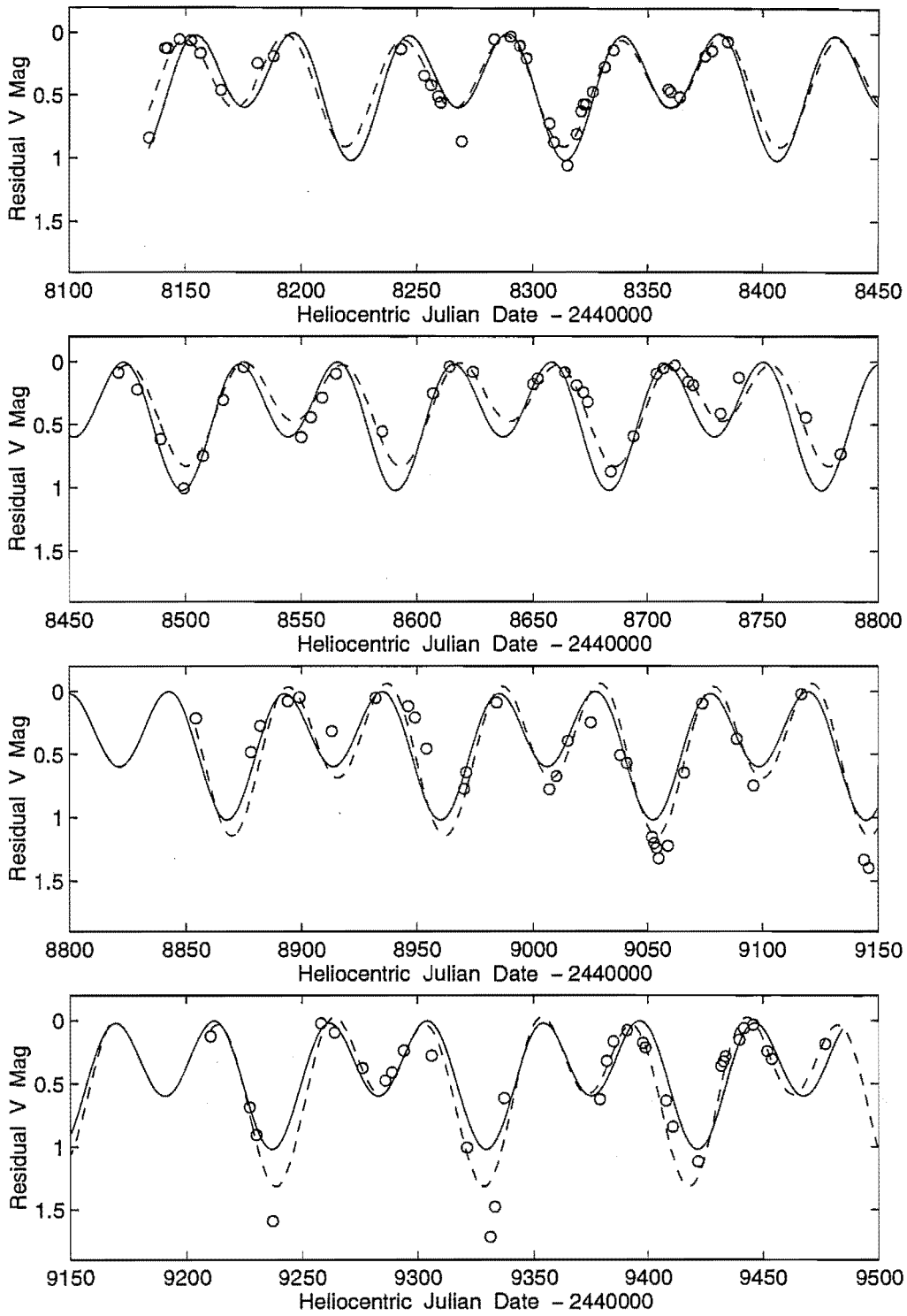

Figure 4.6: The harmonic fit (solid line) to the residual V magnitudes for U Mon. The dashed line shows the synthetic light curve derived from analysing each year of data separately. Top to bottom: 1991, 1992, 1993, 1994.

Table 4.3: The least-squares harmonic fit to the individual years of U Mon V and I photometry.

Data	N^a	f_1 (d^{-1})	P_1 (d)	A_1 (mag)	ϕ_1 (°)	f_2 (d^{-1})	P_2 (d)	A_2 (mag)	ϕ_2 (°)	rms
all V	131	0.02167	46.16	0.39	40	0.01083	92.31	0.21	17	0.192
all I	130	0.02165	46.19	0.32	24	0.01082	92.39	0.13	15	0.127
1991 V	35	0.02121	47.16	0.36	75	0.01060	94.32	0.15	31	0.094
1991 I	35	0.02110	47.40	0.29	64	0.01055	94.80	0.10	33	0.051
1992 V	32	0.02155	46.41	0.31	134	0.01077	92.82	0.18	250	0.089
1992 I	32	0.02155	46.40	0.31	123	0.01078	92.80	0.14	252	0.091
1993 V	31	0.02172	46.05	0.48	239	0.01086	92.09	0.23	296	0.180
1993 I	31	0.02175	45.98	0.37	227	0.01088	91.95	0.14	305	0.123
1994 V	33	0.02232	44.80	0.46	130	0.01116	89.60	0.37	70	0.153
1994 I	33	0.02218	45.09	0.34	164	0.01109	90.17	0.21	82	0.085

[a] N is the number of data points

with the synthetic light curve derived from the year-by-year analysis in Fig. 4.6. The larger amplitude variations in 1993 and 1994 are evident. The V photometry from 1992 (at the long-term minimum) shows the smallest amplitude variations. It is interesting to note that the main increase in the amplitude of the light variation appears to be in the primary minima. The secondary minima do not seem to increase in depth to the same extent that the primary minima do at the maximum of the long-period variation.

4.2 AI Sco

4.2.1 Background

The variability of AI Sco was discovered by Cannon on Harvard plates (as reported by Voûte 1932a). Voûte (1932a) presents a light curve for AI Sco from 1926 to 1930 using photographic magnitudes obtained from Harvard plates. This light curve clearly shows the short and long period variations of this star. A short period of 35.62 d was determined with an amplitude of 2.0 magnitudes.

A continuation of this study until 1939 (Voûte 1941) noted irregularities in the short period variations, but stated a mean of 35.89 d. A light curve representing the long period variations of AI Sco between 1926 and 1939 was also displayed. The long period was found to be 960 d and a gradual amplitude decrease from 1.61 to 0.82 magnitudes was observed over the time of the observations. This amplitude decrease was seen to arise from a variation in the depth of the minima,

since the magnitude at maximum was almost constant. Voûte (1941) noted the similarity of the variations of AI Sco to those of SX Cen and suggested that a new class of variable, the *AI Scorpii type stars*, be recognised.

O'Connell (1933) used earlier photographic plates from 1890 to 1926 to estimate the brightness of the star and combined these estimates with those from Voûte's (1932a) paper. The short period seemed to fluctuate by up to 0.5 d from the mean of 35.50 d. The long period was determined to be 980 d.

Rosino (1951) and Joy (1952) both note the RV Tauri membership of AI Sco, and subsequent to the definition of RVa and RVb photometric subtypes in the second edition of the General Catalogue of Variable Stars (Kukarkin et al. 1958), Preston et al. (1963) classified AI Sco as belonging to the RVb subtype. Sky Catalogue 2000.0 (Hirshfeld & Sinnott 1985) gives a range of 9.5–12.7 for the light variations in V.

The only published photoelectric photometry of AI Sco seem to be single-night observations obtained for the purpose of circumstellar dust-shell modelling and no complete or partial photometric light curves are available.

4.2.2 Photometry from MJUO

AI Sco was an addition to the RV Tauri programme in 1991 August. Between 1991 August and 1994 April a total of 131 good-quality, night-averaged *BVRI* observations of AI Sco were obtained using the B&C and OC 0.61-m telescopes at MJUO. The comparison and check stars were SAO 209445 and SAO 209464 respectively. Table 2.1 presents the V magnitudes and colours that were adopted for these stars. The check star, SAO 209464, has spectral type M2 and a somewhat uncertain III: luminosity class. From the MJUO photometry it is suspected as being a low-amplitude red variable star with light variations that were not noticed at the time of observation. The internal accuracy of the V photometry was therefore unable to be obtained using the check star's V magnitudes.

The V magnitudes and the colour indices obtained for AI Sco are shown in Fig. 4.7 with the individual B, V, R and I magnitudes displayed in Fig. 4.8. As for U Mon, the long-term modulation of the light curve is quite apparent, with the photometric data obtained during the 1992 season (HJD 2448470 to HJD 2448910) appearing much fainter in all filters and slightly redder in all colours than the 1991, 1993 or 1994 season's data. The amplitude of the long-term variation is estimated from the the plotted light and colour curves curves (Table 4.4). The

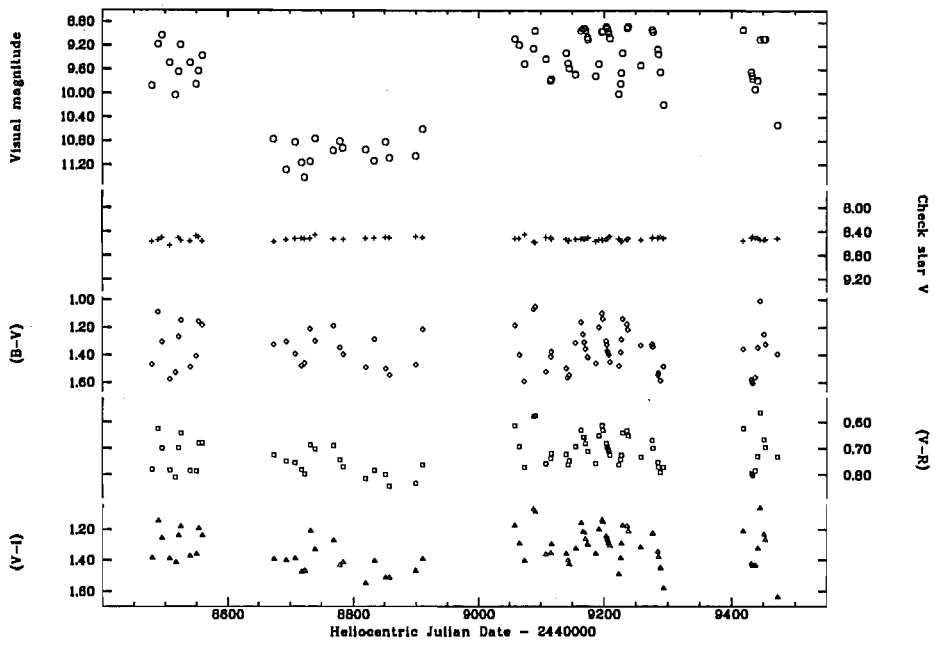

Figure 4.7: The V light curve and $(B–V)$, $(V–R)$ and $(V–I)$ colour curves for AI Sco. The low level variability that is present in the check star, SAO 209464, is just detectable on this scale.

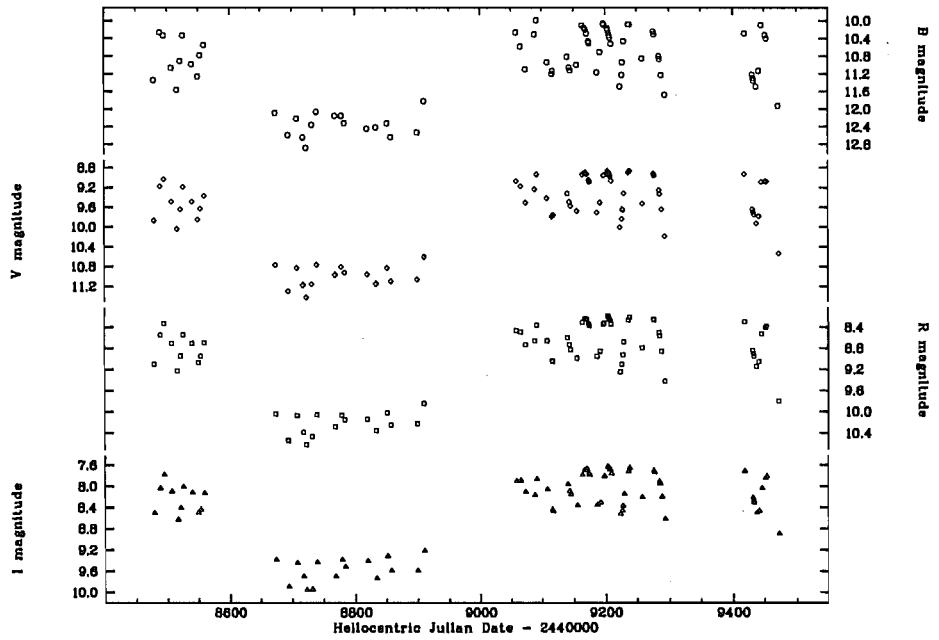

Figure 4.8: Individual B, V, R and I magnitudes for AI Sco.

Table 4.4: The amplitude of the long-term variation in AI Sco.

Filter	Δ mag	$M_{\rm min}{}^a$	$M_{\rm min}{}^b$
B	2.05	10.00	12.05
V	1.90	8.85	10.75
R	1.85	8.15	10.00
I	1.70	7.60	9.30
$(B-V)$	0.16	1.06	1.20
$(V-R)$	0.11	0.57	0.68
$(V-I)$	0.14	1.09	1.23

[a]Magnitude of light maxima during long-term maximum

[b]Magnitude of light maxima during long-term minimum

short-term light variations appear to have a larger amplitude at the maximum of the long-term cycle, as was seen in U Mon. This is most apparent in the bluer filters.

4.2.3 Analysis of the photometric data

The long period evident in the photometry of AI Sco has a distinctly non-sinusoidal shape. A period of about 940 d was obtained from fitting a pure sinusoid to the photometry, but it was quite apparent that the descent to the long period minimum and the rise to maximum were quite abrupt. AI Sco remains at maximum light longer than at minimum light. This confirms Voûte's (1941) estimate of the shape of the light curve for the long period, which was determined from photographic observations of AI Sco. The previously-discussed RVb star, U Mon (Percy 1993), appears to share this characteristic of spending comparatively more time at maximum light with periodic declines to the long-term minimum.

The long-term light variations in AI Sco were modelled by fitting smooth spline curves to the photometric data for each year of observation. This long term trend was then subtracted from the photometry so that the short period could be determined. The long-term trend in the $(B-V)$ photometric data was not subtracted since the slight reddening due to the effect of the long period was very small compared to colour changes arising from the short-term pulsational effects.

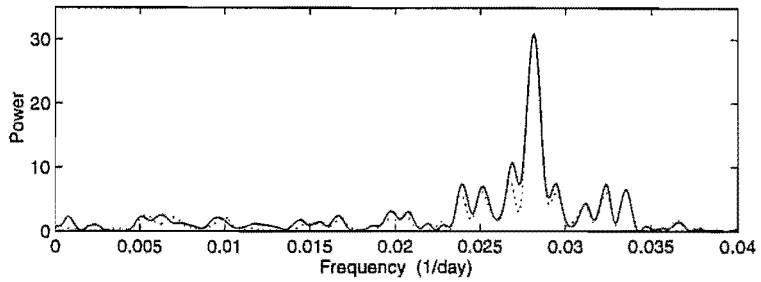

Figure 4.9: The power spectrum for the AI Sco V photometry (solid line). The dominant peak occurs at $f_1 = 0.02814\,\mathrm{d}^{-1}$ ($P_1 = 35.54\,\mathrm{d}$). The dotted line shows the natural window function.

Table 4.5: The analysis of the photometric data for AI Sco. Each data set consists of 78 photometric points.

Data	Fit[a]	f_1 (d^{-1})	P_1 (d)	A_1 (mag)	ϕ_1 (°)	f_2 (d^{-1})	P_2 (d)	A_2 (mag)	ϕ_2 (°)	rms
B	F	0.02814	35.54	0.61	48	0.01407	71.07	0.10	194	0.222
	L	0.02815	35.52	0.55	43	0.01408	71.04	0.12	196	0.216
V	F	0.02814	35.54	0.48	30	0.01407	71.07	0.07	198	0.152
	L	0.02815	35.52	0.42	26	0.01408	71.05	0.07	197	0.147
R	F	0.02814	35.54	0.42	22	0.01407	71.07	0.07	190	0.141
	L	0.02815	35.53	0.38	19	0.01407	71.06	0.07	189	0.137
I	F	0.02816	35.51	0.38	11	0.01408	71.02	0.06	188	0.109
	L	0.02818	35.49	0.34	6	0.01409	70.98	0.06	181	0.104
$(B-V)$	F	0.02814	35.54	0.19	90	–	–	–	–	0.066
	L	0.02816	35.51	0.19	85	0.01408	71.02	0.03	220	0.062
$(V-R)$	F	0.02816	35.51	0.07	71	–	–	–	–	0.032
	L	0.02817	35.50	0.07	68	0.01408	71.00	0.01	224	0.031
$(V-I)$	F	0.02804	35.66	0.13	98	–	–	–	–	0.067
	L	0.02804	35.67	0.13	97	0.01402	71.33	0.01	237	0.066

[a]F is the Fourier harmonic fit; L is the least-squares harmonic fit.

The Fourier power spectrum of the V photometry reveals a dominant periodicity at $f_1 = 0.02814\,\mathrm{d}^{-1}$ corresponding to a period of $P_1 = 35.54\,\mathrm{d}$ (see Fig. 4.9). It can be seen that most of the structure in the power spectrum arises from the 35.54 d periodicity and its associated window function peaks. As with the previous stars, the harmonic fit was used to model the light and colour variations. Due to the low power of any 70 d ($2P_1$) periodicity in the photometry, it was found that the harmonic fit offered only a small reduction in the residuals as compared with the single sinusoid fit. For the colours there was practically no reduction in the residuals when the second periodicity was added to the fit. Although the harmonic fit was employed for the light curves and colour curves to maintain consistency with the analyses of the other RV Tauri stars, the the second ($2P_1$) periodicity was found to have a very low amplitude, particularly for the colour curves (see Table 4.5).

The general trend, both for the RVa stars, and for the RVb star U Mon, is for the amplitude of variation to be greater in the bluer filters than in the redder filters, and for an increasing phase lag for redder filters. This is also what is seen in AI Sco. The synthetic light curve fit to the V photometry for AI Sco is shown in Fig. 4.10. In this figure, the long-term trend has been subtracted from the photometry so residual V magnitudes are being plotted. It appears that the amplitude of the short-term pulsational variations changes from season to season. In the 1992 season (about HJD 2448670 to HJD 2448910) the amplitude of the light variation appears much smaller than in the subsequent seasons. By re-examining the original photometry (see Fig. 4.7) it can be seen that this decrease in amplitude corresponds to the time of the long-term light minimum.

The least-squares analysis of the B, V, R and I photometry was used to derive a mean period for AI Sco. The standard deviation was used to estimate the accuracy of the period determination. The mean period for AI Sco is calculated to be $(35.52 \pm 0.01)\,\mathrm{d}$ which corresponds to a double period of $(71.03 \pm 0.03)\,\mathrm{d}$. The photometric data from MJUO were phased using the 71.03 d period and the light and colour curves are plotted in Figs 4.11 and 4.12.

The bluer light curves show a more asymmetric shape and greater amplitude than the redder light curves. The B light curve has quite a 'sawtooth' shape with a very steep rise from primary minimum. Although a large scatter is quite apparent in the depth of the secondary V minima, the colours are quite consistent at this phase. The colour curves have a more asymmetric appearance during

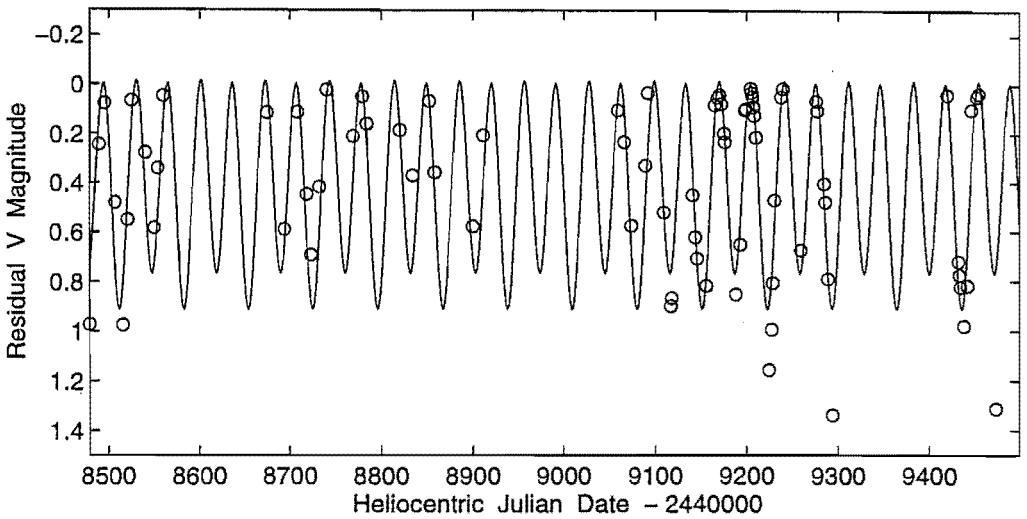

Figure 4.10: The harmonic fit (solid line) to the residual V magnitudes for AI Sco. The long period trend has been subtracted from the photometric data.

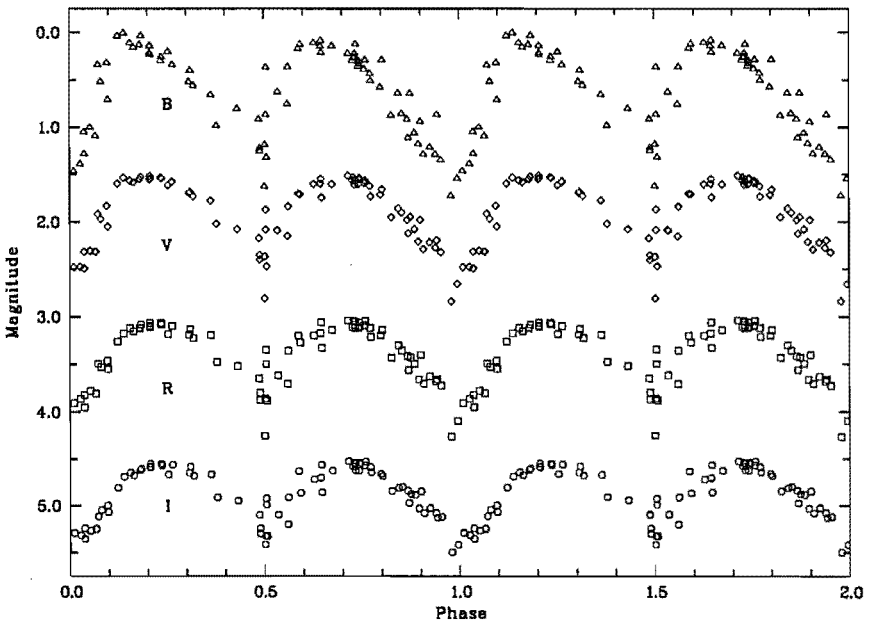

Figure 4.11: The phased (period = 71.03 d) residual B, V, R and I magnitudes for AI Sco. Offsets of 1.5, 3.0, 4.5 magnitudes have been applied to the V, R and I data respectively.

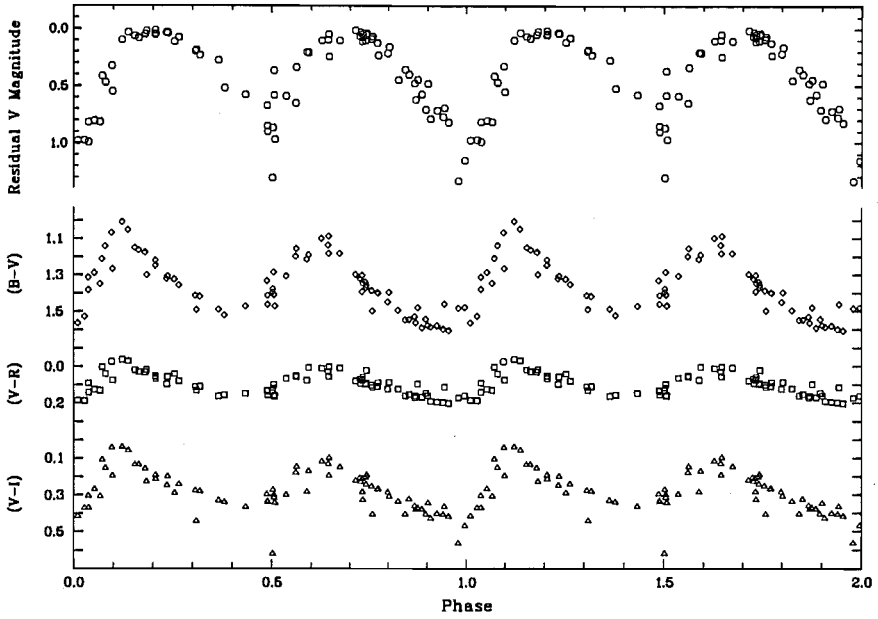

Figure 4.12: The phased residual V, $(V–R)$ and $(V–I)$ colour curves for AI Sco. The long-term trend was not subtracted from the $(B–V)$ data.

phases 0.0–0.5 than during phases 0.5–1.0. The colours are reddest just prior to the primary V minimum. Unlike the majority of the RVa stars and the RVb star U Mon, the colour curves become bluest during the rise from the primary V minimum, rather than from the secondary minimum.

When each year of photometry is analysed[2] separately, the change in amplitude of the light variations becomes apparent. Table 4.6 shows the year-by-year analysis of the V and the I data. Although some seasons have as little as 10 data points, it appears that the variations in the 1992 season have a much smaller amplitude than the 1993 and 1994 seasons. In the 1992 season, both the V and I light curves have a similar amplitude of variation, while in the subsequent seasons, the amplitude of variations in the V filter becomes much larger than those in the I band.

[2] A single-sinusoid fit has been used due to the low amplitude of the second periodicity.

Table 4.6: The analysis of the individual years of AI Sco photometry.

Data	N^a	f (d^{-1})	P (d)	A (mag)	ϕ (°)	rms
all V	78	0.02814	35.54	0.48	30	0.161
all I	78	0.02816	35.51	0.38	11	0.106
1991 V	11	0.03020	33.11	0.38	348	0.149
1991 I	11	0.03028	33.03	0.40	334	0.131
1992 V	16	0.02846	35.14	0.30	203	0.073
1992 I	16	0.02892	34.58	0.27	166	0.089
1993 V	41	0.02798	35.74	0.52	157	0.143
1993 I	41	0.02810	35.59	0.40	136	0.096
1994 V	10	0.03118	33.60	0.66	163	0.227
1994 I	10	0.03118	35.74	0.52	142	0.101

[a] N is the number of data points

4.3 AR Pup

4.3.1 Background

The variability of AR Pup was discovered by O'Leary (1937) from Riverview and Lembang plates. Deep–shallow light variations were observed to occur and these were particularly stable from 1933 to 1935. The double period of 74.58 d appeared more well defined than the single period throughout the whole light curve. Superposed on this short period was a long period of about 1200 d. The light variations of the short period were seen to be larger at long period maximum.

The photographic estimates of O'Leary (1937) were added to 605 observations made by Brenton (Payne-Gaposchkin et al. 1943) and a combined light curve of AR Pup was presented. The period of the long-term variations was determined to be 1218 d and the amplitude of the change in maximum brightness was 1.8 magnitudes. The range in the photographic magnitude of the star was 8.7–10.9. When the phases of the observed minima were plotted versus the epoch, significant departures from the mean period of 75 d were apparent. AR Pup was seen to exhibit interchanges of deep and shallow minima, with about one 'flip' every 8 cycles.

Four-colour *uvby*, Hβ and *VRI* photometric data were presented for AR Pup by Eggen (1986) for slightly more than one 75 d cycle. Raveendran et al. (1989) obtained 63 photometric *BV* observations during 1986–1988 and combined their

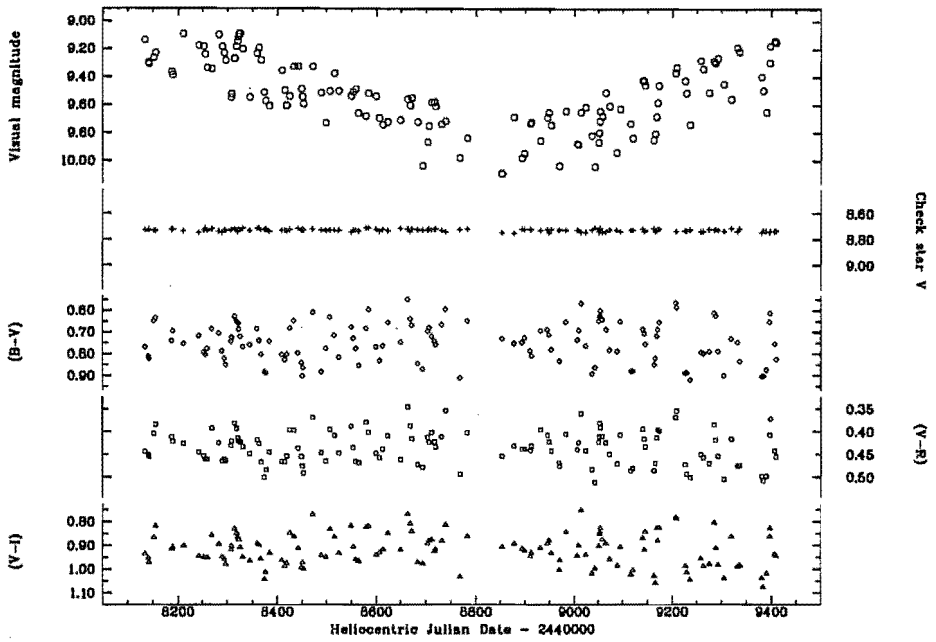

Figure 4.13: The V light curve and $(B–V)$, $(V–R)$ and $(V–I)$ colour curves for AR Pup.

data with Eggen's to produce V light and $(B–V)$ colour curves. In both sets of data it was difficult to ascertain which minima were 'primary' and which were 'secondary'. Much more variability was seen in the V light curve than the $(B–V)$ colour curve. The $(B–V)$ colour curve was seen to lead the V curve by about 0.1 in phase (assuming a 75.0 d period), so that the $(B–V)$ colour attained its bluest value during the ascending branch of the V light curve.

4.3.2 Photometry from MJUO

Between 1990 August and 1994 February, a total of 133 night-averaged $BVRI$ photometric observations were obtained of AR Pup using the 0.61-m B&C and OC telescopes. The adopted magnitudes and colours for the comparison star (SAO 198737) and the check star (SAO 198762) used in the differential photometry are tabulated in Table 2.1. Raveendran et al. (1989) used SAO 198737 as the comparison star for their differential photometry of AR Pup. The standard deviation of the check star's V magnitudes is used to indicate the precision of the AR Pup V photometry. This is calculated to be 0.009 magnitudes.

The colour indices and V magnitudes for AR Pup are displayed in Fig. 4.13

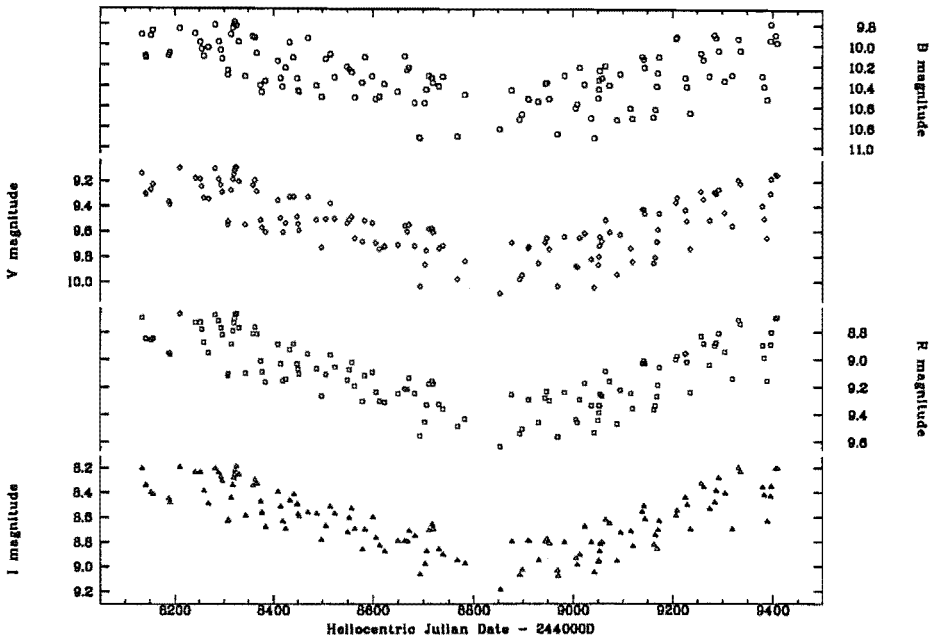

Figure 4.14: Individual B, V, R and I magnitudes for AR Pup.

and the individual B, V, R and I magnitudes are shown in Fig. 4.14. The long-term modulation of the light curves in each of the four filters is quite apparent. Since the MJUO photometry has not sampled the long-term maximum of the light curve, only an estimated lower limit on the amplitude of this light-term light variation can be given (see Table 4.7). The amplitude of the long-term periodicity is very similar in all four filters.

Unlike U Mon and AI Sco, the colour curves (see Fig. 4.13) show very little colour change during the long-term minimum and, if anything, the colours may be slightly bluer during the minimum. There is perhaps a slight increase in the amplitude of the short-term variations from HJD 2449000 to 2449400 following the long-term minimum. The possibility of an amplitude change will be investigated later in the analysis section.

4.3.3 Analysis of the photometric data

Because the long-term trend in the light curves for AR Pup appears to be reasonably sinusoidal in shape, spline fits were not used to model it. Instead, the Fourier analysis was used to determine which low frequencies were a good fit to this long period. The upper panel in Fig. 4.15 shows the Fourier power spectrum

Table 4.7: The amplitude of the long-term variation in AR Pup.

Filter	Amplitude (Δ mag)	M_{max}[a] (mag)	M_{min}[b] (mag)
B	0.63	9.77	10.40
V	0.57	9.09	9.66
R	0.55	8.67	9.22
I	0.55	8.18	8.73

[a]Magnitude of the maxima during long-term maximum

[b]Magnitude of the maxima during long-term minimum

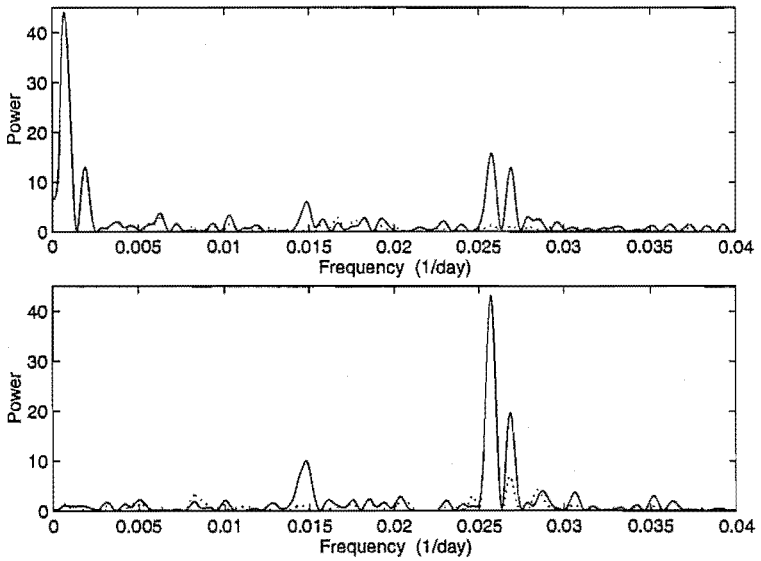

Figure 4.15: The power spectrum for the AR Pup V photometry (solid line). The dotted line shows the natural window function.

Table 4.8: The analysis of the photometric data for AR Pup. There are 133 photometric points in each data set, except for the I and $(V–I)$ data set where there are 132 points.

Data	Fit[a]	f_1 (d^{-1})	P_1 (d)	A_1 (mag)	ϕ_1 (°)	rms
B	F	0.02570	38.91	0.20	252	0.130
	L	0.02571	38.90	0.23	250	0.127
V	F	0.02570	38.91	0.17	228	0.085
	L	0.02571	38.89	0.17	224	0.082
R	F	0.02570	38.91	0.16	217	0.070
	L	0.02571	38.89	0.16	212	0.066
I	F	0.02572	38.88	0.15	198	0.064
	L	0.02571	38.90	0.15	201	0.061
$(B–V)$	F	0.02568	38.94	0.10	300	0.056
	L	0.02568	38.94	0.10	299	0.055
$(V–R)$	F	0.02566	38.97	0.04	302	0.026
	L	0.02567	38.96	0.04	301	0.026
$(V–I)$	F	0.02568	38.94	0.07	296	0.050
	L	0.02569	38.93	0.07	297	0.050

[a]F is the Fourier harmonic fit; L is the least-squares harmonic fit.

resulting from this analysis. A low frequency at $f = 0.00072\,d^{-1}$ ($P = 1389\,d$) is the strongest peak present for the V photometry. The long period from the analysis of the B and R photometry gives the same period, while the analysis of the I photometry gives a low frequency of $f = 0.00074\,d^{-1}$ ($P = 1351\,d$). These derived periods are greater than the time span of the data set and are therefore only intended as a reasonable approximation to the long period in the MJUO photometry. If AR Pup spends more time at long-term maximum than it does at long-term minimum, as is seen in U Mon and AI Sco, then the real period will be longer than the periods obtained from the analysis of the MJUO photometry (where we have not completely sampled the long-term maximum).

The lower panel in Fig. 4.15 shows the Fourier power spectrum once the long period has been subtracted from the photometric data. A strong peak is obvious at a frequency of $f = 0.002570\,d^{-1}$ ($P = 38.91\,d$). The power spectra for the B, V, R and I photometry all show a dominant, long-period peak with a second, short-period peak at about 38.9 d. No strong peak at half this frequency was found. The next strongest peak occurred at about 67.1 d. The colour curves show no long-period peak in their Fourier power spectra. It was noted earlier

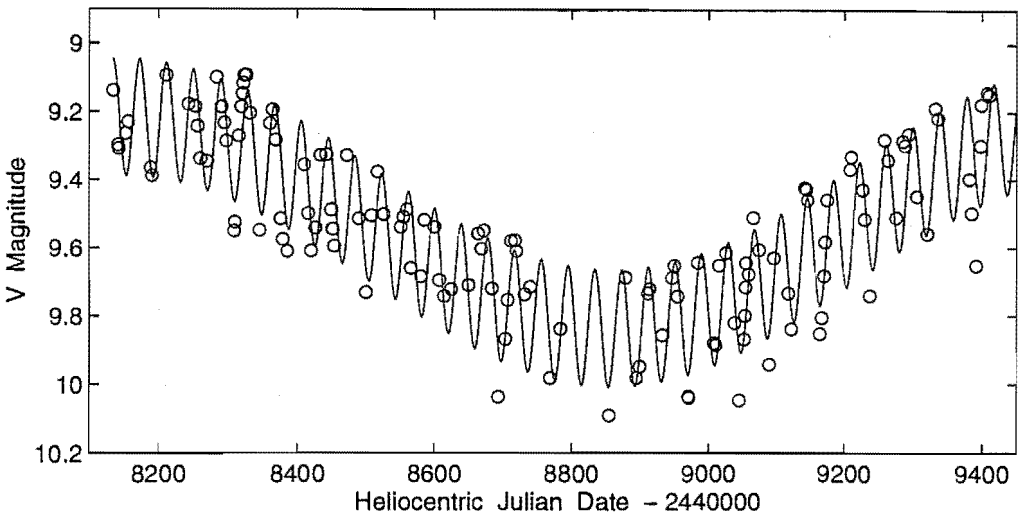

Figure 4.16: The least-squares fit (solid line) to the MJUO V photometry (o) for AR Pup.

that the colours for AR Pup (see Fig. 4.13) show very little change throughout the entire data set. The dominant periodicity for the colour curves is similar to the short period for the light curves.

Once the long period had been derived using the Fourier technique, this was subtracted from the photometry and the short-term periodicities were then derived. Using the least-squares technique, a simultaneous fit using a long and short period was made. The mean long period determined from the least-squares analysis of the B, V, R and I light curves was 1389 ± 30 d. Once again this is an indicative period only. A harmonic fit was not employed for either method since no strong power was seen at this frequency. The results of the Fourier and least squares analyses are shown in Table 4.8 for the short periodicity only. A mean period of 38.896 ± 0.005 d was determined from the analysis of the B, V, R and I photometry.

A synthetic light curve fit to the V photometry for AR Pup is shown in Fig. 4.16. From this figure it can be seen why there is a lack of any strong power at the frequency corresponding to the 'double' period. AR Pup does show deep and shallow minima in its light curve, but these do not appear to alternate in a consistent manner. It is difficult to decide which minima are 'primary' and which are 'secondary'. This star could be undergoing many 'flips' of the two minima or it could be pulsating with just the 38.9 d period and very irregular depths of the minima. In the analysis of the RVa type star, R Sct, it was found that when R Sct

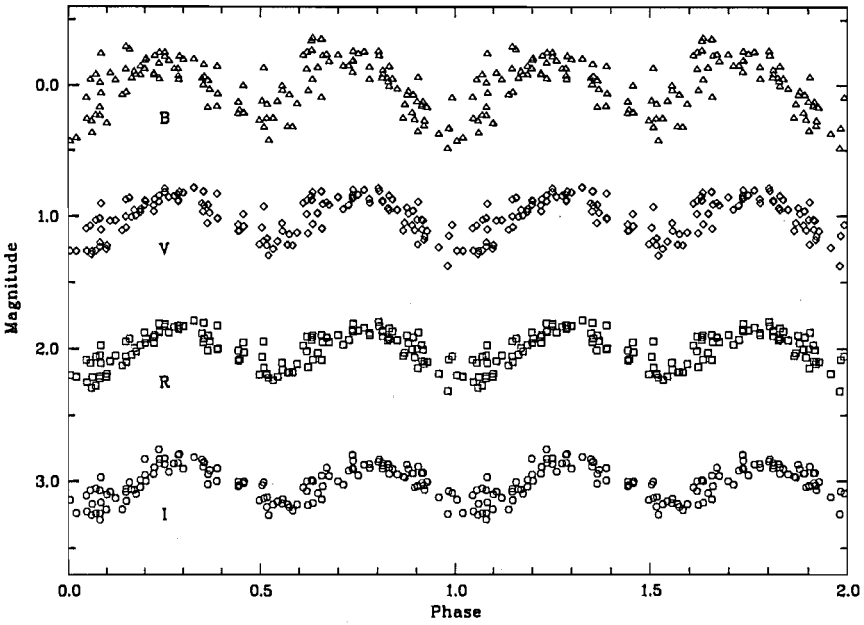

Figure 4.17: The phased (period = 77.79 d) residual B, V, R and I magnitudes for AR Pup. Offsets of 1.0, 2.0, 3.0 magnitudes have been applied to the V, R and I data respectively.

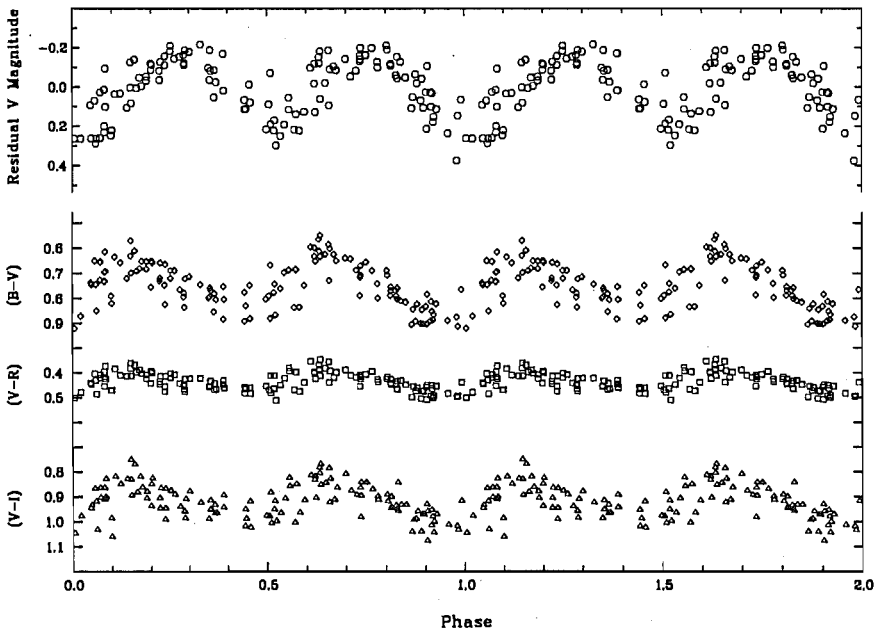

Figure 4.18: The phased residual V magnitudes and $(B–V)$, $(V–R)$ and $(V–I)$ colour curves for AR Pup.

Table 4.9: The long-term colour effects in AR Pup.

time interval HJD 2440000+	description of light curve for this interval	V^a amp (mag)	mean $(B-V)$ (mag)	$(B-V)$ amp (mag)	mean $(V-I)$ (mag)	$(V-I)$ amp (mag)
8100.0–8600.0	decreasing V light	0.17	0.75	0.10	0.91	0.08
8600.0–9050.0	minimum V light	0.17	0.74	0.09	0.91	0.06
9050.0–9450.0	increasing V light	0.18	0.75	0.14	0.95	0.11

[a]This V amplitude is for the short-period variations only.

was pulsating in a very 'irregular' manner, only the 70 d periodicity appeared to be present (the 140 d periodicity was not obvious in the power spectra). The depths of the minima were quite erratic and did not appear to alternate in a deep–shallow manner. This behaviour appears to be quite similar to that seen in AR Pup. In the earlier photographic data of AR Pup (O'Leary 1937, Payne-Gaposchkin et al. 1943), time spans of irregular light variations were interspersed with intervals of reasonably regular, deep–shallow alternating minima and a large number of 'flips' were noted.

In keeping with the analysis of other RV Tauri stars, the double period was used for the phasing of the photometry. The mean period of 77.79 ± 0.01 d was used in this case. Because AR Pup was not displaying the characteristic deep–shallow light variations while it was being observed from MJUO, the distinction between the primary and secondary minima is confused (or non-existent). The phased B, V, R and I light curves are shown in Fig. 4.17. The phased V light and the three colour curves are displayed in Fig. 4.18.

The bluer light curves show more scatter and slighter larger amplitudes than the redder light curves. Some of the scatter in the curves will be introduced by the fact that we are not distinguishing which minima are primary and which are secondary. The minimum at phase 1.0 (which should, by convention be the primary minimum) shows more scatter in its depth and therefore may have more contribution from secondary minima. The colour curves also show a reasonably large amount of scatter. No long period trend was removed from the colour curves so some of this scatter may arise from small amplitude, long-term colour changes.

The photometry was analysed to search for any long-term colour effects. The colour photometry was divided into three subsets of data and each subset was analysed separately to examine whether the mean colour level or the amplitude

of variation had changed. The results of this analysis are displayed in Table 4.9. The $(B–V)$ curve appears to display little colour change, but the $(V–I)$ curve shows that during increasing long-term V light, the colours for this index are slightly redder. This is the opposite to what was seen in U Mon and AI Sco.

The amplitude of the light variations appear to change very little. The amplitude of the colour variations is smallest at long-term light minimum and largest during the long-term light increase for both the $(B–V)$ and the $(V–I)$ indices. This effect is similar to what was seen in U Mon and AI Sco, where the light and colour amplitudes are damped at long-term minimum.

4.4 IW Car

4.4.1 Background

The variability of IW Car was discovered in 1937 by O'Connell (1946, as reported by Wisse & Wisse 1971) from photographic observations. A short period of 67.5 d was determined and a long period variation of about 1500 d. As with U Mon, AR Pup and AI Sco, the short period variations were seen to be larger at the maximum of the long period variation.

Wisse & Wisse (1971) presented 36 UBV photometric observations of IW Car and noted very little phase difference between the V light curve and the $(U–B)$ and $(B–V)$ colour curves. They queried the RVb classification of IW Car, pointing to the lack of alternating deep and shallow minima which is a characteristic of the RV Tauri stars.

Photometric $UBVRI$ observations which cover about one pulsational cycle of IW Car were reported by Eggen (1973). Light curves in the V and R filters were presented together with $(U–B)$ and $(R–I)$ colour curves. A general decrease in the mean magnitude of the light curves was seen.

Wisse (1981) plotted 43 points in his V light and $(U–B)$ and $(B–V)$ colour curves. The light curve showed the maxima of the light variations were increasing in brightness, indicating the star was on the ascending branch of the 1500 d light variation. Wisse (1981) classified IW Car as a semiregular star (SRd) and not an RV Tauri star, due to the lack of emission lines and the zero phase difference between the light and colour curves. However, this conclusion may be somewhat complicated by the fact that IW Car is a known binary with a composite spectral type of (A4 Ib–II: + F7/F8) given in the Michigan Spectral Catalogue (Houk

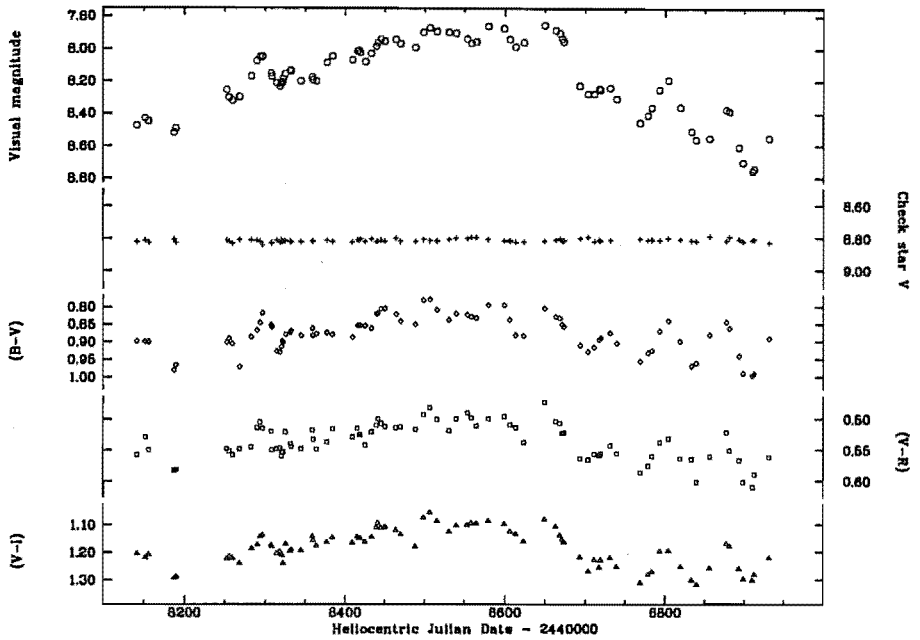

Figure 4.19: The V light curve and $(B–V)$, $(V–R)$ and $(V–I)$ colour curves for IW Car.

1978)

The General Catalogue of Variable Stars (Kholopov et al. 1985) gives a range in photographic magnitude for IW Car of 7.9–9.6. The photometric data from the sources mentioned above give a range in V of 7.7–8.5, although this does not cover an entire cycle of the long period variations.

4.4.2 Photometry from MJUO

Photometric *BVRI* observations of IW Car were obtained with the B&C and OC 0.61-m telescopes at MJUO between 1990 September and 1992 November. A total of 83 good-quality night-averaged observations were obtained. The comparison and check stars were SAO 250565 and SAO 250592 respectively. This is the same comparison star that was used by Wisse & Wisse (1971) for differential photometry and their V magnitude and $(B–V)$ values have been adopted. The V magnitudes and colours that have been adopted for the comparison and check star are presented in Table 2.1. The internal accuracy of the V photometry is 0.010 magnitudes.

The V light curve and the three colour curves for IW Car are shown in Fig. 4.19. The individual B, V, R and I light curves are displayed in Fig. 4.20.

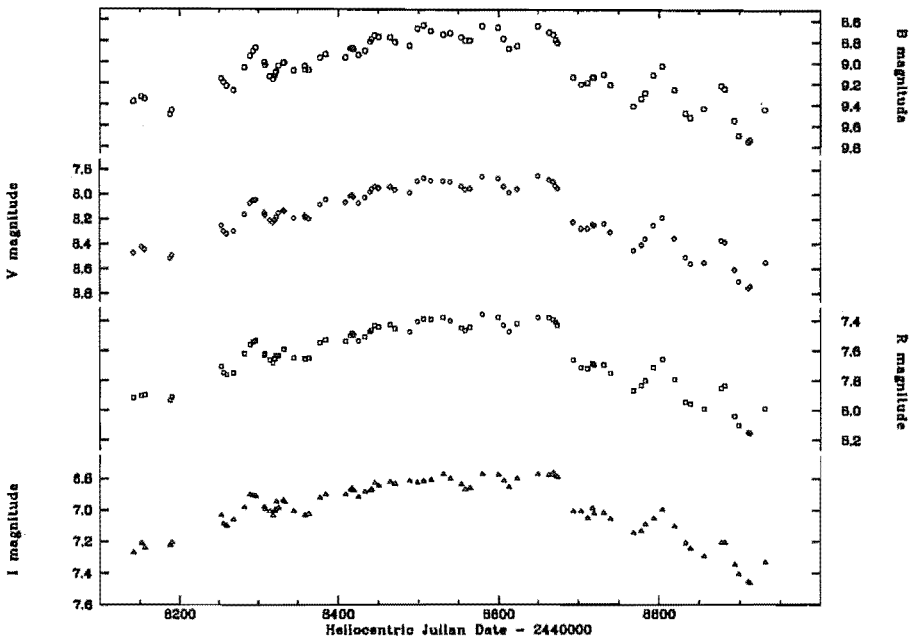

Figure 4.20: Individual B, V, R and I magnitudes for IW Car.

From HJD 2448130 to HJD 2448670 the light and colour curves display a gradual increase in mean value. The variations are quite irregular and are of a small amplitude. The light curves from HJD 24486500 to HJD 2448970 show a general decrease in the mean magnitude with variations that are more distinct, have a larger amplitude and appear to have a longer and more stable period. The colour curves show larger and more well-defined variations, but show little change in the mean value.

4.4.3 Analysis of the photometric data

The 83 photometric observations of IW Car were analysed using both the Fourier and the least-squares techniques. These data were then combined with photometric V data from Wisse & Wisse (1971), Eggen (1973) and Wisse (1981) (hereafter called the WWEW data), to give a total of 185 observation over a time interval of 8263 d (~22.5 years). The analysis of these data should result in a more accurate determination of the long period.

Using the MJUO V data alone, a long period of ~800 d and a short period of ~71 d were revealed using the Fourier analysis. Using the WWEW V data alone, periods of about 1400 d and 73 d were obtained. The Fourier analysis of

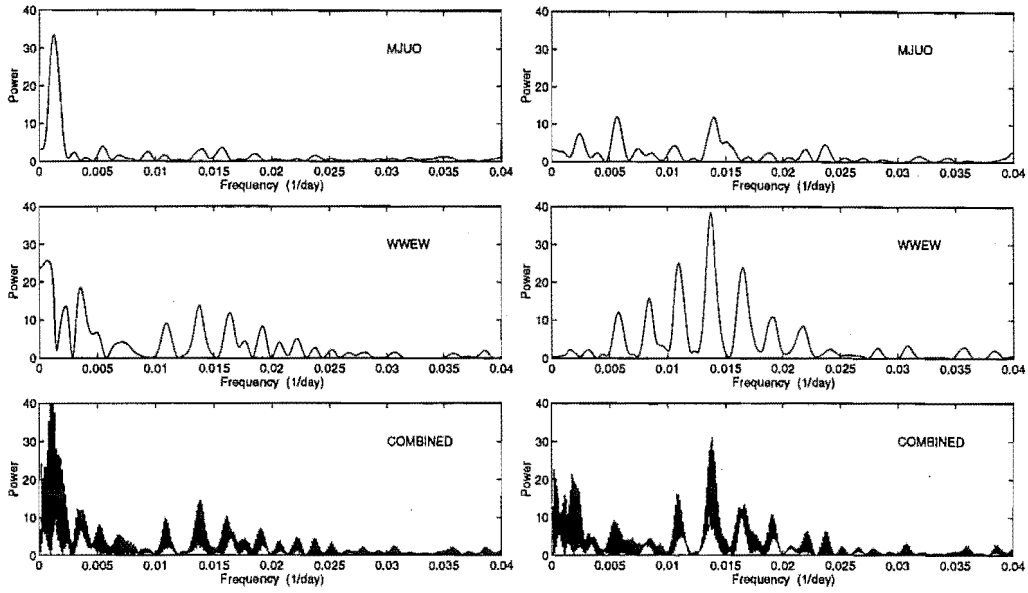

Figure 4.21: The power spectra for the MJUO (top), WWEW (middle) and combined (bottom) IW Car V photometry. The long periodicities are dominant (left panels), while the 72 d period is evident in the prewhitened data (right panels).

Table 4.10: The least-squares analysis of the photometric V data for IW Car.

Data	f_1 (d^{-1})	P_1 (d)	A_1 (mag)	f_2 (d^{-1})	P_2 (d)	A_2 (mag)	rms
V_{MJUO}	0.00947	1056	0.39	0.01389	72.0	0.07	0.074
V_{WWEW}[a]	0.01072	933	0.29	0.01375	72.7	0.19	0.049
$V_{MJUO + WWEW}$	0.00137	730	0.28	0.01384	72.3	0.13	0.128
	0.00069	1444	0.23	0.01397	71.6	0.13	0.147

[a]WWEW indicates Wisse & Wisse (1971), Eggen (1973) and Wisse (1981) photometry.

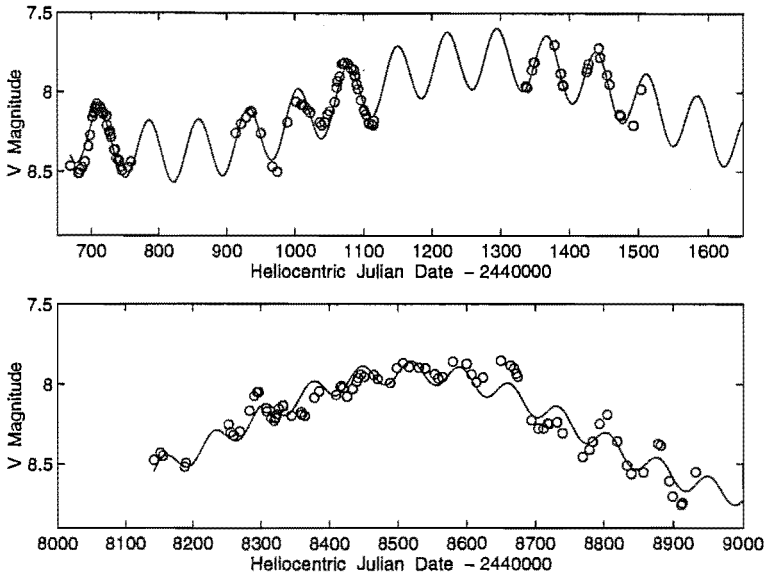

Figure 4.22: The synthetic light curves are shown for the WWEW data (top panel) and for the MJUO data (bottom panel) for IW Car.

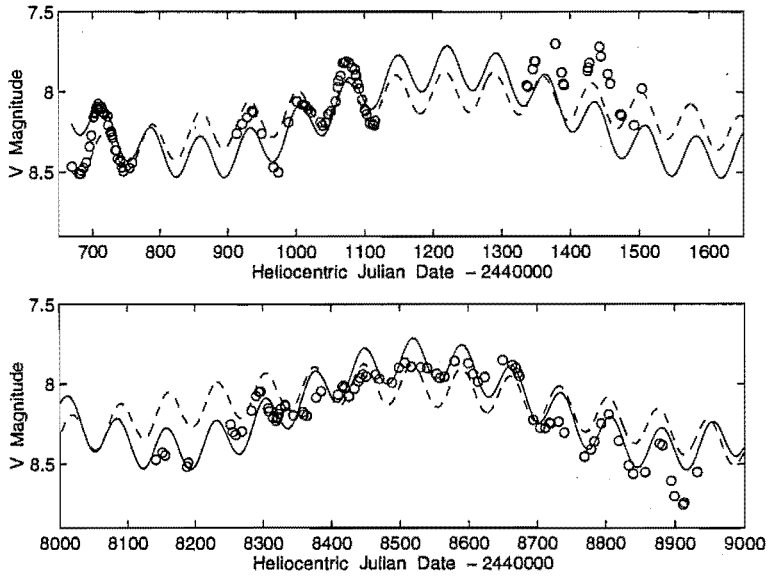

Figure 4.23: The synthetic light curves ate shown for the combined WWEW (top panel) and MJUO (bottom panel) V photometry. The solid line is using a long period of 730 d and the dashed line is for a long period of 1440 d.

the combined data set showed the most power at periods of ~750 d and 72 d. The power spectra from these analyses are displayed in Fig. 4.21. The panels on the left shows the strongest power occurs at the long period. Once this periodicity has been removed from the data, the power spectra shown in the right panels are obtained. These show the strongest power at frequencies of $\sim 0.014\,\mathrm{d}^{-1}$ or periods of approximately 72 d.

The simultaneous least-squares fitting of two sinusoids gave similar results for the short period but rather different results for the long period. This is understandable as the data sets are each much shorter than the long period of ~1500 d reported by O'Connell (1946). It is quite possible that the long period in IW Car has a non-sinusoidal shape which would further affect period-determination from the shorter data sets. The Fourier and the least-squares analyses of the combined V photometry are in good agreement. The results for the analyses are shown in Table 4.10.

The synthetic light curve fit to the WWEW data alone is shown in the top panel of Fig. 4.22 while the bottom panel shows the fit to the MJUO data alone. The synthetic curves using the periods derived from the analysis of the combined V photometry for IW Car are displayed in Fig. 4.23, where the solid line is for periods of $P_1 = 730$ d and $P_2 = 72.3$ d. If we insist that the period is approximately twice this P_1 value, so that it is in better agreement with the period of 1500 d given by O'Connell (1946), then periods of $P_1 = 1444$ d and $P_2 = 71.6$ d are derived. The synthetic curve for these periods is shown in the Fig. 4.23 as the dashed line.

Further photometric observations are obviously required to determine the shape and period of the long-term variation in IW Car.

Chapter 5

Discussion of the RV Tauri photometry

In this chapter we present and discuss the main results from the analysis of the RV Tauri photometric data. Stars from both the RVa and the RVb photometric subclass are considered.

From the analyses of the MJUO photometry presented in Chapters 3 and 4 the following characteristic features of the light and colour curves were noted:

(i) Alternating deep and shallow minima in the light and colour curves;

(ii) Secondary minima depths are more variable than primary minima;

(iii) Bluer light curves generally have larger amplitudes, more asymmetrical shapes and have a phase lead over the redder light curves;

(iv) A mean phase lag exists between the colour and light curves, so that the colours appear bluest during the rising branch of the light curve;

(v) During extremely deep pulsations, the photometric colours get very blue;

(vi) At the minimum of the long-term V variations in the RVb subclass, the amplitude of light variations are 'damped', particularly in the bluer filters;

(vii) The short period RV Tauri stars are generally more regular than long period stars.

In Figs 5.1 and 5.2 we present the V light and $(B–V)$ colour curves for some of the more regular members of the RVa and RVb subtypes. In the case of the

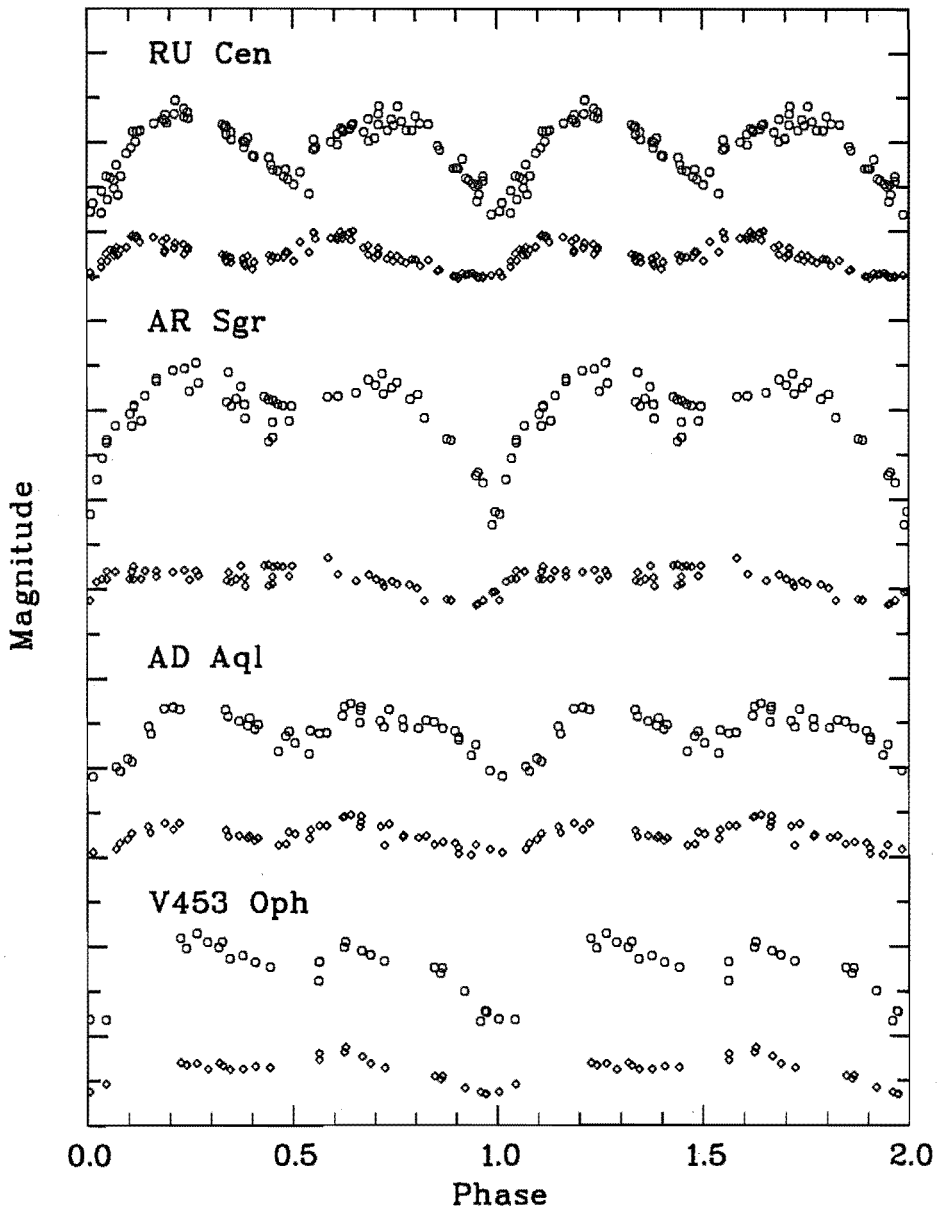

Figure 5.1: Phased V light (circles) and $(B–V)$ colour curves (diamonds) for the more regular members of the RVa subclass: RU Cen, AR Sgr, AD Aql and V453 Oph. Vertical tickmarks correspond to intervals of 0.5 magnitudes.

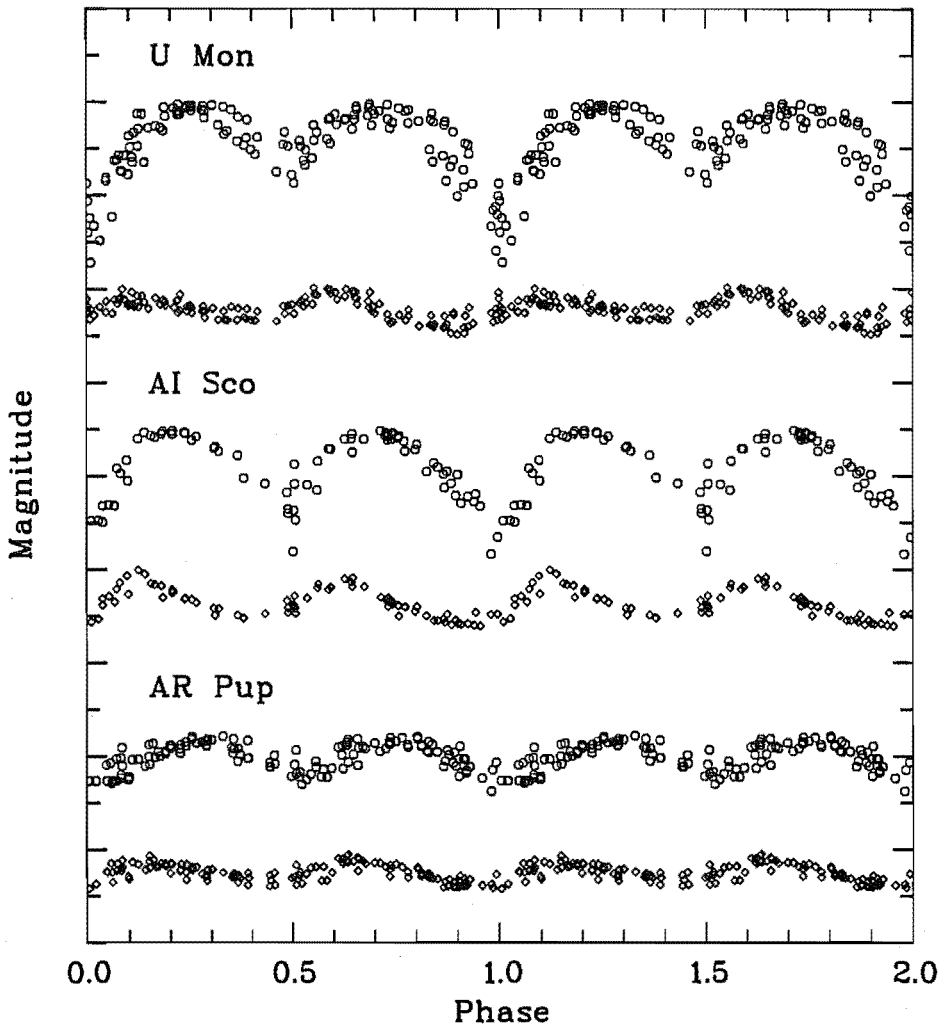

Figure 5.2: Phased V light (circles) and $(B–V)$ colour curves (diamonds) for some members of the RVb subclass: U Mon, AI Sco and AR Pup. Vertical tickmarks correspond to intervals of 0.5 magnitudes.

Table 5.1: A summary of some general photometric characteristics for the RV Tauri stars.

Star	Photometric subclass	Preston type	'Formal' period (days)	V amp[a] $1^{ry}/2^{ry}$ (mag)	$(B-V)$ amp $1^{ry}/2^{ry}$ (mag)
RU Cen	RVa	B	64.60 ± 0.02	1.2/0.7	0.5/0.4
AD Aql	RVa	B?	66.09 ± 0.05	0.8/0.4	0.4/0.3
AI Sco	RVb	A	71.03 ± 0.03	1.2/0.7	0.5/0.3
AR Pup	RVb	B	77.79 ± 0.01	0.4/0.4	0.3/0.3
V453 Oph	RVa	C	80.68 ± 0.10	0.9/0.4	0.5/0.2
AR Sgr	RVa	A	88.86 ± 0.03	1.7/0.6	0.4/0.1
U Mon	RVb	A	92.32 ± 0.04	0.9–1.7/0.6	0.4/0.3
R Sct	RVa	A	140.30 ± 0.08	0.5–2.9/0.5–1.7	0.4
RY Ara	RVa	A?	289.6 ± 1.1	1.5–2.8/0.6	0.6

[a]The first number is the mean depth of the primary minimum, the second number is the mean depth of the secondary minimum.

RVb stars, the long-term variation has been subtracted from the photometry, so that it is the residual V magnitudes that are being plotted.

A summary of some general photometric characteristics for the programme RV Tauri stars, such as photometric subclass, period and the amplitude of the light and colour curves are given in Table 5.1. The stars are arranged in order of increasing period. The stars, V820 Cen and IW Car, are not included in this table since reliable periods were not able to be obtained from the analysis of the MJUO photometry. The irregularity of their photometric variations suggests that it is possible that neither star is an RV Tauri variable.

The alternating deep and shallow nature of both the light and colour curves in the RV Tauri stars (see item (i) above) was able to be modelled by a harmonic $(f + 2f)$ fit. The light curves of the stars from the spectroscopic Preston 'A' type appear to display slightly larger amplitudes than those from the 'B' and 'C' subtypes, although there is less difference in the colour amplitudes. This is shown in Table 5.1, where estimates of the amplitudes are given. In the columns for the amplitude of the light and colour variations, the first number is the amplitude of the deepest minima, while the second number represents the amplitude of the shallower minima. For stars which show a very large variation in either minimum, a range is given for the amplitude.

As is mentioned in item (ii), the depths of the secondary minima (and the following maxima) tend to show a greater variation than the primary minima. This is reasonably obvious in the more regular stars which have a good phase

coverage (e.g. RU Cen, AR Sgr, AD Aql, AI Sco).

One feature of the photometric light curve that is seen in virtually all the stars in Table 5.1, is the difference between the appearance of the B, V, R and I light curves. The bluer light curves generally have larger amplitudes, more asymmetrical sawtooth-type shapes and lead the redder light curve in phase (item (iii) above). In addition, greater scatter is seen in the bluer light curves, particularly around the secondary minima and maxima. It is suggested that this variation may be due to spectral peculiarities at these phases. Shock-produced emission lines (which appear in greater numbers in the bluer filters) have their greatest strength during rising light and variations in the strength of these features could be the cause of the cycle-to-cycle photometric variations.

The colour curves display an extremely asymmetric or 'skew' appearance with the (B–V) and the (V–I) curves having a much greater amplitude than the (R–I) curve. The relative 'skewness' of the light and colour curves results in varying phase differences throughout a cycle. Item (iv) above noted that the colour curves lead the light curves in phase, so that the colours are bluest during the rise from minimum to maximum light. This is consistent with the appearance of shock-related emission lines as outlined above. Unexpectedly, the bluest colours in the majority of the RV Tauri stars that were studied occurred, not during the rise from primary minimum, but during the rise from the *secondary* minimum.

Most spectroscopic studies generally agree that the strongest emission (also the strongest shock wave and photospheric acceleration) occurs just after primary minimum (Lèbre & Gillet 1991a, 1991b). However, Preston (1962) found that the Hα emission intensity in R Sct was strongest during the secondary light maxima. Gillet et al. (1990) used CORAVEL velocities to determine that the acceleration peak associated with the *secondary* minimum was stronger than that for the primary minimum in both AC Her and R Sct[1]. The model of Shenton et al. (1992) for AC Her incorporates a strong non-radial oscillation which requires a much larger photospheric acceleration at secondary minimum than at primary minimum.

It is possible that the occurrence of bluer colours after the secondary minimum could be due the presence of shock-produced emission lines in combination with a less extended (and hence hotter and bluer) photosphere. In addition, the appearance of bands of TiO near minimum light may also cause peculiar colour

[1]However, they suspected their velocities derived from the CORAVEL profiles may have been suspect, due to shock-related emission effects seen around the deep minimum.

behaviour, particularly in the R band. The very large extension of these stars' atmospheres during a pulsation cycle, and the low densities in the outer layers, allows TiO to form rapidly in these cool layers, particularly around minimum light.

The stars that show bluer colours during primary minima are AI Sco, R Sct and RY Ara. The latter two stars displayed quite unusual colour behaviour, a rapid 'blueing' of the colours, during their very deep ($\Delta V > 2.5$ mag) minima (item (v) above). This is unlikely to be purely a temperature effect, since it is mostly the B and V filters that appear to be affected. This behaviour is very reminiscent of that seen in a 'blue' decline of the RCB stars, where broad chromospheric emission appears in the U, B and V bands (Cottrell et al. 1990, Lawson 1990). A spectrum of R Sct obtained during a very deep minimum (Howell et al. 1983) showed a chromospheric spectrum very similar to that seen in RCB stars during a decline. The possibility is raised that this peculiar colour behaviour could arise from a chromospheric contribution.

The features described in item (vi) are an important result obtained from this programme of long time baseline multicolour photometry of stars from the RVb subclass. In the case of U Mon, the long-term variation is evident in both the light and colour curves. There appears to be a slight phase lag so that the minimum of the long-term variation in the B, V, R and I light curves occurs slightly before the reddest colours in this star. In addition, the amplitudes of the short-term (or pulsational) light and colour variations are 'damped' at the long-term minimum. This is particularly obvious for the B light curve and the $(V-I)$ colour curve. In addition, the amplitude of the long-term oscillation is greater for the bluer filters than for the redder filters (see Table 4.1).

Another RVb star, AI Sco, displays very similar photometric characteristics to U Mon. When compared with U Mon, the amplitude of the long-term variation in AI Sco is slightly larger (an amplitude in B of 2.05 magnitudes compared with 1.41 magnitudes for U Mon, see Table 4.4) and the long-term colour variation is smaller.

Rather different behaviour is displayed by AR Pup. The amplitude of the long-term periodicity is similar in all four filters (see Table 4.7), but since the long-term maximum has not been sampled, this is only a lower limit. No reddening of the colours over the long-term variation is evident in AR Pup – if anything, the colours become slightly bluer during the long-term minimum. The short-term

(pulsational) variations are also different from most of the other RV Tauri stars. The light variations do not reveal *consistent* deep–shallow alternations, although stable alternations have been previously reported for this star (O'Leary 1937).

The other star that was included in this programme, IW Car, displayed quite irregular light variations in both period and amplitude. There appear to be no reports that it has ever shown the characteristic deep–shallow RV Tauri alternations. Its RV Tauri classification is therefore rather suspect and it is more likely to be a semiregular variable. In the Michigan Spectral Catalogue it is classified as a binary star. IW Car does show some of the same characteristics as the RVb stars. A long period variation in both the light and colour curves is evident, with the colours redder at long-term minimum. The amplitude of the short-term light and colour variations is greater in the bluer filters. In addition, variable Hα emission is seen in the high-resolution spectra obtained of this object (see Chapter 8).

The last feature (item (vii) above) is that the short period RV Tauri stars seem to have more stable pulsations than the longer period stars. This appears to be particularly true for the short period *carbon-rich* stars (the Preston type 'B' objects), for example RU Cen (see Section 3.1) and AC Her (see Zsoldos 1993a). These two stars are the most stable RV Tauri stars known, with the common characteristic that they are carbon-rich. Another Preston type 'B' star, AD Aql, also appears to have stable pulsations. The other Preston type 'B' star in the programme, AR Pup, displays a stable pulsational period but has quite irregular variations in its amplitude. The most irregular RV Tauri stars are R Sct and RY Ara, which are the longest period stars in the programme. The period for RY Ara is extremely long for an RV Tauri star, suggesting that this star may also be misclassified. However, RY Ara does display the characteristic alternating deep–shallow minima of the RV Tauri class.

5.1 Flux distributions

In order to obtain a better understanding of the RVb subclass and, in particular, the nature of the secondary variability in these objects, the MJUO photometry and some infrared photometry and fluxes from the literature for the bright RVb star, U Mon, is examined in greater detail.

The *BVRI* photometry from MJUO were used together with the infrared (*JHKL*) photometry from SAAO (Lloyd Evans 1985) and the *IRAS Point Source*

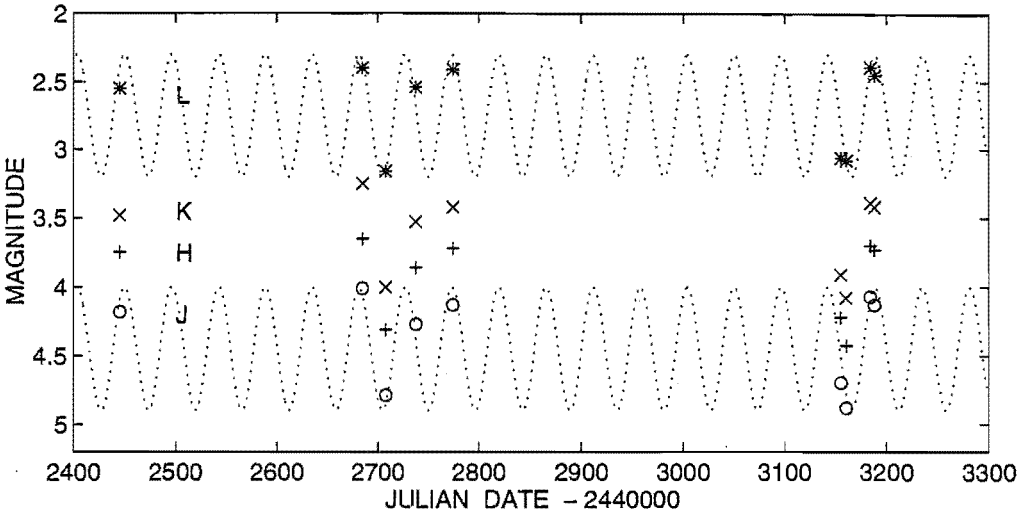

Figure 5.3: The SAAO (Lloyd Evans 1985) *JHKL* photometry for U Mon.

Catalogue (*IRAS* PSC) fluxes to model the contributions from the RVb star, U Mon, and its circumstellar dust shell(s).

The SAAO photometry consisted of nine photometric observations in each of the filters during the time interval from JD 2442445–2443188. These observations are shown in Fig. 5.3. The four SAAO observations taken during the interval JD 2442680–2442775 are taken during a maximum of the long period (at phases 0.60–0.64, where we define phase = 0.0 as the minimum of the long period). The following four observations (JD 2443155–2443190) are taken during the descending branch of the long period at a (long-period) phase of 0.79–0.80.

Although the number of SAAO observations is very small, these near-infrared data appear to be consistent with the 46.16 d periodicity (dotted curve in Fig. 5.3) derived from the analysis of the MJUO optical photometry for U Mon. The amplitude of the pulsational variability seems reasonably well defined. In contrast to what is seen in the optical photometry, the near-infrared photometry for U Mon displays no evidence of a long-term (2600 d) cycle.

SAAO points defining the maximum and minimum of the 46.16 d pulsational cycle were selected. MJUO observations at long-period phases about 0.6 and 0.8 (although in a later cycle to the SAAO observations) were examined and points defining the maximum and minimum of the 46.16 d pulsational cycle in the V curve were selected. The photometric *BVRIJHKL* magnitudes from MJUO and SAAO were dereddened assuming an interstellar reddening of $E(B-V) = 0.10$

Table 5.2: The U Mon flux densities ($\times 10^{-26}$ W m^{-2} Hz^{-1}) calculated from the MJUO *BVRI* and the SAAO *JHKL* photometry.

Filter band	P_L(max)[a] P_S(max)[b]	P_L(max) P_S(min)	$P_L(\phi \sim 0.8)$ P_S(max)	$P_L(\phi \sim 0.8)$ P_S(min)	P_L(min) P_S(max)	P_L(min) P_S(min)
B	16.6	3.67	11.9	3.72	5.10	2.36
V	33.9	7.10	22.2	7.96	11.1	4.49
R_c	41.3	8.74	27.6	10.5	14.6	5.75
I_c	48.6	16.2	33.6	15.9	19.2	8.63
J	41.9	18.8	41.9	18.8	–	–
H	36.2	17.7	36.2	17.7	–	–
K	32.2	15.0	32.2	15.0	–	–
L	31.6	15.5	31.6	15.5	–	–
12μ	124.3	124.3	124.3	124.3	124.3	124.3
25μ	88.4	88.4	88.4	88.4	88.4	88.4
60μ	26.3	26.3	26.3	26.3	26.3	26.3
100μ	9.2	9.2	9.2	9.2	9.2	9.2

[a] P_L indicates the long 2600 d period
[b] P_S indicates the short 92.32 pulsational period

(Cardelli 1985) and converted to flux densities using the absolute flux calibrations of Bessell (1979) and Wilson et al. (1972). The dereddened flux densities for U Mon are shown in Table 5.2.

The *BVRIJHKL* fluxes from MJUO and SAAO were used together with the *IRAS* fluxes to define the flux distribution of U Mon for long period phases of ~ 0.6 and ~ 0.8 and for the maximum and minimum V magnitude of the 'formal' pulsational period of 92.32 d. Although, the *IRAS* data were taken at only one phase, it was assumed that the variability at these wavelengths is relatively small. The flux distribution was fitted by up to three blackbody functions defining the stellar flux and the flux from warm and cold dust. The blackbody fits to the U Mon flux distribution at phases ~ 0.6 and ~ 0.8 are shown in Figs 5.4 and 5.5. These fits make use of three blackbodies. No near-infrared photometry was available for U Mon during a long-period phase of 0.0, so a two blackbody fit was made to the MJUO and *IRAS* fluxes only (Fig 5.6). The temperatures of the blackbodies are indicated on the plots and are tabulated in Table 5.3.

It appears that the temperature variability associated with the pulsations of the star is greater during the maximum of the long period ($\phi \sim 0.6$) than during the descent to minimum ($\phi \sim 0.8$) or at the minimum of the long period itself ($\phi \sim 0.0$).

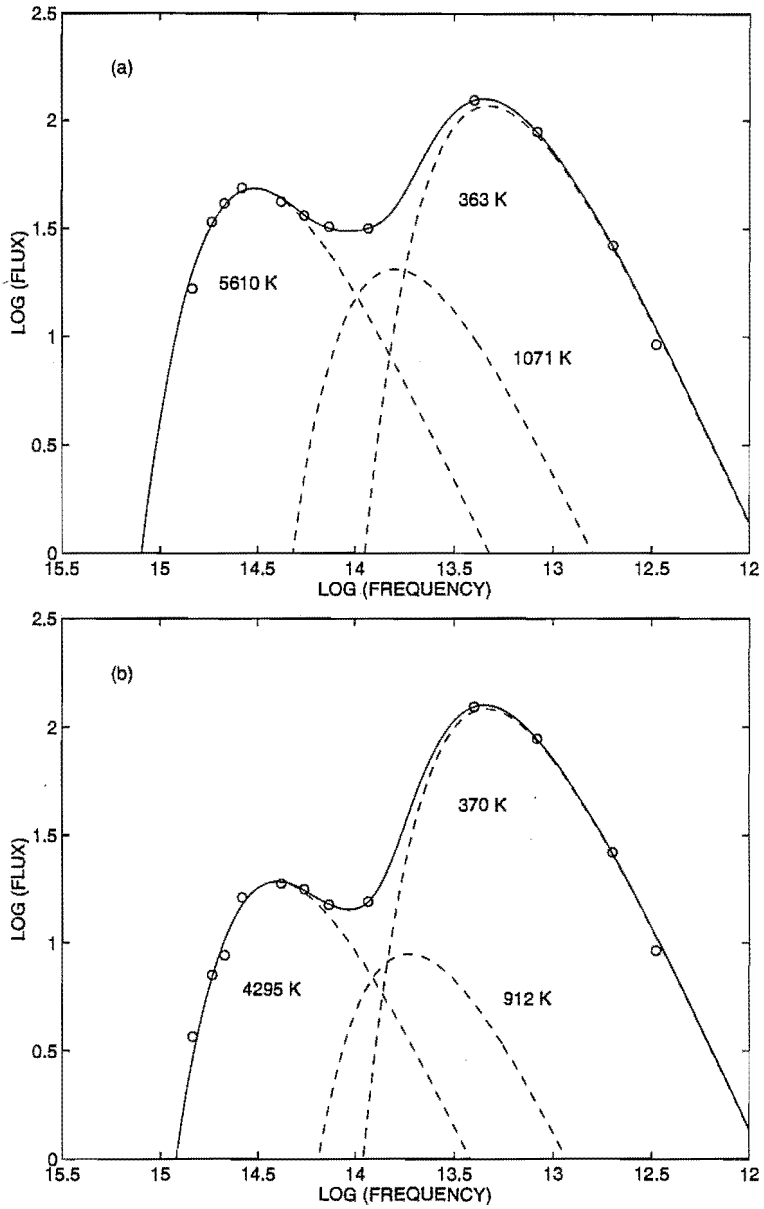

Figure 5.4: The individual blackbody fits (dashed curves) to the U Mon flux distribution during the long period maximum of the V light (long period phase = 0.6) and at short period (a) maximum, and (b) minimum. The solid line is the addition of the three blackbodies. The flux is in units of $10^{-26}\,\mathrm{W\,m^{-2}\,Hz^{-1}}$.

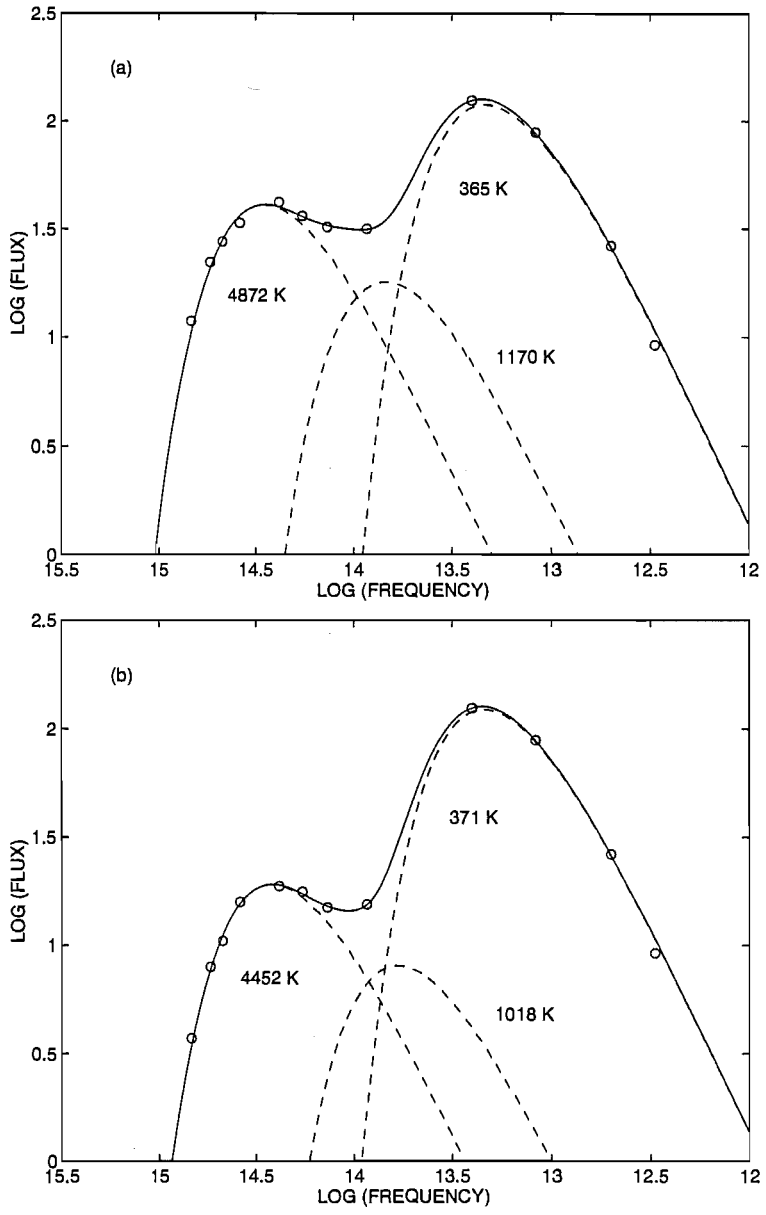

Figure 5.5: The individual blackbody fits (dashed curves) to the U Mon flux distribution during the long-term dimming of the V light (long period phase = 0.8) and at short period (a) maximum, and (b) minimum. The solid line is the addition of the three blackbodies. The flux is in units of 10^{-26} W m^{-2} Hz^{-1}.

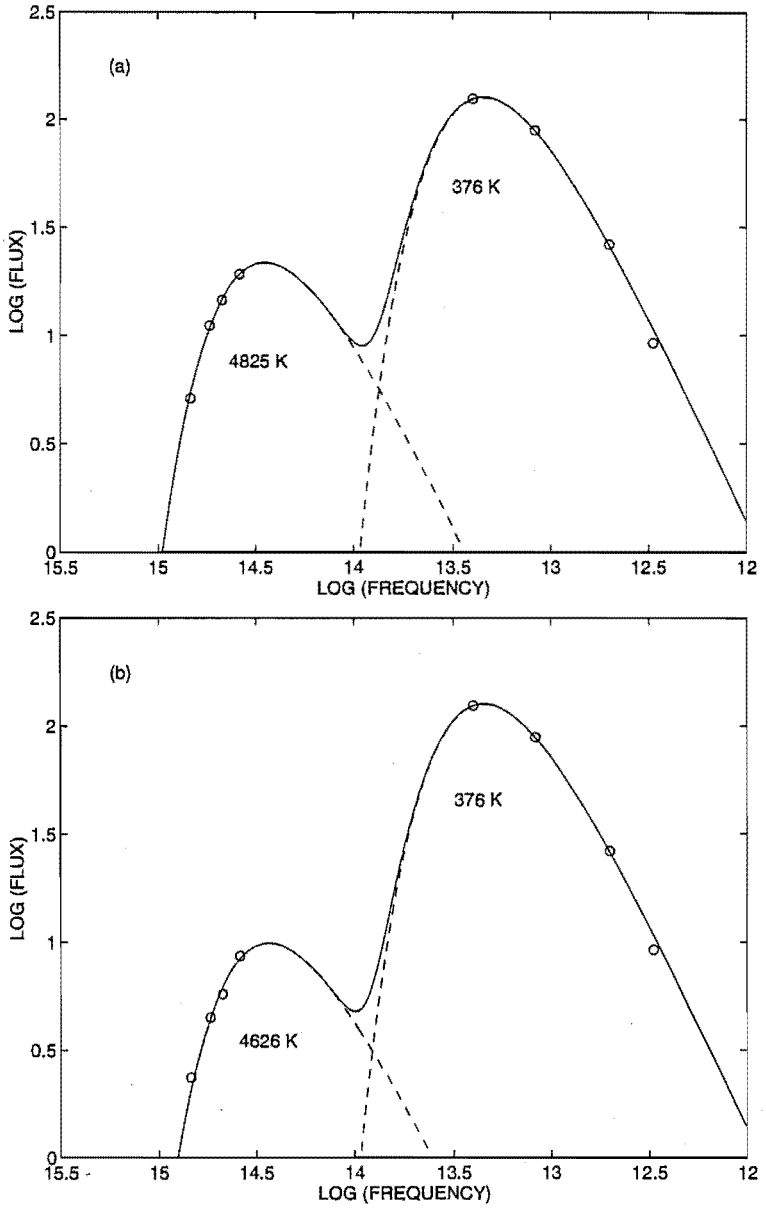

Figure 5.6: The individual blackbody fits (dashed curves) to the U Mon flux distribution during the long period minimum of the V light (long period phase = 0.0) and at short period (a) maximum, and (b) minimum. The solid line is the addition of the two blackbodies. The flux is in units of 10^{-26} W m^{-2} Hz^{-1}.

Table 5.3: Temperatures derived from blackbody fits to the U Mon flux distribution.

Flux contribution	P_L(max) P_S(max)	P_L(max) P_S(min)	$P_L(\phi \sim 0.8)$ P_S(max)	$P_L(\phi \sim 0.8)$ P_S(min)	P_L(min) P_S(max)	P_L(min) P_S(min)
star (U Mon)	5610	4295	4872	4452	4825	4626
warm dust	1071	912	1170	1018	–	–
cool dust	363	370	365	371	376	376

Previous attempts to derive the temperature of U Mon have used a variety of techniques. For each technique, an indication is given of the phases of the long period since this was not considered in any of the studies given below:

- DDO photometry to estimate temperatures at a range of pulsation phases (Dawson 1979, T = 4930–5830 K). These data were obtained at the maximum of the long period.

- MK standards and model fluxes to fit spectrophotometric data near maximum pulsational light (Cardelli 1985, T = 4800–5000 K). These data were obtained at the maximum of the long period.

- An abundance analysis technique to fit model atmospheres to the star near maximum pulsational light (Luck & Bond 1989, T = 4250 K). These spectra were obtained approaching the maximum of the long period.

- Blackbody modelling of optical-infrared fluxes (Alcolea & Bujarrabal 1991, $T_{\text{U Mon}}$ = 5500 K and T_{dust} = 420 + 985 K). Various sources for the optical and infrared data were used.

- Synthetic spectra to fit medium resolution spectra (Wahlgren 1992, T = 4750 K). These spectra were obtained near the minimum of the long period.

Modelling the flux distribution by blackbody fits tends to underestimate the temperature of the star because effects such as line-blanketing and metallicity have not been taken into consideration. Lawson (1990) found that attempts to estimate the temperature of RCB stars by the fitting of blackbody curves gave values that were ~1000 K cooler than spectroscopically derived temperatures. The temperatures determined from the blackbody fits (Table 5.3) are therefore in reasonable agreement with the range of temperatures given above for U Mon.

5.2 Summary

In this chapter the main results from the analysis of the RV Tauri photometric data have been reviewed. The characteristic features of the light and colour curves of the RVa and the RVb photometric subclasses have been discussed. Some similarities between the photometric behaviour of the RV Tauri stars and the RCB stars have been highlighted. The benefit of long-term multicolour photometric monitoring of the RV Tauri stars is evident, with new results of the colour changes in the RVb stars of particular interest.

The MJUO photometry have been combined with infrared photometry and *IRAS* fluxes to derived some stellar and dust shell parameters for the bright RVb star U Mon. These properties and their time variability will be used later (see Chapter 9) in the discussion of the nature of the RVb subclass.

The next three chapters present the spectroscopic instrumentation (Chapter 6), and the results of the RV Tauri spectroscopic programme (Chapters 7 and 8). In Chapter 9 the results from the analysis of the spectroscopy will be be combined with the photometric characteristics reviewed in this chapter, in order to examine a variety of theoretical models that attempt to describe the pulsation mechanisms and the underlying physical nature of the RV Tauri stars.

Chapter 6

Spectroscopic instrumentation and reduction

The instrumentation used to obtain spectra of the stars in the RV Tauri programme at MSO and MJUO are described in this chapter. Section 6.1 describes the instrumentation and the reduction procedures employed at MSO. Descriptions of the MJUO CCD detector system, the 1.0-m reflector telescope and the échelle spectrograph are included in Sections 6.2–6.6.

In addition, the techniques used in the reduction and analysis of the MJUO CCD échelle spectra obtained are described. Reference is made to the MIDAS data analysis system (Sections 6.7–6.9), which was the software package employed for the reduction of the MJUO CCD frames to one-dimensional, wavelength-calibrated spectra.

The FIGARO software package was used for additional processing and analysis of the MSO and MJUO spectra. A brief outline of these steps is also included (Sections 6.10). The analysis of the reduced spectra included line profile fitting and radial velocity measurements and their interpretation. The techniques employed in these analyses are described in Sections 6.11 and 6.12.

6.1 The MSO observations and reductions

Spectroscopic observations of the programme RV Tauri stars were obtained with the 1.9-m reflector at Mt Stromlo Observatory (MSO) at the coudé focus using GEC CCD detectors. The spectra were obtained between 1991 May 9 and 1991 September 12 by W.A. Lawson and the author.

The region around Hα was observed for compatibility with a number of other programmes. The 82-cm camera and 600 line mm^{-1} 'C' grating in the second order gave a reciprocal dispersion of 10 Å mm^{-1}. A slit width of typically 300 μm was used, equivalent to 1.2 arcsec on the sky, 3 pixel resolution and a resolving power, R (defined as $\lambda/\Delta\lambda$), of $\sim$ 13 000.

The spectra were reduced and wavelength calibrated using standard library routines within the IRAF software package by W.A. Lawson (see Lawson et al. 1993) The typical wavelength calibration uncertainty of 0.005 mÅcorresponds to a random error of $\sim$ 0.3 km s^{-1}. Observations of three IAU radial velocity standard stars (β CrV, β Oph and δ Sgr) were also obtained throughout the observing runs. These observations were used to determine the radial velocity zero-point shifts between different observing runs and to convert the MSO radial velocities to absolute (IAU) radial velocities. The mean standard deviation of the corrected standard star velocity residuals was used as an estimate of the uncertainty in the radial velocities. This was calculated to be 1.3 km s^{-1}.

The one-dimensional, wavelength-calibrated spectra were then converted to FITS (Flexible Image Transport System) format. These files were transferred to the University of Canterbury's Sun UNIX system where further processing and analysis was carried out by the author using the FIGARO reduction package.

6.2 The MJUO CCD system

The MJUO CCD detector system is based around the Photometrics 3000 CCD camera system which was purchased in 1988 December from Photometrics Ltd of Tuscon. The commissioning and the preliminary testing of the performance of the CCD system were carried out by W. Tobin and the author. The details of the characteristics and performance of the system are included in this chapter (and in Appendix B). Echelle spectroscopy using the CCD as the detector was not undertaken until these preliminary tests were completed.

The MJUO CCD detector consists of a CH210 camera head connected by cable to a CE200 camera electronics unit and a Photometrics PM3000 computer. When used with the 1.0-m telescope, the CE200 is mounted on the telescope and the PM3000 is situated in the dataroom.

CH210: This is the CCD camera head. It is comprised of a mechanical shutter, CCD detector with its associated cryogenic cooler and a preamplifier which

transfers the analogue data to the camera electronics unit. Attached to the cryostat is the 1-inch inside-diameter Uniblitz shutter and a ring of eight green pre-flash LEDs. The camera head is cooled with liquid nitrogen for which fill tubes are supplied.

CE200: This is the camera electronics unit. The CE200 provides power for the camera electronics and ccd temperature control system and produces CCD timing signals. Analogue image signals from the CCD are amplified, KTC-noise filtered and then digitized to 14 bits with a 50 kHz analogue-to-digital converter.

PM3000: This is the digital image acquisition and processing system. It is based around a camera controller, image memory (to store multiple image frames), video memory (to provide a video display of the image) and a 68020 microprocessor. A $5\frac{1}{4}$-inch floppy disk drive is used for system software installation and backup. A 55-megabyte Winchester disk drive boots up the system after installation of the system software and stores the CCD image data. A 40-megabyte $\frac{1}{4}$-inch DC2000 cartridge tape drive can be used for image storage and transport. The system includes an HDS 3200 graphics and ANSI terminal, and an Electrohome video monitor for image display. A 1600 bpi, 9-track, $\frac{1}{2}$-inch streaming tape drive and Panasonic KX-P1081 dot matrix printer are also interfaced to the PM3000 computer.

More specific details of the MJUO CCD system hardware are included in Tobin (1990) and in the 'Photometrics 3000 User's Manual for the Forth Programming System,' version 3.01, October 1987. The base-level FORTH software provided for CCD control by Photometrics Limited is also described in this latter reference. MJUO extensions to this software have been written (Tobin 1991b) which include site- and instrument-specific commands to improve the ease and convenience of CCD observing.

6.3 The CCD chip

The CCD is a Thomson CSF TH7882 CDA chip overcoated with a fluorescent dye, Metachrome II, for enhanced ultraviolet and blue response. The chip consists of 384 × 576 pixels (columns × rows), with each pixel being 23 μm square. The chip has excellent cosmetic quality as can be seen from the median-clipped

Table 6.1: The gain and other properties of the MJUO CCD system. (Reproduced from Tobin 1992.)

cgain	Gain G (ADU/e$^-$)	Inverse Gain $Q = G^{-1}$ (e$^-$/ADU)	Base level Noise, B_e (e$^-$)	Curvature c ($\times 10^{-6}$)	Full-chip setup + readout time (s)
0	0.062±.002	16.2±.6	11.1±.6	1.1±.5	4.9
33	0.114±.002	8.7±.2	8.0±.2	3.1±.5	7.8
66	0.172±.002	5.8±.1	7.4±.1	5.5±.6	11
100	0.232±.003	4.31±.06	7.1±.1	6.3±.7	14
200	0.405±.006	2.47±.04	6.8±.2	7.2±1.3	23
400	0.738±.015	1.36±.03	7.1±2	14±3	40

dark exposure shown in Fig. 6.1. There is a region of ~ 15 rows next to the output register that shows a significant increase in signal level. This feature has developed over time and seems to be associated with the readout electronics and may not be a property of the chip itself.

A mechanical shutter mounted in front of the quartz cryostat window is opened to admit light during exposures. A flash ring of eight green LEDs is situated between the shutter and the window. The flash ring is normally illuminated for 70 ms before the shutter is opened to begin an exposure. This flash deposits ~ 300 electrons in each pixel of the CCD in order to minimize the reduced efficiency of charge transfer that can occur at very low signal levels.

6.4 Characteristics of the CCD system

6.4.1 Gain and noise of the CCD system

Table 6.1 (taken from Tobin 1992) displays the gain and other properties determined for the MJUO CCD system. The gain, G, is selected by setting the software parameter `cgain` to the appropriate value. The readout noise R_e ($\approx B_e$ for $G^{-1} < R_e$) is ~ 7 electrons.

In addition to the higher base-level noise at `0 cgain`, truncation or digitization noise may be significant at low signal levels. Initial high resolution, échelle spectroscopy was carried out using the system default of `0 cgain`. The digitization noise became very apparent when échelle observations of faint ($\sim$9th magnitude) objects were obtained. For this reason, subsequent échelle observations were taken using a `cgain` of 100. The digitization noise is reduced at this

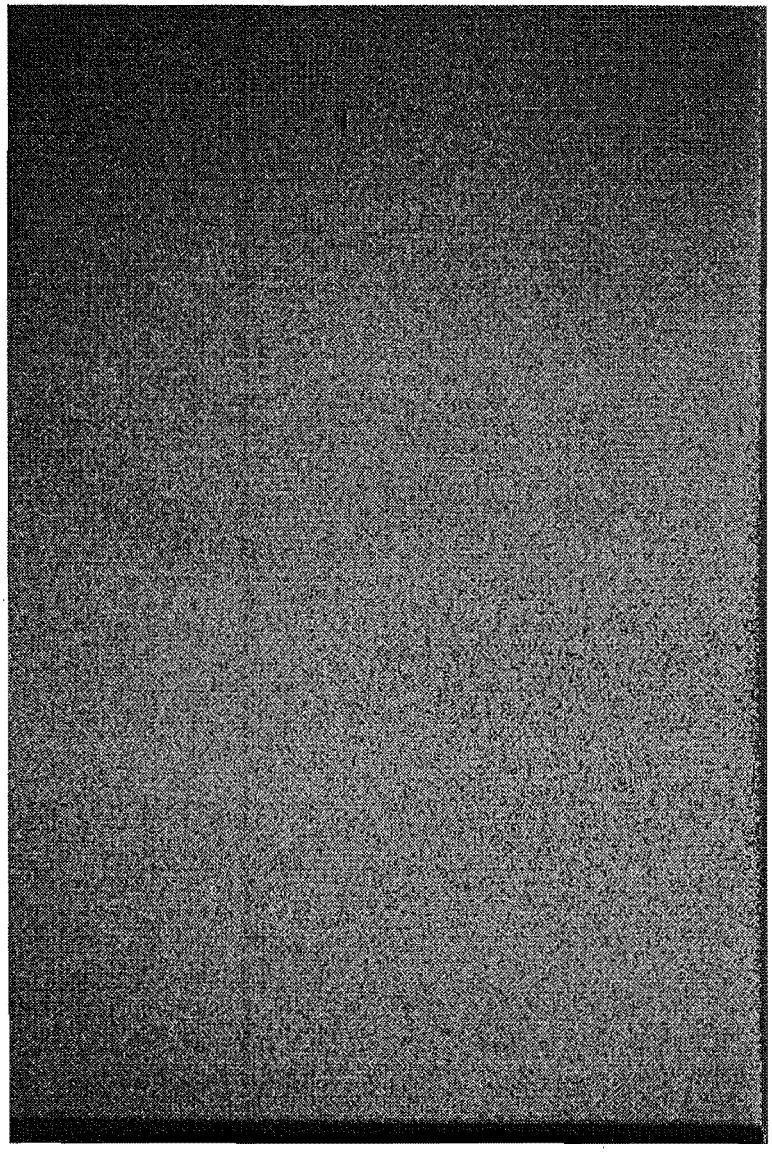

Figure 6.1: A typical dark CCD frame. The non-uniformity of the flash ring illumination is evident.

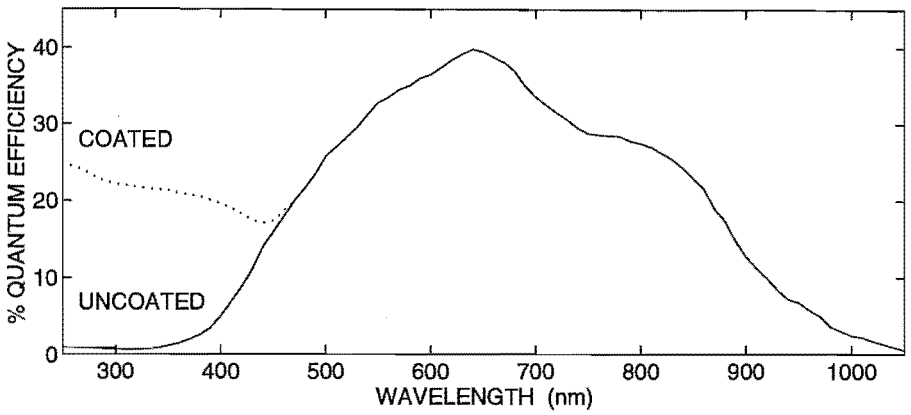

Figure 6.2: The quantum efficiency of a coated and uncoated Thomson TH7882 CCD chip, from Photometrics Ltd.

higher gain, but at the expense of a smaller dynamic range.

6.4.2 Quantum efficiency of the CCD system

Gain should not be confused with sensitivity or quantum efficiency, which relate to the probability that an incoming photon produces a captured charge in the CCD substrate.

Due to the fact that silicon is very absorptive of photons shorter than about 400 nm, the polysilicon electrodes are essentially opaque at these wavelengths and therefore CCD detectors have an intrinsic lack of blue and ultraviolet response. One way to obtain some response at these wavelengths is to overcoat the chip with a fluorescent dye that will absorb blue or UV photons and re-emit visible or red photons. This is what has been done in the case of the MJUO CCD chip, where the fluorescent dye Metachrome II has been used. Photometrics Ltd estimate that the overcoated chip has a quantum efficiency of $\sim 20\,\%$ from 300–400 nm, rising to a peak of $\sim 40\,\%$ at 650 nm, and declining to $\sim 25\,\%$ at 830 nm, $\sim 7\,\%$ at 950 nm, and $\sim 0\,\%$ at 1.05 μm (see Fig. 6.2). It should be noted, however, that the quantum efficiency at a particular wavelength is not the same for each pixel, but varies by up to $\sim 5\,\%$ from its mean value.

6.4.3 Mains pickup during readout

Output signals are affected by AC pickup from the 50 Hz mains supply. This pickup is always present but is most apparent when it beats with the readout rate which results in diagonal bands across images. Because of their inclination they can be very difficult to subtract out in spectroscopy. It is possible to pseudo-randomize the pickup by slight adjustment to either the `cgain` or the area of the chip read out. The peak-to-peak amplitude of the pickup is ~ 9 electrons at all values of cgain.

6.4.4 Cosmic ray detection

Charge can be deposited in the CCD by cosmic rays and probably also as a result of radioactivity in the cryostat materials and elsewhere. Spike-like spots of varying intensities are produced or, less commonly, longer grazing events depending on the obliqueness of incidence of the impinging particle. The number that will be seen in any particular image will depend on the noise level and exposure time. The chip detects ~ 9 cosmic ray events per minute (Tobin 1992) when in the 1.0-m telescope dome at MJUO.

6.4.5 Linearity of the CCD system

One advantage that is often quoted for using CCD systems over photographic and photoelectric detectors is the linearity of CCDs over a large dynamic range. Tests were performed to investigate the linearity of the MJUO CCD and to evaluate over what range of intensities the system is linear. A description of the experimental set-up and details of the analysis and results are presented in Appendix B. The linearity was determined by taking timed exposures of a stable light source. It was found that exposures of less than one second were sensitive to electrical pickup (seen as periodic 'waves' on the displayed image) and had large uncertainties due to the mechanical constraints on the repeatability of the shutter speed[1]. In the range from 30 ADU to 13200 ADU, the linearity of the MJUO chip has been determined to be excellent, with variations from strict linearity of less than 0.4%.

[1]Tobin (1993a) found that the mechanical shutter takes between ~ 5 and ~ 20 ms to open and close, which can increase to ~ 30 ms for very short exposures.

Some CCD detector systems become notably nonlinear slightly before reaching saturation. In most cases where a CCD system has been found to be non-linear, the non-linearity arises in the amplifier or analogue-to-digital converter and not the CCD chip itself. The saturation limit for the MJUO CCD system is set by the analogue-to-digital converter (which saturates at 14 bits or 16383 ADU) and not the full-well pixel capacity. The base level noise has been determined to be ~ 7–11 electrons over the range of values of `cgain` used (see Table 6.1). A higher choice of `cgain` will saturate the CCD system for fewer detected photons, thus the dynamic range of the CCD is reduced for higher values of `cgain`.

If a pixel does become saturated, the excess charge can 'bleed' along the readout columns and, in extreme cases, even across them. Although this is not usually a problem, sometimes excess charge may diffuse into the chip substrate. In following exposures, this excess charge may diffuse back, causing spurious 'remnant images' to appear. Another possible cause of these remnant images is phosphorescence in the fluorescent dye coating of the CCD chip. However, Photometrics claim that the dye used, Metachrome II, has no such phosphorescent characteristics. The remnant images can persist for several hours after the original saturation event and therefore cause a problem in the reduction of these subsequent frames.

6.4.6 The temperature variation of chip sensitivity

Tests were performed on the MJUO CCD system to evaluate the effects of temperature on the spectral response of the chip and also to determine the contribution of the dark current at various temperatures. Appendix B describes the experimental procedure and details of this analysis. The spectral response of the chip as a function of temperature is displayed graphically in this appendix. The results of this series of tests were also used to determine the optimal operating temperature of the CCD chip, based on several considerations:

- The CCD should be operated at a temperature which results in an acceptable dark current. Thermal agitation can produce electron-hole pairs that are indistinguishable from those formed by impinging photons from the observed source. This is known as the dark current of the detector. The dark current can be reduced by cooling the chip but this also reduces the quantum efficiency and charge transfer efficiency of the chip. Photometrics Ltd suggest −90°C as the highest operating temperature, otherwise the dark

noise may dominate the signal.

- A reasonable compromise should be reached for the varying sensitivities at different wavelengths to optimize the response of the chip. Photometrics suggest −130°C as the coolest operating temperature to use, since long wavelength sensitivity is reduced at lower temperatures.

- A heating element and thermostat are used to regulate the chip temperature. To minimize the boil-off of the liquid nitrogen coolant, the coolest acceptable operating temperature should therefore be used.

- The CH210 dewar should be able to maintain the operational temperature of the chip in any telescope position. The coolest temperature at which the CH210 cryostat can maintain the operating temperature of the chip, irrespective of orientation, is −110°C.

- the CCD temperature control only allows operating temperatures, $T_{\rm CCD}$, in the range $-50°\mathrm{C} < T_{\rm CCD} < -150°\mathrm{C}$ to be selected.

The spectral response of the chip for the range of wavelengths tested suggested that the infra-red response was most affected by the cooling of the chip. The sensitivity of the infra-red response was reduced by $\sim 14\%$ in decreasing the temperature from −47°C to −105°C. The tests showed that −55°C was the highest temperature at which the CCD could be used with an acceptable dark current. An operating temperature significantly lower than −110°C is unsuitable since this temperature cannot be held constant when the telescope position is changed. Consequently, −110°C was selected as the operational temperature of the CCD chip. The Photometrics CH210 cryostat can maintain this with a stability of 0.1–0.2°C. This results in no more than a 0.03–0.06% variation in sensitivity.

6.5 The telescope and échelle spectrograph

The échelle spectrograph makes use of a 79 groove mm^{-1} échelle grating with a blaze angle of $\theta_B = \arctan 2 = 36°26'$. Following dispersion by the échelle grating, the incident light is dispersed into spectral orders by a first order cross-disperser. The reciprocal dispersion of the spectrograph is $2\,\mathrm{Å\,mm}^{-1}$ at Hα corresponding to a resolving power, R, of $\sim 30\,000$. Further details on the échelle spectrograph are given by Hearnshaw (1977, 1978).

The spectrograph is directly mounted at the cassegrain focus of the 1.0-m telescope. For the RV Tauri programme, this telescope was primarily used in the f/13.5 configuration which corresponds to a Dall-Kirkham type optical system. Very occasionally, the f/8 configuration of the telescope was employed. A description of the optical systems of the MJUO 1.0-m telescope can be found in Nankivell & Rumsey (1986).

For the RV Tauri programme, the échelle spectrograph is used in conjunction with the CCD detector system to observe three different wavelength regions. The two regions that include the Hα line at 6562 Å (designated the 'Hα region') and the Li I line at 6707 Å (designated the 'Li region') sample approximately 30 Å of each of four orders (usually orders 34–37). For the wavelength region which includes the Na I lines at 5890 Å and 5896 Å (the so-called 'Na region') about 30 Å of five échelle orders (usually orders 38–42) are obtained.

Although this thesis is mainly interested in the relative change in the radial velocities of the programme stars, any comparison with other radial velocity studies requires reference to the standard IAU system.

Recent spectroscopic observations (Albrow 1994 private communication) of three IAU radial velocity standard stars (β CrV, HR6970 and α Tra) obtained with the MJUO CCD and échelle arrangement on the 1.0-m telescope, suggest that the MJUO radial velocities are consistent with the absolute (IAU) system to within $\pm 1.0\,\mathrm{km\,s^{-1}}$, which is within the accuracy required for this project.

6.6 Preparation of échelle spectra for reduction

A typical observing sequence using the échelle spectrograph and the CCD detector consists of an astronomical object image (`OBJ`), a thorium-argon arc image for wavelength calibration (`WLC`) and a tungsten lamp observation (`FLAT`). Three dark exposures are obtained at the beginning of the night (and throughout the night if the bias level is changing). The median of these three images is taken to form a representative `DARK` frame which is then subtracted from all later exposures. The dark-subtracted images are written to 9-track magnetic tape in an idiosyncratic format intrinsic to the Photometrics CCD system. On another 9-track magnetic tape drive attached to a VAXstation II GPX at the University of Canterbury, these tapes are read and the images converted to FITS format on disk. The heliocentric date and airmass are calculated for the stellar observation. (For further details see Tobin 1993b.) The images can now be read into a number of

available software packages, including MIDAS.

6.7 The Munich Image Data Analysis System

The European Southern Observatory – Munich Image Data Analysis System (ESO–MIDAS or simply MIDAS) consists of a set of general tools for image processing and data reduction.

The MIDAS system is designed to allow easy integration of future application modules as well as good flexibility when used interactively. This is achieved through the ability of users to create specific 'procedure files' which are used to perform a simple or complex sequence of MIDAS commands. The MIDAS command language consists of a control language and set of core commands. In addition to these core commands are the context-specific commands. A context is an application module that is selected at the start of the reduction session.

The MIDAS system can be run in both interactive and batch modes. Both VAX/VMS and UNIX compatible versions are available. The spectra described in this thesis were primarily reduced using the 91NOV MIDAS release installed on the University of Canterbury's VAX 7610 computer.

6.8 The MIDAS échelle reduction package

The échelle package provides a set of about thirty basic commands to reduce échelle spectra. These lower level commands are incorporated into several main MIDAS procedures that perform the complete steps of the reduction. Several algorithms are included in most of the main procedures so that the technique best-suited to the data configuration can be chosen. The first ESO instrument to be supported by the échelle package was the Cassegrain Echelle Spectrograph (CASPEC) and procedures have been generalized for other instruments. However, several errors were found in the VMS version of the échelle routines and it was necessary to modify some of the original Fortran codes to handle reductions of échelle spectra from MJUO. These modifications are described at the appropriate stages.

6.9 Description of reduction procedure

The basic data required for the use of the MIDAS échelle reduction package are a wavelength calibration image (WLC), a flat field image (FLAT) and an astronomical object image (OBJ). For absolute or relative flux calibration, a standard star image (STD) is required.

Data preprocessing involves rotating the images so that they have the standard orientation that MIDAS expects:

- dispersion direction horizontal with wavelength increasing from left to right.
- spectral order numbers increasing from top to bottom.

At this point, the descriptor values START and STEP had to be modified (each set to 1.,1.) since the original code did not compensate for the rotation. This problem was reported to ESO and the 91NOV and later releases of MIDAS update these keywords properly after image rotations. In addition, the échelle orders in the standard orientation are expected to be sloping slightly upwards. The MJUO échelle spectra were sloping in the opposite direction, causing problems for the order-tracing algorithm. The échelle spectrograph–CCD camera head interface has since been modified so that the CCD may be rotated slightly to allow easy alignment of the échelle orders along the long axis of the CCD chip. This simplifies the reduction of the échelle spectra since order tracing and extraction is easier and more accurate.

The steps in a typical échelle reduction session are described in the following sections and a flow diagram displaying the steps is shown in Figure 6.3.

More detailed information, including the actual sequence of MIDAS commands and procedures used to perform the reduction steps is included as an appendix to this thesis (Appendix C). Also included in the appendix is a summary of the adopted échelle parameters for reducing the MJUO échelle spectra.

6.9.1 Order definition

There are three algorithms available in MIDAS that automatically locate and trace the échelle orders across the CCD frame. A first guess of the order positions is found by taking a trace perpendicular to the dispersion direction in the centre of

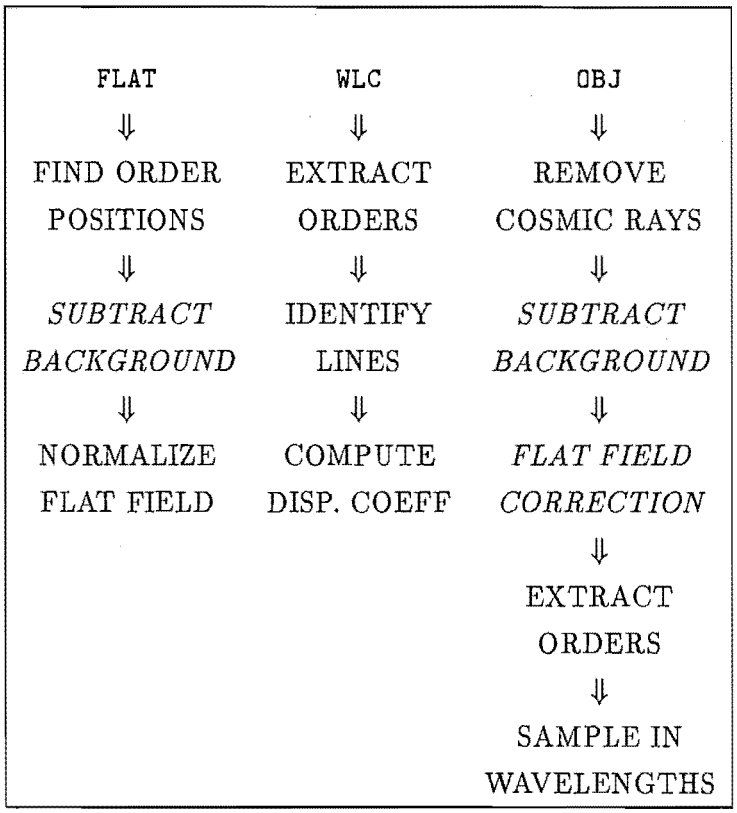

Figure 6.3: The steps in a typical échelle reduction scheme using the MIDAS software package. Optional steps are indicated by slanted type.

the image. The orders are then traced by taking the middle point with respect to the order edges, at intervals along the order. The edges of the orders are detected automatically using a threshold value perpendicular to the dispersion direction. A least-squares fit to the order locations is computed using a bivariate polynomial. In most cases the OBJ frame was used for the order definition, but for some fainter stars, the FLAT image was used.

6.9.2 Background definition

An accurate estimate of the background in an échelle image is required to correct for certain instrumental effects. Once the frames have been dark-subtracted, the remaining background consists of general scattered light in the spectrograph entering via the slit and diffuse light in the interorder space from the adjacent orders. A bivariate polynomial or a smoothing spline is fitted to points in the interorder space to model the background. (At this point, the original code was not using interorder points across the entire chip to estimate the background. The 91NOV release of MIDAS was modified to enable better background estimation after this problem was reported to ESO). The next reduction step (cosmic ray removal) incorporates this background modelling into its procedure.

6.9.3 Cosmic ray removal

One problem with using CCDs as detectors is their sensitivity to cosmic ray events. This is especially true in long CCD exposures. The cosmic ray event may appear as a spike-like spot or, less commonly, as a longer grazing event, depending on the angle at which the CCD is hit.

There are three main steps in MIDAS procedure for removing cosmic rays. In the first step, a median filter is applied to the entire frame. This enables an accurate estimate of the true background, which is then subtracted from the original image in the second step. The third step is the removal of the cosmic ray events from the spectral orders of the background-subtracted image. In this step, a 'true' spatial profile of the order cross-section (similar to a one dimensional point-spread function) is formed as the median of all the individual, normalized profiles along each order. The renormalized flux for all individual pixels along each order is then compared with the appropriate median profile. Any deviation due to cosmic ray events are then obvious and the pixel values are replaced by the median value. The user selects the rejection criteria, based on the inverse gain,

the readout noise and the number of standard deviations for pixel replacement.

The effectiveness of the cosmic ray filtering procedure is verified by comparing the difference between the filtered and unfiltered frames. The final output frame is a merger of the median filtered interorder space and the cosmic ray filtered orders.

(It was found that the Fortran code for the cosmic ray filtering contained several errors. The location of the orders was not correctly input from the order definition step. The limit on the maximum width of the spectral orders was set too small and the calculation of the boundary condition limits for the filtering routine was also incorrect. These problems were probably due to the routine expecting narrow CASPEC orders. Changes were made to the Fortran code and the filtering procedure code in the 91NOV MIDAS release, and the problems reported to ESO.)

6.9.4 Order extraction

The individual échelle orders are extracted by adding the pixel values over a numerical slit lying across the orders. The slit centre is set by the earlier order-definition step. The width of the slit is one pixel with the height being set by the user. The extracted flux is the weighted average of the pixel values. Three types of weighting are available in extracting the spectral orders. The `linear` weighting option adds all the pixels with unit weight, `average` weighting adds all the pixels with a weight dependent on the length of extraction slit used and `optimal` weighting uses the spatial profile to produce optimal weighting of the pixel values. The orders of the `OBJ` image are extracted and exactly the same extraction slit and weighting is used for the `WLC` image. The `linear` weighting option was used for the MJUO spectra.

6.9.5 Wavelength calibration

The extracted orders of the `WLC` image are used to compute the dispersion coefficients for each order. Initially, the arc lines are detected using a simple thresholding algorithm. A gaussian fit to the line profile or a center of gravity method is used to find the line centres. (At this stage, the MIDAS procedure was modified to indicate which arc lines had been detected. This saved a lot of time in the subsequent step, since choosing undetected arc lines gives an unrecoverable error.) There are several algorithms available in MIDAS that perform the arc

line identifications. The pair method requires the identification of two lines in overlapping regions of adjacent échelle orders. The angle method requires a minimum of four arc line identifications. The guess method can be used on images taken with the same instrument set-up. This method uses the dispersion relation from a previous calibration and is not interactive. For the MJUO system, the angle and guess methods were employed. At least ten arc lines were identified interactively on the 2D image display. A set of global dispersion coefficients are then derived. These are used as a first approximation to identify additional arc lines from a thorium-argon line list and then to refine the dispersion coefficients for each order. In a well-calibrated image, the rms residuals of the fit of the dispersion coefficients should be ≤ 0.2 pixel. For the MJUO échelle spectra, the rms residuals of the fit were typically ~ 0.1 pixel, resulting in a standard deviation for each individual order of ~ 0.0020 Å.

6.9.6 Flat-field and instrument response correction

The sensitivity of the MJUO CCD (as with other CCDs) is nonuniform across the image due to a number of factors. These include pixel-to-pixel variations in sensitivity, scattering of light and shadows cast by dust specks on the cryostat window and other optical surfaces as well as telescope vignetting. There are other large scale effects seen in the flat-field that are due to the chromatic response of the CCD chip and the blaze effect of the échelle grating. A flat-field image attempts to represent the combined sensitivity variations of the total échelle spectrograph–CCD configuration.

When using the MJUO CCD system for spectroscopy, the `FLAT` image is known as a 'Smooth-field', since the continuum radiation source has a smooth (not flat) chromatic profile. The `FLAT` frame (and `WLC` frame) is obtained at the same telescope position as the `OBJ` to avoid flexure effects. The `FLAT` frame is normalized by dividing the image by a constant value which is approximately the mean of the signal in the orders. The `OBJ` image is then divided by the normalized `FLAT` image to correct for the sensitivity variations. The instrument response correction may be calculated using a standard star for which the absolute fluxes are known. If a `STD` star was not observed, a model of the blaze effect introduced by the échelle grating can be used.

The next reduction step (reduction of object spectra) incorporates the flat-fielding and instrument response correction into its procedure. Both steps are

optional and must be specified explicitly.

6.9.7 Reduction of object spectra

In the final reduction step the background is determined and subtracted (this step is skipped if the frame has been cosmic-ray filtered already) and the image is optionally divided by the normalized flat-field. The échelle orders are extracted and rebinned into linear wavelength steps using the results from the earlier wavelength calibration. The counts are normalized to an exposure time of one second and the orders are optionally multiplied by the response function. Finally the individual orders are extracted ready for further processing and analysis.

The procedure file for this step was necessarily very general, with many optional steps. For this reason, the procedure file was modified at several stages to optimize its use with the MJUO échelle data. The OBJ frame was always filtered for cosmic ray events and thus the background modelling step was never required at this stage. Since there was no overlap of the échelle orders on the image, the option to merge the orders was removed. The optional response step was not performed.

The one-dimensional, wavelength-calibrated spectra were written out from the MIDAS package at this stage in FITS format. This enabled further processing and analysis to be carried out on the Sun UNIX system at the University of Canterbury using the FIGARO reduction package.

6.10 Further processing

Due to the fact that the CCD samples only ~ 30 Å of the very highly dispersed stellar échellogram, the spectra should be relatively flat. Some (slight) curvature may be introduced by the chromatic profile of the smooth-field lamp, vignetting or the shape of the stellar continuum itself. The spectra are fitted with a continuum profile which is a subjective choice as to the height of the spectrum and the amount of curvature. For high signal-to-noise spectra of warm stars (effective temperature of about 5000 to 7000 K) or phases where the stars appear warm, the choice of the continuum fit is easier and more accurate due to the fact that more regions of stellar 'continuum' (absorption lines absent) are seen. For low signal-to-noise spectra and cooler stars (or phases where the stars are cooler and

TiO bands are visible) the selection of the continuum level is less certain. The stellar spectra are normalized by dividing by the fitted continuum, so that a height of one represents the continuum and zero is total absorption.

A wavelength correction for the Earth's motion around the barycentre (centre of mass) of the solar system is then applied to the spectra. The velocity correction required is calculated using the RADVEL program adapted by K.A. Murdoch, and the VACHEL routine within FIGARO is used to apply the corresponding wavelength correction to the spectra.

The spectra are then lightly smoothed by convolving each spectrum with a running gaussian that has a FWHM less than the effective size of the slit. This should ensure that the high frequency noise is smoothed with little effect on the scientific content of the spectrum.

The MJUO spectra are now in a state that allows line profiles to be analysed and radial velocities to be determined.

6.11 Profile fitting of the Hα line

In order to investigate the phase dependence of the Hα profile and to ascertain what relation this has to the light curve and photometric phase, the Hα line is fitted by a series of Gaussians that reproduce the profile at that particular phase. The gaussian fitting program, GAUSS, in the software reduction package FIGARO, is used for this Hα profile fitting. The position, half-width (the full width at half height) and height (or strength) of each gaussian is interactively adjusted until a reasonable fit is obtained. The GAUSS program then optimizes the fit by minimizing the sum of the square of the residuals. The individual gaussians fitted plus the sum of the gaussians (the fit to the Hα profile) are displayed on the graphics screen together with the residuals for the fit. Fig 6.4 shows the output from the GAUSS program.

The appearance of the Hα profiles for most RV Tauri stars in the MJUO programme could generally be modelled with two gaussians. First, a strong emission component that varied in both height and width, and second, an absorption component added to create the central absorption core of the Hα profile. If required, a further red-shifted absorption component was introduced to improve the fit to the Hα profile in some of the RV Tauri stars.

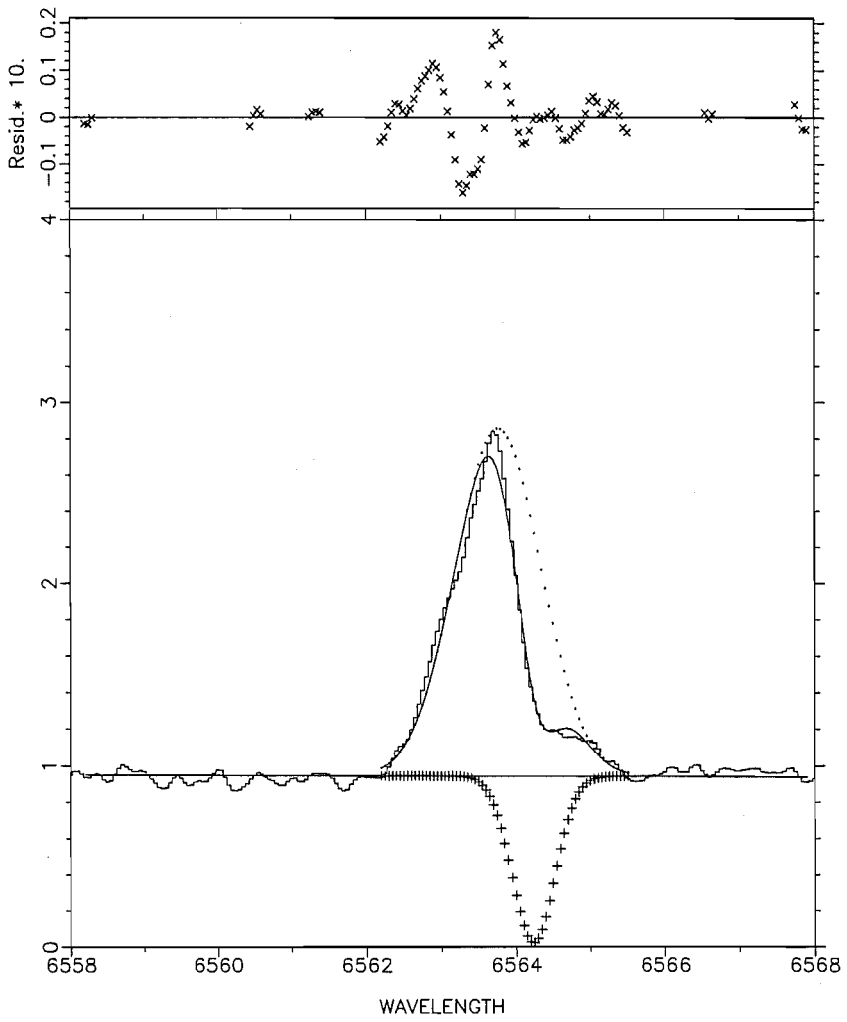

Figure 6.4: The FIGARO program GAUSS is used to model the Hα line with a number of Gaussian profiles.

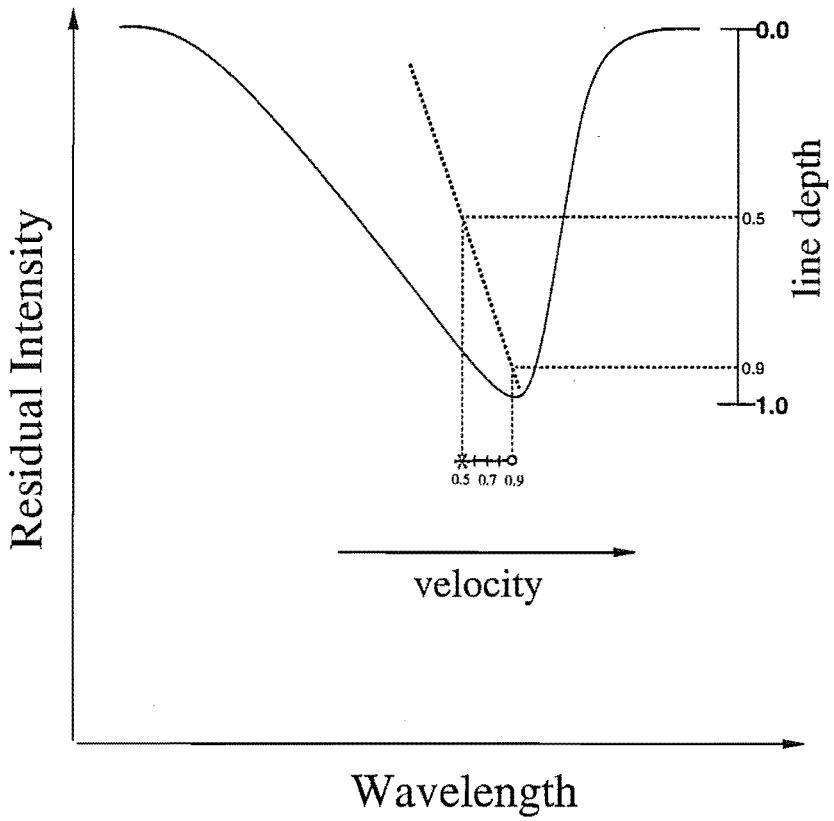

Figure 6.5: Schematic representation of a spectral line, showing how the line bisector and the corresponding velocities are defined. (Reproduced from Albrow 1994.)

6.12 Radial velocity measurements

The line bisector method (Wallerstein et al. 1992, Albrow 1994) was used to calculate the radial velocities. In this method, the continuum is designated as being at depth 0.0 and the core of the spectral line at depth 1.0. The wavelength of the bisector is determined at specific fractions (0.5, 0.6, 0.7, 0.8 and 0.9) of the line depth. Depths of less than 0.5 and greater than depth 0.9 are not used due to possible contamination from neighbouring spectral lines and limits on the algorithm close to depth 1.0 respectively. The corresponding radial velocities at the various depths in the line profile are calculated from the relative shift of the line from its rest wavelength. The average over the velocities derived at depths 0.7, 0.8 and 0.9 were used to produce the radial velocity curves for a particular spectral line. Fig. 6.5 shows a schematic line profile demonstrating the line bisector method for determining radial velocities.

The SPECLINE and HALFVEL programs of M.D. Albrow was used to calculate the line bisectors and radial velocities from the reduced MJUO échelle spectra of the RV Tauri stars.

6.12.1 Orbital analysis

The orbital analysis programs BXT2 of T. Mazeh and SBCM of C. Morbey were used to analyse the long-term radial velocity variations of U Mon. Six parameters or 'orbital elements' uniquely define the position and motion of a star in its orbit around the stellar system's centre of mass as a function of time. These are:

- e, the eccentricity;
- a, the semimajor axis;
- i, the inclination, the angle between the orbital plane and the tangential plane on the celestial sphere;
- Ω, the longitude of the ascending node, the angle between the vernal equinox and the ascending node (point of intersection of the orbit and the tangential plane);
- ω, the longitude of periastron, the angle between periastron (closest approach in the orbit) and the ascending node;
- T_0, the time of periastron passage.

For the orbit of a binary system where the masses are unknown, a seventh element, the period P must be determined. Although we can calculate the value of $a \sin i$ from the orbital analysis, the inclination is undetermined because we are only measuring the radial or line-of-sight component of the velocity. Thus a and i cannot be evaluated separately. The value of Ω is also indeterminable in the case of a single-lined spectroscopic binary.

The two orbital programs compute the orbital parameters: V_γ, K_1, e, ω, T_0, $a \sin i$ and $f(M)$. V_γ is the γ-velocity or the radial velocity of the centre of mass of the binary system, K_1 is the amplitude of the radial velocity of the brighter star and $f(M)$ is the mass function of the system defined by:

$$f(M) = \frac{M_2^3 \sin^3 i}{(M_1 + M_2)^2}$$

The parameters e, ω and T_0 have the same meaning as outlined above.

Chapter 7

Spectroscopy of the RVa stars

Following the format that was used for the chapters dealing with their photometric characteristics, the spectroscopy of the RVa stars and the RVb stars are presented separately. This chapter is concerned with the spectroscopic properties of the RVa stars, while Chapter 8 deals with the members of the RVb subclass.

In this chapter, each programme star is discussed individually. More spectra were obtained of R Sct as a consequence of it being the brightest RV Tauri variable. A more detailed discussion of this star is presented in Section 7.1. Only a few spectra were obtained of some programme RV Tauri stars due to their faintness.

Sequences of stacked MJUO and MSO spectra are presented for each star[1]. The appearance and phase-dependent behaviour of the shock-related spectral features, such as Hα emission, doubled metallic absorption lines and metallic emission lines, is described. For this aspect of the RV Tauri spectroscopy, a more qualitative approach has been adopted.

For every star the phase-dependent behaviour of the Hα emission strength is investigated by measuring the equivalent width of the profile using the ABLINE program within the FIGARO software package. Radial velocity curves are presented for selected metallic lines or, when the metallic lines are too weak to be measured, for the components of the Hα line. Generally, the metallic radial velocities are measured from the Fe I lines with $\chi \sim 2.5\,\mathrm{eV}$ for the Preston 'A' type stars (strong-lined) and the C I line at 6587.622 Å ($\chi = 8.53\,\mathrm{eV}$) for the Preston 'B' type stars (weak-lined, carbon enhanced).

[1]It should be noted that it was not practical to present stacked plots of all the spectra obtained of the programme RV Tauri stars and, therefore, only representative échelle orders or selected phases are presented in most cases.

7.1 R Sct

7.1.1 Previous spectroscopy of R Sct

R Sct, the brightest member of the RV Tauri class of variable, has been a popular target for astronomers for over a hundred years. It displays large variations in its light curve amplitude and spectral type. The range in spectral types for R Sct is from G0e Ia to K0p Ib (Rosino 1951) with the earlier spectral types occurring at maximum light. Later spectral types occur during both minima, and TiO absorption bands, which can be equivalent in strength to those seen in stars of M5 spectral type, may appear during the deep primary minima. Spectral classification based on the rest of the stellar spectrum at this phase corresponds to late-G or early-K type. At extremely deep minima ($V < 8.0$) the metallic line absorption features disappear and strong TiO absorption bands, together with emission features produced in the chromosphere, are apparent (Howell et al. 1983). These chromospheric lines fade rapidly as the star brightens from the deep minimum.

R Sct belongs to the Preston spectroscopic class 'A' (Preston et al. 1963). Dawson (1979) further divides this subclass depending on whether TiO bands are present at minimum light ('A_1') or not ('A_2'). Under this scheme, R Sct is classified as an 'A_1' star.

There are a number of general spectroscopic studies of R Sct, including those by McLaughlin (1939, as described by Tsesevich 1975), Rosino (1951), Preston (1962), Preston et al. (1963) and Howell et al. (1983).

McLaughlin's (1939) study was based on relatively low dispersion spectra of R Sct and yielded a number of interesting results which were discussed by Tsesevich (1975). The amplitudes of variation of the luminosity and the radial velocities appeared to be correlated. A correlation was also found between the amplitude of the previous deep minimum and hydrogen line emission intensity, with stronger emission for deeper primary minima. The γ-velocity was found to vary over a wide range, from 33 to 50 $\mathrm{km\,s^{-1}}$ with an average of 44.2 $\mathrm{km\,s^{-1}}$, but with no apparent periodicity.

Preston's (1962) study was based on 19 medium- and high-dispersion spectrograms obtained over one complete cycle. Using high-dispersion ($R \sim 70\,000$) spectra to investigate Hα line profiles, Preston found that an obvious double-peaked Hα emission profile was visible during both primary and secondary light

maxima, but that the emission intensity was strongest during the *secondary* light maxima. This intensity trend was also seen in the case of the metallic emission lines. Preston (1962) presented the mean radial velocity curve for subordinate Fe I lines with $\chi > 0.9\,\mathrm{eV}$, which showed a large amplitude of variation (about $30\,\mathrm{km\,s^{-1}}$ with an time-averaged mean velocity of $43.8\,\mathrm{km\,s^{-1}}$) and the occurrence of two discontinuities during one luminosity (140 d) cycle due to the doubling of the absorption lines. The radial velocity variations of the ground-term lines of Fe I with $\chi < 0.2\,\mathrm{eV}$ are of much lower amplitude (about $10\,\mathrm{km\,s^{-1}}$ about a mean value of $47\,\mathrm{km\,s^{-1}}$) and do not show any discontinuity. These differences in behaviour were attributed to stratification effects in the envelope. By integrating the discontinuous radial velocity curve, a total displacement of $8 \times 10^7\,\mathrm{km}$ ($114\,R_\odot$) was obtained, which is similar to the assumed stellar radius.

In order to study the dynamics of the atmosphere, radial velocities for R Sct were obtained using high-resolution infrared spectroscopy (Mozurkewich et al. 1987), a combination of high-resolution spectroscopy and CORAVEL observations (Gillet et al. 1989) and high-resolution spectroscopy alone (Gillet et al. 1990, Lèbre 1991, Lèbre & Gillet 1991a, 1991b).

Using high resolution spectroscopy and CORAVEL velocities obtained over several pulsation cycles, Gillet et al. (1989, 1990) have shown the existence of two shock waves and their associated accelerations within the atmosphere during each luminosity period ($\sim$140 d). High-resolution spectroscopy of pure photospheric absorption Fe I lines by Lèbre & Gillet (1991a, 1991b) have confirmed the presence of two acceleration peaks per luminosity period, which are associated with the two shock waves. However, their finding that Fe I lines of very similar excitation potential display very large variations in the velocity amplitude is undoubtedly due to the fact that they have mistakenly used ΔE ($= E_{upper} - E_{lower}$ = energy of transition) as the value of the excitation potential. Consequently, the Fe I lines that they used (all around 6550–6620 Å) have almost exactly the same "excitation potential" of 1.87–1.89 eV. In reality, their pure absorption Fe I lines have excitation potentials of between 1.01 eV and 4.79 eV and thus large variations in the velocity amplitude (due to quite different depths of formation of these Fe I lines) are not unexpected.

Lèbre & Gillet (1991a) observed R Sct over a time interval of 133 days, during which time they expected to sample almost an entire luminosity cycle comprising both a deep and a shallow minimum. However, the AAVSO light curve for R Sct

shows that they observed a very rare event, a 'flip' or interchange of the deep and shallow minima, so that two consecutive deep minima were observed. The first deep minimum they observed was in phase with the previous alternations of deep and shallow minima and the second deep minima was in phase with the subsequent alternating deep and shallow minima (including those regular alternations seen in the MJUO photometry). Lèbre & Gillet (1991a) find that large outward accelerations and strong Hα emission are associated with each shock wave. The acceleration is strongest around phase 0.0 (the primary and strongest shock) and phase 0.6 (the secondary shock). An earlier paper which used CORAVEL velocities (Gillet et al. 1990) found that the *secondary* shock was the strongest in both AC Her and R Sct.

Mozurkewich et al. (1987) studied the velocity structure of R Sct via high-resolution 2μm Fourier-transform spectrograms taken at different pulsational phases. The high-excitation atomic absorption lines which form at deep photospheric layers display a mean velocity of $37\,\mathrm{km\,s^{-1}}$, a net displacement of $5 \times 10^7\,\mathrm{km}$ ($71\,R_\odot$) with a maximum radius of about $1.1 \times 10^8\,\mathrm{km}$ ($157\,R_\odot$) and a continuous (single-lined), repeatable pulsation with a period of about 142 d. This is not consistent with optical studies which show a 70 d period and a discontinuous velocity curve. Mozurkewich et al. (1987) claim that the molecular lines of CO, which form higher in the atmosphere, appear to show a single velocity discontinuity, but Gillet et al. (1989) note that the averaged line profiles show evidence of line-doubling at phases of 0.35 and 0.65. These phases correspond to line-doubling phases of the optical radial velocity curves and would imply a 70 day interval between shock waves. If further high-resolution infrared spectra could be obtained which confirm this CO line-doubling, then Gillet et al. (1989) claim that the infrared CO observations and the optical observations would be consistent. Contemporaneous high-resolution infrared and optical spectroscopy over a single 142 d cycle would be most useful in resolving this issue.

7.1.2 Spectroscopic observations of R Sct

Using the 1.0-m telescope, échelle spectrograph and CCD detector, about 50 high-resolution spectra of R Sct at various wavelength regions were obtained at MJUO between 1991 March and 1993 August. Exposure times were typically 15 to 30 minutes. Twenty high-resolution coudé spectra were obtained using the 1.9-m telescope at Mt Stromlo Observatory (MSO) in Canberra between 1991

May and 1991 September. Exposure times were typically between 2 and 5 minutes. Table 7.1 is a log of the spectroscopic observations for R Sct. The spectra were wavelength-calibrated, continuum-normalized and corrected for barycentric motion. On 1991 May 24, R Sct was observed at both MJUO and MSO. Fig. 7.1 shows the good correspondence between the Hα spectra obtained using the two instrumental set-ups with differing resolutions.

Table 7.1: Spectroscopic observations of R Sct.

UT date	HJD [2] 2440000+	region	site	observer[3]	phase (ϕ)	W_λ(Hα) (Å)	rv(Fe)[4] (km s^{-1})
1991-Mar-26	8342.238	Hα	MJUO	KRP	2.00	−0.15	51.4
1991-Mar-27	8343.211	Li	MJUO	KRP	2.01	–	–
1991-Mar-31	8347.203	Hα	MJUO	KRP	2.03	−0.04	51.8
1991-May-10	8387.180	Hα	MSO	WAL	2.24	−0.07	26.5
1991-May-12	8389.199	Hα	MSO	WAL	2.25	−0.06	28.2
1991-May-20	8397.086	Hα	MJUO	KRP	2.31	+0.10	30.3
1991-May-20	8397.125	Li	MJUO	KRP	2.31	–	–
1991-May-21	8398.121	Li	MJUO	KRP	2.32	–	–
1991-May-21	8398.164	Hα	MJUO	KRP	2.32	+0.18	31.8
1991-May-21	8398.199	Na	MJUO	KRP	2.32	–	–
1991-May-21	8398.246	other	MJUO	KRP	2.32	–	–
1991-May-22	8399.141	Hα	MJUO	KRP	2.32	+0.21	31.8
1991-May-22	8399.168	Li	MJUO	KRP	2.32	–	–
1991-May-23	8400.070	Hα	MJUO	KRP	2.33	+0.18	31.8
1991-May-23	8400.152	Li	MJUO	KRP	2.33	–	–
1991-May-24	8401.102	Li	MJUO	KRP	2.34	–	–
1991-May-24	8401.137	Hα	MSO	WAL	2.34	+0.36	30.4
1991-May-24	8401.141	Hα	MJUO	KRP	2.34	+0.26	30.8
1991-May-26	8403.102	Hα	MSO	WAL	2.35	+0.45	30.4
1991-May-30	8407.211	Hα	MSO	WAL	2.38	+0.44	36.4
1991-May-31	8408.086	Hα	MSO	WAL	2.39	+0.40	39.8
1991-Jun-04	8412.125	Hα	MSO	WAL	2.42	+0.38	41.3
1991-Jun-06	8414.109	Hα	MJUO	KRP	2.43	+0.44	39.8
1991-Jun-06	8414.145	Li	MJUO	KRP	2.43	–	–
1991-Jul-15	8453.105	Hα	MSO	WAL	2.71	−0.38	38.2
1991-Jul-17	8455.145	Hα	MSO	WAL	2.72	−0.18	38.2
1991-Jul-29	8466.945	Hα	MJUO	KRP	2.81	+0.26	30.8
1991-Jul-29	8466.980	Li	MJUO	KRP	2.81	–	–

[2] for mid time of observation

[3] For this, and all subsequent tables listing the spectroscopic observations, the observers are: K.R. Pollard (KRP); W.A. Lawson (WAL); M.D. Albrow (MDA); P.L. Cottrell (PLC).

[4] radial velocity for the Fe I line at 6546.245Å.

1991-Jul-30	8467.906	Hα	MJUO	KRP	2.81	+0.27	32.2
1991-Jul-30	8467.941	Li	MJUO	KRP	2.82	–	–
1991-Aug-02	8470.969	Hα	MJUO	KRP	2.84	+0.40	34.8
1991-Aug-03	8471.961	Hα	MJUO	KRP	2.84	+0.42	35.4
1991-Aug-03	8471.992	Li	MJUO	KRP	2.84	–	–
1991-Aug-21	8489.945	Hα	MSO	KRP	2.97	+0.83	55.9
1991-Aug-24	8492.996	Hα	MSO	KRP	2.99	+0.77	53.5
1991-Aug-26	8495.043	Hα	MSO	KRP	3.01	+0.65	52.0
1991-Aug-31	8500.023	Hα	MSO	KRP	3.04	−0.02	52.8
1991-Sep-02	8502.043	Hα	MSO	KRP	3.05	−0.32	54.2
1991-Sep-03	8503.059	Hα	MSO	KRP	3.07	−0.41	48.9
1991-Sep-05	8505.035	Hα	MSO	KRP	3.08	−0.53	47.9
1991-Sep-07	8507.012	Hα	MSO	KRP	3.09	−0.79	31.6
1991-Sep-09	8509.063	Hα	MSO	WAL	3.11	−0.76	19.6
1991-Sep-12	8512.055	Hα	MSO	WAL	3.13	−0.42	18.7
1991-Sep-25	8524.871	Hα	MJUO	KRP	3.22	+0.54	23.3
1991-Sep-26	8525.914	Hα	MJUO	KRP	3.23	+0.54	23.7
1991-Sep-26	8525.949	Na	MJUO	KRP	3.23	–	–
1991-Sep-27	8526.949	Li	MJUO	KRP	3.24	–	–
1991-Sep-27	8526.957	Hα	MJUO	KRP	3.24	+0.58	24.8
1992-Mar-24	8706.242	Hα	MJUO	KRP	4.51	+0.92	51.1
1992-Mar-24	8706.258	other	MJUO	KRP	4.51	–	–
1992-Apr-11	8724.164	Hα	MJUO	MDA	4.64	+0.28	52.4
1992-May-25	8768.031	Hα	MJUO	KRP	4.92	+0.82	44.0
1992-May-25	8768.117	other	MJUO	KRP	4.92	–	–
1992-May-25	8768.141	Li	MJUO	KRP	4.92	–	–
1992-May-25	8768.164	Na	MJUO	KRP	4.92	–	–
1992-Sep-11	8876.855	Hα	MJUO	KRP	5.73	+0.00	22.2
1992-Sep-11	8877.063	Na	MJUO	KRP	5.73	–	–
1992-Sep-12	8878.004	Hα	MJUO	KRP	5.74	+0.13	23.4
1992-Sep-15	8880.914	Hα	MJUO	KRP	5.76	+0.29	24.8
1992-Sep-17	8882.902	Hα	MJUO	KRP	5.77	+0.37	26.2
1992-Sep-17	8882.922	Li	MJUO	KRP	5.77	–	–
1993-Apr-11	9089.238	Hα	MJUO	PLC	7.22	−0.41	34.1
1993-May-07	9115.168	Hα	MJUO	PLC	7.43	+0.46	51.2
1993-May-09	9117.156	Hα	MJUO	PLC	7.44	+0.53	52.6
1993-May-10	9118.188	Hα	MJUO	PLC	7.45	+0.51	52.8
1993-Aug-25	9224.938	Hα	MJUO	MDA	8.21	−0.10	56.2

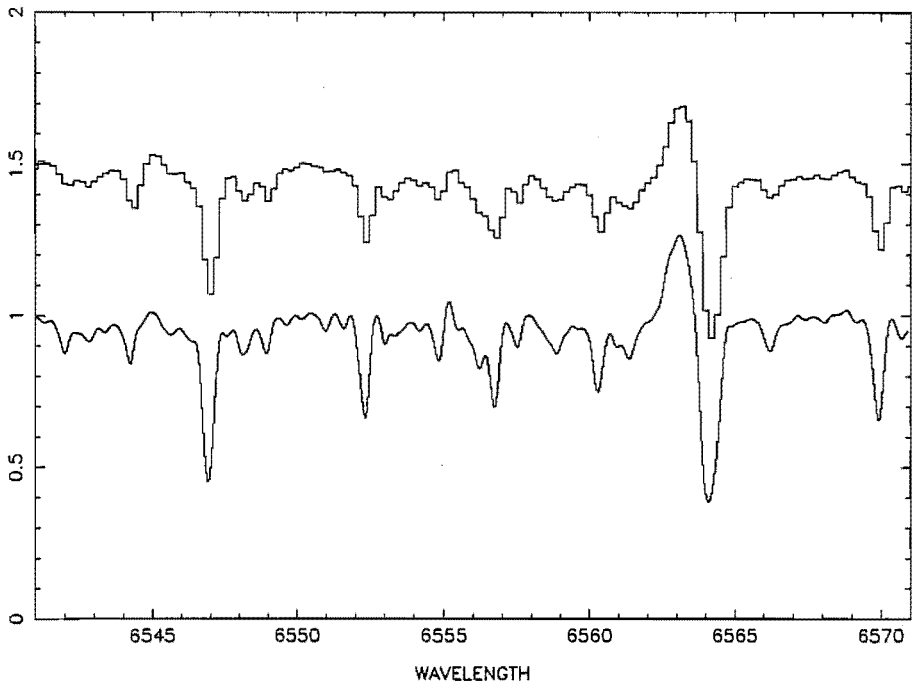

Figure 7.1: Normalized Hα-region spectra of R Sct taken at MSO (top) and MJUO (bottom) on 1991 May 24. The MSO spectrum is offset in intensity by 0.5.

These spectra were then lightly smoothed and their phases calculated according to the average period obtained from the analysis of the B, V, R and I photometric data. The ephemeris used was:

$$\text{Primary (photometric) minimum} = 2448073.05 + 140.30\,E,$$

where phase 0.0 defines the time of the primary V minimum. Due to the fact that R Sct's light variations were reasonably irregular for much of the time that it was observed from MJUO, slight shifts in phase were apparent, particularly at the start of the 'irregular' light variations (HJD $\sim$ 2448320). In instances where the phases calculated from the above ephemeris were inconsistent with the phases calculated from the contemporaneous MJUO light curve, the latter phases were adopted. This was only necessary for a few spectra. The MJUO V photometry and the dates when spectra were obtained at MJUO or MSO are shown in Fig. 7.2 (top panel). The spectral phase coverage and the phased MJUO V observations are shown in the bottom panel in this figure.

The spectra obtained at MJUO were then stacked in a phase sequence, with the earliest phases at the bottom of the figure. Stacked spectra of échelle orders 35 ($\lambda\lambda$6544–6572) and 34 ($\lambda\lambda$6736–6764) are shown in Fig. 7.3 and Fig. 7.4 respectively. The coudé spectra from MSO are shown in Fig. 7.5 where they are also arranged in a phase sequence. The cycle number and phase are indicated to the right of each spectrum. Depending on the size of the CCD that was used at MSO, between 100 and 200 Å of useful spectrum around the Hα line was obtained.

7.1.3 Shock-related spectral features

There are two distinct signatures of a shock wave in the atmosphere of a pulsating star. First, the appearance of line doubling which suggests the presence of two layers that differ in velocity by an amount that exceeds the local sound speed and, second, the appearance of emission lines from shock-heated gas. The combination of doubled absorption lines and recombination emission lines provides strong evidence for shocks in pulsating stars.

In RV Tauri stars both these shock-related features are observed. The sequence of line profiles that are observed suggest that there is a phase lag between the upper and lower atmospheric layers, so that when the lower atmosphere starts moving outwards, the higher layers are still infalling after the passage of a previous shock front. Across the shock front itself, the internal energy of the gas increases

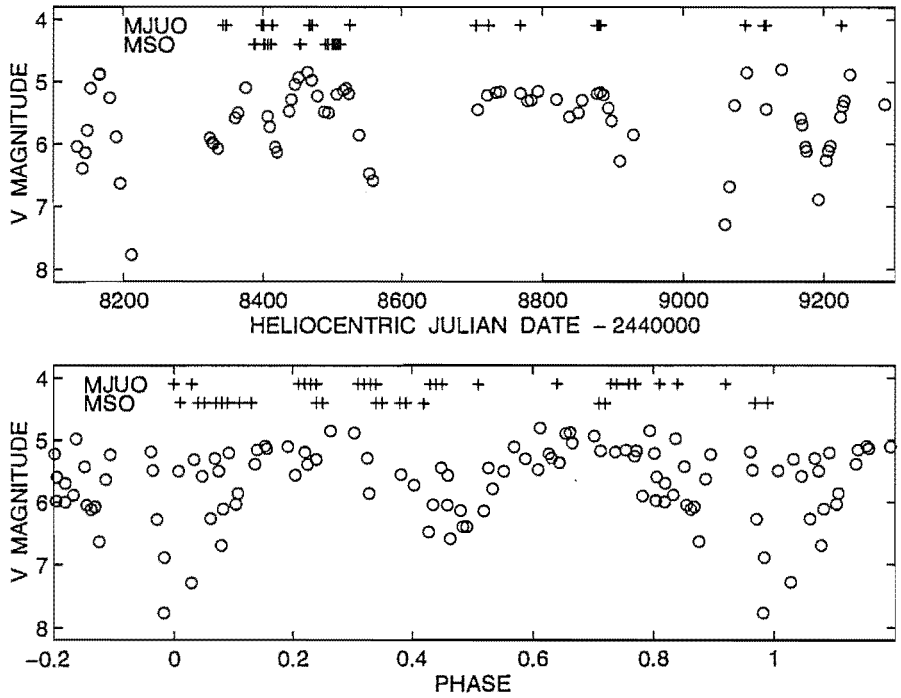

Figure 7.2: Light curves and spectral phase coverage for R Sct. The MJUO photometric observations (o) and spectroscopic observations (+) from both MJUO and MSO are shown versus heliocentric Julian Date (top panel) and versus phase (bottom panel).

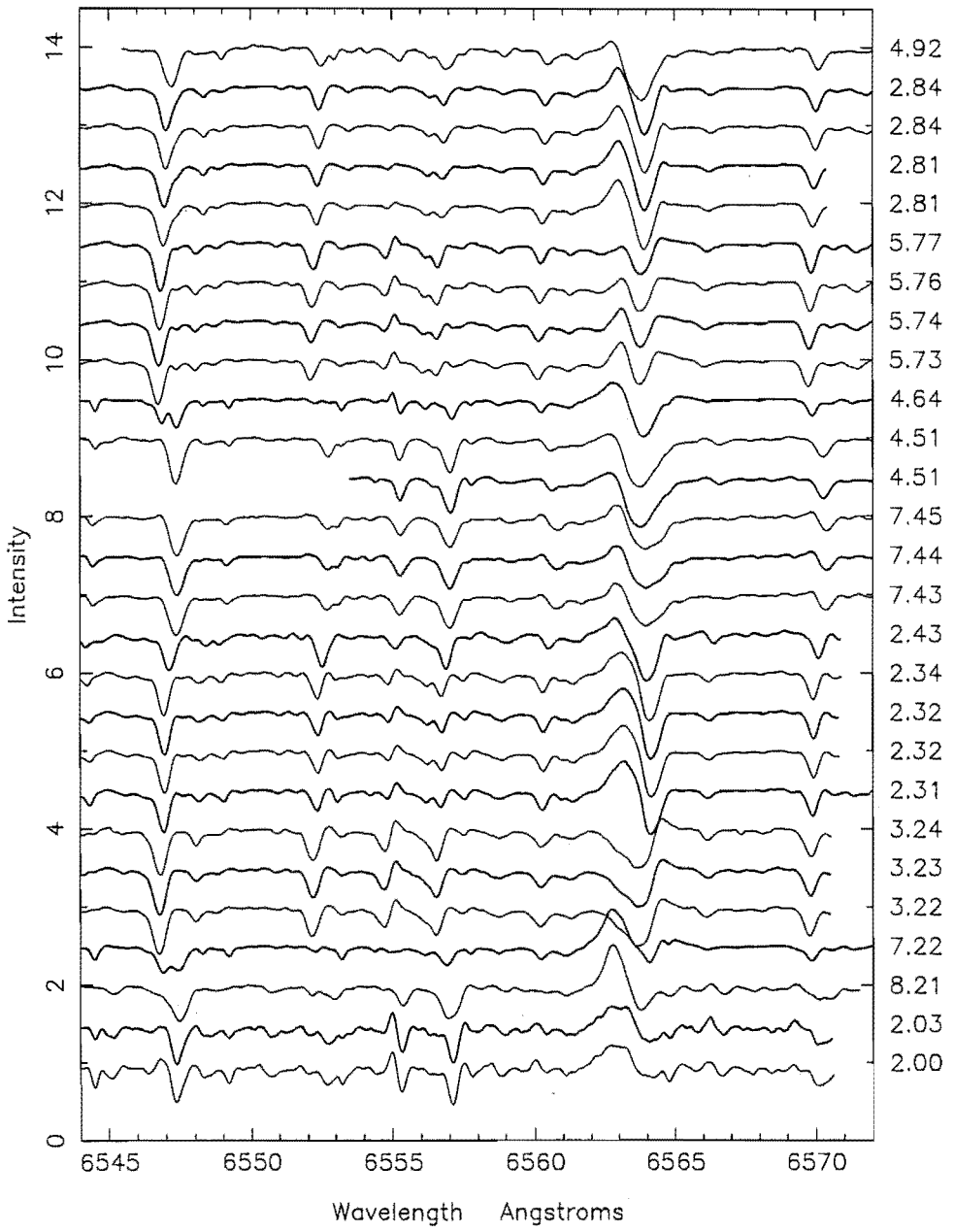

Figure 7.3: Stacked spectra of échelle order 35 for R Sct. The cycle number and phase are indicated to the right of each spectrum.

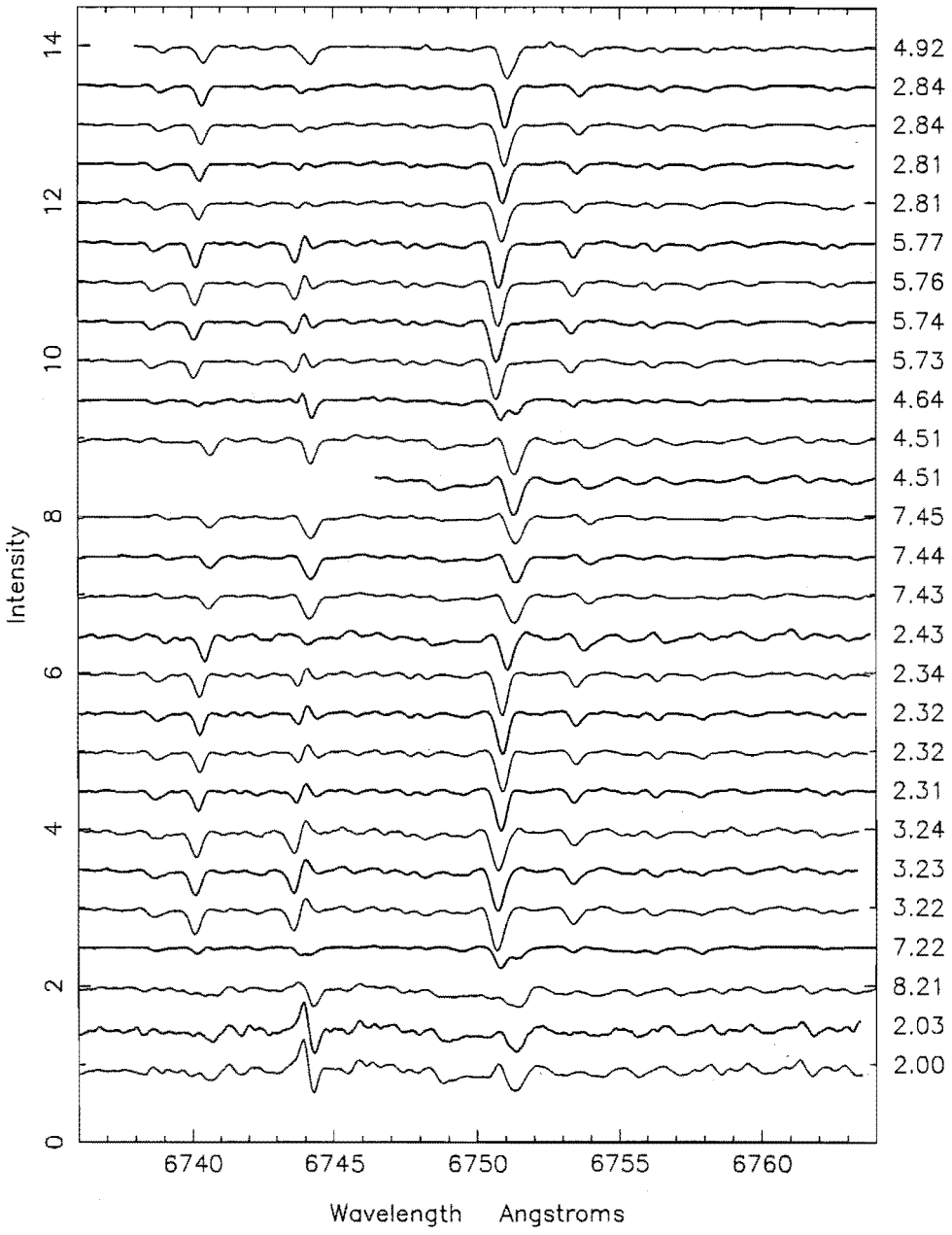

Figure 7.4: Stacked spectra of échelle order 34 for R Sct. The cycle number and phase are indicated to the right of each spectrum.

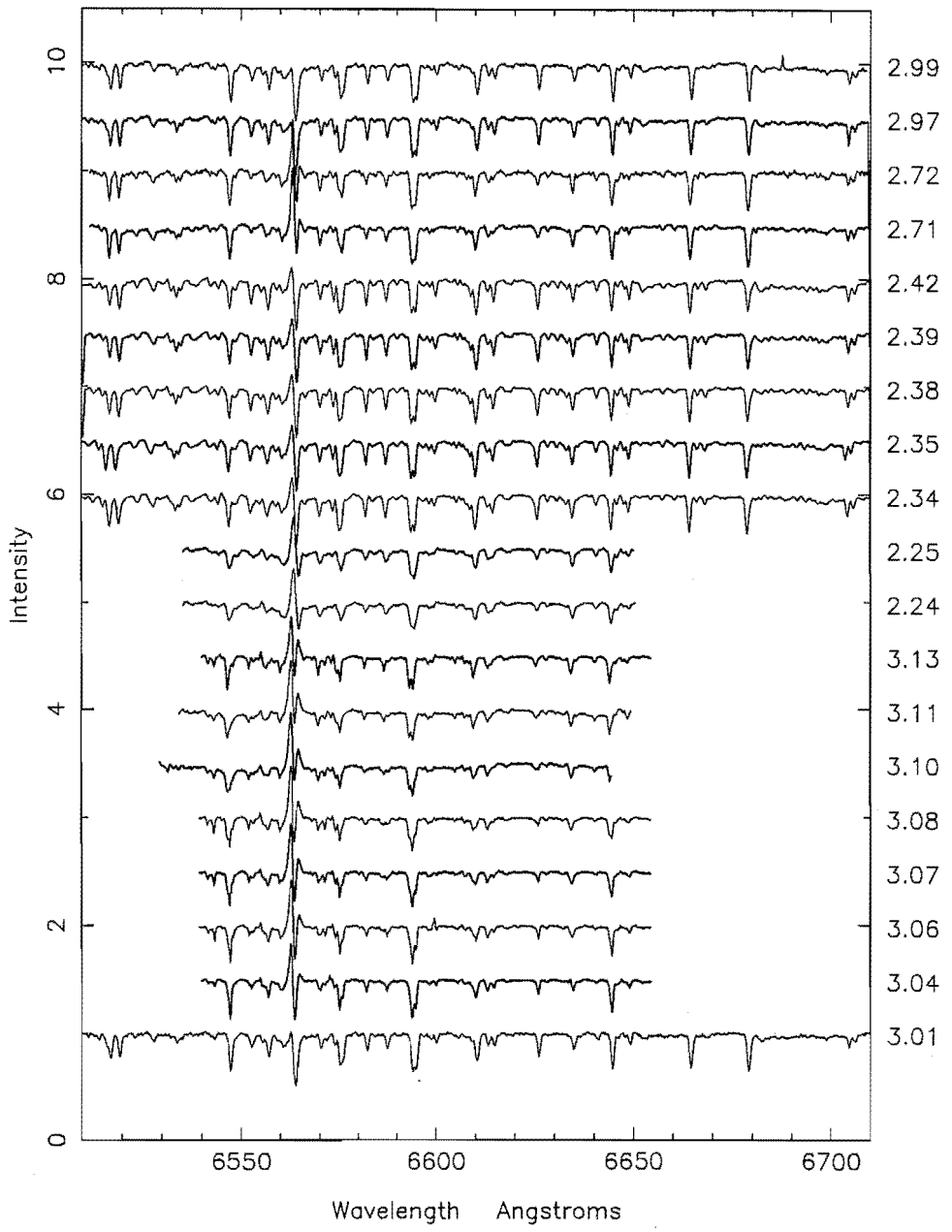

Figure 7.5: Stacked MSO spectra for R Sct. The cycle number and phase are indicated to the right of each spectrum.

dramatically. Compression and heating of the gas occurs immediately behind the shock front leading to ionization of abundant elements, most typically hydrogen. If the shock has sufficient energy, helium may be ionized to yield recombination lines of He I. Such lines are seen at certain phases in some RV Tauri stars, for example U Mon (Preston 1964) and R Sct (Gillet et al. 1989). After atoms have been ionized in the immediate post-shock gas, emission lines are formed through recombination and the subsequent cascading de-excitation. Some emission lines can be caused by collisional excitation of low-lying states as well as by resonant pumping of specific upper atomic levels followed by radiative de-excitation.

The material behind the shock front is pushed upwards, inducing a large extension of the atmospheric layers. The radiative recombination behind the shock front reduces the temperature and pressure behind the shock front and hence reduces the driving force of the shock wave. At the same time however, the density gradient in the stellar atmosphere acts to enhance the shock velocity. The very low density gradients typical of RV Tauri stars and other cool supergiant stars results in the dissipation of shock wave energy throughout the outer layers of the stellar atmosphere.

The most plausible explanation for the characteristic double peaked emission profile of the Hα line at certain phases is that it is the addition of an emission component and an absorption component that form in different layers of the atmosphere. Emission lines form within the de-excitation zone of the shock wave that propagates through the stellar atmosphere, and absorption lines are the result of either photospheric absorption or possibly Hα self-absorption above the shock front.

The Hα line certainly forms over a very extended range of atmospheric layers, much greater than any other photospheric line that we observe in the spectrum. The complex profile of the Hα line is therefore not representative of a single atmospheric layer but has contributions from many different layers. This is consistent with the fact that Hα emission is observed for much of the cycle, whereas the metallic lines display emission only at particular phases. Because the Hα line samples such a extensive range of atmospheric layers, an emission contribution to the Hα line from shock-heated gas is nearly always present. This is in contrast to the metallic lines which display emission components only when the shock wave is traversing the atmospheric layer where these lines are forming.

Large cycle-to-cycle variations in the appearance of the Hα profile have been

noted. These variations may be indicative of differences in the shock intensity and the instantaneous state of the atmosphere, so that after one cycle the star does not return to exactly the same state. If during successive cycles shock waves possessing different intensities are produced, these can subsequently affect the relative extension of the stellar atmosphere and the propagation (and therefore the apparent phase) of the following shock wave. Wallerstein & Elgar (1992) use the analogy of waves breaking on a beach to investigate whether shock waves of differing amplitudes can explain the alternating behaviour of deep and shallow light minima in RV Tauri stars.

7.1.4 The Hα line profile variations

The MJUO spectra show the Hα line from a number of different cycles. A stacked sequence of spectra from both MJUO and MSO from cycles 2 and 3 (using the 140.30 d period) are shown in Fig. 7.6 (top panel). The observatory where the spectra were taken is indicated by the MJ or the MS prefix to the phase.

Although the cycles are not sampled evenly, the spectra are consistent with two increases in the strength of the Hα emission during phases 0.0–0.3 and 0.5–0.8. The emission in cycle 2 during phases 0.0–0.45 is stronger and of longer duration than that seen in cycle 3 during similar phases. (Molecular bands are present at phase 0.00 in cycle 2, which may affect the placement of the continuum level.) This may indicate that more intense shock waves were present in cycle 2.

Fig. 7.6 (bottom panel) shows a phase sequence of selected MJUO spectra from cycles 4 to 8. The strength of the emission in cycles 7 and 8 at phase $\sim$0.2 appears to be similar to that seen in cycle 2. Little emission is present at phases 0.4–0.5 in cycles 7 and 4 but an increase in emission is seen during phases 0.5–0.65. This corresponds to the phase where the second shock would be expected. At phase 0.9 in cycle 4, the emission is quite weak initially before the appearance of the next strong shock wave.

Before cycle 2 and after cycle 6, R Sct displayed very regular deep–shallow light variations with quite deep ($V = 7.0-8.0$) primary minima, whereas between cycle 2 and 5, irregular light variations with minima no deeper than $V \sim 6.5$ were observed. It seems that stronger emission is associated with the deeper and more regular pulsations (cycles 1–2 and 7–9). However, more observations covering several cycles would be required to verify if this is indeed the case. (An indication that the radial velocity amplitude in cycle 7 may be larger than the

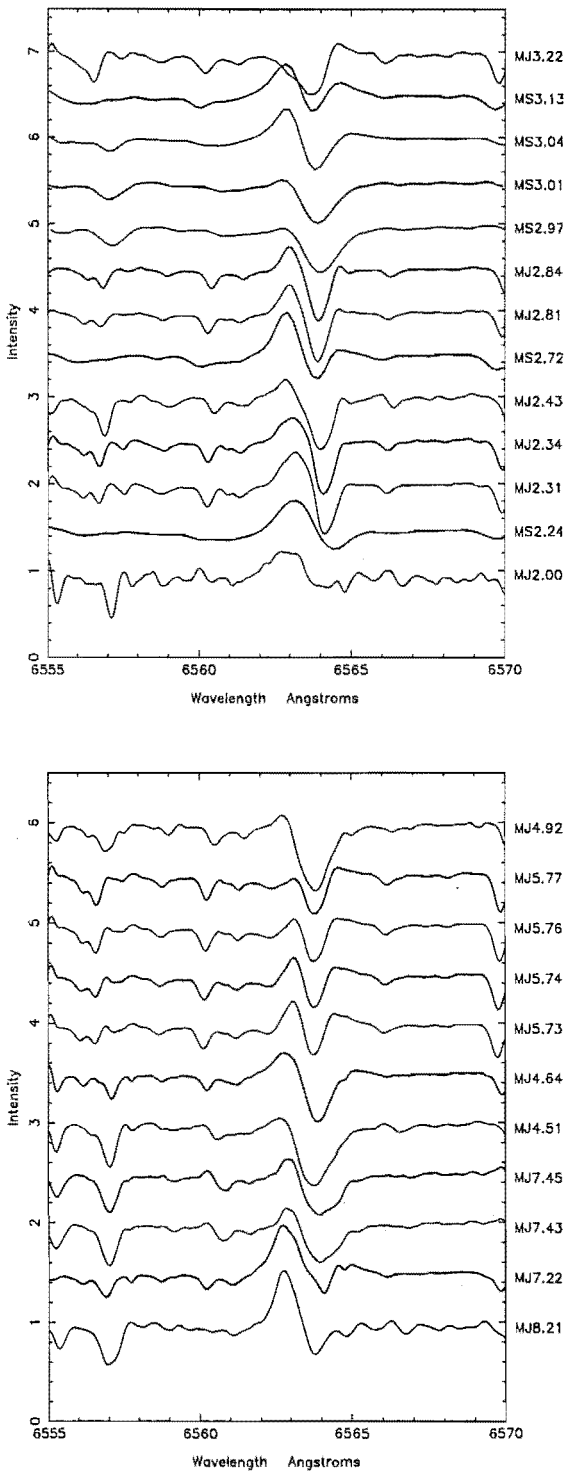

Figure 7.6: A sequence of spectra from cycles 2 and 3 (top panel) and cycles 4 to 8 (bottom panel) showing the Hα line profile variations in R Sct. A period of 140.30 d has been used to phase the spectra.

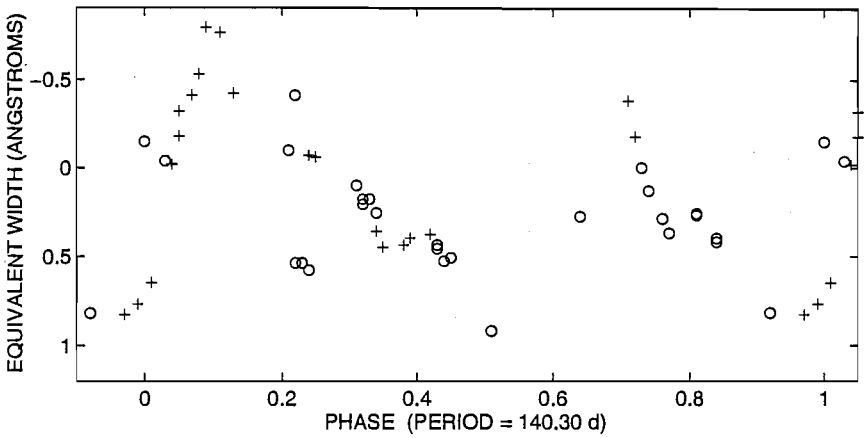

Figure 7.7: The phase dependence of the the Hα equivalent width in R Sct. Equivalent widths were measured on both the MJUO (o) and MSO (+) spectra.

previous cycles is presented in Section 7.1.6).

In order to investigate the phase dependence of the Hα emission strength, the equivalent width of the Hα line was measured for all the spectra. A convention was adopted whereby a positive equivalent width indicates an overall absorption contribution and a negative measurement indicates that there is more emission than absorption. These equivalent widths are listed in Table 7.1 and plotted versus phase in Fig. 7.7.

R Sct shows strong Hα emission (negative equivalent width) just after each light curve minimum at around phases of 0.15 and 0.70. The emission following the primary light minima is associated with the primary shock wave and is stronger than the emission that follows the secondary light minima. The Hα enhancement at phase ~ 0.70 corresponds to the secondary (weaker) shock wave. Fig. 7.7 also shows the cycle-to-cycle variability of the strength of the Hα emission. At around 0.20 in phase, the Hα emission is much less in cycle 3 (with an equivalent width of about 0.55 Å) but in cycles 2, 7 and 8 the emission at a similar phase is much greater (with equivalent widths of between –0.10 Å and –0.40 Å).

7.1.5 The metallic and molecular lines

In contrast to the highly variable strength and appearance of the Hα profile, the metallic lines behave in a much more predictable manner. Lines of a certain

Table 7.2: The phase-dependent behaviour of the metallic and molecular lines in R Sct.

λ (Å)	species	χ (eV)	multiplet	comment
6200.321	Fe I	2.61	207	strong lines, line-doubling at phases ~0.22 &
6213.437	Fe I	2.22	62	~0.64.
6546.245	Fe I	2.76	268	
6570.164	Fe I	2.42	111	
6191.571	Fe I	2.43	169	possible line-doubling at phases ~0.22 &
6739.524	Fe I	1.56	34	~0.64.
6199.186	V I	0.29	19	weak lines showing line-doubling or 'filling-in'
6216.358	V I	0.28	19	by emission at phases ~0.22 & ~0.64.
6554.238	Ti I	1.44	102	emission at phases 0.22–0.34 & 0.64–0.84,
6743.127	Ti I	0.90	48	inverse P Cygni profile at phases 0.00–0.03.
6378.256	Ni I	4.15	247	line-doubling or emission at phases 0.43–0.51.
6380.750	Fe I	4.19	1015	
6551.701	Fe I	0.99	13	
6559.576	Ti II	2.05	91	
6159.1	TiO	–	–	bandheads at primary & secondary light
6214.9	TiO	–	–	minima.
6714.4	TiO	–	–	
6383.906	CN	–	–	
6747.620	CN	–	–	

species can display different behaviour depending on their excitation potential and multiplet number.

At phases ~0.2 and ~0.6, the Fe I lines at 6546.245 Å (excitation potential $\chi = 2.76\,\mathrm{eV}$) and at 6750.164 Å ($\chi = 2.42\,\mathrm{eV}$) display two components. Two values are derived for the star's radial velocity at these phases, leading to a 'discontinuous' radial velocity curve. Such discontinuities indicate that shock waves are propagating through the regions of the stellar atmosphere where these lines are forming.

Similar line-doubling behaviour is also observed in a number of other Fe I lines that have similar excitation potentials (see Table 7.2). When line doubling occurs, the two components are each weaker than the single line would appear. It is quite possible that line-doubling may also occur in weaker lines, but these would be less obvious since the doubled components could be confused with noise near the continuum.

At the phases where the shock wave is propagating through the atmospheric layer in which the Ti I lines are forming, these lines display emission components that indicate that expanding and infalling layers are simultaneously present in the stellar atmosphere. The Ti I lines which display such strong shock-related

behaviour must form higher in the atmosphere than the Fe I lines and this is consistent with the fact that these features occur slightly later in phase than the Fe I line-doubling.

Molecular lines are very strong in the MJUO spectra taken around phases 0.0 in cycle 2, 0.2 in cycle 8 and 0.4 in cycle 2. Some molecular lines are present, but weaker, around phases 0.45 in cycle 7 and 0.5 in cycle 4. This is an indication that the very outer layers of the stellar atmosphere are cool and probably very extended around the phases of the light minima.

Molecular bandheads of the α system of TiO are seen throughout the wavelengths of 6159–6215 Å, with the bandhead at 6159.1 Å apparent on the MJUO spectra at phases of about 0.0 and 0.4 in cycle 2. Possibly associated with the α system of TiO is a bandhead at $\sim$ 6200 Å which is strongest around phases 0.0 in cycle 2 and weaker, but evident, at around phase 0.44 in cycle 2 and phase 0.5 in cycle 4. Molecular bandheads from the TiO γ system are seen at 6714.4 Å and 6719.3 Å at phases of about 0.0 and 0.45 in cycle 2.

The CN bandheads at 6383.906 Å (5,1) and 6747.620 Å (7,3) are detectable in the spectra from cycle 2 at around phases 0.0 and 0.45, and from cycle 4 at phase $\sim$0.5. This corresponds to the phases around the primary and secondary minima.

The MSO spectra at phases 0.0–0.15 from cycle 3 (Fig. 7.5) show no evidence of molecular lines, in contrast to the MJUO spectra obtained around phase 0.0 in cycle 2. Fig. 7.2 shows why this may be the case. The light variations in R Sct are quite irregular during cycles 2 to 5 and the alternation of deep and shallow minima is not strictly adhered to. Phase 0.0 in cycle 3 corresponds to a very shallow minimum ($V \sim 5.5$), whereas phase 0.0 in cycle 2 corresponds to a deeper minimum ($V \sim 6.1$). This indicates that the atmosphere of R Sct is more extended and is cooler during cycle 2 than it is during cycle 3, allowing molecular lines to form in the outer layers of the stellar atmosphere.

7.1.6 The radial velocity curve for R Sct

For the purpose of constructing a radial velocity curve for R Sct, it was decided not to attempt to use velocities derived from metallic lines that showed any emission, whether in the form of P Cygni, inverse P Cygni, pure emission or core-emission profiles, since velocities derived from shock-related emission may bear little resemblance to actual velocities present in the stellar atmosphere. By

choosing lines that do not show this shock-related emission, we are attempting to probe deeper photospheric layers that are affected to a lesser degree by the shock waves.

Radial velocities were obtained from the spectra shown in Figs 7.3 and 7.4 using the line bisector method described in Section 6.12. The Fe I line at 6750.164 Å was used to determine the radial velocities versus phase for R Sct. This line was chosen because it appeared unblended and of sufficient strength to determine the radial velocities at all the observed phases. It has an excitation potential of 2.42 eV.

In order to include the spectra from MSO in this analysis, the radial velocities were measured from the Fe I lines at 6546.245 Å (χ = 2.76 eV) and 6569.224 Å (χ = 4.73 eV, multiplet 1253) on the MJUO and MSO spectra. This latter line also appears in the analysis of R Sct by Lèbre (1991) and Lèbre & Gillet (1991a), which allows comparison of our results with previously published work. The radial velocities measured for the Fe I line at 6546.245 Å are shown in Table 7.1.

By examining the stacked spectra of R Sct, it appears that two radial velocity cycles occur during each 140.30 d luminosity cycle. A period of 70.15 d may therefore be more fundamental for the radial velocity variations and for the dynamics of the stellar envelope. The question of which period is the more intrinsic will be returned to in Chapter 9 where the photometric and spectroscopic evidence from previous studies and from the work in this thesis will be reviewed and discussed in greater detail.

Fig. 7.8 compares the R Sct radial velocity curves calculated with a period of 140.30 d (top two panels) with those calculated using the 70.15 d period (bottom two panels). The latter approach effectively 'folds' the two radial velocity cycles so that they lie on top of each other. In the subsequent discussion of the radial velocity curves all phases refer to the 70.15 d period unless explicitly stated otherwise.

The radial velocities derived from the Fe I lines at 6546.245 Å and 6750.164 Å line agree quite closely. This is to be expected from lines of the same species that have reasonably similar excitation potentials (2.76 eV and 2.42 eV respectively). Some differences in velocity occur between phases 0.20–0.45 where two components of each Fe I line are seen. The bisector method measures the velocity of the deepest component, so that although two components may be present at these phases, only one velocity is plotted. Due to the lower resolution of the

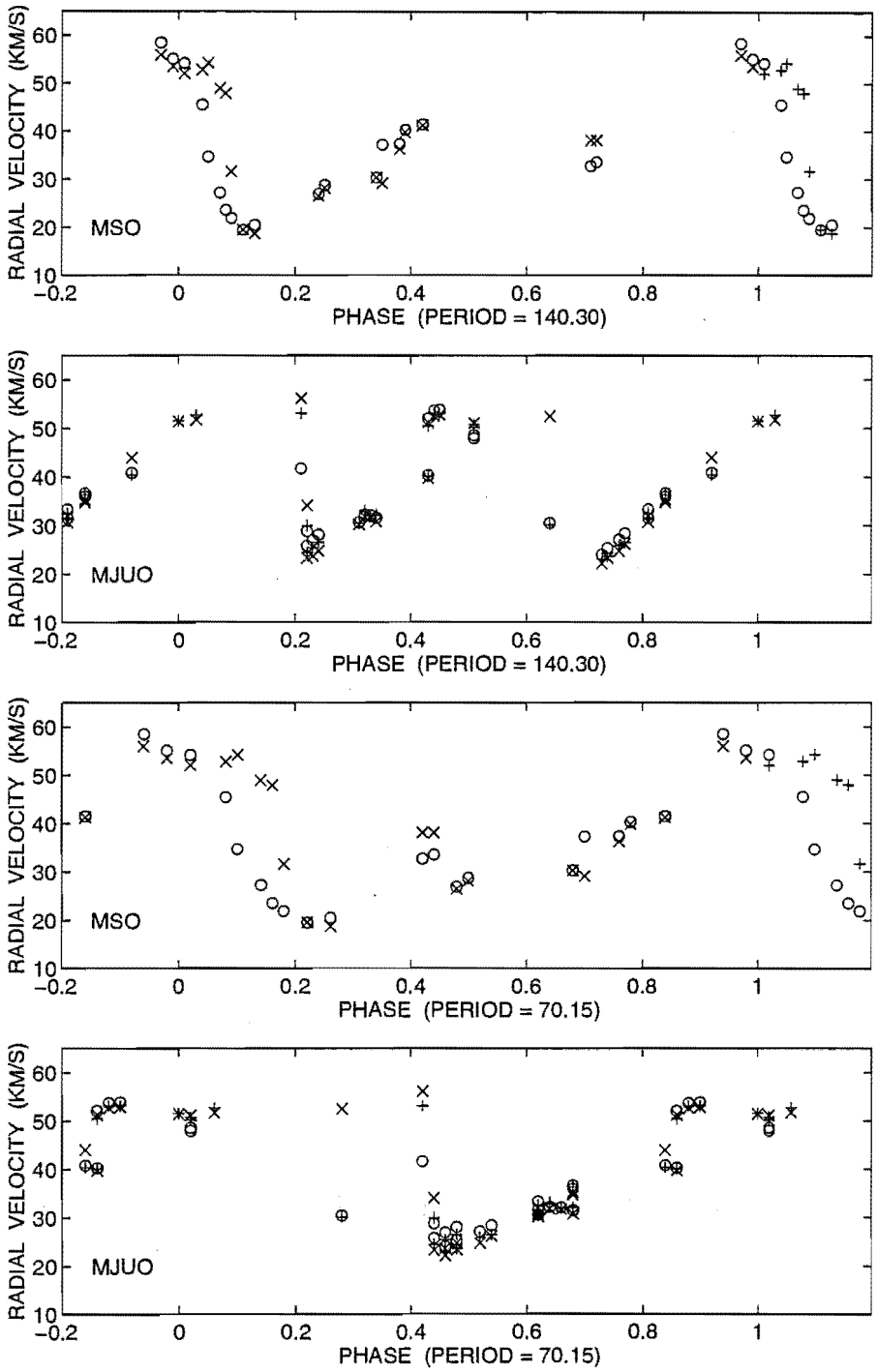

Figure 7.8: Radial velocity curves for R Sct. The radial velocities for the Fe I lines at 6546.245 Å (×), 6569.224 Å (o) and 6750.164 Å (+) are shown for the MJUO spectra, but only the first two lines were available on the MSO spectra. The top two panels are phased using a period of 140.30 d and the bottom two panels used a period of 70.15 d (see text Section 7.1.6 for more details).

MSO spectra, the two components of the Fe I lines appear as a blended line and the derived velocities will be some mean (weighted by the strength of each of the two components) of the velocities that would have been obtained if the two components had been able to be measured individually. This is apparent during phases 0.10–0.25 where a smooth but rapid velocity decrease is observed rather than a discontinuity in the radial velocity curve. Unfortunately, no spectra were obtained at MJUO during the phases 0.10–0.25 where the line doubling (with the components having velocities of $\sim$50 km s^{-1} and $\sim$20 km s^{-1}) takes place. The MSO line profiles indicate line doubling occurs at phases 0.10–0.25 and the MJUO spectra show that the line doubling continues, at least in *some* cycles, up until phases of about 0.42.

Some interesting differences are seen in the radial velocity curve derived from the Fe I line at 6569.224 Å. This line has a higher excitation potential (χ = 4.73 eV) than the other two Fe I lines and is therefore expected to form deeper in the atmosphere. The deeper-forming lines should be affected first by the outwardly moving pulsation and affected less by the related shock fronts. This is evident in the MSO radial velocity curve. The MJUO spectra obtained during phases 0.0–0.42 may also show this phase lag effect, but the small number of spectra and the fact that they are also from different pulsational cycles, make it difficult to draw any firm conclusions from the higher resolution spectra.

One final observation that can be made about the MJUO radial velocity curves is the cycle differences that are apparent in some spectra. During the phases 0.86–0.90 (using the 70.15 d period), five spectra were obtained, the first two during cycle 4 (HJD $\sim$ 2448414) and cycle 8 (HJD $\sim$ 2448768) and the next three during cycle 14 (HJD $\sim$ 2449117). This last cycle corresponds to when R Sct was pulsating in a more regular manner with much deeper primary minima. Although the spectra from cycles 4 and 8 were taken at about the same phase as those from cycle 14, a difference of about 12 km s^{-1} separates the velocities. Cycle 4 and 8 are more consistent with the subsequent spectra which were also from the more irregular part of the R Sct light curve. It appears that the deeper, more regular pulsations may be correlated with larger velocity amplitudes although further observations are required to confirm this finding. This reinforces the need for contemporaneous photometry during spectroscopic campaigns, in order to relate photometric phases to any spectral peculiarities.

7.1.7 Radial velocities for the Na I lines

Four spectra were obtained which included the D lines of Na I (Fig. 7.9). The phases and cycle numbers shown are calculated using the 70.15 d period. The Ni I line ($\lambda_0 = 5892.883$ Å, $\chi = 1.99$ eV) and the two broad, double-peaked stellar Na I lines are seen to vary in wavelength as a result of the stellar pulsation, while the narrow blue-shifted components of the Na I lines are almost stationary. The Na I line profiles are complex with obvious multiple components apparent.

High-resolution observations of Na I line profiles have been used previously to study the motion of the extended atmosphere in R Sct (Lèbre 1991, Lèbre & Gillet 1991b). The strong, narrow and very blue-shifted component that is seen in the MJUO spectra is also reported by Lèbre & Gillet (1991b). There are two possible explanations for the origin of the blue-shifted component, either interstellar or circumstellar. Interstellar sodium lines are quite likely to be seen in the stellar spectrum of R Sct given its low galactic latitude (-1°43′) and its distance (400 pc, Alcolea & Bujarrabal 1991). Making use of the analysis of Crutcher (1982), Lèbre & Gillet (1991b) state that any interstellar sodium lines should have a heliocentric radial velocity of about $-27 \pm 10\,\mathrm{km\,s^{-1}}$, whereas they measure $-13.1 \pm 1\,\mathrm{km\,s^{-1}}$. If the blue-shifted sodium component does have an interstellar origin, then only a small number of intervening interstellar clouds would be able to produce a line that is so narrow.

The case for a circumstellar origin rests on the infrared evidence for a cool circumstellar dust shell, R Sct is an IRAS source, and probable mass loss in the past as indicated by near infrared excesses (Gehrz 1972, Lloyd Evans 1985). Using radial velocity measurements from their own spectra and those presented by Luck (1981), Lèbre & Gillet (1991b) find a slow velocity decrease of about $2.6\,\mathrm{km\,s^{-1}}$ from 1977 to 1990. The scenario that these authors present is that the very blueshifted Na lines arise in a expanding shell of previously ejected matter. In the comoving frame of R Sct (with a systemic velocity of $+42.1\,\mathrm{km\,s^{-1}}$ as reported by Gillet et al. 1989), the blue-shifted component is moving outwards from R Sct (i.e. towards the observer) with a velocity of $55.1\,\mathrm{km\,s^{-1}}$.

In order to examine the profiles and investigate the possibility of a velocity decrease over time, the radial velocities for both narrow, blue-shifted Na D components were measured on the four MJUO spectra. These velocities were derived using two different methods: the line bisector method (as described in

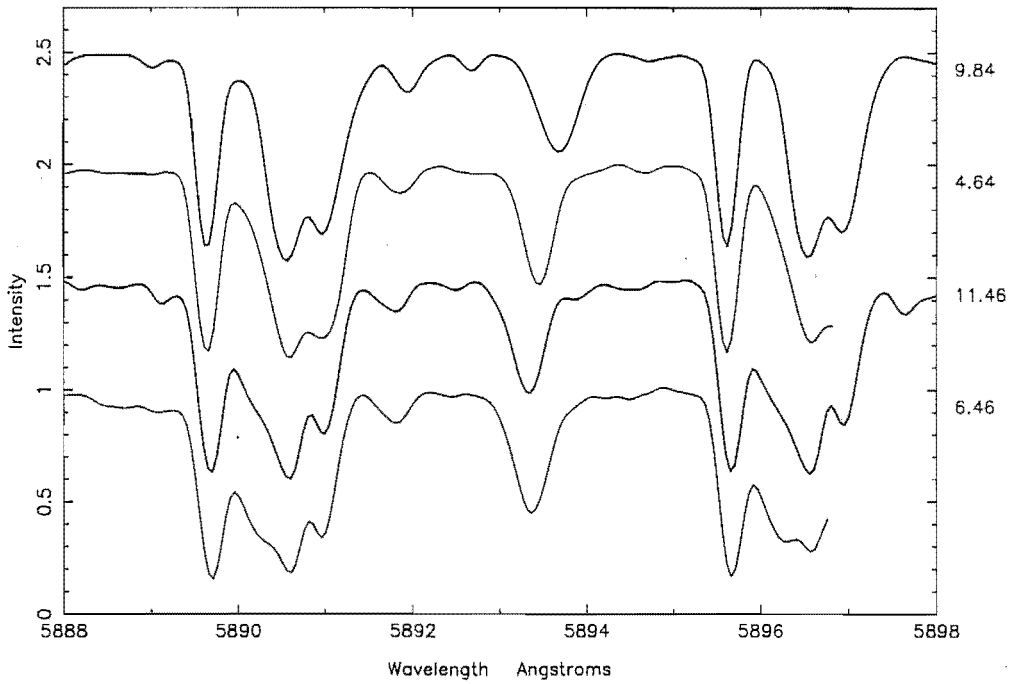

Figure 7.9: Four spectra of R Sct showing the complex profiles of the sodium D lines. Phases (to right of spectra) were calculated using a period of 70.15 d.

Table 7.3: Radial velocities for the sharp blue-shifted component of the Na D lines in R Sct.

Year	N^a	HJD^b (−2440000)	5889.95NaI ($km\,s^{-1}$)	5895.92NaI ($km\,s^{-1}$)	both Na D ($km\,s^{-1}$)	reference
1977	1	3384.5	−58.5±2.0	−56.9±2.0	−57.7±1.4	Luck (1981)
1989	18	7777.9	−55.2±1.0	−54.7±1.0	}−55.1±0.5	Lèbre (1991)
1990	1	8072.5	−55.2±1.0	−55.4±1.0		Lèbre (1991)
1991	2	8462.1	−55.9±2.0	−56.1±2.0	}−56.2±1.5	this thesis
1992	2	8822.6	−56.5±1.8	−56.4±2.0		this thesis

[a] number of spectra
[b] mean HJD given if more than one observation

Section 6.12) and by a Gaussian-fitting technique (similar to the method employed by Lèbre & Gillet 1991b). Both techniques gave very similar velocities. Table 7.3 presents a summary of the radial velocities of the components from the analysis of Lèbre & Gillet (1991b) and from this thesis.

The velocity decrease of about $2.6\,km\,s^{-1}$ over 13 years (from 1977 to 1990) would appear as a $\sim 0.4\,km\,s^{-1}$ decrease from Lèbre & Gillet's observations to the MJUO observations. Although a velocity decrease is not seen between the MJUO observations and the observations of Lèbre & Gillet, our results do not rule out this possibility within the uncertainties given.

A systematic variation in the velocities derived from the MJUO spectra was seen. The velocities for the NaI line at 5889.95 Å were −54.4, −55.1, −57.3 and $-57.7\,km\,s^{-1}$ for phases (including cycle number) of 6.46, 11.46, 4.64 and 9.84 respectively. These velocities are with respect to the rest frame of R Sct. The stacked spectra in Fig. 7.9 show that the stellar sodium lines are closer to the narrow, blue-shifted component in the spectrum taken at phase 0.46 in cycle 6 than they are in the spectrum taken at phase 0.84 in cycle 9. If there is some slight blending with the stellar sodium lines this would shift the sharp, blue-shifted components to longer wavelengths giving smaller velocity shifts, which is exactly the systematic variation that we measure.

The spectra where less blending is apparent (at phase 0.64 in cycle 4 and phase 0.84 in cycle 9) give larger and more consistent velocities for the two sharp, blue-shifted components. The mean velocity is $-57.6\pm0.5\,km\,s^{-1}$.

Luck (1981) stated that the one spectrum of the Na D-region that he obtained (on HJD 244 3385) was taken when the star was near secondary minimum. This is consistent with the phase of 0.415 calculated using the MJUO ephemeris (and

the 140.30 d period) quoted earlier in this section. Using the 70.15 d period, this corresponds to a phase of 0.83. At this phase, the stellar Na I lines and the sharp, blue-shifted components should be well separated, as is apparent from the MJUO spectra obtained at a phase of 0.84 in cycle 9 (Fig. 7.9). The average velocity derived from the two blue-shifted sodium components on the Luck spectrum is $-57.7\pm0.7\,\mathrm{km\,s^{-1}}$ (Lèbre & Gillet 1991b). This agrees well with the mean velocity of $-57.6\pm0.5\,\mathrm{km\,s^{-1}}$ derived from the two MJUO spectra at phases 0.64 (cycle 4) and 0.84 (cycle 9). Lèbre & Gillet do not state whether they fit the narrow, blue-shifted component *simultaneously* with the broad, double-peaked stellar sodium line or not, but their velocities for the blue-shifted component are averages over the entire pulsational cycle. The apparent velocity decrease could be accounted for if the small velocity shift were due to slight blending with the stellar sodium D lines.

If the blue-shifted component does arise from absorption in matter that has been previously ejected from R Sct (as proposed by Lèbre & Gillet 1991b) then the expansion rate of this material appears relatively constant. Finally, the earlier proposal of an interstellar origin for the blue-shifted sodium component cannot be ruled out and this suggestion is strengthened if the velocity of the component is proved to be non-variable.

7.2 RU Cen

7.2.1 Previous spectroscopy of RU Cen

RU Cen is a member of the Preston 'B' subclass of RV Tauri stars that possess unusual spectra of the Fp(R) type. These stars are generally characterized by weak metal line absorption. The members of this group show enhanced carbon.

The spectrum of RU Cen was found to vary from G2 to K2 on six Harvard plates examined by Cannon (Shapley & Walton 1927). Bidelman (1954) obtained a spectrum with a much earlier spectral type of Fpe and found emission in Hβ, Hγ and Hδ, very strong Sr II absorption lines, and an otherwise 'greatly veiled' appearance. With reference to other variable stars, Bidelman further described features in the spectrum: "The feature near 4070 [Å]...is actually a definite characteristic (among others) of a star of the R CrB [RCB] type – that is, a hydrogen-deficient carbon star." This feature was attributed to neutral carbon. Bidelman

concluded that the spectrum of RU Cen was most similar to that of the carbon-rich RV Tauri star, AC Herculis. Houk (1978) gave a classification of G2wF6, indicating a weak-lined object, but no emission was noted.

Using four-colour, Hβ and (RI) photometry, Eggen (1986) found that the Hβ emission is more intense on the rising branch of the light curve near the maximum u magnitude. An estimate of the metallicity for RU Cen from a calibration of the m_1 and $(R-I)$ photometry is estimated to be [Fe/H] = −1.75.

Using high-resolution échelle spectrograms, Luck & Bond (1989) derived a halo or thick-disk metallicity for RU Cen of [Fe/H] = −1.4 and an apparently large overabundance of oxygen, with [O/Fe] = +1.4. They found strong CH and CN bands in RU Cen and nearly solar s-process abundances were determined ([s/Fe] = +0.2). Relative to other low mass supergiants, RU Cen therefore has enhancements of the s-process elements and the authors suggested that this star was possibly related to the Ba II and CH stars.

7.2.2 Spectroscopic observations of RU Cen

Between 1991 January and 1992 September, 17 high-resolution spectra were obtained of RU Cen using the the 1.0-m telescope, échelle spectrograph and CCD detector at MJUO. Exposure times were typically 60 minutes. Using the 1.9-m telescope at MSO, 15 high-resolution coudé spectra were obtained between 1991 May and 1991 September. Exposure times were typically 5 to 10 minutes. A log of the spectroscopic observations for RU Cen is presented in Table 7.4.

The spectra were phased to the mean photometric period of 64.60 d (the 'formal' period) using the ephemeris:

$$\text{Primary (photometric) minimum} = 2448124.570 + 64.60E.$$

Many RV Tauri stars display small deviations in the light and radial velocity variations which can make the calculated phases slightly uncertain. However, photometrically, RU Cen is known to be one of the most regular of the RV Tauri stars (O'Connell 1961). Spectra at phases that have similar cycle numbers are more likely to be consistent than spectra from very different cycles. The spectral phase coverage that was obtained for RU Cen is displayed in Fig. 7.10. This figure shows the MJUO V photometry for RU Cen plotted versus heliocentric Julian Date (top panel) and versus photometric phase (bottom panel). The dates and phases when spectra were obtained are indicated.

Table 7.4: Spectroscopic observations of RU Cen.

UT date	HJD [a] 2440000+	region	site	observer	phase (ϕ)	W_λ(Hα) (Å)	rv(C)[b] (km s^{-1})
1991-Jan-30	8287.125	Hα	MJUO	KRP	2.52	−2.62	–
1991-Mar-29	8345.125	Hα	MJUO	KRP	3.42	−1.05	–
1991-Mar-31	8346.984	Hα	MJUO	KRP	3.44	−1.15	–
1991-May-10	8386.910	Hα	MSO	WAL	4.06	−7.91	–
1991-May-12	8388.930	Hα	MSO	WAL	4.09	−10.49	–
1991-May-20	8396.906	Hα	MJUO	KRP	4.22	−3.29	–
1991-May-21	8398.031	Li	MJUO	KRP	4.23	–	–
1991-May-22	8399.016	Hα	MJUO	KRP	4.25	−2.32	–
1991-May-23	8399.961	Hα	MJUO	KRP	4.26	−1.98	–
1991-May-24	8401.004	Li	MJUO	KRP	4.28	–	–
1991-May-24	8400.957	Hα	MSO	WAL	4.28	−1.78	−55.0
1991-May-25	8401.902	Hα	MSO	WAL	4.29	−1.63	−53.8
1991-May-26	8402.879	Hα	MSO	WAL	4.31	−1.64	−57.9
1991-May-27	8403.965	Hα	MSO	WAL	4.33	−1.52	−51.8
1991-May-28	8404.902	Hα	MSO	WAL	4.34	−1.56	−46.5
1991-May-30	8406.945	Hα	MSO	WAL	4.37	−1.55	−48.1
1991-Jun-05	8412.914	Hα	MJUO	KRP	4.46	−1.70	–
1991-Jul-16	8453.859	Hα	MSO	WAL	5.10	−11.04	−56.4
1991-Jul-18	8455.883	Hα	MSO	WAL	5.13	−8.81	−57.4
1991-Aug-02	8470.816	Hα	MJUO	KRP	5.36	−1.62	–
1991-Aug-03	8471.848	Li	MJUO	KRP	5.38	–	–
1991-Aug-24	8492.922	Hα	MSO	KRP	5.70	−1.50	–
1991-Aug-25	8493.887	Hα	MSO	KRP	5.72	−1.59	−63.5
1991-Sep-01	8500.875	Hα	MSO	KRP	5.83	−1.49	−57.9
1991-Sep-04	8503.879	Hα	MSO	KRP	5.87	−1.44	−58.4
1991-Sep-05	8504.883	Hα	MSO	KRP	5.89	−1.68	−54.1
1992-Mar-23	8705.027	Hα	MJUO	KRP	8.99	−2.36	–
1992-Apr-13	8725.906	Hα	MJUO	MDA	9.31	−1.73	–
1992-May-26	8768.984	Hα	MJUO	KRP	9.98	−1.44	–
1992-Aug-23	8857.809	Hα	MJUO	PLC	11.35	−1.14	–
1992-Sep-12	8877.828	Hα	MJUO	KRP	11.66	−4.20	–
1992-Sep-17	8882.836	Hα	MJUO	KRP	11.74	−2.31	–

[a] for mid time of observation

[b] radial velocity for the C I line at 6587.622Å.

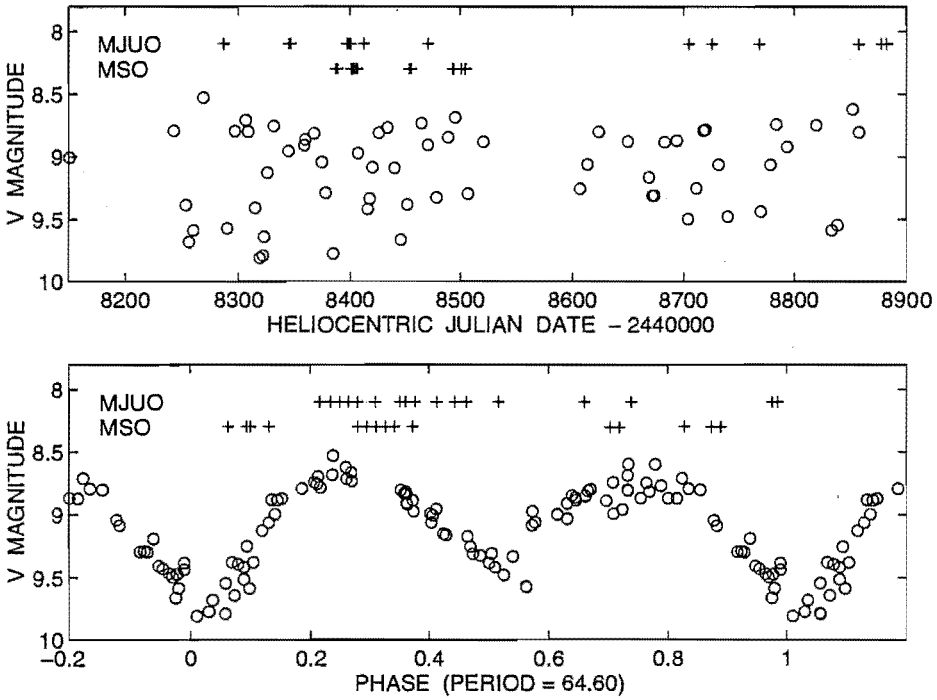

Figure 7.10: Light curves and spectral phase coverage for RU Cen. The MJUO photometric observations (o) and spectroscopic observations (+) from both MJUO and MSO are shown versus heliocentric Julian Date (top panel) and versus phase (bottom panel).

The RU Cen spectra were then stacked in phase order with the cycle number and phase of observation indicated to the right of each plotted spectrum. The region around the Hα line is shown in Figs 7.11 and 7.12 for the MJUO and MSO spectra respectively. These stacked spectra confirm that the metallic lines are weak at all phases in RU Cen. The MSO spectra show a number of telluric H_2O lines around the Hα line. A rather weak line of C I is seen on the MSO spectra at a wavelength of 6587.622 Å. This line is further confirmation of the carbon-enhanced nature of this star. A slight continuum depression is seen at phase 0.52 in cycle 2 at a wavelength of about 6556 Å which resembles the appearance of a molecular bandhead. However, this feature is not seen around the primary minimum when molecular bandheads should be most visible.

7.2.3 The Hα line profiles and radial velocities

A range of Hα profiles are seen in Figs 7.11 and 7.12. The most striking features of the changing profile are the relative strengths of the emission peaks on either side of the absorption core and the overall strength of the emission.

During phases 0.0 to 0.2 the strength of the Hα emission is at its greatest. The heights of the strongest emission peaks are $\sim$3.7 times the continuum level. The emission is very broad with extensive emission wings. Double emission peaks of lesser strength are seen throughout phases 0.20 to 0.50, with a general evolution of the line from more blueward emission to relatively more emission on the red wavelength side of the absorption component. The behaviour in the second half of the cycle is similar to that seen in the first half, with increased Hα emission during phases 0.45 to 0.75 and a trend of first more blueward then more redward emission on either side of the absorption core.

The phase dependence of the Hα emission strength was investigated by measuring the equivalent width on all the MJUO and MSO spectra (as in Section 7.1.4). For every measurement of the Hα line in RU Cen, the equivalent width was found to be negative. The Hα equivalent width measurements are included in Table 7.4. The variation of the Hα equivalent width with phase is displayed in Fig. 7.13.

RU Cen shows enhanced Hα emission just after each light curve minimum around phases of 0.1 and 0.6. The emission at phase 0.1 is extremely strong. Equivalent widths of about -11 Å are obtained for the Hα line. This emission is associated with the strong primary shock wave which is propagating through

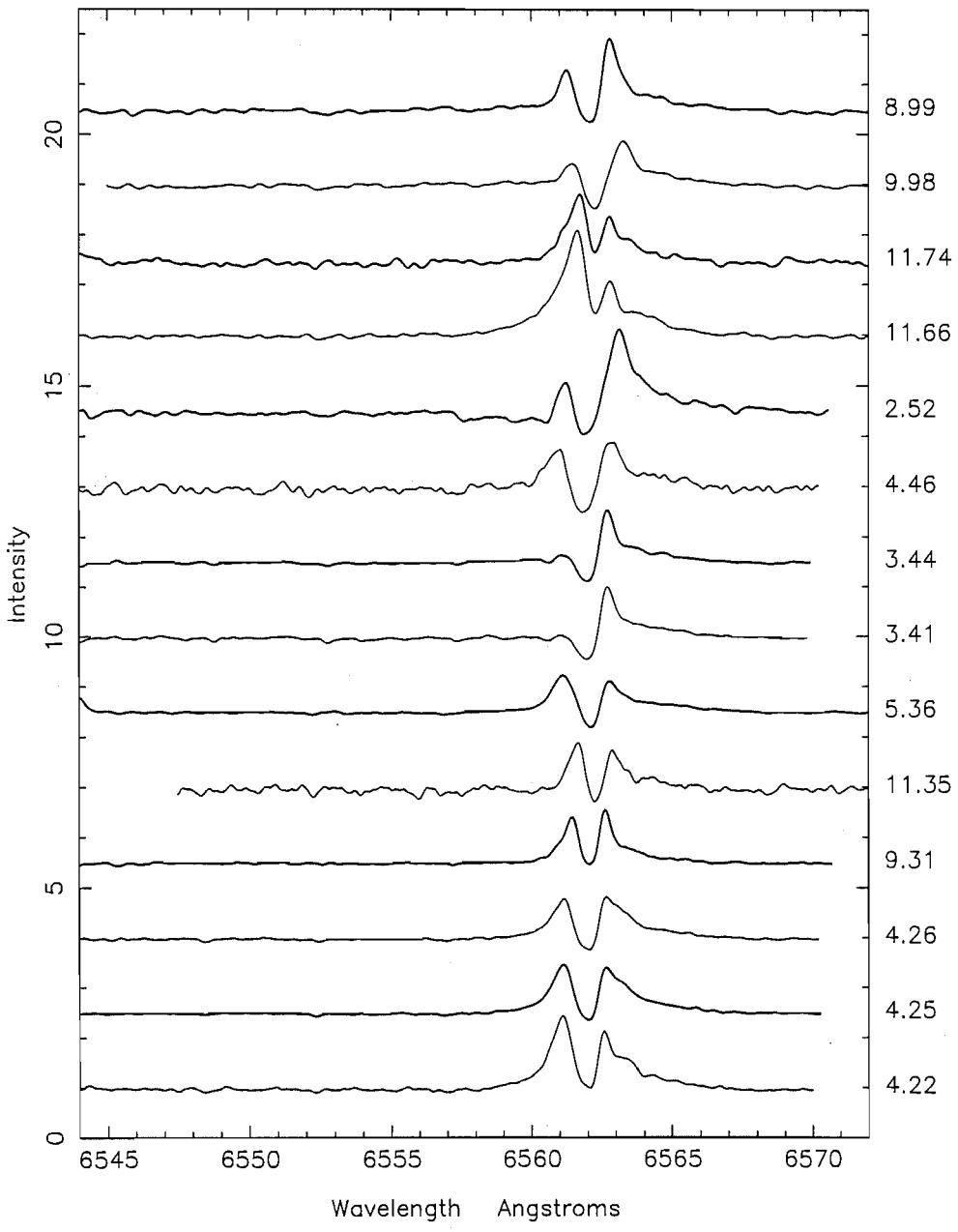

Figure 7.11: Stacked MJUO spectra of échelle order 35 for RU Cen. The cycle number and phase are indicated to the right of each spectrum.

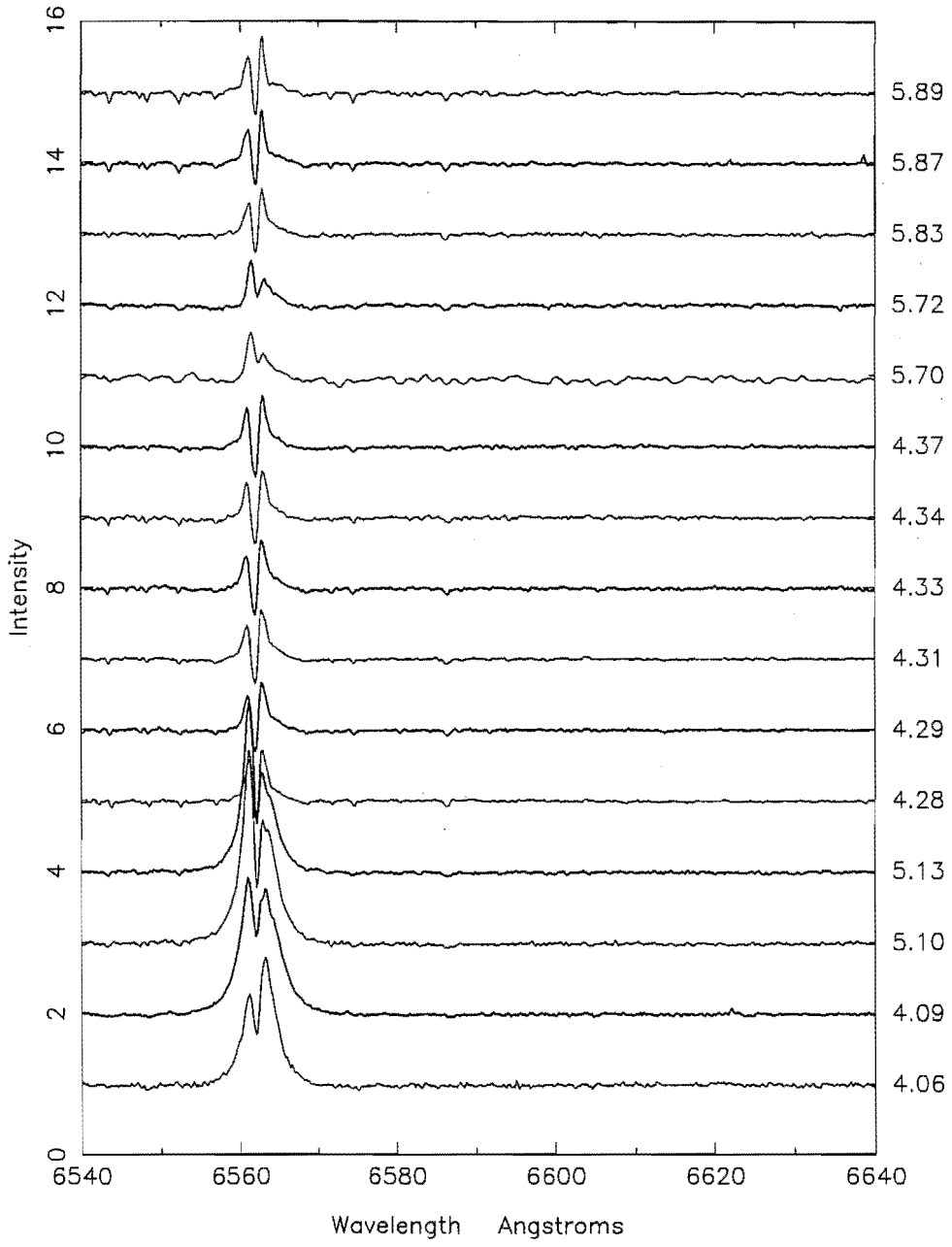

Figure 7.12: Stacked MSO spectra of the region around the Hα line in RU Cen. The cycle number and phase are indicated to the right of each spectrum.

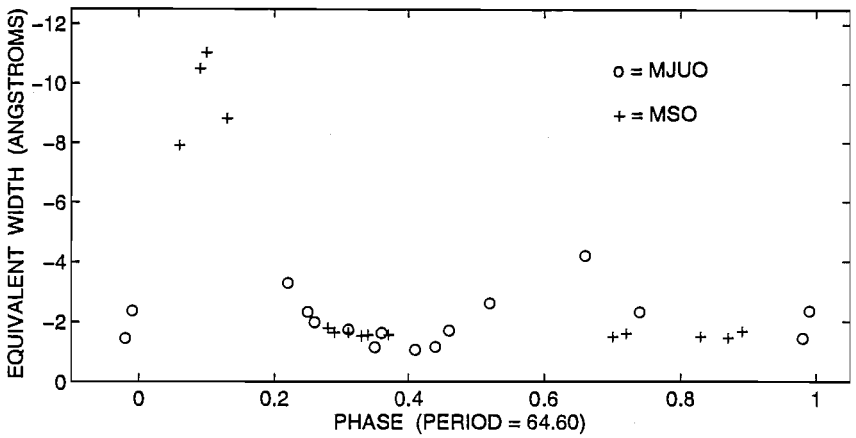

Figure 7.13: The phase dependence of the the Hα equivalent width in RU Cen. Equivalent widths were measured on both the MJUO (o) and MSO (+) spectra.

the lower photosphere at this phase. A further Hα enhancement at a phase of about 0.6 corresponds to the secondary shock wave. Unfortunately, this phase of secondary Hα emission is not sampled well enough to compare the relative strengths of the two Hα enhancements.

The relation between the phase and Hα line velocities was investigated by fitting a series of up to three Gaussians to reproduce the profile at each phase. A strong emission component that varied in both height and width was introduced first. The second Gaussian was a strong absorption component which creates the central absorption core of the Hα profile. If required, a further absorption component which appears to the red of the previous absorption was introduced to the fit. The radial velocities for the strongest emission and absorption components that make up the Hα profile were then plotted versus phase in Fig. 7.14. Although the velocities measured from the Hα profile are quite uncertain, some phase dependent behaviour is apparent.

In addition the radial velocities for the very weak C I line at 6587.622 Å (χ = 8.53 eV, multiplet 22) was measured on twelve MSO spectra for which a line could be detected. The radial velocities, calculated using the line bisector method described in Section 6.12, are plotted in Fig. 7.14 and are also listed in Table 7.4. Despite the small number of spectra obtained and the relatively poor phase coverage, the radial velocity curve for the metallic lines is quite consistent with there being two velocity cycles during each 64.60 d luminosity cycle.

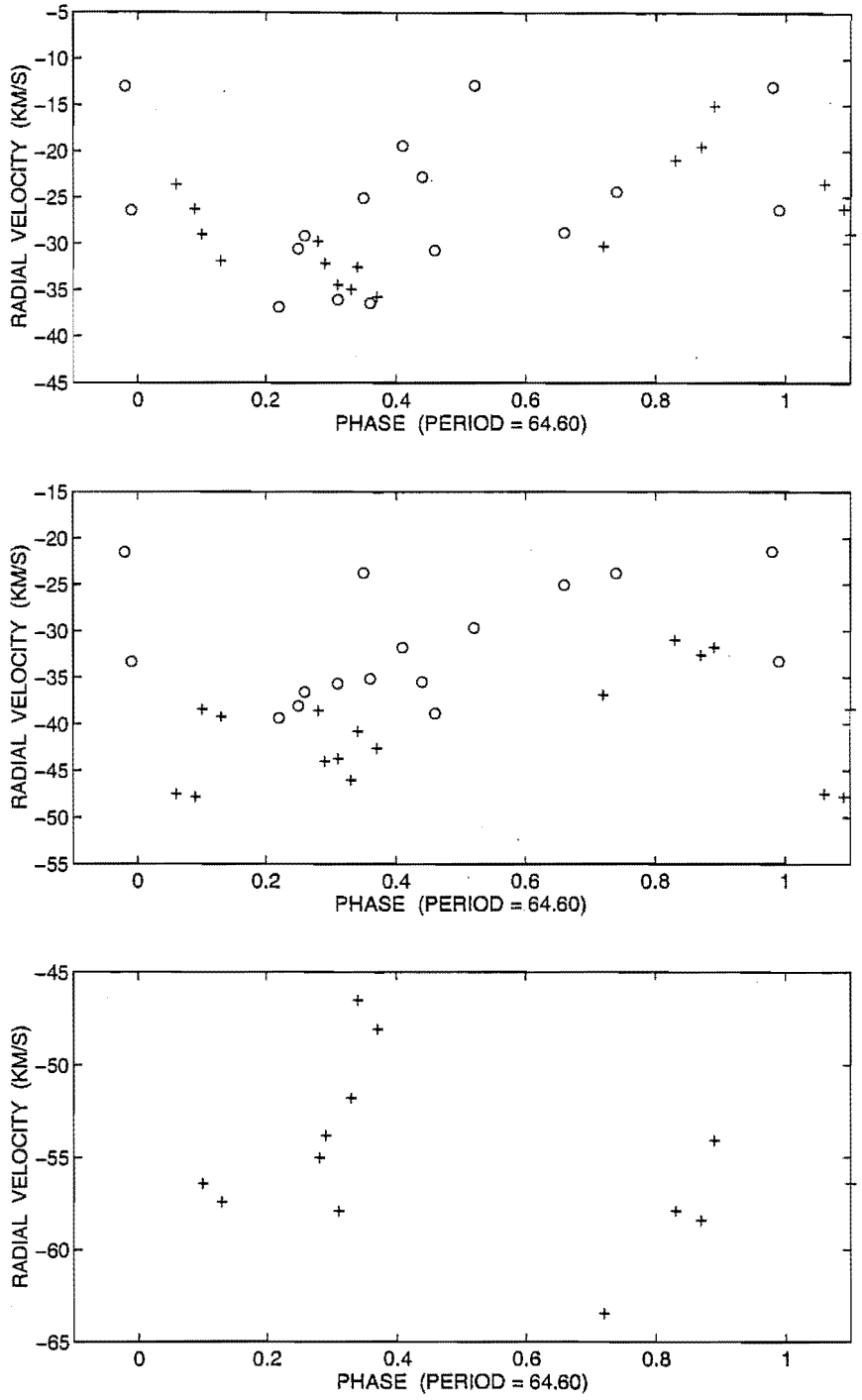

Figure 7.14: Radial velocity curves for the emission (top) and absorption (centre) components of the Hα line in RU Cen. The radial velocities for the C I line at 6587.622 Å are shown in the bottom panel. Velocities are measured from MJUO (o) and MSO (+) spectra.

7.3 AR Sgr

7.3.1 Previous spectroscopy of AR Sgr

From early Harvard observations, Gerasimovič (1929) assigned AR Sgr a spectroscopic class of G. In Joy's (1952) spectroscopic survey of RV Tauri and related stars, eight spectra of AR Sgr showed a spectroscopic range of F5e–G6. No TiO bands were observed, even though one spectrum was obtained at minimum light. The radial velocity was found to have a range of $-88\,\mathrm{km\,s^{-1}}$to $-108\,\mathrm{km\,s^{-1}}$, with a mean of $-100\,\mathrm{km\,s^{-1}}$. The two earliest-type spectral classifications by Joy (1952), F5 and F8, correspond to the smallest values of the radial velocity, –88 and $-90\,\mathrm{km\,s^{-1}}$ respectively, whereas the later spectral types of G0–G6 occur for the larger velocities of –100 to $-106\,\mathrm{km\,s^{-1}}$. Eggen (1986) notes that the small range in radial velocity displayed by AR Sgr is surprising considering the large visual magnitude variations. Preston et al. (1963) included AR Sgr in their list of RV Tauri stars, giving a tentative classification as a Preston type 'A' star.

7.3.2 Spectroscopic observations of AR Sgr

Five Hα-region échelle spectra of AR Sgr were obtained at MJUO between 1991 June and 1992 September. Ten coudé spectra from MSO were obtained between 1991 May and 1991 September. A log of the spectroscopic observations for AR Sgr is given in Table 7.5. The phases at which the spectra were obtained was calculated using the period obtained from the photometric analysis. The ephemeris used was:

$$\text{Primary (photometric) minimum} = 2448362.57 + 88.86\,E.$$

Fig. 7.15 shows the MJUO V photometry plotted versus heliocentric Julian Date and versus phase. This figure shows the dates when spectra were obtained (top panel) and the corresponding spectral phase coverage obtained (bottom panel). The phase coverage is not particularly good around the primary minimum, with only one spectrum obtained between phases 0.90 and 0.20.

The spectra obtained at both MJUO and MSO were then stacked in a phase sequence. The phases and cycle number of the observations are indicated to the right of each plotted spectrum. Stacked MJUO spectra of échelle order 37 ($\lambda\lambda$6192–6220) and 35 ($\lambda\lambda$6546–6574) in the Hα region are shown in Fig. 7.16. It

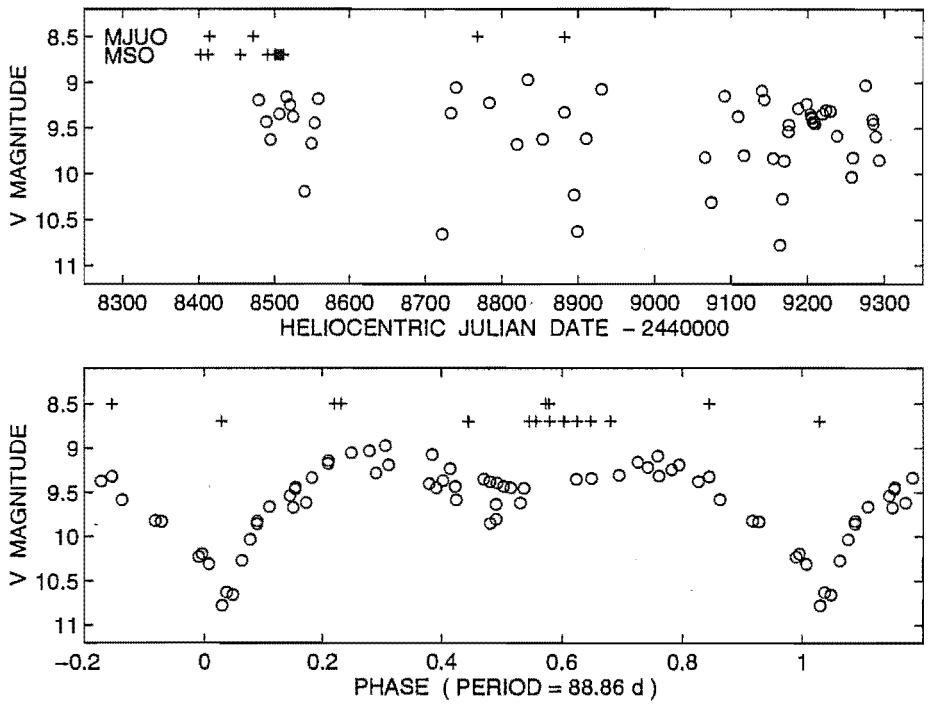

Figure 7.15: Light curves and spectral phase coverage for AR Sgr. The MJUO photometric observations (o) and dates of spectroscopic observations (+) from both MJUO and MSO are shown in the top panel. The bottom panel shows the MJUO photometric V observations (o) and the spectral phase coverage, where a period of 88.86 d has been used to calculate the phases.

Table 7.5: Spectroscopic observations of AR Sgr.

UT date	HJD [a] 2440000+	site	observer	phase ϕ	W_λ(Hα) Å	rv(Hαa) (km s^{-1})	rv(Hαe) (km s^{-1})
1991-May-25	8402.082	MSO	WAL	0.45	−1.39	−99.1	−103.9
1991-Jun-04	8412.121	MSO	WAL	0.56	−1.96	−95.6	−98.8
1991-Jun-06	8414.188	MJUO	KRP	0.58	−2.96	−102.6	−104.9
1991-Jul-16	8454.086	MSO	WAL	1.03	−2.77	−87.9	−89.5
1991-Aug-02	8471.137	MJUO	KRP	1.22	−2.00	−91.0	−90.7
1991-Aug-03	8472.047	MJUO	KRP	1.23	−1.97	−100.0	−100.6
1991-Aug-22	8490.965	MSO	KRP	1.45	−0.16	−97.9	−100.2
1991-Aug-31	8500.094	MSO	KRP	1.55	−0.79	−97.8	−100.0
1991-Sep-03	8503.086	MSO	KRP	1.58	−1.62	−98.0	−100.4
1991-Sep-05	8505.137	MSO	KRP	1.60	−1.46	−96.4	−105.0
1991-Sep-07	8507.117	MSO	KRP	1.63	−1.53	−98.2	−102.4
1991-Sep-09	8509.129	MSO	WAL	1.65	−1.60	−99.7	−104.4
1991-Sep-12	8512.082	MSO	WAL	1.68	−0.88	−100.1	−99.8
1992-May-26	8769.246	MJUO	KRP	4.58	−1.74	−103.1	−106.9
1992-Sep-16	8881.938	MJUO	KRP	5.85	−1.59	−100.7	−100.0

[a]for mid time of observation

can be seen that the relative strength of the metallic lines changes dramatically with phase.

The photospheric absorption lines are all quite deep at phase 0.85 in cycle 5, but are barely detectable at the other phases. P Cygni type profiles are seen for a number of lines at phase 0.85 in cycle 5. Emission is seen in Ti I lines at phase 0.58 in cycles 0 and 4. A summary of the appearance and phase-dependent behaviour of the metallic and molecular lines in AR Sgr is presented in Table 7.6.

The stacked MSO spectra are shown in Fig. 7.17. Metallic absorption lines are strongest at phase 0.03 in cycle 1 and molecular bands are also apparent at this phase. Most obvious are the γ system bandheads of TiO at 6651.5 Å and 6681.1 Å. The CN bandhead at 6631.3 Å may also be present. P Cygni and inverse P Cygni type profiles of the Ti I line at 6554.238 Å are seen during phases 0.45–0.58 in cycles 0, 1 and 4.

7.3.3 The Hα line profiles and radial velocities

Due to the fact that no metallic lines of sufficient strength could be found throughout a complete pulsation cycle, the radial velocities of the metallic lines were not measured. However, the Hα line is very strong in all the spectra. The phase dependence of the strength of this line was investigated by measuring the equivalent

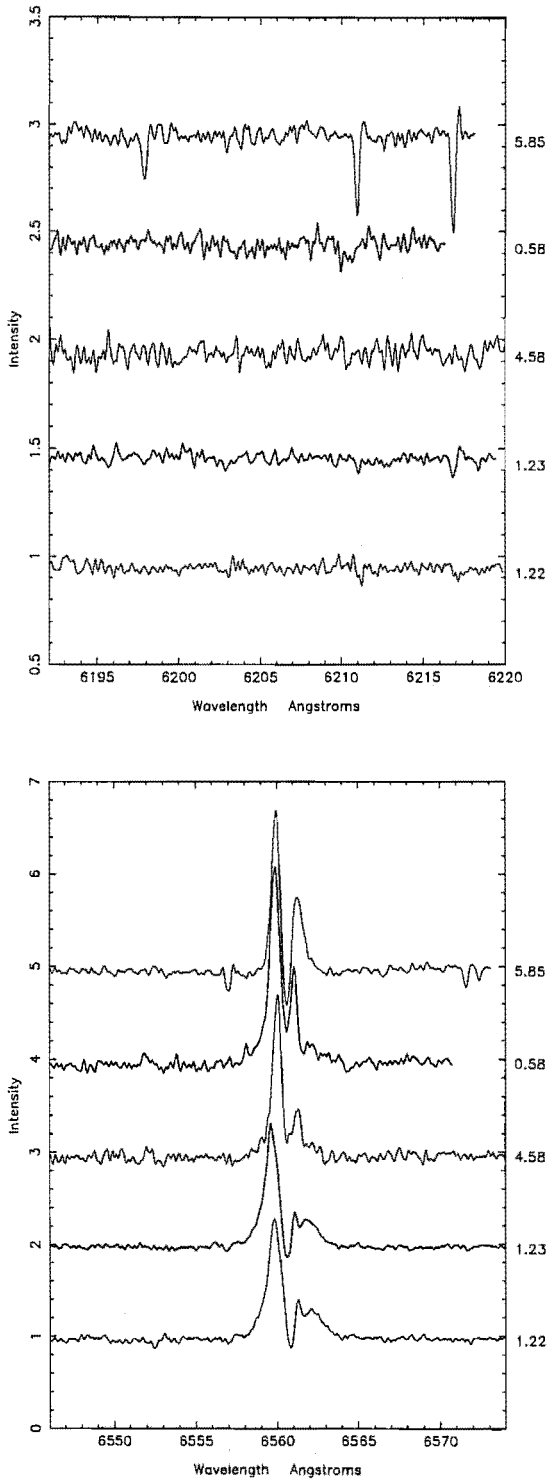

Figure 7.16: Stacked MJUO spectra of échelle orders 37 (top) and 35 (bottom) for AR Sgr. The cycle number and phase are indicated to the right of each spectrum.

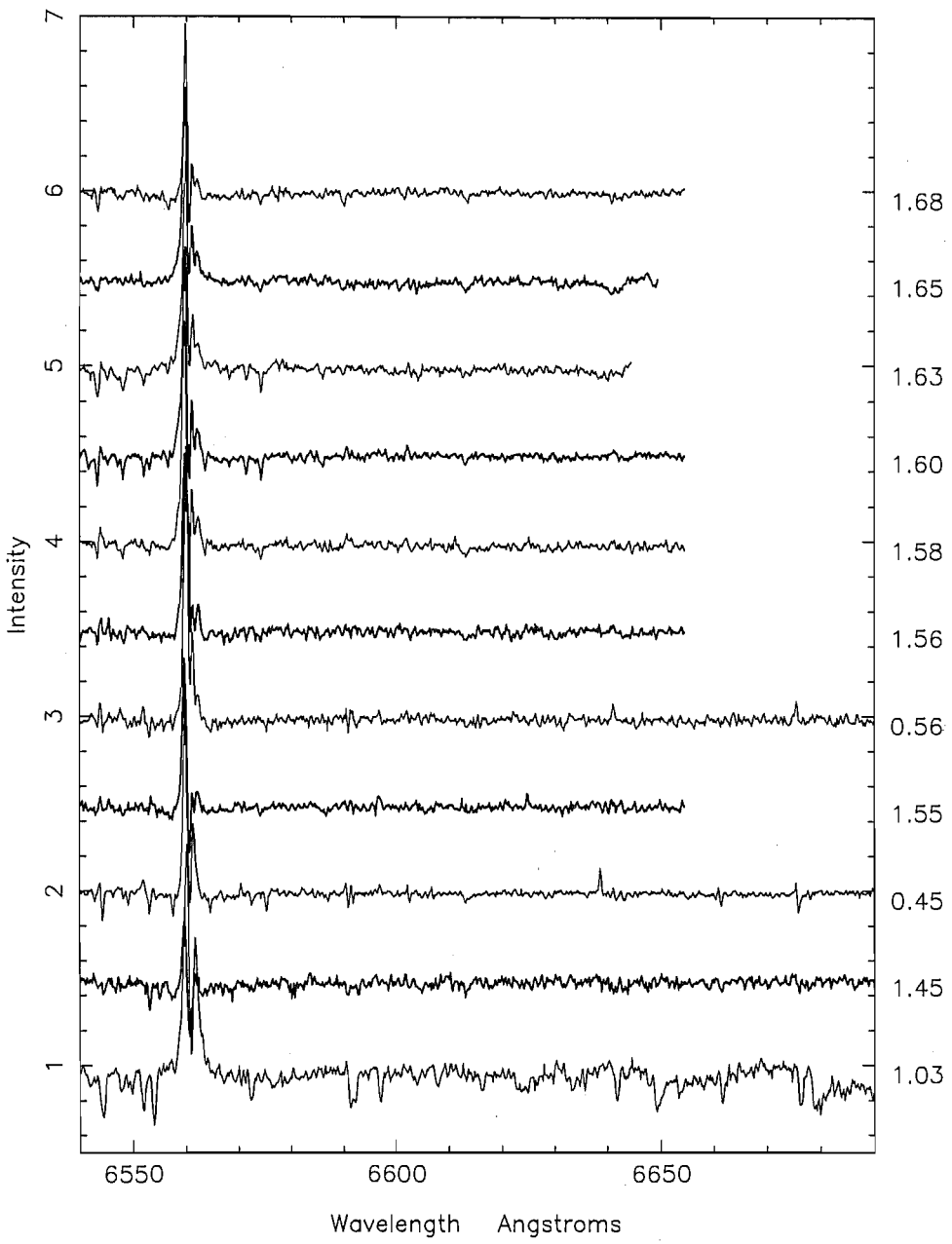

Figure 7.17: Stacked MSO spectra of AR Sgr. The cycle number and phase are indicated to the right of each spectrum.

Table 7.6: The phase-dependent behaviour of the metallic and molecular lines in AR Sgr.

λ (Å)	species	χ (eV)	multiplet	comment
6200.321	Fe I	2.61	207	strong lines, P Cygni profiles at phase 0.85
6213.437	Fe I	2.22	62	in cycle 5.
6219.287	Fe I	2.90	62	
6554.238	Ti I	1.44	102	Emission at phase 0.58 in cycles 0 and 4.
6743.127	Ti I	0.90	48	
6546.245	Fe I	2.76	268	Emission during phases 0.45–0.58 on MSO
6554.238	Ti I	1.44	102	spectra.
6651.5	TiO	–	–	bandheads during primary minimum on MSO
6681.1	TiO	–	–	spectra.
6631.3	CN	–	–	

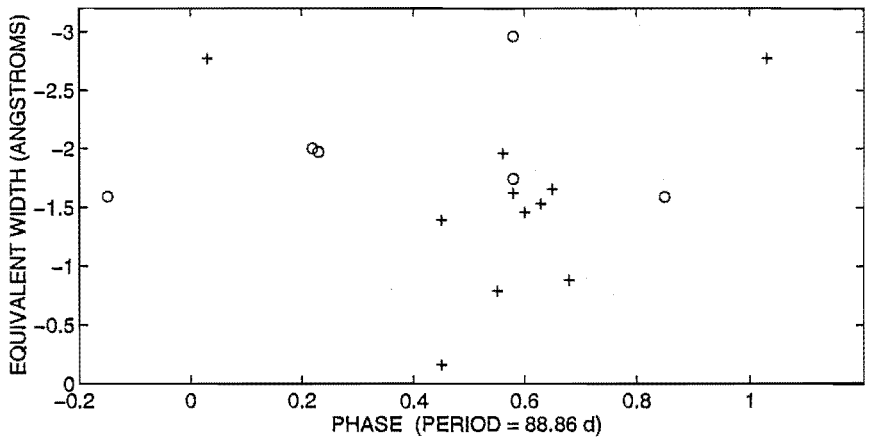

Figure 7.18: The phase dependence of the the Hα equivalent width in AR Sgr. Equivalent widths were measured on both the MJUO (o) and MSO (+) spectra.

width and plotting this value versus phase (Fig. 7.18).

The equivalent width measurement for AR Sgr was always negative, indicating that the emission contribution to the Hα line was greater than the absorption component. The equivalent width measurements for the Hα line are listed in Table 7.5. Cycle-to-cycle variations in the strength of the emission introduce quite a lot of scatter was seen around the secondary minimum (phase 0.5–0.7) where the phase coverage was good. The MSO spectra obtained during phases 0.5–0.7 were mostly from cycle 1 and displayed a peak in emission around phase 0.6.

From Fig. 7.18 and the stacked MSO and MJUO spectra it appears that the

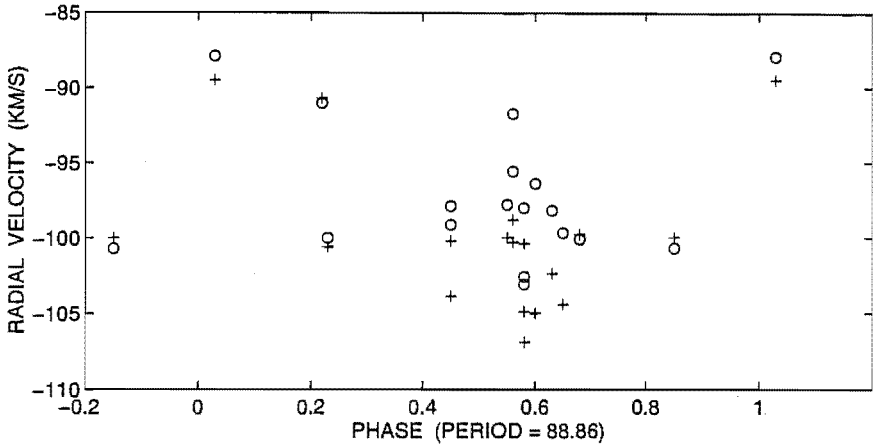

Figure 7.19: The Hα radial velocities for AR Sgr . Velocities of the Hα absorption (o) and emission (+) components are plotted versus phase.

Hα emission from cycle 0 is greater than from the other cycles that have been sampled. The equivalent width measurements from the MJUO spectra at phase 0.58 showed more emission in cycle 0 (equivalent width = −2.96 Å) than cycle 4 (equivalent width = −1.74 Å) and the MSO spectra from cycle 0 also showed stronger emission than cycle 1.

The Hα profile was modelled by fitting a number of Gaussians in order to derive velocities, as in Section 7.2.3. Radial velocities were calculated from the positions of the fitted Gaussians and the phase dependence of these velocities is shown in Fig. 7.19. These velocities are also included in Table 7.5 where the columns rv(Hαa) and rv(Hαe) show the radial velocities for the strong absorption and emission components of the Hα line respectively.

The radial velocity variations for both the absorption and emission components of the Hα profile display a relatively small amplitude of $\sim 16\,\mathrm{km\,s^{-1}}$. The range in radial velocity for the absorption component is from −88 to $-103\,\mathrm{km\,s^{-1}}$ while the range for the emission component is from −90 to $-107\,\mathrm{km\,s^{-1}}$. There are consistent with Joy's (1952) spectroscopic observations which showed a range in velocity from -88 to $-108\,\mathrm{km\,s^{-1}}$.

The radial velocity curves show quite a large scatter which makes it difficult to confirm whether two velocity cycles are present during each 88.86 d luminosity cycle. Previous studies of other RV Tauri stars have shown that there are two radial velocity cycles (Abt 1955, Preston 1962, Sanford 1931), but AR Sgr displays

a very shallow secondary photometric minimum and it is possible that this is also reflected in the radial velocity curve for this star. However, spectroscopic observations with a more complete phase coverage (and preferably within the same or successive cycles) would be needed to investigate whether there is any such effect.

7.4 AD Aql

7.4.1 Previous spectroscopy of AD Aql

In their survey of the RV Tauri stars, Preston et al. (1963) note the Fp(R) spectral type of AD Aql. Based on the presence of the λ3883 Å CN bandhead on a single spectrogram, they tentatively identify AD Aql as a Preston type 'B' object, indicating that it is carbon-rich. No other spectroscopic work on this star appears to have been published.

7.4.2 Spectroscopic observations of AD Aql

Between the dates of 1991 May and 1991 September, eleven high-resolution coudé spectra were obtained of AD Aql using the 1.9-m telescope at MSO. Exposure times were typically between about 10 to 15 minutes. No spectra were obtained at MJUO due to the faintness of the star. A log of the AD Aql spectroscopic observations is presented in Table 7.7.

The spectra were phased to the mean photometric period of 66.09 d using the ephemeris:

$$\text{Primary (photometric) minimum} = 2448086.84 + 66.09E.$$

The MJUO V photometry and the dates when spectra were obtained at MSO are shown in Fig. 7.20 (top panel). The spectral phase coverage and the phased MJUO V observations are shown in the bottom panel in this figure. The phase coverage is reasonable except around the primary and secondary minima.

The MSO spectra of AD Aql were then stacked in a phase sequence (Fig. 7.21). Phases and cycle numbers calculated according to the photometric ephemeris are indicated to the right of each plotted spectrum. These stacked spectra reveal that AD Aql, like RU Cen, has very few metallic lines visible in its spectrum. Unlike the other RV Tauri stars, the Hα line is not double-peaked but always presents an inverse P Cygni type profile. The strength of the emission and absorption

Table 7.7: Spectroscopic observations of AD Aql.

UT date	HJD [a] 2440000+	observer	phase (ϕ)	W_λ(Hα) (Å)	rv(Hαa) (km s^{-1})	rv(Hαe) (km s^{-1})
1991-May-12	8389.219	WAL	4.58	−0.28	72.1	68.2
1991-May-24	8401.145	WAL	4.76	+0.18	53.4	70.4
1991-May-26	8403.094	WAL	4.79	+0.47	48.5	65.1
1991-May-30	8407.219	WAL	4.85	+0.75	47.6	65.9
1991-Jul-16	8454.070	WAL	5.56	+0.11	61.4	82.9
1991-Aug-25	8494.016	KRP	6.16	+0.06	62.5	84.5
1991-Aug-31	8500.035	KRP	6.25	+1.30	32.7	79.1
1991-Sep-01	8501.098	KRP	6.27	+1.27	35.7	81.6
1991-Sep-03	8503.070	KRP	6.30	+1.19	41.0	74.3
1991-Sep-07	8507.023	KRP	6.36	+0.97	41.1	77.3
1991-Sep-09	8509.109	WAL	6.39	+0.65	43.5	72.1

[a]for mid time of observation

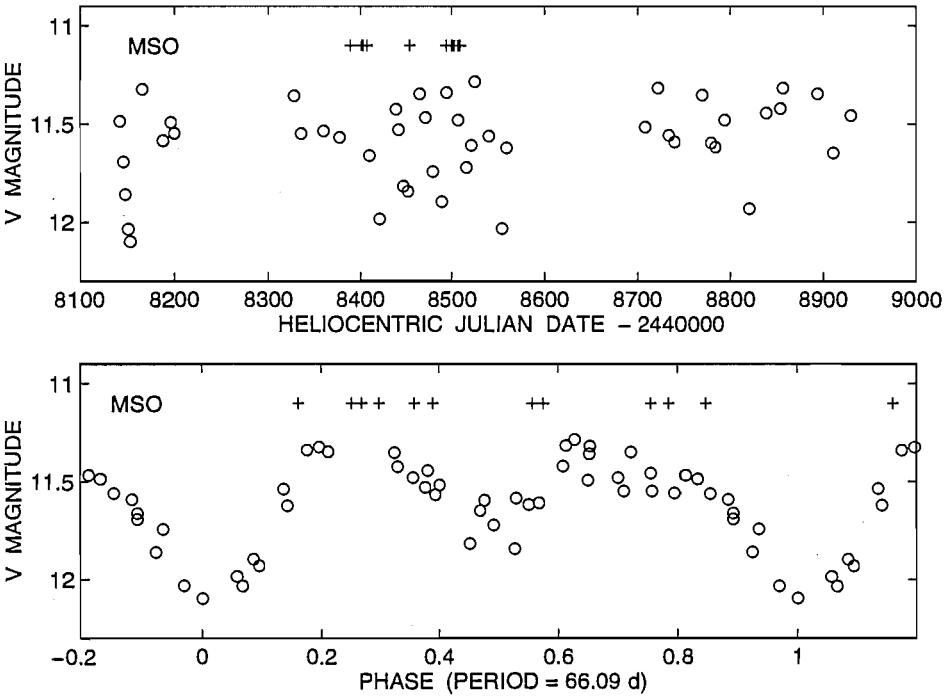

Figure 7.20: Light curves and spectral phase coverage for AD Aql. The MJUO photometric observations (o) and the MSO spectroscopic observations (+) are shown versus heliocentric Julian Date (top panel) and versus phase (bottom panel).

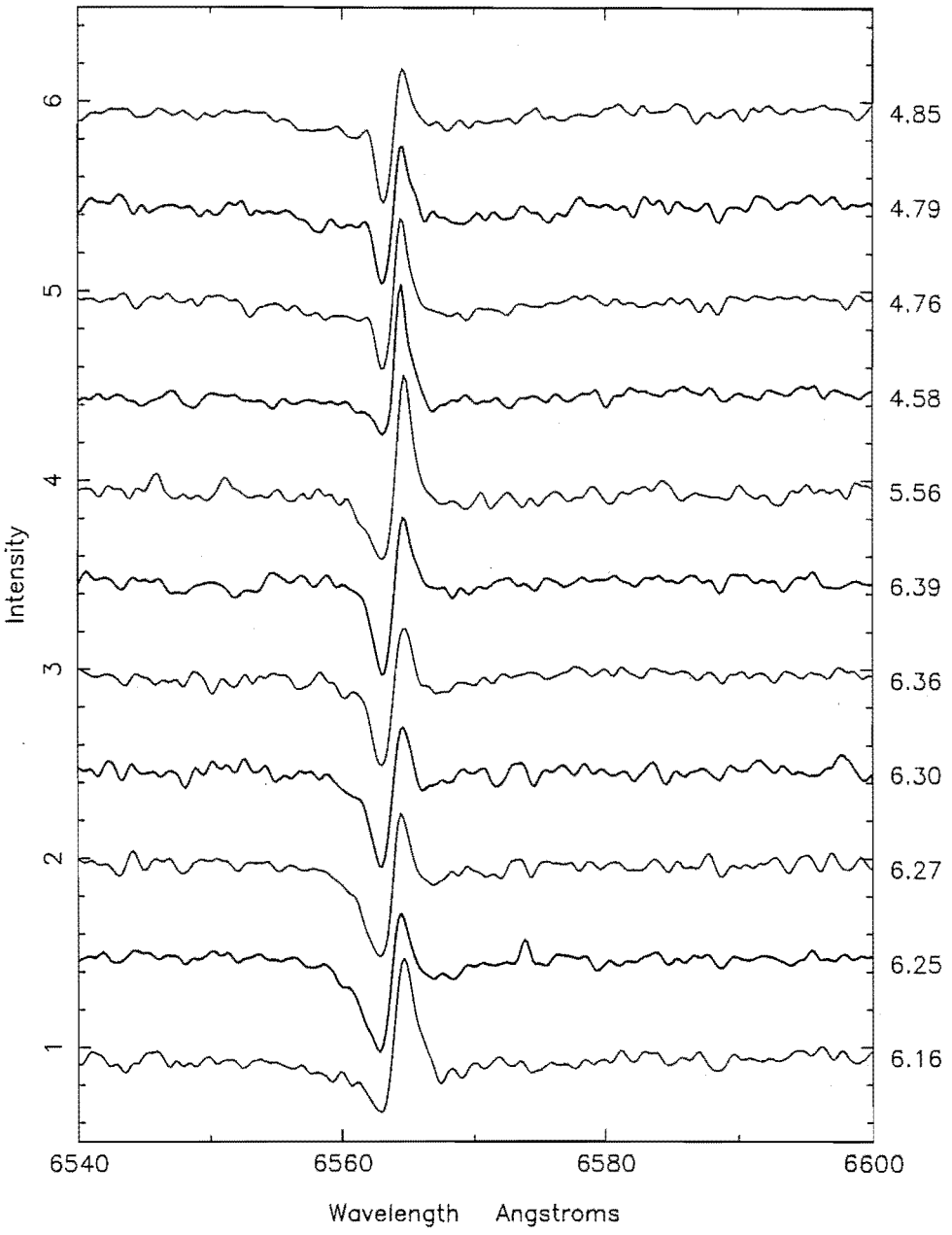

Figure 7.21: Stacked MSO spectra of the region around the Hα line in AD Aql. The phase is indicated to the right of each spectrum.

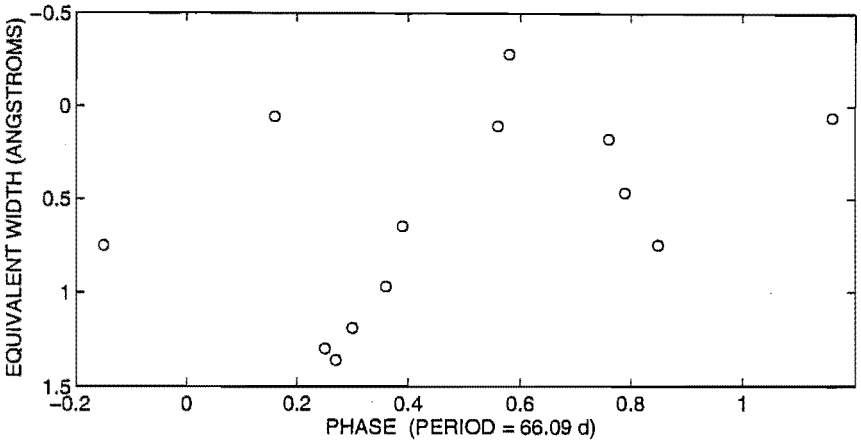

Figure 7.22: The phase dependence of the the Hα equivalent width in AD Aql.

components of the Hα line vary with phase. Around primary and secondary minima, the Hα emission contribution appears quite strong. Some spectra display broad, deep absorption components while at other phases, the absorption is quite narrow. At phases 0.79 and 0.85 in cycle 4, the spectra of AD Aql show a depression in the continuum at a wavelength of about 6556 Å which is quite reminiscent of that seen in RU Cen during a secondary minimum.

7.4.3 The Hα line profiles and radial velocities

The phase dependence of the Hα emission strength was investigated by measuring the equivalent width of the Hα line on all the MSO spectra, as in Section 7.1.4. These equivalent width measurements are included in Table 7.7. Both positive and negative values of the Hα equivalent width were measured for AD Aql. The variation of the Hα equivalent width with phase is displayed in Fig. 7.22.

The variation in the Hα equivalent widths appears quite repeatable in the different cycles. A peak in the Hα emission is seen at phase 0.6, which results from the propagation of the secondary shock wave through the line formation region. Strong Hα emission associated with the primary shock wave is also expected to be seen at phase ~ 0.2. The spectrum obtained at phase 0.16 in cycle 6 shows a large emission component as expected but the poor phase coverage around the primary minimum does not allow us to conclude whether the shock-produced emission is stronger for the primary or the secondary shock.

The relation between the phase and Hα line velocities was investigated by

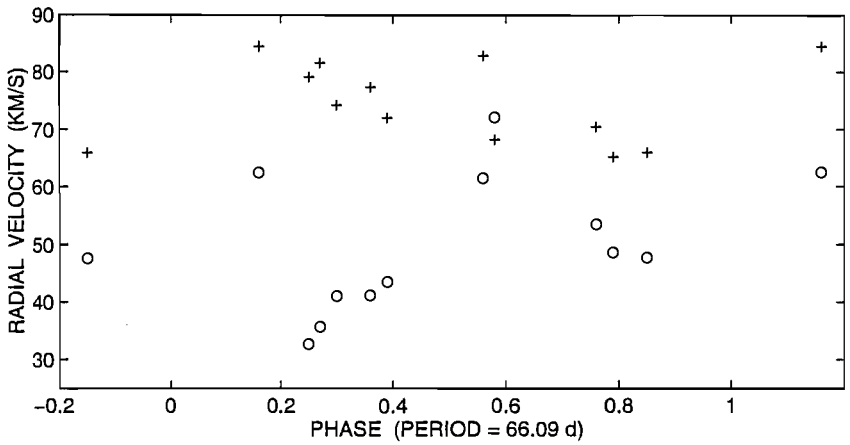

Figure 7.23: The Hα radial velocities for AD Aql. Velocities of the absorption (o) and emission (+) components are plotted for the Hα line.

fitting two Gaussians to the Hα profile at each phase. For AD Aql, an absorption and an emission component were used. The radial velocities are plotted versus phase in Fig. 7.23 and are also included in Table 7.7.

The radial velocity curve for the absorption component of the Hα profile is consistent with two velocity cycles during each 66.09 d luminosity cycle. This radial velocity curve is similar to that obtained for the metallic absorption lines in R Sct. An increase in velocity from phase 0.2 to 0.6 is apparent. Another increase from 0.8 to 0.1 is possible but improved phase coverage would be needed to confirm this. The radial velocities derived from the emission component of the Hα line display a decrease in velocity throughout phases 0.2 to 0.6 (opposite to that of the absorption component velocities) but the amplitude of variation is also smaller ($\sim 20\,\mathrm{km\,s^{-1}}$ compared to $\sim 40\,\mathrm{km\,s^{-1}}$).

7.5 V453 Oph

7.5.1 Previous spectroscopy of V453 Oph

Joy (1950) noted a systemic radial velocity of $-95\,\mathrm{km\,s^{-1}}$ for V453 Oph. Previously classified as a Cepheid, V453 Oph was classified by Preston et al. (1963) as a Preston type 'C' RV Tauri star, with a period of 80 d estimated from their photoelectric observations. The seven spectra that were obtained were assigned

Table 7.8: Spectroscopic observations of V453 Oph.

UT date	HJD [a] 2440000+	observer	phase ϕ	W_λ(Hα) Å	rv(Hαe) (km s^{-1})	rv(Hαa) (km s^{-1})
1991-May-25	8402.184	WAL	0.76	−0.76	−121.7	−117.2
1991-Jul-16	8454.004	WAL	1.41	+0.74	−124.9	−121.1

[a]for mid time of observation

an Fp spectral classification. In Cardelli's (1989) study of the atmospheric properties of several Preston 'B' and 'C' type RV Tauri stars, a range in effective temperature from 5900 K to 7200 K, log g from 1.0 to 2.5 and a metallicity of [Fe/H] = −1.6 was obtained for V453 Oph.

7.5.2 Spectroscopic observations of V453 Oph

Only two coudé spectra were obtained of V453 Oph using the 1.9-m telescope at MSO. These were obtained between 1991 May and 1991 September with exposure times of 10 minutes. No MJUO échelle spectra were obtained due to the faintness of the star. A log of the spectroscopic observations is presented in Table 7.8. The phases for the two spectra were calculated according to the ephemeris:

$$\text{Primary (photometric) minimum} = 2448340.55 + 80.68E.$$

Fig. 7.24 displays the phased MJUO V observations and the phases at which the two spectra were obtained.

The region around the Hα line for the two MSO spectra of V453 Oph is displayed in Fig. 7.25. The spectra show that V453 Oph has few metallic lines visible in its spectrum which is consistent with its spectroscopic classification as a Preston type 'C' (or metal-weak) star.

The metallic lines in V453 Oph appear stronger at phase 0.76. This is similar behaviour to that seen in AR Sgr, where the metallic lines became very strong at phase 0.85 when the star is approaching its coolest temperatures. A strong absorption line is apparent in both spectra at a wavelength of $\sim$ 6615 Å. We have been unable to identify this feature.

The appearance and strength of the Hα line is quite different on the two spectra. At phase 0.41 in cycle 1, the Hα emission is quite weak and the equivalent width of the line is small. At phase 0.76 in cycle 0 the Hα line displays a double-peaked emission profile that is $\sim$ 0.75 times the level of the continuum. This

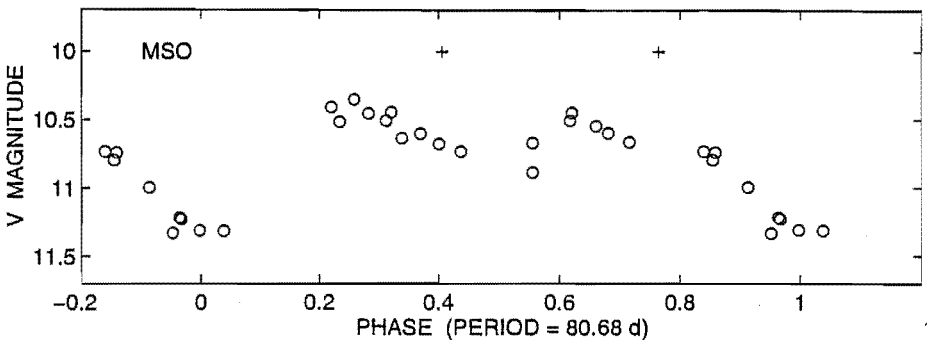

Figure 7.24: The phased light curve and spectral phase coverage for V453 Oph. The MJUO photometric observations (o) and the MSO spectroscopic observations (+) are plotted versus phase.

strong Hα emission occurs at the phase expected for emission associated with the secondary shock wave. At both phases the broad absorption wings of the Hα line are evident.

The equivalent widths for the two Hα profiles were measured and are included in Table 7.8. The Hα profiles were fitted by a number of Gaussians. The radial velocities for the main emission, rv(Hαe), and absorption, rv(Hαa), components are presented in Table 7.8.

7.6 RY Ara

7.6.1 Previous spectroscopy of RY Ara

The General Catalogue of Variable Stars (Kholopov et al. 1985) reports that RY Ara is an RV Tauri star with a spectral range of G5–K0 and a period of 143.5 d. The photometric classification of RY Ara as a member of the RV Tauri class has been questioned in the past due to its lack of infrared excess. There are no known previous spectroscopic observations of this star.

7.6.2 Spectroscopic observations of RY Ara

Eleven high resolution spectra were obtained of RY Ara between 1991 March and 1992 September, using the the 1.0-m telescope, échelle spectrograph and CCD detector at MJUO. Typical exposure times were 60 minutes. Between 1991 May and 1991 September, twelve high resolution coudé spectra were obtained at MSO

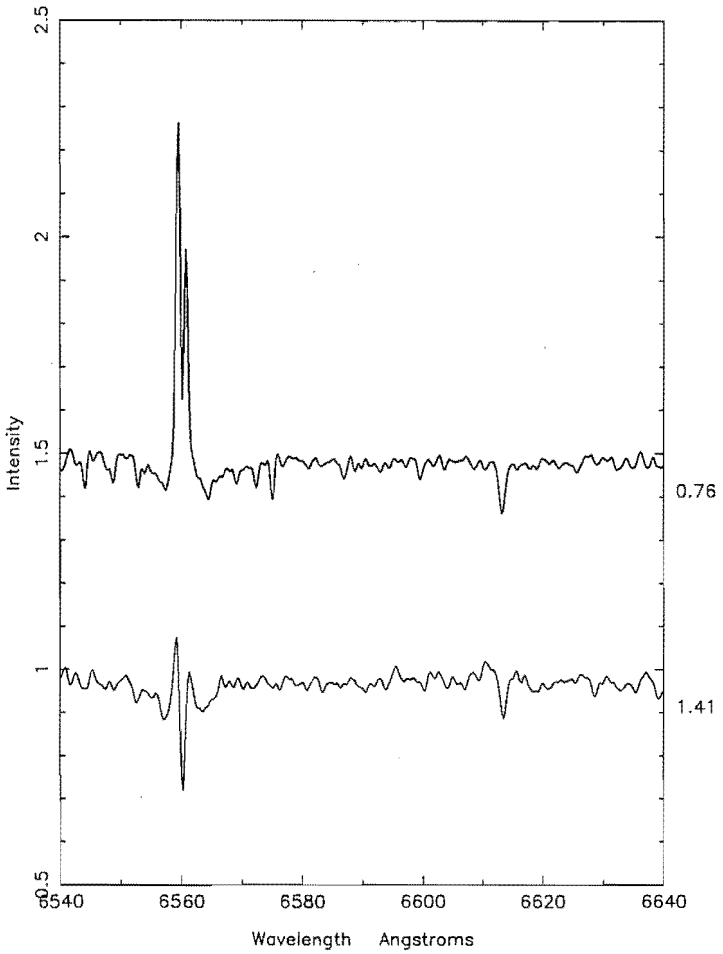

Figure 7.25: The MSO spectra of the region around the Hα line in V453 Oph. The phase is indicated to the right of each spectrum.

Table 7.9: Spectroscopic observations of RY Ara.

UT date	HJD [a] 2440000+	region	site	observer	phase (ϕ)	W_λ(Hα) (Å)	rv(Fe)[b] (km s^{-1})
1991-Mar-30	8346.078	Hα	MJUO	KRP	0.11	+0.40	102.7
1991-May-20	8397.176	Li	MJUO	KRP	0.28	–	–
1991-May-20	8397.254	Hα	MJUO	KRP	0.28	+0.01	92.8
1991-May-23	8400.199	Hα	MJUO	KRP	0.29	–0.13	99.8
1991-May-24	8401.063	Li	MJUO	KRP	0.30	–	–
1991-May-24	8401.113	Hα	MSO	WAL	0.30	–0.10	92.2
1991-May-24	8401.180	Hα	MJUO	KRP	0.30	–0.12	93.7
1991-May-30	8407.047	Hα	MSO	WAL	0.32	–0.04	97.9
1991-Jun-04	8412.074	Hα	MSO	WAL	0.33	–0.03	93.4
1991-Jul-16	8453.977	Hα	MSO	WAL	0.48	–0.07	131.1
1991-Aug-02	8470.875	Hα	MJUO	KRP	0.54	–0.77	130.8
1991-Aug-21	8490.023	Hα	MSO	KRP	0.60	–0.53	111.5
1991-Aug-24	8493.102	Hα	MSO	KRP	0.61	–0.39	107.4
1991-Aug-26	8494.984	Hα	MSO	KRP	0.62	–0.39	113.5
1991-Aug-31	8499.930	Hα	MSO	KRP	0.64	+0.02	107.2
1991-Sep-02	8501.902	Hα	MSO	KRP	0.64	+0.03	113.9
1991-Sep-05	8505.086	Hα	MSO	KRP	0.65	+0.10	108.9
1991-Sep-07	8507.102	Hα	MSO	KRP	0.66	+0.21	114.1
1991-Sep-09	8508.996	Hα	MSO	WAL	0.67	+0.13	110.6
1992-Mar-23	8705.172	Hα	MJUO	KRP	1.35	–0.10	98.3
1992-Apr-12	8725.141	Hα	MJUO	MDA	1.41	+0.11	107.2
1992-May-26	8769.148	Hα	MJUO	KRP	1.57	–1.59	124.7
1992-Sep-11	8876.902	Hα	MJUO	KRP	1.94	+0.40	120.5

[a] for mid time of observation
[b] radial velocity for the Fe I line at 6546.245Å.

using the 1.9-m telescope. Five to ten minute exposures were obtained. A log of the RY Ara spectroscopic observations is presented in Table 7.9.

The spectra were phased to the mean photometric period of 289.6 d using the ephemeris:

$$\text{Primary (photometric) minimum} = 2448315.6 + 289.6E.$$

The MJUO V photometry and the dates when spectra were obtained at MJUO or MSO are shown in Fig. 7.26 (top panel). The spectral phase coverage and the phased MJUO V observations are shown in the bottom panel in this figure.

The MJUO photometry of RY Ara (see Chapter 3) only covered a few cycles due to the very long period of the star. As well as the 289.6 d fundamental period and the 144.8 d first overtone, other shorter periods may have been present in the photometry (as indicated by a number of shallow minima in the light

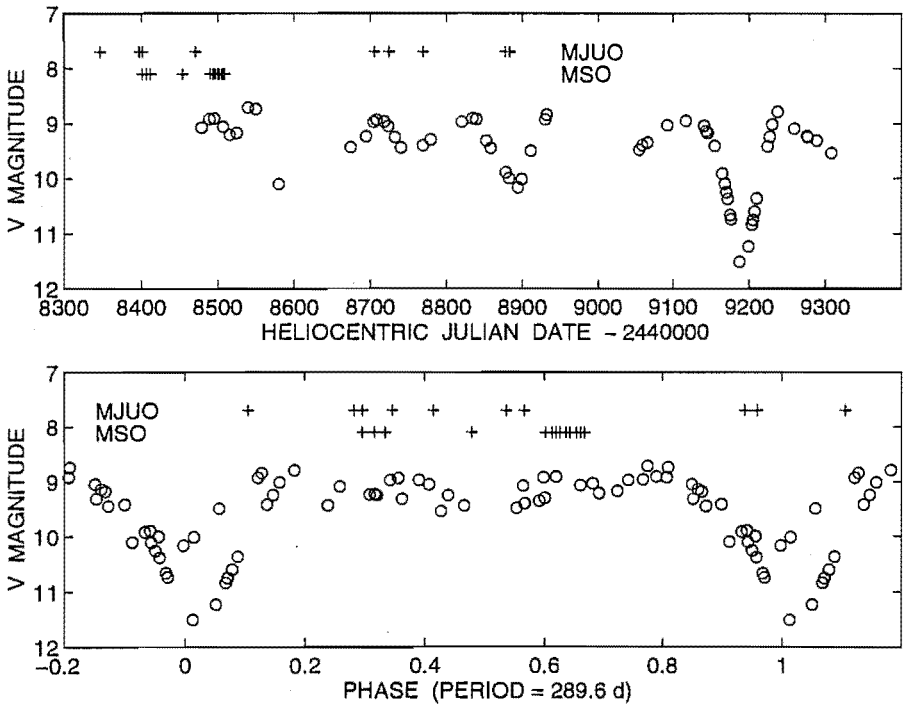

Figure 7.26: Light curves and spectral phase coverage for RY Ara. The MJUO photometric observations (o) and spectroscopic observations (+) from both MJUO and MSO are shown versus heliocentric Julian Date (top panel) and versus phase (bottom panel).

curve, particularly around HJD 2448500). Some spectra were obtained before photometry had been obtained of RY Ara when the form of the light curve was not known. In the case of the MJUO spectra, the phases of spectra from cycle 1 (HJD 2448605.2–2448894.8) appear reasonably consistent with the MJUO V light curve. The MSO spectra from late in cycle 0 (HJD $\sim$ 2448500) were taken just after what appears to be a primary maximum which should correspond to a phase of about 0.3, but the calculated phases are $\sim$0.6. Due to the lack of photometry before HJD $\sim$ 2448480, the photometric behaviour of RY Ara during cycle 0 remains uncertain. Consequently, the phases of spectra taken during cycle 0 are also tentative.

Phase sequences of stacked spectra are shown for the MJUO and MSO spectra of RY Ara in Figs 7.27, 7.28 and 7.29 respectively. The first half of the pulsation cycle (phases 0.0–0.5) is reasonably well sampled but fewer spectra were obtained in the second half of the cycle (phases 0.5–1.0). An obvious characteristic that is apparent from these stacked spectra is that RY Ara, like R Sct, displays numerous, relatively strong metallic lines at all phases. Line-doubling and emission components are present at many phases. The Hα profile is double peaked at many phases with relatively more emission seen on the blueward wing.

7.6.3 The Hα line profile

The equivalent width of the Hα line was measured on all the spectra and plotted versus phase (Fig. 7.30) in order to search for any phase dependence in the emission strength. A range of both positive and negative equivalent widths was obtained for RY Ara and these measurements are listed in Table 7.9.

RY Ara shows enhanced Hα emission just after secondary light minimum at about phase 0.55. No spectra were obtained at around 0.2 when the emission associated with the primary shock wave would be expected. During phases 0.9–0.1 and 0.4–0.5, there is evidence that molecular bands are present and these certainly have some affect on the measurement of the Hα equivalent width due to the uncertain placement of the continuum level and the additional absorption throughout this wavelength region. The MSO spectrum at phase 0.48 in cycle 0 displays particularly strong molecular bands. The strongest emission (about -1.6 Å) is obtained at phase 0.58. This strong emission occurs in cycle 1, whereas the MSO spectra during phases 0.60–0.67 are from cycle 0.

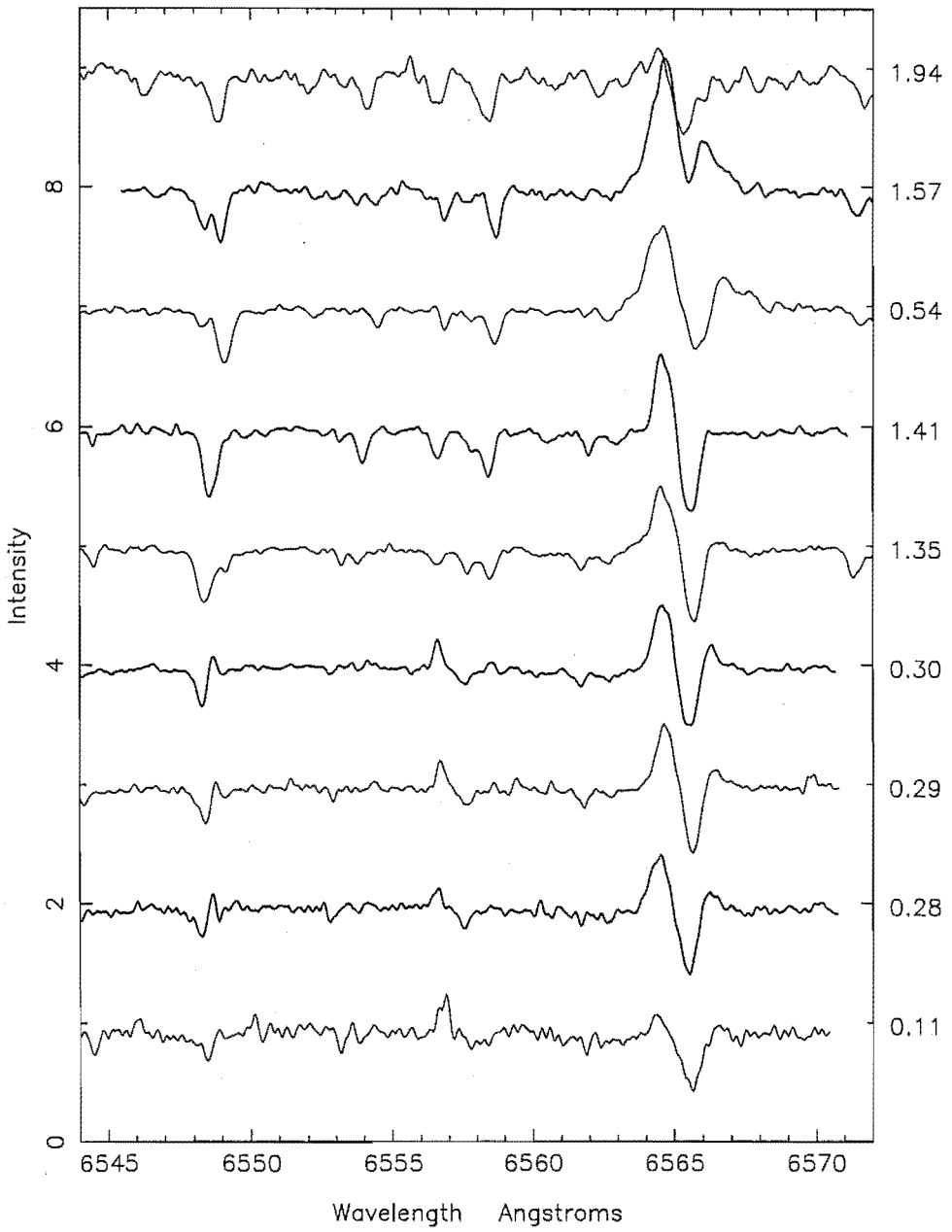

Figure 7.27: Stacked MJUO spectra of échelle order 35 for RY Ara. The cycle number and phase are indicated to the right of each spectrum.

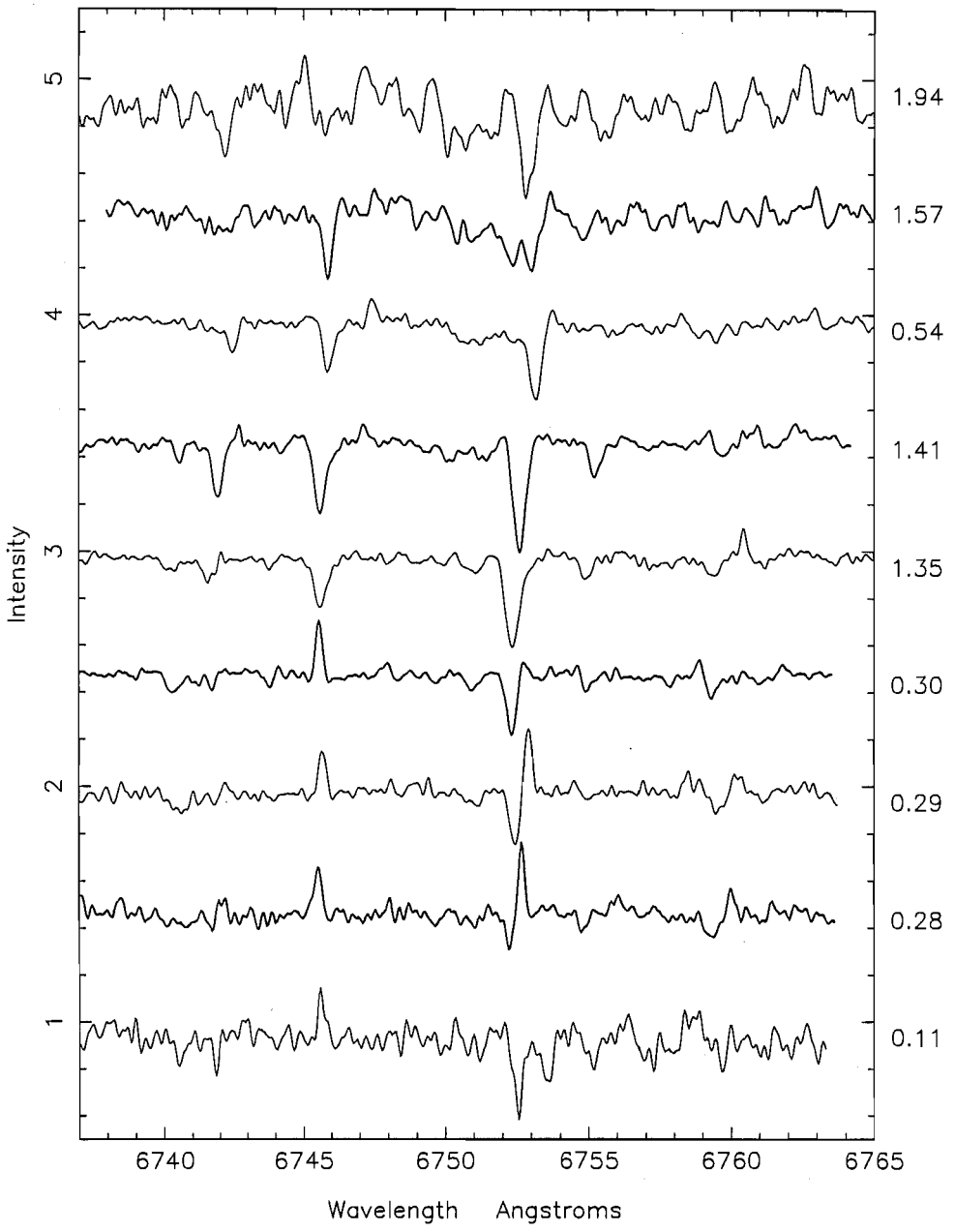

Figure 7.28: Stacked MJUO spectra of échelle order 34 for RY Ara. The cycle number and phase are indicated to the right of each spectrum.

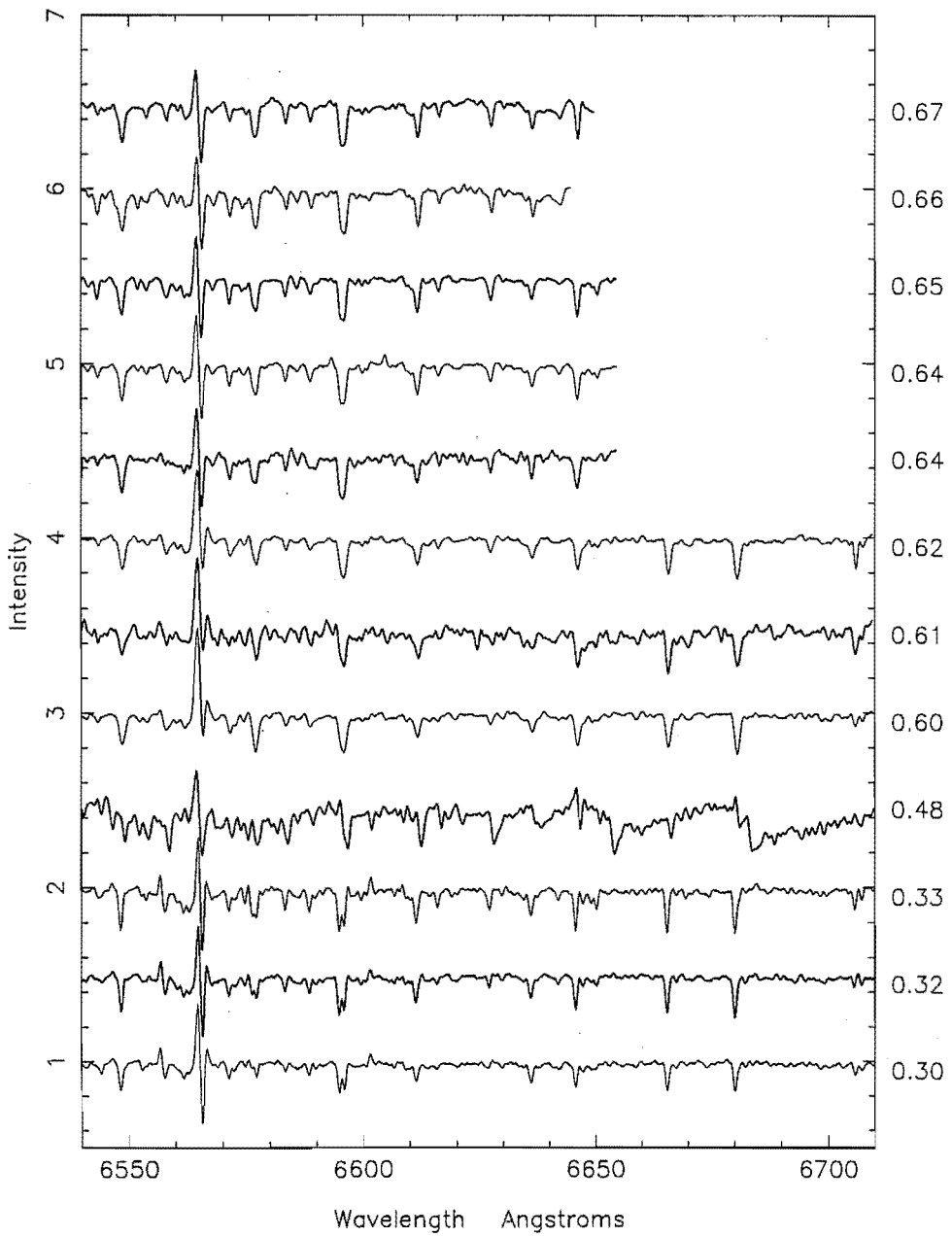

Figure 7.29: Stacked MSO spectra of the region around the Hα line in RY Ara. The phase is indicated to the right of each spectrum.

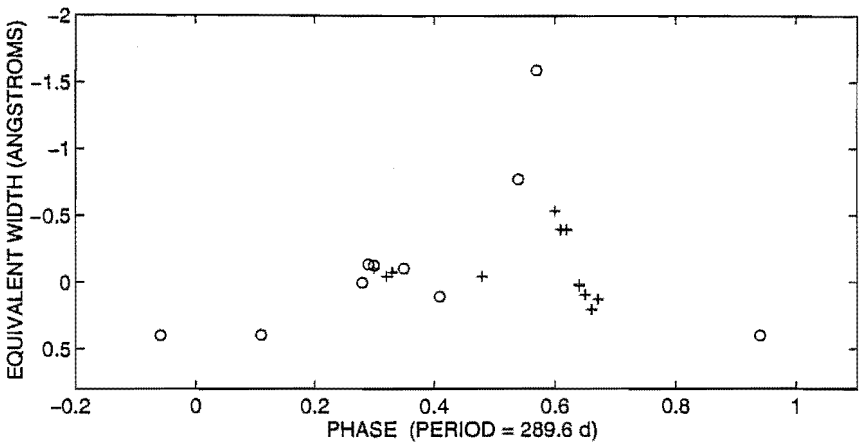

Figure 7.30: The phase dependence of the the Hα equivalent width in RY Ara. Equivalent widths were measured on both the MJUO (o) and MSO (+) spectra.

7.6.4 The metallic and molecular lines

During phases 0.35 and 0.54–0.57, two components of the Fe I line at 6546.245 Å (χ = 2.76 eV) are seen. In addition, P Cygni type profiles are displayed by the line between phases 0.28 and 0.30. Such profiles are indicative of shock waves propagating through the line formation region at these phases. Other Fe I lines with similar excitation potential also display this same behaviour and are listed in Table 7.10.

At the phases where the shock wave is coincident with the atmospheric layer where the Ti I lines are forming, shock-related emission behaviour (P Cygni, inverse P Cygni and pure emission profiles) is apparent. The Ti I and other spectral lines which exhibit this shock-related emission behaviour are also listed in Table 7.10.

Molecular lines are very strong on the MSO spectrum taken at phase 0.48. Molecular bandheads of the γ system of TiO are apparent at the wavelengths of 6651.5 Å and 6681.1 Å. Also evident of the MSO spectrum at this phase is the CN bandhead at 6631.3 Å.

CN bandheads at 6383.906 Å and 6747.620 Åare visible on the MJUO spectra taken during phases 0.54–0.57 and 0.94, that is, around primary and secondary light minima. A bandhead at $\sim$ 6200 Å, which we have tentatively associated with the α system of TiO, is very strong at the same phases.

Table 7.10: The phase-dependent behaviour of the metallic and molecular lines in RY Ara.

λ (Å)	species	χ (eV)	multiplet	comment
6318.027	Fe I	2.43	168	line-doubling during phases 0.35, 0.54–0.57,
6546.245	Fe I	2.76	268	P Cygni profiles at phases 0.28–0.30
6570.164	Fe I	2.42	111	
6191.571	Fe I	2.43	169	similar behaviour to above but complicated by
6213.437	Fe I	2.22	62	blending.
6554.238	Ti I	1.44	102	emission seen during phases 0.11–0.33 and
6743.127	Ti I	0.90	48	0.60–0.62.
6651.5	TiO	–	–	bandheads at phase 0.48 on MSO spectrum
6681.1	TiO	–	–	
6631.3	CN	–	–	
6383.906	CN	–	–	bandheads at phases 0.54–0.57 and 0.94
6747.620	CN	–	–	

7.6.5 The radial velocity curve for RY Ara

The line bisector method described in Section 6.12 was used to calculate radial velocities from the spectra shown in Figs 7.27 and 7.29. In order to make use of both the MJUO and the MSO spectra of RY Ara, the Fe I line at 6546.245 Å was used for this analysis. These radial velocities are included in Table 7.9. Although this Fe I line does display line-doubling and P Cygni type profiles at phases 0.28–0.30, it appeared to be one of the least shock-affected lines that was present on both the MJUO and MSO spectra.

Fig. 7.31 compares the radial velocity curves calculated with periods of 289.6 d (top panel) and 144.8 d (bottom panel). The radial velocity curves have an amplitude of variation of about 40 km s^{-1}, which is typical of amplitudes obtained previously for other RV Tauri stars. The top panel shows that phases 0.2–0.7 are well sampled but phases 0.7–0.2 are rather poorly sampled. The radial velocity curve is consistent with two velocity cycles being present per 289.6 d luminosity period. The velocities in the bottom panel appear to follow a reasonably sinusoidal variation which is rather unusual for RV Tauri stars, which tend to show a slow increase in velocity and then a rapid or discontinuous decrease in velocity. The radial velocity curve calculated with the 144.8 d period is more reminiscent of a Mira or LPV radial velocity curve. It is possible that, due to the lower resolution of the MSO spectra, the line doubling during phases 0.2–0.4 (on the 144.8 d period) may not be resolved, with the doubled Fe I line appearing as a blended line. In this case, the derived velocities will be some mean value of the

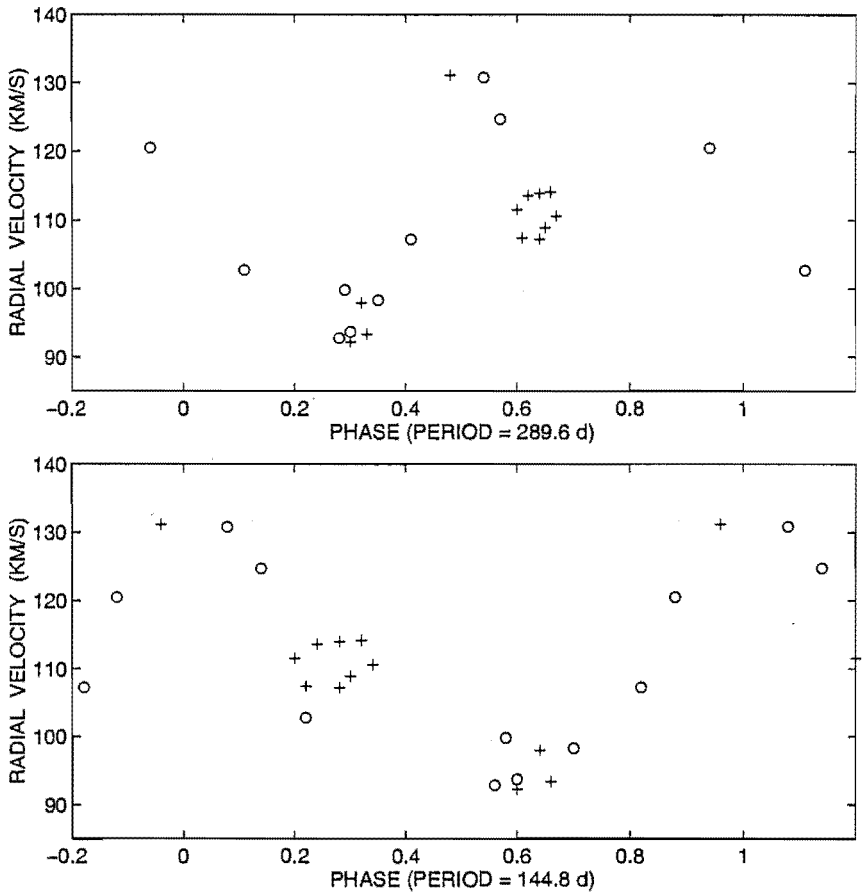

Figure 7.31: The radial velocities for RY Ara, measured from the Fe I line at 6546.245 Å using both MJUO (o) and MSO (+) spectra. The phases in the top panel are calculated using a period of 289.6 d and the bottom panel used a period of 144.8 d.

velocities that would have been obtained if the two components had been able to be measured individually.

7.7 V820 Cen

7.7.1 Previous spectroscopy of V820 Cen

MacConnell et al. (1972) initially classified V820 Cen as an unusual hydrogen-deficient F-type star. Their objective-prism spectra of this star showed strong lines of ionized metals. Strong Hα emission and either stellar or interstellar Na D lines were later noted by Wegner (1976). In this study, a high radial velocity of $+258\,\mathrm{km\,s^{-1}}$ was also noted. A metallicity of [Fe/H] = -2.5 was determined using a differential curve of growth method and and an effective temperature of 4400 K was estimated from photometric observations. Using high-dispersion spectra, Hunger & Kaufmann (1976) compared the line strengths in V820 Cen spectra with those of the hydrogen deficient R Coronae Borealis star, R CrB. They concluded that V820 Cen was not in fact hydrogen-deficient, but was a metal poor giant with a high radial velocity of $+261\,\mathrm{km\,s^{-1}}$. Variable emission in the wings of the Hβ line was also noted.

7.7.2 Spectroscopic observations of V820 Cen

Seventeen high-resolution spectra were obtained of V820 Cen using the 1.0-m telescope, échelle spectrograph and CCD detector at MJUO between 1991 March and 1992 September. Typical exposure times were about 60 minutes. Between 1991 May and 1991 September, fourteen high-resolution coudé spectra were obtained using the 1.9-m telescope at MSO with exposure times of between about 5 and 10 minutes. Table 7.11 presents a log of the spectroscopic observations.

The spectra were phased to the mean photometric period of 159.48 d derived from the MJUO and Eggen (1986) photometry. The ephemeris used was:

$$\text{Primary (photometric) minimum} = 2448338.672 + 159.48E.$$

Due to the very irregular nature of the light variation in V820 Cen, the period and therefore the calculated phases are quite uncertain. The dates when spectra were obtained for V820 Cen are indicated in Fig. 7.32. This figure shows the MJUO V photometry for V820 Cen plotted versus heliocentric Julian Date.

Table 7.11: Spectroscopic observations of V820 Cen.

UT date	HJD [a] 2440000+	region	site	observer	phase (ϕ)	W_λ(Hα) (Å)
1991-Mar-26	8342.203	Hα	MJUO	KRP	0.02	−0.00
1991-Mar-31	8347.027	Hα	MJUO	KRP	0.05	−0.07
1991-May-10	8386.980	Hα	MSO	WAL	0.30	−1.42
1991-May-11	8388.133	Hα	MSO	WAL	0.31	−1.54
1991-May-12	8388.992	Hα	MSO	WAL	0.32	−1.50
1991-May-20	8397.004	Hα	MJUO	KRP	0.37	−1.09
1991-May-21	8398.082	Li	MJUO	KRP	0.37	–
1991-May-22	8399.063	Hα	MJUO	KRP	0.38	–
1991-May-23	8400.020	Hα	MJUO	KRP	0.39	−1.17
1991-May-23	8400.113	Li	MJUO	KRP	0.39	–
1991-May-24	8401.027	Hα	MSO	WAL	0.39	−1.31
1991-May-26	8403.027	Hα	MSO	WAL	0.40	−1.48
1991-May-28	8404.914	Hα	MSO	WAL	0.42	−1.39
1991-Jul-16	8453.949	Hα	MSO	WAL	0.72	−1.95
1991-Jul-18	8455.906	Hα	MSO	WAL	0.74	−2.18
1991-Jul-29	8466.895	Hα	MJUO	KRP	0.80	–
1991-Aug-01	8469.930	Hα	MJUO	KRP	0.82	−2.94
1991-Aug-03	8471.914	Hα	MJUO	KRP	0.84	−3.37
1991-Aug-24	8492.938	Hα	MSO	KRP	0.97	−2.64
1991-Aug-26	8494.938	Hα	MSO	KRP	0.98	−2.58
1991-Sep-01	8500.926	Hα	MSO	KRP	1.02	−2.31
1991-Sep-03	8502.922	Hα	MSO	KRP	1.03	−2.28
1991-Sep-08	8507.914	Hα	MSO	KRP	1.06	−1.98
1991-Sep-09	8508.980	Hα	MSO	WAL	1.07	−2.06
1992-Mar-24	8705.977	Hα	MJUO	KRP	2.30	−1.67
1992-Mar-24	8706.098	Hα	MJUO	KRP	2.30	−1.62
1992-Apr-12	8724.957	Hα	MJUO	MDA	2.42	−1.63
1992-May-25	8767.961	Hα	MJUO	KRP	2.69	−1.74
1992-May-26	8769.031	Hα	MJUO	KRP	2.70	−1.72
1992-Sep-12	8877.867	Hα	MJUO	KRP	3.38	−2.46
1992-Sep-16	8881.863	Hα	MJUO	KRP	3.41	−2.20

[a] for mid time of observation

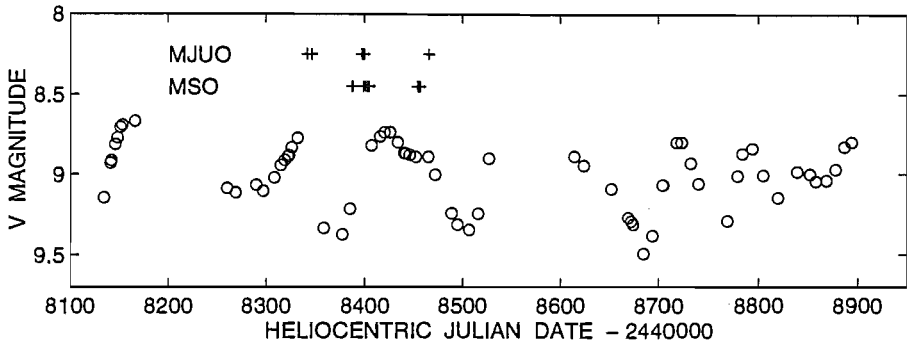

Figure 7.32: The light curve for V820 Cen from MJUO photometry (o) indicating the dates when spectra were obtained (+) at MJUO and MSO .

The MJUO and MSO spectra of V820 Cen were then stacked in phase order with the cycle number and phase of observation indicated to the right of each plotted spectrum. The region around the Hα line is shown in Figs 7.33 and 7.34 for the MJUO and MSO spectra respectively. A number of metallic lines are present but they are weak at all phases. The reported weak-lined nature of V820 Cen and the variability of the hydrogen Balmer lines (Wegner 1976, Hunger & Kaufman 1976) are confirmed by these spectra.

7.7.3 The Hα line profile

A range of Hα profiles are seen in Figs 7.33 and 7.34. An interesting feature of the changing Hα profile is the large variation in the strength and broadness of the central absorption core. Large changes in the overall strength of the emission is also displayed.

The equivalent width of the Hα line was measured on the MJUO and MSO spectra. The equivalent width for every Hα profile was found to be negative, indicating the dominance of the emission contribution. These measurements are included in Table 7.11. Due to the high-velocity nature of this star and correspondingly large wavelength shift, the Hα line sometimes appeared too close to the edge of the frame to measure a reliable equivalent width. Fig. 7.35 compares the variability of the Hα emission strength with the photometric light variations.

The times at which the Hα emission occurs in V820 Cen are different than in the previously presented stars. Strong emission appear to occur during the descending branch of the light curve rather than the ascending branch as for the

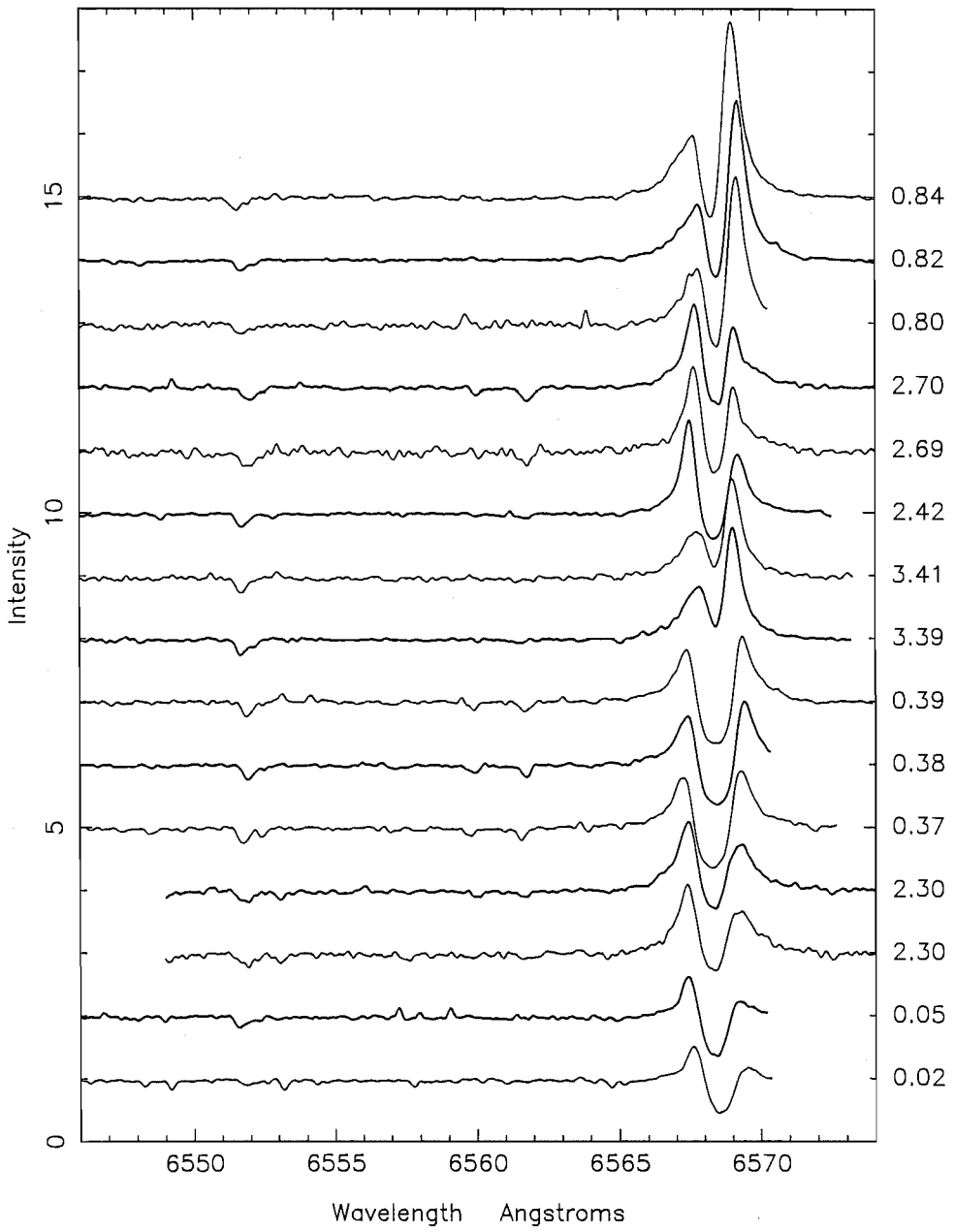

Figure 7.33: Stacked MJUO spectra of échelle order 35 for V820 Cen. The cycle number and phase are indicated to the right of each spectrum.

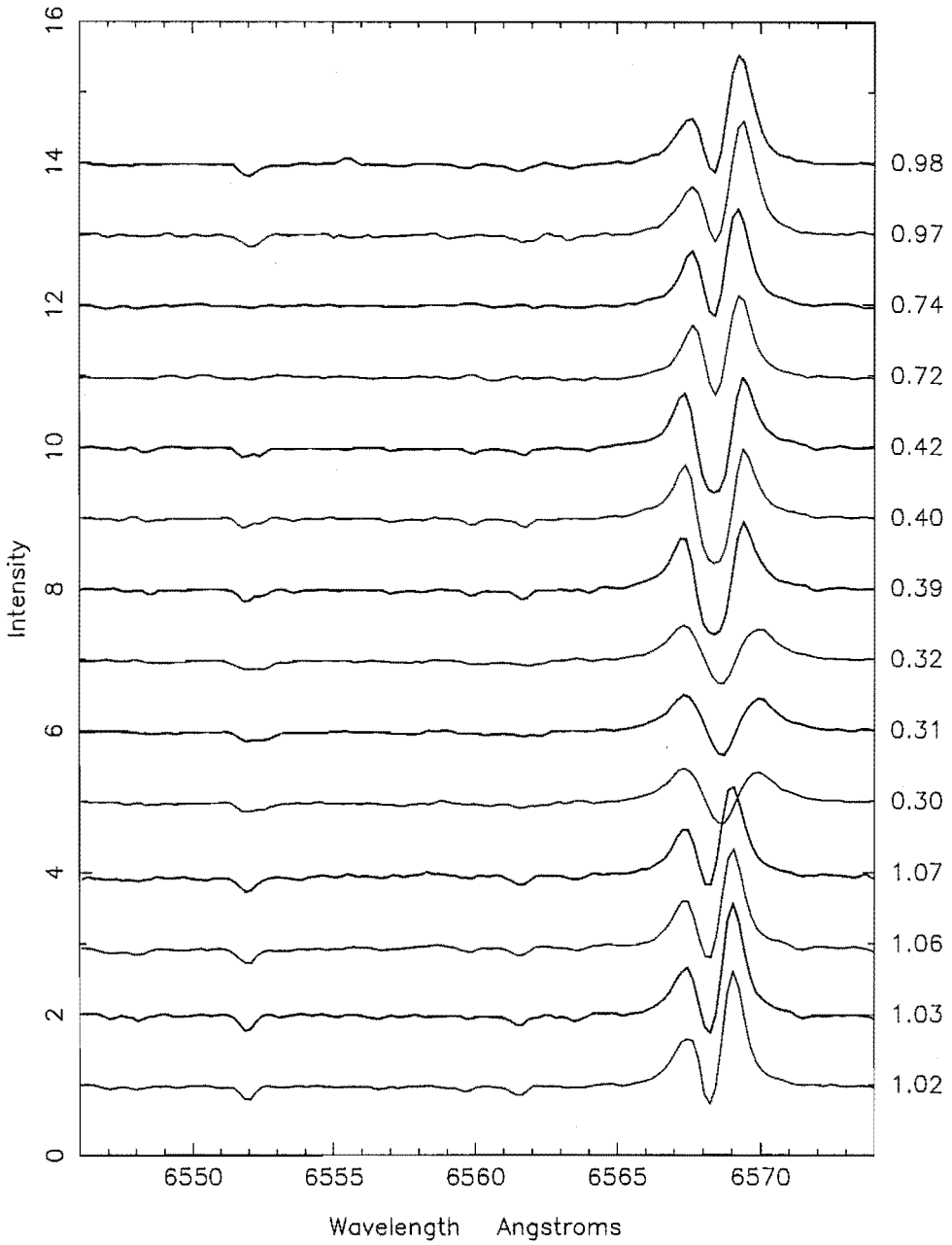

Figure 7.34: Stacked MSO spectra of the region around the Hα line in V820 Cen. The cycle number and phase are indicated to the right of each spectrum.

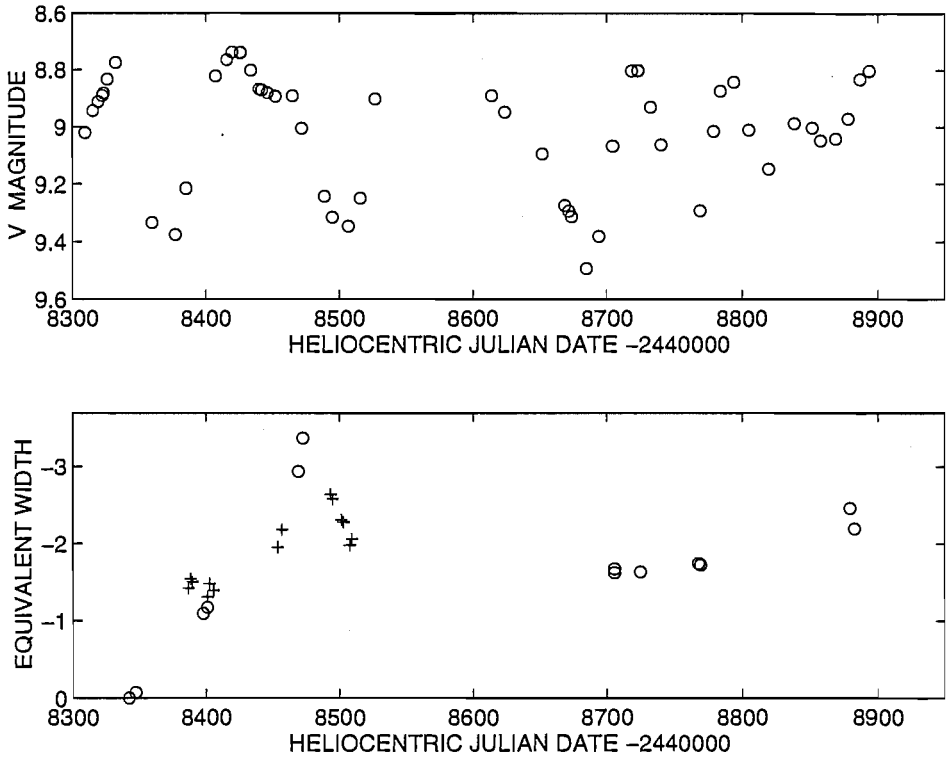

Figure 7.35: The variability of the Hα equivalent width in V820 Cen. Equivalent widths were measured on both the MJUO (o) and MSO (+) spectra.

RV Tauri stars. This is apparent in Fig 7.35 at around HJD 244 8480, where strong emission is seen just after the maximum of the V light curve. This is a further evidence that V820 Cen is not an RV Tauri star, but is a semiregular variable.

Chapter 8

Spectroscopy of the RVb stars

This chapter presents the spectroscopy of the stars of the RVb subclass. Stars of the RVb subclass exhibit long-term radial velocity variations in addition to displaying long-term variability in their light curves. In these stars, short-term radial velocity variations due to pulsations are superimposed onto the slow variation.

Stacked spectra, Hα equivalent widths and radial velocities curves are presented and discussed for each star, in a similar manner as for Chapter 7.

More spectra were obtained of the bright RVb star, U Mon, and a more detailed discussion of this star is presented in Section 8.1. The MJUO radial velocities are combined with previously published velocities to obtain an orbital solution to the long-term radial velocity variations. The possibility that mass loss or transfer is occurring in the binary system is investigated in terms of the derived orbital parameters and the observation of enhanced Hα emission.

In Chapter 9 the spectroscopic properties determined in this chapter and Chapter 7 will be used, together with the photometric characteristics previously discussed, to examine models which attempt to describe the pulsation mechanisms and the underlying physical nature of the RV Tauri stars.

8.1 U Mon

8.1.1 Previous spectroscopy

U Mon is the second brightest RV Tauri star and the brightest member of the photometric RVb subtype. Members of this type display a long-term periodicity in their light curves. In an early study of the RV Tauri variables, Gerasimovič

(1929) listed U Mon and eleven other stars as confirmed members of the class. A double period of 92.26 d and a spectral range of G5–K2 was noted.

Sanford (1933) obtained spectrograms of U Mon over the interval 1922–1932, which show that U Mon possesses a $40\,\mathrm{km\,s^{-1}}$ variation in its centre-of-mass velocity with a period of about 2300 d. Superposed on these long-period variations are short-term radial velocity variations of amplitude $23\,\mathrm{km\,s^{-1}}$, which are due to pulsations with a 92.26 d double period. The γ-velocity of the system was found to be $+34.6\,\mathrm{km\,s^{-1}}$. Variable hydrogen Balmer emission was noted, as well as the presence of TiO bands on a number of spectra obtained around minimum light.

A 220 d campaign involving 21 high-dispersion spectrograms of U Mon (Abt 1955) revealed that the radial velocity curve has a discontinuity at each light maximum. Very large atmospheric displacements ($\sim 80\ \mathrm{R}_\odot$) were inferred from the radial velocity curve. A small decrease in the mean velocity of the system was noted and, comparing these results with those obtained earlier by Sanford, it was suggested that the long period be amended to 2640 d or possibly 1980 d.

Preston (1964) noted metallic emission lines in U Mon spectra taken during rising light and also emission at 5876 Å due to He I. Hα emission was apparent at all phases. The phase-dependent behaviour of the metallic lines was found to be correlated with excitation potential and ionization state, which can be explained by velocity gradients in a stratified atmosphere. Line doubling was reported to be most obvious for lines with $0.5\,\mathrm{eV} < \chi < 1.5\,\mathrm{eV}$ and a shock wave model was used to explain this behaviour. The observed Hα profile was very complex, with at least two absorption components superposed on a variable-strength broad emission component. Radial velocities from 39 spectrograms were used to investigate the long period variations discovered by Sanford (1933). Combining his observations with those of Abt (1955) and the second half of those observations of Sanford (1933), Preston determined a provisional period of roughly 1560 d, which was substantially different from the 2300 d period derived by Sanford.

U Mon was included in Preston et al.ś (1963) spectroscopic survey of the RV Tauri variables where it was classified as a Preston type 'A' object (strong-lined). A change in the circumstellar spectrum of U Mon was noted by Preston (1972). Double circumstellar absorption components of the Ca II H and K lines that were reported eight years earlier (Preston 1964) were found to have been replaced by a single strong absorption line, suggesting merging of two expanding, circumstellar shells.

Previous analyses based on high-resolution spectra of U Mon have suggested quite a range a metallicities. Aliev (1967) used a curve-of-growth analysis to derive [Fe/H] = –2.9, Dawson (1979) used DDO photometry to determine [Fe/H] = –0.3, Cardelli (1985) derived [Fe/H] = –1.0 to 0.0 using spectrophotometry and model atmosphere fluxes, Luck & Bond (1989) obtained [Fe/H] = –0.4 from a model atmosphere abundance analysis technique and Wahlgren (1992) used a synthetic spectrum analysis to obtain [Fe/H] = –0.4. A range in spectral types, temperatures and gravities were also obtained. Most studies note the photometric phase at which the spectrum (or spectra) was obtained but none state the long-term photometric phase. The implicit assumption is that whatever is causing the long-term light, colour, amplitude and radial velocity variations in U Mon is not relevant when using these techniques to derive atmospheric parameters for U Mon.

8.1.2 Spectroscopic observations

Between 1991 January and 1994 April, about 40 high-resolution échelle spectra of U Mon at various wavelength regions were obtained at MJUO using the 1.0-m telescope and CCD detector. The spectra obtained at MJUO typically had exposure times of about 30 to 40 minutes. Between 1991 May and 1991 September eight high resolution coudé spectra were obtained using the 1.9-m telescope at MSO. Exposure times using the MSO set-up were typically 2 to 10 minutes. A log of the spectroscopic observations for U Mon is presented in Table 8.1.

Table 8.1: Spectroscopic observations of U Mon.

UT date	HJD [1] 2440000+	region	site	observer	phase (ϕ)	W_λ(Hα) (Å)	rv(Fe)[2] (km s^{-1})
1991-Jan-21	8278.008	Li	MJUO	KRP	1.60	–	–
1991-Jan-30	8286.969	Hα	MJUO	KRP	1.70	–1.22	+3.5
1991-Mar-29	8344.938	Hα	MJUO	KRP	2.33	–1.12	+25.0
1991-Mar-31	8346.836	Hα	MJUO	KRP	2.35	–1.01	+28.2
1991-May-10	8386.852	Hα	MSO	WAL	2.78	–	–
1991-May-12	8388.906	Hα	MSO	WAL	2.80	–	–
1991-May-21	8397.820	Hα	MJUO	KRP	2.90	–1.51	+31.0
1991-May-22	8398.801	Li	MJUO	KRP	2.91	–	–
1991-May-24	8400.820	Li	MJUO	KRP	2.93	–	–

[1] for mid time of observation

[2] radial velocity for the Fe I line at 6750.164Å.

1991-May-25	8401.848	Hα	MSO	WAL	2.94	–	–
1991-May-29	8405.852	Hα	MSO	WAL	2.99	–	–
1991-Aug-02	8471.285	Hα	MJUO	KRP	3.70	–3.42	+4.6
1991-Aug-25	8494.273	Hα	MSO	KRP	3.95	–	–
1991-Aug-31	8500.277	Hα	MSO	KRP	4.01	–	–
1991-Sep-03	8503.250	Hα	MSO	KRP	4.04	–	–
1991-Sep-09	8509.234	Hα	MSO	KRP	4.11	–	–
1991-Sep-25	8525.148	Hα	MJUO	KRP	4.28	–3.09	+17.9
1991-Sep-26	8526.219	Hα	MJUO	KRP	4.29	–3.37	+18.0
1991-Sep-29	8529.223	Na	MJUO	KRP	4.32	–	–
1991-Nov-14	8575.066	Hα	MJUO	KRP	4.82	–2.62	+18.1
1991-Nov-14	8575.121	Li	MJUO	KRP	4.82	–	–
1991-Nov-15	8576.078	Na	MJUO	KRP	4.83	–	–
1991-Nov-30	8591.117	Hα	MJUO	MDA	5.00	–4.78	+40.3[3]
1992-Mar-13	8694.883	Hα	MJUO	MDA	6.12	–5.56	+48.6
1992-Mar-23	8704.840	Hα	MJUO	KRP	6.23	–4.39	+14.7
1992-Mar-23	8704.863	Hα	MJUO	KRP	6.23	–4.39	+14.8
1992-Apr-10	8722.906	Hα	MJUO	MDA	6.42	–2.29	+37.1
1992-May-26	8768.773	Hα	MJUO	KRP	6.92	–1.72	+29.3
1992-Aug-21	8856.262	Hα	MJUO	KRP	7.87	–0.74	+26.3
1992-Sep-11	8877.215	Hα	MJUO	KRP	8.09	–3.02	+50.7
1992-Sep-12	8878.246	Hα	MJUO	KRP	8.11	–3.20	+52.3
1992-Sep-16	8882.199	Hα	MJUO	KRP	8.15	–2.78	+50.9
1992-Sep-17	8883.207	Hα	MJUO	KRP	8.16	–2.60	+52.1
1992-Nov-20	8947.121	Hα	MJUO	MDA	8.85	–0.65	+26.0
1992-Nov-22	8949.074	Hα	MJUO	MDA	8.87	–0.51	+29.2
1993-Jan-19	9007.043	Hα	MJUO	PLC	9.50	–0.78	+49.8
1993-Feb-15	9033.887	Hα	MJUO	PLC	9.79	–0.91	+28.1
1993-Apr-11	9088.852	Hα	MJUO	PLC	10.39	–0.60	+34.4
1993-Aug-27	9227.270	Hα	MJUO	MDA	11.89	–0.11	+39.4
1994-Feb-04	9387.922	Hα	MJUO	PLC	13.63	–1.90	+19.9
1994-Feb-06	9389.887	Hα	MJUO	PLC	13.65	–1.59	+19.9
1994-Apr-01	9443.820	Hα	MJUO	PLC	14.23	–0.26	+33.9
1994-Apr-03	9445.816	Hα	MJUO	PLC	14.25	–	–
1994-Apr-04	9446.852	Hα	MJUO	PLC	14.26	–0.11	+37.7

[3] this radial velocity was measured from the Fe I line at 6546.245 Å.

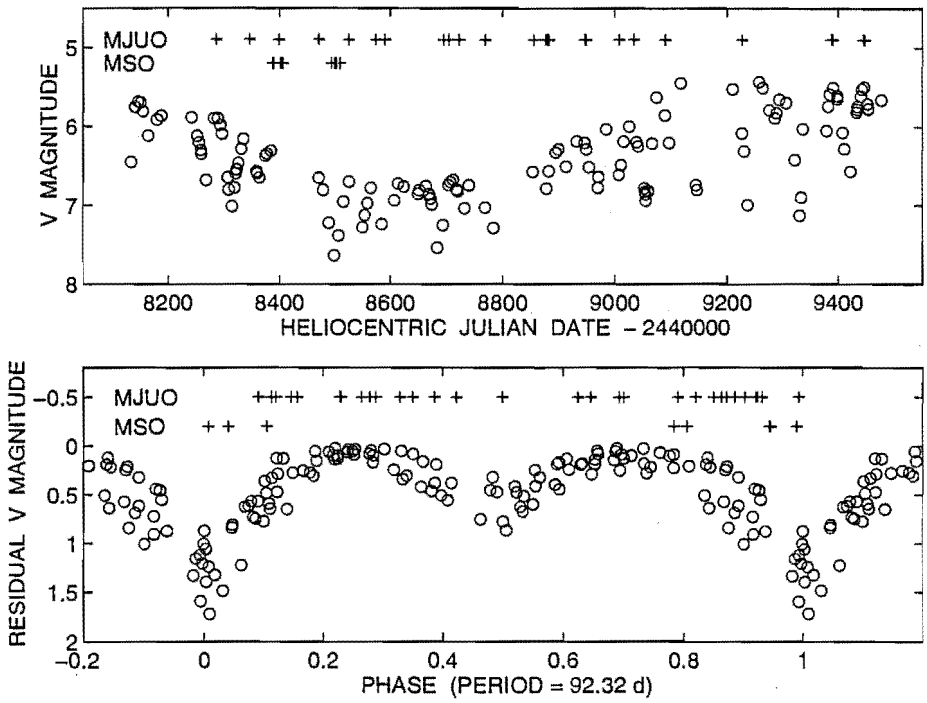

Figure 8.1: Light curves and spectral phase coverage for U Mon. The MJUO photometric observations (o) and dates of spectroscopic observations (+) from both MJUO and MSO are shown in the top panel. The bottom panel shows the MJUO photometric V observations (o) and the spectral phase coverage, where a period of 92.32 d has been used to calculate the phases.

The spectra were wavelength-calibrated, continuum-normalized, corrected for barycentric motion and lightly smoothed. The spectra were phased to the average period obtained from the analysis of the B, V, R and I photometric data. The ephemeris used was:

$$\text{Primary (photometric) minimum} = 2448300.0 + 92.32\,E$$

The dates and phases when spectra were obtained are shown together with the MJUO V photometry for U Mon in Fig. 8.1. The top panel in this figure shows that the MJUO and MSO spectra have sampled from the minimum up to the start of the maximum of the long-term (2600 d) cycle. The bottom panel plots the residual V magnitude after the long-term trend has been subtracted and this shows that a reasonable phase coverage has been obtained of the pulsational period.

The spectra obtained at MJUO were then stacked in phase sequence. Spectra from échelle orders 35 and 34 in the Hα region are shown in Fig. 8.2 and Fig. 8.3 respectively. The coudé spectra from MSO are shown in Fig. 8.4. These spectra are arranged in order of Julian Date, with the cycle number and phase at which the spectra were obtained, indicated to the right of each spectrum.

8.1.3 The Hα line profile variations

An interesting feature of the changing Hα profile is the strength of the emission. Inspecting Fig. 8.2 reveals that the Hα emission strength is greater during cycles 3 to 6, than during the preceding or subsequent cycles. In order to investigate this further, the equivalent width of the Hα line was measured for all the MJUO spectra. The broad wings of the line were included in this measurement as well as the various absorption and emission components that make up the complex profile. For every MJUO spectrum of U Mon, the equivalent width of the Hα line was found to be negative, that is, an emission profile. The equivalent width measurement for U Mon are listed in Table 8.1.

The phase-dependence of the Hα equivalent width is presented in Fig. 8.5. The top panel shows the equivalent width plotted versus photometric phase (including cycle number) which effectively shows the time evolution of the Hα equivalent width. The bottom panel plots the equivalent width versus photometric phase, with different symbols used to differentiate between the different cycles.

It is quite apparent that during cycles 3–6 ($\circ$) the Hα emission is much more intense than during cycles 9–14 ($*$). Cycles 1–2 ($\times$) and 7–8 ($+$) shows the Hα

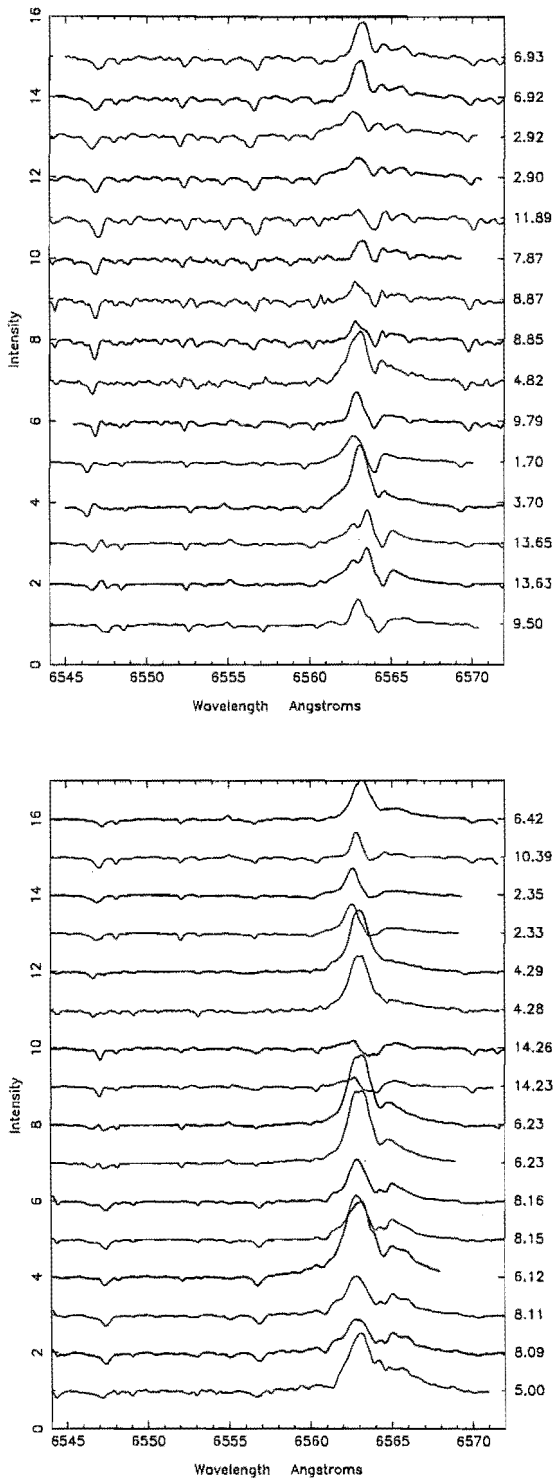

Figure 8.2: Stacked spectra of échelle order 35 for U Mon. Spectra with phases 0.0–0.5 are plotted in the bottom panel and spectra with phases 0.5–1.0 are plotted in the top panel. The cycle number and phase of observation is indicated at the right of each spectrum.

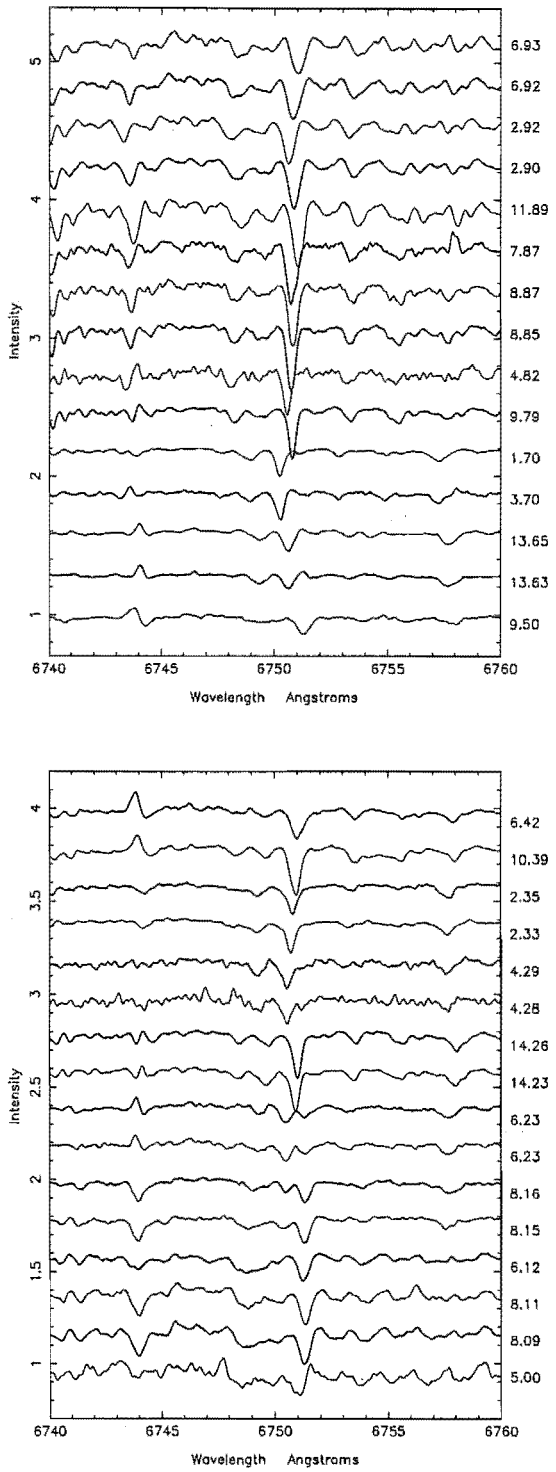

Figure 8.3: Stacked spectra of échelle order 34 for U Mon. Spectra with phases 0.0–0.5 are displayed in the bottom panel and spectra with phases 0.5–1.0 are displayed in the top panel. The cycle number and phase of observation is indicated at the right of each spectrum.

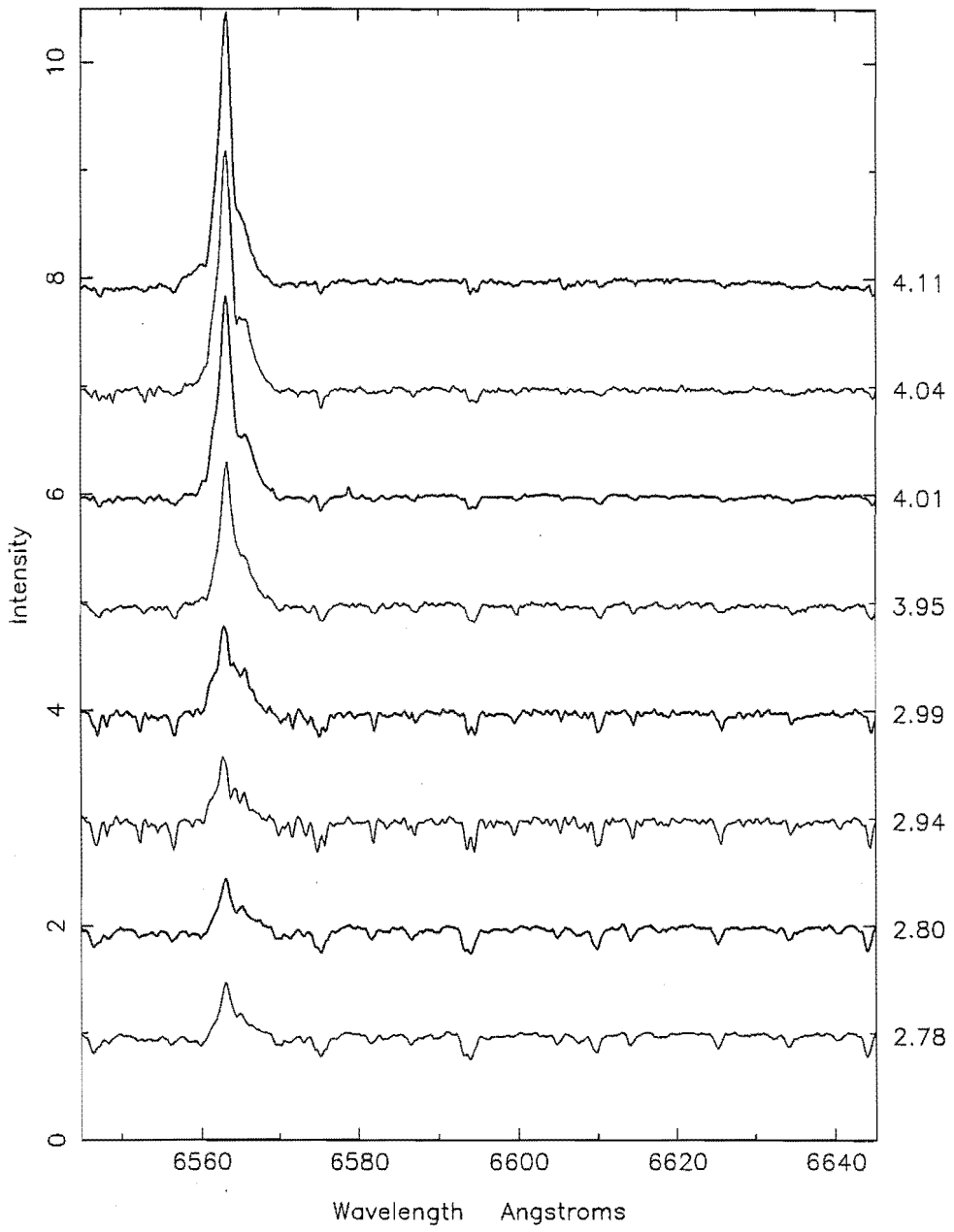

Figure 8.4: The phase sequence of stacked coudé spectra from MSO.

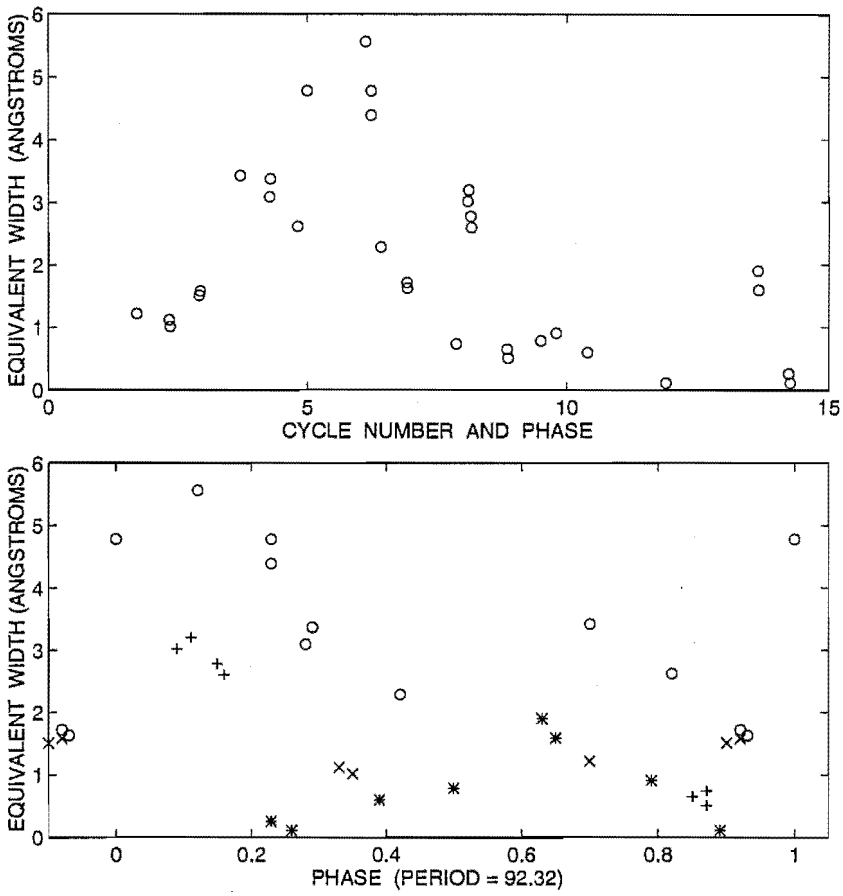

Figure 8.5: The Hα equivalent width plotted versus phase. In the bottom panel, the symbols are as follows: cycles 1–2 (x), cycles 3–6 (o), cycles 7–8 (+) and cycles 9–14 (*).

Table 8.2: The phase-dependent behaviour of the metallic and molecular lines in U Mon.

λ (Å)	species	χ (eV)	multiplet	comment
6191.571	Fe I	2.43	169	line-doubling during phases 0.2–0.3 and
6200.321	Fe I	2.61	207	possibly 0.6–0.7.
6213.437	Fe I	2.22	62	
6546.245	Fe I	2.76	268	
6570.164	Fe I	2.42	111	
6198.655	Ni I	4.26	–	emission at phases 0.2–0.3 and 0.6–0.7.
6210.671	Sc I	0.00	2	
6554.238	Ti I	1.44	102	
6743.127	Ti I	0.90	48	
6159.1	TiO	–	–	bandheads at phases 0.80–0.15.
6214.9	TiO	–	–	
6714.4	TiO	–	–	
6383.906	CN	–	–	bandheads at primary and secondary minima.
6747.620	CN	–	–	

equivalent width increasing and decreasing respectively. As well as Hα emission associated with the two shock waves per luminosity cycle, it appears that there is a further contribution to, or enhancement of, the Hα emission during cycles 3–6. It is likely that the Hα enhancement is related to the long-term period in this RVb type star, since cycles 3–6 correspond to the minimum of the long-term period in U Mon. We shall return to this phenomenon of Hα enhancement later in this chapter in Section 8.1.6 and in Chapter 9.

8.1.4 The metallic and molecular lines

As was seen in R Sct, lines of different excitation potential and multiplet behave in a different, but consistent, manner for each star. Due to the different effective temperatures and other physical conditions (including the composition) in the stellar envelopes, a range in behaviour will be seen for the same key lines in each of the RV Tauri stars in the programme.

During phases 0.2–0.3, most Fe I lines with excitation potentials between $\sim$ 2.0 eV and 3.0 eV display two components. Unfortunately, few spectra were obtained during phases 0.6–0.7 where the line-doubling associated with the second shock wave occurs. Comparing the U Mon spectra with those of R Sct reveals that the doubled components have a larger velocity spacing, indicating a greater intensity of the atmospheric shock wave.

The line-doubling behaviour is also seen in a number of other Fe I lines that

have similar excitation potentials. These are indicated in Table 8.2. It is possible that the Fe I line at 6546.245 Å displays a central emission component at phase 0.22 rather than a line-doubling. However, the line is perturbed in some way by the shock wave at this phase.

There are a variety of lines which display emission components. These may reveal themselves as emission in the cores of the absorption lines, pure emission lines or lines with P Cygni or inverse P Cygni type profiles. During phases 0.20–0.30 and 0.40–0.70, emission behaviour is seen in a range of metallic lines as listed in Table 8.2.

U Mon appears to get very cool during phases 0.80–0.10 as is evident from examining the stacked spectra of order 34 (see Fig. 8.3). Numerous lines of atomic species are apparent and these lines get particularly strong during phases 0.80–0.10. Molecular lines, mostly due to TiO, are quite obvious in the spectra during phases 0.80–0.15. The major bandheads of TiO which are observed in the U Mon spectra around primary minima are listed in Table 8.2. A rather strong bandhead is also seen at $\sim$ 6200 Å which we tentatively associate with the α system of TiO.

The CN bandheads at 6383.906 Å and 6747.620 Å, which were seen in R Sct at both primary and secondary minimum, are also seen in U Mon at the same phases. The latter bandhead is particularly strong.

8.1.5 Radial velocities

Radial velocities were obtained from the spectra shown in Fig. 8.3 using the line bisector method described in Section 6.12. The Fe I line at 6750.164 Å (χ = 2.42 eV, multiplet 111) was chosen because it appeared unblended and of sufficient strength to determine the radial velocities at all the observed phases.

The Fe I line at 6546.245 Å was not used in the analysis of the U Mon radial velocities since emission components of this line were present. To confirm the velocities obtained from the Fe I line at 6750.164 Å, the radial velocities of the Fe I line at 6200.321 Å (χ = 2.61 eV, multiplet 207) were also measured. The radial velocity curves obtained from these spectral lines are shown in Fig. 8.6, where a good agreement between the velocities of the two lines is seen. The phases in the top panel were calculated with a period of 92.32 d and the bottom panel is plotted with a period of 46.16 d, so that the two radial velocity cycles lie on top of each other.

Two discontinuities are obvious for the radial velocity curve plotted with the

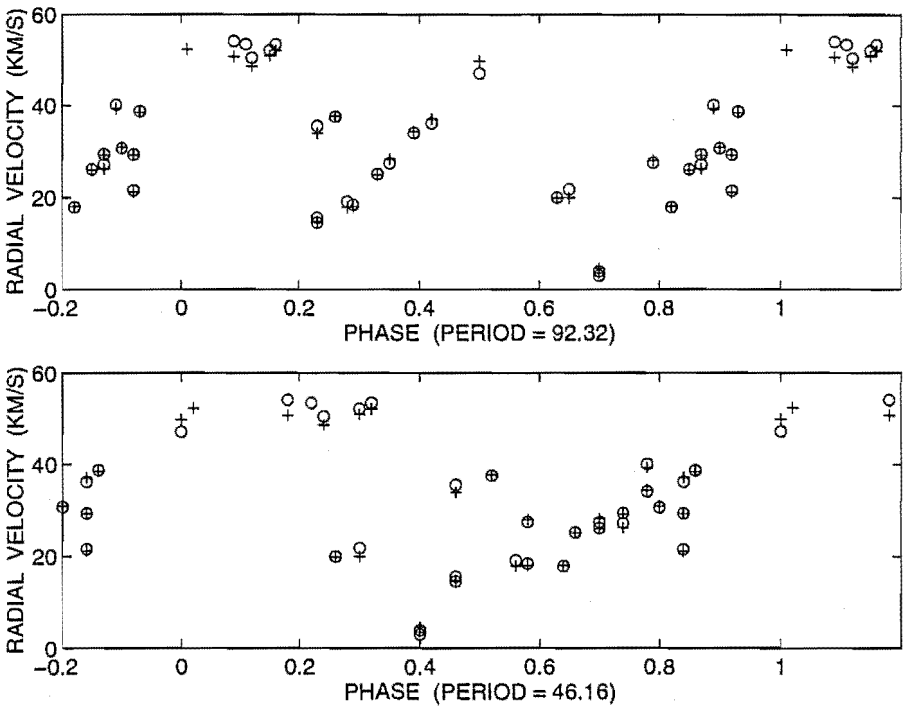

Figure 8.6: Radial velocity curves for U Mon. The radial velocities for the Fe I lines at 6200.321 Å (o) and 6750.164 Å (+) are shown for the MJUO spectra.

92.32-d period. These occur at phases ~ 0.2 and ~ 0.6. As was discussed in the previous section, these discontinuities arise when two components are visible for a particular line (line-doubling) and this behaviour is most apparent in U Mon in Fe I lines that have excitation potentials of $2.2\,\mathrm{eV} < \chi < 2.8\,\mathrm{eV}$. Line-doubling, and hence a discontinuous velocity curve, is evidence for the presence of an atmospheric shock wave. This is further confirmed by the presence of metallic emission lines during phases 0.2–0.3 and 0.6–0.7, as well as strong Hα emission around these phases.

8.1.6 Orbital parameters

A large scatter is seen in the radial velocity curves which is assumed to be as a result of the long-period radial velocity variations that have been reported for this star and other RV Tauri stars of the RVb subclass. The most likely explanation of these long-period radial velocity variations is orbital motion in a binary system. In order to investigate these long-period radial velocity variations further, previously published radial velocity data for U Mon was sought. These older radial velocity data (Sanford 1933, Abt 1955, Preston 1964) were combined with the new MJUO radial velocities in order to obtain an orbital solution. Radial velocities due to pulsational motion were averaged over to obtain a mean velocity for each set of data. Weights were assigned to each set of radial velocity data based on the accuracy of the measurements and the number of spectroscopic observations involved. If a large number of spectra were obtained, then the pulsational variations were much more well-defined and it was easier to estimate the long-period trend in each set of data.

From analysing the radial velocity data for U Mon (Sanford 1933, Abt 1955, Preston 1964, this thesis) the orbital parameters derived are:

- Period, $P = 2597 \pm 6\,\mathrm{d}$
- Centre-of-mass velocity, $V_\gamma = +34.9 \pm 0.7\,\mathrm{km\,s^{-1}}$
- Radial-velocity semi-amplitude, $K_1 = 17 \pm 1\,\mathrm{km\,s^{-1}}$
- Eccentricity, $e = 0.43 \pm 0.05$
- Longitude of periastron, $\omega = (191 \pm 6)^\circ$
- Julian Date of periastron − 2400 000, $T_0 = 27\,573 \pm 58$ d

- $a \sin i = 537 \pm 36\,\mathrm{Gm}$
- Mass function, $f(M) = 0.915 \pm 0.018 M_\odot$

The calculated orbit and the averaged radial velocities are plotted versus orbital phase in Fig. 8.7 (top panel). Phase 0.0 is defined as the time of periastron passage, T_0. The individual radial velocities determined for the Fe I line at 6750.164 Å in U Mon (Section 8.1.5) are shown together with the orbital solution in Fig. 8.7 (bottom panel). These latter radial velocities include both the pulsational variations as well as the long-period variations due to orbital motion.

For a given inclination angle, it is possible to calculate the dimensions of the orbit of the RV Tauri star, U Mon (the semi-major axis a, the semi-minor axis b and the periastron distance) and the mass of the companion star, M_2. If we assume that the typical mass for an RV Tauri star is $M_1 = 0.8 M_\odot$ (the mass is generally considered to be in the range 0.6–1.0 $M_\odot$), then the centre of mass of the system, the separation of the two stars and the size of the Roche lobe for each star can be calculated (Paczyński 1971, de Loore & Doom 1992) for a given inclination angle. The effect of the orbital inclination on the derived value of the companion mass, semi-major axis and the minimum stellar separation are shown in Fig. 8.8.

From the amplitude of the radial velocity variations and the derived value of the companion mass, realistic limits can be placed on the value of i, the inclination angle. The radial velocity amplitude ($\sim 34\,\mathrm{km\,s^{-1}}$ full amplitude) is relatively large compared to other RV Tauri stars which would suggest the orbit is orientated closer to edge-on ($i = 90°$) than face-on ($i = 0°$). For realistic companion masses ($M_2 < 10 M_\odot$), orbital inclinations $i > 30°$ are required.

Using the derived orbital elements and for an inclination angle of 60 degrees, the orbit and Roche lobes for various choices of the U Mon mass have been calculated and are displayed in Fig. 8.9. The relative position of U Mon (large filled circle) and the secondary (small open circle) are shown for the closest approach (periastron) of the two stars. The mean radius of the RV Tauri star is taken to be $\sim 100 R_\odot$ or 70 Gm. U Mon is drawn to scale in the diagram but the (unseen) secondary is not. The solid lines indicate the path of the orbit of U Mon and the size of the Roche lobes for both stars. The centre of mass of the binary system is shown by the asterisk. The semimajor axis is represented by the dotted line. The value of the longitude of periastron obtained from the orbital analysis ($\omega = 191°$) means that the orbit is rotated slightly (11°) towards the Earth. U Mon is thus

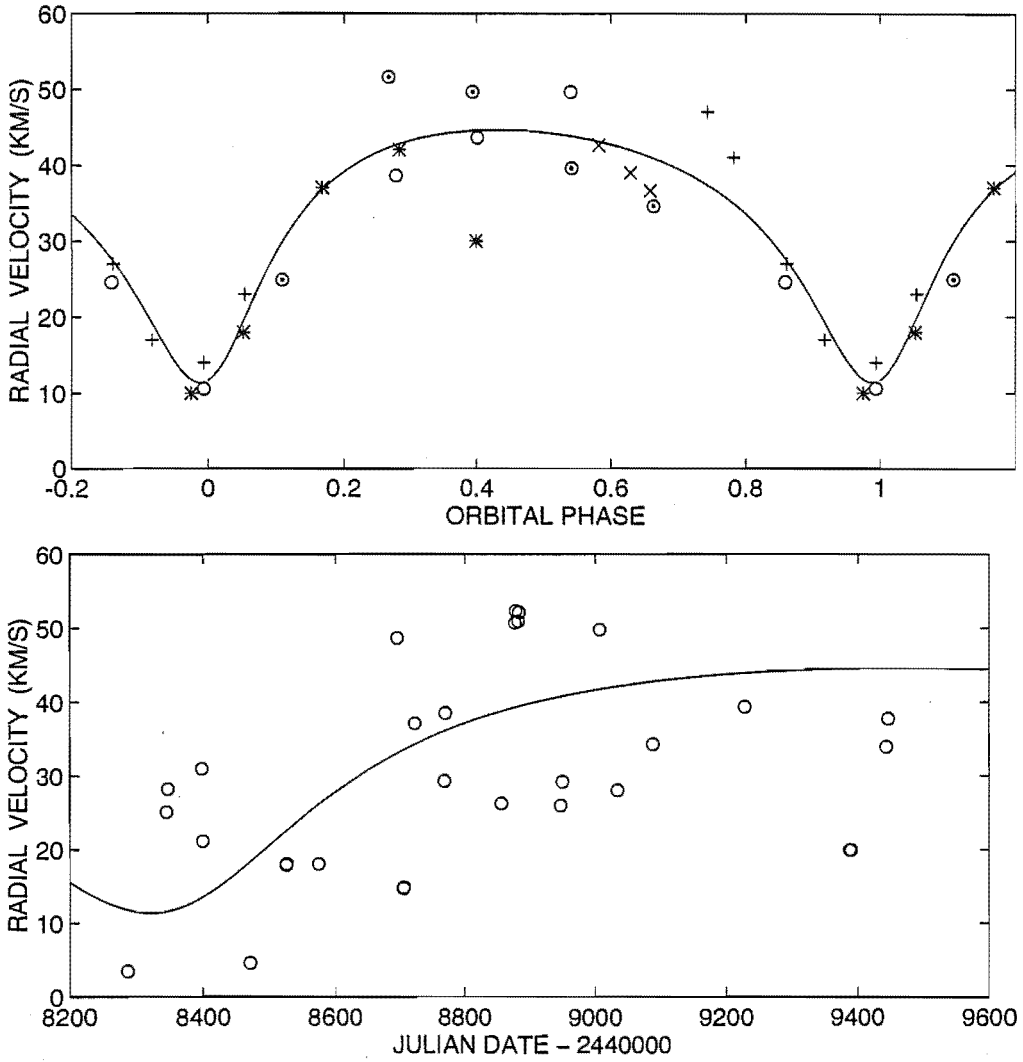

Figure 8.7: The orbital solution for the combined mean radial velocities for U Mon. Symbols: Sanford (1933) data from 1922–1926 (o); Sanford (1933) data from 1927–1932 (⊙); Abt (1955) data (x); Preston (1964) data (+); MJUO data (*). The bottom panel shows the individual MJUO radial velocities and the orbital solution versus Julian Date.

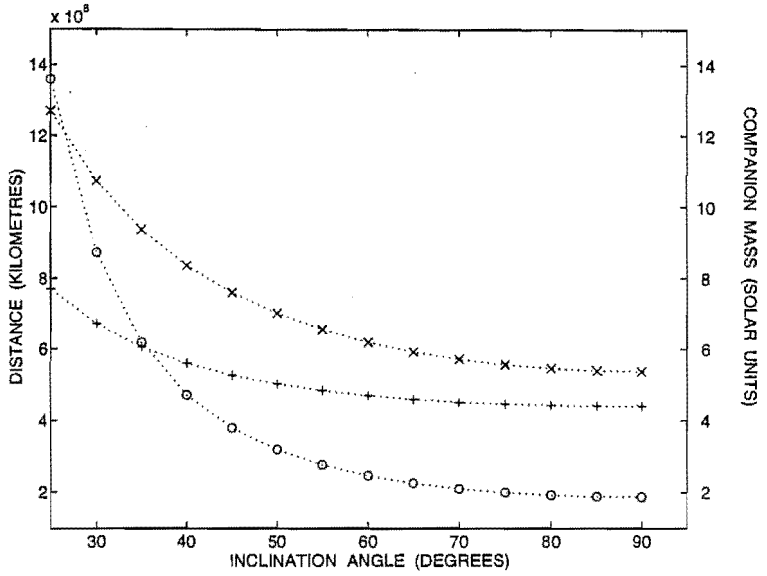

Figure 8.8: The effect of the orbital inclination on the derived value of the companion mass (o), semi-major axis (×) and the minimum stellar separation (+).

closer to the Earth at periastron (as pictured) than at apastron.

The effect of varying the orbital eccentricity was also investigated. The derived value (and formal error) for the eccentricity of the orbit is $e = 0.43 \pm 0.05$. However, certain random and systematic uncertainties have not been accounted for in the calculation of this formal error and the real uncertainty may be much higher. The radial velocities used in the analysis are taken from Sanford (1933), Abt (1955) Preston (1964) and this thesis. Systematic differences between the different sets of radial velocity measurements are likely. These could arise from differences in the instrumental set-up, including the dispersion used, in the techniques of measuring radial velocities and in the particular choice of lines to measure. In addition, poor phase sampling of the spectroscopic observation make it much harder to model the short-term radial velocity variations which will, in turn, make the estimates of the long-term radial velocities more uncertain.

A range of orbital eccentricities was consequently considered. The eccentricity, period and time of periastron passage were held constant, while the orbital parameters V_γ, K_1 and ω were allowed to vary in order to achieve a 'best-fit' orbit for a given eccentricity. The orbital elements were derived for U Mon orbital eccentricities of 0.30, 0.43, 0.50, 0.60, 0.70. Taking $0.8\,M_\odot$ as a reasonable mass

(a) M_1=0.6$M_\odot$, M_2=2.3$M_\odot$

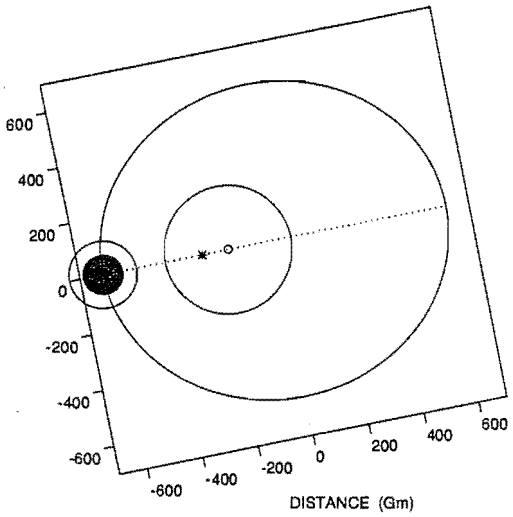

(b) M_1=0.8$M_\odot$, M_2=2.5$M_\odot$

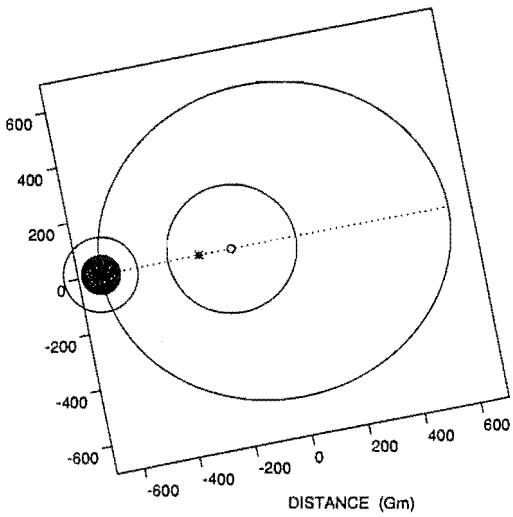

(c) M_1=1.0$M_\odot$, M_2=2.7$M_\odot$

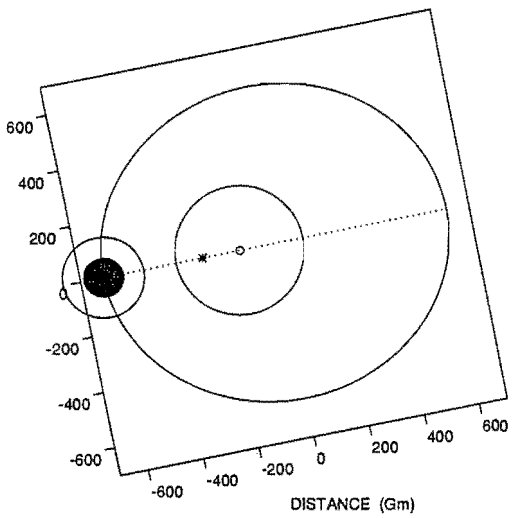

(d) M_1=2.0$M_\odot$, M_2=3.5$M_\odot$

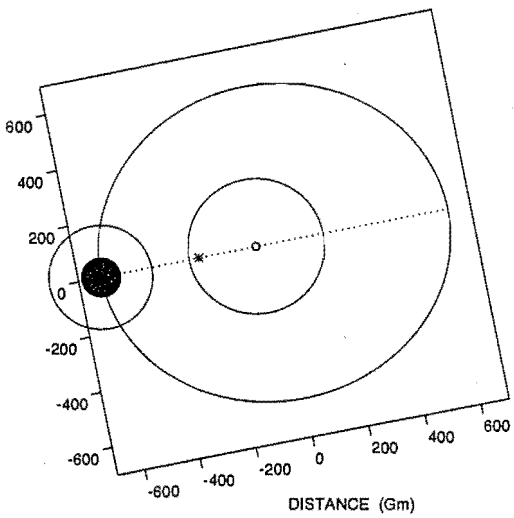

Figure 8.9: The orbit and Roche lobes based on different assumed masses for U Mon, but with $i = 60°$ and e=0.427.

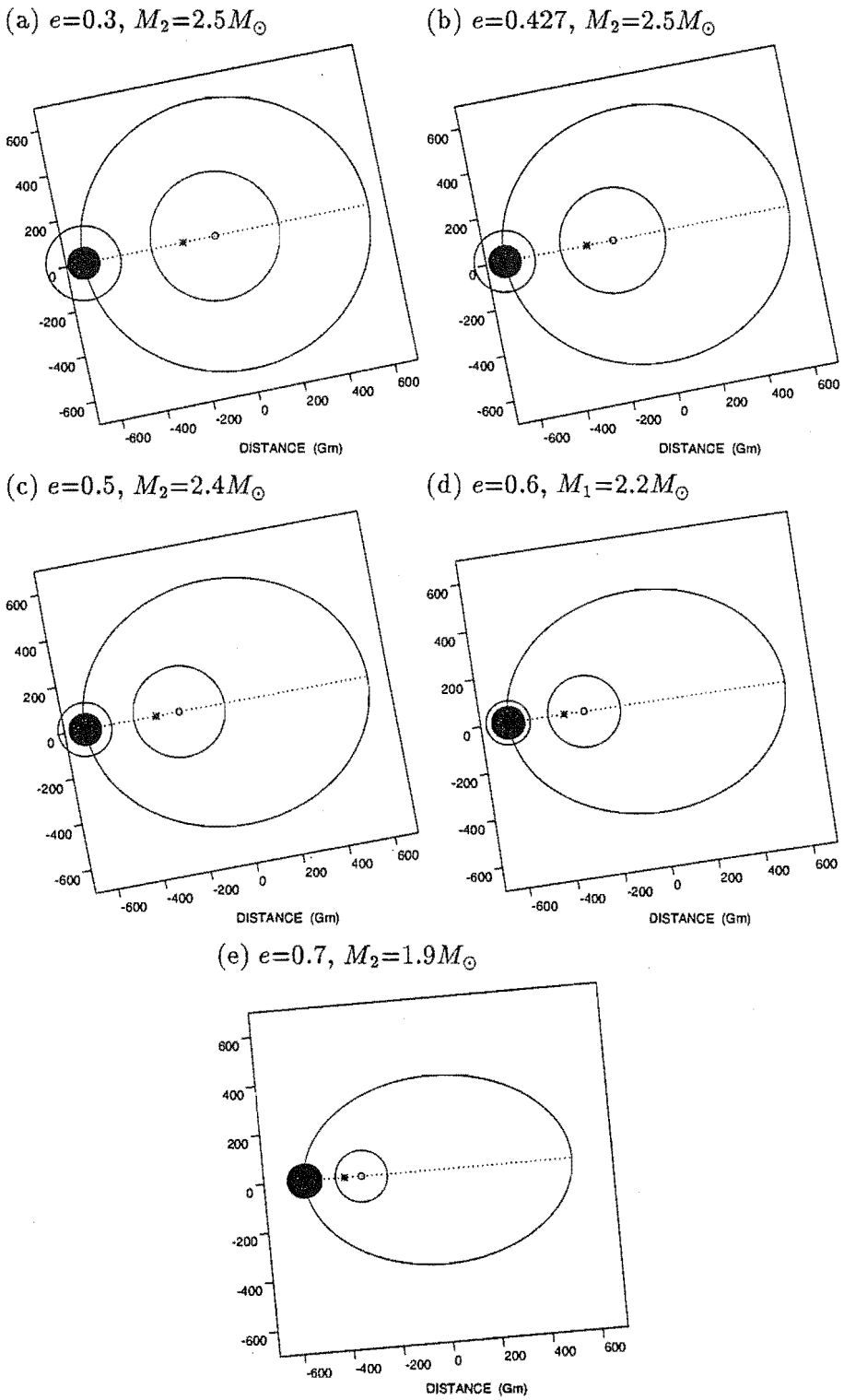

Figure 8.10: The relative dimensions of the U Mon orbit and Roche lobes for various eccentricities, but with $i = 60°$ and M_1=0.8$M_\odot$.

for U Mon, the orbital elements can be used to calculate the companion mass, the dimensions of the orbit and the Roche lobes for both stars as a function of the inclination angle. These are displayed in Fig. 8.10 for an inclination angle of 60°. U Mon is plotted to scale where the mean radius is taken to be $\sim 100 R_{\odot}$ or 70 Gm.

The conditions for mass loss from the RV Tauri star U Mon at periastron passage in the orbit can be investigated using the relative sizes of the Roche lobes and changes in radius of the star during radial pulsations. The sizes of the Roche lobes quite dependent on the choice of RV Tauri star mass and the eccentricity of the orbit which defines the separation of the two binary components. There is only a slight dependence on the inclination angle. The effect of the eccentricity of the orbit was considered by assuming a size of $100 R_{\odot}$ and a mass of $0.8 M_{\odot}$ for U Mon.

For very eccentric orbits, $e > 0.69$, the mean radius of the star exceeds the Roche radius and thus mass loss would occur. For an eccentricity of 0.60, the mean radius of the star is less than the Roche radius, but radius changes of only $\sim 30\,\%$ during pulsation (or $\sim 30\,R_{\odot}$) will result in mass loss. For mass loss at periastron where the orbit has an eccentricity of 0.50, the required change in radius is $\sim 65\,\%$ (or $\sim 65\,R_{\odot}$). A change in radius of $\sim 90\,\%$ for an eccentricity of 0.43, or $\sim 130\,\%$ for an eccentricity of 0.30, will result in mass loss during pulsations. If the mass of U Mon is less than the assumed $0.8 M_{\odot}$, say $0.6 M_{\odot}$, the required radius changes for mass loss to occur are less. For orbital eccentricities of 0.43 and 0.50, radius changes of $\sim 70\,\%$ and $\sim 45\,\%$ during pulsation are required for mass loss to occur at periastron.

One question that we would like to answer is whether we see any evidence of mass loss in the U Mon system, since the calculated orbital solution suggests that this may be possible at periastron passage. Fig. 8.11 shows the orbital phases when spectroscopic observations of U Mon were obtained at MJUO. The cycle numbers which are displayed in this figure correspond to the phasing of the stacked spectra shown previously. The MJUO spectra have sampled almost half an orbital cycle, with the spectroscopic observations starting just before periastron and finishing just before apastron. The evidence we have for possible mass loss in this system includes the enhanced Hα emission that was seen in Fig. 8.5 during (pulsational) cycles 3 to 6 and the orbital phase at which these spectra were obtained. We suggest that the RV Tauri star is losing or transferring mass

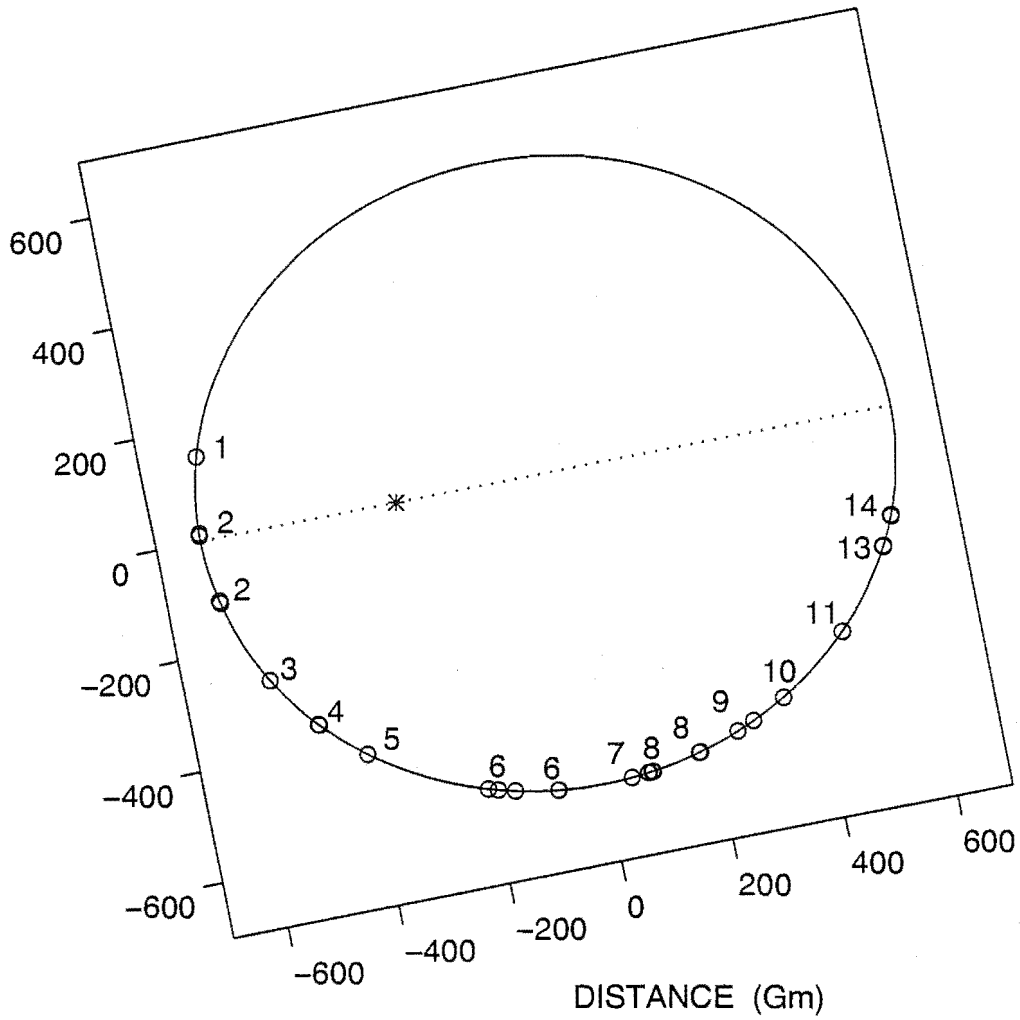

Figure 8.11: The orbital phases at which MJUO spectra of U Mon were obtained.

during the orbital phase at which enhanced Hα emission is observed. However, this does not coincide exactly with the closest approach to the companion star but is a short time afterwards.

A number of possibilities exist that may explain this phenomenon. First, the orbital solution (or more specifically, the value of ω or T_0, the longitude or Julian Date of periastron) may not be quite correct. Second, the enhanced Hα emission that is seen could be evidence of mass loss taking place through the second (or outer) Lagrangian point of U Mon. The phases a which enhanced Hα emission is present are indeed those where the second Lagrangian point would be visible. This would suggest that U Mon is losing mass to a circum-binary shell or disk rather than (or as well as) transferring mass to the companion star. It would be worth investigating whether enhanced Hα emission is seen at the orbital phase when the first (or inner) Lagrangian point of U Mon is visible. The third explanation for enhanced Hα emission occurring slightly after periastron passage is that mass loss is not initiated until periastron passage but, once started, the enhanced Hα emission continues for part of the orbital cycle. This would be the case if the enhanced Hα emission arises from material that is lost or transferred at periastron passage, but which is subsequently visible for a part of the orbital cycle. A final suggestion is that the enhanced Hα emission derives purely from the atmospheric shock waves having greater strength at certain orbital phases due to the proximity of the companion star (for example, gravitational effects such as the increasing non-spherical geometry of the RV Tauri star).

To investigate the first possibility, the orbital velocities were subtracted from the MJUO radial velocities measured from the Fe I lines in U Mon. These residual velocities should therefore be due purely to pulsational variations with no orbital component. These radial velocities are plotted in Fig. 8.12. There does not appear to be any improvement in the scatter of the radial velocity curve from Fig. 8.6 such as we would expect if the scatter was mostly due to orbital effects and assuming that the orbital solution is correct. The points that fall furthest from the radial velocity curve are from cycle 2, which does suggest a possible systematic problem with the orbital solution. However, the semi-regular nature of the pulsational variations in the RV Tauri stars does complicate this analysis.

Further spectroscopic observations are required to confirm and refine this orbital solution. Additional spectroscopic observations would also be useful in verifying at which phases in the orbital cycle the enhanced Hα emission occurs.

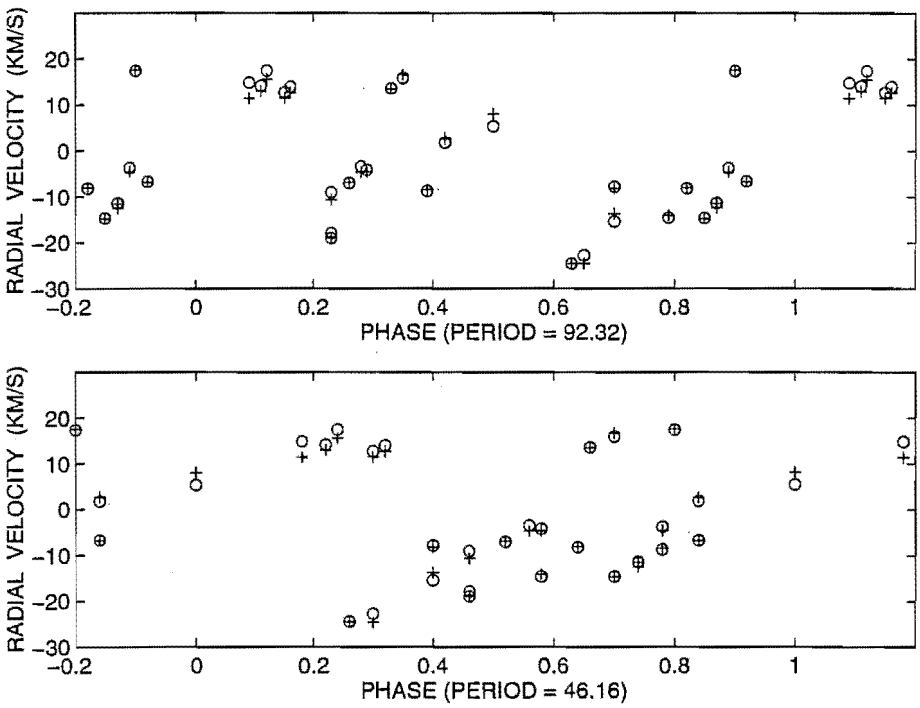

Figure 8.12: Pulsational radial velocity curves for U Mon. The orbital component of the radial velocities has been subtracted, leaving the radial velocity variation due to pulsation. The radial velocities for the Fe I lines at 6200.321 Å (o) and 6750.164 Å (+) are plotted .

This would allow the above suggested possibilities for this enhanced Hα emission to be investigated and the likely cause could thus be determined.

Preston (1972) obtained spectra of U Mon that appeared to show that two expanding, circumstellar shells observed in 1963 may have merged to give a single expanding shell in 1972. This would indicate that current mass loss may indeed be taking place, adding weight to the suggestion that enhanced Hα emission arises from mass loss or transfer initiated at periastron passage.

8.2 AI Sco

8.2.1 Previous spectroscopy of AI Sco

AI Sco was included in Joy's (1952) spectroscopic survey of the RV Tauri and related classes. A spectral range of G0–K2 was found from three plates of the object. The radial velocities varied between −3 and −40 km s^{-1}, with the most negative velocity corresponding to the earliest spectral type of G0. Preston et al. (1963) classified AI Sco as a member of group 'A' (strong-lined) from two spectra of the star.

8.2.2 Spectroscopic observations of AI Sco

Nine high-resolution coudé spectra were obtained of AI Sco using the 1.9-m telescope at MSO between 1991 May and 1991 September. Exposure times were typically between 4 and 10 minutes. Due to the faintness of the star, only one spectrum of AI Sco was obtained at MJUO using the 1.0-m telescope, échelle spectrograph and CCD detector. This 60 minute spectrum was obtained in 1991 August. Table 8.3 is a log of the spectroscopic observations for AI Sco.

These spectra were lightly smoothed and their phases calculated according to the ephemeris:

$$\text{Primary (photometric) minimum} = 2448373.93 + 71.03\,E$$

where phase 0.0 defines the time of primary V minimum. The MJUO V photometry and the dates when spectra were obtained at both MJUO and MSO are shown in Fig. 8.13 (top panel). The spectral phase coverage and the phased MJUO V observations are shown in the bottom panel in this figure. From this figure it can be seen that all the spectra were obtained while AI Sco was at the maximum of its long period light variation.

Table 8.3: Spectroscopic observations of AI Sco.

UT date	HJD [a] 2440000+	site	observer	phase (ϕ)	W_λ(Hα) (Å)	rv(Fe)[b] (km s^{-1})
1991-May-25	8402.070	MSO	WAL	0.40	4.32	−19.5
1991-May-30	8407.152	MSO	WAL	0.47	4.17	−1.9
1991-Jun-04	8412.082	MSO	WAL	0.54	3.82	+8.0
1991-Aug-02	8470.930	MJUO	KRP	1.37	3.20	+0.4
1991-Aug-21	8490.035	MSO	KRP	1.64	1.20	−39.2
1991-Aug-25	8494.059	MSO	KRP	1.69	1.32	−30.0
1991-Aug-31	8499.953	MSO	KRP	1.77	1.52	−21.4
1991-Sep-02	8501.920	MSO	KRP	1.80	1.64	−20.2
1991-Sep-05	8505.098	MSO	KRP	1.85	1.89	−18.5
1991-Sep-07	8507.094	MSO	KRP	1.88	2.05	−10.3

[a] for mid time of observation
[b] radial velocity for the Fe I line at 6546.245Å.

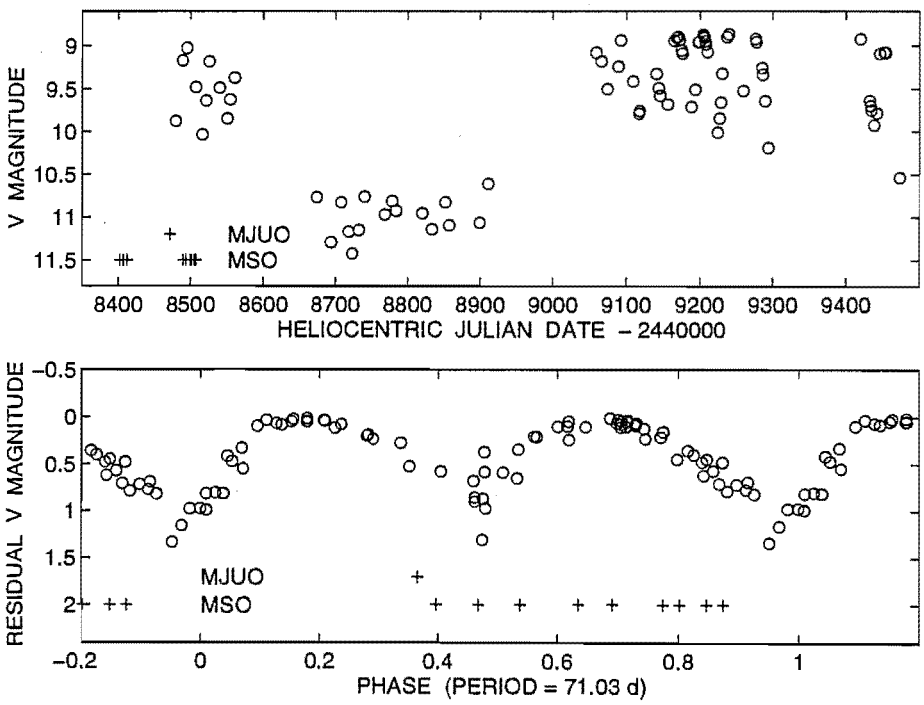

Figure 8.13: Light curves and spectral phase coverage for AI Sco. The MJUO photometric observations (o) and spectroscopic observations (+) from both MJUO and MSO are shown versus heliocentric Julian Date (top panel) and versus phase (bottom panel).

The spectra were then stacked in a phase sequence, with the earliest phases at the bottom of Fig. 8.14. These spectra confirm the strong-lined nature of this star and reveal similarities to R Sct and U Mon, which are also Preston 'A' type stars. Although a reasonable phase coverage was obtained (considering the small number of spectra), little evidence of metallic line-doubling or emission features is seen. It is possible that line doubling or emission may be present during phases 0.54–0.69 when the metallic lines appear to be at their weakest, but may not be resolved on the MSO spectra if the shock intensity is small. (The line doubling for U Mon, which appears to have a relatively large shock intensity as shown by the more widely separated 'doubled-components', was barely resolved on the lower resolution MSO spectra.)

8.2.3 The Hα profile in AI Sco

A dramatic change in the appearance of the Hα profile is apparent on the sequence of stacked spectra. During phases 0.40–0.54 in cycle 0 and at phase 0.37 in cycle 1 the Hα line has a very strong absorption component. The blueward side of the line displays a broad absorption wing, while on the redward side the profile is very steep and a slight emission peak is seen. During phases 0.64–0.88 in cycle 1, the profile changes drastically. The line exhibits an extremely narrow absorption core and emission is apparent on both wings with the redward emission being stronger. Due to the small number of spectra obtained it is difficult to ascertain whether these changes are simply phase-dependent or whether they arise from cycle-to-cycle variations.

The equivalent width of the Hα line was measured on all the MJUO and MSO spectra in order to investigate the phase dependence of the Hα emission strength. These equivalent width measurements are listed in Table 8.3 and indicate a net overall absorption contribution in all spectra. Fig. 8.15 shows the variation of the Hα equivalent width with phase. Cycle 0 and the first half of cycle 1 show a large equivalent width which is associated with a strong broad absorption component that seems to disappear later in cycle 1.

8.2.4 The radial velocity curve for AI Sco

Radial velocities were calculated from the spectra shown in Fig. 8.14 using the line bisector method described in Section 6.12. The radial velocities were measured for the Fe I lines at 6546.245 Å and at 6569.224 Å. The radial velocity measurements

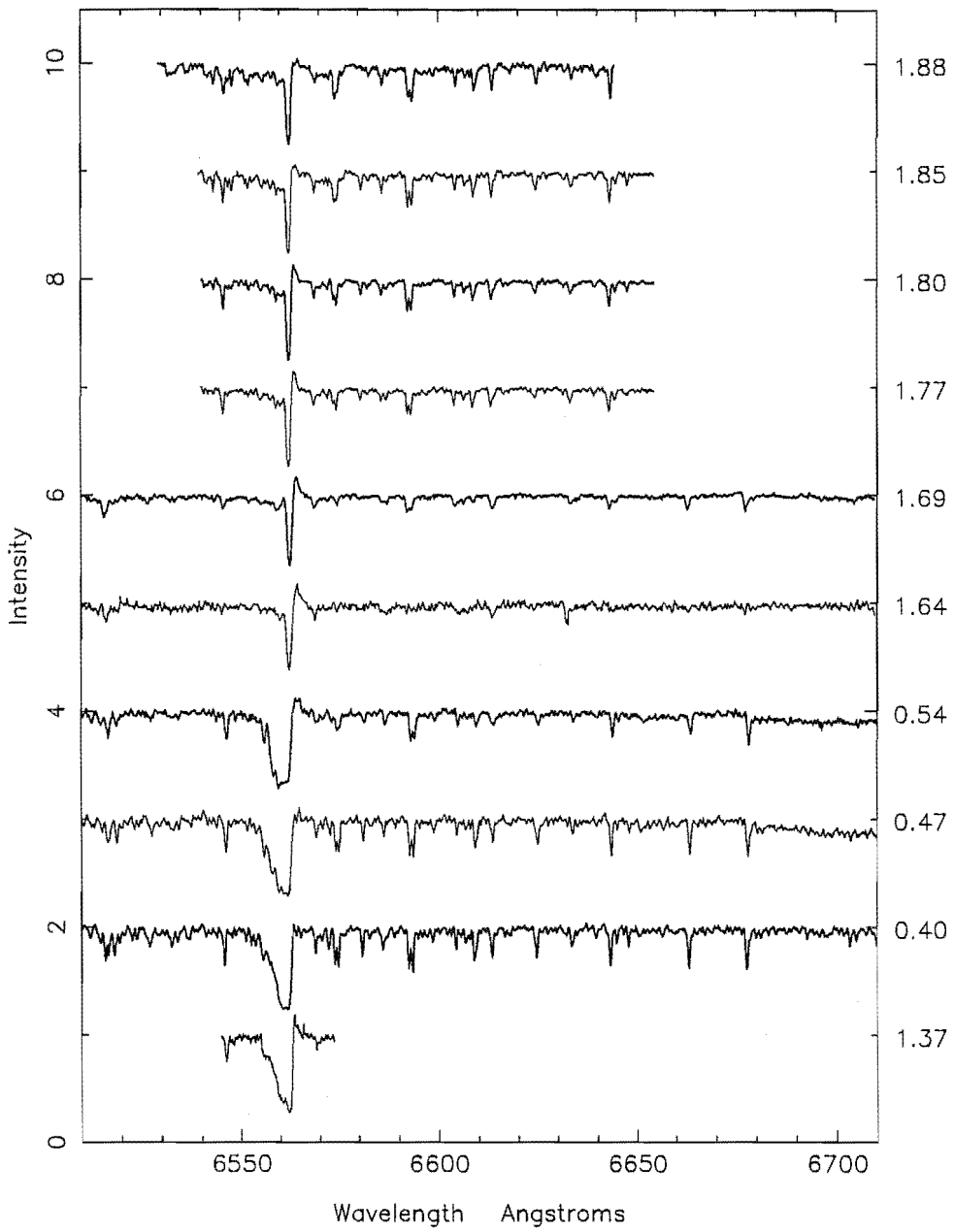

Figure 8.14: Stacked spectra of the Hα region in AI Sco. The cycle number and phase are indicated to the right of each spectrum.

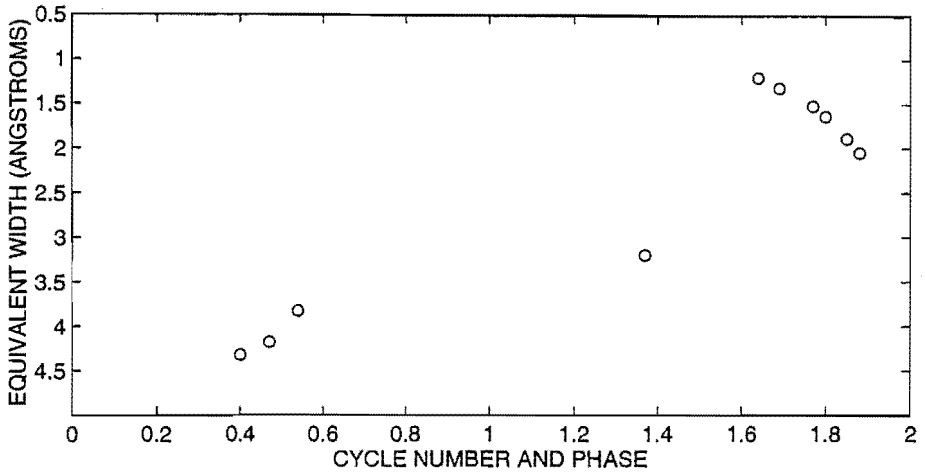

Figure 8.15: The phase dependence of the Hα equivalent widths in AI Sco. The equivalent widths measurement at phase 0.37 in cycle 1 is from the MJUO spectrum while all other measurements are from the MSO spectra.

for the former Fe I line are included in Table 8.3.

Fig. 8.16 compares the radial velocity curves calculated with periods of 70.03 d (top panel) and 35.51 d (bottom panel). The radial velocity curves have a peak-to-peak amplitude of about 50 km s^{-1}, which is one of the largest amplitudes obtained for the programme RV Tauri stars. Plotted with the 70.03 d period, a discontinuity is apparent at phase ~ 0.64. This corresponds to the phase at which the metallic lines are extremely weak. The radial velocity curve is consistent with two velocity cycles being present per 70.03 d luminosity period. This is verified by the good agreement shown between the two radial velocity cycles when they are plotted modulo the 35.51 d period (bottom panel).

8.3 AR Pup

8.3.1 Previous spectroscopy of AR Pup

AR Pup was included in the survey of RV Tauri stars by Payne-Gaposchkin et al. (1943), where the spectral range was noted to be cF0–cF8. Low dispersion spectrograms were used by Rosino (1951) to assign spectral types to a number of RV Tauri stars, including AR Pup. From the one spectrum taken, this star was classified as an Rp type, indicating a carbon-enhanced object.

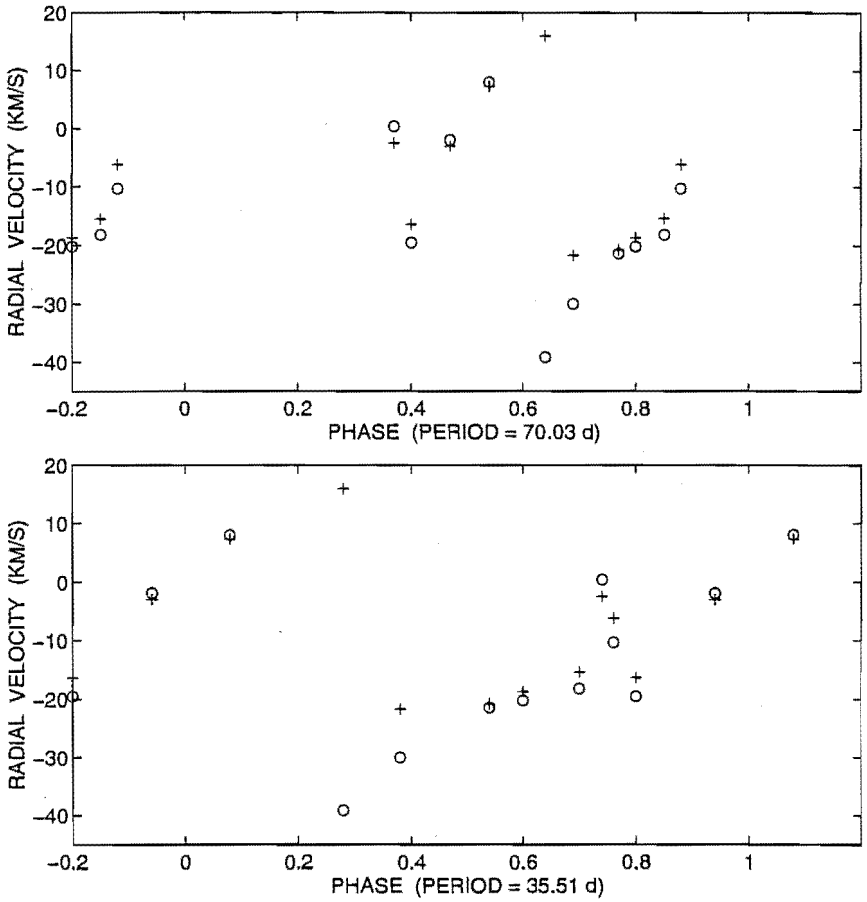

Figure 8.16: The radial velocities for AI Sco, measured from the Fe I lines at 6546.245 Å (o) and at 6569.224 Å (+). The phases in the top panel are calculated using a period of 70.03 d and the bottom panel using a period of 35.51 d.

Table 8.4: Spectroscopic observations of AR Pup.

UT date	HJD [a] 2440000+	region	site	observer	phase (ϕ)	W_λ(Hα) (Å)	rv(C) [b] (km s^{-1})
1991-Mar-31	8346.875	Hα	MJUO	KRP	3.55	−1.55	–
1991-May-10	8386.867	Hα	MSO	WAL	4.06	−1.24	–
1991-May-12	8388.887	Hα	MSO	WAL	4.09	−1.42	–
1991-May-21	8397.875	Hα	MJUO	KRP	4.20	−1.29	–
1991-May-22	8398.855	Li	MJUO	KRP	4.21	–	–
1991-May-23	8399.859	Hα	MJUO	KRP	4.23	−1.06	–
1991-May-24	8400.867	Li	MJUO	KRP	4.24	–	–
1991-May-25	8401.859	Hα	MSO	WAL	4.25	−1.05	41.9
1991-May-26	8402.875	Hα	MSO	WAL	4.27	−0.99	45.2
1991-May-28	8404.879	Hα	MSO	WAL	4.29	−0.86	40.0
1991-Jun-03	8410.820	Hα	MJUO	KRP	4.37	−0.68	–
1991-Aug-25	8494.230	Hα	MSO	KRP	5.44	−0.98	52.0
1991-Aug-31	8500.227	Hα	MSO	KRP	5.52	−1.14	53.7
1991-Sep-03	8503.230	Hα	MSO	KRP	5.56	−1.35	51.8
1991-Sep-09	8509.219	Hα	MSO	WAL	5.63	−1.59	47.7
1991-Dec-03	8494.098	Hα	MJUO	MDA	6.72	−1.41	–
1992-Mar-13	8695.012	Hα	MJUO	MDA	8.02	−1.99	–
1992-Mar-23	8704.898	Hα	MJUO	KRP	8.15	−2.24	–
1992-May-26	8768.816	Hα	MJUO	KRP	8.97	−0.94	–
1992-Sep-12	8878.199	Hα	MJUO	KRP	10.38	−0.74	–
1992-Sep-17	8883.172	Hα	MJUO	KRP	10.44	−0.73	–

[a] for mid time of observation
[b] radial velocity for the C I line at 6587.622Å.

Using factor analysis of the DDO colours of RV Tauri stars, Mantegazza (1984) showed that AR Pup could be a member of one of the metal-weak Preston subtypes (either 'B' or 'C'). Lloyd Evans (1985) classified AR Pup on the Preston scheme as a member of the 'B' spectroscopic subtype (carbon-enhanced).

8.3.2 Spectroscopic observations of AR Pup

Between 1991 March and 1992 September, twelve high-resolution échelle spectra of U Mon at various wavelength regions were obtained at MJUO using the 1.0-m telescope and CCD detector. The spectra obtained at MJUO typically had exposure times of 60 minutes. Between 1991 May and 1991 September nine high resolution coudé spectra were obtained using the 1.9-m telescope at MSO. Exposure times using the MSO spectrograph were typically 5 to 10 minutes. Table 8.4 is a log of the spectroscopic observations for AR Pup.

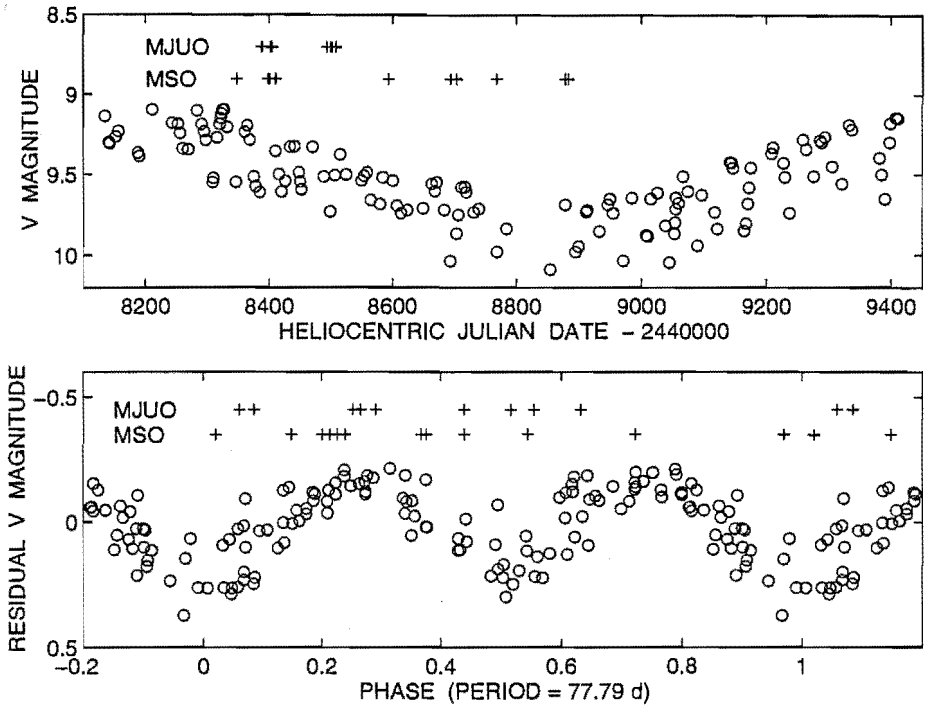

Figure 8.17: Light curves and spectral phase coverage for AR Pup. The MJUO photometric observations (o) and the times when spectroscopic observations (+) were obtained are shown versus heliocentric Julian Date (top panel) and versus phase (bottom panel).

These spectra were then lightly smoothed and their phases calculated according to the ephemeris:

$$\text{Primary (photometric) minimum} = 2448071.09 + 77.79\,E.$$

The MJUO V photometry and the dates when spectra were obtained at both MJUO and MSO are shown in Fig. 8.17 (top panel). The spectral phase coverage and the phased MJUO V observations are shown in the bottom panel in this figure. A reasonable phase coverage for the short (pulsational) period appears to have been obtained. The descending branch and the minimum of the long period light variation has been sampled by the spectroscopic observations.

Stacked spectra of the region around the Hα line are shown in Fig. 8.18 for the MJUO spectra and Fig. 8.19 for the MSO spectra. The most striking feature in the spectra is the single, strong emission line of Hα. The profile appears to be quite simple with no obvious absorption components. The exception is the spectrum obtained at phase 0.97 in cycle 8, where a redward emission wing of

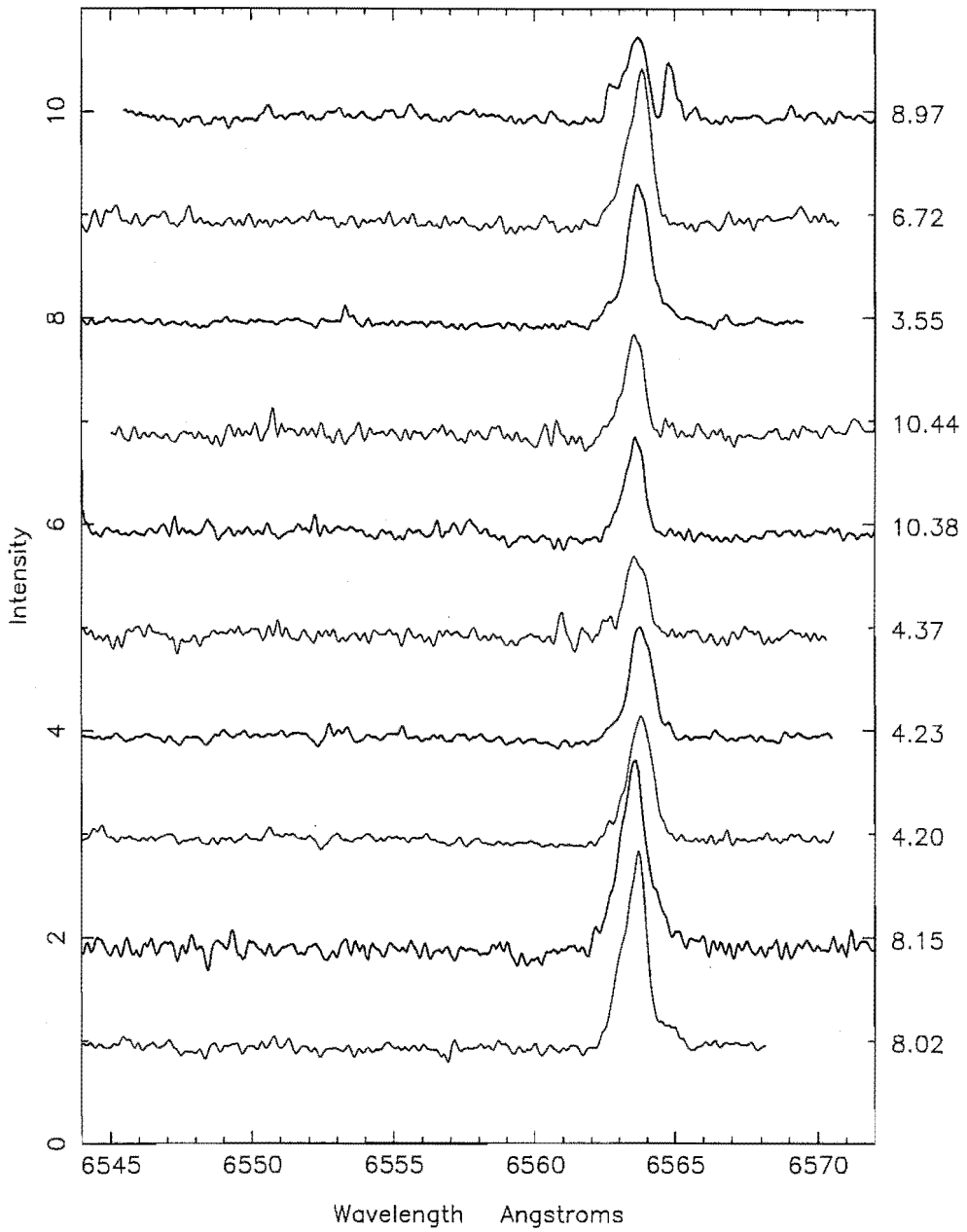

Figure 8.18: Stacked MJUO spectra of échelle order 35, which include the Hα line of AR Pup. The cycle number and phase are indicated to the right of each spectrum.

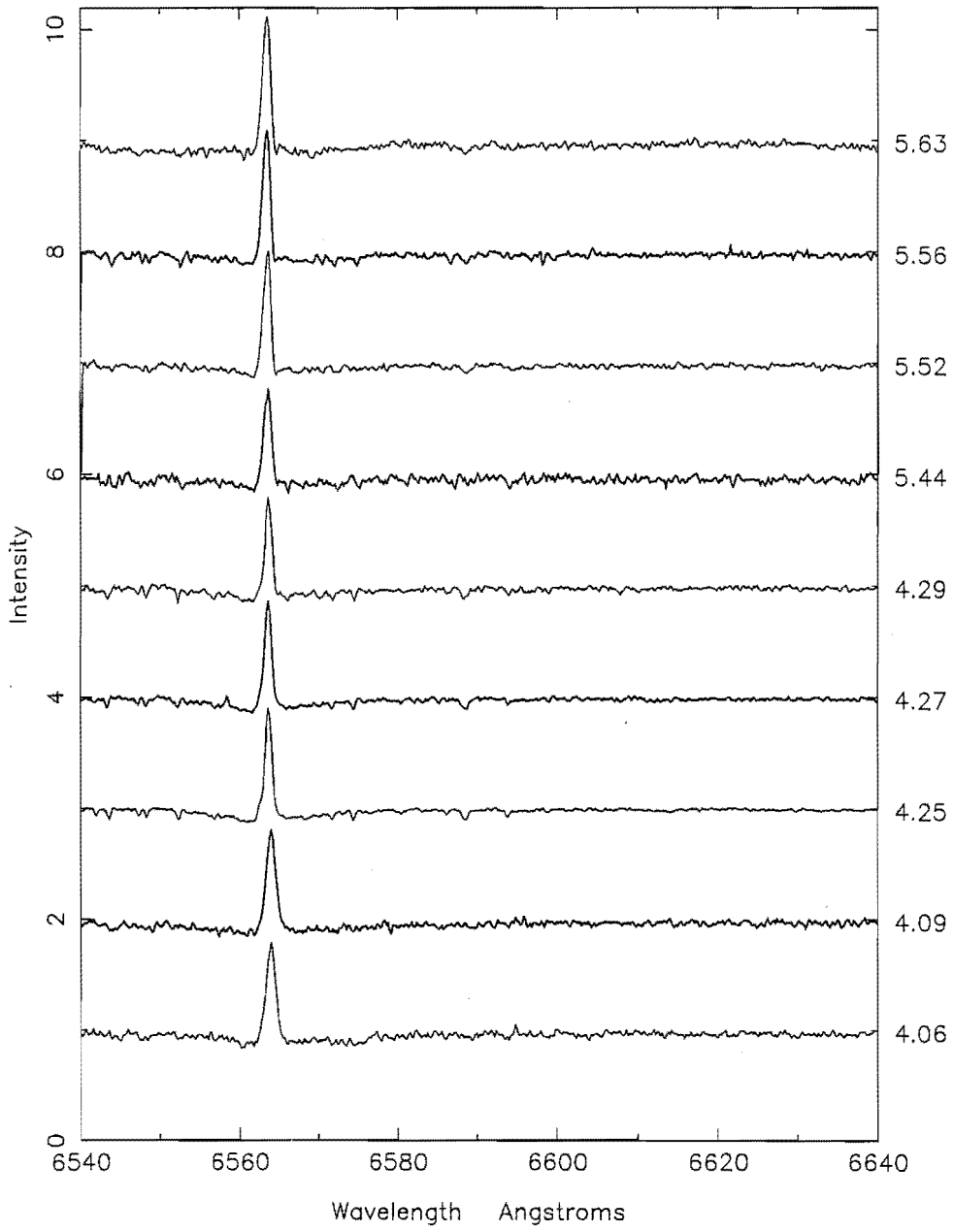

Figure 8.19: Stacked MSO spectra of the region around the Hα line in AR Pup. The cycle number and phase are indicated to the right of each spectrum.

the Hα emission appears. In general, the continuum is depressed on either side of the Hα profile due to broad hydrogen absorption wings. This is most apparent on the sequence of stacked MSO spectra (Fig. 8.19).

Very few metallic lines are visible on the stacked spectra of AR Pup. An extremely weak line of C I is seen on the MSO spectra at a wavelength of 6587.622 Å ($\chi = 8.53$ eV, multiplet 22). Virtually all the other weak lines that appear on the MSO spectra are identified as telluric H_2O lines.

8.3.3 The Hα line profile and radial velocities

The phase dependence of the Hα emission strength was investigated by measuring the equivalent width of the Hα line on all the spectra. A negative equivalent width measurement indicates an overall emission contribution and this was found to be the case for all the AR Pup spectra. These equivalent width measurements are included in Table 8.4. The phase dependence of the Hα equivalent width is displayed in Fig. 8.20.

The periodic nature of the strength of the Hα equivalent width is quite apparent with peaks in the Hα line strength occurring at phases ~ 0.15 and ~ 0.65. This is similar behaviour to what is observed to occur in the other RV Tauri stars and provides evidence for the presence of two shock waves per luminosity period. There appears to be little cycle-to-cycle variation in the strength of the Hα line, except for the very obvious increased strength in cycle 8 at phases 0.02 and 0.15.

At first glance, the Hα line appears to present a simple emission component. However, when the profile is examined in greater detail, the line appears quite asymmetric as if the redward side of the line is affected by an absorption feature. This can be seen in Fig. 8.21, where the Hα profile on the spectrum obtained at phase 0.02 in cycle 8 has been fitted by one (left panel) and two (right) Gaussians. In addition, the spectrum obtained at phase 0.97 in cycle 8 may indicate that the Hα emission that is seen at most phases is merely the violet emission wing of the total Hα profile.

The relation between the phase and Hα line velocities was investigated by fitting either one or two Gaussians to the Hα profile at each phase. The radial velocity for the emission component was then determined from the position of the fitted Gaussian (Fig. 8.22)

Radial velocities were also calculated for the C I line at 6587.622 Å on the seven MSO spectra on which a line could be detected. The line bisector method

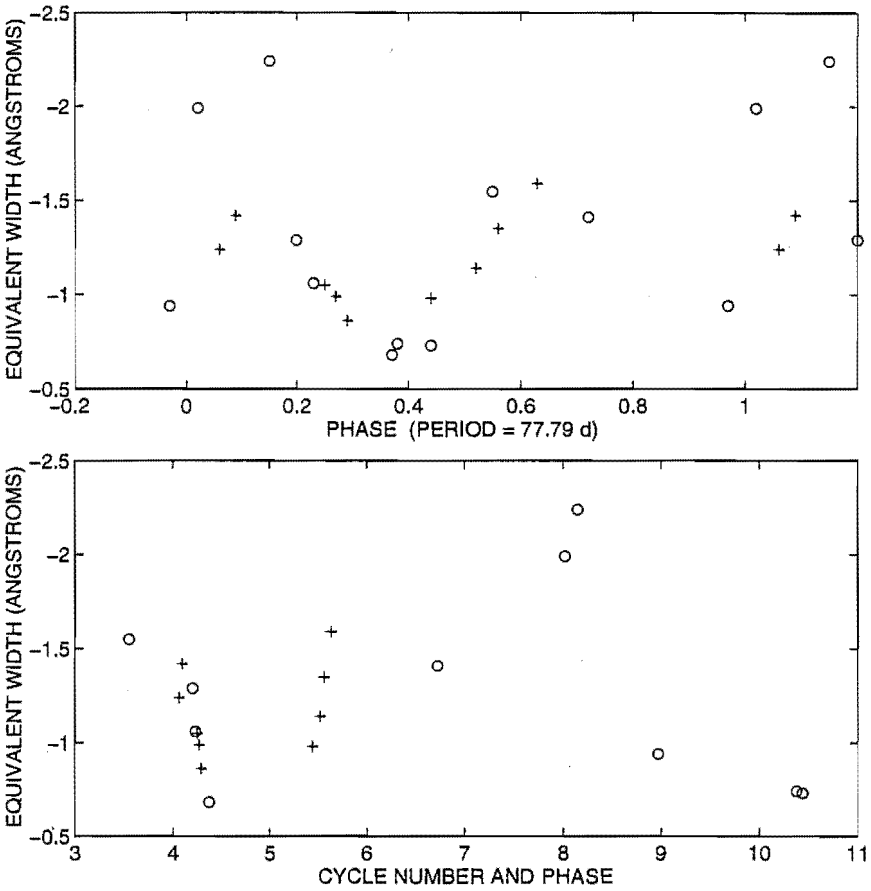

Figure 8.20: The phase dependence of the Hα equivalent width in AR Pup. Equivalent widths for the MJUO (o) and MSO (+) spectra are plotted versus phase (top panel) and versus cycle number and phase (bottom panel).

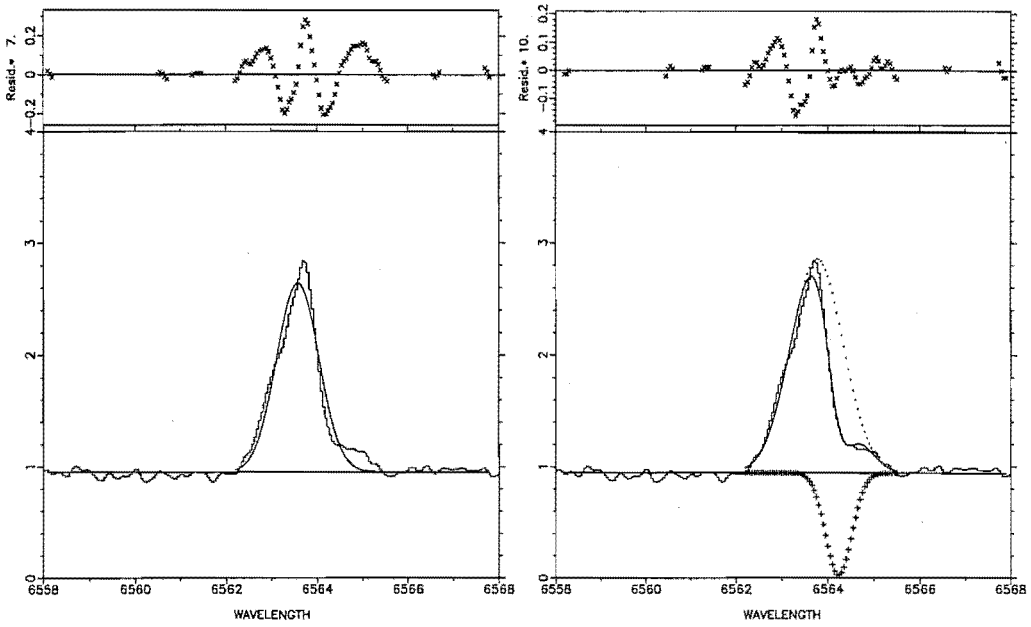

Figure 8.21: Fits to the AR Pup Hα profile at phase 0.02 in cycle 8, using one Gaussian (left) and 2 Gaussians (right).

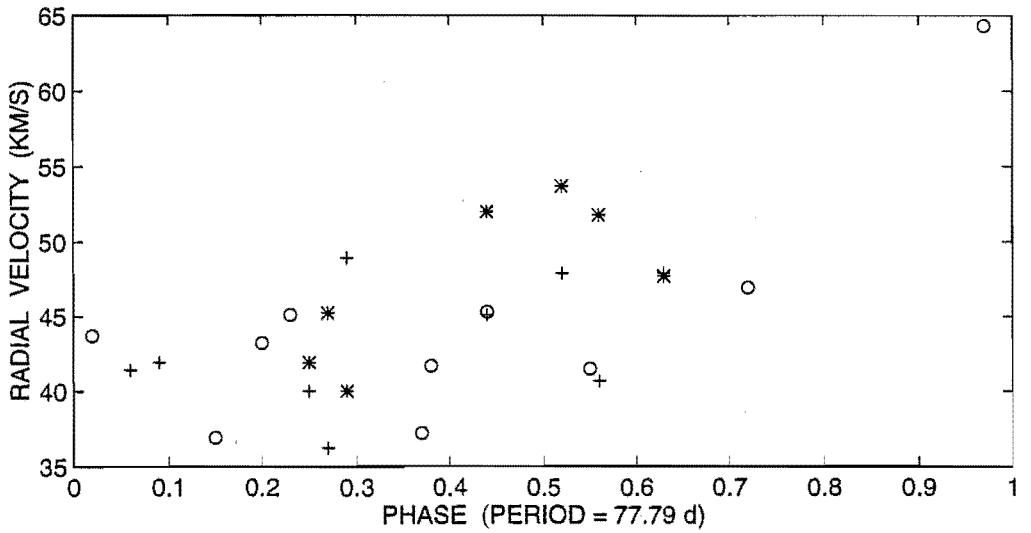

Figure 8.22: The Hα radial velocity curve (o for MJUO spectra, + for MSO spectra) for AR Pup. The radial velocities for the C I line at 6587.622 Å (*) are also shown.

described in Section 6.12 was used. These radial velocity measurements are listed in Table 8.4 and are also included in Fig. 8.22.

The radial velocities are very scattered. The velocities for the C I line are likely to be more reliable than those for the Hα emission component, due to the larger uncertainties that are present for the multiple Gaussian fitting technique. The most positive velocity is measured from the unusual Hα profile obtained at phase 0.97 in cycle 8. The other velocities appear to shown a general increase in velocity through the 77.79 d cycle, although few spectra were obtained in the second half of the cycle (phases 0.5–1.0).

8.4 IW Car

8.4.1 Previous spectroscopy of IW Car

The General Catalogue of Variable Stars (Kholopov et al. 1958) classifies IW Car as an RVb type RV Tauri star but this classification has been brought into question by a number of authors. Based on the results of photoelectric observations (Wisse & Wisse 1971, Eggen 1973, Wisse 1981), Wisse (1981) included IW Car in the semiregular SRd class of variable.

The Michigan Spectral Survey states that IW Car has a composite spectrum of (A4 Ib–II: + F7/F8). Lloyd Evans (1985) classifies IW Car on the system of Preston et al. (1963) as a 'B' (implying carbon-rich) type star.

A recent abundance analysis of IW Car (Giridhar et al. 1994) reports that IW Car is carbon rich and metal poor, with C/O > 1 and [Fe/H] ~ -1.0. It is suggested that the unusual abundances in this star arise from selective removal of certain elements in the stellar photosphere by condensation into dust grains.

8.4.2 Spectroscopic observations of IW Car

Between 1991 March and 1992 September, 25 high-resolution échelle spectra of IW Car were obtained at MJUO using the 1.0-m telescope and CCD detector. Exposure times were typically about 60 minutes for these spectra. Thirteen high resolution coudé spectra were obtained using the 1.9-m telescope at MSO between 1991 May and 1991 September, with exposure times of typically 3 to 15 minutes. Table 8.5 presents a log of the spectroscopic observations for IW Car.

Table 8.5: Spectroscopic observations of IW Car.

UT date	HJD [a] 2440000+	region	site	observer	phase (ϕ)	rv(Hα) (km s^{-1})	rv(metal) [b] (km s^{-1})
1991-Mar-29	8344.988	Hα	MJUO	KRP	3.08	+5.9	+7.8
1991-Mar-31	8346.926	Hα	MJUO	KRP	3.11	+2.5	+3.0
1991-May-10	8386.879	Hα	MSO	WAL	3.67	–	+3.9
1991-May-12	8388.914	Hα	MSO	WAL	3.69	–	-1.0
1991-May-21	8397.926	Hα	MJUO	KRP	3.82	-5.0	+6.9
1991-May-21	8397.980	Li	MJUO	KRP	3.82	–	–
1991-May-22	8398.906	Li	MJUO	KRP	3.83	–	–
1991-May-22	8398.961	Hα	MJUO	KRP	3.83	-10.8	-0.5
1991-May-23	8399.910	Hα	MJUO	KRP	3.85	-6.1	-5.1
1991-May-24	8400.918	Li	MJUO	KRP	3.86	–	–
1991-May-24	8400.949	Hα	MSO	WAL	3.86	-3.3	+3.0
1991-May-25	8401.898	Hα	MSO	WAL	3.87	-7.1	+3.1
1991-May-27	8403.926	Hα	MSO	WAL	3.90	-6.8	+2.8
1991-May-28	8404.887	Hα	MSO	WAL	3.92	-5.4	+5.5
1991-May-31	8407.910	Hα	MSO	WAL	3.96	-8.2	+0.5
1991-Jul-16	8453.848	Hα	MSO	WAL	4.60	-3.2	-11.0
1991-Jul-18	8455.879	Hα	MSO	WAL	4.62	-5.1	-9.0
1991-Jul-30	8467.832	Hα	MJUO	KRP	4.79	-13.2	-7.7
1991-Aug-02	8471.191	Hα	MJUO	KRP	4.84	-21.4	-10.8
1991-Aug-03	8472.195	Hα	MJUO	KRP	4.85	-17.3	-5.1
1991-Aug-25	8494.246	Hα	MSO	KRP	5.16	-16.5	-9.6
1991-Aug-31	8500.242	Hα	MSO	KRP	5.24	-28.2	-9.0
1991-Sep-03	8503.219	Hα	MSO	KRP	5.28	-29.9	-18.3
1991-Sep-09	8509.203	Hα	MSO	WAL	5.36	-31.4	-17.3
1991-Sep-25	8525.227	Hα	MJUO	KRP	5.59	-32.4	-18.4
1991-Sep-26	8526.180	Hα	MJUO	KRP	5.60	-33.5	-15.6
1991-Sep-27	8527.082	Hα	MJUO	KRP	5.61	-31.4	-16.3
1991-Nov-15	8576.129	Hα	MJUO	KRP	6.29	-27.6	-18.9
1991-Nov-29	8590.109	Hα	MJUO	MDA	6.49	-26.3	-24.2
1991-Dec-04	8494.961	Hα	MJUO	MDA	6.56	-25.2	-24.2
1992-Mar-12	8694.125	Hα	MJUO	MDA	7.93	-29.6	-24.5
1991-Mar-23	8705.094	Hα	MJUO	KRP	8.09	-30.4	-24.1
1991-Apr-11	8723.918	Hα	MJUO	KRP	8.35	-26.8	-23.4
1991-May-25	8767.867	Hα	MJUO	KRP	8.96	-23.0	-21.7
1991-May-26	8768.930	Hα	MJUO	KRP	8.97	-22.9	-22.3
1991-Sep-12	8878.082	Hα	MJUO	KRP	10.49	-18.6	-27.2
1991-Sep-16	8882.063	Hα	MJUO	KRP	10.56	-20.5	-30.6
1991-Sep-17	8883.098	Hα	MJUO	KRP	10.34	-20.3	-30.6

[a] for mid time of observation

[b] see text for details of which metallic lines were used to measure radial velocities.

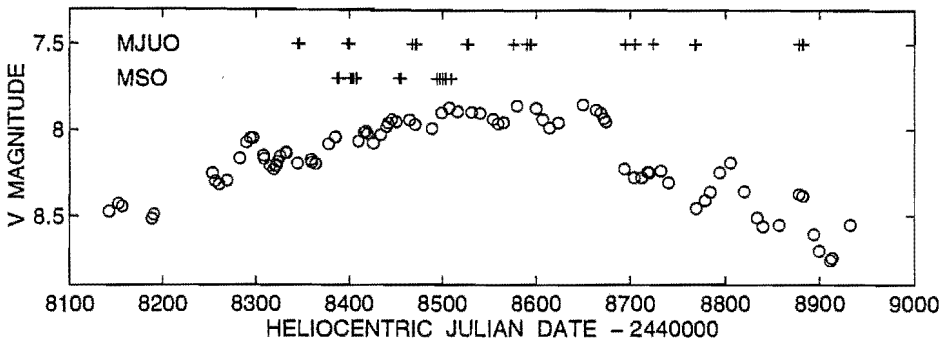

Figure 8.23: The light curve for IW Car and dates when spectra were obtained for IW Car. The MJUO photometric observations (o) and spectroscopic observations (+) from both MJUO and MSO are shown versus heliocentric Julian Date.

These spectra were then lightly smoothed and their phases calculated according to the ephemeris obtained from the analysis of the MJUO V photometry:

$$\text{Primary (photometric) minimum} = 2448123.0 + 72.0\,E.$$

It was found previously that the light variations in IW Car were quite irregular so that phases calculated according the above ephemeris are very uncertain. For the purposes of investigating phase-dependent effects, the above phases were used with caution. The MJUO V photometry and the dates when spectra were obtained at both MJUO and MSO are shown in Fig. 8.23. A reasonable sampling over the long-term period was obtained.

Stacked MJUO spectra of échelle orders 35 and 34 are displayed in Figs 8.24 and 8.25 respectively. Stacked MSO spectra of the region around the Hα line are shown in Fig. 8.26. The MJUO spectra reveal very few metallic lines. This is consistent with the reported low-metallicity of [Fe/H] of ~ -1.0 (Giridhar et al. 1994). Metallic lines that are present on the MJUO spectra are the Si II line at 6371.355 Å (χ = 8.12 eV, multiplet 2) and the S I lines at 6743.575 Å (χ = 7.86 eV), 6748.779 Å (χ = 7.87 eV) and 6757.195 Å (χ = 7.87 eV), all from multiplet 8. The MSO spectra reveal a relatively strong C I line at 6587.622 Å and a number of other weaker lines. A number of weak lines appear throughout the 6540–6580 Å region around the Hα line, but these have been identified as telluric lines of H_2O. Apart from the Hα line, no spectral lines appear to display any emission components.

The Hα line has a rather complex profile with a variable, broad absorption

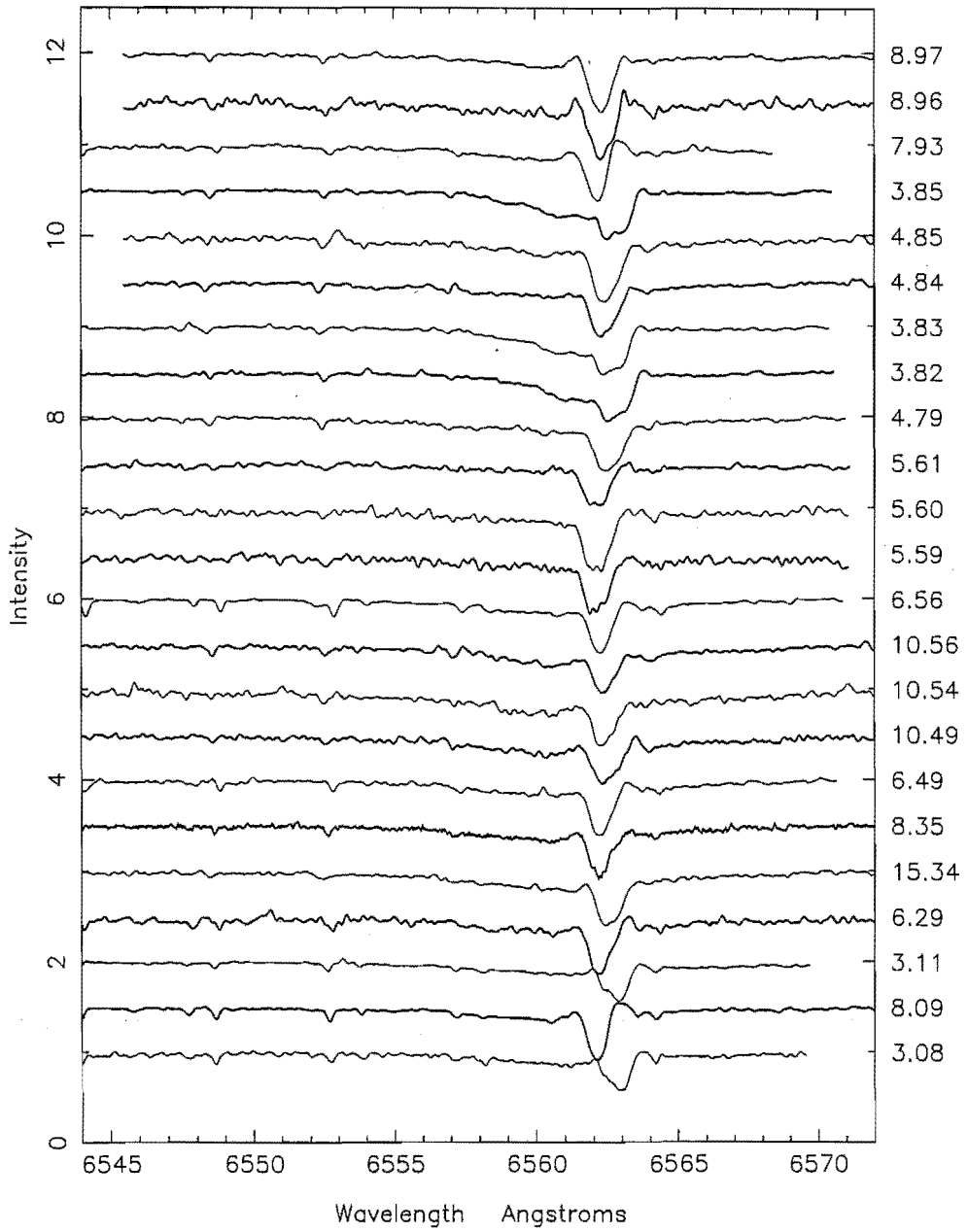

Figure 8.24: Stacked MJUO spectra of échelle order 35 for IW Car. The cycle number and phase are indicated to the right of each spectrum.

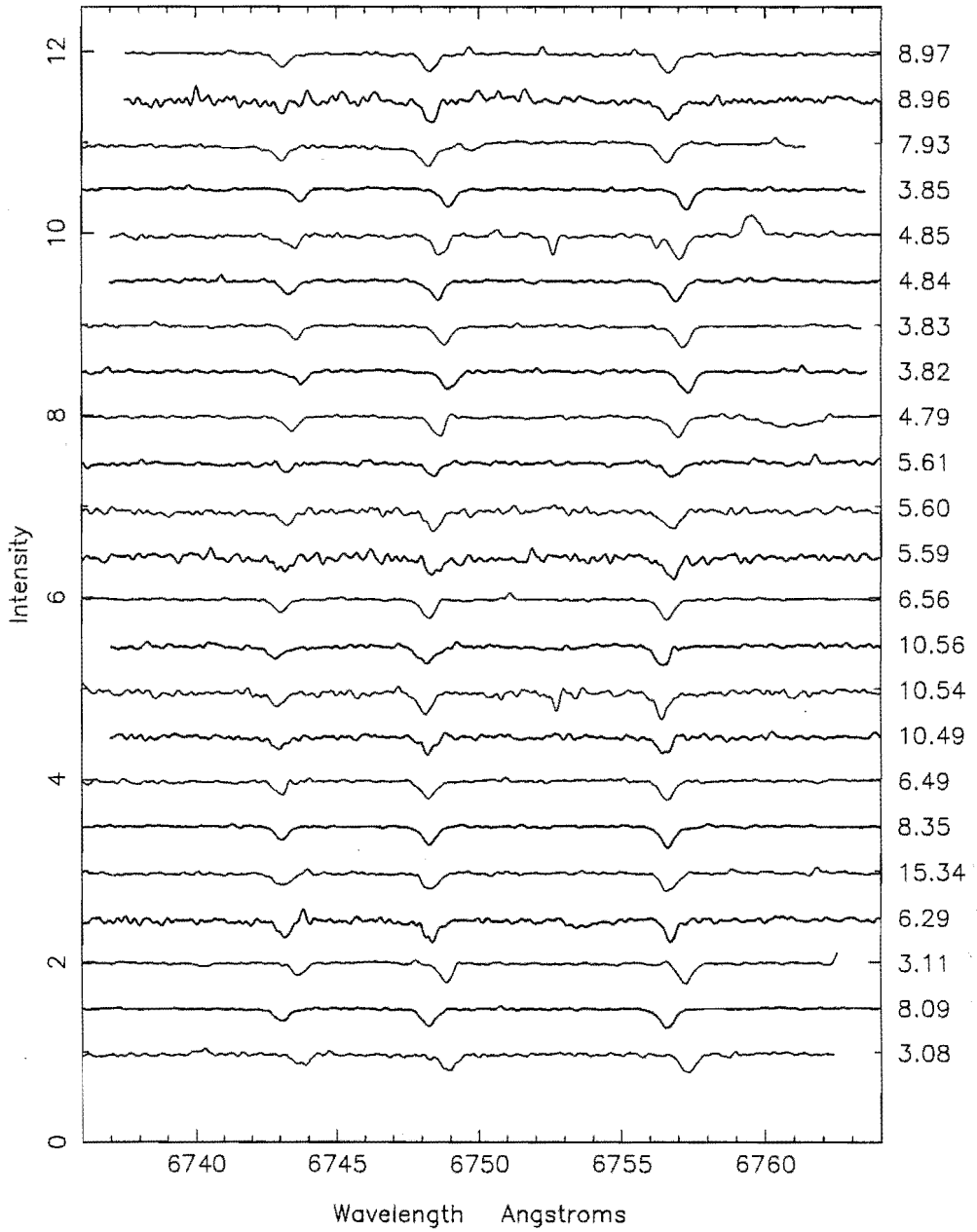

Figure 8.25: Stacked MJUO spectra of échelle order 34 for IW Car. The cycle number and phase are indicated to the right of each spectrum.

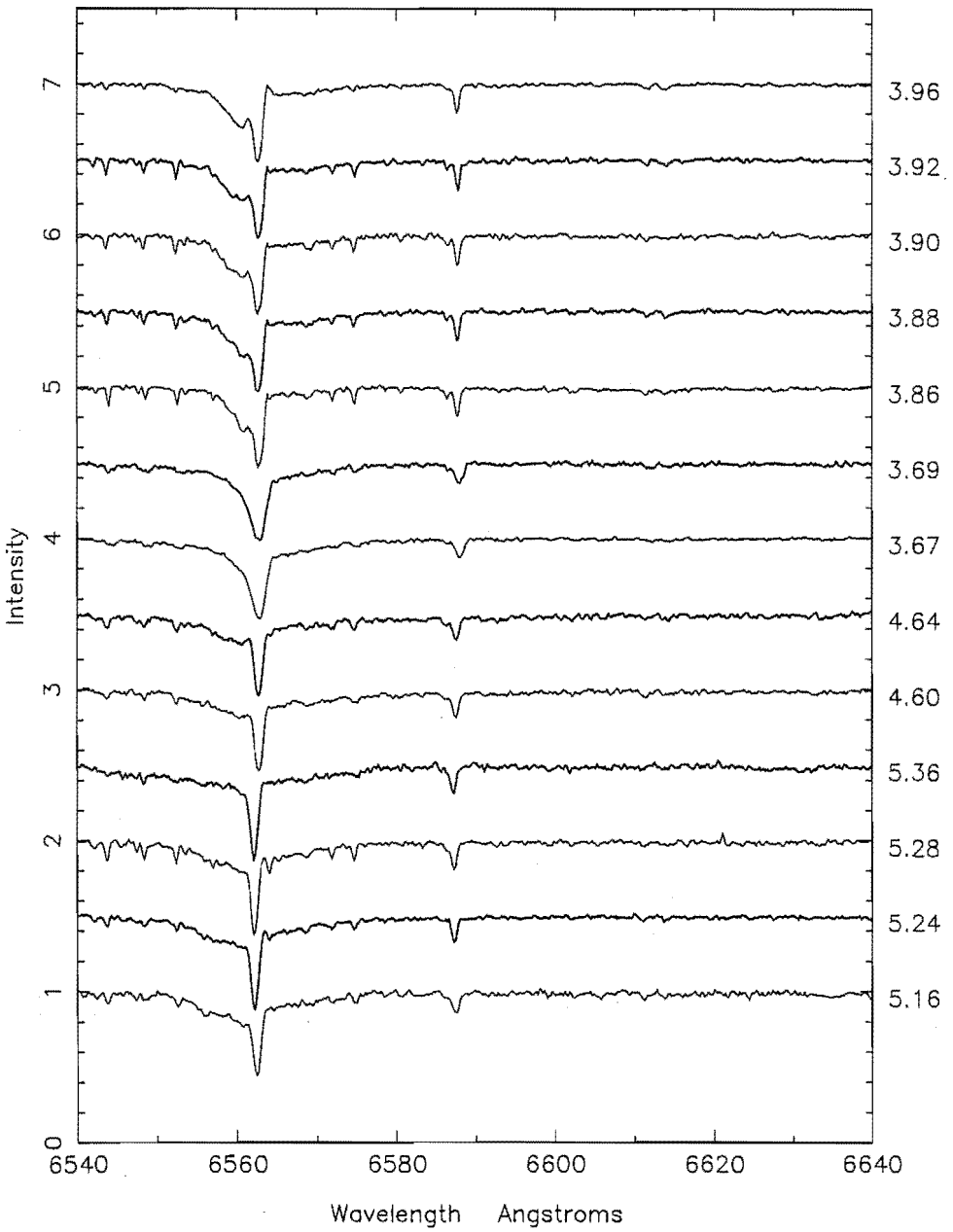

Figure 8.26: Stacked MSO spectra of the Hα region in IW Car. The cycle number and phase are indicated to the right of each spectrum.

component and a deep absorption component with small red and violet emission emission wings on each side of the absorption. The very broad absorption is blue shifted with respect to the narrow absorption feature. The Hα emission in RV Tauri stars arises from radiative recombination following the passage of pulsationally-produced shock waves, but in the case of IW Car, no other shock-related spectral features (metallic emission components or line-doubling) are seen. It is therefore probable that IW Car is not an RV Tauri star (as suspected from its light variations which are relatively irregular and lack the characteristic deep–shallow alternations of RV Tauri stars) and the Hα emission arises from a mass loss to a circumstellar shell or mass transfer in the binary system.

8.4.3 The radial velocity curve for IW Car

Radial velocities were obtained from the spectra shown in Figs 8.24, 8.25 and 8.26 using the line bisector method described in Section 6.12. The radial velocities were measured for the sharp Hα component on both the MJUO and MSO spectra. The MSO spectra at phases 0.67 and 0.69 in cycle 3 were not used for this measurement since poor focussing of the spectrograph led to excessive blending of the broad and narrow Hα components on these spectra.

The radial velocities for the narrow Hα absorption component are included in Table 8.5 and are plotted versus heliocentric Julian Date in Fig. 8.27 along with the contemporaneous photometric V photometry from MJUO. The dominant trend shown by the Hα velocities is correlated with the long-term period in the V variations. The amplitude of the long term radial velocity variations is estimated to be 35 km s^{-1}. This amplitude is only a lower limit since it is uncertain whether both maximum and minimum velocities have been sampled.

The short term phase dependence of the Hα velocities was investigated but no obvious trend with the 72.0 d period was seen. The short term radial velocity variations appeared to have a rather small amplitude of $\sim$ 10 km s^{-1}.

The radial velocities for a number of metallic lines were measured on both the MJUO and MSO spectra. The radial velocities of the S I lines at 6743.575 Å, 6748.779 Å, and 6757.195 Å were measured on the MJUO spectra and the mean value of these three lines is listed in the rv(metal) column of Table 8.5. On the MSO spectra, the radial velocities of the C I line at 6587.622 Å were measured. These velocities are included in Table 8.5, also in the column rv(metal). The radial velocity curves obtained from the S I lines and the C I line on the MSO

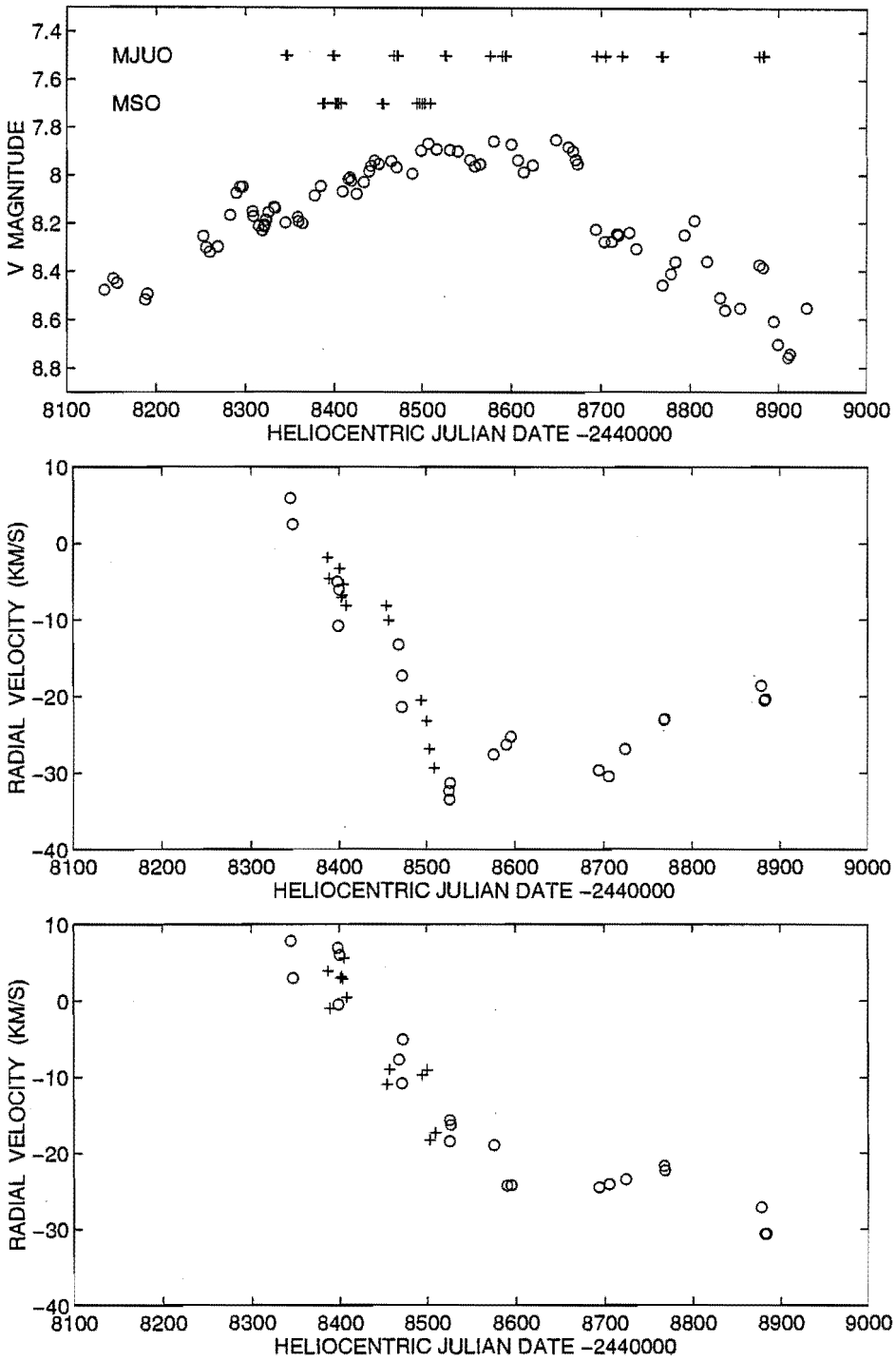

Figure 8.27: The light curve (top), Hα radial velocity curve (middle) and metallic radial velocity curve (bottom) for IW Car. In the middle panel, MJUO (o) and MSO (+) radial velocities are plotted. In the bottom panel, the radial velocities for the S I lines (o) on MJUO spectra and C I lines (+) on MSO spectra are shown.

spectra are shown in the bottom panel of Fig. 8.27. The amplitude of the radial velocity variations for these metallic lines is estimated to be about $30\,\mathrm{km\,s^{-1}}$.

IW Car is reported to be a binary. Houk (1978) gives a spectral classification of (A4 Ib–II: + F7/F8) noting that the A-type star has very sharp lines. However, from the derived MJUO radial velocities, we associate the Hα emission and sharp absorption features in the spectra with the F-type star. It is clear that all of the visible spectral lines are from a single star (giving the same radial velocity) except, perhaps, for the Hα absorption. It is possible that the deep Hα absorption arises from gas that is escaping from the star. It could also be produced by a broad-lined (rapidly rotating) companion star, in this case, the A-type star.

In order to investigate this further, an attempt was made to model the Hα line by a number of Gaussians so that the radial velocities of the broad Hα absorption feature could be obtained. Unfortunately, no unique and acceptable fit to the Hα profile was able to be made.

Chapter 9

Discussion

The preceeding chapters in this thesis have laid out the new photometric and spectroscopic data that are now available on the RV Tauri stars. This current chapter will endeavour to collect these extensive data sets into a consistent model for the RV Tauri stars.

9.1 A model for the RV Tauri stars

Historically, the RV Tauri stars have been classified solely on the nature and period of the variability of their light curves, with the added proviso that they have spectral type F–K and luminosity class I–II in order to exclude the various red variables with otherwise similar variability.

Any proposed physical model for the RV Tauri stars has to explain several, sometimes perplexing characteristics that these stars display both photometrically and spectroscopically. In addition, the model must explain the apparent existence of two *photometric* subclasses of RV Tauri star – the RVa and RVb stars – which show some intriguing similarities and contrasts in photometric and spectroscopic behaviour.

We can further insist that this physical model be related to, and consistent with, an evolutionary scenario for these stars which will produce RV Tauri-type variables with a rather diverse collection of spectral characteristics. It is possible that several different evolutionary scenarios will result in a star exhibiting the typical RV Tauri-type behaviour at a certain stage in its evolution, and that a unique progenitor may not be able to be inferred.

The general characteristics that any physical model of the RV Tauri variables

must predict are briefly outlined below. Each of these properties will then be considered in greater detail, with reference to previous models and the new photometric and spectroscopic data that were collected and analysed for this thesis.

(i) The light curve displays alternating deep and shallow minima with a period of $\sim$50–150 days between deep (primary) minima.

(ii) The radial velocities from optical studies indicate the pulsational period is half the above photometric period.

(iii) Irregularities are seen in the shape and period of the light curve.

(iv) The RVb subclass exhibits an additional periodicity, so that the short-term light variations due to pulsations appear superimposed on a long-term light variation of $\sim$600–2500 days.

(v) Associated with the long-term light variations in the RVb stars are long-term colour variations, where the colours may appear redder at the long-term minimum.

(vi) At the long-term minimum in the RVb stars, the luminosity and colour variations appear 'damped', while at maximum the amplitude of variation is larger with a greater distinction between the deep and shallow minima.

(vii) The RVb subclass display long-term radial velocity variations as well as long-term light variations.

The characteristics described in items (i), (ii) and (iii) above can be associated with the pulsational properties of RV Tauri stars of both the RVa and RVb photometric type and are discussed in the following section (Section 9.1.1).

Items (iv) to (vii) outline the observed photometric and spectroscopic characteristics that distinguish the members of the RVb subclass. However, there are extremes of behaviour within the RVb subclass and any physical model for the RVb phenomenon must be able to explain the subclass as a whole (and perhaps the RV Tauri class as a whole). One RV Tauri star, AC Her, is known to display long-term radial velocity variations with no apparent long-term light variations (Sanford 1931, 1955; Baird 1982). AC Her is thus classed photometrically as an RVa-type star but it displays some spectral characteristics of the RVb subtype. This leads one to suggest that the final model for RV Tauri stars will be

able to describe both RVa and RVb photometric subtypes, with a continuum of characteristics from extreme RVb types to the RVa types.

In Section 9.1.2, the underlying nature of the secondary variability in the RVb subclass is discussed and a possible physical model for the RVb stars is proposed which explains many of the observed properties.

9.1.1 The pulsations in the RV Tauri stars

Many different theories have been proposed in the past that attempt to explain the characteristic, alternating deep–shallow nature of the light curve minima.

- Chaos: decreasing the effective temperature or increasing the luminosity in Population II models can result in a series of period-doubling bifurcations and a transition to chaotic pulsation. The chaotic attractors have been found to correspond to a low-dimensional dynamic system (Buchler & Kovács 1987, Kovács & Buchler 1988, Kolláth 1990, Aikawa 1993).

- Resonance effects between pulsational modes: 2:1 resonance between either the fundamental and the first harmonic (Takeuti & Petersen 1983, Fokin 1993) or the radial pulsation mode and a non-radial mode (Shenton et al. 1992) can be invoked.

- Time-dependent convection: alternation could be caused by coupling between the radial oscillation and large amplitude convective motions (Deupree & Hodson 1976).

Although many different explanations of the alternation of deep and shallow minima in the light curves of the RV Tauri stars have been proposed, it is well established that the variability arises from pulsations in these stars. Spectroscopic studies have suggested that the periodicity associated with the pulsational characteristics (including the observed shock-related phenomena) is half the 'formal' period. The radial velocity curves for many atomic species are discontinuous. However, Mozurkewich et al. (1987) have found that the infrared atomic absorptions in R Sct are always single-lined and trace out a continuous, repeatable pulsation of ~ 142 d which is equal to the 'formal' period. This appears not to be consistent with the optical studies which show an ~ 70 d period and discontinuous velocity curve for R Sct.

A fundamental question that still remains unanswered is whether the underlying period of the RV Tauri stars is the 'formal' period (the time between two

successive deep minima) or the so-called 'fundamental' period (the time between two successive minima). The high-resolution infrared spectroscopic observations of Mozurkewich et al. (1987) suggest the former, while optical studies (Sanford 1933, Abt 1955, Preston 1962, Preston et al. 1963, Preston 1964, Gillet et al. 1989, 1990, Lèbre & Gillet 1991a, 1991b, this thesis), which show two shock waves and two velocity cycles per 'formal' period, suggest the latter. However, it is possible that both studies can be consistent if we realise that when we make use of infrared and optical spectroscopy, we are probing different depths in the star. The $2\,\mu$m region appears to be an important region at which to observe these stars since the H^- opacity is near its minimum and is five times less than at 5000 Å, enabling deeper layers of the star to be investigated. Optical studies sample higher layers in the stellar atmosphere that are affected more by the shock waves.

A recent theoretical study by Fokin (1993) examines non-linear pulsations in RV Tauri star models. Fig. 9.1 is taken from this work. This figure represents the theoretical light curve and radial displacements of different mass zones of a $0.6 M_{\odot}$ (composition X=0.7, Y=0.297) model with an effective temperature of 5400 K, which shows a 'formal' period of 66.8 d and an V amplitude of 1.1 magnitudes. The high non-adiabaticity of the pulsation results in the pulsations having the form of a running wave, that is, non-synchronously moving layers, even in the interior mass zones. Thus the atmosphere is simultaneously composed of both rising and falling gas layers which are separated by a shock wave (Schwarzschild 1952, as described by Wallerstein & Elgar 1992).

The model predicts that two shock waves are produced during each luminosity cycle. The mechanism of the primary shock generation is similar to that found in earlier models of other Population II stars, such as W Vir and RR Lyrae atmospheres (Fokin 1992). This primary shock has an amplitude of $< 40\,\mathrm{km\,s^{-1}}$ which is in good agreement with the shock amplitudes measured for R Sct and AC Her (Gillet et al. 1990). A second shock is also generated near the photosphere just before the secondary light minimum when a large velocity gradient is produced between the rapidly expanding layers below the photosphere and the contracting higher atmospheric layers. The first overtone therefore plays an important role in the generation of the secondary shock.

Fig. 9.1 shows two maxima of the radial displacement curve which result from the first overtone. The secondary shock (of $\sim 20\,\mathrm{km\,s^{-1}}$) is weaker than

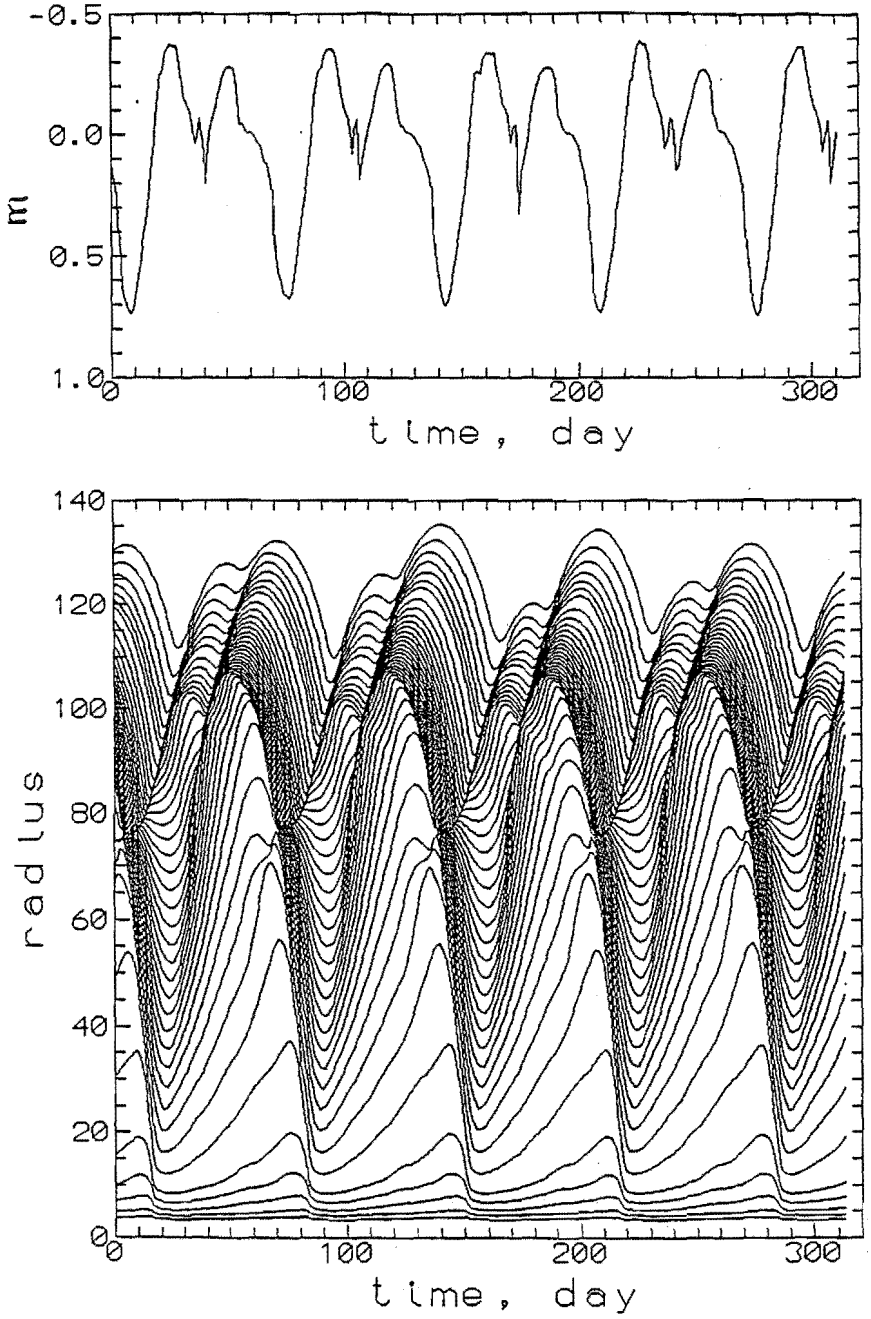

Figure 9.1: The theoretical light curve (top panel) and radial displacements of different mass zones (bottom panel) in solar radii for a $0.6M_{\odot}$ (composition X=0.7, Y=0.297) model with an effective temperature of 5400 K. In the bottom panel the outer layers have a secondary minimum, and hence a period of 33.4 d, whereas the inner layers have a period of 66.8 d.

the first because the infalling pre-shock gas has a lower velocity. The primary and secondary light minima result mainly from rapid hydrogen recombination following the passage of the shock fronts. Just prior to the primary minimum, the higher layers are undergoing a contraction phase. The increase in opacity in the higher atmospheric layers causes strong radiation absorption and results in the photospheric lines forming much further out in the atmosphere. Fig. 9.1 shows the very outer layers of the atmosphere reach their maximum radius just prior to the primary minimum. It is therefore at this phase that the formation of molecules in the very extended, cooler outer layers would be possible.

This model is consistent with the fact that the infrared observations show a period that is equal to the time between successive deep minima since the first overtone is not important in the deeper layers and shock generation occurs above the layer that are being sampled by the infrared spectroscopy. The optical studies, however, sample the region where the two shock waves are produced and the first overtone is an important factor.

9.1.2 The nature of the RVb subclass

We now wish to investigate the nature and cause of the long-term, secondary variability that is a defining characteristic of RVb subclass. The RVb star U Mon is used as our typical example of this subclass, since it is bright and a substantial amount of data has been obtained photometrically and spectroscopically.

To reiterate, the general characteristics that we wish to explain are the long-term light, colour and radial velocity variations, together with the fact that the light and colour variations are damped at long-term light minimum.

First, we consider the long-term radial velocity variations. There are various possibilities which have been suggested: orbital motion, radial or non-radial pulsations, or some form of large scale convective motion in the envelope. The amplitude of the long-term radial velocity variations is too large to be attributed to non-radial pulsations. If the long-term radial velocity variations are assumed to be the consequence of radial pulsations then very large variations in the stellar radii are implied. Tsesevich (1975) reports that radial displacements of approximately $431R_{\odot}$, $568R_{\odot}$ and $1782R_{\odot}$ are implied from the radial velocity variations in RV Tau, R Sgr and U Mon respectively. However, there is no evidence of any variation in the short-term pulsational period from long-term minimum to long-term maximum which would be expected if the star has increased in size by such

an amount. Any increase in the radius of the RV Tauri star should be reflected in a corresponding period change of the short-term pulsations and these are known to be stable, or at least relatively stable, for these stars throughout a long-term oscillation. Additional evidence against the pulsation hypothesis is that the spectral type of the star appears to change very little from long-term minimum to long-term maximum (see Section 8.1).

Preston (1964) combined his radial velocity data of U Mon with the previously published data of Sanford (1933) and Abt (1955) and reached the conclusion that the long-term variation had changed its period or that it was cyclic rather than periodic. Thus the long-term variation would not be able to be described by any kind of orbital motion. A number of authors have used this finding to exclude the binary-model for the long-term radial velocity variations in the RVb stars. However, Preston (1964) also had an alternative suggestion. If the earlier 1922–1926 data of Sanford (1933) were disregarded, then a period of about 1560 d would fit the remaining data. In later papers describing the spectra of U Mon, Preston (1972) states that U Mon is the primary star of a single-line spectroscopic binary with $P \sim 4$ years, $K_1 \sim 20\,\mathrm{km\,s^{-1}}$ and $V_\gamma \sim +35\,\mathrm{km\,s^{-1}}$, quoting his and Sanford's earlier spectroscopic analyses.

In Chapter 8, the U Mon radial velocity data of Sanford (1933), Abt (1955) and Preston (1964) were reanalysed together with the 1990–1994 radial velocity data obtained at MJUO. The reanalysis shows a period of 2597 d is the best fit to the combined radial velocities. This value is in reasonable agreement with Sanford's value of about 2300 d, as well as the values obtained from the analysis of visual estimates by Loreta (1938) and the analysis of visual and photographic estimates by Percy et al. (1991), who derived periods of 2320 d and 2475 d respectively. The 2597 d period compares favourably with Abt's value of 2640 d.

Very little radial velocity data for other RVb stars is available. The MJUO radial velocities for AI Sco and AR Pup are not inconsistent with the long-term radial velocity variations being due to orbital motion in a binary system.

The next two general characteristics of the RVb stars that we will consider are the long-term light and colour variations. The *BVRI* light curves from the MJUO data for U Mon display approximately 'in-phase' long-term light variations. The amplitude is greatest in the B filter ($\sim$ 1.3 mag) and decreases for the redder filters ($\sim$ 0.8 mag in I). The long-term colour variations have a slight phase lag behind the long-term light variations, so that the colours appear reddest after

the star has reached the long-term minimum.

Slow light variability in cool M giants can possibly be explained (Stothers & Leung 1971) by convective supergranules that have sizes only a few times less than that of the stellar radius, but this mechanism is unlikely to be true for RV Tauri stars, since Fokin (1993) has noted that the lifetime of these convective cells is too large for the Kelvin time scales of the RV Tauri stars.

In a binary system an obvious explanation for an observed decrease in the light output of the system is an eclipse of some kind. This could be due to an eclipse of the RV Tauri star by the secondary or an eclipse by dust that has been previously ejected from the RV Tauri star. This latter model is very reminiscent of what is observed in R Coronae Borealis (RCB) variables during their characteristic 'declines'. The declines in RCB stars are obscurations of the star by condensed dust which is mostly composed of carbon. A spectrum of the RV Tauri star R Sct taken during an extremely deep pulsation (Howell et al. 1983) showed many similarities to the RCB decline spectra with many chromospheric emission lines apparent.

The scenario whereby the eclipse of the RV Tauri star is by a companion star is not an attractive one due to several considerations. Only one eclipse is observed to occur during each orbital period. (The orbital period is unlikely to be double the presumed orbital period, since the radial velocities contradict this interpretation.) The amplitude of the long-term light variation for some RVb stars (for example, DF Cyg has an amplitude change of 3.2 magnitude in V) suggests that the companion star must have a relatively large extent to enable it to obscure much of the light from the RV Tauri star. Such a companion would therefore be a giant star and should have been detected unless it is much less luminous than the RV Tauri star. An excess of flux *has* been detected in the near-infrared *JHKLM* pass-bands. For U Mon this flux distribution peaks at about 2.9 μm (equivalent to a blackbody at $\sim$ 1000 K) and varies on the same period as the light variations due to pulsations (see Chapter 5). Therefore, this excess of flux is most likely to be due to 'warm dust' ('cold dust' radiating at $\sim$ 500 K has been detected by the IRAS satellite) associated with the RV Tauri star itself and not due to a companion star.

One of the few companions that would be allowed from evolutionary considerations, assuming that the RV Tauri stars are indeed AGB or post-AGB stars, is a low-mass M-type dwarf. From the orbital analysis of U Mon it was found

that if the RV Tauri star was $\sim 0.8M_{\odot}$, then the derived mass function requires that the companion mass be $\sim 2.5M_{\odot}$ which precludes a low mass companion. If extensive mass loss has occurred in the past (which is quite probable), then the companion star may have been a low mass star initially, but will have accreted material from the RV Tauri star at various stages of evolution, including the recent AGB phase. This state would be similar to what is seen in Algol stars where the (unevolved) companion is actually the more massive of the two stars due to mass transfer in the binary system.

The dust-obscuration model requires the eclipses of the RV Tauri star by the dust to be associated with the orbital motion of the star. The mass previously ejected from the RV Tauri star must be preferentially distributed at one part of the orbit. The eclipses by the dust will then occur in a periodic manner associated with the binary motion. As well as the decrease in light that would be expected by a dust cloud eclipsing the RV Tauri star, we should expect to see the colours of the star get substantially redder, which is indeed what we observe for U Mon. Due to the reddening effects of the dust cloud, the long-term light amplitude should be greater in the bluer filters and very small in the near-infrared.

The MJUO photometry shows that both U Mon and AI Sco display similar characteristics – a long-period variation evident in the light curve (at optical wavelengths) and a reddening of the colours during the long-term minimum. The amplitude of the long-term light variations is largest in the bluest filters and smallest in the I filter. From the near-infrared data of Lloyd-Evans (1985) and Nook (1991) there is no evidence of a long-term variation in the infrared magnitudes. This is consistent with the dust-eclipse model outlined above.

However, AR Pup, which shows a relatively large amplitude in the long-term light variations, does not appear to show any change at all in its colours. AR Pup is also peculiar in that it does not show consistent alternating deep–shallow minima and the amplitude of the short-term light variations (from the MJUO photometric data) does not seem to be dependent on the phase of the long-term oscillation. In contrast, older photographic data (O'Leary 1937) does show extended episodes of reasonably stable, alternating deep–shallow minima and larger amplitudes in the light variations at the maximum of the long period oscillation. Unfortunately, no colour information is available from these photographic data.

Another property of the RVb stars that is difficult to explain by the dust-eclipse model is the decrease in the amplitude of the light and colour variations

at long-term minimum. This 'damping' of the light variations has been reported in most members of the RVb subclass. From the MJUO photometry, U Mon shows a dramatic amplitude change while AI Sco and AR Pup show a smaller amplitude change. The MJUO photometry for AR Pup has covered a long-term minimum and continuing observations through the long-term maximum would be useful.

An alternative explanation for the light and colour variations is that the binary system involving the RV Tauri star is *interacting* at some phase of the binary orbit. This explanation allows for a range of properties observed for the binary system, depending on a number of factors including the eccentricity of the orbit, the relative sizes of the binary components, the inclination angle of the system and the degree of interaction between the two components. Mass loss in an binary system with an eccentric orbit will preferentially occur at periastron. The interaction will possibly involve some kind of mass loss or mass transfer between the components depending on the geometry of the system. At the phase of interaction, the RV Tauri star may appear reddened (as seen in U Mon and AI Sco) due to the presence of gas and dust from a previous or current mass loss event, the binary interaction or possibly tidal forces. The light variations of the RV Tauri star may also be damped at this phase due to the interaction.

In U Mon enhanced Hα emission is seen in the MJUO échelle spectra at the minimum of the long period when we would expect to see the effect of the binary interaction. From analysing the radial velocity data for U Mon (Sanford 1933, Abt 1955, Preston 1964, this thesis) the orbital parameters derived are $P = 2597\,\mathrm{d}$, $V_\gamma = +34.9\,\mathrm{km\,s^{-1}}$, $K_1 = 17\,\mathrm{km\,s^{-1}}$, $e = 0.43$, $\omega = 191°$, $T_0 = 2427573\,\mathrm{d}$, $a \sin i = 537\,\mathrm{Gm}$ and $f(M) = 0.915 M_\odot$, so that the orbit appears quite eccentric. If we combine this with the assumption that the mean size of the RV Tauri star in the U Mon system is about $100\,R_\odot$, then it can be calculated that U Mon and the companion star may be close enough to interact during part of the orbital period. Using this explanation, stars such as U Mon would interact strongly, AI Sco will interact somewhat less, AR Pup will interact but with no colour variation and AC Her does not interact but displays radial velocity variations due to binary motion only.

One clue as to the nature of the long-term period is the different behaviour of the (short-term) pulsations at long-term minimum and long-term maximum. The short-term light and colour variations are smaller at long-term maximum

and the contrast between the deep and shallow minima is less. An interesting question is to consider whether this is due to a real physical effect inherent to the star itself or just an apparent effect resulting from the passage of the starlight through some intervening material.

If the effect is intrinsic to the RV Tauri star, then the mostly probable explanation is that real 'damping' of the stellar envelope is occurring at long-term minimum, as in the 'interaction' scenario above. If, however, this is an extrinsic effect where the star is still pulsating in the same manner but intervening material is affecting what we detect on Earth, then this would be similar to the 'dust-eclipse' scenario.

One piece of additional evidence that would be extremely useful in deciding between the two alternatives given above is the behaviour of the short-term radial velocity variations at different phases of the long-term oscillation. If the star is pulsating in exactly the same manner throughout the long-term cycle ('dust-eclipse') then we would expect to see no change in the radial velocity variations due to the pulsations at either long-term minimum or maximum. However, if the envelope is physically being affected by the binary interaction and actual 'damping' of the pulsation is occurring, then we should expect to see the radial velocities being damped also.

Chapter 10

An abundance analysis of R Coronae Borealis stars in the Galaxy and the LMC

10.1 Introduction

Over the last decade there has been renewed interest in the hydrogen-deficient objects in the luminous region of the HR diagram and other objects, such as RV Tauri stars, in the same part of the diagram. It is particularly important to ensure that connections are investigated between the wide range of hydrogen-deficient objects such as planetary nebulae, Wolf-Rayet stars, extreme helium stars, RCB stars and HdC stars. This chapter describes an analysis of three RCB stars, one in the Galaxy and the other two in the LMC.

The RCB stars are a chemically peculiar group of supergiant stars which provide us with an opportunity to investigate not only the evolutionary connections mentioned above, but also the nucleosynthetic models and mixing theories in both a galactic and an extragalactic environment (for a discussion of evolutionary models, see Renzini 1990).

High-resolution, fine analyses have been completed for only three RCB or HdC stars: R CrB, XX Cam and RY Sgr (Cottrell & Lambert 1982, hereafter CL82; Schönberner 1975, hereafter S75; Jones 1991, hereafter J91). A comprehensive review by Lambert (1986) has discussed CL82, S75 and earlier analyses, including Warner's (1967) analysis of the five southern HdC stars. The general abundance trends for these stars suggest C/H $\geq 10^3$, a [C/Fe] of 1, [X/Fe] approximately solar

for most other species up to the iron peak elements and $^{12}C/^{13}C \geq 100$, indicative of extreme triple-alpha processing. Some analyses have indicated unique chemical peculiarities for particular stars: for example, U Aqr is a cool RCB star that displays enhanced abundances of the light s-process elements, Sr and Y, by up to a factor of 100 times, but normal heavy s-process abundances (Bond et al. 1979, Malaney 1985). Some preliminary results for a further 18 galactic RCB stars have been discussed by Lambert & Rao (1994).

From a number of studies of the chemical composition of the Magellanic Clouds, it is evident that the LMC has an overall metal deficiency relative to the Sun. A mean iron abundance of [Fe/H] = -0.3 ± 0.2 dex has been determined from a study of F-type supergiants in the LMC (Russell & Bessell 1989), with good agreement from studies of other LMC objects. The elemental abundances in the LMC were found to follow the abundance of iron very closely. One exception was the heavy neutron capture elements which seemed to show an enhancement relative to iron in several different studies (for a review of these abundances, see Rolleston 1991).

Earlier spectroscopic studies of the RCB stars in the LMC have consisted of low-resolution spectra used mainly for classification purposes. Rodgers (1970) observed weak C_2 absorption bands with continuum depressions of up to about 8 per cent in W Men. Feast (1972) observed the (1,0) C_2 sequence (band head at 4737 Å) to have a continuum depression of $\sim$ 11 per cent and the (0,0) C_2 sequence (band head at 5165 Å) to have a continuum depression of $\sim$ 15 per cent in W Men. HV 12842 displayed C_2 absorption bands of very similar strength to those in W Men. It was also noted in this latter work that these two LMC stars have C_2 strengths within the same range as the galactic F-type RCB stars RY Sgr and R CrB. Thus we would expect HV 12842 and W Men to have similar effective temperatures ($\sim$ 7000 K) to R CrB and RY Sgr.

Most F- and G-type RCB stars display UV excesses relative to the intrinsic colours of normal-composition supergiants. This is presumably due to the absence of the Balmer continuum absorption. The effect of low metallicity is to enhance these UV and blue excesses, because of the lower strength of the metallic lines which appear in greater numbers in the blue and near-UV. We would therefore expect lower metallicity RCB stars (such as those in the LMC) to show greater UV and blue excesses than solar-metallicity RCB stars.

At a reciprocal dispersion of 100 Å mm^{-1}, Kilkenny & Westerhuys (1990) note

that W Men is spectroscopically comparable to RY Sgr and similar in colour to RY Sgr at its bluest, except that it appears to have a stronger UV excess.

Lawson et al. (1990) have obtained several years of BV photometry for HV 12842 and W Men. They observed the $(B–V)$ of HV 12842 and W Men (outside declines) to have ranges of 0.33 to 0.45 and 0.33 to 0.58 respectively. These authors also present photometry for the galactic, solar-metallicity RCB star RY Sgr. These data indicate a $(B–V)$ range of 0.40 to 0.77 with a very small estimated reddening to RY Sgr. The mean reddening to stars in the LMC has been found to be relatively small, with an $E(B-V)\lesssim 0.1$ mag. If the LMC stars have similar effective temperatures to RY Sgr and R CrB (as is suggested by their C_2 strengths), then they also seem to display slightly bluer $(B–V)$ colours compared with RY Sgr.

10.2 Observations

In this work we make use of spectroscopic observations obtained over the last several years with the Australian National University (ANU) Cassegrain échelle and University College London coudé échelle spectrographs (UCLES) on the 3.9-m Anglo-Australian Telescope. Spectra were obtained of two RCB stars in the LMC, namely HV 12842 and W Men, as well as of the galactic RCB star SU Tau. An extremely metal-deficient star, HD 26169, was observed with the UCLES arrangement, as a check on the response of the detector and to provide information on the presence of telluric lines. Table 10.1 gives a compilation of all the observations.

The frames taken with the ANU Cassegrain échelle contain five orders centred on the indicated wavelength, λ_c. The spectral coverage with this arrangement was $\sim$ 75 Å per order within the wavelength range of 5850–6720 Å. The detector used was the GEC 584 × 386 pixel CCD. This chip is 12.7 × 8.5 mm^2 with a pixel size of 22 μm square.

The frames taken with UCLES cover 14 échelle orders in the λ_c = 6572 and 6707 Å regions and about 28–30 orders in the λ_c = 4373 Å region. A total spectral coverage of $\sim$ 800 Å within the λ range 5550–8450 Å was obtained for the λ_c = 6572 and 6707 Å regions. In the blue, the spectral range from 4600 to 4900 Å was fully observed. The detector used with UCLES was the blue Thompson 1024 × 1024 pixel CCD, which is coated for extended response in the blue. The chip is 19.5 × 19.5 mm^2 with a pixel size of 19 μm square.

Table 10.1: Spectroscopic observations obtained on the AAT for SU Tau, HV 12842, W Men and an extremely metal-poor star, HD 26169.

Star	λ_c	UT date	exp. (sec)	#	R ($\times 10^3$)
HV 12842	6295	1988 Nov 13	1800	2	25
HV 12842	6215	1988 Nov 13	1800	2	25
SU Tau	6215	1988 Nov 13	600	1	25
SU Tau	6295	1988 Nov 14	900	1	25
W Men	6572	1991 Jul 30	1200	1	27
W Men	6572	1991 Jul 31	1200	2	27
W Men	6707	1991 Jul 31	1200	2	27
HV 12842	6707	1991 Jul 31	550	1	27
HD 26169	6707	1991 Jul 31	120	1	27
HV 12842	6707	1991 Aug 1	1800	1	27
HD 26169	6707	1991 Aug 1	240	1	27
W Men	4373	1991 Aug 1	1800	1	12
HD 26169	4373	1991 Aug 1	240	1	12
HD 26169	6572	1991 Aug 1	240	1	27

In Table 10.1, the exposure time for each observation is shown in seconds and the number of exposures of the star taken in each λ_c region is indicated by the # column. The spectra were obtained using a slit width of 1.5 to 2 arcsec on the sky, equivalent to a resolution $\Delta\lambda = 0.25$ to 0.35 Å. This gives a resolving power, R (defined as $\lambda/\Delta\lambda$), of 12 000 to 27 000.

These data have been reduced using either the MIDAS or FIGARO package, and the equivalent widths of key absorption lines have been measured so that atmospheric and abundance analyses can be undertaken. For the galactic RCB star, SU Tau, the signal-to-noise (S/N) ratio achieved for the smoothed spectra was ~ 100, while for the fainter LMC stars, HV 12842 and W Men, the S/N ratios were ~ 30 and ~ 20 respectively. In cases where there were two observations of the same region, the exposures were added with a weight corresponding to their S/N ratios.

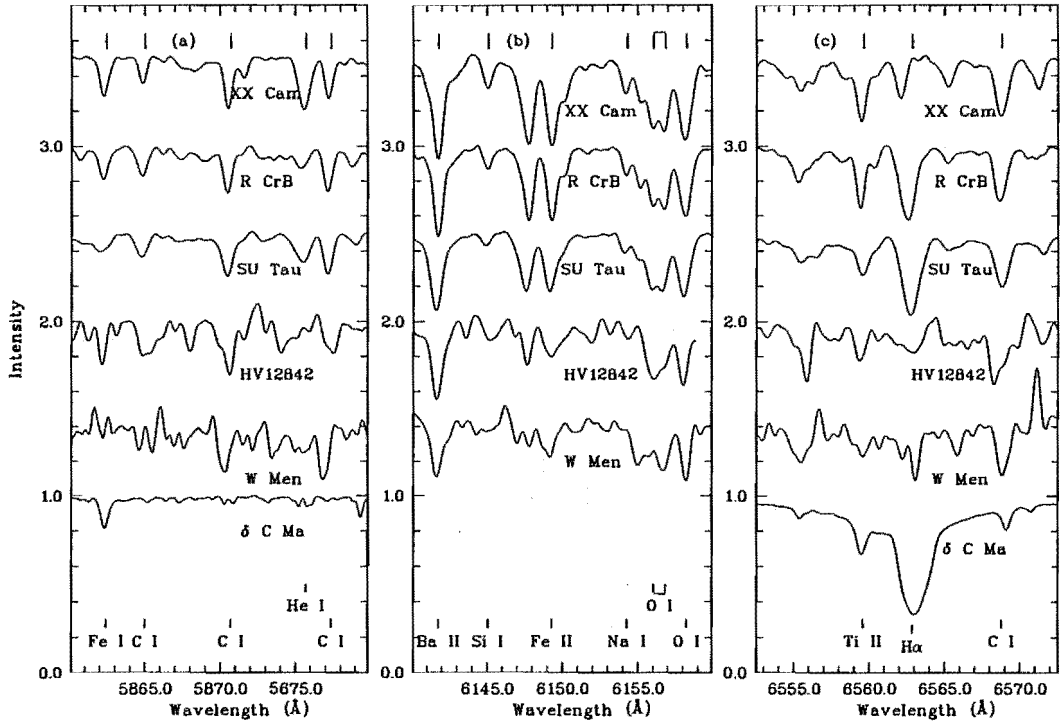

Figure 10.1: Sample spectra (a to e) of RCB stars XX Cam, R CrB, SU Tau, HV 12842 and W Men in a range of different wavelength intervals. A normal, oxygen-rich F8 supergiant, δ CMa, is included for comparison in most of the panels. The XX Cam, R CrB and δ CMa spectra have been reproduced from CL82.

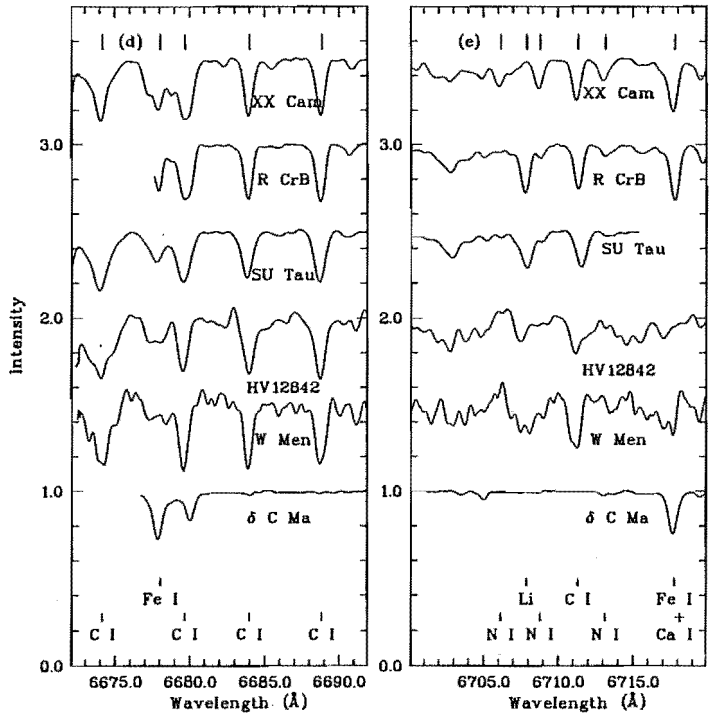

Figure 10.1: (continued). Sample spectra (d and e) of RCB stars, XX Cam, R CrB, SU Tau, HV 12842 and W Men at a range of different wavelength intervals.

A few sample spectra are shown in Figs 10.1(a)–(e). These highlight various spectral regions, e.g., λ5876 He I, λ6150 Ba II/O I, Hα, λ6680 C I and λ6707 Li I/N I, in which the key spectral features are indicated. A normal, oxygen-rich F8 supergiant, δ CMa, is included for comparison.

10.3 Analysis

10.3.1 The data

10.3.1.1 Equivalent widths, W_λ

Using the reduced high-resolution spectra of HV 12842, W Men and SU Tau, the equivalent widths W_λ of lines of a range of species have been measured using a planimeter. We chose to use the planimeter since the relatively low S/N ratios of the LMC spectra rendered the use of Gaussian-fitting-type techniques on the line profiles unreliable. The majority of lines have been taken from the list of CL82, but these have been supplemented using identifications from other sources, e.g. Moore et al. (1966).

In order to make a direct comparison with the results obtained for R CrB by CL82, equivalent widths of lines from CL82's Reticon spectra of R CrB were remeasured using the planimeter. Lines were selected in the range 50 mÅ $< W_\lambda <$ 350 mÅ. These were compared with the original equivalent widths of CL82 which had been calculated by an automated technique of fitting Gaussian profiles to absorption lines.

A linear regression straight line fit to a plot of the CL82 equivalent widths versus the planimeter equivalent widths showed that there was an underestimation using the planimeter method as compared with the Gaussian-fitting method employed by CL82. Specifically, the linear regression gave an experimental underestimation factor of 0.92±0.02 for the planimeter equivalent widths. This was due to the fact that the wings of the absorption lines were not included when drawing in the profiles for planimeter measurements.

For this work it was desirable to have an objective approach to the problem of correcting the W_λs from planimeter values to the total line widths. First, it was assumed that the profile of the absorption line is Gaussian, as was done in the analysis of CL82. If the wing of the profile to be measured by planimeter is drawn as the tangent to the steepest part of the absorption line, then the drawn profile intercepts the continuum of the spectrum at 2σ from the centre of

the line. Thus the integration is cut off at this point, the wings are truncated and the equivalent width underestimated by a certain factor. This theoretical truncation factor was calculated to be 0.925. This is similar to that obtained experimentally. The inverse of this value was subsequently applied to the widths measured by planimeter to correct them to an equivalent width scale which is less subject to systematic error.

10.3.1.2 *gf* values

To undertake the abundance analysis, *gf* values for all lines must be determined. The *gf* values for hydrogen, helium, lithium and oxygen are originally from Wiese et al. (1966). The *gf* values for nitrogen come from the semi-empirical calculations of Kurucz & Peytremann (1975). Carbon *gf* values are from CL82. All other *gf* values were recalculated using a so-called 'reverse abundance analysis' to deduce empirical *gf* values. This involves measuring solar equivalent widths from the continuum-normalized Sacremento Peak integrated solar spectrum (Beckers et al. 1976) using an automated technique of fitting Gaussians to absorption lines (Cottrell & Sneden 1986). A recent Smithsonian Astrophysical Observatory solar model (Kurucz, private communication) was used and standard solar abundances (Ross & Aller 1976) were included with the model atmosphere program WIDTH6 – a derivative of Kurucz's ATLAS5 code (Kurucz 1970). The recalculated *gf* values obtained from this reverse analysis and the equivalent widths for the three programme RCB stars are listed in Table 10.2. Included in this table for comparison are the equivalent widths for R CrB as measured by CL82 from their Reticon spectra. These equivalent widths were used in a reanalysis of R CrB, as described in Section 10.4.1.

10.3.2 The hydrogen-deficient models

The measured equivalent widths have been used as input to the WIDTH6 analysis program. This has been appropriately modified to include a more extensive wavelength range for both the bound-free and free-free opacities due to C I. These opacities are necessary to undertake an analysis of these He- and C-rich atmospheres. The next most important opacity source after the C I and He^- opacities is C^-, which is also included in our version of WIDTH6.

Model atmospheres from S75 have been used to interpret the measured lines. These models were also employed by CL82 in their abundance analysis of R CrB

Table 10.2: Line and equivalent width data.

Line	λ (Å)	Multiplet	χ (eV)	log *gf*	Equivalent width, W_λ (mÅ)			
					SU Tau	HV 12842	W Men	R CrB
H I								
	4861.340	1	10.20	-0.020	–	–	296.8	395.1
	6562.810	1	10.20	0.710	699.8	325.0	296.8	536.0
He I								
	5875.630	11	20.87	0.739	183.3	55.5-131.5	158.5	135.0
Li I								
	6707.780	1	0.00	0.000	136.3	70.3	57.7	146.3
	6707.930	1	0.00	-0.300	68.2	35.2	8.9	73.2
N I								
	6423.030	21.03	11.76	-2.220	3.2	–	–	8.8
	6436.710	21.01	11.76	-1.390	–	54.1	–	10.5
	6437.680	21.01	11.75	-4.690	–	25.0	–	75.2
	6440.940	21.03	11.76	-1.140	–	33.6	–	75.0
	6441.710	21.03	11.76	-2.370	–	41.6	–	30.0
	6457.900	21.01	11.76	-2.170	99.8	74.9	–	123.4
	6468.440	21.01	11.76	-3.740	–	73.4	–	55.9
	6483.750	21	11.75	-1.040	83.3	18.9	14.7	169.5
	6484.800	21	11.76	-0.760	68.7	27.3	53.4	145.1
	6506.310	21	11.76	-3.370	77.0	83.3	14.7	107.0
	6622.540	20	11.76	-1.530	–	–	–	51.0
	6642.000	–	11.75	-1.580	54.3	67.2	–	56.0
	6646.500	20	11.75	-1.660	12.5	54.3	–	45.0
	6656.510	20	11.75	-1.660	10.4	48.0	–	66.0
	6700.500	59	11.84	-2.340	20.9	31.5	–	20.0
	6704.840	59	11.84	-1.350	39.7	72.2	14.7	50.0
	6706.110	59	11.84	-1.800	25.1	–	–	30.0
	6708.760	59	11.84	-1.790	39.7	29.6	35.0	56.2
	6713.110	59	11.84	-2.810	12.5	24.1	–	48.3
	6720.970	58	11.84	-2.650	–	62.9	16.5	47.6
	6722.620	59	11.84	-0.980	–	112.9	42.4	128.0
	6733.320	58	11.84	-1.790	–	–	–	74.2
	6752.030	58	11.84	-1.330	–	–	51.6	30.0
	9798.560	19	11.75	-0.640	–	–	–	122.2
	9810.000	19	11.75	-0.820	–	–	–	122.0
	9814.000	19	11.76	-1.570	–	–	–	96.0
	9822.750	19	11.76	-0.250	–	–	–	205.0
	9834.620	19	11.76	-0.610	–	–	–	173.0
	9863.330	19	11.76	0.000	–	–	–	229.0
	9872.150	19	11.76	-0.650	–	–	–	166.0
O I								
	5958.480	23	10.99	-0.870	252.1	172.9	–	234.5
	6155.980	10	10.74	-0.700	297.8	356.2	267.2	342.0
	6156.770	10	10.74	-0.480	283.2	237.5	398.1	332.1
	6158.180	10	10.74	-0.330	374.9	331.1	357.5	412.6
	6300.310	1F	0.00	-9.694	221.4	238.8	–	–
	6363.790	1F	0.02	-10.250	70.8	52.1	99.5	93.0
	6453.600	9	10.74	-1.350	201.8	201.8	–	182.6
	6454.450	9	10.74	-1.130	178.9	178.9	–	226.0
Na I								
	6154.230	5	2.10	-1.627	72.9	68.8	88.5	113.7
	6160.750	5	2.10	-1.373	187.4	138.9	173.3	210.7

Table 10.2: continued

Line	λ (Å)	Multiplet	χ (eV)	log *gf*	Equivalent width, W_λ (mÅ)			
					SU Tau	HV 12842	W Men	R CrB
Al I								
	6696.030	5	3.14	-1.711	50.1	44.4	–	86.3
	6698.670	5	3.14	-2.013	29.2	26.0	–	63.4
Si I								
	5948.550	16	5.08	-1.595	252.1	133.3	–	257.3
	6131.580	30	5.61	-1.939	36.0	10.4	–	65.8
	6131.860	30	5.61	-1.926	36.9	10.5	–	67.7
	6145.020	29	5.61	-1.689	41.6	75.6	101.3	96.8
	6555.470	62	5.98	-1.248	187.4	79.6	254.4	206.0
	6719.620	–	6.00	-1.972	–	27.8	36.9	70.3
	6721.840	38	5.86	-1.450	–	62.9	84.8	112.7
Si II								
	5978.910	4	10.07	0.074	189.6	156.3	232.2	227.3
	6371.359	2	8.12	-0.477	–	–	689.3	–
S I								
	6536.360	–	8.05	-1.336	–	–	–	73.0
	6743.580	8	7.86	-0.812	–	–	175.1	178.4
	6748.780	8	7.87	-0.687	–	–	191.6	227.8
	6757.200	8	7.87	-0.451	–	–	191.6	241.6
Ca I								
	5857.459	47	2.93	-0.431	–	–	154.8	–
	6122.230	3	1.89	-0.908	327.0	249.9	–	378.1
	6162.180	3	1.90	-0.718	295.8	192.6	160.4	325.6
	6166.440	20	2.52	-1.370	47.9	14.8	–	68.0
	6439.080	18	2.52	-0.581	–	193.5	–	296.7
	6449.820	19	2.52	-1.026	–	77.7	–	217.9
	6471.670	18	2.52	-1.118	110.3	27.3	–	181.2
	6493.790	18	2.52	-0.825	183.1	95.7	169.6	329.7
Sc II								
	6309.890	–	1.50	-1.450	263.1	102.3	191.6	–
	6320.850	28	1.51	-1.799	181.7	104.5	175.1	–
Ti II								
	4865.620	29	1.12	-2.762	–	–	171.4	360.7
	4874.010	114	3.09	-1.070	–	–	–	379.3
	6559.570	91	2.05	-2.442	249.9	262.5	208.3	263.0
V II								
	5928.890	98	2.52	-1.732	–	–	–	154.3
Cr II								
	4812.350	30	3.86	-1.907	–	–	176.9	299.0
	4848.250	30	3.86	-1.367	–	–	318.8	417.1
	4864.320	30	3.86	-0.991	–	–	235.9	421.1
	4876.400	30	3.85	-1.574	–	–	89.7	318.9
	4876.490	30	3.85	-1.522	–	–	59.0	99.2
Fe I								
	4787.830	384	3.00	-2.624	–	–	24.0	27.8
	4788.770	588	3.24	-1.929	–	–	36.9	44.2
	4789.660	753	3.55	-1.304	–	–	42.4	142.7
	4872.140	318	2.88	-1.038	–	–	–	352.5
	5852.228	1178	4.55	-1.260	–	–	24.0	–
	5859.596	1181	4.55	-0.708	–	–	58.1	–
	5862.370	1180	4.55	-0.537	93.8	145.8	63.6	–

Table 10.2: continued

Line	λ (Å)	Multiplet	χ (eV)	log *gf*	Equivalent width, W_λ (mÅ)			
					SU Tau	HV 12842	W Men	R CrB
Fe I								
	5883.810	982	3.96	-1.107	108.4	43.7	–	–
	5916.260	170	2.45	-3.035	–	31.5	–	90.2
	5930.190	1180	4.65	-0.420	–	–	–	179.9
	5934.670	982	3.93	-1.286	–	56.7	–	99.6
	6008.566	982	3.88	-1.147	–	–	66.3	–
	6027.059	1018	4.08	-1.312	–	–	79.2	–
	6056.013	1259	4.73	-0.563	–	–	44.2	–
	6136.620	169	2.45	-1.947	179.1	147.8	130.9	272.4
	6137.700	207	2.59	-1.860	164.6	85.4	–	246.6
	6170.520	1260	4.79	-0.395	66.6	–	–	101.6
	6173.340	62	2.22	-3.080	–	105.6	90.3	116.6
	6188.000	959	3.94	-1.732	–	–	–	43.9
	6191.570	169	2.43	-2.015	–	–	–	288.1
	6200.320	207	2.61	-2.616	–	–	–	72.4
	6301.510	816	3.65	-1.030	102.3	58.7	–	–
	6302.500	816	3.69	-1.426	91.9	33.6	–	–
	6315.810	1014	4.07	-1.695	50.1	22.9	–	–
	6318.027	168	2.45	-2.319	–	–	230.4	–
	6335.340	62	2.20	-2.663	–	–	112.5	–
	6336.830	816	3.69	-1.153	–	–	173.3	–
	6344.155	169	2.43	-3.006	–	–	18.4	–
	6355.035	342	2.84	-2.430	–	–	14.7	–
	6380.750	101	4.19	-1.434	37.5	31.3	44.2	–
	6393.610	168	2.43	-2.047	125.0	68.8	136.4	–
	6419.960	1258	4.71	-0.471	93.8	91.6	–	185.3
	6421.360	111	2.28	-2.459	125.0	62.5	–	215.1
	6430.860	62	2.18	-2.499	137.5	–	–	214.3
	6469.190	1258	4.83	-0.742	–	104.0	–	71.5
	6475.630	206	2.56	-2.918	–	42.0	–	73.6
	6518.373	168	2.83	-2.647	–	–	64.5	–
	6546.250	268	2.76	-2.043	–	–	176.9	154.0
	6592.930	268	2.73	-1.978	150.0	68.5	–	203.0
	6593.880	168	2.43	-2.653	72.9	62.5	–	104.0
	6609.120	206	2.56	-2.814	45.9	20.9	–	–
	6750.160	111	2.42	-2.553	–	–	60.8	84.9
Fe II								
	4833.190	30	2.66	-4.619	–	–	–	211.7
	4840.000	30	2.68	-4.660	–	–	193.5	281.8
	5991.380	46	3.15	-3.746	302.1	249.9	199.0	316.1
	6149.250	74	3.89	-2.951	339.5	214.1	248.8	368.1
	6175.160	200	6.22	-2.332	–	74.1	88.5	236.5
	6179.400	163	5.57	-2.704	–	35.1	57.1	169.2
	6369.460	40	2.89	-4.280	202.0	62.5	158.5	–
	6383.715	–	5.55	-2.280	–	–	130.9	–
	6385.473	–	5.55	-2.636	–	–	158.5	–
	6416.930	74	3.89	-2.884	374.9	364.6	–	330.3
	6432.680	40	2.89	-3.820	287.5	–	–	304.0
	6442.950	–	5.55	-2.527	–	46.2	–	132.0
	6446.400	199	6.22	-2.015	–	42.0	–	119.0
	6493.060	–	5.58	-2.612	122.7	35.7	–	237.3
	6516.080	40	2.89	-3.564	–	–	184.3	356.0

Table 10.2: continued

Line	λ (Å)	Multiplet	χ (eV)	log *gf*	Equivalent width, W_λ (mÅ)			
					SU Tau	HV 12842	W Men	R CrB
Co I								
	4867.870	158	3.12	0.396	–	–	14.7	124.0
Ni I								
	4786.540	98	3.42	-0.386	–	–	55.3	244.4
	4829.030	131	3.54	-0.529	–	–	57.1	155.0
	4831.180	111	3.61	-0.561	–	–	–	151.4
	4857.400	111	3.74	-0.797	–	–	66.3	103.5
	4866.280	111	3.54	-0.445	–	–	160.4	234.7
	6327.600	44	1.68	-3.178	31.4	62.9	92.1	–
	6767.780	57	1.83	-2.436	–	–	94.0	119.3
	6772.320	127	3.66	-1.098	–	–	70.1	64.9
Ni II								
	6195.360	–	14.50	6.077	–	–	–	–
	6433.770	–	15.00	5.259	–	–	–	–
	6459.740	–	14.70	4.473	–	–	–	–
	6487.230	–	15.00	4.652	–	–	53.4	–
	6541.190	–	15.00	5.039	–	–	136.4	–
Y II								
	4883.690	22	1.08	-0.151	–	–	340.9	446.0
	5402.780	35	1.84	-0.430	–	–	–	162.3
	5521.590	27	1.74	-0.910	–	–	–	123.0
Zr II								
	6787.150	–	2.47	-0.947	–	–	66.3	–
Ba II								
	5853.680	2	0.61	-1.297	–	181.5	244.2	459.0
	6141.730	2	0.70	-0.641	454.1	435.3	388.9	432.7
	6496.910	2	0.60	-0.939	441.0	401.6	311.5	508.2
La II								
	6774.260	–	0.12	-1.531	–	–	119.8	–
Nd II								
	4811.350	3	0.06	-0.568	–	–	141.9	63.0
	5431.530	80	1.12	0.050	–	–	–	–
	5842.390	86	1.28	-0.212	–	92.6	66.3	78.0

and XX Cam. There has been some discussion that these models are no longer appropriate for this type of analysis. However, Jones (1991) has recently converged new hydrogen-deficient models for which the derived atmospheric parameters and abundances for R CrB (using the same CL82 equivalent width data) are similar to those found using Schönberner's models (see Table 10.3).

The grid of hydrogen-deficient model atmospheres included models with effective temperatures $T_{\rm eff}$= 6000 K, 7000 K and 8000 K, gravities log g= 0.0, 0.5 and 1.0 and a variety of different composition ratios of hydrogen, helium and carbon. The He:C ratio of a model refers to the composition by number expressed as a percentage of the helium and carbon abundances. This specifies a particular model from the grid of models supplied by Schönberner.

Fig. 10.2 (a)–(c) shows the effect on the temperature structure of altering the He:C ratio, the gravity or the temperature of the hydrogen-deficient model. Differences are plotted relative to a reference model with $T_{\rm eff}$ = 7000 K, log g = 0.5 and He:C = 97:3. The temperature differences of models with He:C ratios of 90:10 (dotted) and 99:1 (solid) are displayed relative to the reference model in Fig. 10.2(a). These are all for models with $T_{\rm eff}$ = 7000 K and log g = 0.5. The dotted and solid lines in Fig. 10.2(b) represent the temperature differences for models with log g of 1.0 and 0.0 respectively. In Fig. 10.2(c), the temperature differences are plotted for models with log g = 0.5, He:C = 99:1 and effective temperatures of 7000 K (solid) and 7200 K (dotted). The model represented by the dashed line is the same as the reference model, except for a $T_{\rm eff}$ of 6800 K. The 6800-K and 7200-K models have been interpolated from the grid of Schönberner's models. From these plots, it can be seen that a change of the He:C ratio from 97:3 to 99:1 has a similar effect on the temperature structure as an increase of the gravity by 0.5 dex. In Fig. 10.2(c), a change in the temperature of 200 K affects the temperature structure in a systematic manner throughout most of the depth of the model atmosphere. The main difference in the temperature structure occurs in the innermost regions of the model atmosphere, and thus the choice of model will have a greater impact on lines that form in the deeper layers of the atmosphere.

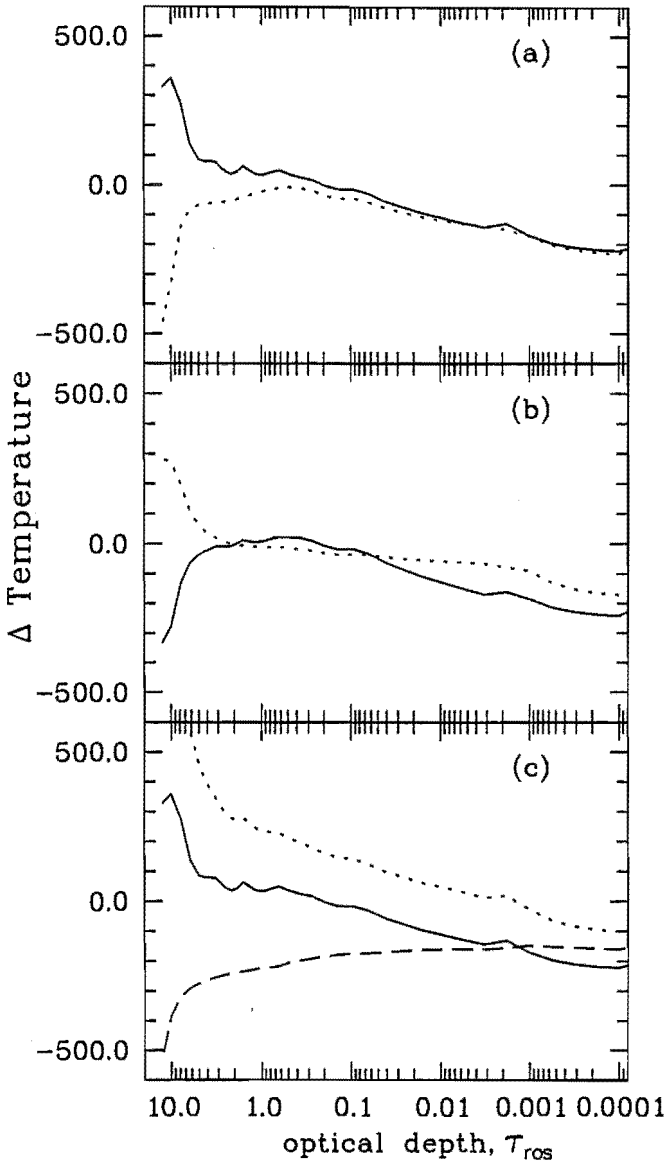

Figure 10.2: Temperature differences (relative to a model at $T_{\rm eff}$ =7000 K, log g = 0.5 and He:C of 97:3) for various RCB model atmospheres are plotted versus the Rosseland mean optical depth ($\tau_{\rm ros}$). (a) solid line: $T_{\rm eff}$ =7000 K, log g =0.5, He:C=99:1; dotted line: $T_{\rm eff}$ =7000 K, log g =0.5, He:C=90:10. (b) solid line: $T_{\rm eff}$ =7000 K, log g =0.0, He:C=97:3; dotted line: $T_{\rm eff}$ =7000 K, log g =1.0, He:C=97:3. (c) solid line: $T_{\rm eff}$ =7000 K, log g =0.5, He:C=99:1; dotted line: $T_{\rm eff}$ =7200 K, log g =0.5, He:C=99:1; dashed line: $T_{\rm eff}$ =6800 K, log g =0.5, He:C=97:3.

10.3.3 Atmospheric parameters

10.3.3.1 $T_{\rm eff}$

The combination of the forbidden O I line at 6363 Å (with an excitation potential of $\chi \sim 0$ eV) together with several O I lines ($\chi \sim 11$ eV) gives a large χ baseline which results in a good indication of excitation temperature and hence the $T_{\rm eff}$ through the model atmosphere. The derived O I abundance must be independent of the lower excitation potential at the correct $T_{\rm eff}$. Neutral and ionized lines of iron are used as secondary temperature indicators. In SU Tau the λ6363 [O I] line is reasonably clean and unblended. For HV 12842 and W Men it is blended slightly but measurable. The λ6300 [O I] line is severely blended with an Si I line and has not been used in the analysis.

10.3.3.2 log g

The surface gravity is determined by the condition that the neutral and ionized lines of a given element give the same abundance. The best species for this purpose is iron, for which we have measured about twenty Fe I lines and about ten Fe II lines in each of the three programme stars.

10.3.3.3 Microturbulence, $\xi_{\rm t}$

The microturbulent velocity characteristic of these stars is obtained from the requirement that the derived abundance of an element be independent of the reduced width (log W_λ/λ) of the line. Following CL82, we have used Fe I, Fe II and O I lines, as these species have the largest range in reduced width, enabling the microturbulence to be determined more accurately.

10.3.3.4 Opacity considerations and the C/He ratio

The major atmospheric constituents (in this case He and C) determine the dominant opacity source(s) and consequently the zero-point in the scale of abundances. This determination is dependent upon our assumption that the λ5876 He I line is of photospheric origin. This was the same assumption employed by CL82. Although this line may have some chromospheric contribution, which will affect the C/He ratio and hence the overall metallicity (through the continuous opacity), the relative abundances (element/Fe) can be considered to be much more reliable.

(When expressing the C/He ratio in this form we are referring to the input, or output, abundance ratios in the model atmosphere program, WIDTH6.)

In the hydrogen-deficient, helium- and carbon-rich atmospheres of RCB stars, we expect carbon to be the dominant contributor to the continuous opacity, unless either the C/He ratio is very small or the H/C ratio is quite large. The carbon opacity is due to the photoionization of neutral carbon, as well as the carbon free-free interaction of $C^+ + e^-$. Carbon also provides electrons for the next most important opacity source, He^-. Thus carbon effectively determines the transparency of the stellar atmosphere. However, helium is by far the most abundant element in RCB star atmospheres, being the main contributor to the mean molecular weight and therefore the gas pressure.

One key point to note is that, because carbon opacities are the dominant continuous opacity source in all the stars analysed in this work, any given C I line will have the same or similar strength in each star (see Figs 10.1a and 10.1d). This is a good illustration of the principle that the line strength is proportional to the ratio of line to continuum opacity. Since carbon contributes to both these quantities, the ratio is independent (at least to first order) of the carbon abundance. This is valid as long as carbon is the dominant contributor to the continuous opacity, which CL82 have shown to be the case for C/He $\geq$ 0.002.

Fig. 10.3(a) shows the total continuous opacity as well as the the main contributors to this opacity for the depths where the continuum is forming for a typical hydrogen-deficient model. This specific model has $T_{\rm eff}$ = 7000 K, log g = 0.5, He:C = 97:3 and an input C/He ratio of 0.004. By varying the carbon abundance we effectively vary the C/He ratio since the He abundance is $\sim$1. If the C/He ratio is decreased to 0.002, as was done for the model in Fig. 10.3(b), the contributions from both the C I and C^- opacity sources will be diminished. Neutral carbon is no longer the dominant opacity source, but is equalled by the He^- opacity contribution. This is called the 'critical' C/He ratio.

Upper and lower limits can be placed upon the C/He ratio as discussed by S75 and CL82. Because the RCB stars are not extreme Population I objects, we can set the upper limit on the C/He ratio by requiring that the derived metal abundances for galactic RCB stars do not exceed the solar value. The lower limit is set by the observed equivalent widths of weak C I lines. (These equivalent widths will be constant if the C/He ratio exceeds a certain minimum value.) The limits set by CL82 for R CrB were 0.003 $\leq$ C/He $\leq$ 0.03. The He I line at

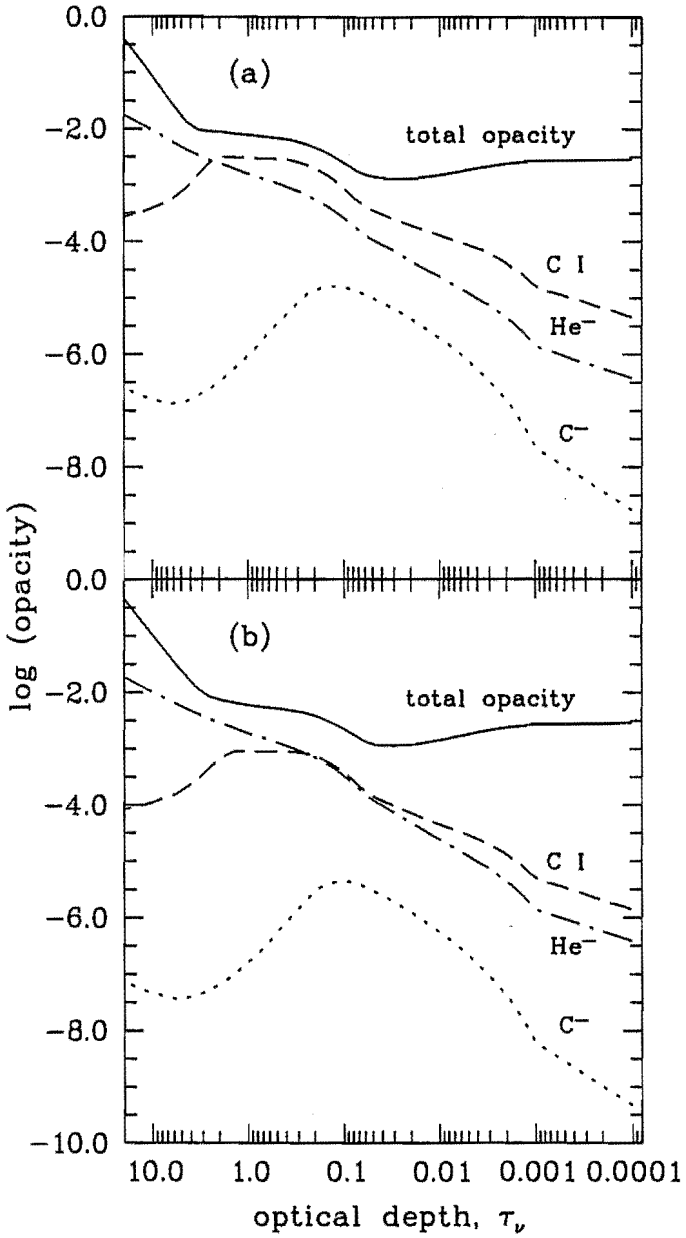

Figure 10.3: The total opacity, and dominant opacity sources at the depths where the continuum is forming, are plotted versus the optical depth at 650 nm (τ_{650}) for two different C/He ratios. Panel (a) shows a model at $T_{\rm eff}$ =7000 K, log g = 0.5, He:C = 97:3 and C/He = 0.004. Panel (b) has C/He = 0.002 (the 'critical' C/He ratio) and all other parameters as for (a).

Table 10.3: A comparison of previous abundance analyses for the galactic RCB star, R CrB.

Parameter	S75	CL82	J91
$T_{\rm eff}$(K)	6900 ± 600	7000 ± 250	7400 ± 500
log g(cgs)	0.15 ± 0.65	0.50 ± 0.30	0.55 ± 0.25
ξ_t (km s^{-1})	6.5 ± 1	8 ± 1	8 ± 2
C/He	0.03	0.004	0.005

5876 Å is used to determine the C/He ratio (assuming that this line has a purely photospheric origin) when a self-consistent C/He ratio is derived from the model input abundances and from the He I line.

10.4 Results of the abundance analysis

10.4.1 R CrB reanalysed

A reanalysis of R CrB was completed using the newly computed *gf* values. The equivalent widths given in CL82 and the Schönberner grid of hydrogen-deficient models were used. The atmospheric parameters derived for R CrB are as follows:

(i) $T_{\rm eff}$= 6900 K from O I lines (see Fig. 10.4a) and also the Fe I and Fe II lines, with further confirmation by other species, e.g., Ca I;

(ii) log g = 0.5 from the requirement that the Fe I and Fe II lines give the same abundance (see Fig. 10.4c), and

(iii) ξ_t = 8 km s^{-1} from O I lines (see Fig. 10.4b) and the Fe I and Fe II lines (see Fig. 10.4d).

A C/He ratio of 0.0034 was determined self-consistently from the He I line at 5876 Å. The abundance determination made use of the 99:1 He:C model and a solar mix of metals. The effect of the newly determined *gf* values on the derived atmospheric parameters and abundances is very small for most species and well within the uncertainties of the abundance analysis (see Section 10.4.3). Table 10.3 shows the atmospheric parameters derived from previous fine analyses of R CrB. There is good agreement between this reanalysis of R CrB and the previous abundance analyses shown for this star.

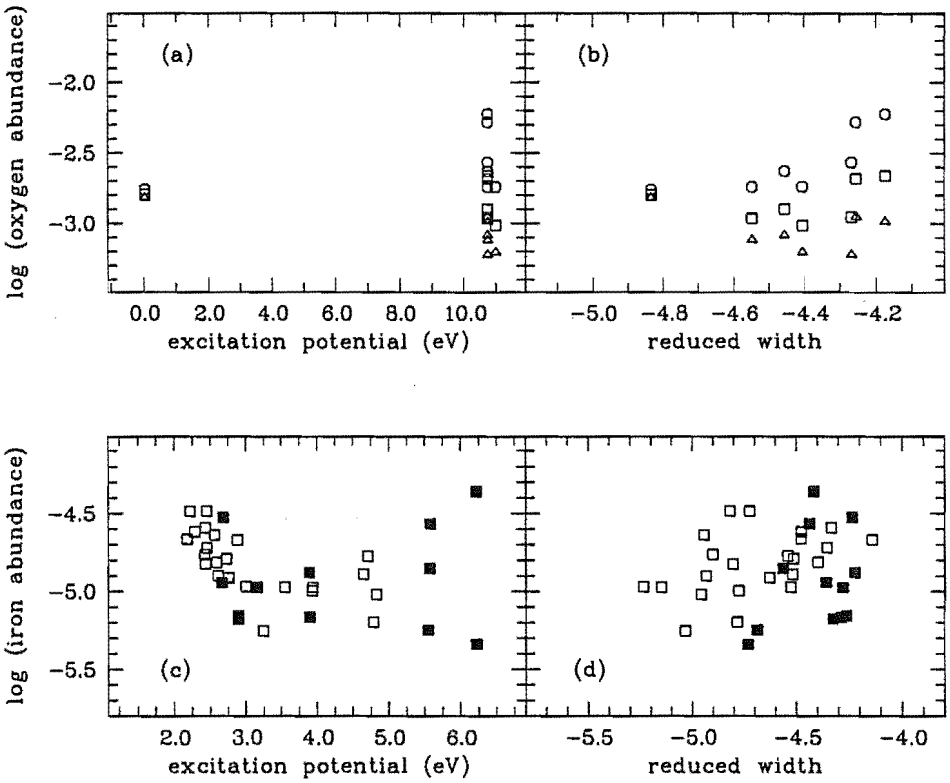

Figure 10.4: Derived oxygen (a and b) and iron (c and d) abundances for R CrB plotted against the excitation potential of the transition and the reduced width of the line. The model parameters are $T_{\rm eff}$ = 6900 K, log g = 0.5 and He:C = 99:1 with a range of microturbulent velocities. These indicate the appropriateness of the atmospheric parameters derived. In panels (a) and (b) the abundances are plotted for $\xi_{\rm t}$ = 6 (circles), 8 (squares) and 10 km s^{-1} (triangles). In all panels, neutral lines are indicted by open symbols and ionized lines by filled symbols.

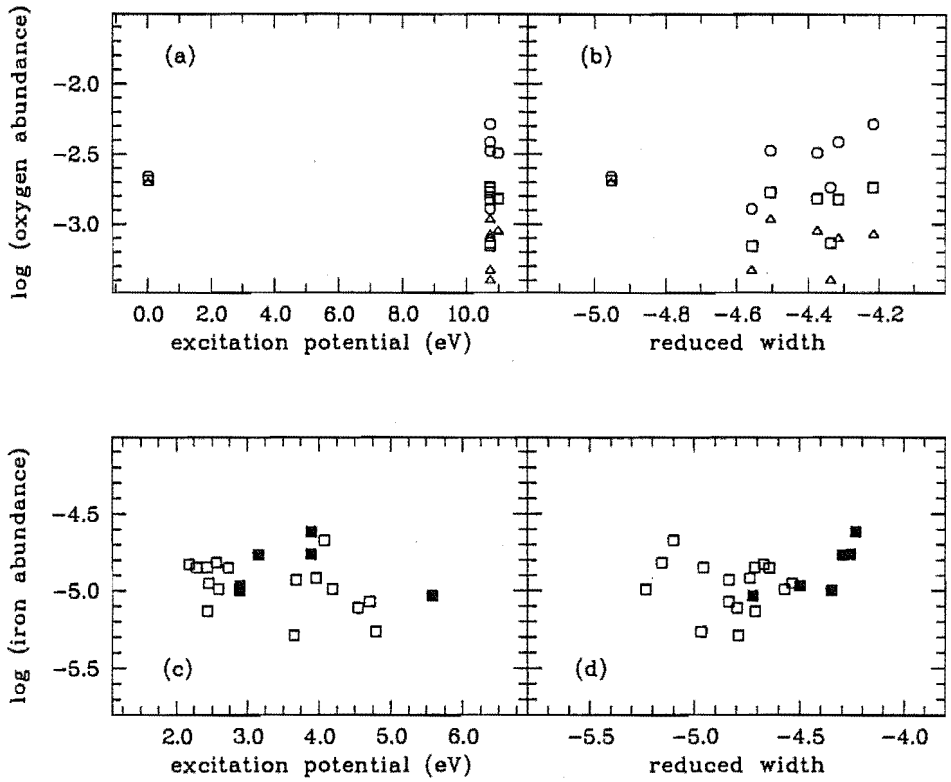

Figure 10.5: As for Fig. 10.4 but for SU Tau with model parameters as described in Table 10.4. In panels (a) and (b) the abundances are plotted for $\xi_t = 5$ (circles), 7 (squares) and 9 $\mathrm{km\,s^{-1}}$ (triangles).

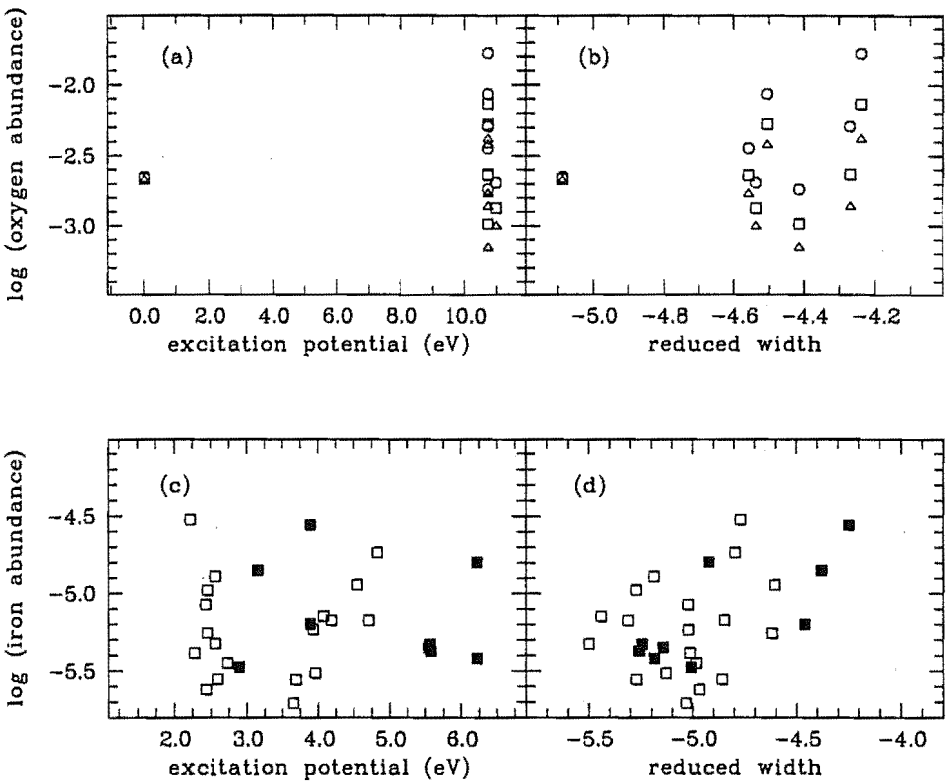

Figure 10.6: As for Fig. 10.4 but for the LMC RCB star, HV 12842, with model parameters as described in Table 10.4. In panels (a) and (b) the abundances are plotted for $\xi_t = 6$ (circles), 8 (squares) and 10 $\mathrm{km\,s^{-1}}$ (triangles).

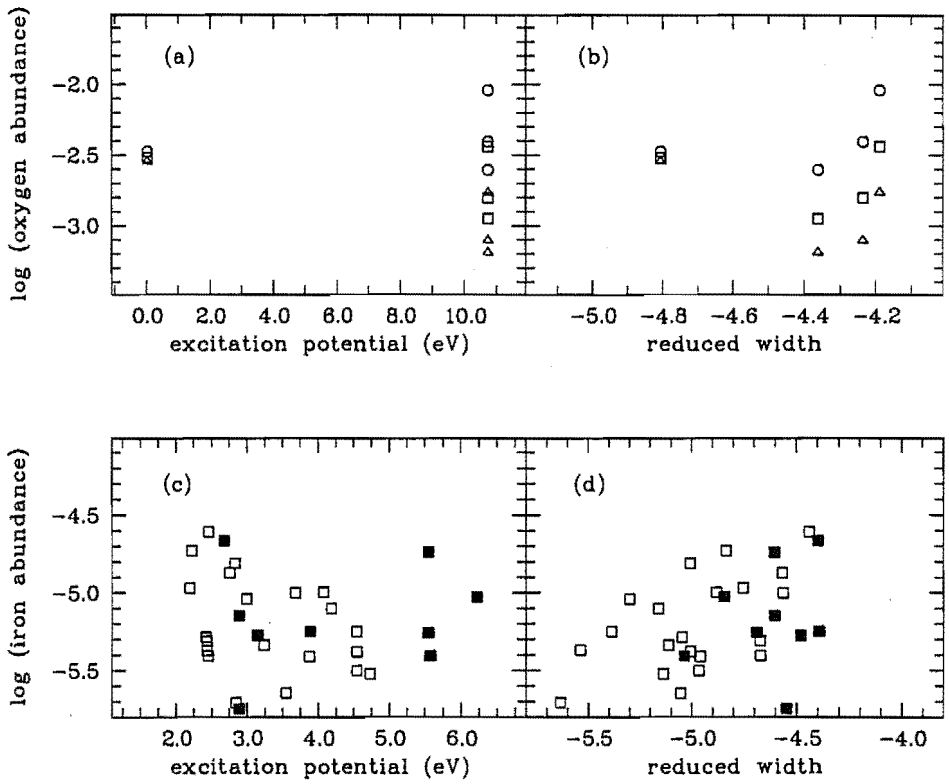

Figure 10.7: As for Fig. 10.4 but for the LMC RCB star, W Men, with model parameters as described in Table 10.4. In panels (a) and (b) the abundances are plotted for $\xi_t = 5$ (circles), 7 (squares) and 9 km s^{-1} (triangles).

Table 10.4: The atmospheric parameters determined from an abundance analysis of the four RCB stars: R CrB, SU Tau, HV 12842 and W Men. Previous analyses for R CrB, XX Cam and RY Sgr are included for comparison.

Parameter	R CrB (CL82)	XX Cam (CL82)	RY Sgr (J91)	R CrB	SU Tau	HV 12842	W Men
$T_{\rm eff}$ (K)	7000	7000	7000	6900	6800	6800	6700
	±250	±250	±500	±250	±250	±500	±500
log g (cgs)	0.5	0.0	0.65	0.5	0.5	1.0	0.75
	±0.3	±0.3	±0.25	±0.25	±0.25	±0.35	±0.35
ξ_t (km s^{-1})	8	8	10	8	7	8	7
	±1	±1	±2	±1	±1	±2	±2
C/He	0.004	0.003	0.004	0.0034	0.004	0.011	0.004

10.4.2 The RCB stars SU Tau, HV 12842 and W Men

The atmospheric parameters derived for SU Tau, HV 12842 and W Men are displayed in Table 10.4. The previous analyses for R CrB, XX Cam and RY Sgr by CL82 and J91, as well as the reanalysis of R CrB in this paper, are included for comparison. The usual criteria have been employed to determine the most appropriate atmospheric parameters, namely consistency of the derived abundance with excitation potential, with reduced width and between ionization states. These comparisons are shown for SU Tau in Figs 10.5(a)–(d), HV 12842 in Figs 10.6(a)–(d) and W Men in Figs 10.7(a)–(d).

Panel (a) in each figure shows the determination of the effective temperature, when the derived oxygen abundances are independent of the lower excitation potential of the line. Other species, such as Fe and Ca, were used as secondary temperature indicators. The determinations of the gravity and the microturbulence are shown in panels (b)–(d).

The abundance analysis for SU Tau, HV 12842 and W Men made use of model atmospheres with structure based on the 97:3 He:C models. Some interpolation in the grid of models for temperature and gravity was employed. The derived abundances for SU Tau, HV 12842 and W Men, as well as the reanalysis of R CrB, are displayed in Table 10.5. Comparison is made with the abundances derived for R CrB and XX Cam (CL82) and for RY Sgr (J91).

The relative abundances derived in this study for R CrB, SU Tau, HV 12842 and W Men are displayed in Fig. 10.8. These generally follow the solar distribution for all elements heavier than oxygen. (Individual elemental abundances will be discussed in Section 10.4.4). The lower overall abundance of the heavier

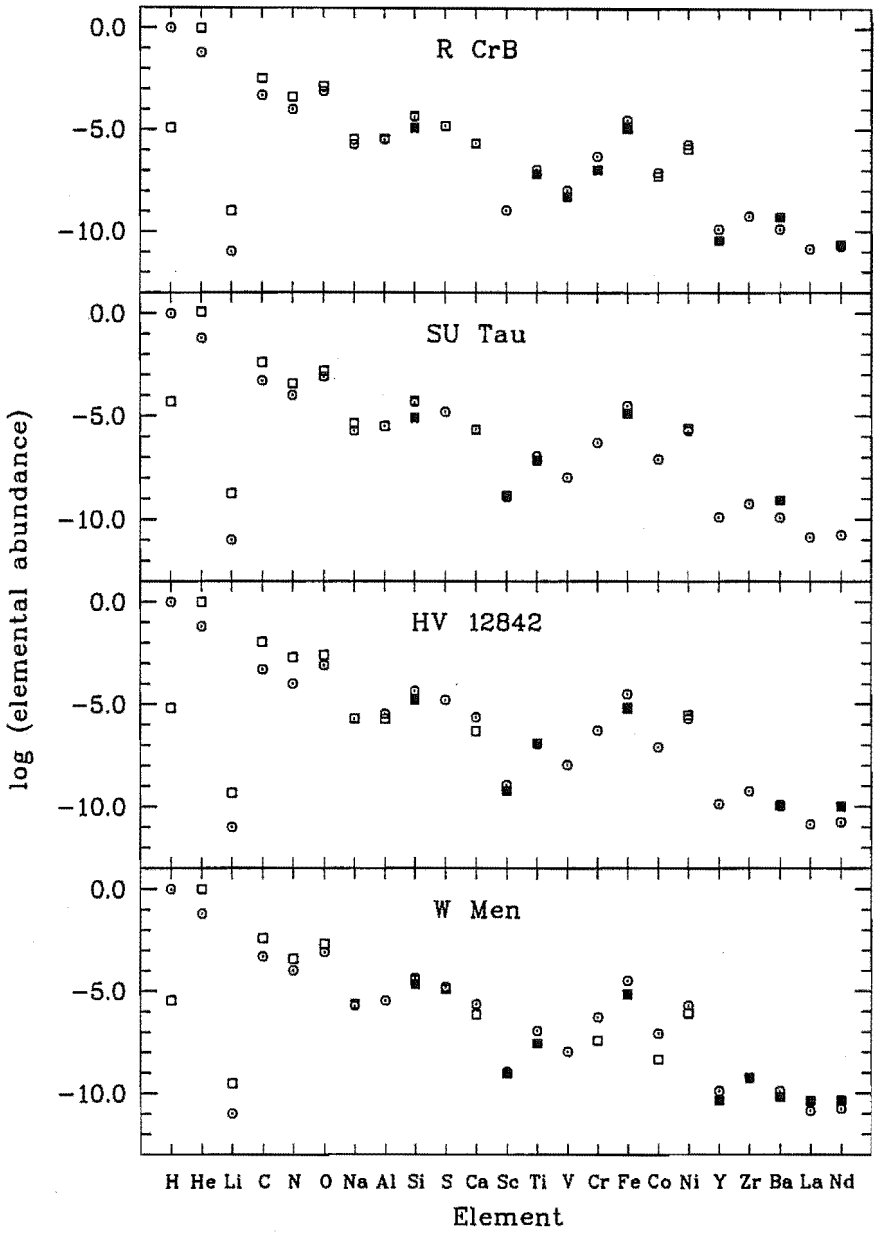

Figure 10.8: Elemental abundances for R CrB, SU Tau, HV 12842 and W Men compared with the Sun (⊙ symbols). The RCB stars are shown with open squares for neutral lines and filled squares for ionized lines. This figure shows the same general trend of abundances for the four RCB stars, with large enhancements of Li and N, and of course He and C. Hydrogen is depleted by more than a factor of 10^4. Iron is depleted in the LMC objects by factors of $\sim$2 relative to the galactic RCB stars and $\sim$5 relative to the Sun.

Table 10.5: The abundance ratios determined from the abundance analysis.

Quantity	R CrB (CL82)	XX Cam (CL82)	RY Sgr (J91)	R CrB	SU Tau	HV 12842	W Men
[H/He]	−5.9	< −8.6	−4.4	−5.9	−5.4	−6.2	−6.5
[Fe/total]	−1.1	−0.8	−0.4	−0.4	−0.4	−0.7	−0.7
[Li/Fe]	+2.7	<+1.4		+2.4	+2.6	+2.4	+2.1
[C/Fe]	+1.5	+1.2	+1.0	+1.2	+1.3	+2.0	+1.6
[N/Fe]	+1.1	+1.4	+1.7	+1.0	+1.0	+2.0	+1.2
[O/Fe]	+0.9	+0.8	−0.2	+0.6	+0.6	+1.2	+1.1
[Na/Fe]	+0.7	+1.0	+0.6	+0.6	+0.7	+0.7	+0.7
[Al/Fe]			+0.9	+0.4	+0.3	+0.4	
[Si/Fe]			+0.4	+0.4	+0.4	+0.3	+0.5
[Ca/Fe]			−0.3	+0.4	+0.3	0.0	+0.2
[Ni/Fe]			+1.4	+0.2	+0.4	+0.9	+0.2
[Y/Fe]			+0.4	+0.2			+0.5
[Zr/Fe]							+0.7
[Ba/Fe]			+0.1	+1.0	+1.1	+0.6	+0.4
[La/Fe]							+1.2
[Nd/Fe]			+1.9	+0.5		+1.4	+1.1

elements in the Magellanic Cloud stars is indicative of the overall deficiency (by up to a factor of 2 or more) determined from other LMC objects.

10.4.3 Uncertainties in the abundance analysis

The spectra of the two LMC RCB stars have significantly lower S/N ratios ($\sim$ 20–30) than the spectra obtained for the galactic RCB star SU Tau (S/N $\sim$ 100). Consequently, we would expect the random uncertainty in the measured equivalent widths for these stars to be higher. An increased scatter in the derived abundances is observed where there are several lines of the same species. An illustration of this effect can be seen in panels (c) and (d) of Figs 10.4 to 10.7, where we have plotted the derived iron abundances for the four stars R CrB, SU Tau, HV 12842 and W Men.

The derived *gf* values are another source of random error. By using a 'reverse abundance analysis' from the solar spectrum we hope to derive a consistent set of *gf* values to use in the abundance analysis.

By using as many lines as possible, we hope to minimize the effects of the random errors mentioned above.

Another uncertainty arises in determining the C/He ratio. The procedure we adopted was to use the C/He ratio that produced a consistent result from the

He I line at 5876 Å, and to verify that this fell within the range of C/He required to produce the observed strength of C I lines.

The choice of the most appropriate atmospheric parameters, and therefore the best atmospheric model, was based on certain criteria as described in Section 10.3.3. The selection of a slightly different input model will have an effect on the derived elemental abundances. However, the errors resulting from uncertainties in the atmospheric parameters are minimized when the relative abundances (element/Fe) are considered.

The effect of adopting slightly different atmospheric parameters is displayed in Fig. 10.9. In this figure, we plot the differences between the abundances derived for SU Tau using the adopted atmospheric parameters (see Table 10.4) and those using a slightly different model. The triangles in this figure illustrate the effect of using a different He:C model from that adopted. To produce consistent results, the temperature and the C/He ratio needed to be adjusted slightly. The effect on the derived abundances of decreasing the gravity (but with all other parameters the same) is indicated by the circles. The squares show the dependence of the derived abundances on the microturbulent velocity that is chosen. The effect of a change in the microturbulence of 1 $\mathrm{km\,s^{-1}}$ is displayed.

The derived elemental abundances from H I, He I, C I, N I, O I, Sc II, Ti II and Fe II lines are not greatly affected by changing the gravity. The different-composition model has little effect upon the abundances from lines of H I, He I, Na I, Al I and Si I, but there is a systematic difference of about −0.15 dex for the C I, N I and O I lines. The derived abundances from C I, N I, Na I, Al I, Fe I and Ni I lines are not greatly affected by altering the microturbulence. The s-process element Ba is affected by the largest amount (±0.40 dex) with the use of the different-gravity model or the different microturbulence. This is due to the fact that the Ba abundance is derived from very strong lines, which are affected more strongly by the final choice of atmospheric parameters. The systematic effects of the atmospheric parameter uncertainties for specific groups of elements are presented in Table 10.6.

It can be seen from Fig. 10.9 and Table 10.6 that the derived atmospheric abundances may differ by up to $\sim$ 0.15 dex (excluding the Ba abundances) due to uncertainties in the adopted atmospheric parameters.

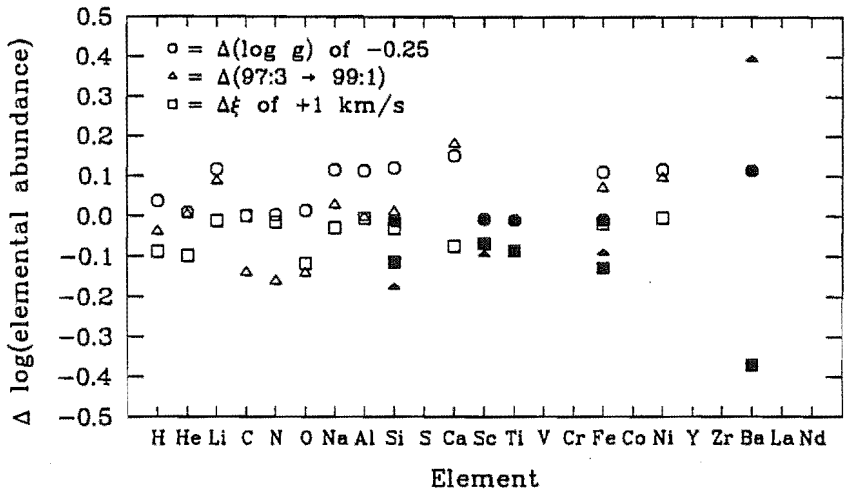

Figure 10.9: The effect on the derived abundances of altering the atmospheric parameters for SU Tau. The circles represent changing log g from 0.5 to 0.25 with other parameters the same as in the adopted model. The triangles are for a model with a higher He:C ratio of 99:1. Other parameters are adjusted slightly to keep consistency ($T_{\rm eff}$ = 7200 K, C/He = 0.003 and log g = 0.5). The squares indicate the effect of choosing a model with a microturbulence of 8 km s^{-1} rather than 7 km s^{-1}, with other parameters the same as in the adopted model. The open symbols represent neutral lines while the filled symbols represent ionized lines.

10.4.4 Discussion of elemental abundances

If HV 12842 and W Men are LMC analogues of galactic RCB stars, such as R CrB and SU Tau, then some interesting differences in abundances are evident. Since we are looking at similar objects in different chemical environments, it may be more meaningful to look at the comparison of these LMC stars with the galactic RCB stars. This provides us with the opportunity to study the effect of a different chemical environment on the appearance and the evolution of these peculiar objects.

Both LMC stars are more hydrogen-deficient than either of the galactic stars R CrB and SU Tau. This is probably not significant, since a huge range in hydrogen abundance is known to exist for these stars. The [H/He] ratios for SU Tau and HV 12842 have been determined from the Hα line and the 5876-Å line of He I. For W Men and the reanalysis of R CrB, the Hβ line was also used. SU Tau displays a greater [H/He] ratio (−5.4) than R CrB (−5.9), while the two

Table 10.6: Systematic errors from uncertainties in the derived atmospheric parameters.

Elements	$\Delta(\log g)$ $0.50 \rightarrow 0.25$	Δ He:C $97{:}3 \rightarrow 99{:}1$	$\Delta\ \xi_t$ $7 \rightarrow 8$
H, He [a]	$<+0.05$	$< \pm 0.05$	$\sim+0.10$
C, N, O [a]	$<+0.02$	~-0.15	$-0.12 \rightarrow 0.00$
Na, Al, Si [a]	$\sim +0.12$	$<+0.03$	$< \pm 0.03$
Sc, Ti, Fe [b]	$< \pm 0.01$	~-0.10	~-0.10
Fe, Ni [a]	$\sim+0.12$	$\sim+0.08$	~-0.05
Ba [b]	$\sim+0.40$	$\sim+0.11$	~-0.40

[a]neutral species; [b] ionized species

LMC stars, HV 12842 and W Men, have slightly lower [H/He] ratios of −6.2 and −6.5 respectively. Due to this extreme deficiency, hydrogen can be regarded as a trace element with little effect on the atmospheric structures of these stars.

The C/He ratio (or, equivalently, the helium abundance) was derived from the 5876-Å line of helium, assuming that this line has no chromospheric or non-LTE contribution. The validity of these assumptions has been discussed for some time, without any definitive conclusion. The C/He ratio is of vital importance in the RCB stars but is a very difficult quantity to obtain with known accuracy. This ratio determines the abundance scale, since it defines the continuous opacity and hence the transparency of the atmosphere of the RCB star. Any uncertainty in the C/He ratio will affect the derived abundances of all the elements.

One interesting result is the positive identification of lithium in both SU Tau and HV 12842 and an indication of its presence in W Men (see Fig. 10.1e). These lead to abundance enhancements (relative to iron) of several hundred for both SU Tau and HV 12842. The presence of this line requires some unique nucleosynthetic interpretation because this element is easily destroyed during main-sequence and giant branch evolution. To explain the enhanced lithium both the ^{7}Be transport mechanism, $^3\mathrm{He}(\alpha,\gamma)^7\mathrm{Be}(\mathrm{e}^+\nu)^7\mathrm{Li}$, and various spallation processes have been invoked (see the discussion in CL82). Both scenarios have their drawbacks, not the least of which for the Be mechanism is that it requires the presence of hydrogen, a species extremely deficient in these objects.

The CNO abundances and ratios are important as they are key elements in both the CNO cycle and the triple-alpha process. The carbon abundance was determined from the C/He ratio required to produce self-consistency. The

nitrogen abundance was determined from lines of specific multiplets, since the scatter of abundances between multiplets was very large (presumably due to uncertain *gf* values). CL82 used lines from multiplet 19 (near 9650 Å) which had experimentally determined *gf* values. However, the region containing these lines was not observed for any of the three stars in this programme. In the reanalysis of R CrB, lines from multiplet 59 gave abundances in good agreement with lines from multiplet 19. The nitrogen abundance was therefore determined primarily from lines of this multiplet. Most of the lines that were used to determine the oxygen abundance were reasonably strong (in the range 170–380 mÅ). However, with access to the weak forbidden line at 6363 Å in all three stars, reliable abundances were able to be derived.

There is a substantial enhancement of carbon, nitrogen and oxygen in all objects (see Table 10.5). Together with the extreme hydrogen deficiency, this indicates that substantial mixing of nuclear processed material has occurred during the evolution of these stars. The larger values of [C/Fe], [N/Fe] and [O/Fe] in HV 12842 and W Men, compared to the galactic RCB stars, is a reflection of the overall metal deficiency in the LMC. For R CrB, SU Tau, HV 12842 and W Men the ratios of C:N:O are 8:1:4, 11:1:4, 10:1:6 and 12:2:3, respectively. In comparison, the Sun has a C:N:O ratio of 5:1:9. A mixture of both CNO cycle and triple-alpha processed material is required to explain these C:N:O ratios observed in the atmospheres of the RCB stars.

When the CNO cycle reaches its equilibrium, there are specific ratios of the various isotopes of carbon, nitrogen and oxygen. Although these will be altered as further nuclear processing occurs, certain isotopes are key indicators of the extent and nature of further processing. The CNO cycle has a characteristic equilibrium $^{12}C/^{13}C$ ratio of ~ 3.4. The (1,2) $^{12}C^{12}C$ band head at 5585.5 Å was not observed for SU Tau or HV 12842. The band head in W Men is as strong as that observed in R CrB by CL82. No evidence of the $^{12}C^{13}C$ band head at 5577.0 Å is seen. Hence the $^{12}C/^{13}C$ ratio is estimated to be similar to that determined by CL82 for R CrB, that is, a value greater than ~ 40. This is quite at variance with the equilibrium ratio for the CNO cycle.

For the elements Na, Al, Si, S and Sc, the LMC RCB stars have [element/Fe] ratios similar to those of the galactic RCB stars. There is an indication that the observed light α-elements (O, Si, S) may be slightly overabundant in W Men relative to the galactic stars. The [Ca/Fe] ratios in both HV 12842 and W Men

are somewhat lower than in the galactic stars.

Spectra of W Men taken in the blue contain a number of Cr II and Ni I lines. The [Cr/Fe] abundance ratio for W Men is slightly less than that determined for the galactic star R CrB. The Ni abundance is very uncertain for SU Tau and HV 12842, as there are few unblended lines of Ni within the spectral regions that were observed for these stars. However, spectra of both R CrB and W Men contain a number of Ni I lines and the abundance is more well defined. The [Ni/Fe] ratio in W Men is similar to that of the galactic RCB stars.

The [Fe/total] abundance ratios for R CrB and SU Tau are −0.4, and a similar [Fe/total] is derived by J91 for RY Sgr (see Table 10.5). This indicates that the galactic stars are slightly metal-poor relative to the solar composition. This is consistent with these stars being members of a slightly older population than the Sun. For both HV 12842 and W Men, a value of −0.7 has been determined for the [Fe/total] abundance ratio. The LMC stars are depleted in iron by factors of ∼5 relative to the solar composition and ∼2 relative to the galactic RCB stars. This depletion factor of ∼2 (or 0.3 dex) is similar to the mean metal deficiency of the LMC.

Russell & Bessell (1989) give the mean metallicity of the LMC relative to the Sun (derived from a study of F-type supergiants in the LMC) as [Fe/H] = −0.3 dex. A value of [Fe/H] = −0.2 dex is quoted by Russell & Dopita (1992) as the mean iron deficiency in the interstellar medium (ISM) of the LMC, relative to the solar vicinity ISM. The fact that the [Fe/total] abundance ratios of the LMC RCB stars relative to galactic RCB stars are similar to the metal deficiency of the LMC is a good indication that the adopted C/He ratios (defining the overall abundance scales, or metallicities of the stars) are correct. The derived C/He ratios are all within the limits set by CL82 for R CrB.

Table 10.7: A summary of s-process abundance ratios for Galactic and LMC RCB stars.

Star	[Fe/total]	[Sr/Fe]	[Y/Fe]	[Zr/Fe]	[Ba/Fe]	[La/Fe]	[Ce/Fe]	[Nd/Fe]	[Sm/Fe]	[Y+Nd/Fe]
R CrB[a]	−1.1									+0.3
XX Cam[a]	−0.8									−0.2
RY Sgr[b]	−0.4		+0.9		+1.0			+0.5		
U Aqr[c]	−0.3	+1.7	>+2.4		+0.1					
U Aqr[d]	+0.2	+1.4	+1.2	+0.4	−0.1					
R CrB[e]	−0.4		+0.9		+1.0			+0.5		
SU Tau[e]	−0.4				+1.1					
HV 12842[e]	−0.7				+0.6			+1.4		
W Men[e]	−0.7		+0.7	+0.7	+0.4	+1.2		+1.1		
LMC[f]	−0.3	−0.23	−0.03	−0.16	0.00	+0.16	+0.10	+0.50	+0.04	
LMC[g]	−0.3	−0.16	−0.03	−0.09	+0.07	+0.23	+0.17	+0.51	+0.27	

[a]CL82; [b] J91; [c] Bond et. al (1979); [d] Malaney (1985) abundances relative to HD182040; [e] this paper; [f] Russell & Bessell (1989); [g] Russell & Dopita (1992)

Lines of s-process elements were observed for SU Tau (Ba), HV 12842 (Ba and Nd) and W Men (Y, Zr, Ba, La and Nd). CL82 measured the s-process elements Y, Ba and Nd for R CrB. The [element/Fe] abundance ratios for these s-process elements are plotted in Fig. 10.10. These abundances are derived from measurements of one to three lines for each element in question. All three lines of Ba II and one line of Y II are reasonably strong and consequently have larger abundance uncertainties. From Fig. 10.10, there is an indication that the LMC stars have an enhancement of the s-process elements, in particular, the heavier neutron capture elements, La and Nd. The abundances for these elements are based on weaker lines ($W_\lambda \lesssim 150$ mÅ) which should be more reliable.

The enhancement of s-process elements requires an effective neutron source. The most commonly presented reaction for producing neutrons in low-mass stars depends on the production of ^{13}C, by mixing down protons from a hydrogen-rich to the helium-rich layer during thermal pulses while the star is evolving up the asymptotic giant branch. Neutrons are then produced by the reaction ^{13}C(α,n)^{16}O.

There are obviously problems with this model in RCB stars, where the envelopes are extremely hydrogen-deficient, unless the s-process elements are produced prior to the hydrogen-rich envelope being ejected or engulfed by a final helium-shell flash. Light s-process element enhancements have been observed in some RCB stars (Bond et al. 1979, Lambert & Rao 1994), all of which are metal-poor objects. Bond et al. (1979) suggested that a single exposure to neutrons at the helium-core flash could be responsible for the tremendous overabundance of the light s-process elements (Sr and Y) which is observed in U Aqr.

Russell & Dopita (1992) described the overall abundance patterns of the Magellanic Clouds. One of their results was that the s-process sequence was found to be as effective in the LMC as in the local interstellar medium for elements as massive as Ba, but to have a much reduced effectiveness for heavier elements. They found that the r-process had to be invoked to successfully describe the pattern of abundances for elements heavier than Ba. The analysis of the light neutron capture elements Y and Zr by Russell & Bessell (1989) indicated normal abundances relative to iron in the Magellanic Clouds. The heavy neutron capture elements Nd and Sm were found to be enhanced with respect to iron. Similar results of heavy element overabundance were reported by Spite et al. (1989) for three young F–G supergiants in the SMC.

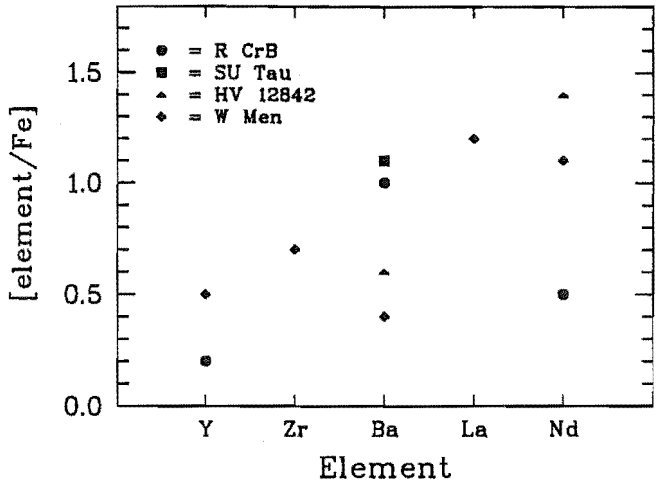

Figure 10.10: The s-process abundance ratios for R CrB, SU Tau, HV 12842 and W Men relative to iron.

Table 10.7 displays a summary of the s-process abundance ratios derived for various studies of Galactic and LMC RCB stars. The s-process abundances ratios for the LMC, derived from a study of F-type supergiants and abundance ratios for the interstellar medium of the LMC, are also included for comparison. Abundances are calculated relative to the Sun, i.e. $[X/Fe] = [X/Fe]_{RCB} - [X/Fe]_{\odot}$, except for the U Aqr analyses where the abundances are relative to HD 182040, a nonvariable HdC star, i.e. $[X/Fe] = [X/Fe]_{RCB} - [X/Fe]_{HD182040}$.

These heavy s-process element overabundances suggest that there may be significant differences between our Galaxy and the Magellanic Clouds in terms of their star formation and chemical enrichment histories.

10.4.5 The abundances related to evolutionary scenarios

The most serious constraint on most proposed evolutionary scenarios for the production of RCB stars is the production of the observed peculiar surface abundances. In particular, the overabundances of He, ^{12}C, N and O, with residual traces of H, ^{7}Li and s-process enhancements, must be explained.

There have been two main evolutionary schemes proposed to explain the formation and characteristic appearance of RCB stars. Both theories involve recycling of white dwarf stars, which are then re-evolved up to the luminous

region of the HR diagram. Renzini (1990) presents the main characteristics of these two evolutionary scenarios and their resulting predictions.

The first theory involves the coalescence of a He–CO white dwarf binary (Webbink 1984, Iben & Tutukov 1985) to form an RCB star of the appropriate mass. This proposed scenario begins with a hydrogen-deficient progenitor, and thus avoids the difficult process of evolving such an unusual star from the conventional post-AGB evolutionary processes of mixing and nuclear burning, or hydrogen envelope ejection. This model also accounts for the rarity of binary systems in these stars. The double degenerate model explains the absence of ^{13}C (since the merging white dwarfs have virtually none of this isotope), but has difficulty accounting for some of the observed surface abundances, especially of H and Li, and possibly the overabundance of carbon.

The second theory involves a single white dwarf undergoing a final thermal pulse when the helium shell ignites. The final flash model predicts the photospheric compositions with more ease. One problem with this model, however, is that large quantities of ^{13}C are produced, giving an expected $^{12}C/^{13}C$ ratio close to the CNO cycle equilibrium ratio of ~ 3.4. The observed $^{12}C/^{13}C$ ratio (from the apparent absence of the $^{12}C^{13}C$ band head) in RCB stars is found to be very large. A value of $\gtrsim 40$ has been reported by CL82 for R CrB and a similar value for W Men has been estimated in this paper. However, there is a mechanism within the bounds of this model, by which the absence of ^{13}C can be explained. During the shell flash, the products of hydrogen burning (^{13}C and ^{14}N) are mixed down to the helium-burning shell. The reaction $^{13}C(\alpha,n)^{16}O$ is suddenly ignited, resulting in the star having a lower He-burning shell and an upper ^{13}C-burning shell. Thus ^{13}C is effectively removed from the photospheric layers. The release of neutrons from the ^{13}C-burning reaction may result in the production of ^{15}N, and an enhanced $^{15}N/^{14}N$ ratio is predicted by Renzini (1990). Neutrons that escape capture by ^{14}N could be involved in the production of s-process elements, which are observed in the photospheres of some of the RCB stars (see Table 10.7).

10.5 Conclusions and further work

Although the composition of the galactic RCB star SU Tau does not provide many differences with respect to previous analyses (see table I of Lambert 1986), it does provide additional evidence that these objects have a reasonably consistent set of properties. The extragalactic observations indicate that it is possible for

this phenomenon to exist in different nucleosynthetic environments.

As was discussed by CL82 and others, enhancement of both carbon and nitrogen requires triple-alpha processing followed by CN-processing to have occurred during the later stages of the evolution of these stars. The latter of these processes requires hydrogen to be consumed, and is possibly an indication that a final flash model may be able to prove an explanation for both the enhanced nitrogen and enhanced lithium. This final flash model may also be able to account for the observed enhancements of s-process elements found in some of the RCB stars.

The abundances derived here will enable modelling to be undertaken which should be able to produce the RCB phenomenon in both Galactic and Magellanic Cloud environments. The complete evolutionary history of these stars, including the metallicity of the progenitor, the effect of the variety of nucleosynthetic processes on the composition and structure of these stars and the physical processes, such as convective mixing and mass loss, must result in a similar outcome in both circumstances. One connection may be that the galactic objects have been linked to an older population (the old disc, due to their positions in the Galaxy and their kinematics) which may have a similar metallicity to that of other objects in the Large Magellanic Cloud.

Chapter 11

Summary and future work

A programme of photometric and spectroscopic observations has been undertaken in order to investigate the physical and chemical characteristics of the RV Tauri and R Coronae Borealis stars. These characteristics have, in turn, been used to examine a variety of theoretical models that attempt to describe the pulsation mechanisms, the underlying physical nature and the evolutionary status of these low mass supergiant variables.

BVRI photometry was obtained over intervals of between 750 and 1300 days for most of the RV Tauri stars in the programme. RV Tauri stars from both the RVa (constant mean magnitude) and RVb (varying mean magnitude) photometric subclasses and from all three spectroscopic Preston subtypes (A, B and C types) were included. Two methods of period analysis (the Fourier power spectrum method and the simultaneous least-squares fitting technique) were used to derive the dominant periodicities and the stability of the light and colour variations in these stars. Properties such as the periods, amplitudes, phases and rms errors were tabulated for each star. The Fourier spectra for most of the programme stars revealed two dominant periodicities which had a period ratio of close to 2:1. In most cases, a harmonic ($f + 2f$) fit was found to be a good representation of the deep–shallow nature of both the light and colour curves. Amplitude variations in the light and colour curves were investigated for many stars.

The main results from the analysis of the RV Tauri photometry were presented Chapters 3 and 4 and discussed in Chapter 5. The photometry for V820 Cen and IW Car showed irregularities in both period and amplitude and no consistent deep–shallow alternations were observed. It is probable that neither of these stars is an RV Tauri star. They are most likely to be members of the semiregular

class of variable. For AR Pup, the MJUO data did not show consistent deep–shallow alternations, although these have been observed in the past. The period for AR Pup is quite stable, but the depths of the minima appear to be rather variable. The shorter period stars, in particular the carbon-rich (Preston type 'B') objects, appeared to display more regular light curves. With the notable exceptions of the longer period variables R Sct and RY Ara, the secondary light minima were more variable than the primary minima.

General properties of the light and colour curves (such as the shape, asymmetry, amplitude, phase lag and repeatability) were discussed for each star. Some of the characteristics of these curves were linked to their spectroscopic properties. For example, the blueness of the colour curves during the rising branch of the light curve can be attributed to the appearance of numerous shock-related emission lines. The variability in the strength of these emission lines is a likely explanation for the cycle-to-cycle variations in the photometric light curves, especially in the the bluer filters where the photospheric lines occur in greater numbers.

One unexpected feature of the colour curves was that the majority of stars showed the bluest colours during the rise from secondary light minimum. Most recent spectroscopic studies generally agree that the strongest emission (also the strongest shock wave and photospheric acceleration) occurs just after primary minimum, although there are a few studies (Preston 1962, Gillet et al. 1990, Shenton et al. 1992) which suggest that the secondary shock is the strongest. It is possible that the occurrence of bluer colours after the secondary minimum could be due to the presence of shock-produced emission lines in combination with a less extended (and hence hotter and bluer) photosphere. In addition, the appearance of strong TiO bands around the primary and secondary minima may also cause colour peculiarities.

The peculiar 'blueing' of the colours during the very deep minima observed in R Sct and RY Ara was compared with previous observations of a deep minimum in R Sct (Howell at al. 1983). These very blue colours appear to arise when a chromospheric spectrum is evident and this is very similar behaviour to that seen in the RCB stars during their characteristic declines (Cottrell et al. 1990, Lawson 1990).

An important result from the photometric programme arose from the analysis of the RVb stars. The two stars U Mon and AI Sco were found to have very similar properties. The long-term variation is evident in the light and colour curves. In

U Mon, there appears to be a slight phase lag so that the long-term light minimum occurs slightly before the reddest colours. In both stars, the amplitudes of the short-term (pulsational) light and colour variations are 'damped' at the long-term minimum. The amplitude of the long-term oscillation is greater for the bluer filters than for the redder filters.

AR Pup appears to be a little different in an number of ways. No consistent deep–shallow alternations were seen in the MJUO photometry of this star. Although the short-term colour variations are damped at the long-term minimum (as was seen in U Mon and AI Sco), the colours are also bluer (rather than redder) at this time.

The main results from the analysis of the RV Tauri spectroscopy were presented in Chapters 7 and 8 and discussed in Chapter 9. Sequences of spectra stacked in phase order were presented for each star. Shock-related features, such as doubled absorption lines and recombination emission lines, were observed in most stars. Emission components for the Hα line were observed for most of the pulsation cycle and for every star in the RV Tauri programme. Since the Hα line samples such a extensive range of atmospheric layers, an emission contribution to the Hα line from shock-heated gas is nearly always present. This is in contrast to the metallic lines which display emission components only when the shock wave is traversing the relatively thin atmospheric layer where these lines are forming.

The phase dependent behaviour of the Hα emission was examined. In most cases, the observed Hα profiles were consistent with increased Hα emission following the passage of the primary and secondary shock waves through the photosphere around phases 0.2 and 0.6. The appearance and the phase-dependent behaviour of the metallic and the molecular lines was investigated. Quite different behaviour was observed to occur in the Fe I, Ti I and Hα lines, although consistency between lines of the same element and similar excitation potential was seen. The sequence of line profiles that was observed suggests that there is a phase lag between the upper and lower atmospheric layers, so that when the lower atmosphere starts pulsating outwards, the higher layers are still infalling after the passage of a previous shock front.

Radial velocity curves were presented for the metallic lines or, when the metallic lines were too weak to be measured, for the components of the Hα lines. In most RV Tauri stars, a discontinuous radial velocity curve with a period half that of the 'formal' or luminosity period was observed. However, many stars did not

have sufficient phases coverage to do more than suggest the form of the radial velocity curve. In addition, cycle-to-cycle variations complicate the interpretation of the RVb stars, which show long-period trends in their radial velocities.

The MJUO radial velocities for the RVb star U Mon were combined with previously published velocities (Sanford 1933, Abt 1955, Preston 1964) to obtain an orbital solution to the long-term periodicity in the radial velocities. The orbit obtained was reasonably eccentric ($e = 0.43$) and suggested that at periastron passage, U Mon may come close to filling its Roche lobe, thus inducing mass loss or transfer in the binary system which appears as Hα emission. It was found that the Hα line appeared to have a extra enhancement of emission during cycles 3 to 6, which corresponds to the orbital phases just after periastron. A number of scenarios were presented that could explain his enhanced Hα emission at these orbital phases. These scenarios included mass loss to a circumbinary disk or shell, mass transfer to the binary companion or an interaction between the RV Tauri star and its companion.

The spectroscopic and the photometric characteristics that have been determined in this thesis have been used to examine a variety of theoretical models that attempt to describe the pulsation mechanisms and the underlying physical nature of the RV Tauri stars. The theoretical RV Tauri model of Fokin (1993) was used to examine the difference between the optical and the infrared radial velocities and periods.

The nature of the RVb subclass and the interpretation that the RVa and RVb stars actually represent a continuum of properties is discussed in detail. A model of a binary system which undergoes periodic eclipses by dust or which interacts at certain orbital phases was presented. The observed photometric and spectroscopic properties previously determined in this thesis for the RV Tauri stars were used to examine the particular details and predictions of each model. The interaction model generally has better agreement with the observed properties although it is quite likely, in a system where circumstellar and/or circumbinary material is known to exist, that a combination of obscuration and interaction is possible.

The last chapter in this thesis presented a detailed analysis of the chemical composition of a number of RCB stars in the Galaxy and the LMC. This work made use of high-resolution échelle spectra obtained at the Anglo-Australian

Telescope. The analysis involved the use of the hydrogen-deficient model atmospheres of Shönberner and the stellar atmosphere code WIDTH6 (adapted for use with hydrogen-deficient and helium- and carbon-rich atmospheres). The results for the galactic star, SU Tau, revealed very similar properties to a number of other warm galactic RCB stars, most notably R CrB. This was the first abundance analysis completed for any extragalactic RCB stars and showed a similar abundance distribution to the galactic RCB stars. All these objects (galactic and extragalactic) have a reasonably consistent set of properties, proving that it is possible for this phenomenon to exist in different nucleosynthetic environments.

11.1 Future Work

In Chapter 9, an outline was presented of a specific programme of photometric and spectroscopic observations that would be required to address a number of outstanding issues concerning the nature of the RV Tauri stars.

One of the outstanding questions is the exact cause of the long-term secondary variation in the RVb stars. A number of scenarios have been proposed in this work which go some way to explaining the peculiar photometric and spectroscopic variations that we observe in the RVb stars (and at least one of the RVa-type stars). If this effect is intrinsic to the RV Tauri star then this provides evidence that real 'damping' of the stellar envelope is occurring at long-term minimum, as was indicated in the 'interaction' scenario above. However, if this is an extrinsic effect, where the star is still pulsating in the same manner but intervening material is affecting what we detect on earth, then this would be similar to the 'dust-eclipse' scenario.

Further observations will be needed to verify which of these explanations is is closest to the truth and to refine future models of these stars. One piece of spectroscopic evidence that would allow us to choose between the two alternatives above is the behaviour of the short-term radial velocity variations at different phases of the long-term oscillation. If the star is pulsating in exactly the same manner throughout the long-term cycle ('dust-eclipse') then we would expect to see no change in the radial velocity variations due to the pulsations at either long-term minimum or maximum. However, if the envelope is physically being affected by the binary interaction and actual 'damping' of the pulsation is occurring, then we should expect to see the radial velocities being damped also.

Specific observations that should be undertaken to investigate the possibilities

outlined above are contemporaneous visual (*UBVRI*) and infrared (*JHKLMN*) photometry and high- (or medium-) resolution spectroscopy through several pulsation cycles at long-term light minimum and at long-term light maximum. The large number of observations will allow the radial velocity behaviour of the pulsations to be modelled and therefore allow the long-term radial velocities to be determined more accurately.

The optical and infrared photometry indicates the regularity of the pulsations and allows peculiarities to be noted. Colour variations can indicate temperature changes but also spectral peculiarities such as emission lines. Visual and infrared fluxes can be calculated to determine if the long-term variation is present in the infrared. Infrared photometry would also be extremely useful in the context of examining the pulsational models for the RV Tauri stars, since it has been suggested (Shenton et al. 1992) that nonradial pulsations are required to describe the sinusoidal appearance of the infrared light curves.

Contemporaneous high-resolution spectroscopy should be obtained with particular emphasis on a variety of spectral lines: lines that do not show shock-related features and are thus likely to be formed deeper in the photosphere; lines of Ti I that exhibit strong shock-related emission features; and lines of Fe I that display two components also indicative of shocks. In addition, accurate and well-sampled radial velocities should be obtained through several pulsation cycles at long-term light minimum and long-term light maximum. Of fundamental importance is the question: are the radial velocity variations 'damped' at long term minimum or not? This is a *crucial question* since the answer will allow us to decide if the envelope of the star is being physically 'damped' or otherwise affected by the interaction with the binary companion.

In addition, an abundance analysis of a reasonable sample of the RV Tauri and related stars would be useful for a more quantitative assessment of the interrelationship among the members of the three spectroscopic subtypes. The knowledge of the physical properties of individual stars is an important step towards a better understanding of the evolutionary status and the relationship that exists between members of this class and other classes of variable star. The difficulties at this stage arise from the tremendously dynamic nature of the photospheres of these stars. There a number of complications that must also be considered, such as the presence of strong atmospheric shocks with the subsequent huge extension of the atmosphere and the complex emission behaviour of many photospheric lines.

Acknowledgements

First I would like to thank my supervisor, Peter Cottrell, for his unswerving enthusiasm and for suggesting the original project to me. Although it changed a little along the way, Peter was always prepared to get involved, listen and offer helpful advice on all aspects of my work.

I would also like to thank my co-supervisor, William Tobin, for encouraging me to become involved in the commissioning and testing on the CCD system, for helpful suggestions and for sitting in front of a terminal with me for hours trying to understand what MIDAS was doing.

Pam Kilmartin and Alan Gilmore were responsible for taking the photometric observations for this project, and without their dedication, long-term photometric monitoring of such stars as the RV Tauri variables would not be possible. Mike Clark set up the telescope, spectrograph and CCD detectors, helped with equipment problems and late-night gremlins at MJUO. Peter Cottrell and Michael Albrow took observations at MJUO for this project, often at crucial phases. Warrick Lawson kindly put my RV Tauri stars on his MSO observing programme, obtained and reduced a large number of spectra for me and helped me out when I was observing on the 1.9-m telescope at MSO. Warrick provided me with the Lomb-Scargle Fourier code and offered helpful suggestions regarding its use.

Other astronomers who have contributed with useful discussions, suggestions and preprints have been: Frank Bateson, George Wallerstein, John Percy, Dimitar Sasselov, Agnes Lèbre, Warrick Lawson, Michael Albrow, John Hearnshaw, Andrew Fokin, Mike Bessell and David Lambert.

I would also like to thank Detlef Schönberner for providing the model atmospheres for the abundance analysis of the RCB stars. Peter Cottrell, Warrick Lawson, Mike Bessell, Peter Wood and Don Pollaco helped in the acquisition of the AAT observations of the RCB stars.

During the course of this work, I was supported by a New Zealand University

Grants Committee Scholarship and a Ministry of Research, Science and Technology Women's Study Award. I am grateful to Zonta International for their support via an Amelia Earhart Award, and particularly to the local branches of Zonta for their fundraising efforts which maintain this award.

I would like to acknowledge the financial support which allowed me to attend the 1990 Vatican Summer School in Observational Astronomy and Astrophysics, conferences at Bologna, Italy in 1990 and Victoria, Canada in 1992, and to observe at MSO. This support was provided by: The Kingdon-Tomlinson bequest of the Royal Astronomical Society of New Zealand, the Vatican Observatory, the Royal Society of New Zealand's Young Scientist's Fund, the Frank Bradshaw and Elizabeth Pepper Wood Fund and the IAU.

I would like to thank the other members of the astronomy group who made my time as a PhD student so enjoyable: Warrick, Kaylene, Michael, Donna, Steve, Alan, Lyndon, David, Frank, John, Irene, Ben and Saskia.

Thanks also to my Mum, Dad and brothers for their support and encouragement over the years.

Final thanks must go to Michael for making it all worth while.

References

Abt H.A., 1955, ApJ, 122, 72

Aikawa T., 1991, ApJ, 374, 700

Aikawa T., 1993, MNRAS, 262, 893

Aikawa T., Bruegman O., 1987, Ap&SS, 137, 115

Albrow M.D., 1994, PhD thesis, University of Canterbury

Alcolea J., Bujarrabel V., 1991, A&A, 245, 499

Aliev A.A., 1967, Sov. Astron., 10, 794

Andreasen G.K., 1987, A&A, 186, 159

Antonello E., Mantegazza L., Poretti E., 1986, A&A, 159, 269

Argelander F.W.A., 1869, Beobachtungen und Rechnungen uber Veränderliche Sterne, Adolf Marcus, Bonn, 7, 379

Baird S.R., 1981, ApJ, 245, 208

Baird S.R., 1982, PASP, 94, 850

Baird S.R., 1984, PASP, 96, 72

Beckers J.M., Bridges C.A., Gilliam L.B., 1976, A high resolution spectral atlas of the solar irradiance from 380 to 700 nm, Air Force Geophysics Laboratory, Sacremento Peak Observatory

Bessell M.S., 1976, PASP, 88, 557

Bessell M.S., 1979, PASP, 91, 589

Bidelman W.P., 1954, ApJS, 1, 205

Bond H.E., Luck R.E., Newman M.J., 1979, ApJ, 233, 205

Brancewicz H., Dworak T.Z., Kreiner J.M., 1976, IAU Inf. Bull. Var. Stars 1198, 1

Breger M., 1982, Vienna Internal Report 82/2

Buchler J.R., Kovács G., 1987, ApJ, 320, L57

Cardelli J.A., 1985, AJ, 90, 1494

Cardelli J.A., 1989, AJ, 98, 324

Cardelli J.A., Howell S.B., 1989, AJ, 98, 311

Cottrell P.L., Lambert D.L., 1982, ApJ, 261, 595 [CL82]

Cottrell P.L., Lawson W.A., Buchhorn M., 1990, MNRAS, 244, 149

Cottrell P.L., Sneden C. 1986, A&A, 161, 314

Cousins A.W.J., 1983, Circ. South African Astr. Obs., 7, 36

Crutcher R.M., 1982, ApJ, 254, 82

Dawson D.W., 1979, ApJ, 41, 97

Dawson D.W., Patterson C.R., 1982, PASP, 94, 574

de Loore C.W.H., Doom C., 1992, Structure and Evolution of Single and Binary Stars, Kluwer, Dordrecht, p. 319

Deupree R.G., Hodson S.W., 1976, ApJ, 208, 426

Drilling J.S., 1986, in Hunger K., Schönberner D., Kameswara Rao N., eds, Proc. IAU Coll. 87, Hydrogen Deficient Stars and Related Objects, Reidel, Dordrecht, p. 9

DuPuy D.L., 1973, ApJ, 185, 597

Eggen O.J.,1973, PASP, 85, 42

Eggen O.J, 1978, Inf. Bull. Var. Stars, 1425

Eggen O.J, 1986, AJ, 91, 890

Erleksova G.E., 1979, Perem Zvezdy Prilozh, 3, 627

Fadeyev Y.A., 1984, Ap&SS, 100, 329

Feast M.W., 1972, MNRAS, 158, 11P

Fokin A.B., 1992, MNRAS, 256, 26

Fokin A.B., 1993, preprint

Gehrz R.D., 1972, ApJ, 178, 715

Gehrz R.D., Ney E.P., 1972, PASP, 84, 768

Gehrz R.D., Woolf N.J., 1970, ApJ, 161, L213

Gerasimovič B.P., 1928, Harv. Coll. Obs. Circ., 333, 1

Gerasimovič B.P., 1929, Harv. Coll. Obs. Circ., 341, 1

Gillet D., 1992, A&A, 259, 215

Gillet D., Burki G.,, Duquennoy A., 1990, A&A, 237, 159

Gillet D., Duquennoy, Bouchet P., Gouiffes C., 1989, A&A, 215, 316

Gilmore A.C., Tobin W., 1991, Mt John Photometrics CCD System: Use and Performance Note Number 5

Giridhar S., Kameswara Rao N., Lambert D.L., 1994, preprint

Goldsmith M.J., Evans A., Albinson J.S., Bode M.F., 1987, MNRAS, 227, 143-159

Hearnshaw J.B., 1977, Proc. Astron. Soc. Australia, 3, 102

Hearnshaw J.B., 1978, Sky & Telescope, 56, 6

Hertzsprung E., 1928, B.A.N., 4, 160

Hirshfeld A., Sinnott R.W. eds, 1985, Sky Catalogue 2000.0, Cambridge University Press

Hoffmeister C., Richter G., Wenzel W, eds, 1985, Variable Stars, Springer-Verlag, Berlin, p. 265

Houk N., 1978, Michigan Spectral Catalogue of Two-dimensional Spectral Types for the HD Stars, Ann Arbor, Univ. of Michigan

Howell S.B., Bopp B.W., Noah P.V., 1983, PASP, 95, 762

Hunger K., Kaufmann J.P., 1976, A&A, 50, 133

Iben I.Jr, Tutukov A.V., 1985, ApJS, 58, 661

Jones K.N., 1991, PhD thesis, St Andrews University [J91]

Joy A.H., 1950, PASP, 62, 60

Joy A.H., 1952, ApJ, 115, 25

Jura M. 1986, ApJ, 309, 732

Kapteyn J.C., 1896, Cape Ann., 3, 93

Kholopov P.N., Samus N.N., Frolov M.S.,Goranskij V.P., Gorynya N.A., Kireeva N.N., Kukarkina N.P., Kurochkin N.E., Medvedeva G.I., Perova N.B., Shugarov S.Yu., eds, 4th edition, 1985, <<Nauka>> Publishing House, Moscow

Kilkenny D., Westerhuys J.E., 1990, Observatory, 110, 90

Kolláth Z., 1990, MNRAS, 247, 377

Kovács G., Buchler J.R., 1988, ApJ, 334, 971

Kukarkin B.V., Parenago P.P., Yu N., Kholopov P.N., 1958, General Catalogue of Variable Stars, 2nd edition, Academy of Sciences of USSR, Moscow

Kurucz R.L., 1970, SAO Special Report, No. 309

Kurucz R.L., Peytremann, E., 1975, A Table of Semi-empirical gf values, SAO Special Report, No. 362

Lambert D.L., 1970, MNRAS, 182, 249

Lambert D.L., 1986, in Hunger K., Schönberner D., Kameswara Rao N., eds, Proceedings IAU Colloquium 87, Hydrogen deficient stars and related objects, Reidel:Dordrecht, p.127

Lambert D.L., Kameswara Rao, N., 1994, J. Astrophys. Astron., 15, 47

Lawson W.A., 1990, PhD Thesis, University of Canterbury

Lawson W.A., Cottrell P.L., Kilmartin P.M., Gilmore A.C., 1990, MNRAS, 247, 91

Lawson W.A., Cottrell P.L., Kilmartin P.M., Gilmore A.C., 1992, MNRAS, 256, 339

Lawson W.A., Kilkenny D., Marang F., van Wyk F., Pollard K.R., Ryder S.D., 1993, MNRAS, 265, 351

Lèbre A., 1991, PhD Thesis, Observatoire de Haute-Provence, Université de Montpellier II

Lèbre A., Gillet D., 1991a, A&A, 246, 490

Lèbre A., Gillet D., 1991b, A&A, 251, 549

Lloyd Evans T., 1985, MNRAS, 217, 493

Lomb N.R., 1976, Astrophys Space Sci, 39, 447

Loreta E., 1938, AN, 267, 399

Luck R.E., 1981, PASP, 93, 211

Luck R.E., Bond H.E., 1984, ApJ, 279, 729

Luck R.E., Bond H.E., 1989, ApJ, 342, 476

MacConnell D.J., Frye R.L., Bidelman W.P., 1972, 84, 388

MacFarlane G.G., McLean T.P., Quarrington J.E., Roberts V., 1958, Phys. Rev., 111, 1245

McLaughlin D.B., 1939, Publ. Obs. Univ. Michigan, 7, 57

Malaney R.A., 1985, MNRAS, 216, 743

Mantegazza L., 1985, A&A, 151, 270

Moore C.E., Minnaert M.G.J., Houtgast J., 1966, The Solar Spectrum 2935Å to 8770Å, NBS Monograph 61

Mozurkewich D., Gehrz R.D., Hinkle K.H., Lambert D.L., 1987, ApJ, 314, 242

Nankivell G., Rumsey N., 1986, in Hearnshaw J.B., Cottrell P.L., eds, Proc. IAU Symp. 118, Instrumentation and Research Programmes for Small Telescopes, Reidel, Dordrecht, p. 101

Nook M.A., 1991, private communication

Nook M.A., Cardelli J.A., Nordsieck K.H., 1990, AJ, 100, 2004

Nook M.A., Nordsieck K.H., 1991, private communication

O'Connell D.J.K., 1933, Harv. Coll. Obs. Bull., 893, 14

O'Connell D.J.K, 1946, Riverview Coll. Obs. Publ., 2, 46

O'Connell D., 1961, Spec. Astron. Vat. Ric .Astron., 6, 341

O'Leary W., 1937, Ann. Bosscha Sterrenwacht, Lembang, VIII, 17

Paczyński B., 1971, Ann. Rev. Astron. Astrophys., 9, 183

Payne-Gaposchkin C., Brenton V.K., Gaposchkin S., 1943, Harv. Ann., 113, 1

Percy J.R., Sasselov D.D., Alfred A., Scott G, 1991, ApJ, 375, 691

Percy J.R., 1993, in Sasselov D.D., ed, ASP Conf. Ser. 45, Luminous High-Latitude Stars, Astron. Soc. Pac., San Francisco, p. 295

Pigott E., 1797, Phil. Trans., 87, 133

Pollard K., 1989a, The Mt John Photometrics CCD System: Use and Performance Note Number 2, *Evaluation of the linearity of the Mt John CCD*

Pollard K., 1989b, The Mt John Photometrics CCD System: Use and Performance Note Number 3, *Evaluation of the spectral response for various operating temperatures of the Mt John CCD*

Pollard, K.R., Cottrell P.L., Lawson W.A., 1994, MNRAS, 268, 544

Pollard, K.R., Kilmartin P.M., Gilmore A.C., Cottrell P.L., 1993, Southern Stars, 35, 53

Polyakova T.A., 1992. Sov. Astron., 36, 52

Poretti E., 1989, A&A, 220, 144

Poretti E., Mantegazza L., Riboni E., 1992, A&A, 256, 113

Preston G.W., 1962, ApJ, 136, 866

Preston G.W., 1964, ApJ, 140, 173

Preston G.W., 1972, ApJ, 172, L105

Preston G.W., Krzeminski W., Smak J., Williams, J.A., 1963, ApJ, 137, 401

Raveendran A.V., 1989, MNRAS, 238, 945

Raveendran A.V., Kameswara Rao, N., 1988, A&A, 192, 259

Raveendran A.V., Kameswara Rao N., Anandaram M.N., 1989, MNRAS, 240, 823

Renzini A., 1990, in Cacciari C., Clemintini G., eds, ASP Conference Series Vol 11, Confrontation between Stellar Pulsation and Evolution, p 549

Rodgers A.W., 1970, Observatory, 90, 197

Rolleston R.W.J., 1991, Irish Astr. J., 20, 60

Rosino L., 1951, ApJ, 113, 60

Ross J.E., Aller L.H., 1976, Science, 191, 1223

Russell S.C., Bessell M.S., 1989, ApJS, 70, 865

Russell S.C., Dopita M.A., 1992, ApJ, 384, 523

Rybka E., 1934, Lwów Cont., 2, 7

Rybka E., 1935, Lwów Cont., 4, 22

Saitou M., Takeuti M., Tanaka Y., 1989, PASJ., 41, 297

Sanford R.F., 1931, ApJ, 73, 364

Sanford R.F., 1933, ApJ, 77, 120

Sanford R.F., 1934, ApJ, 79, 77

Sanford R.F., 1955, ApJ, 121, 318

Sasselov D.D., 1992, CfA Preprint Series No. 3479

Scargle J.D., 1982, ApJ, 263, 835

Schönberner D., 1975, A&A, 44, 383 [S75]

Schwarzschild M., 1952, Transactions of the IAU VII, Oosterhoff P.Th., ed, Cambride Univ. Press, Cambridge, p. 811

Shapley H., Walton M., 1927, Harv. Coll. Obs. Circ., 313

Shenton M., Albinson J.S., Barrett P.,Davies J.K., Evans A., Goldsmith M.J., Hutchinson M.G., Maddison R.C., Weight A., 1992, A&A, 262, 138

Spite F., Spite M., François P., 1989, A&A, 210, 25

Stothers R., Leung R., 1971, A&A, 10, 290

Takeuti M., Petersen J.O., 1983, A&A, 117, 352

Tobin W., 1990, The Mt John Photometrics CCD System: Use and Performance Note Number 1, *Description of the System*

Tobin W., 1991a, The Mt John Photometrics CCD System: Use and Performance Note Number 7, *Time Keeping on the Photometrics CCD System*

Tobin W., 1991b, The Mt John Photometrics CCD System: Use and Performance Note Number 8, *Forth Acquisition Software*

Tobin W., 1992, Southern Stars, 34, 421 (same as below)

Tobin W., 1992, The Mt John Photometrics CCD System: Use and Performance Note Number 10, *Gain, Noise and related charateristics of the Mt John Photometric CCD System*

Tobin W., 1993a, The Mt John Photometrics CCD System: Use and Performance Note Number 11, *Shutter Map*

Tobin W., 1993b, The Mt John Photometrics CCD System: Use and Performance Note Number 13, *Christchurch VMS-based Software*

Tsesevich V.P., 1975, in Kukarkin B.V., ed, Pulsating Stars, Wiley, New York, p. 112

Tuchman Y., Lèbre A., Mennessier M.O., Yarri A., 1993, A&A, 271, 501

Vaníček P., 1971, Ap&SS, 12, 10

Velduizen T., Percy J.R., 1989, J. AAVSO, 18, 97

Voûte J.G., 1932a, Ann. Bosscha Sterrenwacht, Lembang, II, D5

Voûte J.G., 1932b, Ann. Bosscha Sterrenwacht, Lembang, II, D63

Voûte J.G., 1939, Ann. Bosscha Sterrenwacht, Lembang, VIII, 46

Wahlgren G.M., 1993, in Sasselov D.D., ed, ASP Conf. Ser. 32, Luminous High-Latitude Stars, Astron. Soc. Pac., San Francisco, p. 270

Wahlgren G.M., 1992, AJ, 104, 1174

Wallerstein G., Cox A.N., 1984, PASP, 96, 677

Wallerstein G., Elgar S., 1992, Science, 256, 1531

Wallerstein G., Jacobsen T.S., Cottrell P.L., Clark M., Albrow M.D., 1992, MNRAS, 259, 474

Warner B., 1967, MNRAS, 137, 119

Webbink R.F., 1984, ApJ, 277, 355

Wegner G., 1976, Observatory, 96, 13

Wiese W.L., Smith M.W., Glennon B.M., 1966, Atomic Transition Probabilities (NSRDS–NBS4)

Wilson W.J., Schwartz P.R., Neugebauer G., Harvey P.M., Becklin E.E., 1972, ApJ, 177, 523

Wisse P.N.J., 1981, A&AS, 44, 273

Wisse P.N.J., Wisse M., 1971, A&A, 12, 143

Wisse P.N.J., Wisse M., 1973, A&A, 23, 463

Yoshioka K., 1979, PASJ, 31, 23

Zsoldos E., 1993a, A&A, 268, 149

Zsoldos E., 1993b, Observatory, 113, 305

Appendix A

RV Tauri photometric data

This appendix contains the tabulated *BVRI* photometry for the programme RV Tauri stars. The programme stars are presented in alphabetical order according to the constellation name of the RV Tauri star. The column HJD refers to the heliocentric Julian Date of observation (– 2440000).

Table A.1: AD Aql photometry from MJUO

HJD	V	$(B-V)$	$(V-R)$	$(V-I)$
8141.938	11.487	0.854	0.506	1.030
8145.892	11.691	0.962	0.526	1.103
8147.967	11.861	0.973	0.556	1.169
8150.986	12.035	0.912	0.522	1.003
8152.985	12.097	0.942	0.539	1.028
8165.934	11.324	0.687	0.440	0.957
8187.930	11.584	0.692	0.339	0.767
8195.903	11.492	0.659	0.425	0.855
8199.874	11.547	0.868	0.512	1.040
8328.203	11.358	0.607	0.377	0.889
8335.183	11.548	0.748	0.493	1.200
8360.228	11.538	0.654	0.446	0.980
8377.231	11.569	0.813	0.487	1.058
8410.248	11.661	0.898	0.470	1.153
8421.113	11.986	0.908	0.511	1.074
8439.118	11.425	0.764	0.477	0.946
8442.192	11.530	0.782	0.468	1.088
8447.133	11.818	0.865	0.537	0.944
8452.104	11.843	0.792	0.503	1.081
8465.023	11.348	0.624	0.432	1.018
8471.088	11.467	0.762	0.492	1.033
8479.150	11.742	0.861	0.554	1.114

8489.001	11.896	0.798	0.485	1.142
8494.984	11.339	0.618	0.394	0.908
8506.919	11.481	0.756	0.504	1.126
8515.927	11.722	0.741	0.473	1.064
8520.923	11.609	0.648	0.417	1.027
8524.899	11.285	0.526	0.368	0.751
8539.894	11.561	0.828	0.499	1.146
8553.879	12.035	0.842	0.568	1.172
8558.885	11.622	0.722	0.434	1.074
8708.187	11.518	0.786	0.483	1.062
8722.202	11.316	0.544	0.367	0.834
8734.211	11.557	0.783	0.483	1.024
8740.146	11.591	0.843	0.490	1.048
8769.191	11.353	0.692	0.468	1.046
8779.270	11.596	0.717	0.471	1.069
8784.156	11.617	0.646	0.436	–
8794.084	11.479	0.654	0.455	1.066
8820.134	11.930	0.733	0.490	1.133
8839.023	11.445	0.759	0.485	1.106
8854.051	11.422	0.554	0.356	0.894
8857.002	11.319	0.543	0.392	0.901
8893.941	11.348	0.615	0.405	0.840
8910.939	11.648	0.850	0.477	0.967
8929.882	11.458	0.770	0.498	0.950

Table A.2: RY Ara photometry from MJUO

HJD	V	$(B-V)$	$(V-R)$	$(V-I)$
8479.112	9.072	1.186	0.630	1.134
8488.935	8.918	1.169	0.630	1.104
8495.043	8.908	1.166	0.633	1.101
8507.031	9.059	1.203	0.655	1.123
8516.021	9.208	1.199	0.645	1.124
8525.010	9.170	1.143	0.652	1.091
8539.957	8.712	0.963	0.556	0.941
8549.949	8.738	1.088	0.592	0.956
8579.935	10.095	1.162	0.600	1.547
8674.086	9.434	1.234	0.672	1.261
8694.178	9.237	1.163	0.635	1.129
8704.237	8.976	1.203	0.621	1.034
8708.069	8.933	1.230	0.634	1.160
8718.202	8.966	1.339	0.678	1.208
8723.040	9.051	1.364	0.680	1.288

8732.209	9.251	1.362	0.690	1.313
8740.087	9.441	1.298	0.665	1.320
8769.273	9.398	1.215	0.627	1.290
8779.147	9.296	1.265	0.662	1.329
8820.090	8.966	0.987	0.563	0.992
8834.054	8.902	1.133	0.618	1.049
8839.056	8.919	1.202	0.635	1.102
8852.012	9.313	1.352	0.700	1.303
8858.025	9.444	1.362	0.672	1.353
8877.967	9.890	1.248	0.632	1.558
8882.020	9.995	1.222	0.625	1.561
8894.047	10.161	1.102	0.594	1.557
8898.993	10.010	1.086	0.581	1.506
8911.005	9.492	1.074	0.582	1.304
8929.897	8.926	1.139	0.618	1.128
8931.907	8.839	1.130	0.586	1.072
9025.144	9.546	1.311	0.646	1.320
9055.020	9.478	1.199	0.622	1.239
9059.108	9.391	1.236	0.614	1.189
9066.137	9.346	1.251	0.628	1.170
9074.108	9.212	1.237	0.634	1.169
9092.038	9.028	1.152	0.624	1.135
9117.056	8.950	0.999	0.569	0.972
9141.020	9.043	1.232	0.617	1.095
9143.994	9.137	1.287	0.637	1.148
9145.914	9.178	1.319	0.621	1.166
9155.089	9.411	1.423	0.663	1.264
9164.920	9.911	1.453	0.673	1.504
9168.084	10.097	1.434	0.675	1.570
9170.095	10.247	1.447	0.695	1.647
9172.049	10.372	1.422	0.687	1.704
9175.072	10.660	1.365	0.652	1.757
9175.913	10.738	1.369	0.665	1.809
9188.033	11.508	1.015	0.604	1.906
9199.097	11.231	0.811	0.501	1.992
9204.104	10.837	0.858	0.499	1.919
9205.006	10.748	0.875	0.505	1.895
9207.152	10.597	0.922	0.559	1.869
9209.982	10.358	0.980	0.529	1.790
9223.967	9.418	1.199	0.615	1.400
9226.962	9.238	1.181	0.634	1.294
9229.991	9.015	1.139	0.627	1.171
9237.101	8.785	1.032	0.572	1.012
9258.903	9.098	1.149	0.636	1.084

9275.922	9.227	1.260	0.671	1.173
9276.979	9.250	1.253	0.673	1.167
9288.891	9.309	1.321	0.691	1.223
9307.908	9.536	1.373	0.700	1.249

Table A.3: IW Car photometry from MJUO

HJD	V	$(B-V)$	$(V-R)$	$(V-I)$
8142.197	8.475	0.898	0.558	1.205
8152.206	8.430	0.900	0.529	1.220
8156.210	8.447	0.900	0.550	1.208
8188.086	8.517	0.981	0.583	1.294
8190.150	8.493	0.966	0.581	1.289
8253.025	8.254	0.902	0.548	1.223
8256.007	8.301	0.891	0.552	1.215
8260.033	8.320	0.906	0.558	1.222
8268.907	8.298	0.971	0.548	1.239
8282.973	8.167	0.886	0.545	1.186
8289.993	8.075	0.868	0.514	1.173
8294.012	8.049	0.846	0.505	1.143
8296.979	8.048	0.817	0.515	1.137
8308.060	8.152	0.852	0.520	1.174
8308.916	8.172	0.858	0.550	1.178
8314.933	8.212	0.927	0.548	1.204
8318.993	8.231	0.930	0.547	1.197
8320.950	8.214	0.914	0.560	1.208
8321.925	8.207	0.898	0.554	1.212
8323.003	8.187	0.902	0.553	1.240
8325.938	8.155	0.880	0.521	1.170
8331.935	8.132	0.873	0.540	1.196
8332.948	8.138	0.868	0.544	1.190
8344.917	8.198	0.882	0.548	1.193
8359.064	8.175	0.862	0.518	1.142
8359.950	8.192	0.882	0.533	1.157
8364.144	8.200	0.878	0.549	1.176
8378.007	8.085	0.874	0.537	1.162
8384.905	8.045	0.880	0.516	1.146
8409.975	8.067	0.888	0.529	1.165
8415.901	8.016	0.854	0.515	1.144
8417.919	8.009	0.852	0.525	1.149
8419.891	8.023	0.854	0.526	1.149
8425.903	8.078	0.855	0.542	1.162
8433.859	8.029	0.862	0.521	1.145

8439.950	7.983	0.820	0.510	1.110
8441.936	7.961	0.819	0.500	1.094
8445.897	7.939	0.806	0.507	1.112
8450.868	7.953	0.805	0.512	1.109
8464.896	7.941	0.822	0.514	1.120
8470.844	7.967	0.842	0.513	1.135
8489.252	7.992	0.851	0.517	1.178
8499.135	7.898	0.782	0.493	1.074
8507.194	7.869	0.779	0.482	1.055
8516.176	7.892	0.809	0.501	1.087
8531.071	7.896	0.838	0.519	1.125
8540.075	7.901	0.820	0.500	1.103
8554.104	7.937	0.823	0.490	1.101
8559.089	7.963	0.829	0.498	1.094
8565.125	7.955	0.833	0.511	1.095
8580.020	7.858	0.796	0.500	1.086
8600.023	7.872	0.796	0.496	1.099
8606.967	7.938	0.837	0.509	1.125
8614.007	7.987	0.882	0.514	1.134
8624.005	7.958	0.884	0.538	1.161
8650.035	7.852	0.805	0.473	1.080
8663.964	7.883	0.829	0.504	1.107
8668.969	7.901	0.833	0.507	1.139
8671.934	7.935	0.851	0.523	1.154
8673.941	7.953	0.858	0.522	1.163
8693.943	8.227	0.911	0.564	1.219
8704.007	8.278	0.929	0.566	1.271
8711.985	8.278	0.916	0.557	1.229
8717.923	8.245	0.895	0.559	1.257
8719.896	8.251	0.890	0.556	1.230
8731.913	8.239	0.875	0.543	1.220
8739.876	8.308	0.905	0.556	1.253
8769.036	8.457	0.957	0.587	1.312
8778.919	8.411	0.932	0.576	1.282
8783.845	8.362	0.926	0.560	1.272
8793.880	8.250	0.870	0.538	1.197
8805.002	8.191	0.841	0.532	1.194
8819.840	8.359	0.900	0.564	1.254
8833.827	8.511	0.970	0.565	1.302
8839.852	8.562	0.961	0.602	1.319
8856.925	8.553	0.882	0.561	1.259
8878.140	8.375	0.845	0.522	1.169
8882.074	8.386	0.863	0.551	1.178
8894.120	8.608	0.942	0.567	1.262

8899.108	8.704	0.990	0.602	1.298
8911.056	8.758	0.997	0.610	1.304
8913.084	8.744	0.992	0.590	1.282
8931.990	8.552	0.892	0.562	1.222

Table A.4: RU Cen photometry from MJUO

HJD	V	$(B-V)$	$(V-R)$	$(V-I)$
8133.910	8.882	0.552	0.347	0.765
8141.859	8.664	0.704	0.397	0.943
8147.831	8.817	0.823	0.439	0.980
8150.848	9.007	0.880	0.466	1.016
8243.095	8.793	0.880	0.446	0.986
8253.112	9.386	1.013	0.504	1.091
8256.087	9.683	1.002	0.496	1.119
8260.095	9.589	0.757	0.454	0.852
8269.101	8.529	0.629	0.351	0.923
8290.121	9.576	0.729	0.440	0.940
8297.059	8.797	0.499	0.326	0.786
8306.962	8.710	0.811	0.416	0.913
8309.011	8.802	0.821	0.439	0.958
8315.005	9.408	0.983	0.522	–
8319.041	9.811	0.987	0.517	1.123
8322.057	9.791	0.893	0.505	1.108
8323.049	9.644	0.825	0.484	1.042
8326.038	9.127	0.673	0.419	0.907
8331.989	8.756	0.734	0.436	0.957
8334.991	8.955	0.774	0.457	0.980
8359.125	8.910	0.555	0.355	0.813
8360.026	8.862	0.576	0.366	0.818
8368.060	8.814	0.830	0.449	0.975
8375.086	9.045	0.939	0.500	1.048
8378.060	9.291	1.003	0.522	1.073
8384.938	9.775	0.954	0.510	1.111
8407.108	8.972	0.845	0.452	0.967
8415.959	9.419	0.731	0.443	0.918
8417.940	9.334	0.616	0.412	0.897
8419.980	9.083	0.505	0.349	0.794
8425.981	8.809	0.596	0.381	0.865
8433.914	8.769	0.821	0.439	0.960
8439.979	9.089	0.925	0.505	1.031
8442.002	9.316	0.978	0.532	1.198
8445.987	9.665	1.014	0.530	1.113

8450.976	9.493	0.769	0.612	0.970
8452.010	9.381	0.743	0.414	1.000
8464.942	8.732	0.677	0.434	0.918
8470.918	8.906	0.765	0.460	0.982
8478.966	9.325	0.787	0.461	1.023
8488.868	8.846	0.504	0.352	0.797
8494.868	8.685	0.747	0.400	0.935
8506.828	9.296	1.001	0.506	1.068
8520.842	8.884	0.538	0.367	0.877
8607.117	9.255	0.830	0.471	1.028
8614.079	9.060	0.579	0.349	0.857
8624.065	8.803	0.764	0.446	0.938
8650.088	8.877	0.537	0.352	0.789
8669.055	9.163	0.842	0.473	1.044
8671.999	9.312	0.774	0.460	1.018
8674.000	9.308	0.724	0.396	0.937
8683.088	8.882	0.532	0.357	0.836
8694.004	8.870	0.810	0.462	1.028
8704.075	9.499	0.985	0.518	1.113
8712.045	9.252	0.674	0.417	0.945
8717.982	8.791	0.562	0.372	0.813
8719.951	8.784	0.577	0.382	0.851
8732.076	9.064	0.854	0.483	1.078
8739.930	9.479	0.832	0.471	1.072
8769.911	9.438	1.001	0.516	1.123
8778.991	9.063	0.554	0.358	0.824
8783.922	8.741	0.610	0.409	0.891
8793.977	8.920	0.829	0.467	1.046
8819.914	8.746	0.761	0.428	0.966
8833.889	9.588	1.014	0.550	1.145
8838.882	9.547	0.831	0.471	1.032
8851.894	8.622	0.640	0.405	0.903
8857.888	8.805	0.758	0.430	1.004
8932.133	9.386	0.780	0.442	0.975
8947.107	8.807	0.744	0.436	0.926
8970.096	9.516	0.763	0.459	1.012
8971.116	9.380	0.699	0.423	0.958
9007.133	8.851	0.513	0.344	0.799
9010.107	8.741	0.655	0.380	0.901
9025.032	9.191	0.967	0.481	1.061
9038.028	8.996	0.564	0.374	0.835
9044.178	8.684	0.679	0.403	0.891
9052.033	8.833	0.787	0.416	0.987
9053.004	8.886	0.789	0.442	0.995

9054.945	8.993	0.800	0.436	0.986
9058.992	9.173	0.762	0.427	0.971
9066.014	8.973	0.517	0.319	0.773
9073.981	8.889	0.679	0.400	0.930
9088.996	9.298	1.023	0.498	1.107
9092.135	9.476	1.008	0.520	–
9116.920	8.831	0.837	0.443	0.962
9120.967	9.152	0.919	0.486	1.042
9140.951	8.596	0.685	0.398	0.930
9143.895	8.597	0.774	0.402	0.930
9155.904	9.470	0.963	0.508	1.089
9163.897	9.420	0.706	0.410	0.942
9167.952	8.870	0.617	0.377	0.857
9171.890	8.696	0.705	0.403	0.935
9174.945	8.715	0.753	0.417	0.952
9197.875	8.997	0.576	0.359	0.837
9198.947	9.031	0.590	0.402	0.869
9203.928	8.992	0.758	0.462	0.920
9204.883	8.958	0.791	0.454	0.979
9206.912	8.869	0.804	0.448	0.990
9209.878	8.869	0.850	0.468	0.998
9219.847	9.431	0.973	0.539	1.096
9227.874	9.396	0.698	0.423	0.939
9230.906	8.805	0.451	0.350	0.831

Table A.5: V820 Cen photometry from MJUO

HJD	V	$(B-V)$	$(V-R)$	$(V-I)$
8133.948	9.144	1.194	0.644	1.350
8140.934	8.930	1.164	0.613	1.318
8141.885	8.915	1.121	0.617	1.258
8145.919	8.813	1.083	0.609	1.214
8147.877	8.772	1.046	0.597	1.208
8150.898	8.704	1.057	0.577	1.184
8152.915	8.691	1.033	0.573	1.193
8165.863	8.668	1.048	0.584	1.179
8260.123	9.087	1.235	0.653	1.329
8269.114	9.114	1.163	0.629	1.296
8290.076	9.067	1.105	0.603	1.269
8297.083	9.105	1.174	0.623	1.307
8309.049	9.021	1.223	0.661	1.361
8315.040	8.944	1.218	0.656	1.352
8319.080	8.912	1.191	0.644	1.329

8322.075	8.891	1.145	0.636	1.323
8323.075	8.882	1.136	0.641	1.315
8326.053	8.834	1.138	0.615	1.284
8332.030	8.775	1.097	0.602	1.270
8359.168	9.333	1.243	0.657	1.407
8377.061	9.375	1.147	0.646	1.393
8384.967	9.215	1.209	0.642	1.373
8407.158	8.822	1.123	0.614	1.272
8416.009	8.764	1.091	0.608	1.244
8420.027	8.738	1.104	0.605	1.220
8426.007	8.739	1.079	0.604	1.199
8433.937	8.801	1.045	0.601	1.177
8440.011	8.868	1.040	0.588	1.160
8442.033	8.871	1.041	0.565	1.131
8446.017	8.881	1.016	0.564	1.141
8451.977	8.893	0.983	0.556	1.125
8464.968	8.892	1.060	0.590	1.198
8471.943	9.006	1.149	0.630	1.290
8488.909	9.243	1.255	0.674	1.371
8494.899	9.315	1.236	0.676	1.394
8506.854	9.347	1.178	0.648	1.387
8515.842	9.249	1.150	0.631	1.342
8526.848	8.902	1.065	0.583	1.216
8614.112	8.891	1.136	0.595	1.234
8624.097	8.948	1.133	0.621	1.263
8652.097	9.095	1.251	0.657	1.400
8669.097	9.274	1.182	0.639	1.460
8672.065	9.294	1.190	0.641	1.465
8674.041	9.314	1.184	0.631	1.451
8685.074	9.495	1.182	0.646	1.454
8694.042	9.383	1.150	0.623	1.391
8704.100	9.068	1.099	0.608	1.297
8718.179	8.803	1.127	0.615	1.250
8722.988	8.802	1.154	0.632	1.280
8732.122	8.932	1.244	0.660	1.342
8739.974	9.062	1.290	0.683	1.389
8769.105	9.293	1.171	0.638	1.377
8779.024	9.016	1.107	0.612	1.281
8783.948	8.874	1.089	0.614	1.260
8793.994	8.842	1.106	0.616	1.264
8805.052	9.010	1.203	0.642	1.319
8819.931	9.147	1.198	0.660	1.379
8838.904	8.987	1.077	0.633	1.265
8851.934	9.004	1.122	0.619	1.231

8857.867	9.047	1.151	0.624	1.263
8868.902	9.041	1.216	0.636	1.301
8877.884	8.972	1.267	0.656	1.331
8886.875	8.832	1.226	0.636	1.278
8893.877	8.802	1.224	0.626	1.317

Table A.6: U Mon photometry from MJUO

HJD	V	$(B-V)$	$(V-R)$	$(V-I)$
8134.244	6.456	1.095	0.566	1.212
8141.188	5.750	0.922	0.468	0.910
8142.224	5.752	0.922	0.480	0.927
8147.240	5.684	0.993	0.514	0.979
8152.234	5.698	1.085	0.537	1.014
8156.221	5.807	1.157	0.573	1.051
8165.184	6.112	1.151	0.579	1.111
8181.088	5.915	0.840	0.492	0.877
8188.117	5.866	0.931	0.495	0.935
8242.996	5.889	1.088	0.519	1.018
8253.060	6.123	1.188	–	–
8255.974	6.205	1.192	0.601	1.146
8259.034	6.300	1.193	0.573	1.153
8260.013	6.352	1.197	0.595	1.170
8268.939	6.682	1.126	0.582	1.203
8282.951	5.897	0.965	0.511	0.987
8289.971	5.896	1.136	0.554	1.042
8293.978	5.983	1.201	0.528	1.057
8296.950	6.094	1.264	0.586	1.103
8306.921	6.649	1.282	0.627	1.271
8308.881	6.805	1.242	0.623	1.307
8314.891	7.011	1.108	0.575	1.290
8318.940	6.776	1.003	0.542	1.167
8320.897	6.598	0.988	0.523	1.090
8321.880	6.546	0.985	0.526	1.068
8322.941	6.549	0.985	0.534	1.075
8325.911	6.463	1.014	0.560	1.071
8331.034	6.283	1.041	0.514	1.043
8334.868	6.159	0.992	0.522	1.044
8358.877	6.571	1.070	0.556	1.087
8359.910	6.595	1.064	0.569	1.098
8363.981	6.654	1.040	0.561	1.081
8374.916	6.376	0.977	0.504	1.016
8377.891	6.348	1.026	0.527	1.056

8384.868	6.310	1.174	0.583	1.095
8471.264	6.651	1.125	0.575	1.131
8479.260	6.808	1.226	0.605	1.224
8489.232	7.224	1.192	0.620	1.317
8499.199	7.632	0.982	0.544	1.245
8507.218	7.387	0.944	0.510	1.160
8516.225	6.958	1.066	0.595	1.227
8525.168	6.705	1.136	–	1.272
8550.069	7.281	1.117	0.631	1.218
8554.096	7.126	1.003	0.564	1.137
8559.081	6.973	0.981	0.586	1.197
8565.089	6.783	1.115	0.609	1.259
8585.044	7.244	1.157	0.650	1.348
8606.925	6.941	1.058	0.610	1.220
8613.945	6.725	1.152	0.622	1.272
8623.985	6.765	1.155	0.640	1.299
8649.970	6.855	0.970	0.584	1.157
8651.930	6.810	0.998	0.557	1.182
8663.907	6.758	1.191	0.648	1.299
8668.947	6.858	1.256	0.657	1.290
8671.901	6.915	1.262	0.658	1.312
8673.885	6.989	1.246	0.671	1.345
8683.926	7.535	1.077	0.574	1.417
8693.913	7.251	1.008	0.570	1.257
8703.950	6.747	1.101	0.631	1.268
8706.942	6.702	1.151	0.630	1.265
8711.923	6.676	1.181	0.624	1.288
8717.852	6.799	1.184	0.670	1.324
8719.866	6.825	1.188	0.655	1.305
8731.872	7.040	1.126	0.640	1.268
8739.847	6.746	1.013	0.591	1.189
8768.818	7.025	1.266	0.636	1.401
8783.799	7.288	1.064	0.585	1.312
8854.226	6.578	1.351	0.678	1.323
8878.172	6.785	1.137	0.607	1.323
8882.231	6.565	1.179	0.655	1.279
8894.215	6.332	1.208	0.633	1.263
8899.138	6.287	1.208	0.642	1.269
8913.136	6.510	1.231	0.651	1.267
8932.021	6.188	1.163	0.555	1.130
8946.138	6.208	1.351	0.659	1.234
8949.067	6.288	1.366	0.677	1.269
8954.103	6.518	1.359	0.689	1.353
8970.066	6.777	1.130	0.615	1.267

8971.044	6.641	1.114	0.618	1.208
8984.089	6.032	1.149	0.643	1.197
9007.045	6.610	1.108	0.639	1.229
9010.027	6.493	1.028	0.603	1.139
9015.027	6.190	0.938	0.548	1.028
9024.980	5.999	1.177	0.601	1.132
9037.941	6.201	1.319	0.640	1.227
9040.961	6.251	1.347	0.673	1.223
9051.955	6.787	1.281	0.675	1.361
9052.925	6.831	1.261	0.650	1.362
9053.919	6.864	1.250	0.649	1.359
9054.869	6.942	1.208	0.681	1.387
9058.924	6.825	1.184	0.616	1.298
9065.931	6.215	1.058	0.593	1.082
9073.886	5.633	0.973	0.526	1.032
9088.910	5.859	1.221	0.606	1.068
9095.901	6.209	1.246	0.611	1.133
9116.829	5.450	0.927	0.455	0.882
9143.840	6.745	1.139	0.610	1.277
9145.833	6.808	1.072	0.556	1.279
9210.237	5.529	1.103	0.496	0.883
9227.218	6.092	1.303	0.601	1.130
9230.171	6.313	1.299	0.561	1.183
9237.236	6.996	1.096	0.505	1.399
9258.126	5.436	1.061	0.490	0.925
9264.092	5.510	1.046	0.507	0.981
9276.118	5.794	1.040	0.527	0.968
9286.083	5.893	0.920	0.507	0.897
9289.036	5.829	0.849	0.494	0.879
9294.122	5.658	0.906	0.434	0.799
9306.051	5.697	1.156	0.534	0.986
9320.990	6.426	1.277	0.600	1.233
9331.018	7.134	1.002	0.501	1.432
9333.029	6.899	0.978	0.481	1.332
9337.030	6.033	0.944	0.482	0.928
9381.980	5.743	0.845	0.430	0.822
9384.926	5.590	0.790	0.442	0.776
9390.939	5.505	0.946	0.455	0.875
9397.945	5.609	1.112	0.515	0.954
9398.950	5.647	1.131	0.511	0.960
9407.908	6.075	1.189	0.526	1.064
9410.890	6.281	1.158	0.537	1.166

Table A.7: V453 Oph photometry from MJUO

HJD	V	$(B-V)$	$(V-R)$	$(V-I)$
8421.024	11.312	1.123	0.685	–
8439.042	10.407	0.801	0.506	–
8442.146	10.353	0.806	0.525	–
8447.145	10.446	0.831	0.543	–
8451.114	10.602	0.874	0.578	–
8466.036	10.885	0.771	0.519	–
8471.067	10.507	0.685	0.458	–
8479.003	10.664	0.861	0.561	–
8488.970	10.734	0.947	0.588	–
8494.935	10.997	1.082	0.643	–
8498.971	11.218	1.157	0.689	–
8504.932	11.316	1.037	0.646	–
8520.873	10.517	0.829	0.554	–
8524.851	10.453	0.872	0.560	–
8708.089	10.670	0.699	0.470	–
8718.233	10.596	0.813	0.539	–
8732.221	10.798	0.983	0.603	1.144
8740.105	11.333	1.132	0.730	1.371
8769.165	10.508	0.800	0.549	1.116
8779.166	10.732	0.853	0.560	1.126
8794.048	10.449	0.633	0.440	0.861
8821.950	11.229	1.154	0.692	1.308
8851.975	10.635	0.872	0.570	1.060
8856.959	10.678	0.841	0.557	1.073
8877.907	10.548	0.731	0.509	0.978
8893.897	10.742	0.943	0.581	1.149

Table A.8: AR Pup photometry from MJUO

HJD	V	$(B-V)$	$(V-R)$	$(V-I)$
8134.223	9.138	0.768	0.444	0.935
8141.206	9.297	0.812	0.451	0.953
8142.210	9.308	0.822	0.455	0.971
8152.192	9.264	0.650	0.404	0.866
8156.197	9.229	0.635	0.384	0.819
8188.100	9.365	0.741	0.412	0.916
8190.164	9.388	0.695	0.422	0.907
8211.081	9.094	0.754	0.427	0.901
8242.978	9.178	0.719	0.446	0.945
8253.043	9.185	0.793	0.454	0.951
8255.990	9.242	0.805	0.461	–

8260.026	9.338	0.777	0.461	0.952
8268.923	9.345	0.685	0.393	0.857
8282.964	9.100	0.707	0.425	0.896
8289.984	9.186	0.790	0.465	0.949
8293.999	9.232	0.823	0.461	0.959
8296.962	9.286	0.852	0.464	0.980
8308.006	9.550	0.744	0.431	0.918
8308.893	9.524	0.726	0.421	0.903
8314.904	9.271	0.629	0.382	0.830
8318.952	9.186	0.650	0.394	0.849
8320.913	9.147	0.657	0.414	0.865
8321.893	9.117	0.663	0.414	0.867
8322.972	9.093	0.689	0.421	0.877
8325.925	9.093	0.721	0.424	0.909
8331.049	9.204	0.769	0.434	0.950
8344.894	9.548	0.760	0.449	0.965
8359.897	9.234	0.687	0.419	0.893
8363.994	9.194	0.741	0.427	0.899
8367.941	9.283	0.804	0.467	0.957
8374.940	9.514	0.885	0.501	1.044
8377.907	9.575	0.889	0.484	1.013
8384.886	9.610	0.745	0.446	0.933
8409.941	9.356	0.805	0.466	0.964
8415.886	9.499	0.829	0.467	0.988
8419.850	9.609	0.803	0.454	0.976
8425.866	9.541	0.683	0.397	0.849
8433.823	9.328	0.650	0.398	0.863
8441.867	9.326	0.798	0.437	0.913
8448.831	9.488	0.841	0.456	0.993
8450.844	9.545	0.903	0.476	0.973
8452.844	9.595	0.865	0.492	1.000
8471.253	9.329	0.609	0.369	0.770
8489.175	9.514	0.884	0.447	0.942
8499.177	9.732	0.776	0.465	0.950
8507.206	9.506	0.632	0.396	0.832
8516.213	9.377	0.715	0.409	0.864
8525.146	9.502	0.816	0.448	0.933
8550.044	9.539	0.679	0.389	0.819
8554.076	9.510	0.730	0.436	0.906
8559.060	9.488	0.778	0.466	0.959
8565.098	9.661	0.854	0.469	0.967
8579.992	9.685	0.685	0.380	0.824
8585.052	9.519	0.598	0.402	0.819
8600.049	9.539	0.769	0.448	0.940

8606.937	9.696	0.832	0.458	0.930
8613.956	9.743	0.764	0.439	0.917
8623.994	9.723	0.658	0.410	0.848
8649.980	9.711	0.748	0.462	0.919
8663.950	9.559	0.550	0.346	0.768
8668.957	9.604	0.640	0.388	0.808
8671.918	9.550	0.669	0.416	0.841
8683.937	9.721	0.845	0.473	0.971
8693.928	10.037	0.871	0.479	0.977
8703.964	9.868	0.697	0.413	0.893
8706.954	9.754	0.681	0.424	0.879
8711.936	9.581	0.720	0.403	0.876
8717.889	9.580	0.744	0.423	0.923
8719.878	9.610	0.759	0.434	0.915
8731.885	9.738	0.666	0.412	0.882
8739.860	9.716	0.595	0.354	0.813
8768.835	9.982	0.912	0.494	1.033
8783.817	9.838	0.650	0.403	0.862
8854.238	10.092	0.731	0.454	0.906
8878.156	9.689	0.753	0.432	0.893
8894.183	9.982	0.748	0.439	0.915
8899.123	9.949	0.728	0.439	0.922
8911.108	9.735	0.788	0.442	0.946
8913.121	9.723	0.809	0.432	0.932
8932.007	9.857	0.695	0.396	0.911
8946.124	9.690	0.689	0.408	0.891
8949.076	9.654	0.713	0.423	0.879
8954.122	9.744	0.781	0.443	0.932
8970.052	10.036	0.835	0.469	1.004
8971.055	10.040	0.833	0.476	0.964
8984.098	9.645	0.655	0.406	0.843
9007.061	9.880	0.737	0.441	0.945
9010.037	9.886	0.692	0.425	0.900
9015.036	9.653	0.569	0.361	0.751
9024.990	9.616	0.765	0.443	0.939
9037.955	9.821	0.892	0.484	1.018
9044.105	10.047	0.865	0.512	0.998
9051.966	9.869	0.651	0.424	0.904
9052.935	9.800	0.633	0.412	0.852
9053.929	9.717	0.624	0.382	0.844
9054.885	9.646	0.602	0.392	0.827
9058.934	9.679	0.643	0.411	0.876
9065.941	9.512	0.689	0.425	0.892
9073.897	9.607	0.784	0.450	0.958

9088.920	9.942	0.790	0.471	0.986
9095.911	9.631	0.651	0.408	0.906
9116.842	9.735	0.881	0.486	1.023
9120.895	9.839	0.879	0.481	1.005
9140.859	9.424	0.687	0.395	0.870
9143.858	9.428	0.707	0.417	0.919
9145.846	9.460	0.758	0.434	0.843
9163.837	9.852	0.851	0.486	1.030
9166.845	9.806	0.820	0.470	1.059
9169.859	9.683	0.718	0.414	0.827
9171.823	9.583	0.688	0.397	0.881
9174.819	9.459	0.656	0.400	0.826
9208.239	9.369	0.565	0.369	0.783
9210.227	9.332	0.586	0.355	0.786
9227.180	9.429	0.891	0.473	0.988
9230.159	9.516	0.889	0.494	1.014
9237.225	9.741	0.921	0.501	1.045
9259.100	9.282	0.794	0.451	0.957
9264.080	9.342	0.799	0.458	0.988
9276.105	9.511	0.790	0.470	0.979
9286.092	9.286	0.612	0.385	0.805
9289.023	9.299	0.625	0.419	0.912
9294.108	9.265	0.788	0.455	0.982
9306.036	9.449	0.901	0.505	1.040
9321.000	9.559	0.732	0.417	0.863
9333.040	9.189	0.747	0.476	0.990
9337.043	9.218	0.836	0.475	0.985
9381.991	9.397	0.905	0.499	1.040
9384.938	9.498	0.903	0.509	1.077
9390.950	9.653	0.874	0.498	1.018
9397.972	9.298	0.654	0.408	0.863
9398.965	9.177	0.614	0.373	0.828
9407.918	9.142	0.755	0.443	0.938
9410.900	9.148	0.825	0.456	0.945

Table A.9: AI Sco photometry from MJUO

HJD	V	$(B-V)$	$(V-R)$	$(V-I)$
8479.074	9.876	1.471	0.782	1.386
8488.952	9.174	1.090	0.626	1.141
8495.031	9.028	1.305	0.700	1.255
8506.999	9.488	1.578	0.784	1.389
8515.975	10.036	1.528	0.811	1.415

8520.990	9.644	1.267	0.699	1.240
8524.990	9.186	1.151	0.644	1.179
8539.943	9.491	1.489	0.786	1.374
8549.962	9.852	1.410	0.788	1.359
8553.965	9.629	1.157	0.681	1.191
8559.904	9.370	1.184	0.680	1.239
8674.103	10.771	1.325	0.726	1.394
8694.197	11.295	1.307	0.750	1.402
8708.111	10.828	1.394	0.756	1.388
8718.233	11.172	1.480	0.782	1.475
8723.095	11.422	1.462	0.799	1.468
8732.240	11.152	1.212	0.687	1.211
8740.123	10.762	1.300	0.703	1.332
8769.244	10.968	1.191	0.690	1.274
8779.233	10.812	1.347	0.744	1.433
8784.123	10.926	1.398	0.772	1.413
8820.169	10.956	1.491	0.816	1.548
8834.041	11.142	1.286	0.784	1.406
8852.028	10.824	1.499	0.800	1.511
8858.046	11.095	1.548	0.846	1.511
8899.912	11.058	1.473	0.833	1.470
8910.959	10.605	1.216	0.763	1.391
9059.140	9.079	1.185	0.614	1.172
9066.164	9.183	1.402	0.693	1.291
9074.147	9.506	1.592	0.773	1.403
9089.091	9.240	1.069	0.578	1.066
9092.072	8.942	1.051	0.574	1.082
9109.232	9.418	1.523	0.759	1.363
9117.042	9.792	1.414	0.738	1.355
9118.002	9.760	1.378	0.720	1.294
9140.912	9.326	1.497	0.724	1.358
9144.027	9.496	1.564	0.763	1.402
9145.901	9.580	1.544	0.748	1.428
9155.941	9.683	1.314	0.693	1.326
9164.907	8.943	1.164	0.631	1.157
9167.897	8.911	1.251	0.658	1.216
9170.129	8.899	1.308	0.659	1.221
9172.077	8.935	1.356	0.682	1.264
9175.103	9.055	1.414	0.713	1.297
9175.933	9.090	1.419	0.712	1.302
9188.064	9.710	1.462	0.758	1.360
9193.104	9.509	1.199	0.653	1.201
9197.895	8.961	1.100	0.613	1.139
9199.075	8.956	1.139	0.632	1.152

9204.093	8.872	1.299	0.682	1.244
9205.039	8.891	1.327	0.696	1.250
9206.044	8.908	1.371	0.695	1.265
9207.028	8.948	1.388	0.704	1.276
9208.091	8.983	1.400	0.712	1.292
9210.020	9.072	1.450	0.726	1.308
9224.050	10.012	1.480	0.763	1.491
9226.997	9.847	1.382	0.743	1.391
9228.062	9.660	1.289	0.727	1.290
9230.018	9.324	1.141	0.642	1.174
9237.080	8.901	1.177	0.633	1.178
9238.995	8.868	1.220	0.653	1.212
9258.956	9.528	1.334	0.734	1.318
9275.910	8.924	1.322	0.670	1.229
9276.944	8.963	1.342	0.700	1.224
9284.886	9.260	1.546	0.754	1.346
9285.896	9.337	1.530	0.772	1.381
9288.878	9.648	1.587	0.792	1.450
9293.922	10.195	1.484	0.773	1.582
9419.190	8.925	1.358	0.624	1.211
9432.077	9.639	1.580	0.795	1.424
9433.150	9.698	1.599	0.798	1.429
9434.156	9.751	1.607	0.803	1.439
9438.153	9.927	1.563	0.785	1.436
9442.127	9.785	1.348	0.731	1.326
9446.133	9.090	1.008	0.563	1.059
9452.118	9.077	1.247	0.667	1.234
9454.120	9.079	1.322	0.697	1.267
9473.099	10.532	1.396	0.732	1.638

Table A.10: R Sct photometry from MJUO

HJD	V	$(B-V)$	$(V-R)$	$(V-I)$
8134.027	6.040	1.530	0.769	1.696
8141.020	6.395	1.448	0.749	1.856
8141.919	6.394	1.457	0.746	1.800
8145.875	6.141	1.355	0.731	1.668
8147.954	5.786	1.327	0.726	1.485
8152.970	5.101	1.184	0.660	1.152
8164.933	4.892	1.222	0.641	1.229
8165.920	4.877	1.274	0.665	1.169
8180.936	5.261	1.473	0.752	1.470
8189.889	5.885	1.537	0.768	1.712

8195.888	6.631	1.543	0.789	2.002
8210.871	7.769	1.599	0.765	2.316
8323.145	5.907	1.426	0.733	1.586
8326.171	5.978	1.370	0.734	1.603
8328.216	6.001	1.299	0.712	1.607
8335.166	6.072	1.233	0.689	1.686
8360.244	5.582	1.366	0.712	1.477
8364.205	5.501	1.383	0.728	1.431
8375.146	5.096	1.292	0.726	1.244
8407.195	5.557	1.546	0.794	1.485
8410.230	5.729	1.553	0.789	1.546
8418.083	6.049	1.496	0.789	1.661
8421.098	6.130	1.475	0.776	1.681
8439.101	5.472	1.380	0.727	1.402
8442.174	5.289	1.371	0.736	1.337
8447.118	5.044	1.329	0.715	1.261
8452.090	4.935	1.329	0.711	1.235
8465.007	4.850	1.401	0.737	1.256
8471.104	4.978	1.466	0.765	1.317
8479.135	5.233	1.513	0.823	1.410
8488.986	5.485	1.454	0.771	1.449
8494.972	5.501	1.392	0.748	1.409
8506.937	5.206	1.262	0.706	1.241
8515.913	5.135	1.369	0.734	1.259
8520.909	5.107	1.436	0.727	1.278
8524.885	5.194	1.469	0.767	1.361
8539.909	5.860	1.474	0.757	1.713
8553.894	6.471	1.392	0.707	1.919
8558.901	6.584	1.266	0.682	1.929
8708.169	5.450	1.362	0.747	1.434
8722.181	5.221	1.290	0.718	1.298
8734.197	5.171	1.364	0.735	1.290
8740.136	5.161	1.388	0.733	1.282
8769.177	5.189	1.455	0.751	1.339
8779.257	5.311	1.423	0.766	1.365
8784.143	5.295	1.402	0.741	1.338
8794.099	5.159	1.363	0.712	1.264
8820.149	5.292	1.484	0.746	1.391
8839.011	5.565	1.392	0.724	1.489
8852.058	5.501	1.318	0.729	1.429
8857.022	5.304	1.288	0.694	1.293
8878.002	5.194	1.425	0.749	1.315
8882.866	5.177	1.476	0.746	1.371
8886.992	5.220	1.495	0.773	1.424

8893.956	5.428	1.506	0.761	1.537
8898.942	5.633	1.504	0.738	1.628
8910.921	6.272	1.426	0.748	1.855
8929.895	5.861	1.277	0.714	1.499
9059.175	7.288	1.185	0.720	1.969
9066.214	6.691	0.994	0.569	1.839
9074.205	5.389	1.193	0.669	1.425
9092.119	4.854	1.330	0.733	1.340
9118.046	5.443	1.364	0.756	1.415
9141.037	4.807	1.192	0.704	1.218
9144.068	4.842	1.269	0.719	1.237
9168.117	5.595	1.520	0.786	1.524
9170.069	5.699	1.520	0.758	1.555
9175.114	6.049	1.480	0.756	1.677
9176.070	6.114	1.485	0.750	1.691
9193.142	6.892	1.114	0.633	1.816
9204.013	6.261	1.179	0.645	1.676
9207.091	6.109	1.216	0.656	1.615
9210.032	6.033	1.235	0.688	1.627
9224.089	5.566	1.352	0.701	1.580
9227.009	5.393	1.398	0.708	1.489
9229.005	5.312	1.376	0.760	1.472
9238.021	4.882	1.296	0.709	1.193
9285.885	5.360	1.368	0.728	1.305

Table A.11: AR Sgr photometry from MJUO

HJD	V	$(B-V)$	$(V-R)$	$(V-I)$
8479.093	9.193	0.848	0.499	0.969
8489.019	9.433	0.872	0.514	0.965
8495.019	9.632	0.864	0.515	0.965
8506.948	9.347	0.652	0.418	0.793
8515.944	9.158	0.842	0.509	0.938
8520.976	9.246	0.915	0.525	0.954
8524.978	9.375	0.952	0.532	0.993
8539.930	10.195	1.163	0.661	1.233
8549.978	9.668	0.804	0.498	0.920
8553.954	9.443	0.747	0.507	0.917
8558.921	9.176	0.799	0.510	0.893
8709.242	9.530	1.080	0.533	0.871
8722.222	10.660	1.123	0.621	1.386
8734.229	9.335	0.794	0.494	0.848
8740.167	9.055	0.809	0.499	0.935

8784.077	9.218	0.890	0.506	0.951
8820.186	9.672	0.804	0.500	0.902
8834.070	8.969	0.798	0.491	0.916
8854.116	9.620	0.853	0.504	0.925
8882.049	9.321	0.991	0.560	1.008
8894.885	10.228	1.176	0.642	1.327
8899.023	10.632	1.031	0.571	1.382
8911.006	9.615	0.887	0.549	0.996
8929.913	9.074	0.811	0.518	0.999
9066.188	9.820	1.116	0.632	1.136
9074.166	10.313	1.127	0.632	1.262
9092.087	9.144	0.860	0.497	0.890
9109.242	9.369	0.888	0.534	1.022
9117.071	9.804	0.940	0.531	0.987
9140.924	9.093	0.932	0.506	0.942
9144.086	9.189	0.946	0.536	0.964
9155.955	9.833	1.123	0.619	1.183
9164.955	10.780	1.037	0.592	1.331
9167.911	10.272	0.920	0.569	1.107
9170.145	9.859	0.886	0.544	0.995
9175.141	9.539	0.889	0.543	1.002
9175.948	9.463	0.891	0.551	0.994
9188.095	9.283	0.892	0.530	0.997
9199.128	9.234	0.739	0.460	0.828
9204.118	9.348	0.735	0.431	0.793
9205.053	9.379	0.728	0.448	0.803
9206.073	9.394	0.754	0.439	0.797
9207.041	9.431	0.741	0.441	0.801
9208.107	9.447	0.748	0.446	0.810
9210.064	9.454	0.743	0.440	0.821
9220.054	9.341	0.834	0.475	0.907
9224.063	9.305	0.906	0.513	0.989
9230.031	9.315	0.973	0.560	1.037
9239.019	9.585	1.128	0.622	1.136
9258.011	10.034	0.884	0.512	0.940
9259.000	9.826	0.798	0.474	0.878
9275.934	9.030	0.785	0.469	0.902
9284.900	9.404	0.906	0.536	1.058
9285.912	9.449	0.921	0.527	0.998
9288.905	9.589	0.967	0.556	0.987
9293.936	9.849	0.959	0.570	0.974

Appendix B

Characteristics of the MJUO CCD system

This appendix presents the results of two experiments that were performed on the MJUO CCD system which incorporates a 384×576 pixel (columns $\times$ rows) Thomson CSF TH7882 CDA chip. These test were devised in order to test the linearity of the CCD system (Section B.1) and to test the variation of the sensitivity of the CCD system at a number of different wavelengths and for various operating temperatures of the chip (Section B.2). This last test was used to determine the best temperature at which to operate the MJUO CCD.

B.1 Linearity of the CCD

One aspect in which CCD systems have an advantage over photographic and photoelectric detectors is their linearity over a large dynamic range. When a CCD chip is exposed to light, charge accumulates in the potential wells of the two-dimensional imaging area called the parallel (or imaging) register. Charge can accumulate over an extended period of time – the total amount of accumulated charge should be proportional to the product of the light intensity and the exposure time if the system has a linear response. Some CCD detectors become notably non-linear slightly before reaching saturation. However, in most cases where CCD systems have been found to be non-linear, the non-linearity arises in the amplifier or analogue-to-digital converter and not the CCD chip itself.

Tests were performed to investigate the linearity of the MJUO CCD and to evaluate over what range of intensities the system is linear. The linearity

was determined by taking images of a stable light source with exposure times ranging from 0.5 s to 1024 s. A synthetic aperture of 100×100 pixels was used to determine the minimum, maximum, mean intensity and mean intensity rms of a specific area of the stable light source image. Signal levels with a mean value from 13 ADU to 13200 ADU were obtained, and the linearity was determined over this range.

B.1.1 Experimental procedure

Stable light source

Observations of varying exposure length were made of a stabilized light source. This consisted of a 'top hat' arrangement, whereby the depolished crown of the hat was illuminated by LEDs mounted inside. Four set of coloured LEDs were available, with only one set selected at a time. The current to the LEDs was provided by a controlled stabilized power supply and altered by setting a coarse and fine adjustment. In this way, the intensity of the LEDs was varied as required.

The six red LEDs (at a wavelength of 655 nm), mounted in a circular pattern behind a depolished window in the top hat, were used for the testing of the linearity. The brightness was set at medium on the coarse scale and 2.0 (outer scale) for the fine adjustment, so that a 20 minute exposure would give an image that had intensities close to the saturation level of the CCD. The LEDs were turned on and left overnight to stabilize before the testing began. Because the response of the the LEDs is slightly dependent on temperature, the top hat, CCD dewar and electronics unit were set up in the Phys201 wet darkroom which maintained a reasonably constant temperature. The Photometrics 3000 computer and the experimenter were in the neighbouring dry darkroom. The drift of the LEDs was monitored by taking a 10 second reference observation at the beginning and end of the tests and between each set of timed observations. To ensure no light was being detected from other sources, all lights on the CE210 electronics unit were taped over.

CCD camera

The CCD camera head was mounted on an optical bench at a distance of approximately 0.5 m from the stabilized light source. A 50 mm Pentax camera lens was then attached to the camera head and focused on the illuminated crown of the

top hat. Before the test began, the CCD chip was cooled with liquid nitrogen to an operating temperature of −111.9°C.

B.1.2 Observations

The MJUO CCD system makes use of base-level FORTH software for controlling the CCD. An observation is obtained by typing: `t obs` where `t` is the duration of the exposure in deciseconds. This command closes the shutter, clears the CCD array twice, preflashes the chip, opens the shutter for the specified time and reads the CCD out into the current image cache.

In order to give as large a dynamic range as possible, the `cgain` parameter was set to 0, giving a CCD system gain of $0.062\,\mathrm{ADU/e^-}$. A series of images of varying exposure length were obtained of the stable light source. This enabled the response of the CCD to a reference light source to be sampled at both ends of the dynamic range of the CCD system. The minimum exposure was 0.5 seconds, with the exposure length being doubled for each subsequent exposure up to a maximum of 1024 seconds. The 0.5 s images contained counts that were little above the base-level noise and the 1024 s exposures resulted in images that were close to saturation level. Each set of timed observations of the stable light source by the CCD consisted of:

- a dark exposure of `t` deciseconds;
- a first observation (a) of `t` deciseconds;
- a second observation (b) of `t` deciseconds.

The dark frame contained the standard bias component as well as the dark current accumulated over `t` deciseconds. The dark CCD frame was inspected for any cosmic ray events that would affect the analysis of the images. Two observations of the same duration were then obtained of the stable light source. The associated dark frame was subtracted from observations (a) and (b) and both images were saved on DC2000 cassette tape. Reference observations of the stable light source, each being a 10 s exposure, were obtained between each pair of timed observations and also at the beginning and end of the entire test. In this way, the drift of the LEDs was monitored and could be interpolated for each set of timed exposures.

B.1.3 Image Analysis

The analysis of the dark-subtracted images was done with the PM3000 computer and video monitor. Each full frame image was displayed with intensity varying linearly between two selected values of minimum and maximum. A reasonably constant-intensity region of the stable light source was chosen near the middle of the circular array of LEDs. The FORTH commands `sb` and `pcur` enabled a 100×100 pixel box to be positioned at the chosen region on the image (centre: column 215, row 185). The `stats` command gave values of maximum, minimum, mean intensity and the rms of the mean intensity over the 10 000 pixels enclosed by the indicated box. This enabled a mean intensity to be obtained over the same region of the constant light source, and over identical pixels of the CCD chip, for differing exposure times.

B.1.4 Results

Tobin (1993a) found that the mechanical shutter of the CCD normally takes between ~ 5 and ~ 20 ms to open and close, which can increase to ~ 30 ms for very short exposures. Tests suggest the shutter map is variable at the few millisecond level, but a mean correction for the shutter speed can be determined from the shutter map (see Fig. 2 of Tobin 1993a). In testing the linearity of the CCD system, the same region of the chip is used and the shutter correction is therefore the same for all the observations. From the shutter map, it was determined that the actual exposures were 15 ms longer than the requested exposure time. The corrected exposure times are shown in Table B.1. The uncertainty due to shutter speed variations is estimated to be 5 ms.

In addition, the internal CCD clock used to time the observations in this experiment has been found to run 4.3/affected in a systematic manner and will therefore not alter the results obtained, the correction for this timing error has not been applied.

Counts from the reference exposures obtained before and after the pair of timed observations were averaged to give a representative mean for that exposure time, $\overline{C_{\rm ref}}$. These mean reference counts are displayed together with the associated exposure time in Table B.1. The mean reference exposures of the stable light source indicate that the intensity of the LEDs varied by less than 1% for the duration of the test (see Fig. B.1), but that the greatest change was in the latter half of the experiment. For the longer exposures (64 s to 1024 s) it was

Table B.1: Mean reference counts from 10 second exposures of the stable light source.

exposure time E (s)	log (E)	mean reference counts $\overline{C_{\rm ref}}$ (per 10 s)
1.015	0.0065	128.382
2.015	0.3043	128.422
4.015	0.6037	128.502
8.015	0.9039	128.468
16.015	1.2045	128.415
32.015	1.5054	128.397
64.015	1.8063	128.338
128.015	2.1073	128.273
256.015	2.4083	128.165
512.015	2.7093	127.963
1024.015	3.0103	127.651

necessary to interpolate the reference counts for the mid-time of each exposure because of the changing brightness of the stable light source.

The mean reference counts were subsequently used in the analysis of the series of images of varying exposure length. The 0.5 second exposures showed electrical pickup (seen as periodic 'waves' on the displayed image) and also had a comparatively large uncertainty due to shutter speed variations which made up a not-insignificant part of the short exposure time. The 0.5 s exposure was therefore not included in further analysis.

The raw counts obtained for the various pairs of timed exposures were scaled to account for the fluctuations in the stable light source which were determined from the mean reference exposures. The raw counts were scaled by the (normalized) mean reference counts associated with that exposure. The normalization made use of the mean reference counts determined for the 1 s exposure time. These scaled counts, C_s, for each pair of observations of the same exposure length were averaged, $\overline{C_s}$. The logarithm of the mean scaled counts was then taken, $\log(\overline{C_s})$. The exposure time and counts obtained for the series of images of the stable light source are displayed in Table B.2.

A weighted least-squares linear regression was calculated for the data set of log(exposure time) and $\log(\overline{C_s})$. The weighting of each data point was dependent on the uncertainty associated with that measurement.

One contribution to the uncertainty is from the reference exposures. The statistical uncertainty associated with the reference exposures was determined to be 2×10^{-4} (or $\sim 0.02\%$) for the $\overline{C_s}$ measurement. This is calculated from

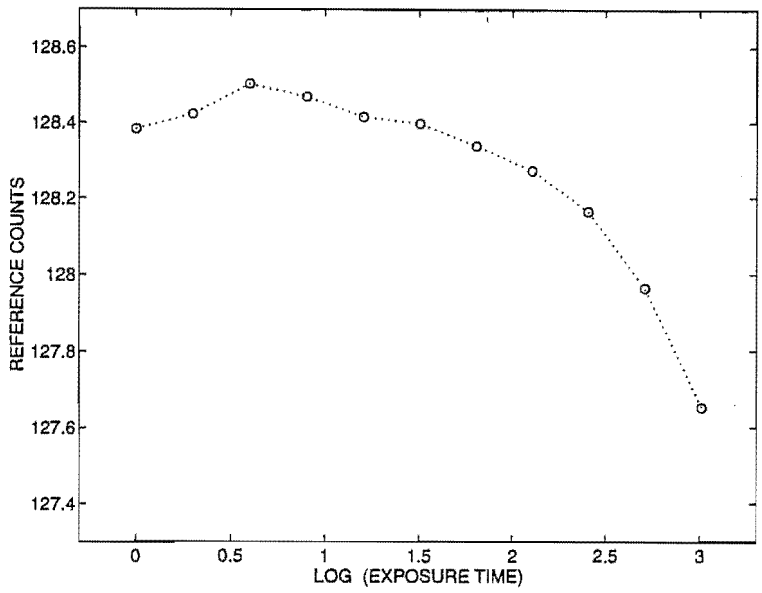

Figure B.1: Reference counts from 10 second exposures of the stable light source. The statistical uncertainty in each intensity is approximately the size of the plotted circles.

Table B.2: Exposure times and counts for the timed observations of the stable light source.

exposure time E (s)	log (E)	counts, C (ADU)	scaled counts C_s (ADU)	log (C_s)
1.015	0.0065	13.317	13.317	1.1244
		13.314	13.314	
2.015	0.3043	26.157	26.149	1.4176
		26.180	26.172	
4.015	0.6037	51.842	51.794	1.7143
		51.857	51.809	
8.015	0.9039	102.914	102.845	2.0122
		102.941	102.872	
16.015	1.2045	205.388	205.335	2.3124
		205.352	205.299	
32.015	1.5054	410.221	410.173	2.6130
		410.243	410.195	
64.015	1.8063	819.731	820.012	2.9139
		819.798	820.252	
128.015	2.1073	1638.630	1640.022	3.2148
256.015	2.4083	3275.940	3281.487	3.5162
		3275.804	3282.795	
512.015	2.7093	6549.314	6570.759	3.8177
		6546.342	6571.835	
1024.015	3.0103	13109.646	13184.719	4.1201
		13097.806	13186.137	

$1/\sqrt{S}$ where S is the signal determined as: $S = 10\,000$ (pixels) $\times$ 128 ADU $\times$ $16\,e^-$/ADU.

A further uncertainty is introduced by the non-reproducibility of the shutter speed. In the case of a 1 s exposure, a shutter speed variation of 5 ms would results in percentage errors in the exposure time of 0.5%. It was evident that the shorter exposures had a comparatively larger uncertainty than the longer exposures due to this variability in the shutter speed and therefore the shorter observations had a lower weight in the regression analysis. The uncertainty for each measurement was calculated using a 5 ms uncertainty in the shutter speed.

An additional uncertainty derives from the interpolation of the reference exposures for the scaling of the mean counts. This was the most difficult uncertainty to quantify. By using two different interpolation techniques and looking at the variations in the scaled counts, an estimate of the uncertainty produced by the interpolation method was able to be made. This resulted in uncertainties for the longer exposures (where the reference light source intensity was changing by the greatest amount) of 1×10^{-4} (or $\sim 0.01\%$) for the $\overline{C_s}$ measurement. The uncertainty contributions were added together and used as the weight for each measurement of the mean counts.

The straight line obtained from the weighted least-squares linear regression is plotted together with the experimental points on a graph of log(exposure time) versus $\log(\overline{C_s})$ in Fig. B.2. The slope of the straight line fit in this figure, together with the residuals of the data points from the fit, gives a good indication of the linearity of the response of the MJUO CCD system.

The (O–C) residuals from the best least-squares fit to the data is presented in Fig. B.3. A systematic trend is apparent, which seems to indicate a slight deviation from linearity. The maximum deviation from the straight line fit occurs for the shortest exposures which have the larger percentage uncertainties. This maximum deviation occurs for the 1 s exposure where the calculated residual of 0.01 represents a deviation from linearity of 0.9%.

In order to investigate this systematic trend in the residuals, a weighted least-squares linear regression was calculated for the same data set with the regression coefficient (the slope) set to exactly 1. The weighting of each data point was the same as for the previous analysis. The fit from the weighted least-squares linear regression to the experimental points is compared with the previous analysis in Fig. B.4. The residuals for both fits are similar. Since the residuals follow a trend

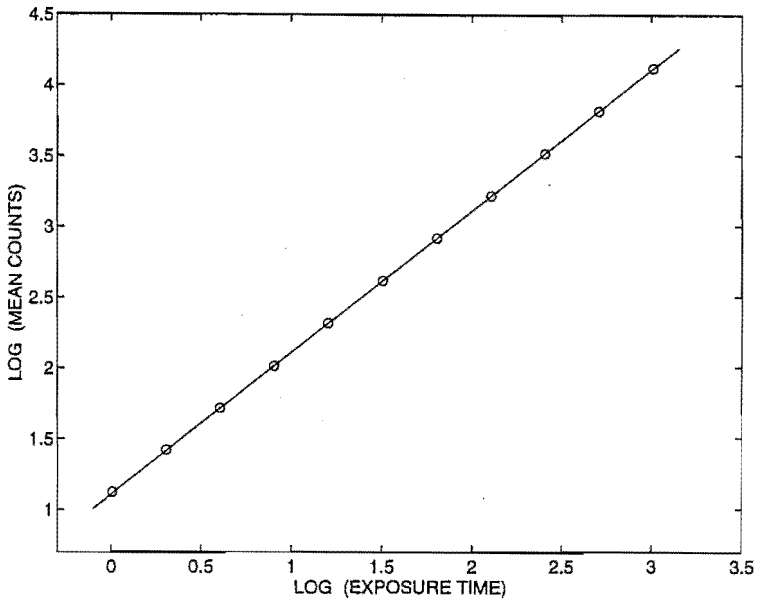

Figure B.2: The experimental data points are displayed together with the fit from the weighted least-squares linear regression to the data.

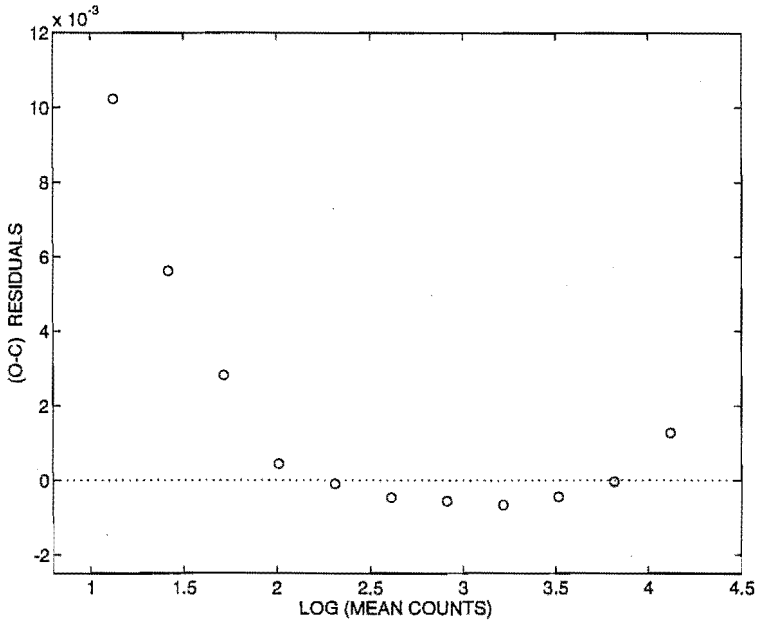

Figure B.3: The residuals from the weighted least-squares linear regression to the experimental points. The dotted line indicates no deviation from linearity.

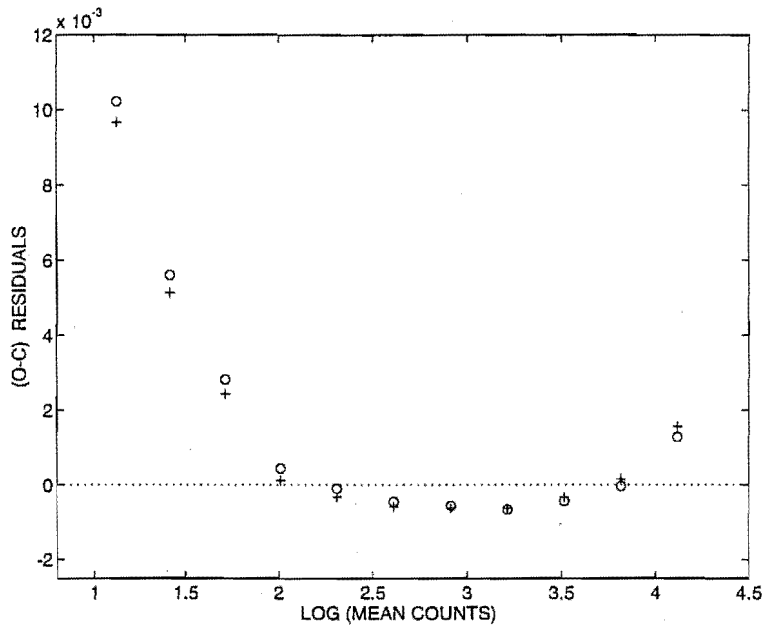

Figure B.4: The residuals from the weighted least-squares linear regression to the experimental points is compared with the previous analysis. Plus (+) symbols represent the residuals from fitting a straight line of unit slope to the data, while the circle (o) symbols are the residuals from the regression when both the slope and intercept are fitted.

Table B.3: Linear regression parameters.

Description of regression fit	Regression coefficient	Regression constant	Figure for residuals
fit slope and intercept	1.0003 ± 0.0001	1.1077 ± 0.0002	B.3
fit intercept only	1.0 (set)	1.108 ± 0.002	B.4

similar to that shown by the reference counts, it may be possible that there is some related uncertainty that has not been accounted for. For this reason, the experimental procedure would have been improved if the exposure times had not been taken in sequence, but in some random manner.

The values determined for the regression constant and regression coefficient from both weighted linear regressions are shown in Table B.3.

B.1.5 Conclusion

It was seen from Fig. B.1 that the reference light source was stable to about 1% for the duration of the experiment. The counts obtained for each timed set of exposures were scaled to take account of these fluctuations. Exposures less than one second were found to be overwhelmed by the effects of electrical pickup (seen as periodic 'waves' on the displayed image). From the shutter map, it was determined that the actual exposures were 15 ms longer than the requested exposure time, with an uncertainty of about 5 ms. This correction was applied to all the exposure times in the linearity test. It was evident that the shorter exposures had a comparatively larger uncertainty than the longer exposures due to the mechanical constraints on the repeatability of the shutter speed. The shorter observations therefore had a proportionally lower weight in the regression analysis.

The results of the weighted linear regression of the log(exposure time) versus $\log(\overline{C_s})$ data, shows that the MJUO CCD system is linear over the range of intensities 13 ADU to 13200 ADU to better than 0.9%. The largest variations (and uncertainties) occur at the lower signal levels. Over the intensity range from 30 ADU to 13200 ADU, the response of the system is linear to better than 0.4%.

B.2 Temperature dependence of CCD sensitivity

When a CCD chip is exposed to light, photons that penetrate the silicon substrate of the CCD produce electron-hole pairs. The covering electrodes of the CCD create potential wells. The electrons which do not combine with the lattice accumulate in these potential wells until they are read out. On average, red photons penetrate further into the silicon substrate than blue photons, since silicon becomes increasingly transparent at longer wavelengths. Thermal fluctuations in the silicon lattice can produce free electrons that are indistinguishable from electrons produced by photons. Cooling the CCD reduces the contribution of thermally-generated charge or 'dark current'. This cooling reduces sensitivity in the red because the gap between the valence and conduction bands in the silicon increases from 1.10 eV at 300 K to 1.15 eV at 100 K (MacFarlane et al. 1958) and also because the absorption of lower energy photons requires the presence of higher energy phonons in the silicon lattice. These are rarer at lower operating temperatures.

The aim of the procedure reported here was to investigate the sensitivity of the MJUO TH7882 CDA chip over a range of operating temperatures of the CCD and at four different wavelengths. In addition, the determination of the contribution of the dark current as function of operating temperature was used to choose the optimal operating temperature to use for CCD observations at Mt John. The experimental set-up was very similar to that used in the testing of the linearity of the CCD system. A sequence of 10 s exposures were taken of a stable light source as the CCD chip was cooled down from room temperature (~ 23°C) to its coolest setting (approximately −145°C). The stable light source was illuminated by LEDs at wavelengths of 830 nm, 655 nm, 555 nm and 480 nm to investigate the sensitivity of the CCD at a range of different operating temperatures and wavelengths.

B.2.1 Experimental procedure

CCD Temperature Control

The CCD temperature is regulated by a thermoelectric cooler. A small heater with a temperature sensor and feedback circuit maintains the CCD at a constant temperature above the uncontrolled temperature. If power is disconnected from

Table B.4: The colour, wavelength and brightness settings for the stable light source LEDs.

LED colour	Wavelength (nm)	LED brightness control setting coarse setting	fine (outer scale)
infrared	830	low	5.0
red	655	high	3.0
green	555	high	10.0
blue	480	high	10.0

the CE200 camera electronic unit, the CCD will cool to the minimum temperature allowed by the ambient temperature. The status of the CCD temperature regulation circuit is indicated by the 'heating' and 'cooling' LEDs on the back of the CE200 unit.

A temperature control dial and digital readout on the front of the CE200 unit allows the observer to adjust and optimize the CCD temperature. The temperature control dial has a range of 100°C and is nominally calibrated to cover a range from −50 to −150°C The dial is graduated from 0 to 1000 with 1000 representing approximately −150°C. Photometrics suggest a highest operating temperature of −90°C (so that the dark noise will not dominate the signal) and a lowest operating temperature of −130°C (due to the fact that long wavelength quantum efficiency and performance deteriorate with a decrease in temperature).

Stable light source and CCD camera

The experimental set-up was essentially the same as for the testing of the linearity of the CCD (see Section B.1).

The stabilized light source contained an arrangement of infrared, red, green and blue LEDs which were mounted in a circular pattern behind a depolished window in the top hat. There were six LEDs of each colour, except in the case of the blue LEDs, where only two were available. Only one set of LEDs could be selected at a time. The brightness of the set of LEDs was regulated by a coarse and fine adjustment and the setting for each arrangement of LED is given in Table B.4. The LEDs were turned on and left for several hours to stabilize before use. It was assumed that the LEDs had negligible drift over the duration of the experiment. This assumption is justified for the purposes of this experiment by examination of Fig. B.1 in Section B.1, where the light source is seen to be stable to about 1%.

B.2.2 Observations

Observations of the stable light source were made at differing temperatures of the CCD array, from ambient room temperature ($\sim 23°C$) down to about $-145°C$. The coldest setting for the temperature control was selected and liquid nitrogen was then introduced into the CCD dewar. A sequence of 10 s exposures of the stable light source were then taken as the CCD chip cooled down, at approximate intervals of 15°C. This was done at four different wavelengths to test the sensitivity of the CCD as a function of both temperature and wavelength.

An observation with an exposure time of 100 deciseconds is obtained by typing: `100 obs`. For temperatures hotter than $-90°C$, each set of timed observations of the stable light source by the CCD consisted of: a 10 second dark exposure, a 10 second observation of the stabilized light source and a second 10 second dark exposure.

Since the chip was cooling down throughout the experiment, this observing sequence enabled an interpolated dark exposure to be calculated from the darks taken before and after the observation of the light source. For temperatures cooler than $-90°C$, the rate of temperature decrease had slowed sufficiently for only one dark exposure to be required.

The dark frames contained the standard bias component (which should be approximately constant for a set value of `cgain`) as well as the dark signal. In this case, a `cgain` of 0 was used. The dark frames and observations were saved on DC2000 cassette tape for further analysis.

B.2.3 Image Analysis

The images were analysed using the PM3000 computer and video monitor. A reasonably constant-intensity region of the light source image was chosen for each set of LEDs. The FORTH commands `sb` and `pcur` enabled a 50×50 pixel box to be positioned at the selected region of the light source image. The `stats` command gave values of maximum, minimum, mean intensity and the rms of the intensity over the 2500 pixels enclosed by the box. Each temperature sequence was analysed in this manner, so that the mean counts of the chosen region could be determined as a function of the CCD chip operating temperature. This was done at the four wavelengths provided by the different coloured LEDs. The dark current was determined by analysing the same area on the dark images that were used in the analysis of the CCD response in the red.

Table B.5: The temperature dependence of the CCD dark current.

CCD temperature (°C)	Mean dark counts (per 10 seconds)
+23.5	34153
−0.2	1826
−15.1	619
−31.6	350
−46.8	317
−59.9	315
−75.0	315
−90.1	315
−105.3	315
−120.3	316
−135.1	316
−140.5	316
−145.0	317

B.2.4 Results and discussion

A graph of the mean counts obtained in the dark frames as a function of the CCD temperature is displayed in Fig. B.5. For temperatures hotter than −90°C, an interpolated dark exposure was calculated from the darks taken before and after each observation of the stable light source. The mean counts were then calculated from this interpolated image. For temperatures cooler than −90°C, the mean counts were calculated from the single dark exposure that was taken before each observation.

Table B.5 shows the operating temperature of the CCD and the corresponding mean dark counts. The mean counts show the average over 2500 pixels of a dark exposure of 10 s duration. To avoid saturation of the CCD system, the room temperature observation was a 2 s exposure, which was later scaled to a 10 s exposure. The observations of the stable light source were taken while the CCD chip was cooling down. The temperatures therefore are averages and are accurate to about 1°C. The mean counts shown for the dark current include the 'dark' or 'offset' signal of ~ 315 ADU. However, the offset signal varies with ambient temperature as shown by Gilmore & Tobin (1991) and includes ~ 10 ADU that come from the 70 ms illumination of the chip by the LED preflash ring.

It can be seen from Fig. B.5 that cooling the CCD dramatically reduces the dark current. Specifically, the dark current $I_{\rm dark}$ diminishes with the absolute operating temperature of the device T as

$$I_{\rm dark} = Ae^{-E_g/2kT}$$

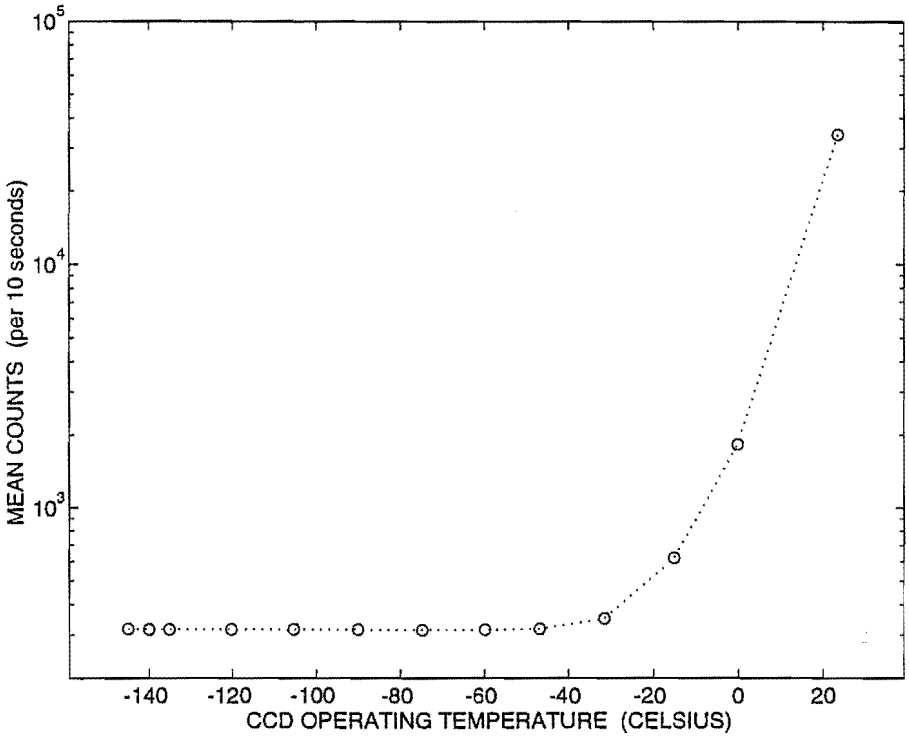

Figure B.5: The temperature dependence of the CCD dark current. The mean counts obtained from the 10 s dark frames are plotted against the corresponding CCD operating temperature.

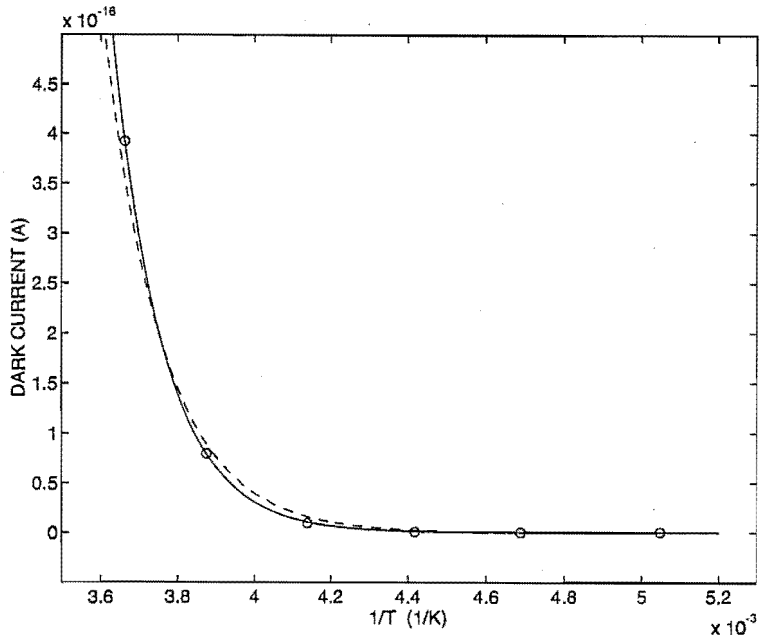

Figure B.6: The best least-squares fit of an exponential function to the dark current (solid line) gives a value for E_g of 1.31eV. The dotted line is the curve calculated for $E_g = 1.13\,\mathrm{eV}$.

where A is a dark rate constant, k is Boltzmann's constant and E_g is the silicon band gap in electron volts. In reality, the dark rate constant A is also slightly temperature dependent. The band gap is a function of absolute temperature, T, and can be calculated as

$$E_g(T) = 1.1557 - (7.021 \times 10^{-4}T^2)/(1108 + T).$$

As seen in Fig. B.5, the mean dark counts decrease to the offset value at approximately −55°C and merely fluctuate about this value for temperatures cooler than −55°C. A linear drift of the offset with temperature was assumed and this was modeled for temperatures cooler than −75°C. This offset was then subtracted from the mean dark counts. The mean dark counts were converted to the dark current in amps by using the value of the inverse gain ($16.2 \pm 0.6\,\mathrm{e^-}$/ADU at 0 `cgain`).

As the operating temperature of the CCD is lowered from 273 K to 128 K, the band gap is expected to increase from 1.12 eV to 1.15eV. An exponential function was fitted to the dark current versus inverse temperature graph and the best least-squares fit gave a value for E_g of 1.31eV. This value is about 14% different from

the expected value (see Fig. B.6). A 5% uncertainty could be expected from the ADU-to-electron conversion and further systematic uncertainties are introduced by ignoring the temperature dependence of the dark rate constant A. In addition, it is possible that cooling the CCD chip quickly is not a reliable technique for measuring the dark current. Residual dark current from operating the chip at the hotter temperatures may persist as the chip is cooled. This residual dark current will depend on the time constant of any surface traps in the Si–SiO_2 interface that have been occupied by thermally-generated electrons.

The 2 s exposure was not used in the above analysis since it was realised that the measured dark current was not just the charge generated during the timed exposure, but also included charge accumulated during the readout of the chip (which takes 4.9 seconds at a cgain of 0). The dark current measured for the 2 s exposure therefore cannot be multiplied by five to get a corresponding 10 s exposure time.

The mean intensity (or mean counts) represents the sensitivity of the CCD at a particular wavelength, assuming that the light source is constant. In the linearity test (see Section B.1), the light source was found to be stable to $\sim 1\%$.

The mean counts of the stable light source was determined as a function of the CCD chip operating temperature. This was done at the four wavelengths provided by the different coloured LEDs. Graphs of mean counts (as a measure of the chip sensitivity) versus CCD chip operating temperature are shown in Figs B.7 to B.10. It can be seen that the CCD chip sensitivity at 830 nm increases monotonically with increasing temperature. At 655 nm, a peak in sensitivity occurs at approximately –90°C. At 555 nm, there may be a peak in sensitivity at approximately –140°C with the sensitivity decreasing for higher chip operating temperatures. The sensitivity at 480 nm decreases monotonically with increasing temperature.

In order to compare the sensitivity of the CCD chip at different wavelengths, the counts at each wavelength were scaled to the counts obtained from the observations of the red LED counts at –145°C. Tables B.6 to B.9 show the operating temperature of the CCD chip, the mean counts obtained from the 10 s exposures and the scaled mean counts.

The variation in CCD sensitivity over the entire temperature range, from 23°C down to –145°C, can be described by a percentage defined by

$$\frac{(\text{maximum counts}) - (\text{minimum counts})}{\text{mean counts}} \times 100 \quad (\%).$$

Table B.6: The temperature dependance of CCD sensitivity in the infrared (830 nm)

Temperature (°C)	Mean counts (per 10 seconds)	Scaled mean counts (per 10 seconds)
+23.2	3640	8985
−0.9	3446	8505
−17.4	3361	8297
−32.3	3261	8048
−46.9	3155	7787
−61.6	3037	7496
−76.2	2978	7350
−90.1	2863	7066
−105.0	2731	6740
−121.9	2601	6420
−136.2	2472	6101
−140.8	2430	5997
−145.1	2386	5889

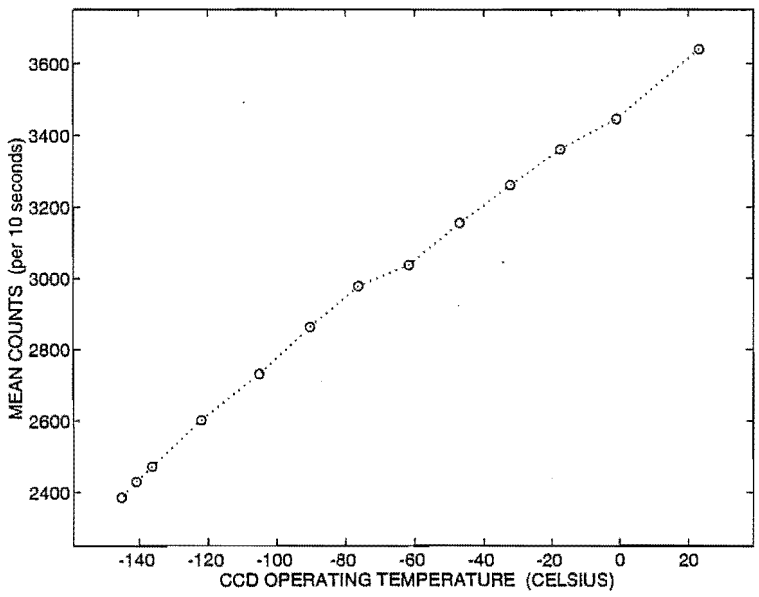

Figure B.7: The temperature dependence of the CCD sensitivity in the infrared (830 nm). The mean counts from Table B.6 are plotted for the corresponding CCD operating temperature.

Table B.7: The temperature dependance of CCD sensitivity in the red (655 nm)

Temperature (°C)	Mean counts (per 10 seconds)
+23.5	5705
−0.2	5864
−15.1	5865
−31.6	5948
−46.8	6018
−59.9	6059
−75.0	6076
−90.1	6086
−105.3	6044
−120.3	6013
−135.1	5950
−140.1	5921
−145.0	5889

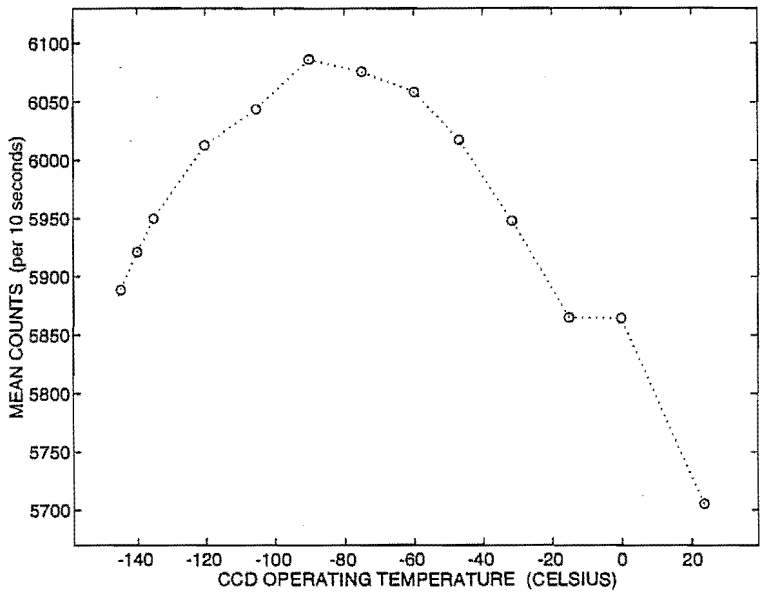

Figure B.8: The temperature dependence of the CCD sensitivity in the red (655 nm). The mean counts from Table B.7 are plotted for the corresponding CCD operating temperature.

Table B.8: The temperature dependance of CCD sensitivity in the green (555 nm)

Temperature (°C)	Mean counts (per 10 seconds)	Scaled mean counts (per 10 seconds)
+22.4	1514	4961
−1.6	1620	5019
−16.2	1693	5247
−30.7	1729	5358
−46.7	1767	5474
−61.8	1803	5589
−76.5	1820	5640
−90.4	1847	5724
−105.3	1874	5806
−120.3	1894	5868
−135.1	1903	5896
−140.0	1903	5897
−145.0	1900	5889

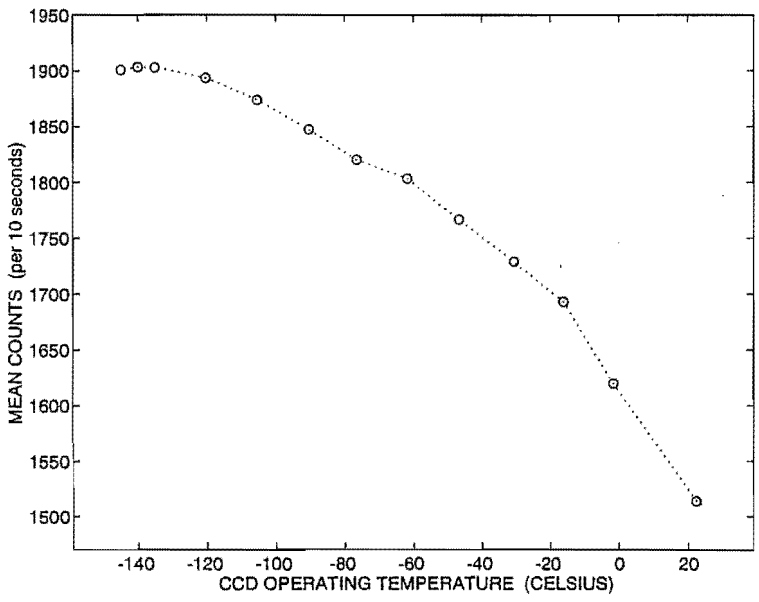

Figure B.9: The temperature dependence of the CCD chip sensitivity in the green (555 nm). The mean counts from Table B.8 are plotted for the corresponding CCD operating temperature.

Table B.9: The temperature dependance of CCD sensitivity in the blue (480 nm)

Temperature (°C)	Mean counts (per 10 seconds)	Scaled mean counts (per 10 seconds)
+23.8	302.6	3796
-2.7	326.3	4094
-17.0	386.6	4851
-32.3	404.0	5069
-47.5	418.3	5249
-61.5	429.0	5383
-76.2	434.9	5457
-90.4	444.6	5579
-105.3	454.6	5704
-120.2	462.6	5804
-135.1	467.5	5866
-140.0	468.8	5882
-144.8	469.3	5889

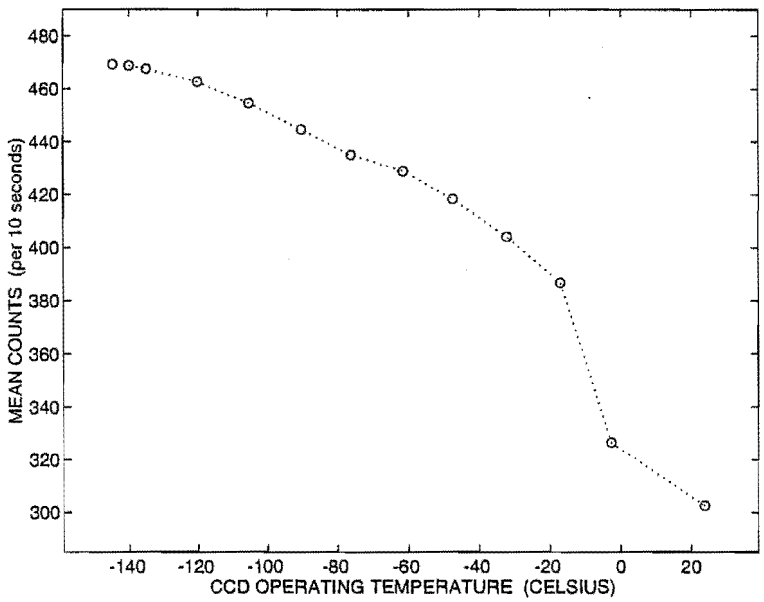

Figure B.10: The temperature dependence of the CCD chip sensitivity in the blue (480 nm). The mean counts from Table B.9 are plotted for the corresponding CCD operating temperature.

Table B.10: The percentage variation in CCD chip sensitivity over the entire temperature range, from 23°C down to −145°C.

LED	Wavelength (nm)	Variation in chip sensitivity	Temperature of max sensitivity (°C)
infrared	830	43%	>+23
red	655	6%	−90
green	555	22%	−105
blue	480	40%	<−145

The percentage variation in the sensitivity of the CCD over the range of operating temperatures is shown in Table B.10 for each wavelength tested. The relative variations in sensitivity at the four different wavelengths are shown in Fig. B.11. In this composite graph, the mean counts, scaled relative to the red LED counts at −145°C, are plotted against CCD operating temperature.

From the results for the dark current presented in Fig. B.5 and Table B.5, we can see that the CCD chip operating temperature should be cooler than about −55°C to avoid excessive dark current. Photometrics suggest −90°C as the highest operating temperature to use for this same reason. For exposures as long as an hour, chip operating temperatures should be as cool as possible to minimize this accumulated dark current. However, cooling the chip also decreases the quantum efficiency and charge transfer efficiency of the chip.

Limits on the coldest operating temperatures are imposed by the requirement that the CH210 should be able to maintain the operating temperature of the chip irrespective of orientation. Experiments showed that the coolest operating temperature that can be maintained is −110°C. Operating the cryostat at the lowest maintainable temperature has the advantage of minimizing the liquid nitrogen boil-off, because the thermostat circuit switches the chip heater on less often.

Fig. B.11 shows that the precise choice of chip operating temperature does not alter the sensitivity at different wavelengths significantly. Sensitivity in the infrared (830 nm) is most affected by the particular choice of cooler operating temperatures.

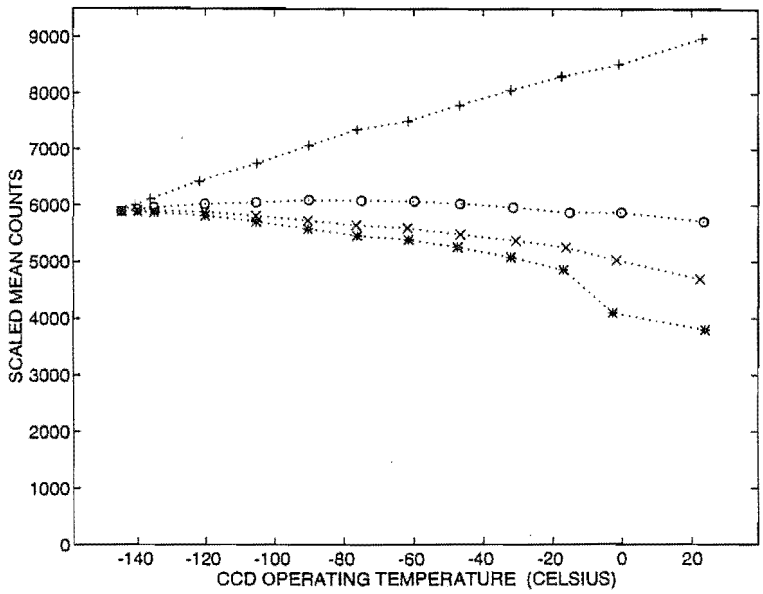

Figure B.11: The temperature dependence of the MJUO CCD chip sensitivity at four wavelengths: + = infrared (830 nm), o = red (655 nm), x = green (555 nm), and * = blue (480 nm). The mean counts are all scaled to the red counts at -145°C.

B.2.5 Conclusion

The optimum operating temperature is dependent on the wavelength region at which the observations are being made, since the CCD chip has different sensitivities at different wavelengths. The infrared sensitivity could be enhanced by operating the CCD at higher temperatures, although there would some trade-off with the higher dark current that would be generated. The length of a typical exposure should also be considered when selecting the chip operating temperature, since the exposure time determines the accumulated dark current. The dark current analysis of the 10 s exposures seems to indicate that −55°C would be the highest temperature the CCD could be used at.

An operating temperature lower than approximately −110°C is unsuitable since this temperature cannot be held constant when the telescope position is changed. Operating the cryostat at the lowest maintainable temperature has the advantage of minimizing the liquid nitrogen boil-off, and therefore increasing the 'hold-time' of the cryostat.

Based of the considerations presented above, a chip operating temperature

of between −110°C and −100°C would be suitable for the MJUO CCD system. At present, an operating temperature of −110°C is used. Since the Photometrics CH210 can maintain this operating temperature to a stability of 0.1–0.2°C there will be a maximum variation in chip sensitivity of 0.03–0.06%.

Appendix C

Reductions of CCD échelle spectra

As outlined in Chapter 6, this appendix presents the actual sequence of MIDAS commands and procedures used to perform the échelle reduction. This is basically a practical user's guide to the reduction of échelle spectra from MJUO using the MIDAS software package. Also included in this appendix are a summary of the adopted échelle parameters for reducing the MJUO échelle spectra.

C.1 The Munich Image Data Analysis System

The European Southern Observatory – Munich Image Data Analysis System (ESO–MIDAS or simply MIDAS) consists of a set of general tools for image processing and data reduction. Specialized reduction routines are included for ESO instruments at La Silla.

The versatility of the MIDAS system arises from the use of table structures and also device independent interfaces for plotting and image display. These features enable a large data base to be easily maintained, manipulated and displayed.

MIDAS makes use of a number of data structures:

- *Images* are arrays of numbers representing data values of the same physical significance in one to three dimensions. The data must be sampled with constant stepsize along all axes.

- *Tables* are a structure for handling data which can be arranged in two

dimensional arrays of columns and rows. Many commands take their input from¿ or output their results to tables.

- *Fit-files* are used to store the functions and parameter values needed for fitting functions to data values.
- *Descriptors* are variables associated with frames, tables or fit-files describing the contents and structure of them. They are similar to FITS keywords in a FITS file header.
- *Catalogs* contain lists of images, tables or fit-files for the purpose of grouping data together within MIDAS. They can be used for input to various commands or merely for reference.
- *Keywords* are global variables in the MIDAS environment that are used to pass information from one MIDAS program to the next or to store intermediate results temporarily.

C.2 Sequence of MIDAS commands

The sequence of commands and a brief description each one are given in this section. Parameters are included where required. Note that a '?' in place of a parameter when using MIDAS indicates that the default value should be used. Reduction of the MJUO échelle spectra requires a colour display terminal for image analysis.

`set default uoc$scratch:[scratch.phys159.s136]`
: change the default directory to the one you wish to work in.

`inmidas`
: starts the midas session

`create/display 0 576,384,0,0`
: creates an image display window 576 pixels wide by 384 pixels tall (the size of the MJUO CCD chip) at position 0,0 on the screen.

`create/graphics`
: creates a graphics window of default size.

`set/context echelle`
: loads in the échelle context commands and initializes the échelle parameters.

`init/echelle s135`
: reads in the default échelle parameters from the session saved as 's135'.

`intape/fits 1-30 s136_ s136_`

reads in the fits files 's136_0001.mt' to 's136_0030.mt' and writes as MIDAS image files 's136_0001.bdf' to 's136_0030.bdf'.

`create/icat s136 *.bdf`

creates an image catalogue called 's136.cat' containing the names of all .bdf (image) files in the current subdirectory.

`rotate/echelle s136 s136 ROTATE`

rotates all the images in the catalogue s136.cat so they are in the standard orientation for reduction. The file s136_0001.bdf is rotated and called s1360001.bdf, for example.

`define/echelle s1360001 18,80,5 STD 1,2`

locates and tracks the échelle orders on the object image s1360001. The width of the order is 18 pixels at the threshold value of 80 counts and 5 is the slope parameter. The standard (STD) algorithm is used and a bivariate polynomial of degree 1 (along the order) and order 2 (perpendicular to the order) is used as the fit to the échelle orders.

`@@ select s1360001`

makes a cut through the center of the image s1360001 (usually the `OBJ` frame) and plots this cross-section on the graphics screen. The extraction slit width and the offset of the orders from the fitted échelle orders can be determined. The procedure file 'select.prg' is not a MIDAS file but was written specifically for the MJUO échelle reductions.

`set/echelle slit=18 offset=0`

this sets the echelle parameter 'slit' to a value of 18 and the parameter 'offset' to 0. When the orders are extracted, 18 pixels will be extracted at an offset of 0 pixels from the fit done in the previous step (`define/echelle`).

`show/echelle`

shows all the échelle parameters and their current value.

`extract/echelle s1360002 arc 18,0`

extracts the échelle orders for the `WLC` frame 's1360002.bdf' and call the frame containing the one-dimensional orders 'arc.bdf'. The extraction slit and offset are the same for the `WLC` frame as for the `OBJ` frame.

`search/echelle arc 5,500`

this searches the one-dimensional orders in the 'arc.bdf' frame to detect any arc lines above the threshold of 500 counts.

EITHER

`ident/echelle s1360002 thar ? ? ? angle`

In the 'angle' method of wavelength calibration, the user interactively indicates at least four arc lines on the 2-D `WLC` image and then is prompted for the order number of the first line and wavelengths for all the lines. The table file 'thar.tbl' is the line list of thorium-argon arc line wavelengths. The default values are taken for the degree of the polynomial, the maximum rms error of the global échelle relation and the maximum error of further arc line identifications.

OR

`ident/echelle s1360002 thar ? ? ? guess s135`

If the 'guess' method is used, the arc solution from the previously saved session 's135' is used as an initial starting point for the arc line identifications. This method is not interactive.

`set/echelle medfilt=1,1,10 bkgmtd=POLY bkgpoly=0,0`

this sets the filtering parameters for the median filter that is applied to the frame to be filtered. This enables the background to be estimated correctly. The background modelling method is a polynomial fit and the order of fit of the bivariate polynomial is set to 0,0. Other methods may be used and these have different parameters.

`set/echelle crfilt=15,41,3`

this sets some parameters for cosmic ray filtering. A box of 15 pixels (along the order) and 41 pixels (perpendicular to the order) is used for the filtering. The number of iterations for the filtering is set to 3.

`set/echelle ccdfilt=7.1,4.3,7`

this sets the filtering parameters for the cosmic ray filtering. These parameters are the read-out noise (in e^-), the inverse gain (in e^-/ADU) appropriate to the value of `cgain` used, and the number of standard deviations for removal of cosmic rays. This last parameter needs to be optimized for different frames.

`@s echkaren s1360001 s1360001f`

performs the cosmic ray filtering on the `OBJ` image 's1360001.bdf' and calls the filtered image 's1360001f.bdf'. The échelle parameters for the filtering should have been updated previously.

`set/echelle sample=0.05`

this sets the stepsize (in Å) for rebinning the reduced échelle orders into wavelength space.

IF NO FLAT FIELDING IS REQUIRED:

`set/echelle ffopt=NO respopt=NO`

the optional flat-field and response correction options will not be done.

`reduce/echelle s1360001f f01`

this reduces the cosmic ray filtered object frame 's1360001f' to individual, one-dimensional, wavelength-calibrated échelle orders. These are designated 'f010001.bdf','f010002.bdf', 'f010003.bdf' and 'f010004.bdf' for the first to the fourth orders respectively.

IF FLAT FIELDING IS REQUIRED:

`set/echelle ffopt=YES correct=FLAT03`

the optional flat-field correction options will be done.

`compute/image FLAT03 = s1360003/10000`

the FLAT frame is normalized by dividing through by a representative value of the signal in the orders.

`reduce/echelle s1360001f g01`

this time the object is reduced with the flat-field option activated.

`save/echelle s136`

this saves all the échelle parameters that have been defined in this session so that these can be used in the future reductions. The table files s136back.tbl, s136line.prg and s136orde.tbl are created. These table store the positions on the chip to use for background-determination, the arc line identifications and dispersion coefficients of the wavelength calibration, and the bivariate polynomial fit to the échelle orders together with the current échelle parameters.

C.3 Echelle parameters

The current échelle parameters are shown by the command `show/echelle`. When the échelle context is first started up, the échelle parameter values are set to the system defaults. Parameters can be changed to the required values using the command: `set/echelle parameter=value`. A typical reduction session involving CCD èchelle spectra from MJUO should have the values for the échelle parameters similar to those given below.

```
**********  Echelle Parameters  ******************
```